

**HEMILABILE LIGANDS SUPPORTING CATIONIC INDIUM COMPLEXES: TUNING
REACTIVITY IN CATALYSIS**

by

Chatura Goonesinghe

B.Sc., The University of Colombo, 2016

A THESIS SUBMITTED IN PARTIAL FULFILLMENT OF
THE REQUIREMENTS FOR THE DEGREE OF

DOCTOR OF PHILOSOPHY

in

THE FACULTY OF GRADUATE AND POSTDOCTORAL STUDIES
(Chemistry)

THE UNIVERSITY OF BRITISH COLUMBIA
(Vancouver)

August 2023

© Chatura Goonesinghe, 2023

The following individuals certify that they have read, and recommend to the Faculty of Graduate and Postdoctoral Studies for acceptance, the dissertation entitled:

Hemilabile ligands supporting cationic indium complexes: tuning reactivity in catalysis

submitted by Chatura Goonesinghe in partial fulfilment of the requirements for

the degree of Doctor of Philosophy

in Chemistry

Examining Committee:

Parisa Mehrkhodavandi, Professor, Chemistry, UBC

Supervisor

Laurel Schafer, Professor, Chemistry, UBC

Supervisory Committee Member

Michael Wolf, Professor, Chemistry, UBC

University Examiner

Zachary Hudson, Associate Professor, Chemistry, UBC

University Examiner

Additional Supervisory Committee Members:

Keng Chang Chou, Professor, Chemistry, UBC

Supervisory Committee Member

Abstract

Over the years, numerous neutral indium catalysts have been studied for polymerization reactions. However, recent research conducted by Mehrkhodavandi and co-workers has shed light on the potential of cationic indium species in catalytic applications.

In a comprehensive study, the impact of carefully designed hemilabile ligands on the stability, reactivity, and catalytic behavior of indium complexes is explored. Specifically, a family of cationic alkyl indium complexes supported by hemi-salen type ligands with hemilabile heterocyclic pendant donor arms are investigated. The stability and stable lifespan of these complexes directly correlate with the affinity of the pendant donor group to the indium center. The reactivity of the complexes exhibits the opposite trend in the cationic ring-opening polymerization of epoxides. Notably, the most stable complex, bearing a pyridyl donor arm, displays the remarkable ability to polymerize racemic lactide without an external initiator.

The same air-stable cationic alkyl indium complex with the pyridyl pendant arm is employed to selectively produce high-molecular-weight cyclic poly(lactide) (c-PLA). This complex enables the reproducible synthesis of c-PLA with low dispersity ($\bar{M}_w/\bar{M}_n \sim 1.30$) and molecular weights reaching up to $416,000 \text{ g mol}^{-1}$. Importantly, the complex remains active even after prolonged exposure to high-humidity air. Furthermore, it could form high-molecular-weight c-PLLA, c-PDLA, and their stereocomplex without inducing epimerization. The polymerization occurs through a cooperative Lewis-pair-based coordination–insertion mechanism, involving the coordination of monomers to the cationic indium center and the ring-opening of lactide facilitated by the pyridine donor group.

Finally, these complexes are used to delve into the mechanism of the selective synthesis of spiro-orthoesters, a unique pre-sequenced monomer capable of producing perfectly alternating

poly(ether-*alt*-ester). Structure function investigations and computational studies were conducted to elucidate the reaction mechanism. These findings reveal that this reaction follows Michaelis-Menten type saturation kinetics, which can be attributed to the low Lewis acidity of the indium catalysts, providing a basis for their exceptional selectivity.

Lay Summary

Researchers have long been investigating the use of neutral indium-based catalysts, but recent work by the Mehrkhodavandi lab has shed light on the potential of cationic indium species in catalytic applications. This PhD work explores the impact of specifically designed ligands on the stability, reactivity, and behavior of indium catalysts, offering valuable insights into the workings of indium in catalysis. One exciting application of these catalysts was their use to selectively produce large cyclic poly(lactide), a bio-degradable polymer. This addressed a significant challenge in the field and opened doors for further advancements in the synthesis of such polymers. Additionally, these indium complexes proved instrumental in studying the mechanism of a novel reaction, providing valuable information for the improved design of catalysts in the future.

Preface

The thesis introduction in Chapter 1 is partially based on an invited review article in preparation. The sections presented in this thesis were written by myself, while other sections in the manuscript were written by Joseph Chang, a master's student and Kimia Hosseini, a former undergraduate student, and Takeo Iwase, a PhD student. The manuscript was edited by Prof. Parisa Mehrkhodavandi.

1. **Goonesinghe, C.;** Chang, J.; Hosseini, K.; Iwase, T.; Mehrkhodavandi, P. Indium (III) in catalysis. (*Manuscript in preparation*)

Chapter 2 is based on the manuscript published in the journal *Chemical Science*. The manuscript was written by myself and edited by Prof. Parisa Mehrkhodavandi. Hootan Roshandel, a former undergraduate student, fully characterized complexes **47c** and **48c** and conducted reactivity studies with CHO for those complexes. Former doctoral students Dr. Hyuk-Joon Jung and Dr. Carlos Diaz assisted in initial complex synthesis and *in situ* NMR studies respectively. Crystollographical characterization was done by the PhD student, Kudzanai Nyamayaro. Dr. Maria Ezhova assisted with additional NMR characterization of complex behavior.

2. **Goonesinghe, C.;** Roshandel, H.; Diaz, C.; Jung, H. J.; Nyamayaro, K.; Ezhova, M.; Mehrkhodavandi, P. Cationic Indium Catalysts for Ring Opening Polymerization: Tuning Reactivity with Hemilabile Ligands. *Chem. Sci.* **2020**, *11* (25), 6485–6491.

The work presented in Chapter 3 has been published in the journal *ACS Catalysis*. This work was done in collaboration with former PhD student Dr. Hyuk-Joon Jung, who conducted

initial reactivity studies for c-PLA formation using **48c**. Former PhD student Dr. Hassan Baalbaki assisted with kinetic studies while the former undergraduate student Kimia Hosseini assisted with large scale synthesis of ligand **Lc**. The final manuscript was written by myself and edited by Prof. Parisa Mehrkhodavandi.

3. **Goonessinghe, C.[‡]**; Jung, H-J.[‡]; Roshandel, H.; Diaz, C.; Baalbaki, H. A.; Nyamayaro, K.; Ezhova, M.; Hosseini, K.; Mehrkhodavandi, P. An Air Stable Cationic Indium Catalyst for Formation of High-Molecular-Weight Cyclic Poly(Lactic Acid). *ACS Catal.* **2022**, *12*, 7677–7686. (*These authors contributed equally)

Work presented in Chapter 4 was done in collaboration with former undergraduate mentee Kimia Hosseini, who synthesized complexes **48e-h** and conducted kinetic studies. Prof. Paula Diaconescu and Hootan Roshandel from UCLA conducted computational studies. Crystal structures were collected and solved by Kudzanai Nyamayaro. This work is soon to be submitted for publication in the journal *ACS Catalysis*.

4. Hosseini, K.[‡]; **Goonessinghe, C.[‡]**; Roshandel, H.; Chang, J.; Nyamayaro, K.; Jung, H-J.; Diaconescu, P. L.; Mehrkhodavandi, P. Mechanistic insights into the selective indium catalyzed formation of spiro-orthoesters. *ACS Catal.* **2023** (*These authors contributed equally) (*Manuscript accepted, Manuscript ID cs-2023-03450h*)

Table of Contents

Abstract.....	iii
Lay Summary	v
Preface.....	vi
Table of Contents	viii
List of Tables	xii
List of Figures.....	xiii
List of Abbreviations and symbols	xxii
Acknowledgements	xxviii
Dedication	xxx
Chapter 1: Introduction	1
1.1 Indium(III) in catalysis	1
1.2 Polymerization reactions.....	5
1.2.1 Mechanisms of indium catalyzed ring-opening polymerizations	8
1.2.2 Polymerization reactions by neutral indium catalysts	11
1.2.2.1 Indium catalysts with monodentate ligands.....	11
1.2.2.2 Indium catalysts with bidentate ligands.....	13
1.2.2.3 Indium catalysts with tridentate ligands	19
1.2.2.4 Indium catalysts with tetradentate ligands	26
1.2.3 Polymerization reactions by cationic indium catalysts.....	43
1.3 Scope of the thesis	48

Chapter 2: Tuning the stability and reactivity of cationic alkylindium complexes using hemilabile ligands.....	50
2.1 Introduction.....	50
2.2 Results and discussion	55
2.2.1 Synthesis and characterization of proligands L_{a-d}	55
2.2.2 Synthesis and characterization of neutral alkylindium complexes 47a-d	56
2.2.2.1 Solution state behavior of 1a-d	58
2.2.3 Synthesis and characterization of cationic alkyl indium complexes 48a-d	58
2.2.3.1 Analysis of ¹ H NMR spectra of 48a-d	60
2.2.3.2 Analysis of NOESY NMR spectra of 48a-c	61
2.2.4 Hemilabile behavior of complexes	62
2.2.4.1 Temperature dependent hemilabile behavior of 48a-c	62
2.2.4.2 External donor effect on the hemilabile behavior of 48b	65
2.2.5 Reactivity Studies	68
2.2.5.1 Polymerization of epichlorohydrin	69
2.2.5.1.1 Reaction progression monitoring	70
2.2.5.2 Polymerization of cyclohexene oxide	71
2.2.5.3 Polymerization of ε-caprolactone	72
2.2.5.4 Polymerization of racemic-lactide	73
2.2.6 Mechanistic considerations	74
2.3 Conclusions.....	75
2.4 Experimental	76

Chapter 3: Synthesis of high molecular weight cyclic poly(lactic acid) using an air stable cationic indium catalyst.....	87
3.1 Introduction.....	87
3.2 Results and discussion	91
3.2.1 Generation and characterization of cyclic PLA	91
3.2.2 Catalytic behaviour of 48c	94
3.2.3 Mechanistic discussion	96
3.2.4 Kinetics of c-PLA formation	101
3.2.5 Exploration of polymer tacticity	104
3.3 Conclusions.....	106
3.4 Experimental	107
Chapter 4: Hemilability as a tool: exploring the mechanism of indium catalyzed coupling of epoxides and lactones.....	112
4.1 Introduction.....	112
4.2 Results and discussion	114
4.2.1 Synthesis of compounds	115
4.2.2 Evaluation of catalytic competency	117
4.2.2.1 Role of the alkyl ligands in determining reactivity.....	117
4.2.2.2 Role of the α -substituent on the hemilabile pendant arm in reactivity	118
4.2.3 Kinetics of spiro-orthoester formation.....	119
4.2.3.1 Michaelis-Menten kinetic analysis	120
4.2.4 Nature of the active catalyst.....	121
4.2.4.1 Temperature dependent behavior of catalysts.....	121

4.2.4.2	Substrate coordination	123
4.2.5	Proposed mechanism for spiro-orthoester formation.....	127
4.2.5.1	Computational studies.....	128
4.3	Conclusion	130
4.4	Experimental	131
Chapter 5: Conclusions and future directions		142
5.1	Conclusion	142
5.2	Future directions for cationic group 13 catalysts	144
Bibliography		149
Appendices.....		178
Appendix A - Data associated with Chapter 2.....		178
Appendix B - Data associated with Chapter 3.....		239
Appendix C - Data associated with Chapter 4.....		257

List of Tables

Table 2.1. Summary of cationic complex synthesis, storage, and longevity.	60
Table 2.2. Polymerization of epichlorohydrin with cationic alkylindium complexes.	69
Table 2.3. Polymerization of cyclohexene oxide with cationic alkylindium complexes.	72
Table 2.4. Polymerization of ϵ -CL with cationic alkylindium complexes.	73
Table 2.5. Polymerization of <i>rac</i> -LA with cationic alkylindium complexes.	74
Table 3.1. Formation of c-PLA by ring opening polymerization of <i>rac</i> -LA using complex 48c . 91	
Table 3.2. Formation of c-PLA using 48c by consecutive addition of <i>rac</i> -LA	95
Table 3.3. Reported T_m values of cyclic and linear PLLA,PDLA and stereocomplexes of cyclic and linear-PLLA/PDLA.....	105
Table 4.1 Synthesis of SOE from ϵ -caprolactone (ϵ -CL) and 1,2-epoxy-7-octene (EOE) using various cationic indium complexes.....	117

List of Figures

Figure 1.1. Reaction of a Lewis acid and a Lewis base to form a Lewis adduct.....	2
Figure 1.2. Different modes of substrate activation by indium (III) catalysts.....	3
Figure 1.3. General reaction types catalyzed by In(III) species.	4
Figure 1.4. a) Chain growth polymerization and b) step-growth polymerization.	5
Figure 1.5. Microstructures of poly(lactic acid) (PLA) depict polymer tacticity.	7
Figure 1.6 a) The coordination-insertion mechanism and b) the activated monomer mechanism of lactide polymerization.....	9
Figure 1.7. Intermolecular and intramolecular transesterification reactions.	10
Figure 1.8. a) Living polymerization and b) immortal/ chain-transfer polymerization.....	11
Figure 1.9. The proposed structure of the InCl ₃ /BnOH catalyst 1 reported by Tolman <i>et al.</i>	12
Figure 1.10. a) Polymerization of styrenics with InCl ₃ or InBr ₃ and b) Proposed mechanism for the In(III) catalyzed formation of polyolefins.	13
Figure 1.11. Indium Amino pyrrolate complexes (2-4) reported by Huang <i>et al.</i>	14
Figure 1.12. Indium alkoxide complexes (5-7) reported by Arnold and Okuda.....	14
Figure 1.13. Stereoselective polymerization of <i>rac</i> -LA by the dinuclear alkoxide complexe (8) reported by Horeglad <i>et al.</i>	15
Figure 1.14. Indium thiolate complexes (9 and 10) reported by Briand <i>et al.</i>	16
Figure 1.15. Alkylindium iminophenolate complexes (12a-f) reported by Carpentier <i>et al.</i>	17
Figure 1.16. Bimetallic indium iminophenolate complex (13) reported by Carpentier <i>et al.</i>	18
Figure 1.17. Indium bis(iminophenolate) complexes (14a-d) reported by Chakraborty <i>et al.</i>	19
Figure 1.18. Dinuclear indium diamino phenolate complexes (15a-f) reported by Mehrkhodavandi <i>et al.</i>	19

Figure 1.19. Block copolymerization reaction catalyzed by 15a and 15b	20
Figure 1.20. a) The dinuclear mechanism for LA polymerization and the b) mononuclear mechanism for BBL polymerization.....	21
Figure 1.21. Indium diamino phenolate complexes with aryloxy initiators (15g-k) reported by Mehrkhodavandi <i>et al.</i>	22
Figure 1.22. Indium diamino phenolate complexes with various <i>ortho</i> -phenol substituents (15l-n) reported by Mehrkhodavandi <i>et al.</i>	23
Figure 1.23. Indium diamino phenolate complex with an achiral backbone (16) reported by Mehrkhodavandi <i>et al.</i>	23
Figure 1.24. Indium bis(diaminophenolate) complex (17) reported by Mehrkhodavandi <i>et al.</i> ..	24
Figure 1.25. Block copolymerization of <i>rac</i> -LA and ϵ -CL by the (aminoethyl)iminophenolate (18a,b) and phosphininiminophenolate (18c) complexes reported by Mehrkhodavandi <i>et al.</i>	25
Figure 1.26. a) ROCOP of CO ₂ and CHO to form polycarbonate and possible side products, b) bimetallic (19a) and monometallic (19b) indium iminophenolate complexes reported by Mehrkhodavandi <i>et al.</i> , and c) the proposed intramolecular initiation mechanism.....	26
Figure 1.27. Indium (1,2)-diphenylethylene-salen complexes (20a-c) reported by Carpentier <i>et al.</i>	27
Figure 1.28. Dinuclear indium salen complexes (21a-e) reported by Mehrkhodavandi <i>et al.</i>	28
Figure 1.29. Mononuclear indium salen complexes (22a-c) reported by Mehrkhodavandi <i>et al.</i>	29
Figure 1.30. Dinuclear SalBinam complexes (23a and 23b) reported by Mehrkhodavandi <i>et al.</i>	30
Figure 1.31. Indium dialkoxy diimino complexes (24a and 24b) reported by Carpentier <i>et al.</i> ..	31
Figure 1.32. Indium SalBinam dialkoxy diimino complex (26) reported by Carpentier <i>et al.</i>	31

Figure 1.33. Ferrocene backboned indium salen complex (27) reported by Diaconescu and Quan and its monomer scope.....	32
Figure 1.34 Redox active indium ferrocene phosphasalen complexes (28a and 28b) reported by Diaconescu <i>et al.</i>	33
Figure 1.35. Indium phosphasalen complexes (29a-f) for <i>rac</i> -LA polymerization reported by Williams <i>et al.</i>	34
Figure 1.36. Indium phosphasalen complexes (29b-29g-l) ROCOP of CO ₂ and CHO reported by Williams <i>et al.</i>	35
Figure 1.37. Proposed mechanism for the ROCOP of CO ₂ and CHO by indium phosphasalen complexes.	36
Figure 1.38. Indium salen complex with a phosphine pendant arm (30) reported by Mehrkhodavandi <i>et al.</i>	37
Figure 1.39. Proposed mechanism for the ROCOP of CO ₂ and CHO by 30	38
Figure 1.40. Air and moisture stable dinuclear indium salan complexes (31a and 31b) reported by Mehrkhodavandi <i>et al.</i>	39
Figure 1.41. Indium salan complexes (32a and 32b) reported by Buchard and Jones.	40
Figure 1.42. Indium (OSSO)-salan complexes (33a-c) reported by Okuda <i>et al.</i>	41
Figure 1.43. Indium tertiary amine phenolate complex (34) reported by Sun <i>et al.</i>	42
Figure 1.44. Various indium complexes (35a-d,36,37 , and 38) reported Mountford <i>et al.</i>	43
Figure 1.45. Proposed mechanisms for the temperature triggered formation (a) and polymerization (b) of SOEs using 39	45
Figure 1.46. Cationic indium salen complexes (40a-g) reported by Mehrkhodavandi <i>et al.</i>	46

Figure 1.47. Polymerization reactions promoted by 40c and 40g . a) Polymerization of epoxides, b) statistical copolymerization of epoxides and cyclic ethers and, c) block copolymerization of epoxides and <i>rac</i> -LA.....	47
Figure 1.48. Proposed mechanism for the a) cationic polymerization of cyclic ethers and the b) block copolymerization of epoxides and <i>rac</i> -LA.	48
Figure 2.1. Behavior of a metal complex [(XL)M], bearing a hemilabile ligand in the presence of a coordinating ligand, Y.....	50
Figure 2.2. Previously reported aluminum and indium complexes bearing hemilabile ligands (41-46) and cationic indium complexes reported by the Mehrkhodavandi group (39,40b, 40d and 40f).....	51
Figure 2.3. (a) Decomposition of a metal complex by de-coordination of labile ligand. (b) Stabilization of metal complex by reversible de-coordination and re-coordination of a hemilabile ligand.....	52
Figure 2.4. Controlling reactivity at metal center using a hemilabile ligand by (a) stabilizing transition states and (b) regulating access to coordination sites at the reactive center.	53
Figure 2.5. (a) Substrate activation by the metal center for reaction with a proximal donor ligand. (b) Enhancing the ability of leaving groups to dissociate by hemilabile donors.	54
Figure 2.6. Synthesis of proligands L_{a-d}	56
Figure 2.7. Synthesis of neutral dialkylindium complexes 47a-d	57
Figure 2.8. Complexes 47c and 47d are isostructural and have similar distance between the indium center and the donor group.	57
Figure 2.9. ³¹ P{ ¹ H} NMR spectra of OPET ₃ with 47a-d show a similar acceptor ability. ³¹ P{ ¹ H} NMR (160 MHz, C ₆ H ₆ , 25 °C) chemical shift of free OPET ₃ appears at 45 ppm.....	58

Figure 2.10. Synthesis of cationic alkyl indium complexes 48a-d	59
Figure 2.11. (a) Methylene protons (H [★]) are an AB pair in 47a and 47b .(b) In 48a and 48b they act like an AX pair. (¹ H NMR at 300 MHz in CDCl ₃ at 25 °C)	60
Figure 2.12. Most apparent through-space NOE interactions observed between heterocyclic protons and isobutyl ligand for 48a-c (NOESY NMR spectra 400 MHz, CDCl ₃ , 25 °C).	62
Figure 2.13. VT NMR spectra of 48a show the irreversible decomposition of isolated complex when the temperature is increased from 25-105 °C (¹ H NMR at 400 MHz in C ₆ D ₅ Br).	63
Figure 2.14. (a-d) Spectra showing downfield migration of the α proton of the furfuryl group in 48b (★) at 25-125 °C. (e) ¹ H NMR spectrum of the free ligand (Lb) at 125 °C (¹ H NMR at 400 MHz in C ₆ D ₅ Br).....	64
Figure 2.15. Significant change is not observed in the VT NMR spectra of 48c temperature is increased from 25-130 °C (¹ H NMR at 400 MHz in C ₆ D ₅ Br).....	64
Figure 2.16. Downfield shift of the furfuryl α proton signal of 48b (★) in the presence of (b) THF, (c) pyridine, (d) triethylphosphine oxide and (e) epichlorohydrin (¹ H NMR at 400 MHz in C ₆ D ₆ at 25 °C).....	65
Figure 2.17. Molecular structures of complex 48b.2THF (depicted with thermal ellipsoids at 50% probability and H atoms, minor disorders as well as solvent molecules and counter anion omitted for clarity).	67
Figure 2.18. DOSY NMR spectrum of 48b with excess THF in C ₆ D ₆ , shows the independent diffusion of THF and the complex. (¹ H NMR, diffusion time (Δ) = 0.85 s, gradient length (δ) = 400 μs, 400 MHz, C ₆ D ₆ , 25 °C).....	68
Figure 2.19. Percentage monomer conversion vs. time plots (average of a minimum of two trials) for ECH with 48a and 48b at (a) 10 °C (b) 25 °C (c) 35 °C and (d) 60 °C.....	71

Figure 2.20. Proposed behavior of cationic complexes with (a) increasing temperature, (b) in the presence of a low concentration of epoxide and (c) at high concentration of epoxide resulting in cationic polymerization.....	74
Figure 3.1. Catalysts capable of producing cyclic poly(lactide).....	88
Figure 3.2. Representative mechanisms of the three major groups of catalysts.	89
Figure 3.3. (a) Magnified MALDI-TOF spectrum of c-PLA (Table 3.1, entry 1). (b) Mark-Houwink plots for high molecular weight c-PLA (Table 3.1, entry 2) and linear PLA (Table B.2, entry 3)	92
Figure 3.4. The relationship of molecular weight and dispersity at each addition of monomer at 24 h intervals.....	95
Figure 3.5. Proposed mechanism of the polymerization of LA to form c-PLA by complex 48c . 96	
Figure 3.6. $^{31}\text{P}\{^1\text{H}\}$ NMR spectra (162 MHz, C_6D_6 , 25 °C) of a) the neutral dialkyl complex 47c b) 48c and c) InBr_3 after the addition of 0.8 equivalents of triethylphosphine oxide. The free OPEt_3 shift is determined by the addition of a capillary inside the NMR tube containing a solution of OPEt_3 in C_6D_6	97
Figure 3.7. The molecular structure of the cation of 48c . (depicted with thermal ellipsoids at 50% probability and H atoms, $\text{Bar}^{\text{F}}_{24}$ counterion, solvent molecules as well as minor disorders omitted for clarity)	98
Figure 3.8. <i>rac</i> -LA methine proton region of ^1H NMR spectra (400 MHz in Tol-d_8) of a 1:1 mixture of 48c and <i>rac</i> -LA a) at 100 °C 0 h, b) at 100 °C for 12 h, observed at 25 °C, c) after an additional 1 h at 25 °C and d) re-heated to 100 °C in the spectrometer.	99

Figure 3.9. Imine (I) and methylene (II) proton regions of ^1H NMR spectra (400 MHz, 25 °C in CDCl_3) of a) 47c , b) complex 48c and c) 1:1 mixture <i>rac</i> -LA and 48c heated at 100 °C for 24 h	100
Figure 3.10. a) Conversion vs. time plot for the synthesis of c-PLA using 48c (Reactions were performed in toluene at 100 °C, [<i>rac</i> -LA] = 0.8 M, conversion determined by ^1H NMR spectroscopy). b) Initiation efficiency vs. [LA]/[1] plot for the synthesis of c-PLA (Table 3.1	102
Figure 3.11. a) Reaction profile raised to power zero. b) Reaction profile raised to power 0.5. c) Reaction profile raised to power 1. d) Reaction profile raised to power 1.5. Reaction conditions: [LA] = 0.633 M; toluene d_8 ; T= 100 °C. (Integration determined with respect to 1,3,5-trimethoxybenzene internal standard).	103
Figure 3.12. a) Reaction profile raised to power zero. b) Reaction profile raised to power 0.5. c) Reaction profile raised to power 1. d) Reaction profile raised to power 1.5. Reaction conditions: [48c] = 0.0316 M; toluene d_8 ; T= 100 °C. (Integration determined with respect to 1,3,5-trimethoxybenzene internal standard).	103
Figure 4.1. Prior studies in the coupling of epoxides and lactones.	113
Figure 4.2. Synthesis of neutral and cationic indium complexes.	116
Figure 4.3. The molecular structure of 48h depicted with thermal ellipsoids at 50% probability and H atoms, $\text{BAr}^{\text{F}}_{24}$ counterion, solvent molecules, as well as minor disordered counterparts, omitted for clarity.	116
Figure 4.4. Conversion vs. time plots of 48b , 48e , and 48f for the formation of SOE monitored by ^1H NMR spectroscopy (60 °C, C_6D_6 , 400 MHz).	118

Figure 4.5. Conversion vs. time plots of 48b , 48g , and 48h for the formation of SOE monitored by ^1H NMR spectroscopy (60 °C, C_6D_6 , 400 MHz) showing comparable reactivity regardless of substituents on the furan pendant arm.	119
Figure 4.6. a) VTNA plot to determine the order with respect to $[\epsilon\text{-CL}]$. ($[\mathbf{48b}] = 0.0127\text{ M}$, $[\text{EOE}] = 0.507\text{ M}$ at 60 °C in benzene- d_6). b) VTNA plot to determine the order with respect to $[\text{EOE}]$ ($[\mathbf{48b}] = 0.0127\text{ M}$, $[\epsilon\text{-CL}] = 0.507\text{ M}$ at 60 °C in benzene- d_6). c) VTNA plot to determine the order with respect to $[\mathbf{48b}]$ ($[\text{EOE}] = 0.507\text{ M}$, $[\epsilon\text{-CL}] = 0.507\text{ M}$ at 60 °C in benzene- d_6)..	120
Figure 4.7. a) Saturation plot of 48b . Line is plotted with K_M and V_{max} values extracted from the b) Eadie–Hofstee plot for 48b	121
Figure 4.8. a) Downfield shift of the α proton of the furfuryl pendant arm relative to 25 °C, b) VT ^1H NMR (400 MHz, $\text{C}_6\text{D}_5\text{Br}$, 25–125 °C) spectra showing downfield migration of the α proton of the furfuryl group of 48e and c) 48b	122
Figure 4.9. Percent buried volume (at a 3.5 Å radius around the indium center) calculation to determine steric bulk of different alkyl ligands on 48e , 48b , and 48f	123
Figure 4.10. Possible pathways for substrate coordination and product formation by 48b	124
Figure 4.11. Coordination of $\epsilon\text{-CL}$ followed by attack of the epoxide is expected to result in the formation of cyclic ether-esters, which are not observed.	125
Figure 4.12. (a) Broad $^{31}\text{P}\{^1\text{H}\}$ NMR spectral peak arising from the coordination of one TEPO molecule to 48b and (b) the sharp $^{31}\text{P}\{^1\text{H}\}$ NMR spectral peak from the coordination of two TEPO molecules to 48b	126
Figure 4.13. Relative stabilization energies (kcal mol^{-1}) of a truncated version of complex 48e bound to one or two epoxides.	126
Figure 4.14. Formation of the active catalyst by coordination of epoxide to 48b	127

Figure 4.15. Proposed mechanism for spiro-orthoester formation by complex 48b	127
Figure 4.16. Reaction profile of the proposed mechanism of SOE formation by a truncated version of 48e	128
Figure 4.17. Buried volume (at a 3.5 Å radius around the indium center) calculation to determine steric bulk of different alkyl ligands on 48e -SOE, 48b -SOE, and 48f -SOE.	129
Figure 5.1. Potential sulfur containing monomers for polymerization by indium catalysts.	144
Figure 5.2. Previously reported dialkyl cations of group 13 metals stabilized by monodentate ligands.	146
Figure 5.3. The synthesis of cationic dialkylgallium and indium complexes.....	148

List of Abbreviations and symbols

\pm	Racemic
$^{\circ}$	Degree
$^{13}\text{C}\{^1\text{H}\}$	Proton-decoupled carbon
\AA	Angstrom
ACN	Acetonitrile
Ac	Acyl
Anal.	Analysis
Ar	Aromatic
$\text{BAr}^{\text{F}}_{20}$	Tetrakis(pentafluorophenyl)borate
$\text{BAr}^{\text{F}}_{24}$	Tetrakis(3,5-bis(trifluoromethyl)phenyl)borate
BBL	β -butyrolactone
Binam	1,1'-binaphthyl-2,2'-diamine
Bn	Benzyl
Boc	tert-butyloxycarbonyl
cal	calories
Calcd.	Calculated
Cat.	Catalyst
CHO	Cyclohexene oxide
CL	Caprolactone
c-PLA	Cyclic PLA

CoCp ₂	Cobaltocene
Conv.	Conversion
COSY	Correlation spectroscopy
CTA	Chain transfer agent
Cumyl	-C(CH ₃) ₂ Ph
Da	Dalton
DACH	Diaminocyclohexane
DCM	Dichloromethane
DFT	Density function theory
DHB	2,5-dihydroxybenzoic acid
D _N	Donor number
DOSY	Diffusion ordered spectroscopy
D _s	Donor strength
DSC	Differential scanning calorimetry
<i>D</i>	Dispersity
EA	Elemental analysis
ECH	Epichlorohydrin
ee	Enantiomeric excess
EOE	1,2-epoxy-7-octene
Eq	Equivalent
equiv	Equivalent
Et	Ethyl

Et ₂ O	Diethyl ether
FT-IR	Fourier-transform infrared spectroscopy
g	Gram
GC-MS	Gas chromatography-mass spectrometry
GPC	Gel permeation chromatography
h	Hour
HMBC	Heteronuclear multiple bond correlation spectroscopy
HSQC	Heteronuclear single quantum coherence spectroscopy
HRMS	High resolution mass spectrometry
Hz	Hertz
<i>i</i> *	Initiation efficiency
ⁱ Bu	Isobutyl
ⁱ Pr	Isopropyl
<i>K</i> _M	Michaelis-Menten constant
LA	Lactide
M	Molarity
MALDI-TOF	Matrix-assisted laser desorption ionization-time of flight
Me	Methyl
MeOH	Methanol
Me-THF	2-methyltetrahydrofuran
<i>M</i> _n	Number average molecular weight of polymer
<i>M</i> _n	Calculated number average molecular weight of polymer

M_w	Weight average molecular weight of polymer
MW	Molecular weight
NHC	N-heterocyclic carbene
NMR	Nuclear magnetic resonance
NOE	Nuclear Overhauser Effect/Enhancement
NOESY	Nuclear Overhauser Enhancement Spectroscopy
PCL	Poly(caprolactone)
PDI	Poly dispersity index
PDLA	Poly(D-lactide)
Ph	Phenyl
PHB	Polyhydroxybutyrate
PLA	Poly(lactide)
PLLA	Poly(L-lactide)
PO	Propylene oxide
ppm	Parts per million
PPNCl	Bis(triphenylphosphine)iminium chloride
R	Alkyl group
<i>R</i>	<i>Rectus</i> (Latin for right) in R/S chirality
<i>rac</i>	Racemic
ROP	Ring-opening polymerization
ROCOP	Ring-opening copolymerization
<i>S</i>	<i>Sinister</i> (Latin for left) in R/S chirality

salan	A compound synthesized by reduction of a salen compound
salen	Bisiminophenolate
Schiff base	An imine bearing a hydrocarbyl group on the nitrogen atom
SOE	Spiro-orthoester
[TBA]N ₃	Tetrabutylammonium azide
THMB	Tri(hydroxymethyl)benzene
^t Bu	tert-butyl
Temp.	Temperature
TEPO	Triethylphosphine oxide
<i>T_g</i>	Glass transition temperature
TGA	Thermogravimetric analysis
THF	Tetrahydrofuran
THP	Tetrahydropyran
<i>T_m</i>	Melting temperature
TMC	Trimethylene carbonate
TMS	Trimethylsilyl
Tol	Toluene
Tosyl	-SO ₂ PhMe
Triflate	Trifluoromethyl sulfonate
<i>V_{max}</i>	Maximum rate
VT	Variable temperature
VTNA	Variable time normalization analysis

β -BL	β -butyrolactone
δ	Chemical shift downfield from tetramethylsilane in ppm
$\Delta\delta$	Difference in chemical shift
δ -VL	δ -valerolactone
ε -CL	ε -caprolactone

Acknowledgements

This thesis would never have seen the light of day if not for the enormous amounts support that I received from many good people at many places at many times. First among these is Professor Parisa Mehrkhodavandi, who was my supervisor, mentor, and friend through the most turbulent of times. I will be forever grateful to her for giving me a place in the Mehr lab and for having faith in my work, for being there when we needed her. Although I could write pages upon pages about the many times Prof. Mehrkhodavandi has been the MVP, all I will say is that working for her has been a joy and an honor.

I would like to thank the staff at UBC Chemistry. Especially, Dr. Maria Ezhova for spending all those hours with me poring over hundreds of NMR spectra and for being a mentor and collaborator. A special thanks to Ben Herring, George Kamel, and Brian Ditchburn for being heroes in hours of desperation. Thank you, Helen Wright, for keeping all of us alive for most of my tenure at UBC. I am equally thankful to Sheri Harbour, Sabrina Fried and others for keeping things running smoothly at UBC Chemistry. I would also like to thank all those unsung heroes from the NMR facilities, mech shop, electronic shop, IT services, and the custodial services for making UBC chemistry what it is. I would also like to thank my UBC Chemistry teaching family in the 3XX organic labs, especially Dr. Monserrat Rueda for all those lively conversations (and the TA candy).

I owe a very special thank you to all the past and present members of the Mehr group. Especially, my amazing undergraduate collaborators, Hootan, Kimia, Joseph, Ana, and Salik. It was such a joy to have you in my life. I would also like to thank Kudzi, Hassan, and Joon, the old-guard of the group, for being my constant collaborators and friends. Nor will I ever forget all the

good times I have had in and out of the lab with Afagh, Takeo, Jason, and Kritika. It was an incredible experience to work with such good friends.

I would also like to thank my undergraduate mentors Profs. Nalin de Silva and Rohini de Silva for believing in me and giving me so many opportunities. I am ever thankful to my parents Kamal and Samantha and my sibling Maneka and Minaka for supporting my dreams. I wish my grandparents could see me today. I am grateful to my uncle and aunt Satish and Renuka for helping me when I first started research all those years ago. Lastly, I need to thank my partner, Cathy, for reminding me how wonderful life can be and making these years infinitely more glorious.

අත දිවයිනක නූපන් පරපුරක් වෙනුවෙන් දිවි දුන් දහස් සංඛ්‍යාත ශිෂ්‍ය වීරයින්ට...

*To the thousands of student heroes who gave their lives for an unborn generation in an island far
away...*

Chapter 1: Introduction

The reactivity of indium(III) catalysts is defined to a great extent by their ligand architectures. In this thesis, I propose that by adding tethered hemilabile donor groups, the stability, reactivity, and reactive mechanism of cationic alkyl indium complexes can be fine-tuned. The controlled reactivity of these complexes can be used to determine synthetic mechanisms and to produce novel polymer architectures.

1.1 Indium(III) in catalysis

Although it is often overlooked in favor of its group 13 siblings in synthetic chemistry, indium has seen a steady increase in its applications over the past 50 years.^{1,2} This soft, silver metal in its elemental form, with the atomic number 49 and symbol In, possesses unique properties that have attracted the attention of researchers in a variety of fields.³⁻⁵ Indium-based catalysts have demonstrated remarkable selectivity and efficiency in promoting challenging reactions, making them valuable in numerous synthetic transformations.⁶ As our understanding of its capabilities continues to grow, the significance of indium in catalysis is gaining new recognition, paving the way for innovative advancements in chemical synthesis.

The electronic configuration of indium, $[\text{Kr}]4d^{10}5s^25p^1$, affords two stable oxidation states, In(I) and In(III). Between these, In(III) is more stable, making it the most frequently encountered oxidation state of the metal.⁷ The popularity of In(III) compounds in catalysis mainly arises from their ability to accept electron pairs *i.e.*, their Lewis acidity. Lewis acidity can be broadly defined as the ability of a chemical species to accept electron pairs. Conversely, the ability to donate non-bonding electron pairs is called Lewis basicity. The reaction between a Lewis acid and a Lewis base results in the formation of Lewis adducts (Figure 1.1). While compounds of group 13 elements boron, aluminum, and gallium exhibit strong Lewis acidity, indium species tend to be

less acidic owing to the much larger ionic radius of the metal. Unlike other members of group 13, In(III) species have greater functional group tolerance with lower affinity to amines, hydroxides and, even aqueous reaction conditions, making them an enticing option as Lewis acidic catalysts for many chemical transformations.^{8,9}

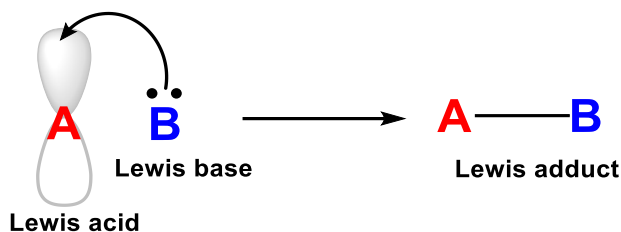


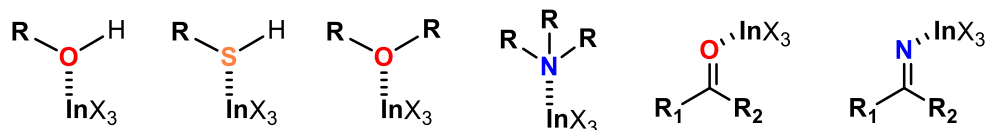
Figure 1.1. Reaction of a Lewis acid and a Lewis base to form a Lewis adduct.

Indium compounds used in catalysis range from simple salts to well-defined organometallic complexes with polydentate ancillary ligands.^{6,10,11} The magnitude of the Lewis acidity of In(III) species and the associated reactivity is largely defined by the ligand environment around the metal center. The most popular In(III) catalysts are indium (III) halide salts, predominantly used in organic reactions utilizing mild Lewis acid catalysts.^{6,12–15} When a stronger Lewis acid is called for, organometallics such as In(III) triflate (trifluoromethanesulfonate) and related compounds have been used.¹⁶ Indium complexes with more complicated multidentate ligands have been used mostly as polymerization catalysts.¹⁷ Other reactions requiring stronger Lewis acidity and functional group tolerance have turned towards cationic indium species with additional vacant sites and increased reactivity.¹⁰

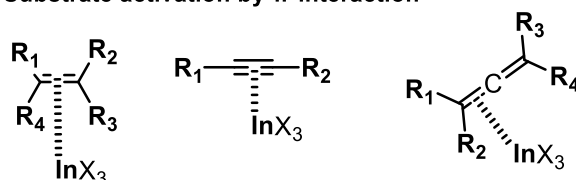
Although indium catalysts can take many forms, a common theme in reactive mechanisms is the formation of a Lewis adduct with Lewis basic substrates and the indium center. Lewis adduct formation could occur through several possible routes, a) σ -interactions with carbonyl, hydroxy, amine, imine, or thiol groups (Figure 1.2a) b) π -interaction with alkynes, alkenes, or allenes

(Figure 1.2b) and c) Multiple interactions or dual-mode activations (Figure 1.2c). The formation of such Lewis adducts cause substrate activation by increasing the electrophilicity of adjacent atoms increasing their reactivity towards nucleophiles.¹⁸

a. Substrate activation by σ -interactions



b. Substrate activation by π -interaction



c. Multi-site substrate activation

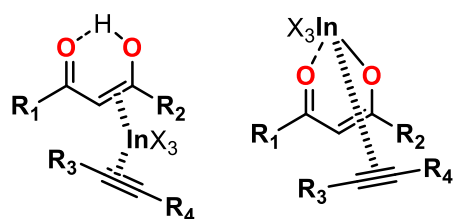


Figure 1.2. Different modes of substrate activation by indium (III) catalysts.

These reactive modes have been utilized in numerous organic reactions, including, but not limited to, ring-forming reactions, addition reactions, substitution reactions, reductive aminations, hetero-cyclization reactions, rearrangement/isomerization reactions, protection/deprotection reactions, and polymerization reactions (Figure 1.3). Various aspects of these and other reactions have been reviewed in detail over the last two decades. The use of In(III) catalysts in organic synthesis was reviewed in detail by Frost⁵, Podlech¹⁹, and Augé.²⁰ Ranu¹⁴, Vaccaro²¹, and Yadav²² and focuses on describing reactions promoted by various In(III) salts. The use of InCl₃ as a catalyst was the focus of the reviews by Datta⁶ and Singh¹⁵ while Kazemi and Yu¹² focused on InBr₃. Maiti

described the use of In(III) triflate to catalyze various organic reactions.¹⁶ The review by Mehrkhodavandi looked at cationic indium species as catalysts in various reactions.¹⁰ Chan⁸ and Loh⁹ reviewed the use of In(III) catalysts in aqueous media. In(III) catalysts in reactions involving alkynes and C-C unsaturated systems were described by Selander²³ and Sestelo¹⁸ respectively. Enantioselective reactions catalyzed by In(III) species was reviewed by Pellissier²⁴ while Yadav²⁵ and Pineiro²⁶ described In(III) catalyzed multi-component reactions. The review by Jaisankar described the use of InCl₃ in various heterocycle forming reactions.¹³ Finally, Dagorne¹⁷ and Garden^{27,28} have reviewed some of the polymerization reactions catalyzed by In(III) complexes.



Figure 1.3. General reaction types catalyzed by In(III) species.

While catalysis by In(III) has been predominantly focused on fine chemical synthesis in organic chemistry, most of the defined organometallic In(III) complexes have been utilized in polymer synthesis. Since the first such complexes were reported by Huang²⁹ and Mehrkhodavandi³⁰ a number of In(III) complexes supported by a diverse set of ligands have been reported over the years. The next section of this chapter will focus on the fundamental aspects of polymer synthesis and the In(III) catalysts used in these reactions, focusing on their ligand architectures in order of increasing complexity.

1.2 Polymerization reactions

A significant amount of new research on indium catalysis has focused on polymerization reactions. There are two main types of polymerizations, chain growth polymerization where the monomer units are added one-by-one to a polymer chain end until the termination of polymerization (Figure 1.4a). The second type is step growth polymerization where pairs of monomer units of various lengths can react until larger polymer units are formed (Figure 1.4b). Most indium mediated polymerization reactions belong to the former class.

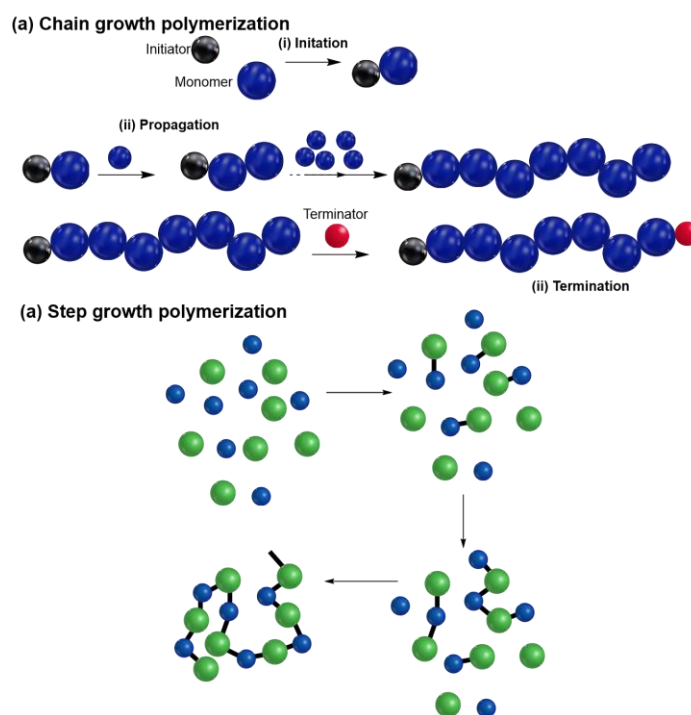


Figure 1.4. a) Chain growth polymerization and b) step-growth polymerization.

Chain growth polymerizations have three distinct stages beginning with initiation. This step usually involves the activation of a single monomer molecule to enable reaction with incoming monomers. The second step is propagation; the majority of chain growth occurs during this stage as new monomer molecules add to a reactive chain end, increasing the size of the growing polymer chain. The last step of polymerization is termination or chain termination. In this

step, polymerization ends as the reactive chain ends are quenched by various mechanisms. The reactions kinetics of these will govern how catalysts can control polymer formation.

Polymers are characterized using a few fundamental parameters. Polymer molecular weight is one of these. As polymer samples consist of molecules that vary in size, it is not possible to determine the precise molecular weight of the polymer. Consequently, the averages of several factors to represent the molecular weight of the polymer are used. Molecular weight can be defined using several methods, but number average molecular weight (M_n), calculated using the mole fraction of each molecular weight in a sample, (Equation 1.1a) and weight average molecular weight (M_w), calculated using the weight fraction of each molecular weight, (Equation 1.1b) are the most widely used and applied. The ratio between these two, M_w/M_n , gives polymer dispersity, D , (also known as Polydispersity Index, PDI). A dispersity value of close to 1.0 indicates a narrow distribution of molecular weights, whereas a high dispersity signifies a broad distribution of molecular weights. A narrow dispersity is generally desirable for many applications as it results in more uniform properties, whereas a broad dispersity can lead to variable or unpredictable properties.

$$\begin{array}{lll} \text{a)} & \text{b)} & \text{c)} \\ M_n = \frac{\sum M_i N_i}{\sum N_i} & M_w = \frac{\sum M_i^2 N_i}{\sum M_i N_i} & D = \frac{M_w}{M_n} \end{array}$$

Equation 1.1 Equations for a) Number average molecular weight and b) weight average molecular weight and c) dispersity.

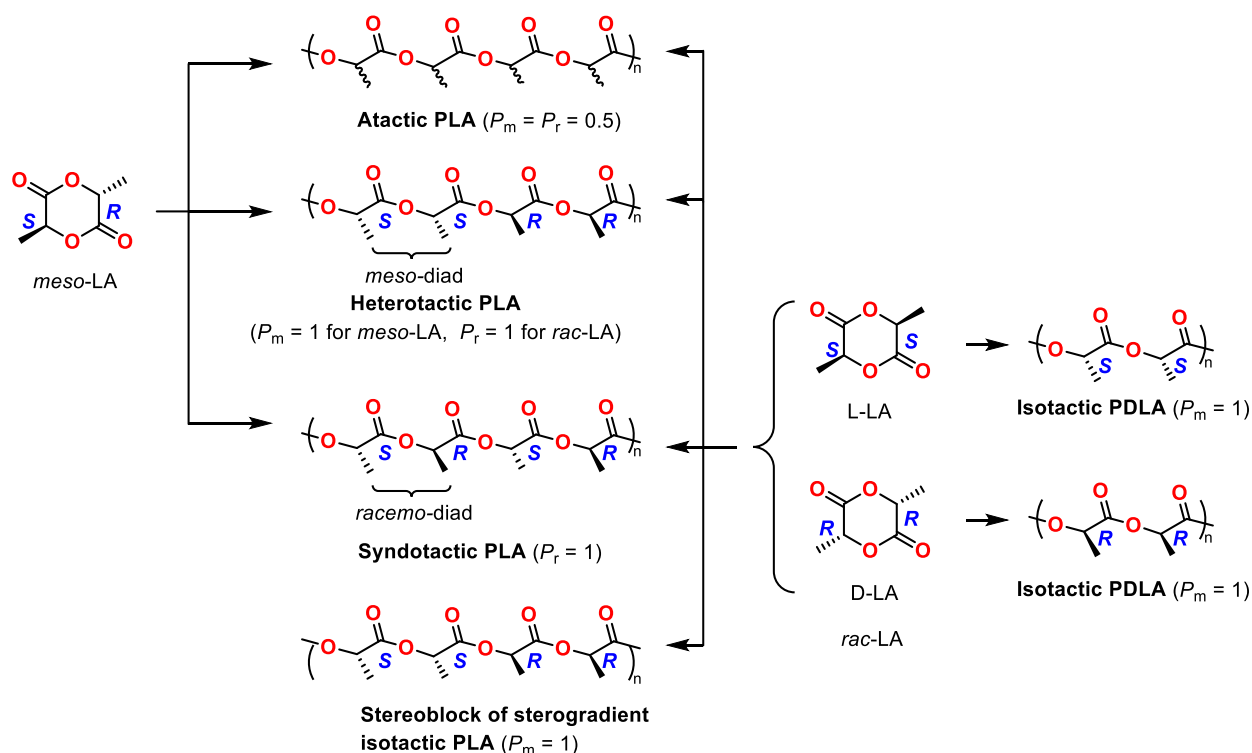


Figure 1.5. Microstructures of poly(lactic acid) (PLA) depict polymer tacticity.

Another factor that is important in determining polymer properties is the spatial arrangement of monomer units. The term ‘tacticity’ is commonly by polymer chemists used to describe the regularity or irregularity of the stereochemistry of monomers along the polymer chain. The degree of tacticity is quantified using the probability of finding the same (P_m) or opposing (P_r) stereochemistry in two adjacent monomer units (Figure 1.5). There are four types of tacticity: isotactic, syndiotactic, heterotactic, and atactic. Isotactic polymers have a regular, repeating pattern of monomer units with all the side groups positioned on the same side of the polymer backbone with a P_m close to 1. Syndiotactic polymers have a regular pattern of alternating side group positions along the polymer backbone, thus, the probability that two adjacent repeat units have the same configuration is close to zero *i.e.*, P_m is close to 0. Atactic polymers have a random arrangement of monomer stereocenters making the probability $\frac{1}{2}$, hence, P_m is close to 0.5. In

heterotactic polymers, monomer units are arranged in an ordered, alternating sequence with P_r close to 1. Polymer molecular weight, dispersity, and tacticity are important factors in determining the physical and chemical properties of polymers, such as their mechanical strength, thermal stability, and solubility, and therefore have important implications for its potential applications.

Control of polymer stereochemistry *i.e.*, stereocontrol is achieved through two different mechanisms. The first is enantiomorphic site control where the stereochemistry of the polymer is determined by the stereochemistry of the catalyst/initiator. Hence the stereochemistry of the product is determined by the overall chiral environment of the growing chain end. The second mechanism is chain end control where the stereochemistry of the growing polymer chain is determined by the stereochemistry of the previously added monomer unit and is independent of the stereochemistry of the catalyst.

1.2.1 Mechanisms of indium catalyzed ring-opening polymerizations

The monomer scope, polymerization control, and mechanism of polymerization will be largely dependent on the type of indium catalyst used. The vast majority of polymerization reactions catalyzed by neutral indium complexes involve the ring opening polymerization (ROP) of lactones. Among these, lactide (LA), a cyclic dimer of lactic acid, is one of the most extensively used monomers owing to the biodegradable nature of its polymer, poly(lactide) (PLA). Indium catalyzed polymerization LA and other lactones can be achieved by two alternate mechanisms. The first of these, the coordination-insertion mechanism, involves the activation of a carbonyl group on the monomer by coordination to indium making it susceptible to nucleophilic attack and ring-opening by an alkoxy, alkyl, amide, or halide nucleophile attached to the metal center (Figure 1.6b). The ring-opened monomer forms a new indium alkoxy insertion product which acts as a

nucleophile for subsequent monomers that coordinate to indium, making this the propagation step. The polymer chain is usually terminated by protonation by water or alcohols. The initiation step for the second mechanism *i.e.*, the activated monomer mechanism, proceeds in much the same way as the coordination-insertion mechanism by carbonyl activation (Figure 1.6a). However, the monomer is ring-opened through nucleophilic attack by an external nucleophile, typically an alcohol. The propagation and termination steps for this mechanism follow a similar pattern to the coordination-insertion pathway.

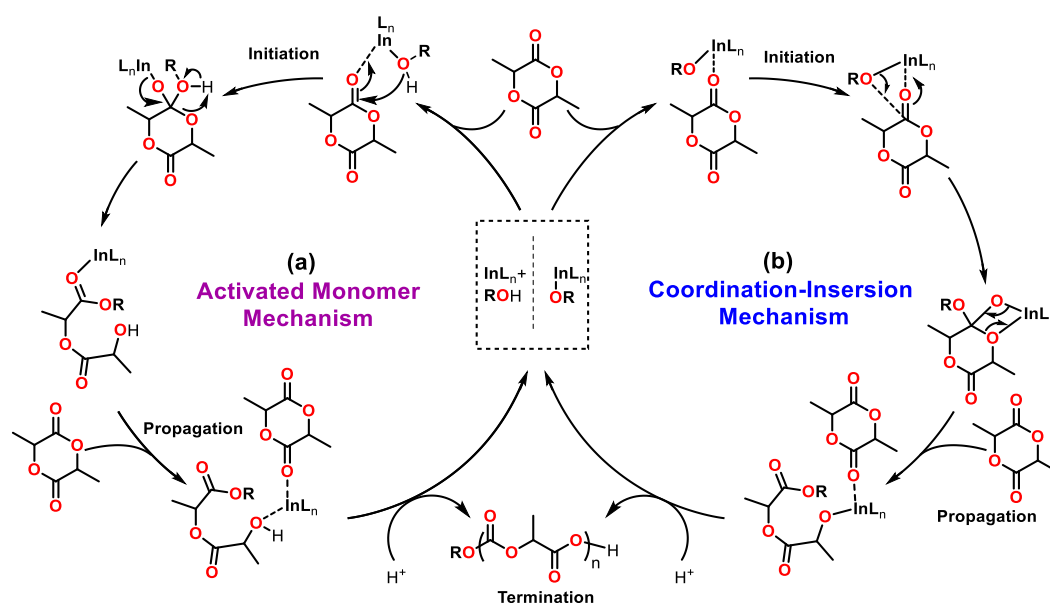


Figure 1.6 a) The activated monomer mechanism and b) the coordination-insertion mechanism of lactide polymerization.

During both mechanisms the undesired process known as transesterification can result in truncated polymer chains and increased dispersity (Figure 1.7). This could take the form of intramolecular transesterification, also called “backbiting”, or intermolecular transesterification between two polymer chains. Catalyst design and reaction conditions are often optimized to avoid these side reactions.

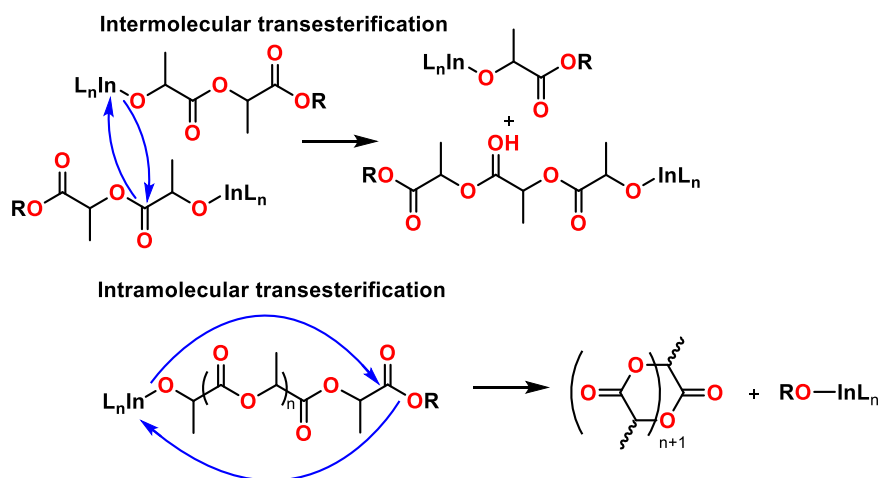


Figure 1.7. Intermolecular and intramolecular transesterification reactions.

Many indium catalyzed polymerization reactions involving coordination-insertion and activated monomer mechanisms are living in nature (Figure 1.8a). These are polymerization reactions which enable precise control over the shape and size of polymer chains through the ability to pause and resume the reaction. The propagating alkoxide species can be deactivated and reactivated as required, thus consecutive additions of monomer result in a longer chain length with each monomer addition. In contrast, non-living polymerizations are uncontrolled, and reaction cannot be stopped or restarted once it has begun. A subset of living polymerization reactions is called immortal polymerization (Figure 1.8b). These reactions employ chain transfer agents (CTAs) to reversibly take up the growing polymer chain from the metal center. The polymer chains attached to the CTA do not grow any further. However, these chains can be reactivated by chain exchange between the CTA and the metal center. One of the main limitations of immortal polymerization is the instability of most metal-based initiators when exposed to significant quantities of CTAs, notably alcohols.

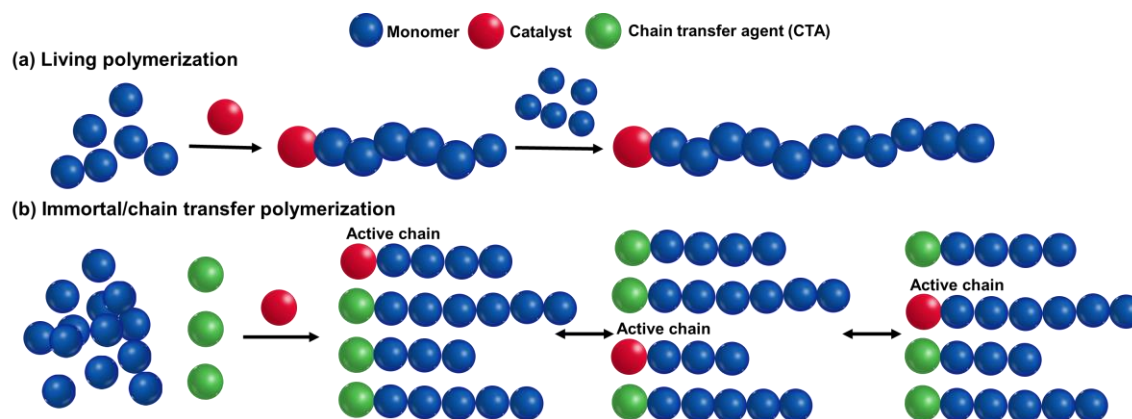


Figure 1.8. a) Living polymerization and b) immortal/ chain-transfer polymerization.

Reaction mechanism and control of polymerization (molecular weight, dispersity, tacticity, *etc.*) are largely dependent on ligand environment around the indium metal. Fine-tuning ligand architectures can have a pervasive impact on the activity of the catalyst as well as the microstructure of the resultant polymers. Thus, unlike most indium catalysts used for reactions in organic chemistry, catalysts used in polymerization reactions tend to be well-characterized, discreet organometallic complexes. The next section will focus on ligand architecture and structure-function relationships of various indium catalysts used in polymerization reactions.

1.2.2 Polymerization reactions by neutral indium catalysts

Indium complexes used in polymerization reactions can be broadly classed into neutral/uncharged catalysts and cationic catalysts. This subsection will look at various ligand architectures used in uncharged indium complexes. Looking at progressively complicated ligand environments.

1.2.2.1 Indium catalysts with monodentate ligands

One of the simplest systems was the *in situ* generation of bridged dinuclear indium alkoxide species (**1**) from a 2:1:1 mixture of InCl_3 , NEt_3 , and benzyl alcohol (BnOH) reported by Hillmyer and Tolman (Figure 1.9).³¹ Catalyst **1** could polymerize *rac*-LA to give high conversions,

molecular weights up to 159 kg mol^{-1} and, low dispersity. This system selectively produced highly heterotactic PLA ($P_r = 0.97$) demonstrating excellent stereocontrol without the use of specialized ancillary ligands. The polymerization followed a typical coordination-insertion mechanism at two indium centers initiated by an *in situ* generated alkoxide species. The function of the amine was to act as a base and be the counterion to the propagating species. The identity of the halide species dictated the rate of reaction, with InBr_3 and InI_3 being significantly slower than InCl_3 . However, the mode of stereoselectivity was not well understood.

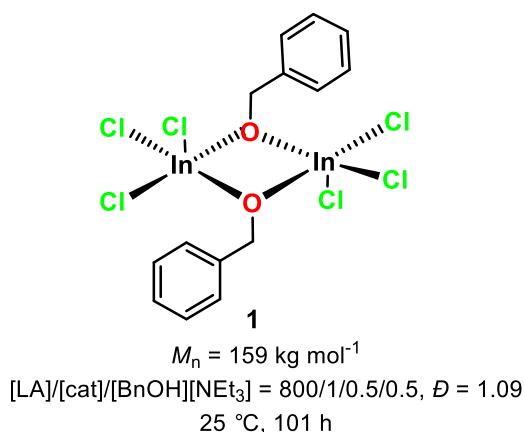


Figure 1.9. The proposed structure of the $\text{InCl}_3/\text{BnOH}$ catalyst **1** reported by Tolman *et al.*

In a deviation from the usual lactone polymerization reactions, InCl_3 and InBr_3 were used in conjunction with alkyl halides by Carpentier and co-workers for the polymerization styrene and related compounds through a cationic mechanism to form polyolefins (Figure 1.10).³² The polymerization was initiated by halide abstraction from the alkyl halide initiator which resulted in an electrophilic carbocation that could propagate with monomer addition. While this system mostly produced oligomers, chains with lesser than 100 repeating units, more controlled reactivity could be obtained when a small amount of donor cosolvent such as di(isopropyl)ether was used to stabilize intermediates and to solubilize the catalyst. Additionally, cationic co-oligomerization of styrene and α -methyl styrene could also be achieved with InCl_3 .

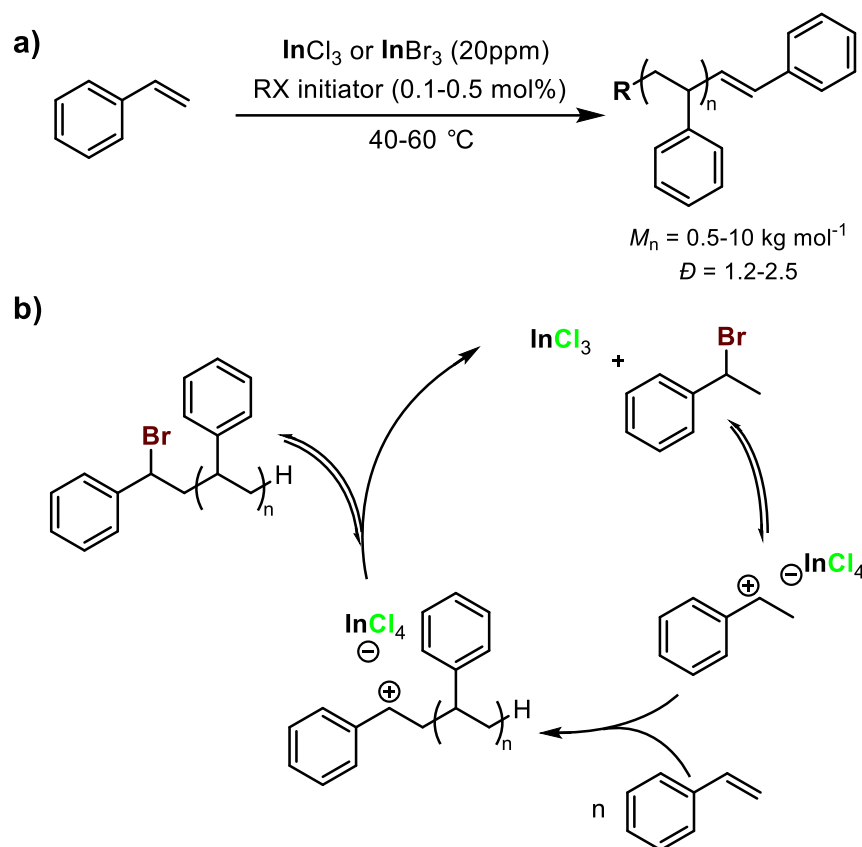


Figure 1.10. a) Polymerization of styrenics with InCl_3 or InBr_3 and b) Proposed mechanism for the In(III) catalyzed formation of polyolefins.

1.2.2.2 Indium catalysts with bidentate ligands

Slightly more intricate are the indium complexes supported by bidentate ligands systems. The very first indium complexes reported for the polymerization of lactones, reported by Huang and co-workers, used a bidentate (dimethylaminomethyl)pyrrolate ligand system (**2-4**) for the polymerization of the seven-membered lactone, ϵ -caprolactone (ϵ -CL), to form polycaprolactone (PCL) (Figure 1.11).²⁹

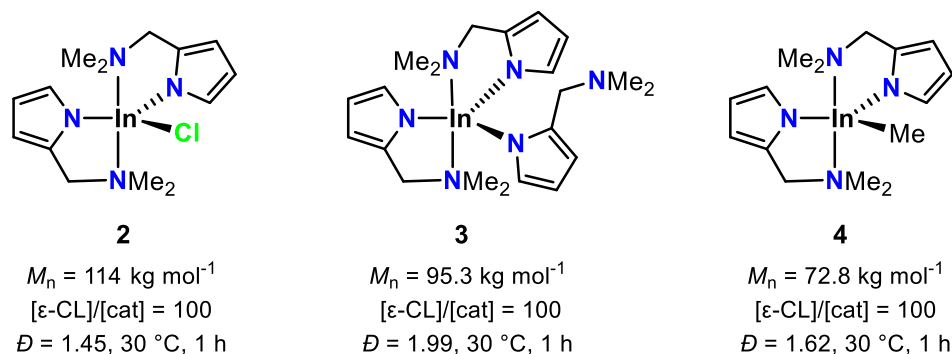


Figure 1.11. Indium amino pyrrolate complexes (**2-4**) reported by Huang *et al.*

Indium complexes with bidentate alkoxide ligands could act either as ancillary ligands or initiators. The indium species with phosphine oxide-alkoxide chiral ligand systems (**5-7**) reported by Arnold and Okuda are prime examples of this type of catalyst (Figure 1.12).³³ These catalysts could produce isotactic PLLA and PDLA from *rac*-LA. The polymers produced by **5-7** possessed $\text{-N}(\text{SiMe}_3)_2$, -OAr , and alkoxy-ligand chain-ends respectively, indicating a coordination-insertion mechanism of polymerization. The alkoxy chain-end of polymers formed with **7** pointed to a possibly labile phosphine oxide moiety and a penta-coordinate active catalyst. Additionally, the reactivity patterns as indicated by monomer conversions showed that LA prefers to insert into an indium-alkoxy bond followed by aryloxy and amido bonds in turn.

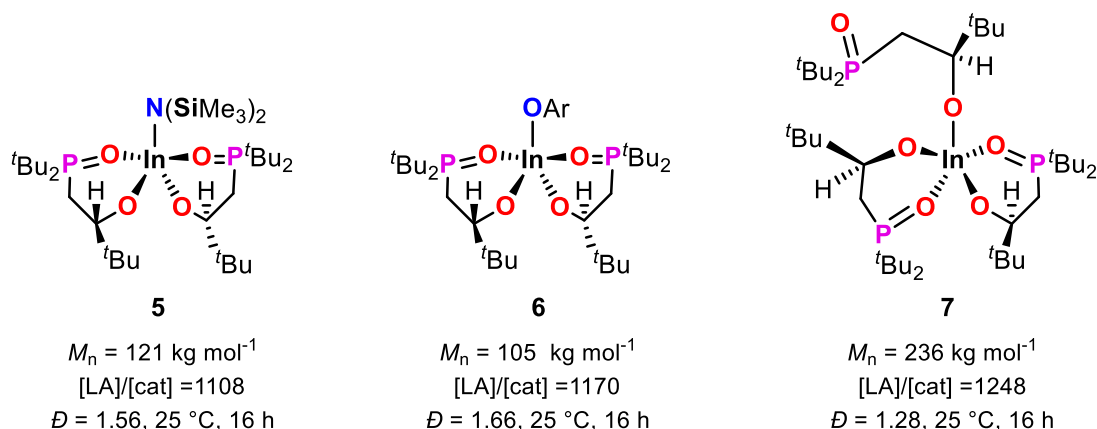


Figure 1.12. Indium alkoxide complexes (**5-7**) reported by Arnold and Okuda.

The simplicity of alkoxide ligands has also been leveraged to investigate mechanisms of polymerization reactions, as in the case of the dinuclear dimethylindium alkoxide species used by Horeglad and co-workers to explore stereoselectivity in PLA formation (Figure 1.13).³⁴ Reacting $\text{In}(\text{CH}_3)_3$ with *rac*-methyl lactate gave a mixture of (*R,R*)-**8** and *rac*-**8** in a 3:2 ratio. Introducing an excess of a Lewis basic amine species formed a mixture of homochiral (*R,R*)-**8** and (*S,S*)-**8**. This was caused by Lewis base coordination to the fifth coordination site of indium which promoted rapid chiral recognized ligand exchange. Polymerization studies of *rac*-LA with (*S,S*)-**8**/amine indicated that that stereoselectivity was largely dependent on the proportion of excess homochiral catalyst species with Lewis bases that promoted greater exchange to produce more homochiral indium complex resulting in more heterotactic enriched PLA.

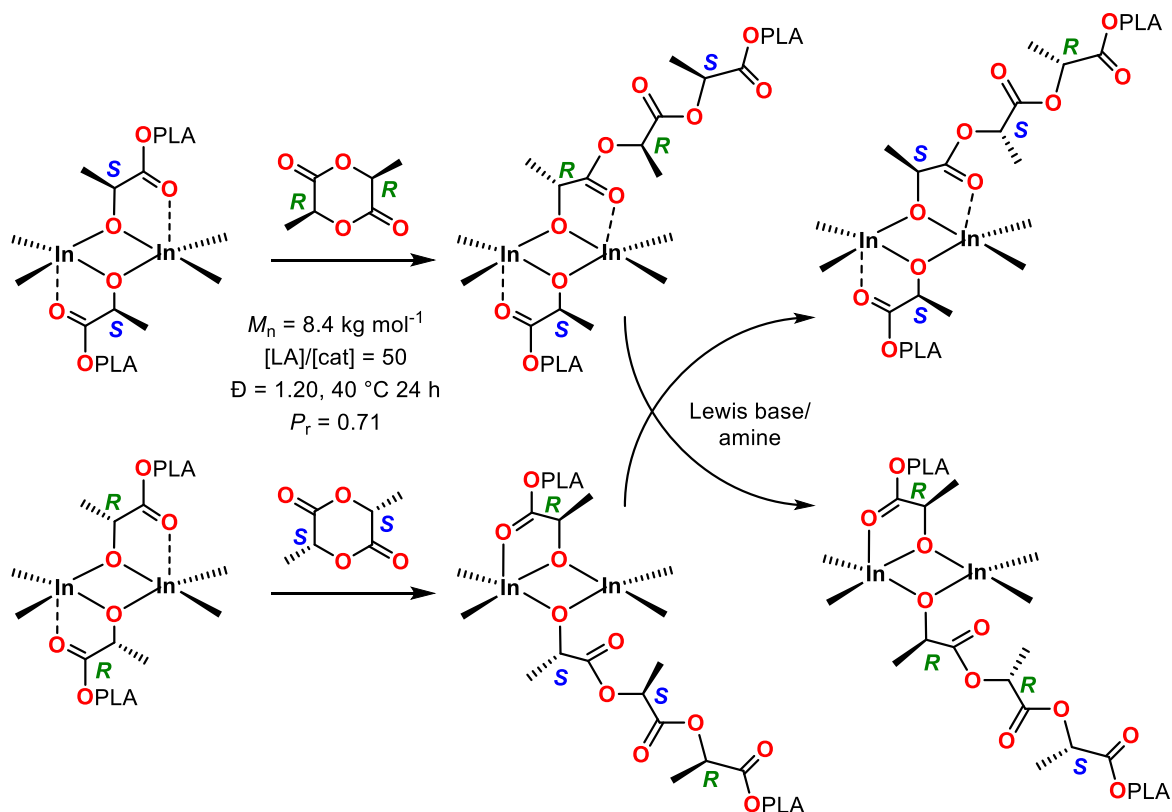


Figure 1.13. Stereoselective polymerization of *rac*-LA by the dinuclear alkoxide complex (**8**) reported by Horeglad

et al.

The indium thiolate complexes reported by Briand and co-workers shared a similar structural motif indium to alkoxide complexes (Figure 1.14).³⁵ The formation of insoluble indium sulfides was avoided by using bidentate ligands with ester (**9**) and amine (**10**) donor groups to occupy additional coordination sites on indium. The In-O(ester) secondary interaction of **9** was significantly weaker than the In \cdots S interaction resulting in a dinuclear complex. However, the stronger In-N(amine) interaction of **10** was sufficient to prevent dimerization of the complex. Both **9** and **10** could initiate the polymerization of *rac*-LA in the presence of BnOH. While **9** showed lower M_n and greater dispersity due to transesterification, **10** showed excellent control of polymerization. However, in the absence of BnOH both catalysts indicated lower initiation and conversion. Complexes **9** and **10** are proposed to form an alkoxide species with BnOH which then undergoes a coordination-insertion mechanism to produce PLA.

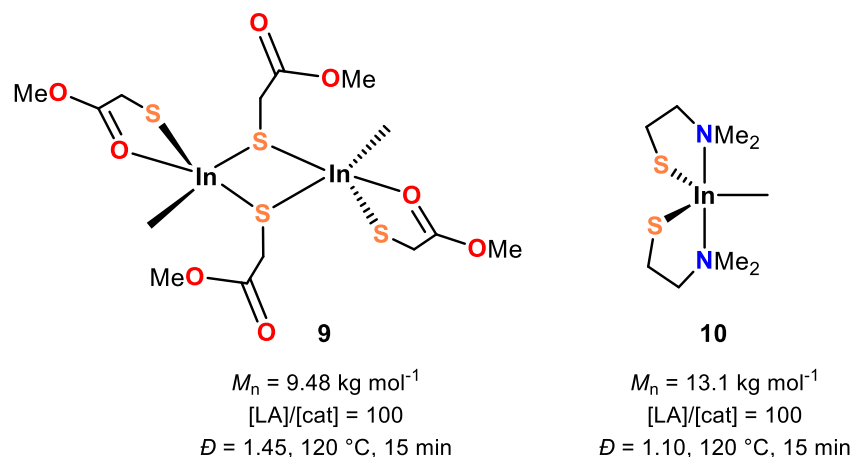
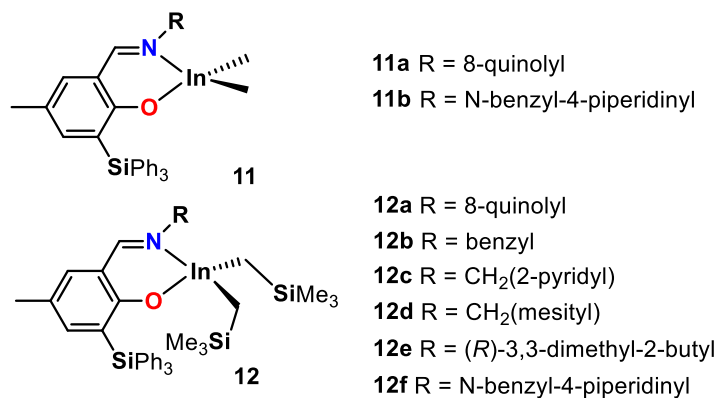


Figure 1.14. Indium thiolate complexes (**9** and **10**) reported by Briand *et al.*

Imino- or aminophenolate ligands, formed by coupling salicylaldehyde derivatives with amines, have been some of the most widely used ligand systems in indium-based polymerization catalysts. The series of iminophenolate dialkylindium complexes (**11a,b** and **12a-f**) with various imino substituents, reported for the ROP of LA by Carpentier and co-workers possess this

structural motif (Figure 1.15).³⁶ The dimethylindium complexes **11a** and **11b** showed good performance in the ROP of *rac*-LA in toluene at 80 °C when combined with 1 or 2 equivalents of isopropyl alcohol with monomodal but broadened dispersities ($\bar{D} = 1.33$ -1.96). Higher monomer loading led to lower molecular weights of the PLAs, indicating poor control over polymerization. Interestingly, using a larger excess (10 equiv) of CTA during polymerization resulted in PLA with molecular weights that matched the theoretical M_n values and had narrow dispersity. The bis((trimethylsilyl)methyl)indium (-CH₂TMS) complexes (**12a-f**) showed similar control over polymerization in the presence of a larger excess of isopropyl alcohol. These systems efficiently transferred between the growing polymer chains and dormant alcohols, indicating good control over polymerization parameters, and showing evidence for immortal polymerization. In contrast to an analogous aluminum system that showed coordination-insertion ROP of *rac*-LA, kinetic studies of the **12f** indicated that indium catalysts follow an activated monomer mechanism.



11a $M_n = 26.6 \text{ kg mol}^{-1}$, [LA]/[cat] = 500, $\bar{D} = 1.90$, 80 °C, 16 h
11b $M_n = 11.8 \text{ kg mol}^{-1}$, [LA]/[cat] = 1000, $\bar{D} = 1.60$, 80 °C, 15 h, 10 eq. iPrOH
12a $M_n = 13.7 \text{ kg mol}^{-1}$, [LA]/[cat] = 1000, $\bar{D} = 1.12$, 80 °C, 18 h
12b $M_n = 9.5 \text{ kg mol}^{-1}$, [LA]/[cat] = 1000, $\bar{D} = 1.13$, 80 °C, 16 h
12c $M_n = 14.4 \text{ kg mol}^{-1}$, [LA]/[cat] = 1000, $\bar{D} = 1.08$, 80 °C, 19 h
12d $M_n = 13.3 \text{ kg mol}^{-1}$, [LA]/[cat] = 1000, $\bar{D} = 1.07$, 80 °C, 16 h
12e $M_n = 12.8 \text{ kg mol}^{-1}$, [LA]/[cat] = 1000, $\bar{D} = 1.10$, 80 °C, 15 h
12f $M_n = 6.8 \text{ kg mol}^{-1}$, [LA]/[cat] = 1000, $\bar{D} = 1.06$, 80 °C, 3 h

Figure 1.15. Alkylindium iminophenolate complexes (**12a-f**) reported by Carpentier *et al.*

While a bimetallic analogue of **12f** (**13**) showed similar reactivity to the monometallic complex (Figure 1.16),³⁷ an aluminum analogue of **13** could significantly accelerate the polymerization of *rac*-LA. This contrast in reactivity was attributed to the different ROP mechanisms preferred by the two metals.

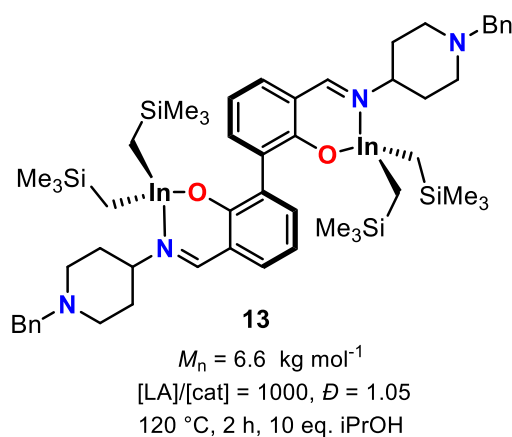


Figure 1.16. Bimetallic indium iminophenolate complex (**13**) reported by Carpentier *et al.*

Bis(iminophenolate) ligands, a variant of the iminophenolate motif, were used by Chakraborty and co-workers to construct a family of bis(*tert*-butyl)indium complexes with various imino substituents (**14a-d**) (Figure 1.17).³⁸ These complexes possessed a bidentate coordination mode with one of the imine moieties remaining pendant to the indium. All the complexes showed controlled polymerization of *rac*-LA and L-LA, obtaining close to theoretical molecular weights and narrow dispersity. In the case of *rac*-LA, the resultant polymer was isotactic enriched ($P_m = 0.70\text{-}0.76$) indicating moderate isoselectivity. Based on analysis of low molecular weight polymer produced with a gallium analogue of **14b**, ROP of LA was proposed to proceed through a coordination-insertion mechanism initiated by LA insertion into the M-O(phenoxy) bond for both metals.

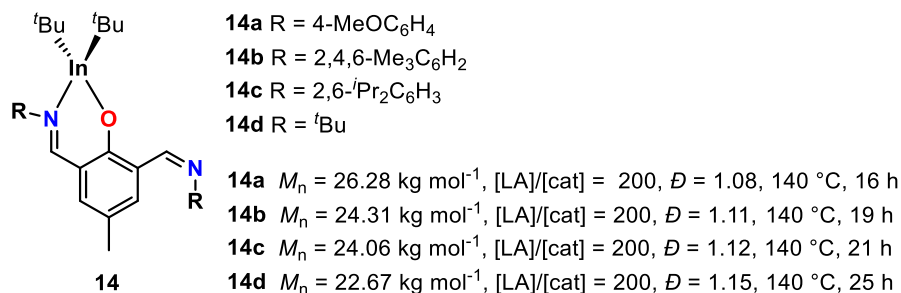


Figure 1.17. Indium bis(iminophenolate) complexes (**14a-d**) reported by Chakraborty *et al.*

1.2.2.3 Indium catalysts with tridentate ligands

A tridentate diamino phenolate ancillary ligand was used by Mehrkhodavandi and co-workers in the first indium complex (**15a**) reported to polymerize *rac*-LA (Figure 1.18).³⁹ Much of the foundational studies on indium catalyzed ROP reactions of lactones was accomplished using **15a** and its myriad descendants. The dinuclear complex **15a** showed homochirality with only (*RR,RR*)-**15a** or (*SS,SS*)-**15a** forming, excluding the formation of heterochiral (*RR,SS*)-**15a**. This homochirality was credited with the slight iso-enrichment of the PLA produced ($P_m = 0.60$). Additionally, **15a** could perform living and immortal polymerization of *rac*-LA. Subsequent work showed that the catalyst was also capable of the immortal polymerization of the cyclic ester β -butyrolactone (BBL) to produce poly(hydroxybutyrolactone) (PHB).

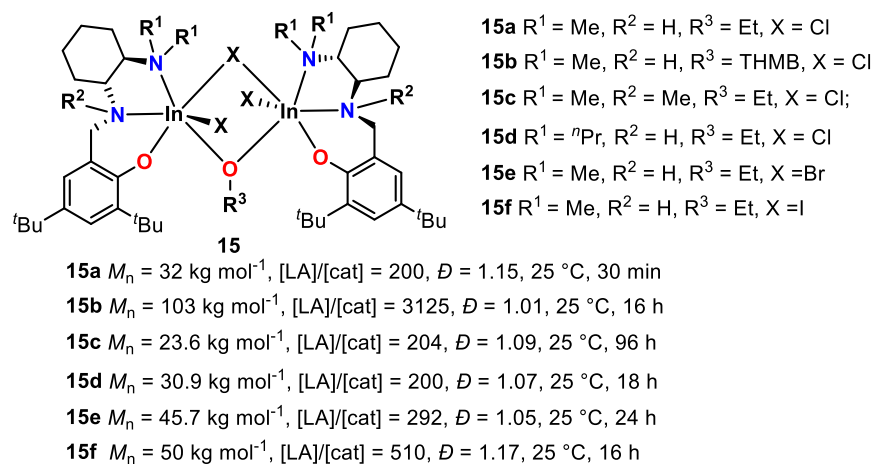


Figure 1.18. Dinuclear indium diamino phenolate complexes (**15a-f**) reported by Mehrkhodavandi *et al.*

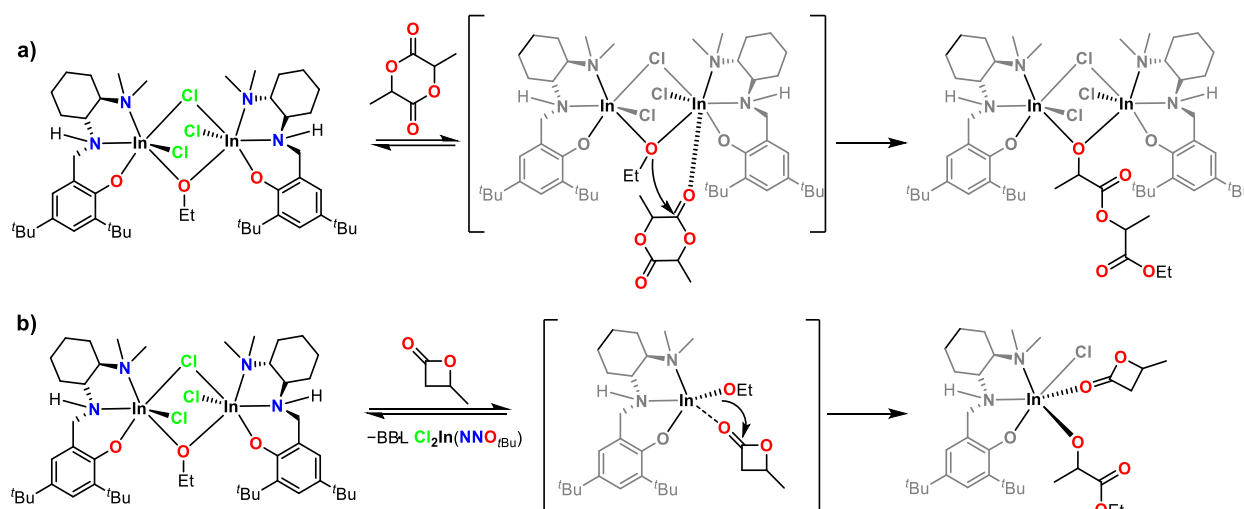


Figure 1.20. a) The dinuclear mechanism for LA polymerization and the b) mononuclear mechanism for BBL polymerization.

The reactivity and isoselectivity of **15a** could be significantly influenced by changing the ligand environment around the complex. Subsequent work by Mehrkhodavandi and co-workers modified **15a** through changing the ligand chirality, substituents on the terminal and central amines (**15c,d**), bridging ligands (halogens, alkoxides, aryloxides, and hydroxides), phenolate substituents, and ligand backbone.³⁹ The replacement of the central secondary amine donor of **15a** with a tertiary amine donor (**15c**) resulted in over a 100-fold decrease in activity, potentially due to the absence of N-H hydrogen bonding and consequent dissociation of the dinuclear complex. When a bulkier N substituent is used in the terminal tertiary amine (**15d**) there was loss of isoselectivity due to the dissociation of the dinuclear complex. Indicating that isoselectivity was associated with the dinuclear mechanism of ROP.

The rate of LA polymerization increased when moving from chloride to iodide bridging ligands (**15a**, **15e**, and **15f**) due to the lowered electrophilicity of the indium centers of **15e** and **15f**.³⁹ The polymerization rates of derivative complexes with bridging aryloxy ligands (**15g-k**) was correlated to the electron donating ability of each aryloxy initiator (Figure 1.21). Strongly electron

withdrawing, *para*-nitro substituted complex **15k** showed only low conversions even at longer reaction times. While more electron donating phenoxides (**15g-j**) showed increased activity, they were still less active with slow initiations and less control compared to the ethoxy bridged parent complex, **15a**.

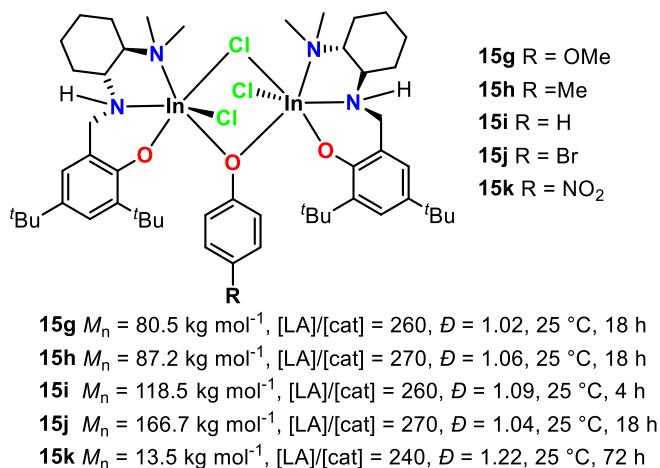


Figure 1.21. Indium diamino phenolate complexes with aryloxy initiators (**15g-k**) reported by Mehrkhodavandi *et al.*

The steric bulk of the *ortho* substituent of these complexes influenced the tacticity of the resulting polymer. The use of the silyl substituted catalyst **15l** in the polymerization of *rac*-LA resulted in atactic PLA ($P_m \sim 0.5$). While bulky adamantyl (**15m**) or cumyl (**15n**) substituents had a small effect on reaction rate, the stereoselectivity was similar to the parent complex, **15a** (Figure 1.22). One possible explanation for the decreased stereoselectivity observed with a bulkier catalyst could be the dissociation of the dinuclear catalyst in the presence of lactide in solution.

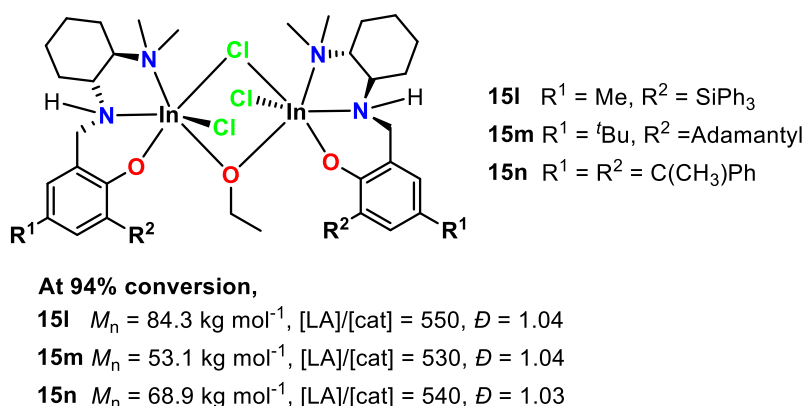


Figure 1.22. Indium diamino phenolate complexes with various *ortho*-phenol substituents (**15l-n**) reported by Mehrkhodavandi *et al.*

Changing the ligand backbone from chiral diaminocyclohexane (**15a**) to achiral ethylenediamine (**16**) did not significantly alter reactivity (Figure 1.23). However, the ROP of *rac*-LA resulted in purely atactic PLA ($P_m = 0.5$) indicating the importance of ligand environment in determining polymer microstructure and properties.

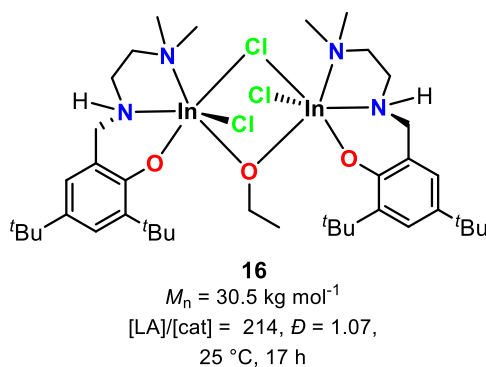
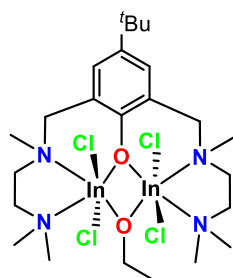


Figure 1.23. Indium diamino phenolate complex with an achiral backbone (**16**) reported by Mehrkhodavandi *et al.*

In the hopes of preventing dissociation of indium centers and encouraging tandem reactivity Mehrkhodavandi and co-workers used a bis(diaminophenolate) ligand (a similar structural motif to **14a-d**) to produce the dinucleating indium complex **17** by (Figure 1.24).⁴¹ However, catalyst **17** displayed a rigid octahedral structure and a congested active site. This was unlike a majority of previously described indium catalysts featuring square-pyramidal or square-

planar structures which provide a free coordination site that can be utilized for LA coordination. This resulted in very slow activity in contrast to **16** or **15a**. Nevertheless, **17** showed good heteroselectivity in the ROP of *rac*-LA ($P_r = 0.87$). Considering the lack of chirality in **17**, this stereoselectivity was attributed to chain-end control.



17

$M_n = 17.1 \text{ kg mol}^{-1}$
 $[LA]/[cat] = 200$, $\bar{D} =$
 1.06,
 25 °C, 8 days

Figure 1.24. Indium bis(diaminophenolate) complex (**17**) reported by Mehrkhodavandi *et al.*

Mehrkhodavandi and co-workers went on to develop another family of indium complexes with tridentate (aminoethyl)imino- (**18a,b**) and phosphininimino-phenolate (**18c**) ligands capable of ROP of *rac*-LA and ϵ -CL (Figure 1.25).⁴² While all three complexes exhibited controlled reactivity, the presence of the potentially hemilabile morpholine group on **18b** caused a 20-fold decrease in the rate of ROP of *rac*-LA, possibly due to the morpholine moiety competing with monomer. However, **18b** showed a small heterotactic bias ($P_r = 0.63$) compared to the other complexes. Catalysts **18a-c** were also capable of fast ROP of ϵ -CL, albeit with a significant loss of molecular weight and dispersity control. Sequential polymerization of ϵ -CL and *rac*-LA with **18a** resulted in PCL-*b*-PLA block co-polymer while only **18c** produced PLA-*b*-PCL with a reverse order of polymerization. When *rac*-LA and ϵ -CL were added at the same time only **18a** formed

PLA-*b*-PCL copolymers. It is noteworthy that ϵ -CL conversion was noticeable only after *rac*-LA was fully converted.

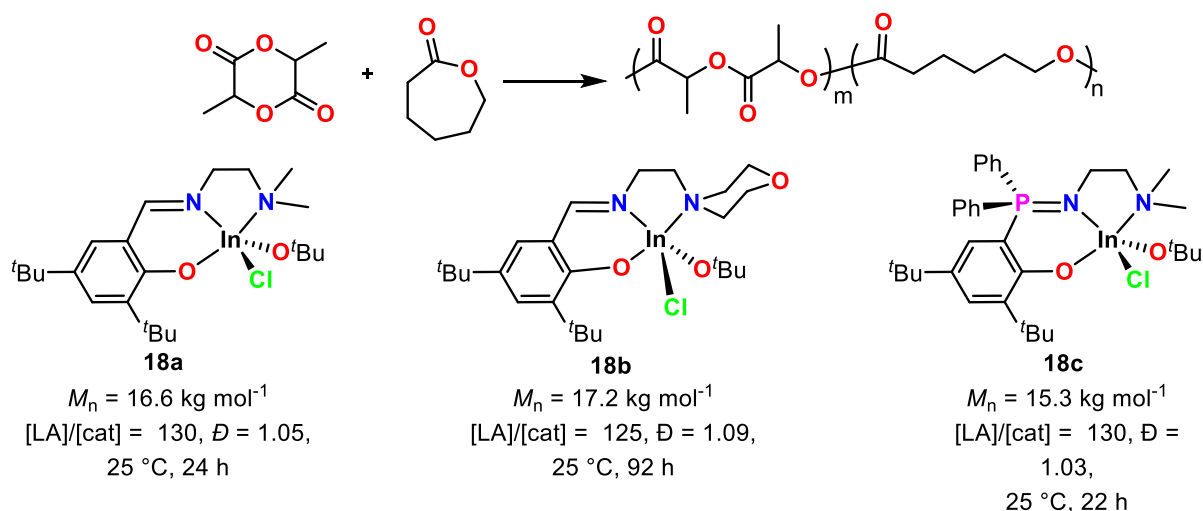


Figure 1.25. Block copolymerization of *rac*-LA and ϵ -CL by the (aminoethyl)iminophenolate (**18a,b**) and phosphininiminophenolate (**18c**) complexes reported by Mehrkhodavandi *et al.*

In another variation of the tridentate iminophenolate motif, Mehrkhodavandi and co-workers connected two (aminoethyl)iminophenolate ligands through a binaphthol linker and fashioned a bimetallic indium complex (**19a**) for the ring opening copolymerization (ROCOP) of CO_2 and cyclohexene oxide (CHO) to selectively produce polycarbonate precluding the formation of undesirable side products such as cyclic carbonate and polyether (Figure 1.26a and 1.6b).⁴³ The monometallic analogue of this complex, **19b** showed significantly lower conversion and produced a mixture of products. The stark contrast in reactivity between **19a** and **19b** can be explained through a cooperative intramolecular initiation mechanism whereby one indium center activated a coordinated epoxide and a chloride from second indium center ring opens the monomer allowing for CO_2 insertion (Figure 1.26c). It is also possible that the In-In spacing prevents ‘backbiting’ and forming cyclic carbonates.

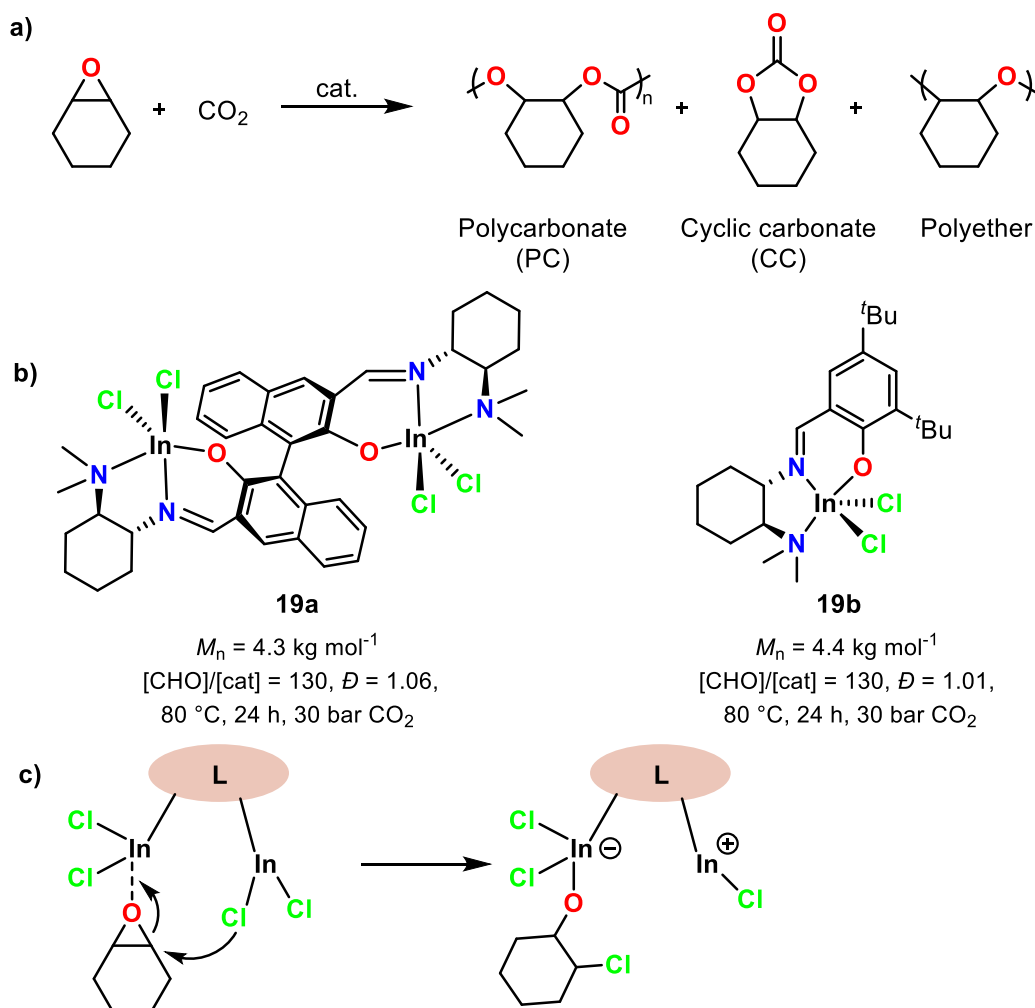


Figure 1.26. a) ROCOP of CO_2 and CHO to form polycarbonate and possible side products, b) bimetallic (**19a**) and monometallic (**19b**) indium iminophenolate complexes reported by Mehrkhodavandi *et al.*, and c) the proposed intramolecular initiation mechanism.

1.2.2.4 Indium catalysts with tetradentate ligands

Many of the tetradentate ligands used in indium catalysts are based on the (ONNO)-salen ligand motif composed of a diimino-bis(phenolate) backbone. Carpentier and Sarazin used chiral (1,2)-diphenylethylene-salen ligands to synthesize the alkylindium complexes **20a-c** (Figure 1.27).⁴⁴ These complexes could polymerize *rac*-LA with 1.0 equiv. of BnOH through the activated monomer mechanism. While **20a-c** were faster than analogous aluminum complexes, they did not

show any stereocontrol in the ROP of *rac*-LA. According to kinetic studies, an increase in electronic density and steric congestion at the metal atom led to a decrease in catalytic activity in the following order **20c** > **20a** > **20b**.

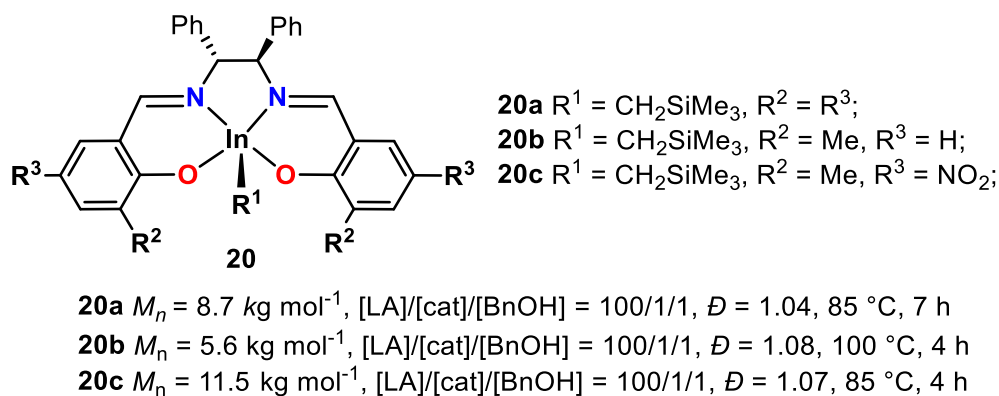
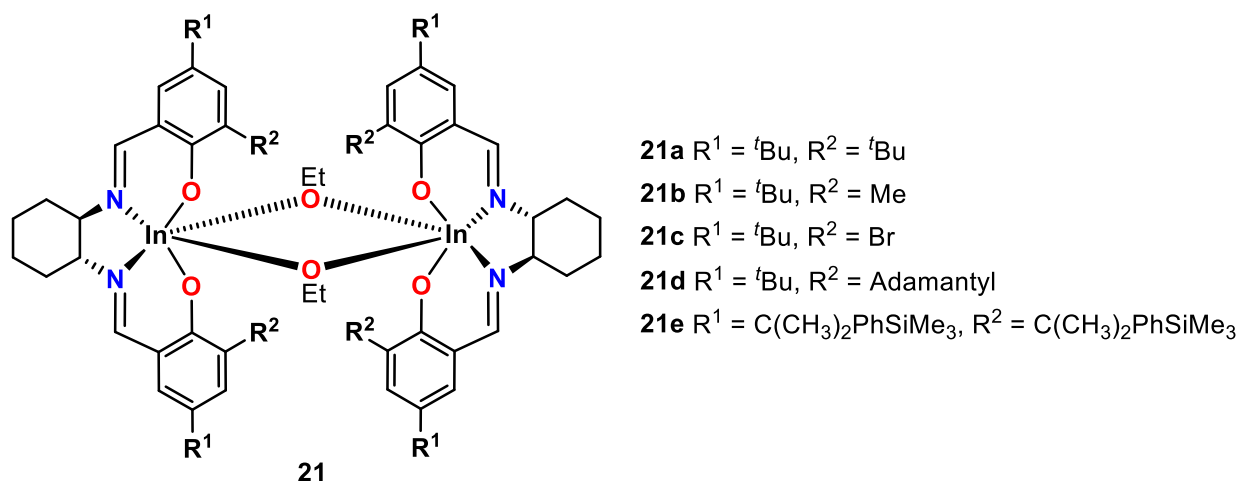


Figure 1.27. Indium (1,2)-diphenylethylene-salen complexes (**20a-c**) reported by Carpentier *et al.*

Mehrkhodavandi and co-workers used ‘Jacobsen’s ligand, a salen ligand with a diaminocyclohexyl backbone, to support the dinuclear indium ethoxy complex, **21a**, for the living polymerization of *rac*-LA (Figure 1.28).³⁹ When homochiral (*RR,RR*)-**21a** was used for the ROP of *rac*-LA, iso-enriched PLA could be obtained ($P_m=0.77$) through an enantiomeric site control mechanism. (*RR,RR*)-**21a** preferentially consumes L-LA monomers, resulting in a polymer chain enriched with L-LA and a high P_m value. The depletion of L-LA caused more D-LA to be incorporated. With increasing conversion, the latter half of the polymer chain is mainly composed of D-LA, indicating the formation of a stereoblock polymer. Further mechanistic studies indicated that **21a** dissociates in the presence of donors and the active catalytic species is mononuclear in nature. This was confirmed when less bulky *ortho*-phenyl substituents on homochiral (*RR,RR*)-**21b** and (*RR,RR*)-**21c** resulted in lowered reactivity and stereoselectivity. While increasing the steric bulk of the *ortho*- substituents ((*RR,RR*)-**21c** and (*RR,RR*)-**21d**) increased the rate of reaction, it did not have a significant impact on isoselectivity.



21a $M_n = 34.8 \text{ kg mol}^{-1}$, $[LA]/[cat] = 200$, $\bar{D} = 1.39$, 25°C , 1 h

21b $M_n = 5.6 \text{ kg mol}^{-1}$, $[LA]/[cat] = 200$, $\bar{D} = 1.19$, 25°C , 2 h

21c $M_n = 11.5 \text{ kg mol}^{-1}$, $[LA]/[cat] = 200$, $\bar{D} = 1.15$, 25°C , 2 h

21d $M_n = 8.7 \text{ kg mol}^{-1}$, $[LA]/[cat] = 200$, $\bar{D} = 1.42$, 25°C , 1 h

21e $M_n = 5.6 \text{ kg mol}^{-1}$, $[LA]/[cat] = 200$, $\bar{D} = 1.56$, 25°C , 1 h

Figure 1.28. Dinuclear indium salen complexes (**21a-e**) reported by Mehrkhodavandi *et al.*

To exclude the effects of aggregation on reactivity a series of mononuclear indium-salen complexes were prepared by substituting the ethoxy initiator with 2-pyridinemethoxide (**22a-c**) (Figure 1.29).³⁹ The dinuclear (*RR,RR*)-**21a** and the mononuclear analogue (*RR,RR*)-**22a** behaved similarly during polymerization except for a short initiation stage in (*RR,RR*)-**21a**. Both had similar activity, isoselectivity, and kinetic profiles. However, less bulky catalysts such as (*RR,RR*)-**21b** had longer initiation periods which disappear entirely in their mononuclear analogues ((*RR,RR*)-**22b**). This further highlights that the mononuclear species is responsible for propagation in these indium salen complexes and dissociation of dimers was necessary for initiation of LA polymerization.

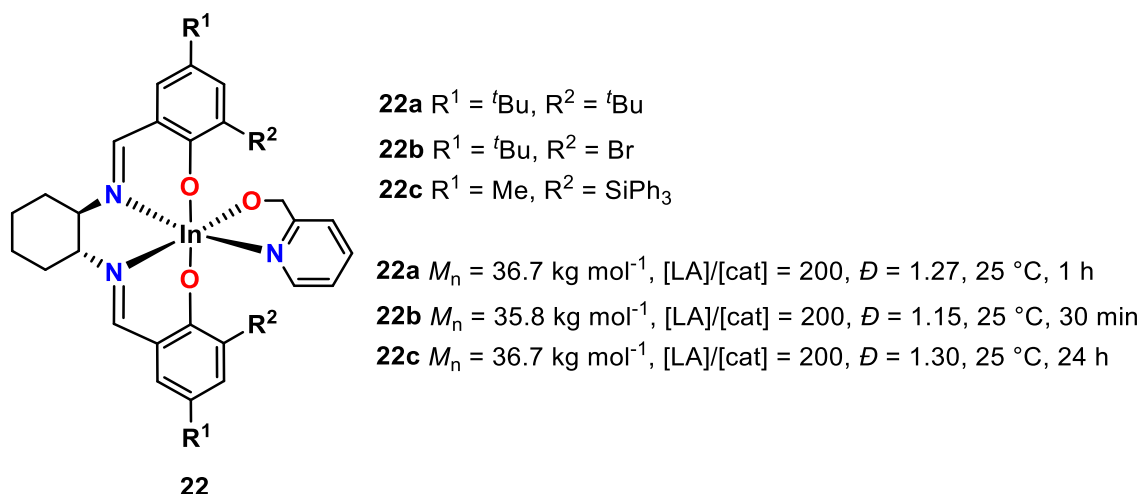


Figure 1.29. Mononuclear indium salen complexes (**22a-c**) reported by Mehrkhodavandi *et al.*

When the salen backbone is replaced by binam(1,1'-binaphthyl-2,2'-diamine) the aggregation issue became more severe in the resulting SalBinam complexes **23a** and **23b** (Figure 1.30).³⁹ The polymerization of *rac*-LA using **23a** was sluggish and needed high temperatures to reach complete conversion, resulting in atactic PLA with higher than anticipated molecular weights. Complex **23b** was even more unreactive and it was discovered that **23a** transformed into inactive **23b** during the polymerization process. It was hypothesized that the slower polymerization in the dinuclear complex **23a** was due to increased steric hindrance. Aggregation played a significantly larger role compared to the aluminum and gallium counterparts, illustrating the importance of ligand design for indium catalysts.

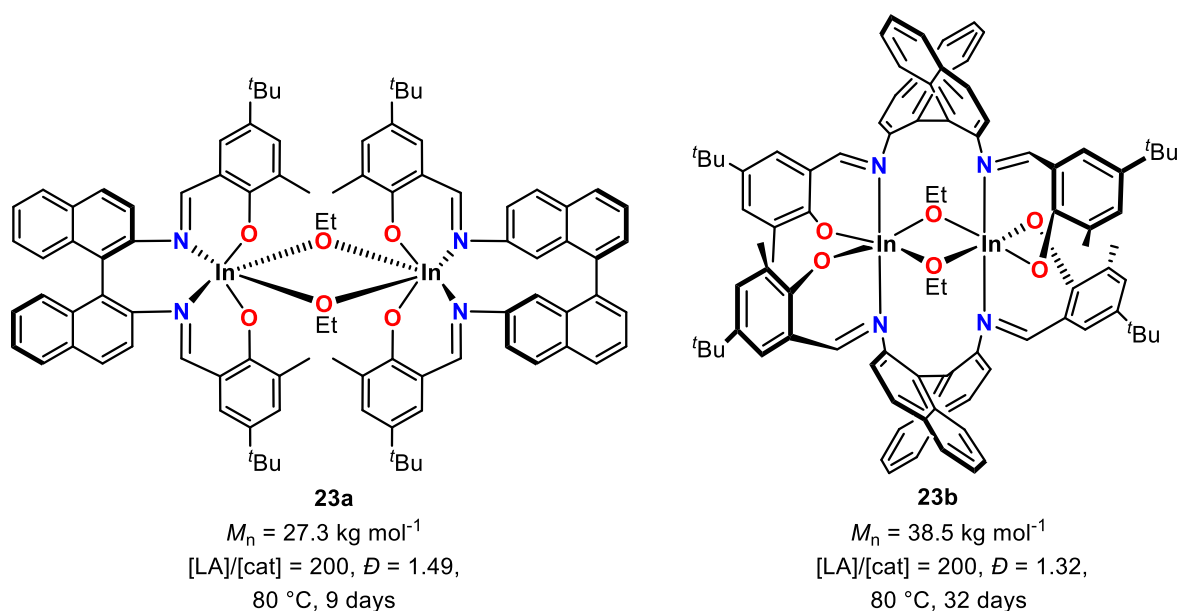


Figure 1.30. Dinuclear SalBinam complexes (**23a** and **23b**) reported by Mehrkhodavandi *et al.*

As another derivative of the salen ligand motif, ethylenediamine (**24a** and **25a**) and diamnocylohexane (**24b** and **25b**) spined salen-like tetradentate dialkoxy diimino ligands were used by Carpentier and co-workers for indium complexes capable of polymerizing *rac*-LA (Figure 1.31).⁴⁵ Interestingly, an attempt to form a methylindium complex with these ligands from InCl_3 and MeLi resulted in the heterobimetallic complexes **24a** and **24b** centered around a chelated lithium atom. The alkylindium complexes **25a** and **25b** showed some moderate reactivity in the ROP of *rac*-LA with low initiation efficiencies owing weak nucleophilicity of the alkyl group in the coordination-insertion mechanism. Both complexes showed improved control over polymerization though an activated monomer mechanism in the presence of isopropyl alcohol (*i*PrOH). The heterobimetallic complexes **24a** and **24b** were also capable of alkyl-initiated ROP of *rac*-LA, albeit with increased initiation efficiency. Additionally, **24a** and **24b** displayed a slight

heterotactic bias ($P_r \sim 0.60$). The increased activity was attributed to the ejected indium center having lower steric hindrance.

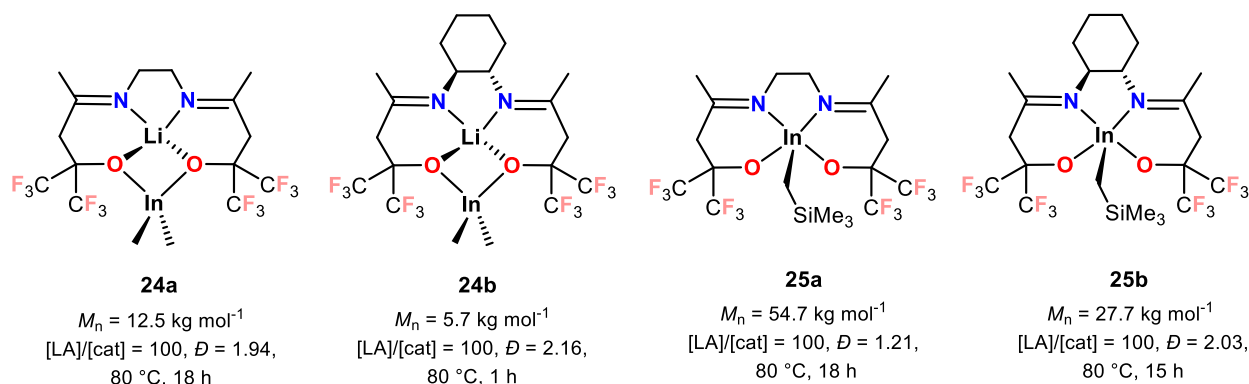


Figure 1.31. Indium dialkoxy diimino complexes (**24a** and **24b**) reported by Carpentier *et al.*

The SalBinam complex **26** (Figure 1.32) could slowly polymerize *rac*-LA to produce atactic PLA in the presence of 1 equiv. of BnOH in toluene.⁴⁶ However, using a polar solvent such as THF slightly increased reactivity and showed an increased heterotactic bias ($P_r = 0.70$) suggesting that THF may act as a non-innocent co-ligand. The lack of alcoholysis, when **26** is mixed with BnOH, pointed to an activated monomer mechanism of polymerization.

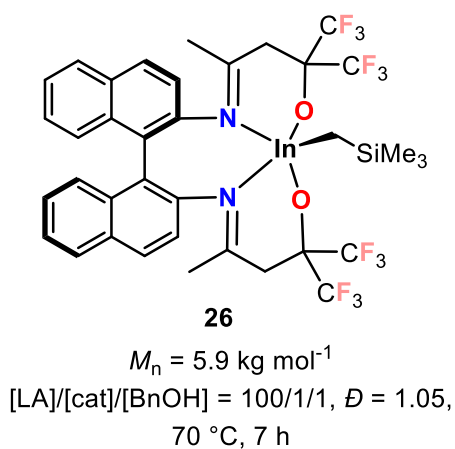


Figure 1.32. Indium SalBinam dialkoxy diimino complex (**26**) reported by Carpentier *et al.*

A unique modification of the ONNO-salen ligand type incorporating a ferrocene backbone was used in an indium alkoxy complex (**27**) that was capable of ROP of various lactones was

reported by Diaconescu and Quan (Figure 1.33).⁴⁷ Complex **27** was capable of polymerizing L-LA, *rac*-LA, and trimethylene carbonate (TMC) with good control. The most remarkable reactivity was towards ϵ -CL, δ -valerolactone (δ -VL), and BBL. These monomers were polymerized to completion within minutes at ambient temperatures giving high molecular weight polymers. Notably, **27** was the first indium catalyst reported for the polymerization of δ -VL. However, all the polymerizations showed low initiation efficiencies indicating a slow initiation step in the coordination-insertion mechanism.

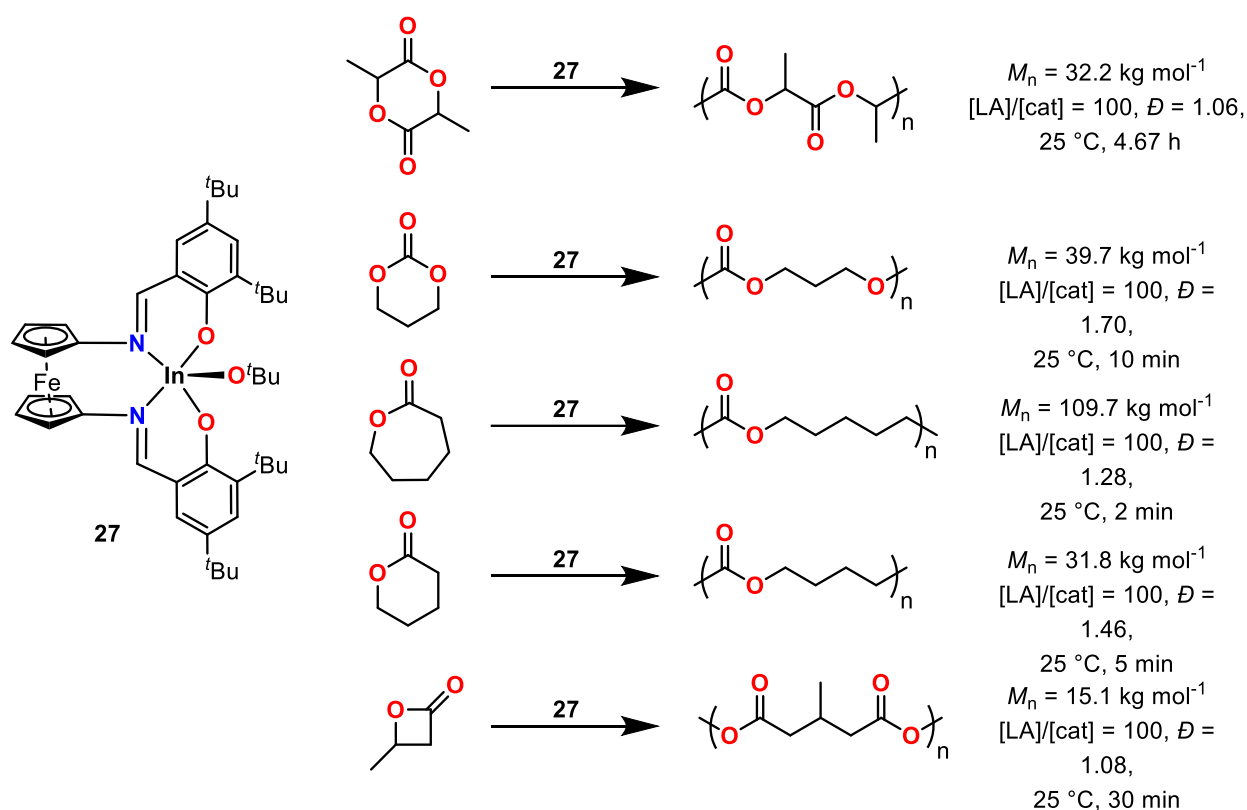


Figure 1.33. Ferrocene backboned indium salen complex (**27**) reported by Diaconescu and Quan and its monomer scope.

A variation with phosphinimine bonds replacing the imine bonds of **27** was used as a redox switchable catalyst (**28a** and **28b**) (Figure 1.34).⁴⁸ Complex **28a** and **28b** contained Fe(II) and Fe(III) in the ligand backbones respectively. These could be interconverted readily by oxidizing

28a with ferrocenium tetrakis(3,5-bis(trifluoromethyl)phenyl)borate ($\text{FcBAR}^{\text{F}}_{24}$) or by reducing **28b** with cobaltocene (CoCp_2). The reduced complex **28a** was inactive in the ROP of TMC at ambient temperature. However, when oxidized to **28b** conversions of up to 49% were observed at the end of 24 h. These results suggested that withdrawing electrons from indium through the oxidation of the ligand backbone increases the rate of polymerization of TMC.

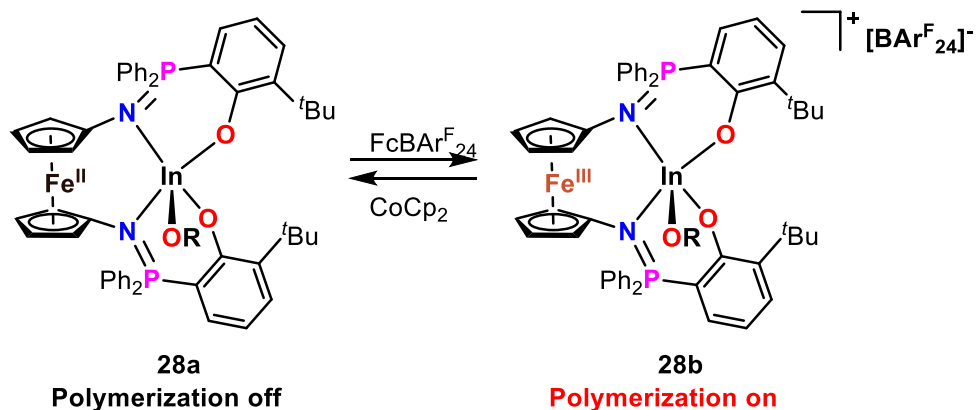


Figure 1.34 Redox active indium ferrocene phosphasalens complexes (**28a** and **28b**) reported by Diaconescu *et al.*

The first indium phosphinimine salen (phosphasalens) catalysts (**29a-f**) for the ROP of *rac*-LA were reported by Williams and co-workers (Figure 1.35).^{49,50} Phosphasalens ligands contain an iminophosphorane backbone that can provide higher electron density to the metal center, resulting in faster reaction rates compared to salen analogues. Complexes **29a** and **29b** were capable of rapid, controlled, living polymerization of *rac*-LA with a high degree of isoselectivity to produce stereoblock PLA. However, **29a** was 4-times faster than **29b** and showed a greater degree of isoselectivity ($P_m = 0.85\text{--}0.87$ vs. $0.72\text{--}0.75$). This was attributed to the bulky *ortho*-cumyl substituents on **29a** having a greater directing effect. Substituting the ethylene linker with propylene (**29c**) and dimethyl propylene (**29d**) resulted in notably slower rates of polymerization. Asymmetric *tert*-butyl and phenyl substituents on each phosphorus resulted exclusively in *meso*-isomers of indium complexes (**29e** and **29f**) with *R,S* stereochemistry at each phosphorus. While

slightly slower than **29a**, **29e** and **29f** showed significantly enhanced isoselectivity ($P_m > 0.90$) arising from a chain-end control mechanism. These complexes were also active for the rapid polymerization of ϵ -CL (**29a**, **29c**, **29d**, and **29f**), BBL (**29a**, **29c**, and **29f**), ϵ -decalactone (**29a**, **29c**, and **29f**), and δ -hexalactone (**29a** and **29c**).

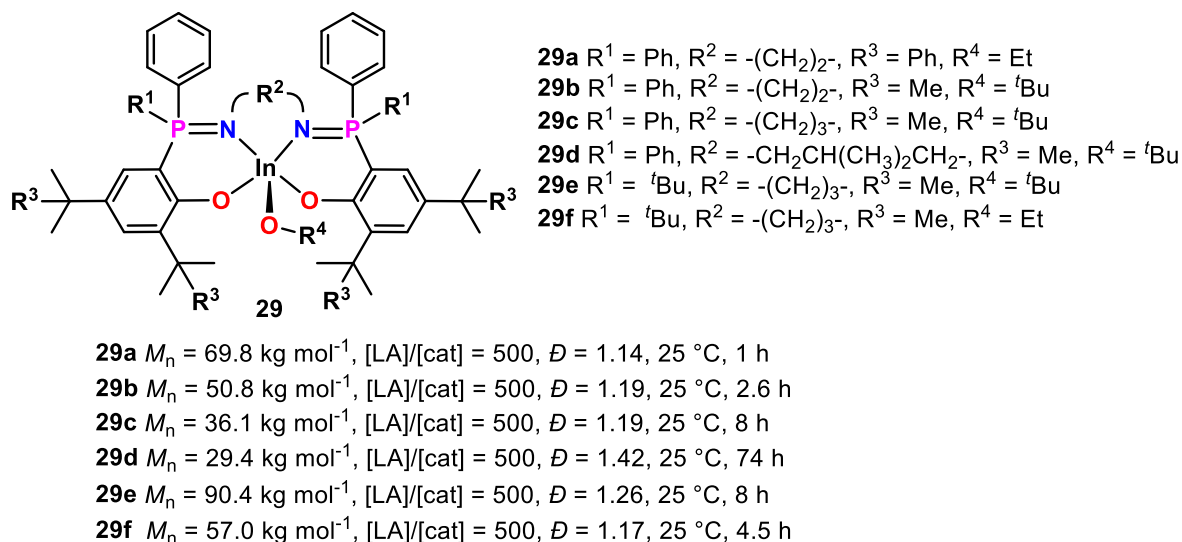
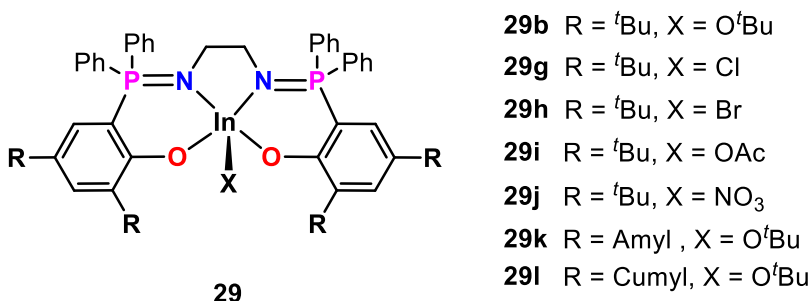


Figure 1.35. Indium phosphasalen complexes (**29a-f**) for *rac*-LA polymerization reported by Williams *et al.*

Williams and co-workers proceeded to use a series indium phosphasalen complexes (**29b**, **29g-l**) as the first indium catalysts for the ROCOP of CO_2 and CHO to form polycarbonate (Figure 1.36).⁵¹ Complex **29g** was active for the ROCOP reaction under low CO_2 pressure (1 bar) in the absence of co-catalysts but showed polymodal molecular weight distributions. The presence of co-catalysts either inactivated **29g** or produced cyclic carbonate. As Br was a better leaving group that facilitates ‘backbiting’, **29h** produced mostly cyclic carbonate. Complex **29i** was inactive for this reaction while **29j** produced polymers with largely ether linkages. However, the alkoxy complex **29b** showed high selectivity for polycarbonate giving monomodal polymer with a narrow dispersity. The more sterically hindered **29l** with a cumyl ortho-phenolate substituent was twice as

active as **29b**. Catalysts **29b**, **29k**, and **29l** also showed chain end control of isoselectivity ($P_m = 0.76-0.86$) in the **29b** < **29k** < **29l** increasing order.



At 1 bar CO₂,

29b $M_n = 1.41 \text{ kg mol}^{-1}$, $[\text{CHO}]/[\text{cat}] = 100$, $D = 1.23$, 60°C , 48 h

29g Polymodal M_n distribution, $[\text{CHO}]/[\text{cat}] = 100$, $D = 1.23$, 60°C , 48 h

29h M_n = N/A kg mol⁻¹, [CHO]/[cat] = 100, \bar{D} = N/A, 60°C, 48 h

29i $M_n = \text{N/A kg mol}^{-1}$, $[\text{CHO}]/[\text{cat}] = 100$, $D = \text{N/A}$, 60°C , 48 h

29j $M_0 = 7.50 \text{ kg mol}^{-1}$, $[\text{CHO}]/[\text{cat}] = 100$, $D = 1.44$, 60°C , 48 h

29k $M_0 = 1.60 \text{ kg mol}^{-1}$, $[\text{CHO}]/[\text{cat}] = 100$, $D = 1.23$, 80°C , 48 h

29l $M_0 = 3.40 \text{ kg mol}^{-1}$, $[\text{CHO}]/[\text{cat}] = 100$, $D = 1.32$, 60°C , 23 h

Figure 1.36. Indium phosphasalen complexes (**29b-29g-l**) ROCOP of CO₂ and CHO reported by Williams *et al.*

Based on kinetic and mechanistic studies Williams and co-workers proposed a monometallic mechanism different from the previously reported bicomponent or bimetallic mechanisms (Figure 1.37). The initiation step proceeded with the formation of 1,2-cyclohexanediol through ring-opening of CHO by trace amounts of water. This diol acted as a CTA and formed a new cyclohexanediol alkoxide which was inactive for epoxide polymerization, precluding ether linkage formation. After initiation, CO₂ was rapidly inserted to form a stable hexacoordinate indium carbonate species as the catalyst resting state. This was followed by the coordination of an epoxide molecule and slow ring-opening to form a new alkoxide bond, regenerating the active catalyst. The reduced Lewis acidity of indium phosphasalen complexes as well as the steric bulk of *ortho*-phenolate substituents was proposed to destabilize the indium carbonate intermediate allowing further epoxide coordination. Additionally, by virtue of its larger

ionic radius, indium could potentially allow for *cis*-coordination of epoxide and carbonate, which could in turn lower the barrier to insertion and enable the mononuclear polymerization pathway

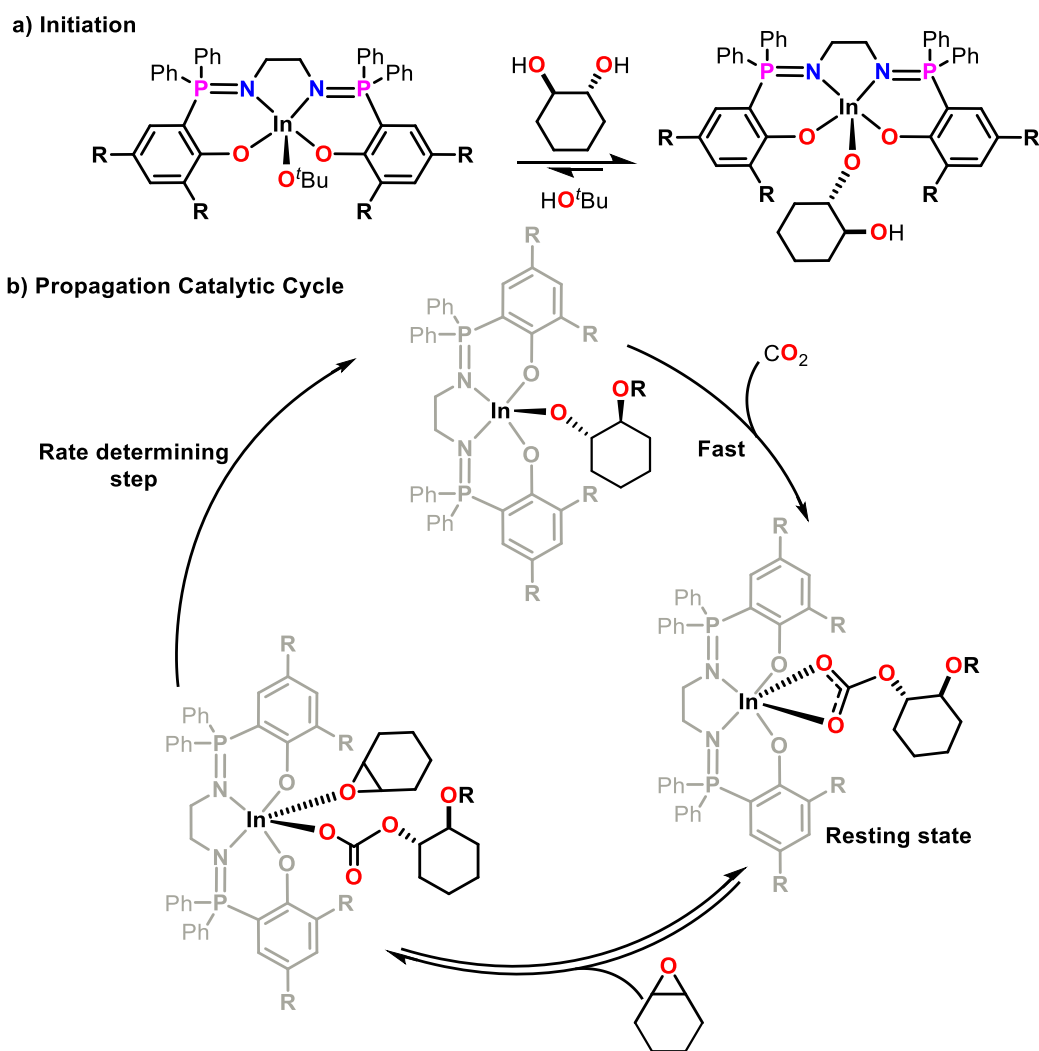


Figure 1.37. Proposed mechanism for the ROCOP of CO₂ and CHO by indium phosphasalen complexes.

The salen framework was further modified by Mehrkhodavandi and co-workers to produce a PNNO-type asymmetric hemi-salen indium complex possessing a hemilabile phosphine donor arm (**30**) for the ROCOP of CO₂ and epoxide (Figure 1.38).⁵² Unlike the phosphasalen complexes **29b**, **29k**, and **29l**, **30** was only active in the presence of co-catalysts and at high CO₂ pressures (30 bar). Using 0.5 equiv. tetrabutylammonium azide ([TBA]N₃) as a co-catalyst produced the

best selectivity for polycarbonate formation (91%). Analogous aluminum and gallium complexes showed significantly reduced selectivity for polycarbonate formation.

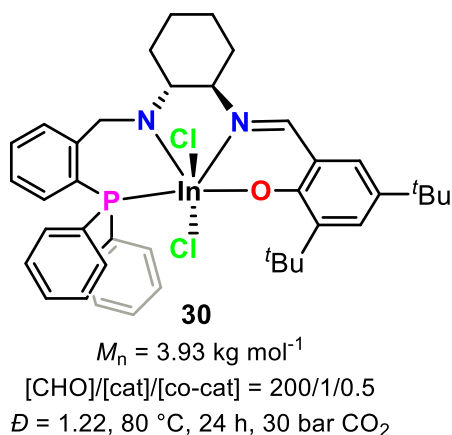


Figure 1.38. Indium salen complex with a phosphine pendant arm (**30**) reported by Mehrkhodavandi *et al.*

The complex **30**/[TBA] N_3 system followed a bicomponent mechanism in the formation of polycarbonate initiated by the coordination of CHO to the indium center (Figure 1.39). The activated CHO is ring opened by external nucleophilic attack by an N_3^- ion. CO_2 is inserted into the new indium alkoxide bond to form an indium carbonate intermediate. Polycarbonate is formed by the insertion of additional CHO and CO_2 . The propagating chain dissociates from the indium center allowing additional CHO coordination and ring opening by the dissociated carbonate chain end. As an example of using ligand architecture to modulate the Lewis acidity of indium the phosphine donor arm played two pivotal roles in the system, first, it was responsible for reducing the electrophilicity of the indium center to polarize the In-OR bond, permitting chain dissociation. Second, the bulky phosphine arm competes with CHO for coordination space, controlling CHO coordination and suppressing ether linkage formation.

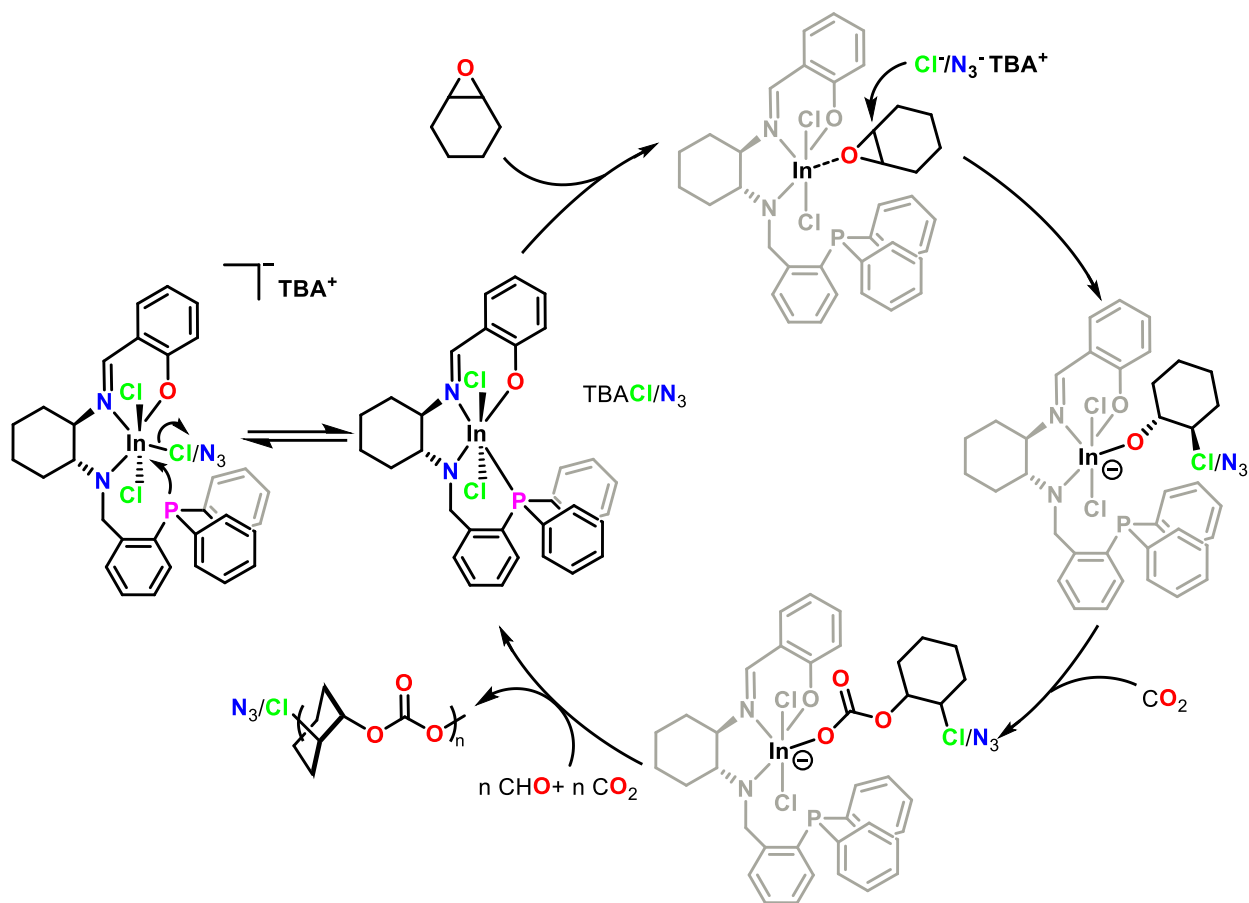


Figure 1.39. Proposed mechanism for the ROCOP of CO_2 and CHO by **30**.

The salen ligand motif can be further modified by reducing the imine moieties to secondary amines forming tetradentate salan ligands. This minor change in the ligand backbone can have far-reaching consequences for the reactivity of indium complexes. This was exemplified by the work of Mehrkhodavandi and co-workers in the formation of an air and moisture stable indium complex (*RR,RR*)-**31b** (Figure 1.40).⁵³ When the alkoxy bridged complex (*RR,RR*)-**31a** was exposed to trace amounts of water the hydroxy bridged, water and air stable catalyst (*RR,RR*)-**31b** was formed. Immortal polymerization of *rac*-LA in air with 10 equiv. ethanol as a CTA with (*RR,RR*)-**31b** produced highly controlled polymerization products. Catalyst (*RR,RR*)-**31b** was capable of controlled melt polymerization of up to 10 000 equiv. of *rac*-LA and tolerating up to 100 equiv.

of alcoholic CTAs. When THMB was used as a CTA, high molecular weight star-shaped PLA could be obtained from unpurified commercial grade *rac*-LA. Additionally, diblock PLLA-*b*-PDLA, PHB-*b*-PLA, and triblock PLLA-*b*-PDLA-*b*-PLLA star-shaped block copolymers were synthesized by sequential addition of enantiopure monomers. While the analogous salen complex **21a** decomposed within hours of air or moisture exposure, (*RR,RR*)-**31b** was stable for up to 2 months exposed to air or to 100 equiv. of water. Monomer purity or atmosphere (inert or air) had no impact on the polymer products.

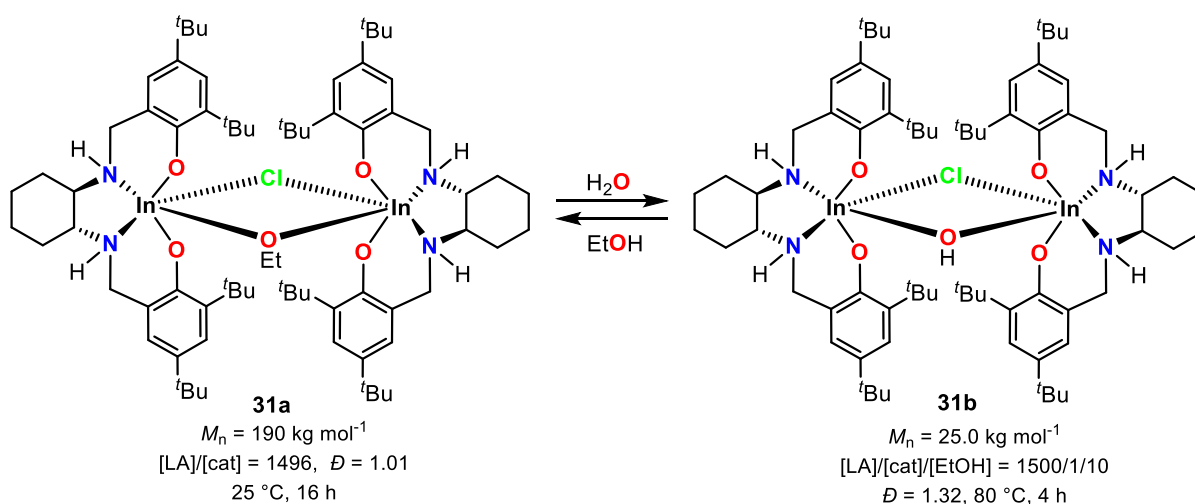


Figure 1.40. Air and moisture stable dinuclear indium salen complexes (**31a** and **31b**) reported by Mehrkhodavandi *et al.*

Two other salen ligands with chiral 2,2'-bipyrrolidine (**32a**) and achiral methyl substituted ethylenediamine (**32b**) backbones to support indium chloride complexes were reported by Buchard and Jones (Figure 1.41).⁵⁴ Much like the InCl_3 based system **1**, efficient ROP of *rac*-LA could only be achieved in the presence of BnOH and NEt_3 . Complex **32a** showed improved heteroselectivity ($P_r = 0.82$) and control of polymerization compared to **1**. The achiral **32b** was significantly less selective ($P_r = 0.73$) with less control over molecular weight. The ROP of *rac*-LA with **32a** and **32b** was proposed to undergo a coordination-insertion mechanism with an *in situ* generated

alkoxide species, much like **1**. Analogous aluminum and gallium complexes were completely inactive. This differential reactivity was probably due to the larger ionic radius of indium allowing monomer coordination or the weaker M-X bond allowing the formation of the metal alkoxide active catalyst. The relative decrease in activity for these complexes in comparison to **15a** and **31a** could potentially be caused by the tertiary amine donors, similar to **15c**.

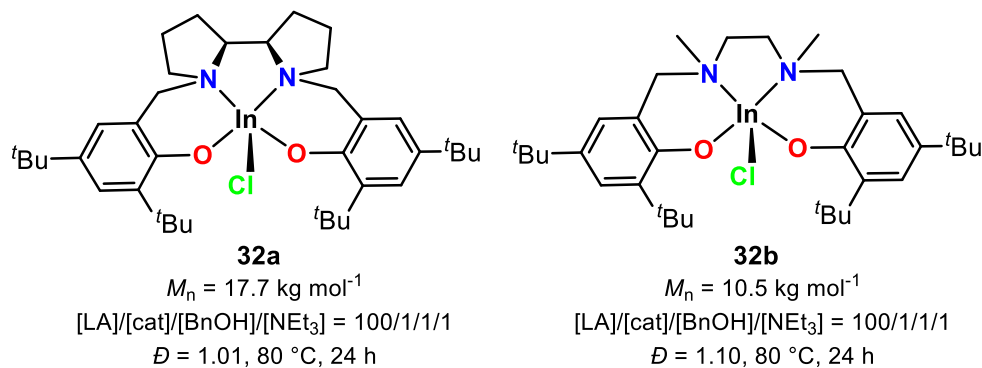


Figure 1.41. Indium salan complexes (**32a** and **32b**) reported by Buchard and Jones.

Indium catalysts (**33a-c**) bearing a tetradentate ligand system based on the salan motif composed of a (OSSO)-type ligand in place of the usual (ONNO)-salan was reported Okuda co-workers for the ROP of L-, *rac*-, and *meso*-LA giving isotactic, atactic, and syndiotactic PLA respectively (Figure 1.42).^{55,56} These were the first reports of tetradentate ligands supporting indium catalysts. Complex **33a** had a dinuclear solution structure while **33b** and **33c** bearing bulkier *ortho-para* cumyl substituents were mononuclear in solution. The mononuclear **33b** displayed a faster rate of polymerization in comparison to **33a**. Additionally, solution state NMR spectroscopic studies showed that the coordination of LA to the indium center of **33a** forms a mononuclear species, indicating that the active catalyst was mononuclear in nature. While **33a** and **33b** produced atactic PLA from *rac*-LA, the chiral complex **33c** showed enhanced heteroselectivity ($P_r = 0.77$) in THF.

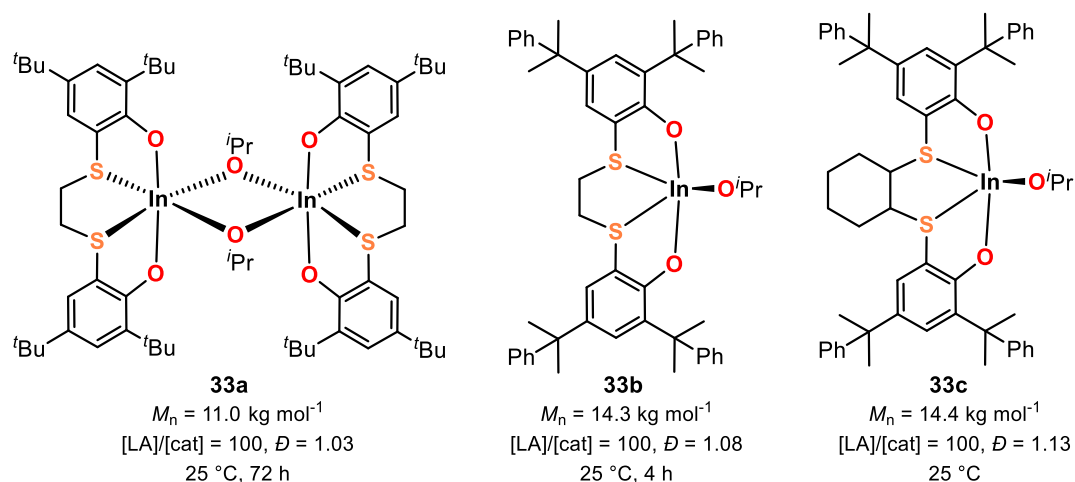


Figure 1.42. Indium (OSSO)-salan complexes (**33a-c**) reported by Okuda *et al.*

Deviating widely from the salen/salan ligand motif are tetradentate ligands that centered around tertiary amino N atom. These ligands coordinate to the metal center through the central tertiary amino group and three surrounding donor moieties, superficially resembling a ‘scorpionate’ ligand assembly. This type of asymmetric tertiary amine ligand with two phenolate groups and a pyridyl group was used by Sun and co-workers to support a water bridged dinuclear indium catalyst capable of polymerizing *rac*-LA (**34**) (Figure 1.43).⁵⁷ The restriction of motion upon coordination causes the central nitrogen atom to form a chiral center resulting in two homochiral water bridged species, N(*R,R*)-**34** and N(*S,S*)-**34**. The polymerization of *rac*-LA was unaffected by the presence of air, water, or alcohols, giving similar conversions, molecular weights and dispersities independent of conditions. Additionally, this system also showed a small heterotactic bias ($P_r = 0.65$) regardless of the polymerization conditions.

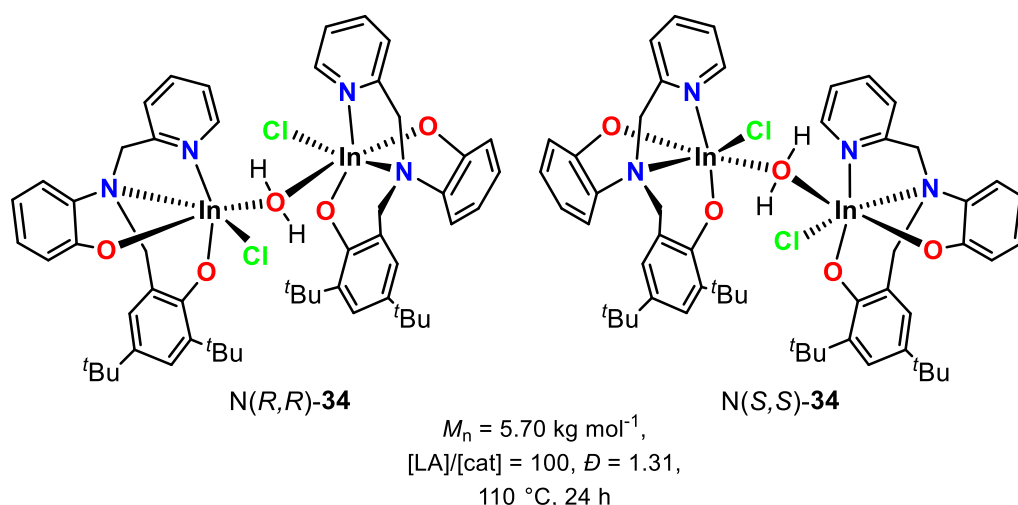


Figure 1.43. Indium tertiary amine phenolate complex (**34**) reported by Sun *et al.*

Another series of tertiary amine ligands were used by Mountford and co-workers to explore the effect of directing ligands on the ROP of *rac*-LA(**35a-d**,**36**,**37**, and **38**) (Figure 1.44).⁵⁸ Complexes **35a-d** and **36** included the bis(sulfonamide) amine ligands that were purported “phenolate mimics” due to the reduced basicity of the amide moieties from the electron withdrawing effects of the tosyl (-SO₂PhMe) groups. Complex **36** existed as a heterobimetallic indium ‘ate’ complex bridged by an isopropoxide to a lithium atom. A tertiary amine bis(phenolate) with a pyridine pendant arm supported the alkylindium complex **37**. Lastly, **38** was a dinuclear bridged alkoxide without directing ligands. While all these complexes were active to varying degrees, **35a**, **35d**, and **37** showed the best reactivity in the ROP of *rac*-LA owing to the strong donor effects of the pendant pyridyl moiety. Catalysts **35b** and **35c** were about 25-times slower in their reactivity due to lack of strong donor species to activate initiation. However, all these catalysts produced polymers with higher-than-expected molecular weights *i.e.*, with a low initiation efficiency, indicating that only 15-50% of the complex was participating in catalysis. The heterobimetallic complex **36** was very slow to react but had greater initiation efficiency and controlled polymerization as result of the superior initiating ability of alkoxides over alkyls or

amides. Kinetic studies indicated that the lithium atom may play an active role in the catalytic cycle. The directing ligand-free **38** exhibited rapid and controlled polymerization, with a 99.5% initiation efficiency. This reactivity was persistent even during melt polymerization. Additionally, when benzyl amine was used as a CTA, **35a** and **38** demonstrated well-controlled immortal ROP of *rac*-LA.

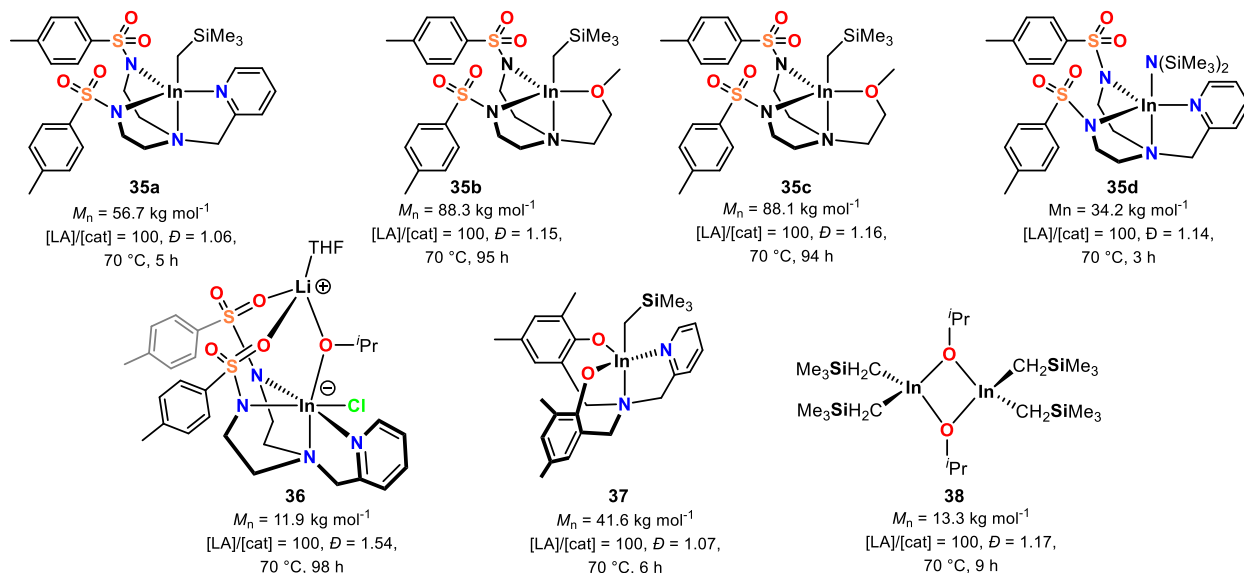


Figure 1.44. Various indium complexes (**35a-d**, **36**, **37**, and **38**) reported Mountford et al.

1.2.3 Polymerization reactions by cationic indium catalysts

While there are a few documented cases of cationic indium being used in catalysis, it is not as prevalent as the use of neutral indium catalysts. Moreover, out of the limited instances where cationic indium is employed in catalysis, only a small subset is utilized in polymerization reactions. However, the enhanced Lewis acidity of cationic indium complexes has allowed them to be used as initiators in polymerizations through cationic mechanisms. The ligands used for these catalysts largely resemble their neutral counterparts.

The first cationic indium complex to catalyze a polymerization reaction consisted of an alkylindium (aminocyclohexyl)iminophenolate species stabilized by a donor THF molecule and a

weakly coordinating $[\text{BAr}^{\text{F}}_{20}]$ (tetrakis(pentafluorophenyl)borate) counter ion (**39**) (Figure 1.45).⁵⁹ Complex **39** was able to polymerize ϵ -CL at 60 °C in dilute conditions. However, it was not capable of polymerizing epoxides under the same conditions. When epoxides and ϵ -CL reacted together at 60 °C under the same reaction conditions, **39** catalyzed the quantitative coupling of the two reactants to form spiro-orthoesters (SOEs). This reaction occurred through epoxide activation by coordination of the cationic indium center and the subsequent nucleophilic attack by the lactone. Increasing the temperature to 110 °C resulted in the double-ROP polymerization of SOEs to give perfectly alternating poly(ether-*alt*-ester) copolymer in high molecular weights and good control. The same result could be obtained in one pot by reacting the monomers at coupling conditions, removing the solvent, and subsequently increasing the temperature to polymerization conditions. Polymerization was proposed to proceed through a cationic mechanism initiated by activation of the SOE by indium. Control of polymerization was achieved through a combination of the moderate Lewis acidity of **39** and stabilization of the cationic growing chain end of the polymer by the bulky, weakly interacting $[\text{BAr}^{\text{F}}_{20}]$ counterion.

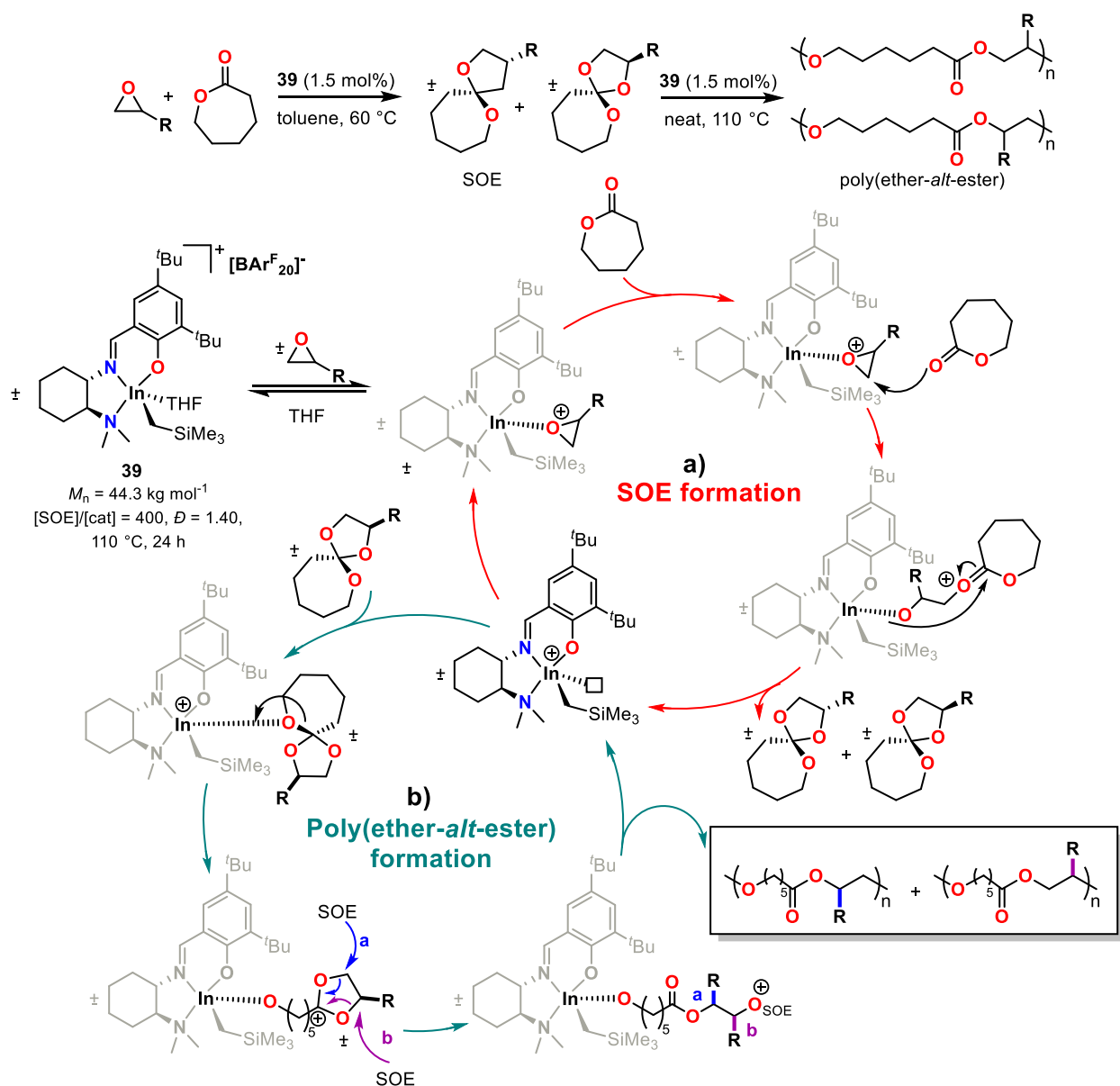


Figure 1.45. Proposed mechanisms for the temperature triggered formation (a) and polymerization (b) of SOEs using **39**.

Another series of cationic indium complexes (**40a-g**) were reported by Mehrkhodavandi and co-workers using the salen ligand motif (Figure 1.46).^{60,61} Each of these complexes were stabilized by two coordinated donor solvent molecules and a weakly interacting counterion. Unlike **40a-f**, owing to the more stable counter ion $[\text{BAR}^{\text{F}}_{24}]$ (tetrakis(3,5-

bis(trifluoromethyl)phenyl)borate), **40g** could be synthesized in diethyl ether and was isolated with two diethyl ether molecules coordinated. All the complexes, **40a-g** were active for the cationic ROP of epoxides (Figure 1.47a). However, **40c** showed higher activity in comparison to **40a**, **40b**, and **40d** due to the greater stabilizing effect of the $[\text{SbF}_6]^-$ counter ion on the cationic growing chain end of the polymer. Additionally, the donor solvents with higher donicity (the ability of a ligand to donate electrons to a central metal ion) had a deactivating effect with significantly slower initiation rates in the order **40e** > **40c** > **40f**. The polymerization of equimolar mixtures of epichlorohydrin (ECH) and another cyclic ether (THF, oxetane, or oxepane) with **40c** resulted in poly(A-*stat*-B) type statistical polyether copolymers, where the repeating unit distribution was a function of the ratio of comonomers (Figure 1.47b). While **40c** could not homopolymerize *rac*-LA, polymerization of ECH and subsequent addition of *rac*-LA at high conversions of ECH resulted in the poly(ether-*b*-lactide) block copolymer. The more stable species **40g** could form the block copolymer faster with greater control over polymerization in the presence of triphenylphosphine (PPh_3) (Figure 1.47c).

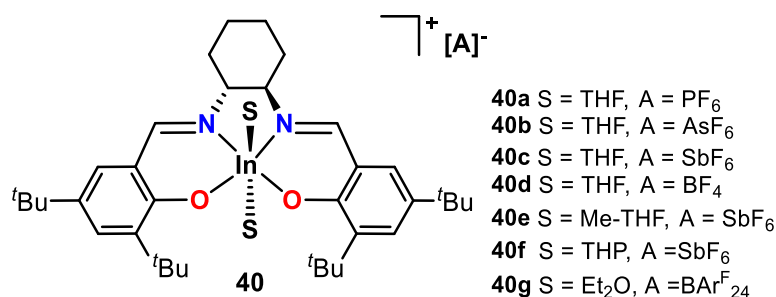


Figure 1.46. Cationic indium salen complexes (**40a-g**) reported by Mehrkhodavandi *et al.*

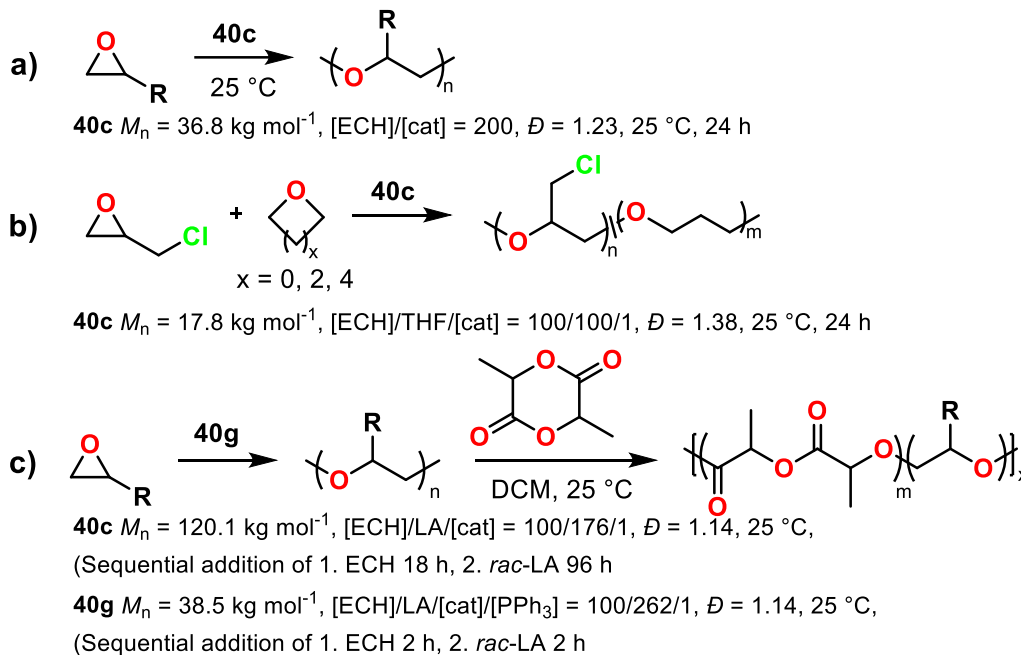


Figure 1.47. Polymerization reactions promoted by **40c** and **40g**. a) Polymerization of epoxides, b) statistical copolymerization of epoxides and cyclic ethers and, c) block copolymerization of epoxides and *rac*-LA.

The polymerization of epoxides was initiated through epoxide activation by coordination to the cationic indium center forming an oxonium ion (Figure 1.48a).⁶⁰ A subsequent nucleophilic attack by an incoming monomer, ring opens the first epoxide and forms a new indium alkoxide species. The cationic chain end grows by addition more monomer units. The addition of PPh_3 stabilized the cationic chain end and prevented further epoxide polymerization. At the opposite chain end the indium alkoxide acted as an initiator in the coordination-insertion mechanism of *rac*-LA polymerization (Figure 1.48b). The propagating species in the ROP *rac*-LA was the same as **21a**. Like **21a**, **40g** showed a degree of enantiomorphic site control giving an iso-enriched PLA block ($P_m = 0.72$).

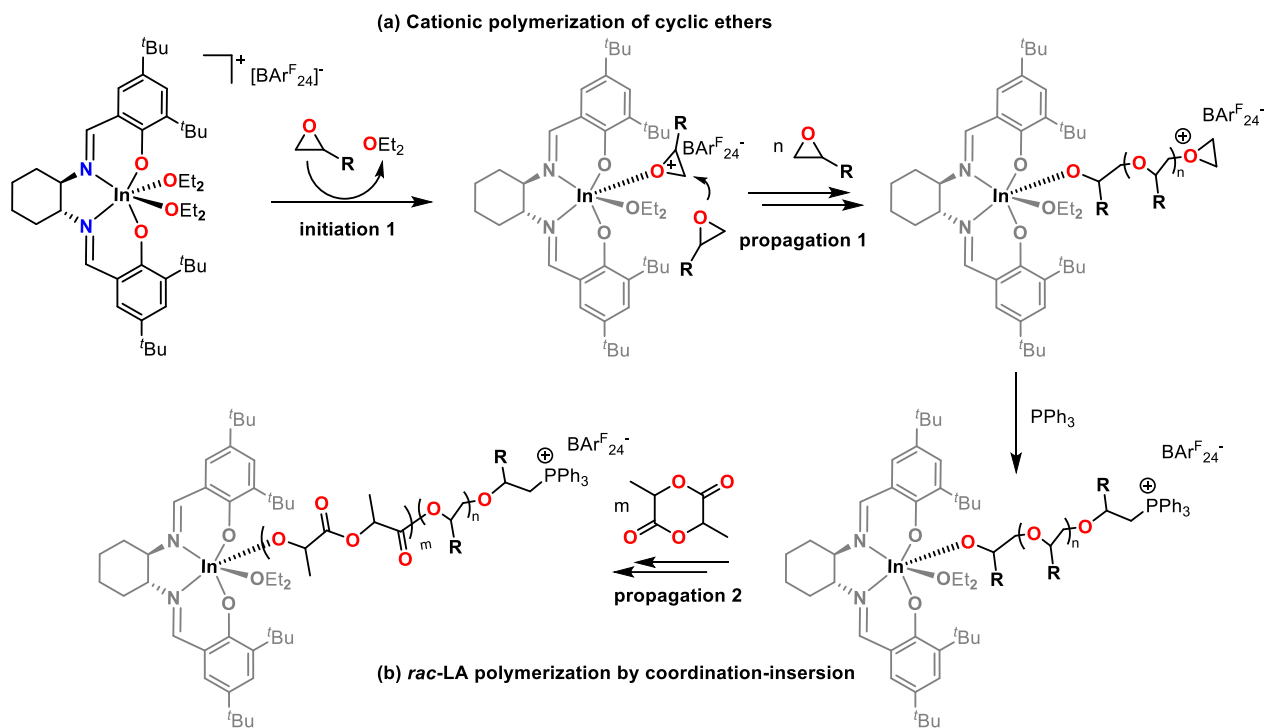


Figure 1.48. Proposed mechanism for the a) cationic polymerization of cyclic ethers and the b) block copolymerization of epoxides and *rac*-LA.

1.3 Scope of the thesis

While a wide assortment of ligands has been utilized to explore the reactivity of neutral indium complexes in polymerization chemistry, cationic indium species remain largely under explored. Based on the wildly diverse ligand defined reactivity patterns seen for neutral indium catalysts, there is potential new ligand designs specifically meant for cationic indium catalysts aimed at expanding their reactivity scope. This work attempts to do this by introducing new ligand systems and reactivities for cationic indium complexes.

In Chapter 2, the synthesis and characterization of a new family of cationic alkylindium (cyclohexylamino)iminophenolate complexes with hemilabile pendant donor is discussed. The effects of the pendant arm on the stability and reactivity are explored through spectroscopic techniques and the cationic polymerization of epoxides. Chapter 3 focuses on one of these

complexes, bearing a pyridine pendant donor arm, and its ability to form very high molecular weight cyclic-PLA. The polymers are characterized, and the mechanism of catalysis is explored using spectroscopic and kinetic techniques. In chapter 4, a related set of ligands is used to support cationic alkylindium complexes to control and slow their reactivity allowing mechanistic studies into the indium catalyzed formation of spiro-orthoesters by the coupling of epoxides and lactones.

Ultimately, Chapter 5 delves into the prospective paths that can be taken in the continuation of these studies, presenting potential applications and modifications for these indium complexes.

Chapter 2: Tuning the stability and reactivity of cationic alkylindium complexes using hemilabile ligands.

2.1 Introduction

Hemilabile ligands, bearing both substitutionally inert and substitutionally labile bonding sites, offer a great degree of tunability to the geometry and electronics around a metal center in an organometallic complex.⁶² The inert bonding sites on these ligands act as strong anchors to the metal center while the labile portion can be displaced by substrates with stronger affinity to the metal center. The re-coordination of the labile portion of the ligand can be achieved when the bound molecules are either transformed to a more weakly-coordinating entity or when they are exhausted from a reaction mixture. While a wide array of ligands with these characteristics can be designed, the basic features of hemilabile ligands remain similar. Hemilabile ligands tend to be polydentate chelates containing at least two different bonding sites with differing bonding capabilities (Figure 2.1). One group binds strongly to the metal center (X) and remains innocent throughout reactive processes while the second group coordinates weakly (L), allowing for easy displacement by substrate or solvent molecules (Y). While the labile group can be displaced, it remains in close proximity to the metal center capable of re-coordination to the metal center under favorable conditions.^{62–65}

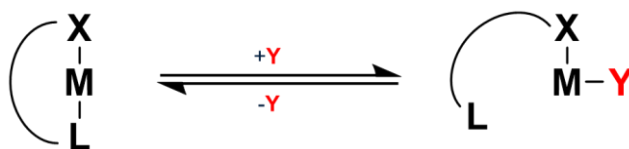


Figure 2.1. Behavior of a metal complex [(XL)M], bearing a hemilabile ligand in the presence of a coordinating ligand, Y.

Hemilabile ligands have been used extensively to stabilize metal complexes, control, and even alter reactivity.^{63,64} A wide array of elegant hemilabile ligand architectures support transition metal centers with catalytic activity in processes such as carbonylation,^{66,67} alkylation,⁶⁸ amination,⁶⁹ cross-coupling,^{70,71} and olefin metathesis⁷² among others.^{73–75}

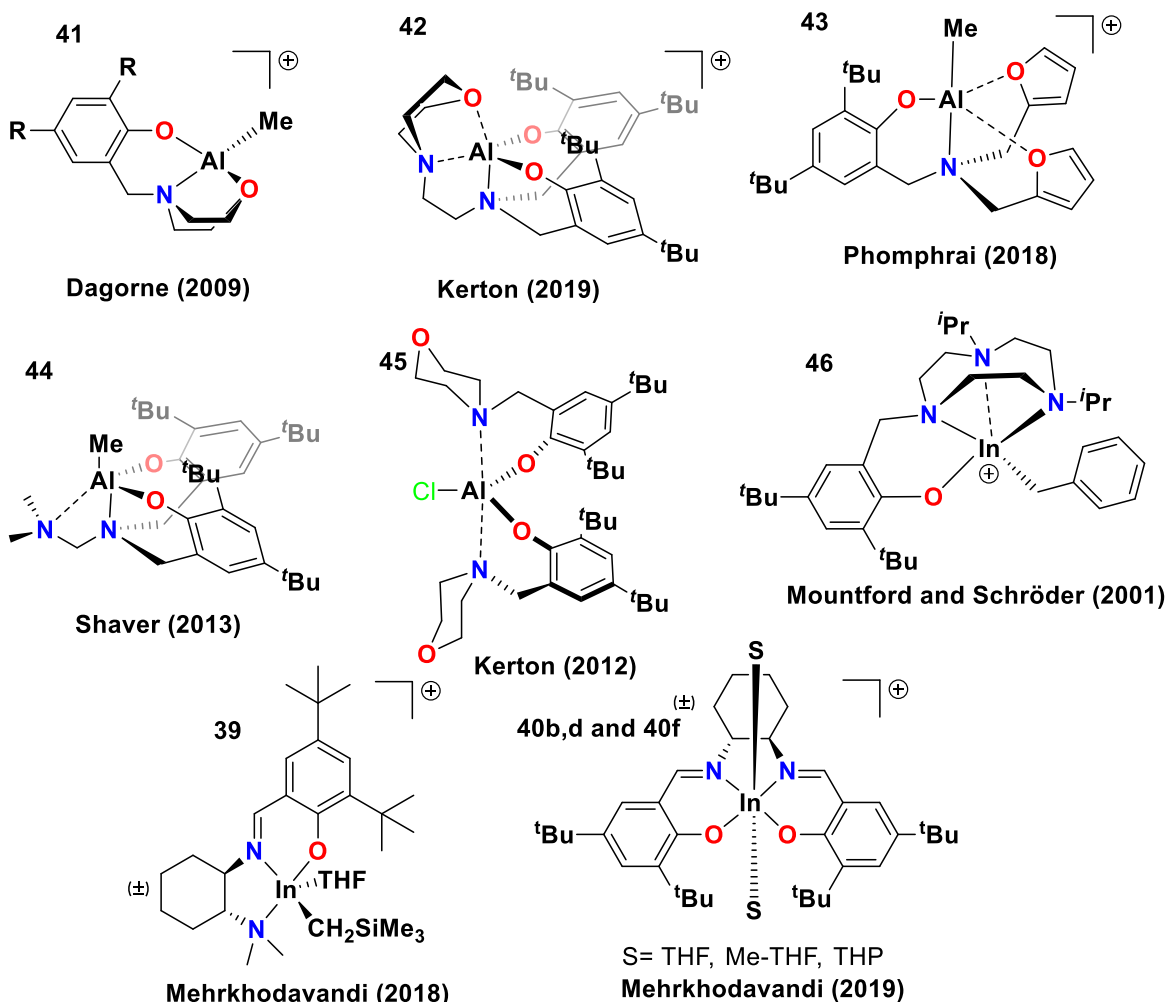


Figure 2.2. Previously reported aluminum and indium complexes bearing hemilabile ligands (**41-46**) and cationic indium complexes reported by the Mehrkhodavandi group (**39, 40b, 40d** and **40f**).

In contrast, there are only a handful of reports of the use of hemilabile ligands with main group metals.^{76–79} Due to their tunable Lewis acidity and oxophilic nature, complexes of group 13

elements, especially aluminum^{80,81} and indium^{39,51} have been used in a variety of reactions ranging from ring opening polymerization (ROP) of cyclic polar monomers to functionalization of small molecules.^{17,82–84} However, among the group 13 metals, almost all reports focus on aluminum complexes (Figure 2.2).

The outer sphere donor groups on these hemilabile ligand frameworks have been utilized mainly to achieve one or a combination of three outcomes.

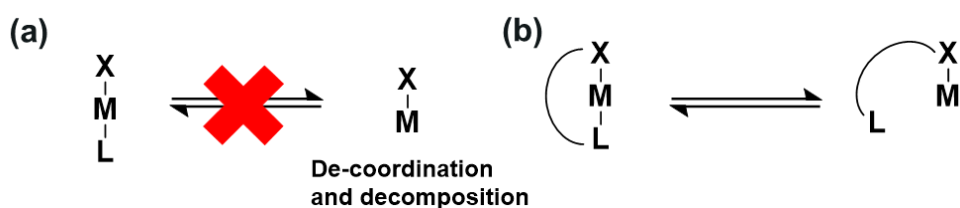


Figure 2.3. (a) Decomposition of a metal complex by de-coordination of labile ligand. (b) Stabilization of metal complex by reversible de-coordination and re-coordination of a hemilabile ligand.

First, hemilabile ligands stabilize metal complexes by providing a proximal, anchored donor group (Figure 2.3). In the absence of such a donor arm, external ligands are necessary to stabilize the metal center. Dissociation of unanchored labile ligands results in either adduct formation or decomposition of the metal complex. However, due to the proximity of the hemilabile donor groups, re-coordination is facilitated, stabilizing the metal complex. Using this strategy as a compromise between stability and reactivity, Dagorne and co-workers reported a series of cationic alkylaluminum complexes, **41**, supported by tridentate aminophenolate ligands with piperazine and morpholine pendant arms.⁸⁵ These complexes were proposed as a more stable alternative to solvent stabilized cationic alkylaluminum catalysts. Consequently, they mark the first use of hemilabile ligands in a group 13 catalyst. These complexes were used in the ROP of propylene oxide and ϵ -caprolactone (ϵ -CL). However, they produce low molecular weight (\sim 2500-4000 Da)

polyethers along with poly(ϵ -CL) of high dispersity (\bar{D} = 1.6-2.0). Kerton and co-workers reported the ROP of ϵ -CL using a cationic aluminum complex **42** stabilized by a morpholinyl donor arm in an aminobis(phenolate) ligand.⁸⁶ In the presence of an alcohol initiator, **42** could produce poly(ϵ -CL) of narrow dispersity (\bar{D} = 1.00-1.05). Using computational methods, they demonstrated **42** was more stable in comparison to hypothetical structures where the morpholinyl oxygen does not coordinate to the cationic aluminum center. Another cationic aluminum alkyl complex for the ROP of ϵ -CL, **43**, proposed to be stabilized by two hemilabile furfuryl pendant arms on an aminophenolate ligand was reported by Phomphrai and co-workers.⁸⁷

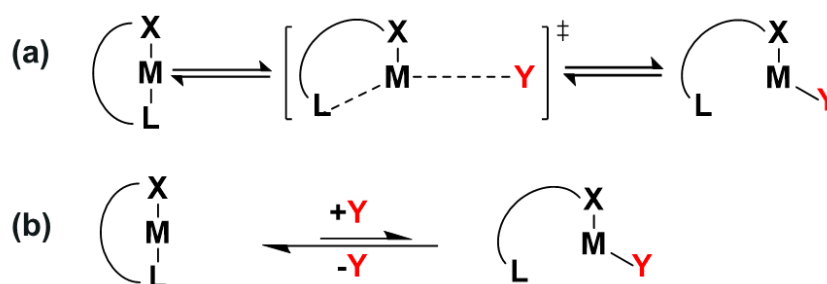


Figure 2.4. Controlling reactivity at metal center using a hemilabile ligand by (a) stabilizing transition states and (b) regulating access to coordination sites at the reactive center.

The second use of hemilabile ligands is to provide greater control to reactivity (Figure 2.4). This can occur through the stabilization of transition states or by regulating access to coordination sites at the reactive metal center. This type of reactivity control using hemilability was demonstrated by Shaver and co-workers by showing that the coordination of various donor arms to an aluminum center in a series of complexes, **44**, was key to obtaining control in the ROP of *racemic* lactide (*rac*-LA) and ϵ -CL.⁸⁸

Finally, the presence of hemilabile donor groups can completely alter the reactivity of some metal complexes (Figure 2.5). This could either occur through the activation of the substrate followed by reaction with the donor moiety or when the dissociation of a strongly binding ancillary

ligand is enhanced by a hemilabile donor. Kerton and co-workers proposed that a morpholinyl hemilabile side arm facilitated the displacement of an ancillary chloride ligand in the neutral aluminum aminophenolate complex **45** to initiate the ring-opening copolymerization (ROCOP) of CO₂ and cyclohexene oxide CHO.⁸⁰ They suggested that the interaction between the morpholinyl-oxygen and the aluminum center facilitates de-coordination of the chloride ancillary ligand increasing the Lewis acidity of the aluminum center allowing the coordination and subsequent ring-opening of the epoxide.⁸¹ The same complex was capable of polymerizing ε-CL initiated by the insertion of monomer molecules into the Al-Cl bond assisted by the morpholinyl donor arm.⁸⁰

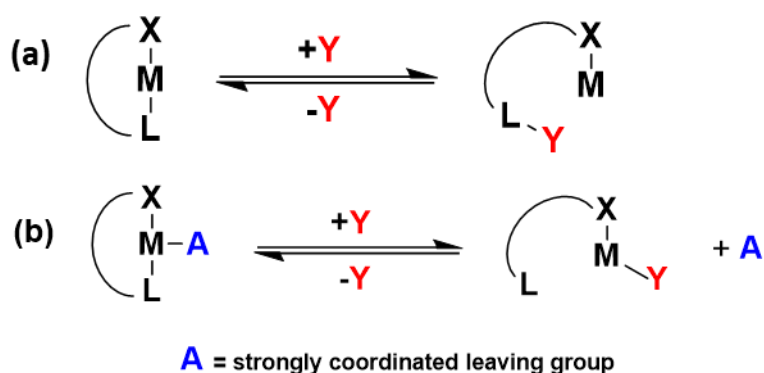


Figure 2.5. (a) Substrate activation by the metal center for reaction with a proximal donor ligand. (b) Enhancing the ability of leaving groups to dissociate by hemilabile donors.

Based on available information, the only known indium complex bearing a hemilabile ligand architecture was described by Mountford and Schröder who reported a cationic alkylindium aminophenolate complex **46** stabilized by a 1,4,7-triazacyclononane hemilabile pendant arm. However, this complex was reportedly unreactive towards all nucleophiles and reagents examined.⁸⁹ It is notable that the hemilabile donor moieties have been primarily used for enhanced stability of cationic complexes. Whereas in neutral complexes, the main role of donor group was connected to reactivity regulation.

Mehrkhodavandi and coworkers have reported cationic indium catalysts supported by tridentate⁹⁰ and tetradentate⁶¹ amino/imino phenolate ligands as catalysts for ROP reactions. Due to the increased electrophilicity and coordinative unsaturation, these complexes have been used to study the coupling of epoxides and ϵ -CL to form spiro-orthoesters (**39**) and the copolymerization of cyclic ethers and lactide (**40b**, **40d** and **40f**). However, these complexes required solvent molecules for stabilization, and the isolated complexes suffered from rapid decomposition when the labile solvent molecules were lost. Nevertheless, a ligand architecture with a hemilabile pendant donor moiety could stabilize the cationic indium center, afford greater control of reactivity, and potentially change the reactivity pattern altogether.

In the following sections, the synthesis and characterization of the first catalytically active cationic alkylindium complexes supported by ligands bearing hemilabile pendant donor arms will be discussed. This is followed by a discussion on the effects of the donor ability of the hemilabile pendant arm on regulating the stability and reactivity in the ROP of epichlorohydrin, cyclohexene oxide, ϵ -CL, and *rac*-LA.

2.2 Results and discussion

2.2.1 Synthesis and characterization of proligands **L_{a-d}**

Proligands **L_{a-d}** are synthesized through the route described in Figure 2.6. Commercially acquired (\pm)-*trans*-1,2-diaminocyclohexane is reacted with one equivalent of hydrochloric acid before asymmetric protection of one amine by a *tert*-butoxycarbonyl (Boc) group. The Boc hemi-protected diamine is alkylated with pendant donor arms via reductive aminations with 2-carbaldehydes of thiophene (**L_a**), furan (**L_b**), pyridine (**L_c**) and benzene (**L_d**) with sodium cyanoborohydride. Deprotection of Boc hemi-protected diamine forms an asymmetrically mono-alkylated intermediate. Condensation reaction of the diamine intermediate and 2,4-cumyl

disubstituted salicylaldehyde followed by recrystallization in pentane forms the prolignands **L_{a-d}** in ~65% yield. The ¹H NMR spectra of the ligands show one characteristic singlet between 8-9 ppm corresponding to the N=CH resonance. In the ¹³C{¹H} spectra, the N=CH resonances appear the most downfield at chemical shifts of >165 ppm. **L_a** was synthesized as a control to approximate the steric bulk of the donor arms in **L_{a-c}** without the donating ability.

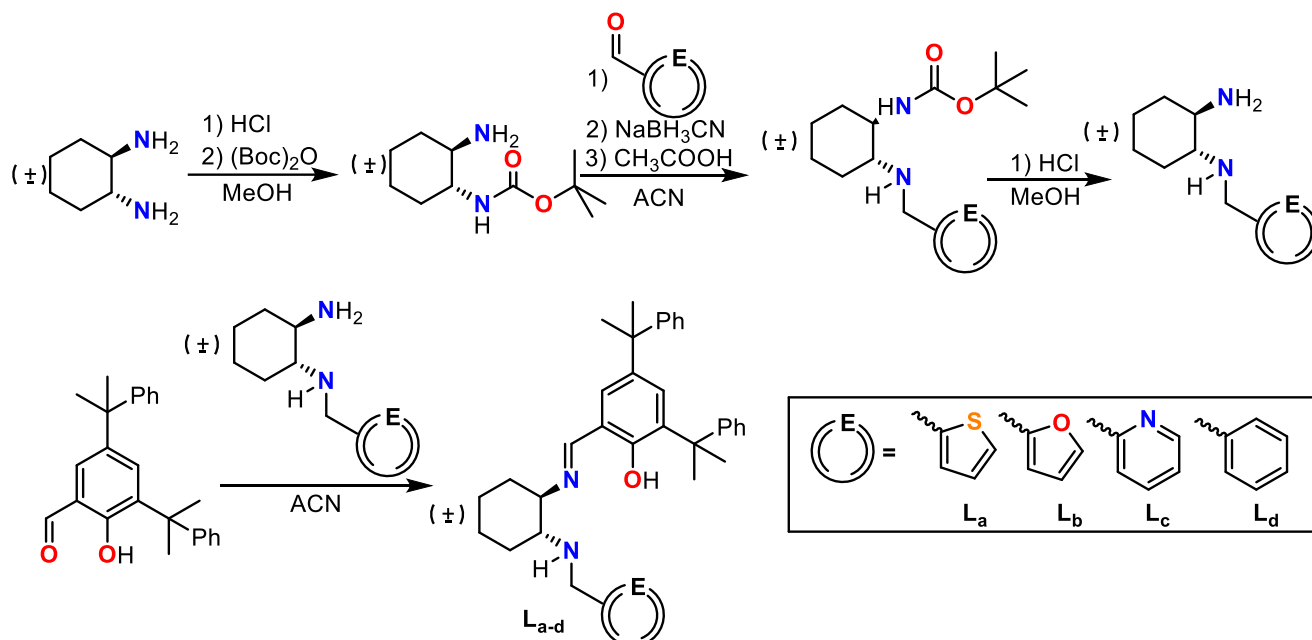


Figure 2.6. Synthesis of prolignands **L_{a-d}**

2.2.2 Synthesis and characterization of neutral alkylindium complexes **47a-d**

Treatment of **L_{a-d}** with In(^{*i*}Bu)₃ at room temperature in hexanes results in the almost quantitative formation of dialkylindium complexes **47a-d** (Figure 2.7). Solid-state structures of **47a-d** determined by single-crystal X-ray crystallography feature distorted square pyramidal indium centers (Figures A.57-A.60).

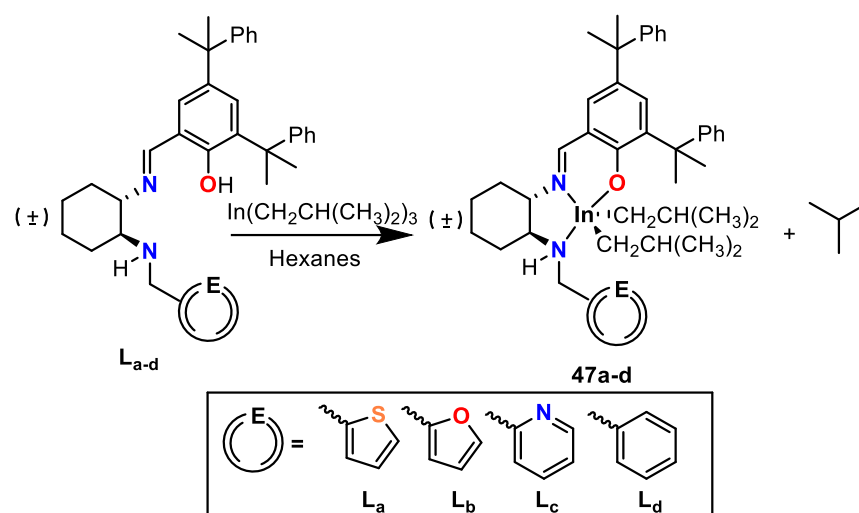


Figure 2.7. Synthesis of neutral dialkylindium complexes **47a-d**

Dialkylindium species **41a-d** are isostructural in the solid-state with the distance between the heterocyclic heteroatoms and the indium center in **47a-c** indicating the absence of significant interactions. This is most apparent in comparison of this distance in **47c** and the analogous distance to the indium center from the *ortho*-C of the benzyl group in **47d**, where no interaction is expected (Figure 2.8). The ^1H and $^{13}\text{C}\{^1\text{H}\}$ NMR spectra obtained for **47a-d** in CDCl_3 agree with the solid-state structures (Figures A.17-A.35)

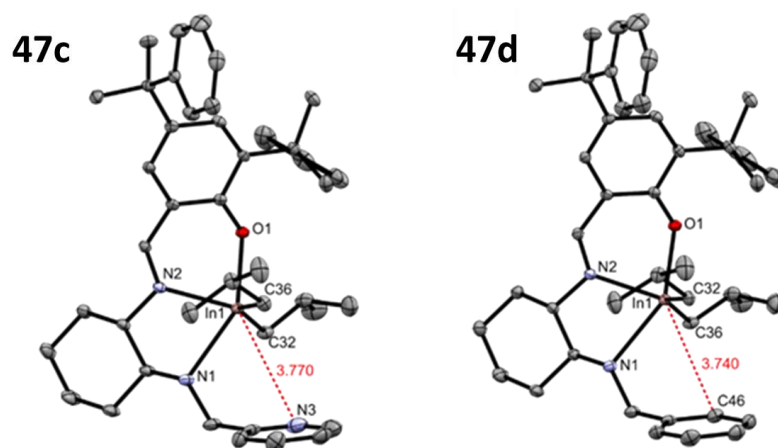


Figure 2.8. Complexes **47c** and **47d** are isostructural and have similar distance between the indium center and the donor group.

2.2.2.1 Solution state behavior of 1a-d

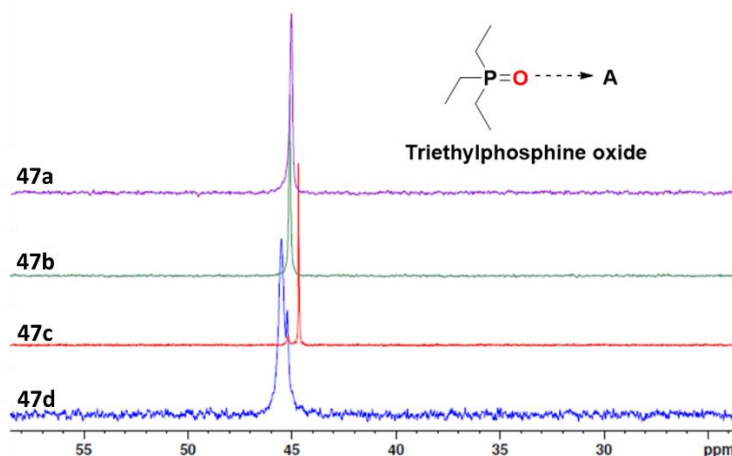


Figure 2.9. $^{31}\text{P}\{^1\text{H}\}$ NMR spectra of OPEt_3 with **47a-d** show a similar acceptor ability. $^{31}\text{P}\{^1\text{H}\}$ NMR (160 MHz, C_6H_6 , 25 $^\circ\text{C}$) chemical shift of free OPEt_3 appears at 45 ppm.

To determine donor group interaction in the solution-state, a modified Gutmann-Beckett method was used to determine relative acceptor ability (Figure 2.9).⁹¹⁻⁹³ This method involves the addition of triethylphosphine oxide (OPEt_3), to form an adduct with the metal complex. As a response to adduct formation, the ^{31}P nucleus chemical shift of OPEt_3 in $^{31}\text{P}\{^1\text{H}\}$ NMR spectra change relative to free OPEt_3 . A capillary tube containing a solution of free OPEt_3 is added to the NMR tubes as an internal standard. Complexes **47a-d** did not show a significant change in $^{31}\text{P}\{^1\text{H}\}$ chemical shifts relative to free OPEt_3 , indicating that the indium centers of **47a-d** have electronically similar environments. This excludes the possibility of pendant donor interaction in the solution-state.

2.2.3 Synthesis and characterization of cationic alkyl indium complexes 48a-d

The reaction of **47a-d** with the Brønsted acid $[\text{HNMe}_2\text{Ph}][\text{BAr}^{\text{F}}_{24}]$ ($\text{BAr}^{\text{F}}_{24}$ = Tetrakis[3,5-bis(trifluoromethyl)phenyl]borate) in THF forms the cationic species **48a-d** (Figure 2.10). After several hexane washes, residual THF can be removed from complexes **48a-c**, while for complex

2d THF cannot be removed. This is reminiscent of the similar alkyl indium cationic catalyst **39** (Figure 2.2).⁴³ Complexes **48a-c** can be synthesized in non-coordinating solvents such as DCM and benzene, indicating that external donor groups are unnecessary for complex stabilization. However, attempts to synthesize **48d** in DCM and benzene formed decomposition products. The stability of the complexes in the absence of donor solvents is related to the affinity of the heteroatom to the indium center (Table 2.1). Complex **48d** is highly unstable at ambient temperatures, decomposing almost immediately. While it can be synthesized at -30 °C, **48d** cannot be isolated in high purity. Complex **48a** is stable for up to 48 hours under inert conditions in ambient temperatures. However, **48a** begins decomposition at higher temperatures even under inert conditions but can be stored at -30 °C for several weeks. The furfuryl bearing **48b** is stable under inert conditions at ambient temperature for several weeks. In contrast, **48c** is stable under inert conditions at room temperature for several months. Surprisingly, for a cationic species, **48c** shows extraordinary stability, being able to withstand exposure to moist air for up to 10 days (Figure A.62).

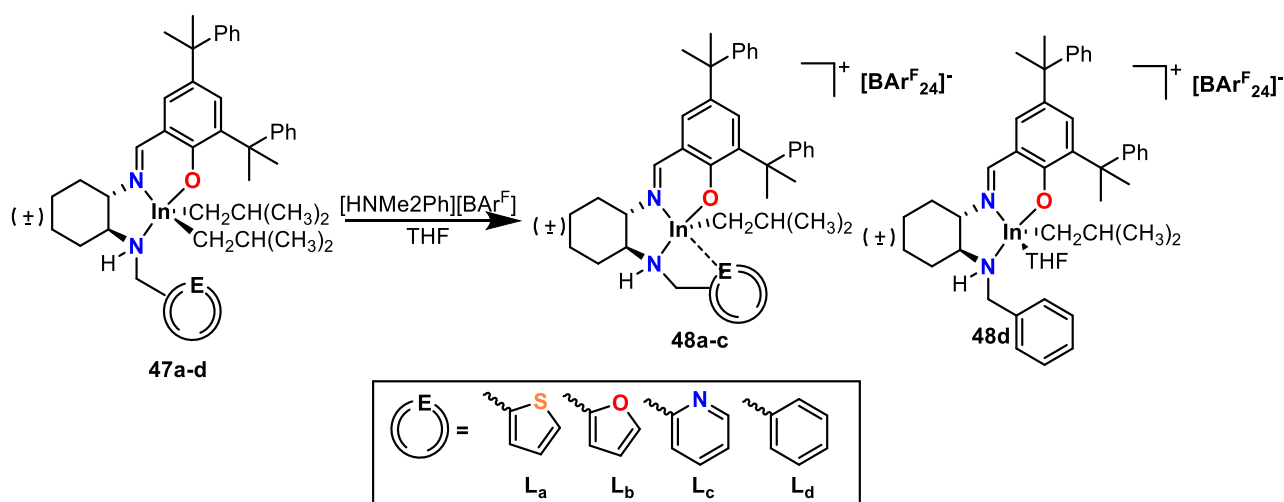


Figure 2.10. Synthesis of cationic alkyl indium complexes **48a-d**

Table 2.1. Summary of cationic complex synthesis, storage, and longevity.

Complex	48a	48b	48c	48d
Pendant group donor strength ^a D _s ⁹⁴	11	10	33	-
Synthesis temperature	Ambient temperature	Ambient temperature	Ambient temperature	-30 °C
Synthesis solvents	THF, DCM, C ₆ D ₆	THF, DCM, C ₆ D ₆	THF, DCM, C ₆ D ₆	THF
Stable lifespan (Stored under dry N ₂ unless otherwise stated)	~48 h at r.t. ~2 weeks at -30 °C	Stable up to 10 weeks at r.t.	Stable up to 10 weeks at r.t. Up to 10 days exposed to moist air	~20 mins at r.t. ~ 1 day at -30 °C

^a Lewis basicity calculated through the stretching vibrational frequency of HgBr₂ in a given donor solvent.

2.2.3.1 Analysis of ¹H NMR spectra of 48a-d

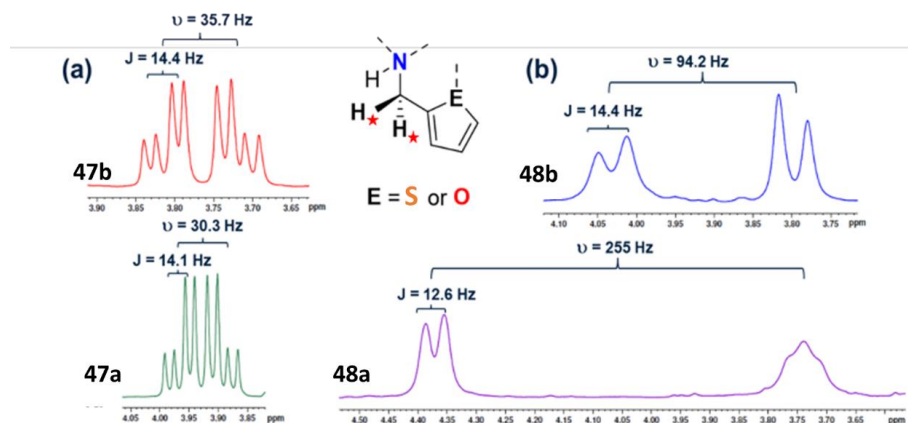


Figure 2.11. (a) Methylene protons (H*) are an AB pair in **47a** and **47b**. (b) In **48a** and **48b** they act like an AX pair. (¹H NMR at 300 MHz in CDCl₃ at 25 °C)

The disappearance of the peaks corresponding to one of the isobutyl groups attached to the indium center at $\delta = 0-1$ ppm in ¹H NMR spectra of **47a-d** is indicative of protonolysis of an alkyl

group from the neutral complex. The clean downfield shift of the imine proton signals from $\delta = \sim 8.10$ ppm in ^1H NMR spectra of **47a-d** to $\delta = \sim 8.20$ ppm in **48a-d** shows the formation of a single product. The peaks arising from the heterocyclic protons in **48a-c** shift significantly upfield compared to the neutral species **47a-c**, suggesting substantial shielding of these protons on the formation of cationic complexes.

Further analysis of the ^1H NMR spectrum of **48c** shows that the AB multiplet ($\nu < 10$ J) arising from the diastereotopic methylene protons of the pendant arm broaden and shift downfield by ~ 0.2 ppm compared to **47c**. In **48a** and to a lesser extent in **48b**, the $\Delta\delta$ for these protons increase, in relation to **47a** and **47b**, resembling an AX coupling ($\nu \geq 10$ J, Figure 2.11). Based on these observations, the upfield shift of heterocyclic proton signals arise when the outer-sphere donor group approaches the cationic indium center, enhancing shielding of the heterocyclic protons. Coordination of the pendant donor groups to the cationic center restricts the free rotation around the methylene carbon on the linker arm, thereby “locking” the methylene protons in position giving them distinct magnetic environments increasing the $\Delta\delta$ of these protons.

2.2.3.2 Analysis of NOESY NMR spectra of **48a-c**

Coordination of the pendant donor group causes the heterocycle to be spatially near the isobutyl ligand attached to the indium center. NOESY NMR spectra of neutral complexes **47a-c** show no through space interaction between heterocyclic protons and isobutyl protons (Figure A.40, A.47, and A.54). However, the α (6.86 ppm) and β (7.05 ppm) protons of the thiophenyl group of **48a** show Nuclear Overhauser Effect (NOE) interactions to isobutyl methylene and methyl protons respectively (Figure A.40). The α (6.14 ppm) proton on the furfuryl group of **48b** show NOE to the isobutyl methyl protons (Figure A.47). In **48c**, the γ proton (7.70 ppm) of the

pyridyl group shows NOE to the isobutyl methyl protons (Figure A.54). The spatial proximity shown by the heterocycles to the isobutyl methyl groups, in **48a-c** in contrast to **47a-c**, lends further credence to the solution state coordination of the pendant donor groups in the cationic complexes (Figure 2.12).

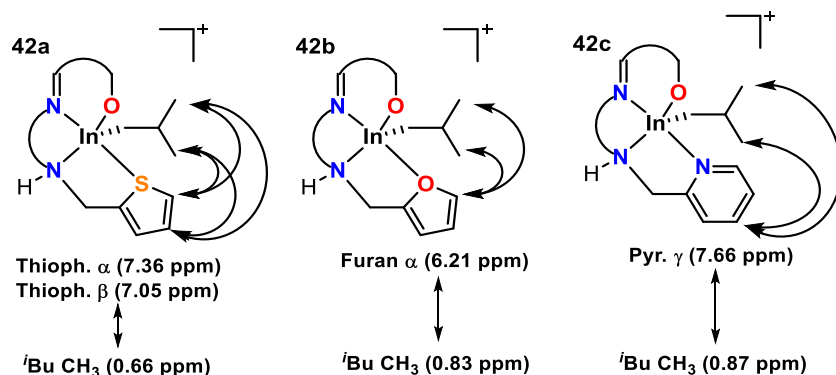


Figure 2.12. Most apparent through-space NOE interactions observed between heterocyclic protons and isobutyl ligand for **48a-c** (NOESY NMR spectra 400 MHz, CDCl_3 , 25 °C).

2.2.4 Hemilabile behavior of complexes

Although several pendent donor stabilized complexes of group 13 metals have been reported, the hemilability of the donor moiety is rarely, if ever, explored in detail. To bridge this gap in knowledge, the following section explores the fluxional nature of the donor arm interaction under varied temperature and in the presence of external donor species. Due to its easily discernible furan α proton, the latter section will largely focus on complex **48b**.

2.2.4.1 Temperature dependent hemilabile behavior of **48a-c**

In previously reported studies with aluminum complexes bearing hemilabile ligands, temperature was a defining factor in complex stability and reactivity. Phomphrai and coworkers reported the decomposition of the cationic aluminum complex **43** at 70 °C with Shaver and coworkers reporting a loss of control in polymerization of ϵ -CL at higher temperature (**44**).^{87,88} It

is likely that decomposition or loss of control occurs with the de-coordination of hemilabile groups at higher temperatures. The decomposition of **48a** with an increase in ambient temperature warranted an exploration into the temperature effect on **48a-c**.

Variable temperature (VT) ^1H NMR spectroscopy (25-125 $^\circ\text{C}$, $\text{C}_6\text{D}_5\text{Br}$) of cationic complexes **48a-b** show significant changes, while the neutral analogues do not change in this temperature range (Figures A.63-A.65). The thiophene complex **48a** shows significant and irreversible decomposition beginning at 45 $^\circ\text{C}$, while the pyridyl complex **48c** was highly stable, with only minor changes in chemical shifts even at 120 $^\circ\text{C}$. (Figure 2.13 and 2.15). In contrast, the furan complex **48b** shows a gradual downfield migration of the α furfuryl proton with increasing temperature, a $\Delta\delta$ of ~ 0.6 ppm (Figure 2.14). At higher temperatures (125 $^\circ\text{C}$, $\text{C}_6\text{D}_5\text{Br}$) the chemical shift of the α proton approaches that of the free ligand **L_b** ($\delta = 7.20$ ppm). This change is reversible when the temperature is lowered to 30 $^\circ\text{C}$. The de-shielding of the α proton occurs as its proximity to the indium center decreases with increasing fluxional behavior of the In-O_{furan} interaction at higher temperatures.

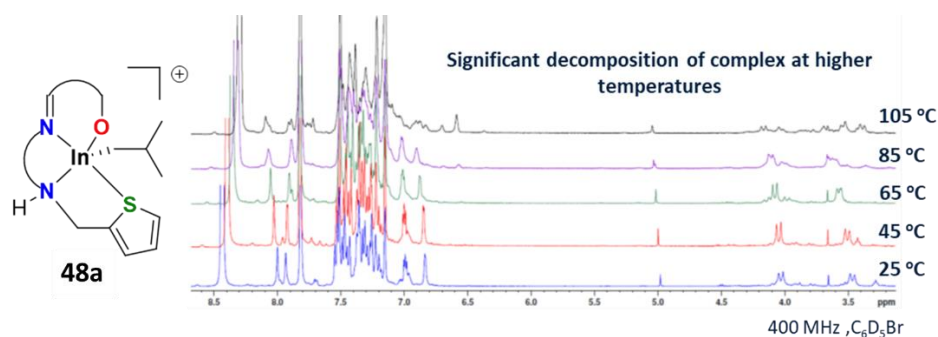


Figure 2.13. VT NMR spectra of **48a** show the irreversible decomposition of isolated complex when the temperature is increased from 25-105 $^\circ\text{C}$ (^1H NMR at 400 MHz in $\text{C}_6\text{D}_5\text{Br}$).

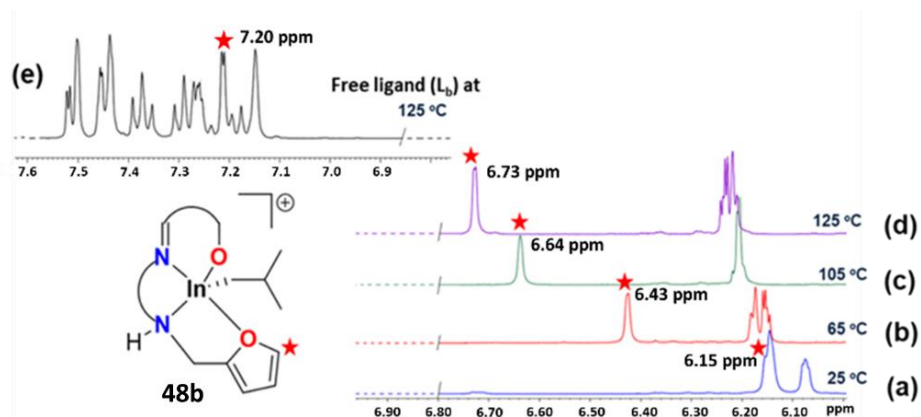


Figure 2.14. (a-d) Spectra showing downfield migration of the α proton of the furfuryl group in **48b** (★) at 25-125 °C. (e) ^1H NMR spectrum of the free ligand (**Lb**) at 125 °C (^1H NMR at 400 MHz in $\text{C}_6\text{D}_5\text{Br}$).

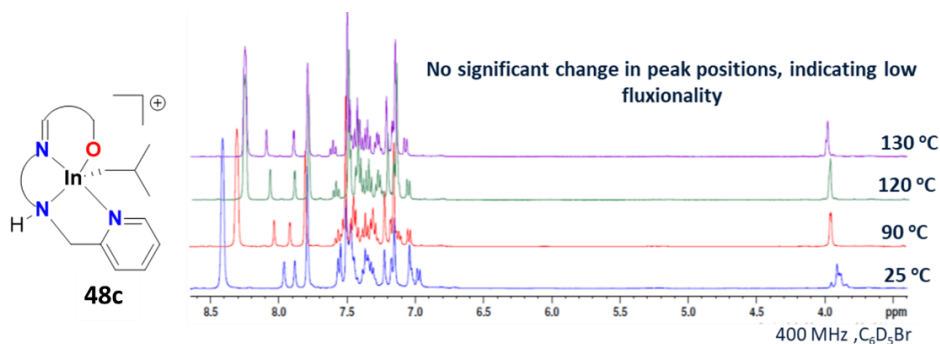


Figure 2.15. Significant change is not observed in the VT NMR spectra of **48c** temperature is increased from 25-130 °C (^1H NMR at 400 MHz in $\text{C}_6\text{D}_5\text{Br}$).

The fluxional behavior of **48a-c** is directly related to the donor ability of the heterocyclic pendant groups. Pyridine having a far greater donor ability (donor strength, $D_s = 38$) than furan and thiophene accounts for the unexpected stability of **48c**.^{94,95} Thiophene and furan have comparable donor strengths ($D_s = 11$ and 10 respectively). Therefore, the donor strength alone does not explain the dramatic difference in stability between **48a** and **48b**. However, when the greater aromaticity of thiophene and the availability of electrons in furan for bonding are considered, the higher stability of **48b** can be accounted.⁹⁶

2.2.4.2 External donor effect on the hemilabile behavior of **48b**

While many of the reported group 13 complexes with reversibly coordinating donor arms have been proposed to have hemilabile behavior, the de-coordination of pendant donor groups in the presence of external donors has not been explicitly demonstrated. For these complexes to be truly hemilabile the pendant donor arm should be able to change its bonding in response to other coordinating ligands or solvent molecules possessing greater donor ability.⁶³ In order to explore the hemilabile behavior of these cationic alkyl indium complexes, **48b** was chosen to be studied in detail due to the easily observable α proton chemical shift in ^1H NMR spectra and its middling ‘Goldilocks’ stability compared to **48a** and **48c** (Figure 2.16).

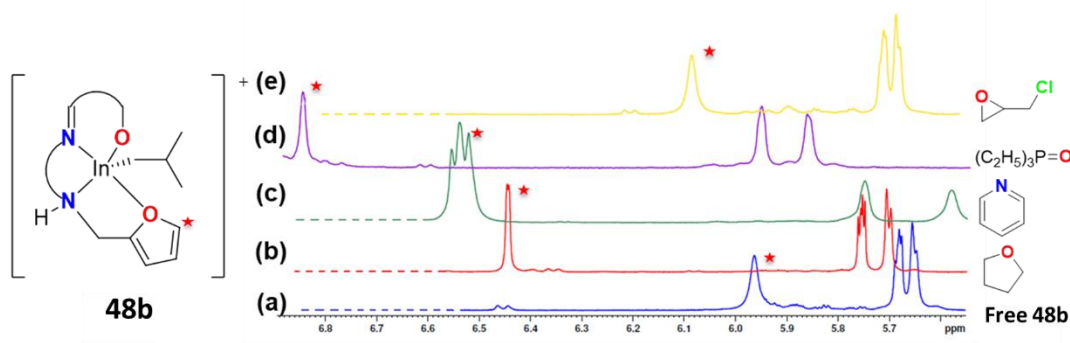


Figure 2.16. Downfield shift of the furfuryl α proton signal of **48b** (★) in the presence of (b) THF, (c) pyridine, (d) triethylphosphine oxide and (e) epichlorohydrin (^1H NMR at 400 MHz in C_6D_6 at 25 °C)

To ascertain the effect of external donor ligands on the hemilabile donor arm ^1H NMR spectroscopy was used to observe the downfield shift of the furfuryl α proton signal of **48b** in the presence of donors in C_6D_6 as solvent. With the addition of THF ($D_S = 17$) to **48b**, a ~ 0.5 ppm downfield shift of the α -proton signal was observed in the ^1H NMR spectrum (C_6D_6) of the mixture, indicating a loss of proximity of the furan moiety (Figure 2.16b). With a weaker donor such as epichlorohydrin (ECH), only a ~ 0.1 ppm downfield shift is observed (Figure 2.16e), while

addition of pyridine ($D_s = 38$, donor number* $D_N = 33.1 \text{ kcal mol}^{-1}$) causes a ~ 0.6 ppm downfield shift. (Figure 2.16c).^{95,97} Addition of OPEt_3 had the greatest effect with a ~ 0.9 ppm downfield shift (Figure 2.16d). While, OPEt_3 has a lower donor number ($D_N = 24 \text{ kcal mol}^{-1}$) than pyridine, the predominantly anionic nature of the oxygen leads to a stronger interaction with the cationic indium center and a greater fluxionality of the $\text{In-O}_{\text{furan}}$ interaction.⁹⁸

The behavior of the pendant arm in the presence of external donor groups can also be observed using the furfuryl methylene signals in the ^1H NMR spectra. The chemical shift changes for these peaks are within 0.2 ppm for THF, pyridine or ECH mixed samples. The unchanged diastereotopic nature of the methylene proton signals show that interactions with donor species such as THF, pyridine or ECH with **48b** does not cause the complete de-coordination of the furfuryl donor group in the solution phase at 25°C , only leading to increased fluxionality correlated to the donor ability of each external donor. However, in the presence of OPEt_3 , the methylene proton signals lose their diastereotopic nature and merge to appear as a singlet in the ^1H NMR spectrum. Further, the new signals arise ~ 0.5 ppm downfield to the methylene signals of the ^1H NMR spectrum of unadulterated **48b**. Both changes in the spectrum along with the large downfield shift of the α proton signal, point to the unhindered free rotation of the furfuryl donor arm due to complete de-coordination in the presence of OPEt_3 (Figure A.73).

A single crystal of solvated **48b** (**48b.2THF**) complex suitable for X-ray crystallographic analysis was obtained through the slow evaporation of a THF/hexamethyldisiloxane solution (Figure 2.7). The structure of **48b.2THF** reveals a distorted octahedral cationic indium center with

* The negative enthalpy for the 1:1 adduct formation between a Lewis base and the Lewis acid SbCl_5 , in 1,2-dichloroethane expressed in kcal mol^{-1}

two THF molecules in the axial positions. The bond distances and angles of this structure resemble that of the cationic salen indium complex **40b** (Figure 2.2) previously reported by the Mehrkhodavandi group.⁶¹ The de-coordination of the furfuryl pendant arm in presence of an external donor entity shows that **48b** displays true hemilabile behavior in the presence of a strong donor ligand.

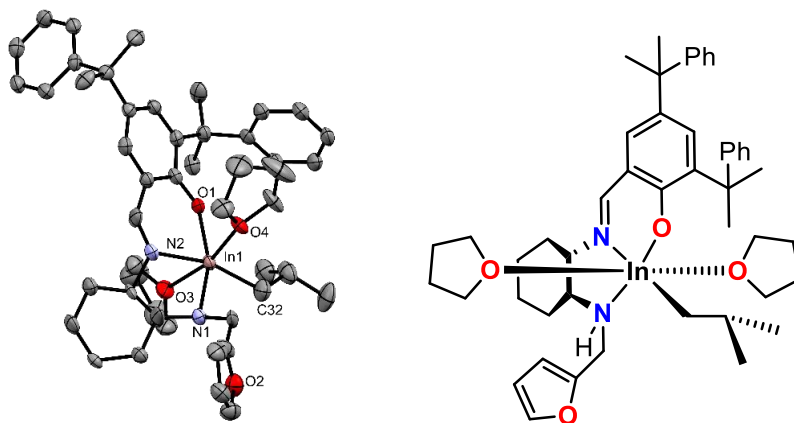


Figure 2.17. Molecular structures of complex **48b.2THF** (depicted with thermal ellipsoids at 50% probability and H atoms, minor disorders as well as solvent molecules and counter anion omitted for clarity).

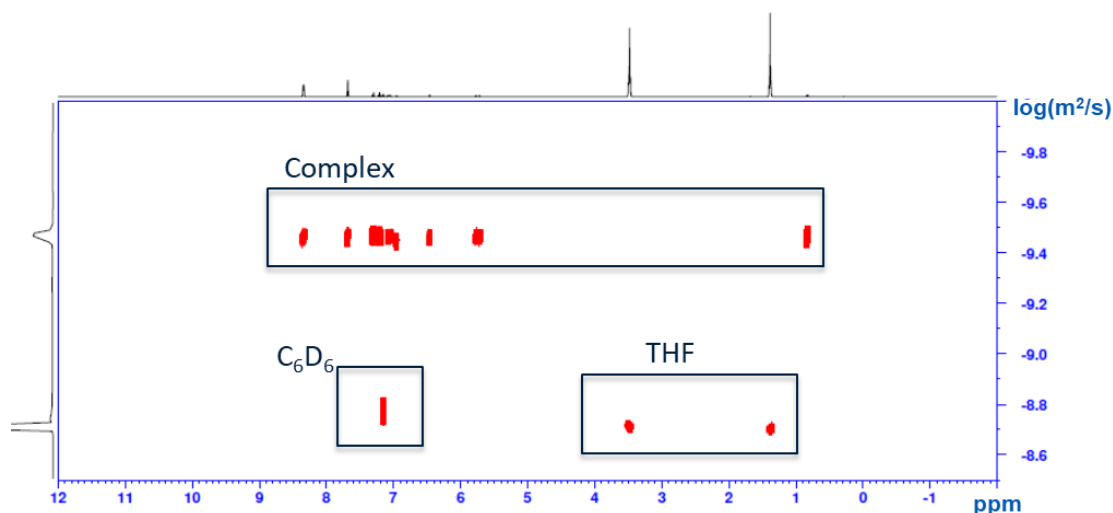


Figure 2.18. DOSY NMR spectrum of **48b** with excess THF in C_6D_6 , shows the independent diffusion of THF and the complex. (1H NMR, diffusion time (Δ) = 0.85 s, gradient length (δ) = 400 μs , 400 MHz, C_6D_6 , 25 $^{\circ}C$)

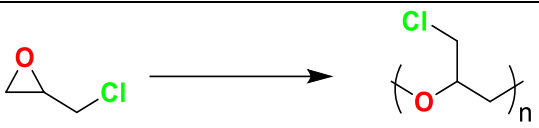
Although the solid-state structure of **48b.2THF** shows the coordination of two THF molecules and the complete de-coordination of the pendant donor arm, the structure is different in solution. The DOSY NMR spectrum (C_6D_6) exhibits independent diffusion of **48b** and THF (Figure 2.18). These results point to a weak association of **48b** with THF in solution phase. This observation held true for DOSY NMR of mixtures of **48a** and **48c** with THF as well (Figures A.70 and A.72). It is possible that this apparent independent diffusion of the complexes and THF is due to fast exchange occurring relative to the NMR time scale at 25 $^{\circ}C$ at 400 MHz.

2.2.5 Reactivity Studies

In this section the influence of the hemilabile donor groups on the reactivity patterns of **48a-c** is discussed using the ROPs of epichlorohydrin (ECH), cyclohexene oxide, ϵ -CL and *rac*-LA.

2.2.5.1 Polymerization of epichlorohydrin

Table 2.2. Polymerization of epichlorohydrin with cationic alkylindium complexes.

							
Entry	Temp. (°C)	Catalyst	Conv. ^a (%)	M_n cal ^b (Da)	M_n^c (Da)	\bar{D}^d	i^{*e}
1	25	48a	59	16 900	27 000	1.42	0.61
2	35	48a	61	16 900	21 300	1.56	0.80
3	60	48a	59	16 400	19 300	1.22	0.85
4 ^f	25	48a	<1	-	-	-	-
5 ^g	25	48a	<1	-	-	-	-
6	25	48b	34	9 400	24 000	1.23	0.39
7	35	48b	61	16 900	29 300	1.33	0.58
8	60	48b	55	15 300	21 200	1.30	0.72
9 ^f	25	48b	<1	-	-	-	-
10 ^g	25	48b	<1	-	-	-	-
11	25	48c	<1	-	-	-	-
12	60	48c	<1	-	-	-	-
13	80	48c	<1	-	-	-	-
14 ^h	25	48d	73	20 400	20 500	1.50	0.99

Reactions were performed in C₆D₆ for 24 h. [ECH] = 6.37 M, [cat] = 20 mM. [ECH]/[cat] = 300. ^a Conversion was monitored by ¹H NMR spectroscopy. ^b M_n Cal = Calculated number averaged molecular weight = [ECH]/[cat] × conversion × molar mass of ECH. ^c M_n determined using GPC in THF. ^d Dispersity = M_w/M_n . ^e Initiation efficiency = (M_n Cal/ M_n). ^f With the addition of triphenylphosphine. ^g [ECH] = 2.94 M, [cat] = 10 mM, [ECH]/[cat] = 300. ^h Catalyst was not isolable.

The cationic ROP of epichlorohydrin (ECH) in C₆D₆ was used as a model reaction to determine the effect of hemilabile donor groups on reactivity (Table 2.2). Lacking a side arm donor group to affect the electronic environment of the cationic indium center, complex **48d** shows the highest activity at 25 °C with an initiation efficiency of 99%.⁹⁹ In contrast, **48c** with strong pyridine donor arm does not polymerize ECH even at 80 °C. Complexes **48a** and **48b** catalyze the ROP of ECH at 25 °C with 61% and 39% initiation efficiencies respectively. The initiation efficiency (M_n

cal/M_n) of **48b** approaches that of **48a** at higher temperatures indicating that both complexes achieve similar reactivity at elevated temperatures. This is consistent with the temperature-dependent fluxional behavior observed for **48b**. De-coordination of the pendant donor arm occurs more readily with increasing temperature resulting in **48a** and **48b** behaving in an electronically similar manner. Additionally, when triphenylphosphine is added to the reaction mixture, polymerization of the epoxide halts through the formation of a stable quaternary phosphonium species at the cationic chain end.¹⁰⁰ This confirms the cationic nature of the polymerization mechanism (Table 2.2, entries 4,9).

2.2.5.1.1 Reaction progression monitoring

To further understand the reactivities of **48a** and **48b** in the cationic ROP of ECH, the progression of reaction was monitored in a range of temperatures using *in situ* real-time ^1H NMR spectroscopy. These spectra are utilized to construct percentage conversion of monomer vs. time plots at 10 °C, 25 °C, 35 °C and 60 °C (Figure 2.19). The polymerization of ECH follows the general trend of a linear increase in conversion followed by a gradual plateauing of monomer conversion. As a relative measurement of comparison between the activities of **48a** and **48b** the rate of percentage conversion of monomer in the initial linear portion of the plot is considered. While the rate of conversion increases with temperature for both **48a** and **48b**, the conversion of monomer occurs ~3 times faster with **48a** compared to **48b** at 10 °C and 25 °C (Figure 2.19a and b). At 35 °C the ratio of conversion rates of **48a** to **48b** drop to ~1.5 pointing to the higher initiation efficiency of **48b** at increased temperature (Figure 2.19c). The reaction occurs too fast at 60 °C to measure rates of conversion. However, monomer conversions with both **48a** and **48b** reach a

plateau approximately in the same period (Figure 2.19d), establishing that **48b** behaves similarly to **48a** as the furfuryl donor arm de-coordinates more readily at higher temperatures.

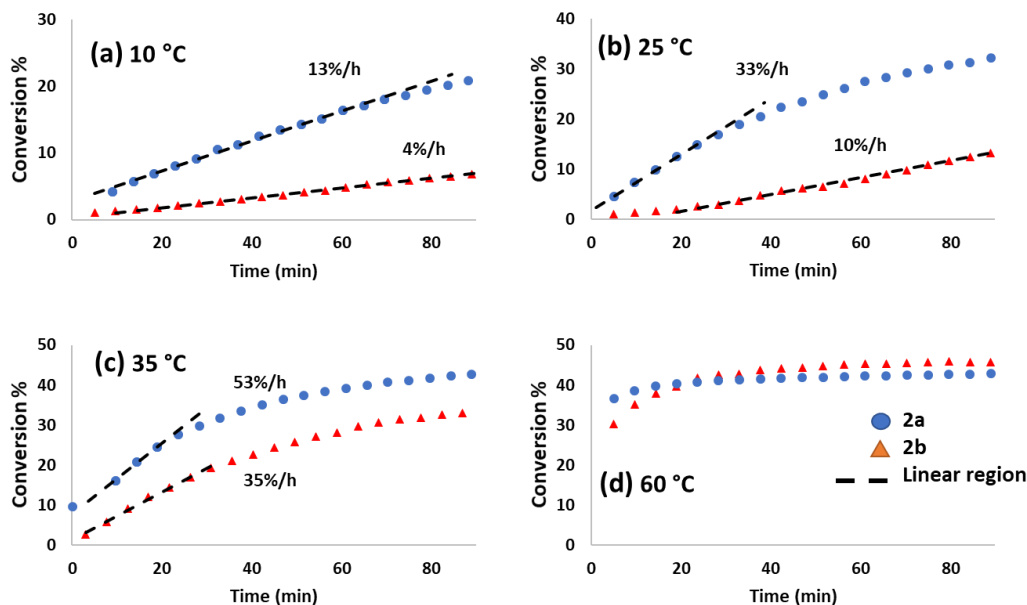


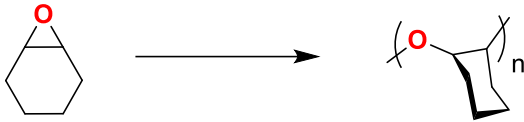
Figure 2.19. Percentage monomer conversion vs. time plots (average of a minimum of two trials) for ECH with **48a** and **48b** at (a) 10 °C (b) 25 °C (c) 35 °C and (d) 60 °C

2.2.5.2 Polymerization of cyclohexene oxide

The polymerization of highly reactive cyclohexene oxide (CHO)¹⁰¹ provides a dramatic example of the tuning of reactivity through the introduction of a hemilabile donor arm (Table 2.3). Under neat, dilute and even low temperature conditions **48a** and **48b** polymerize CHO in a violently uncontrolled fashion, forming polymers with high dispersity and irreproducible molecular weights. In contrast to these species, **48c** reacts slowly to produce higher molecular weight, lower dispersity poly(cyclohexene oxide), even in neat conditions (Table 2.3, entry 7). With increasing temperature, the conversion of monomer is increased with a small improvement in dispersity. When the reaction is conducted in solution, the molecular weight increases further

with a significant lowering of dispersity (Table 2.3, entry 9). Although **48c** is not highly controlled in general, this change in reactivity shows the significant impact of the hemilabile arm.

Table 2.3. Polymerization of cyclohexene oxide with cationic alkylindium complexes.

							
Entry	Temp. (°C)	Catalyst	Solvent	Conv. ^a (%)	M_n Cal ^b (Da)	M_n^c (Da)	\bar{D}^d
1	25	48a	neat	f	-	~ 13 000	~ 7
2	25	48a	C ₆ D ₆	f	-	~ 20 000	~ 4
3	0	48a	Toluene	f	-	~ 19 000	~ 3
4	25	48b	neat	f	-	~ 14 000	~ 5
5	25	48b	C ₆ D ₆	f	-	~ 30 000	~ 3
6	0	48b	Toluene	f	-	~ 24 000	~ 3
7	25	48c	neat	58	113800	80 800	2.23
8	60	48c	neat	93	182500	82 800	1.78
9	25	48c	C ₆ D ₆	91	26800	108 600	1.47
10 ^e	25	48c	neat	-	-	-	-

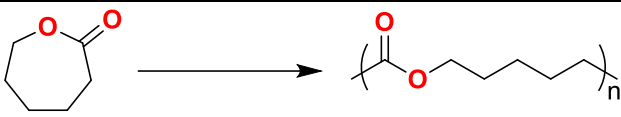
Reactions were performed for 24 h. In solution [CHO] = 8.0 M, [cat] = 5.6 mM. [Epoxide]/[cat] = 300, in neat conditions [epoxide]/[cat] = 2000. ^a Conversion was monitored by ¹H NMR spectroscopy. ^b M_n Cal = calculated number averaged molecular weight = [CHO]/[cat] × conversion × molar mass of CHO. ^c M_n determined using GPC in THF. ^d Dispersity = M_w/M_n . ^e With the addition of triphenylphosphine. ^f Not determined due to uncontrolled reaction.

2.2.5.3 Polymerization of ϵ -caprolactone

The cationic alkyl indium complex **39** previously reported by the Mehrkhodavandi group was capable of polymerizing ϵ -CL in the absence of an external initiator.⁹⁰ Attempts to conduct the ROP of ϵ -CL using **48a-c** at 60 °C and 80 °C did not result in monomer conversion. However, at 100 °C polymerization ensues with **48a** and **48b** exhibiting almost complete conversion of monomer (Table 2.4). The resultant polymer shows similar molecular weights, with **48b** giving a slightly lower dispersity than **48a**. However, **48c** exhibits only 67% conversion with a lower

molecular weight polymer and a dispersity approaching unity. The reduction in conversion and dispersity is directly correlated to the stabilization of the indium center by the hemilabile donor groups. With **48c** giving the highest control in polymerization then **48b** followed closely by **48a**.

Table 2.4. Polymerization of ϵ -CL with cationic alkylindium complexes.

					
Entry	Temp. (°C)	Catalyst	Conv. ^a (%)	M_n^c (Da)	\bar{D}^d
1	100	48a	>99	17 600	1.30
2	100	48b	95	17 400	1.16
3	100	48c	67	11 100	1.05

Reactions were performed for 24 h in toluene. $[\epsilon\text{-CL}] = 3.0\text{ M}$, $[\text{cat}] = 8.5\text{ mM}$. $[\epsilon\text{-CL}]/[\text{cat}] = 350$. ^aConversion was monitored by ^1H NMR spectroscopy. ^c M_n determined through GPC in THF. ^dDispersity = M_w/M_n

2.2.5.4 Polymerization of racemic-lactide

Based on the body of previous work by the Mehrkhodavandi group involving the use of indium complexes for the polymerization LA, an exploration of the reactivity of **48a-c** in the polymerization of *rac*-LA was warranted.^{30,39,40,53,102,103} Under the reaction conditions **48a** does not polymerize *rac*-LA, while **48b** exhibits only 20% conversion of monomer. Possibly due to the formation of low molecular weight oligomers, the products could not be isolated. In contrast, **48c** produced high molecular weight, low dispersity polymer with high conversion. (Table 2.5, entry 3). The polymerization of *rac*-LA in the absence of an external initiator by cationic complex, **48c** is unexpected. This behavior is discussed in more detail in Chapter 3.

Table 2.5. Polymerization of *rac*-LA with cationic alkylindium complexes.

Entry	Catalyst	Conv. ^a (%)	M_n cal ^b (Da)	M_n ^c (Da)	\bar{D}	i^* ^d
1	2a	<1	-	-	-	-
2	2b	20	-	-	-	-
3	2c	94	34 000	130 000	1.32	0.26

Reactions were performed for 24 h in toluene at 100 °C. [*rac*-LA] = 1.6 M, [cat] = 6.4 mM. [*rac*-LA]/[cat] = 250.

^a Conversion was monitored by ¹H NMR spectroscopy. ^b M_n Cal = Calculated number averaged molecular weight = [*rac*-LA]/[cat] × conversion × MW of *rac*-LA. ^c Determined through GPC in THF. ^d Initiation efficiency = (M_n cal/ M_n).

2.2.6 Mechanistic considerations

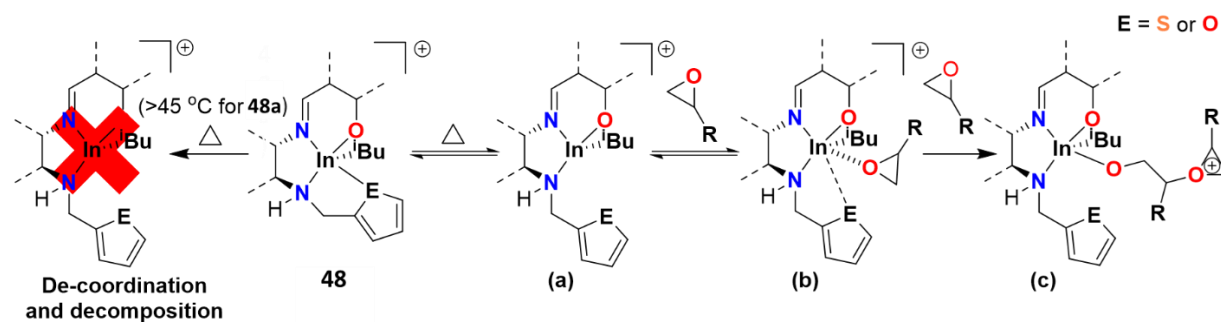


Figure 2.20. Proposed behavior of cationic complexes with (a) increasing temperature, (b) in the presence of a low concentration of epoxide and (c) at high concentration of epoxide resulting in cationic polymerization.

Based on the behavior of the complexes in the polymerizations of ECH and CHO and their temperature dependent behavior the following salient features can be proposed (Figure 2.20). At high temperature with the de-coordination of the pendant donor arm the stability of the cationic indium center is lost and decomposition of the complex occurs. However, at a narrow temperature range for **48a** and at a broader range for **48b**, the hemilabile behavior of the metal-donor (In-E) interaction becomes more pronounced with increasing temperature (Figure 2.20a). This, in turn,

facilitates the competitive coordination of monomer, resulting in higher initiation efficiencies at elevated temperatures (Figure 2.20b). The initiation of polymerization is also concentration dependent. At low concentrations the coordination of epoxide to the cationic indium center occurs reversibly (Table 2.2, entries 5 and 10). At higher concentrations epoxide ring opening and propagation of polymerization ensues with the attack by a second monomer molecule resulting in the irreversible de-coordination of the pendant donor arm and the formation of an alkoxide bond to the indium center (Figure 2.20c).

2.3 Conclusions

In conclusion, the donor ability of the heterocyclic moiety profoundly affects the labile behavior of the pendant donor arms, and thus the stability and the reactivity of the complexes. Through the addition of the hemilabile donor groups all three of the main outcomes expected from hemilabile ligands were achieved. First, the complex stability and stable lifespan was significantly improved in hemilabile ligand bearing complexes **48a-c** relative to the solvent stabilized **48d**. The stability followed the **48d**<**48a**<**48b**<**48c** trend pointing to direct correlation of complex stability and donor ability of the pendant groups.

Second, reactivity was controlled by regulating the coordination of reactants to the indium center. The reactivity is inversely related to stability. Complexes **48a** and **48b** are both active for the ROP of ECH. Unusually for a cationic species, **48c** showed controlled reactivity towards ROP of CHO in neat conditions. The polymerization of ϵ -CL could be carried by **48a-c** with the reactivity being in the following order **48a**>**48b**>**48c**. The ROP of epoxides and ϵ -CL provide instances of reactivity control brought about by the hemilabile ligand system.

Third, typical reactivity of cationic alkyl indium complexes was completely altered by the addition of the pyridine pendant group in **48c**. Complex **48c** was capable of ROP of *rac*-LA. This is an example of completely altering reactivity at the metal center by a hemilabile ligand system. The initiation mechanism for this reaction is discussed in further detail in Chapter 3.

2.4 Experimental

General Considerations. Unless otherwise indicated, all air- and/or water-sensitive reactions were carried out under dry nitrogen using either an MBraun glove box or standard Schlenk line techniques. NMR spectra were recorded on a Bruker Avance 300 MHz, 400 MHz and 600 MHz spectrometers. ^1H NMR chemical shifts are reported in ppm versus residual protons in deuterated solvents as follows: δ 7.27 CDCl_3 , δ 7.16 C_6D_6 , δ 7.16 $\text{C}_6\text{D}_5\text{Br}$ $^{13}\text{C}\{^1\text{H}\}$ NMR chemical shifts are reported in ppm versus residual ^{13}C in the solvent: δ 77.2 CDCl_3 . $^{19}\text{F}\{^1\text{H}\}$ NMR chemical shifts are reported in ppm and externally referenced to neat CFCl_3 at 0 ppm. $^{31}\text{P}\{^1\text{H}\}$ NMR chemical shifts are reported in ppm and externally referenced to 85% H_3PO_4 at 0 ppm.

Diffraction measurements for X-ray crystallography were made on a Bruker X8 APEX II diffraction and a Bruker APEX DUO diffraction with graphite monochromated Mo-K α radiation. The structures were solved by direct methods and refined by full-matrix least-squares using the SHELXTL crystallographic software of Bruker-AXS. Unless specified, all non-hydrogens were refined with anisotropic displacement parameters, and all hydrogen atoms were constrained to geometrically calculated positions but were not refined.

EA CHN analysis was performed using a Carlo Erba EA1108 elemental analyzer. The elemental composition of unknown samples was determined by using a calibration factor. The calibration factor was determined by analyzing a suitable certified organic standard (OAS) of a known elemental composition.

Polymer molecular weights were determined by triple detection gel permeation chromatography (GPC-LLS) using a Waters liquid chromatograph equipped with a Water 515 HPLC pump, Waters 717 plus autosampler, Waters Styragel columns (4.6×300 mm) HR5E, HR4 and HR2, Water 2410 differential refractometer, Wyatt tristar miniDAWN (laser light scattering detector) and a Wyatt ViscoStar viscometer. A flow rate of 0.5 mL min^{-1} was used and samples were dissolved in THF (2 mg mL^{-1}). Narrow molecular weight polystyrene standards were used for calibration purposes. Matrix-assisted laser desorption/ionization time-of-flight (MALDI-TOF) mass spectrometric analysis of isolated polymers was performed on a Bruker Autoflex MALDI-TOF equipped with a nitrogen laser (337 nm). The accelerating potential of the Bruker instrument was 19.5 kV. The polymer samples were dissolved in tetrahydrofuran (ca. 1 g/mL). The concentration of a cationization agent, sodium trifluoroacetate, in tetrahydrofuran was 1 mM. The matrix used was *trans*-[3-(4-*tert*-butylphenyl)2-methyl-2-propenylidene]malononitrile (DCTB) at the concentration of 20 mg/mL . A sample solution was prepared by mixing polymer, matrix, and salt in a volume ratio of 5:5:1, respectively.

Materials. Solvents (THF, pentane, toluene, hexane and diethyl ether) were collected from a Solvent Purification System from Innovative Technology, Inc. whose columns were packed with activated alumina. CDCl_3 was dried over CaH_2 , collected by vacuum distillation and degassed through a series of freeze-pump-thaw cycles. Dimethylanilinium Tetrakis(3,5-bis(trifluoromethyl)phenyl)borate ($[\text{HNMe}_2\text{Ph}][\text{BAr}^{\text{F}}_{24}]$) was generated by reacting dimethylanilinium chloride with sodium $\text{BAr}^{\text{F}}_{24}$ in diethyl ether at room temperature for 4 h.⁹⁰ The solvent was removed under high vacuum, and addition of hexane to the residual precipitated a white solid. The white solid was isolated by vacuum filtration and dried in *vacuo* for 4 h. InCl_3 was purchased from Strem Chemicals and used without further purification. Isobutylmagnesium

chloride (2.0 M in Et₂O) and dimethylanilinium chloride ([HNMe₂Ph]Cl) were purchased from Aldrich and Alfa Aesar, respectively, and used as received. *Rac*-lactide was recrystallized three times from dry toluene and dried under vacuum. ϵ -caprolactone were dried over CaH₂, distilled and stored under molecular sieves. In(^{*i*}Bu)₃ was synthesized according to a previously reported procedure.¹⁰⁴ Proligands L_{a-d} were synthesized by the modification of a previously reported procedure.¹⁰⁵

Synthesis of proligand L_a. (±)- trans-N-(thiophen-2-ylmethyl)cyclohexane-1,2-diamine (4.38 g, 20.8 mmol) was dissolved in 50 ml of acetonitrile (ACN) and 3,5-dicumylsalicylaldehyde (7.45 g, 20.8 mmol) was added while stirring. The solution was heated under reflux for 8 hours, and the solvent was removed under reduced pressure. The residue was dissolved in a minimum amount of ethyl acetate and crystallized by slow evaporation at low temperature to yield a pale-yellow solid (yield 63%). HRMS [M+H]⁺, calculated m/z = 551.3096. Found m/z = 551.3100. ¹H NMR (400 MHz, CDCl₃, 25 °C) δ 13.23 (1H, br. s., Ar-OH), 8.33 (1H, s, -N=CH-Ar), 7.03 - 7.41 (11H, m, ArH), 7.05 (1H, s, ArH), 7.13 (1H, m, Thioph α), 6.89 (1H, m, Thioph β), 6.74 (1H, m, Thioph γ), 3.97 (1H, d, ²J_{H-H} = 14 Hz, -CH₂- of thiophenyl), 3.86 (1H, d, ²J_{H-H} = 14 Hz, -CH₂- of thiophenyl), 2.95 (1H, m, -CH- of DACH), 2.63 (1H, m, -CH- of DACH), 1.02 - 1.74 (17H, m, -CH₂- of DACH and -CH₃ of cumyl), ¹³C{¹H} NMR (101 MHz, CDCl₃) δ 165.7 (N=CH-Ar), 157.8 (Ar C), 150.9 (Ar C), 139.8 (Ar C), 129.2 (Ar C-H), 128.2 (Ar C-H), 128.1 (Ar C-H), 126.9 (Ar C-H), 125.0 (Ar C-H), 124.3 (Thioph α), 126.8 (Thioph β), 125.2 (Thioph γ), 74.4 (C-H of DACH), 59.5 (C-H of DACH), 42.8 (-CH₂- of thiophenyl) 31.1 (-CH₃ of cumyl), 30.0 (-CH₃ of cumyl), 29.3 (-CH₃ of cumyl).

Synthesis of proligand L_b. (±)- trans-N-(furan-2-ylmethyl)cyclohexane-1,2-diamine (6.28 g, 32.3 mmol) was dissolved in 100 ml of acetonitrile (ACN) and 3,5-

dicumylsalicylaldehyde (11.6 g, 32.3 mmol) was added while stirring. The solution was heated under reflux for 8 hours, and the solvent was removed under reduced pressure. The residue was dissolved in a minimum amount of hot hexane and crystallized by slow evaporation at low temperature to yield a yellow solid (yield 61%). HRMS $[M+H]^+$, calculated $m/z = 535.3325$. Found $m/z = 535.3334$. 1H NMR (400 MHz, $CDCl_3$, 25 °C) δ 13.22 (1H, br. s., Ar-OH), 8.35 (1H, s, -N=CH-Ar), 7.02 - 7.43 (11H, m, ArH), 7.07 (1H, s, ArH), 7.16 (1H, m, furan α), 6.24 (1H, m, furan β), 5.98 (1H, m, furan γ), 3.73 (1H, d, $^2J_{H-H} = 15$ Hz, -CH₂- of furfuryl), 3.69 (1H, d, $^2J_{H-H} = 15$ Hz, -CH₂- of furfuryl), 2.95 (1H, m, -CH- of DACH), 2.57 (1H, m, -CH- of DACH), 1.06 – 2.12 (17H, m, -CH₂- of DACH and -CH₃ of cumyl), $^{13}C\{^1H\}$ NMR (101 MHz, $CDCl_3$) δ 165.8 (N=CH-Ar), 157.8 (Ar C), 153.8 (Ar C), 150.8 (Ar C), 139.8 (Ar C), 136.2 (Ar C), 142.0 (Ar C-H), 128.2 (Ar C-H), 128.1 (Ar C-H), 126.9 (Ar C-H), 125.2 (Furan α), 110.1 (Furan β), 107.0 (Furan γ), 74.2 (C-H of DACH), 59.3 (C-H of DACH), 43.1 (-CH₂- of furfuryl), 31.1 (-CH₃ of cumyl), 29.8 (-CH₃ of cumyl), 29.2 (-CH₃ of cumyl).

Synthesis of proligand L_c(±)- trans-N-(pyridin-2-ylmethyl)cyclohexane-1,2-diamine (7.54 g, 36.8 mmol) was dissolved in 100 ml of acetonitrile (ACN) and 3,5-dicumylsalicylaldehyde (13.2 g, 36.8 mmol) was added while stirring. The solution was heated under reflux for 8 hours, and the solvent was removed under reduced pressure. The residue was dissolved in a minimum amount of hot pentane and crystallized by slow evaporation at low temperature to yield a bright yellow solid (yield 64%). HRMS $[M+H]^+$, calculated $m/z = 546.3484$. Found $m/z = 546.3483$. 1H NMR (400 MHz, $CDCl_3$, 25 °C) δ 8.37 (1H, s, -N=CH-Ar), 7.03 - 7.41 (12H, m, ArH), 7.42 (1H, m, Pyr. α), 7.08 (1H, m, Pyr β), 8.25 (1H, m, Pyr γ), 7.01 (1H, m, Pyr δ), 3.88 (1H, d, $^2J_{H-H} = 15$ Hz, -CH₂- of pyridyl), 3.82 (1H, d, $^2J_{H-H} = 15$ Hz, -CH₂- of pyridyl), 3.05 (1H, m, -CH- of DACH), 2.52 (1H, m, -CH- of DACH), 1.09 – 2.14 (20H, m, -CH₂- of DACH

and -CH₃ of cumyl), ¹³C{¹H} NMR (101 MHz, CDCl₃) δ 165.3 (N=CH-Ar), 159.7 (Ar C), 157.6 (Ar C), 150.8 (Ar C), 139.6 (Ar C), 128.9 (Ar C-H), 126.7 (Ar C-H), 125.6 (Ar C-H), 125.1 (Ar C-H), 136.3 (Pyr α), 127.9 (Pyr β), 149.2 (Pyr γ), 122.0 (Pyr δ), 74.4 (C-H of DACH), 59.5 (C-H of DACH), 51.8 (-CH₂- of pyridyll), 30.9 (-CH₃ of cumyl), 30.1 (-CH₃ of cumyl).

Synthesis of proligand L_d. (±)- trans-N-benzylcyclohexane-1,2-diamine (5.62 g, 27.4 mmol) was dissolved in 100 ml of acetonitrile (ACN) and 3,5-dicumylsalicylaldehyde (9.83 g, 27.4 mmol) was added while stirring. The solution was heated under reflux for 8 hours, and the solvent was removed under reduced pressure. The residue was dissolved in a minimum amount of pentane and crystallized by slow evaporation at low temperature to yield a bright yellow solid (yield 71%). HRMS [M+H]⁺, calculated m/z = 545.3532. Found m/z = 545.3543. ¹H NMR (400 MHz, CDCl₃, 25 °C) δ 8.35 (1H, s, -N=CH-Ar), 7.03 - 7.45 (17H, m, ArH), 3.81 (1H, d, ²J_{H-H} = 14 Hz, -CH₂- of benzyl), 3.61 (1H, d, ²J_{H-H} = 14 Hz, -CH₂- of benzyl), 2.97 (1H, m, -CH- of DACH), 2.61 (1H, m, -CH- of DACH), 1.00 – 2.24 (20H, m, -CH₂- of DACH and -CH₃ of cumyl), ¹³C{¹H} NMR (101 MHz, CDCl₃) δ 165.6 (N=CH-Ar), 157.8 (Ar C), 150.7 (Ar C), 140.4 (Ar C), 139.7 (Ar C), 136.0 (Ar C), 129.1 (Ar C-H), 128.5 (Ar C-H), 127.9 (Ar C-H), 126.7 (Ar C-H), 125.6 (Ar C-H), 125.0 (Ar C-H), 74.2 (C-H of DACH), 59.8 (C-H of DACH), 50.9 (-CH₂- of benzyl), 30.9 (-CH₃ of cumyl), 29.7 (-CH₃ of cumyl), 29.2 (-CH₃ of cumyl).

Synthesis of complex 47a. A 20 mL scintillation vial was charged with proligand L_a (186 mg, 0.345 mmol) in hexane (5 ml). triisobutylindium, In(CH₂CH(CH₃)₂)₃ (100 mg, 0.345 mmol) was added to the stirring mixture. The reaction mixture was stirred for 4 h at room temperature and concentrated in vacuo, the residue was cooled to -30 °C to give yellow crystals. The solid was washed with hexane (3 × 3 mL) and dried under high vacuum for 4 hours. (Yield 94%) Anal. Calcd. For C₄₄H₅₉InN₂OS: C 67.84; H 7.65; N 3.60. Found: C 67.56; H 7.55; N 3.70. ¹H NMR

(400 MHz, CDCl₃, 25 °C) δ 8.02 (1H, s, -N=CH-Ar), 7.10 - 7.32 (11H, m, ArH), 7.18 (1H, m, Thioph α), 6.93 (1H, m, Thioph β), 6.86 (1H, m, Thioph γ), 6.79 (1H, s, ArH), 3.96 (1H, dd, $^2J_{H-H}=7$, 15 Hz, -CH₂- of thiophenyl), 3.69 (1H, d, $^2J_{H-H}=7$, 15 Hz, -CH₂- of thiophenyl), 2.94 (1H, m, -CH- of DACH), 2.58 (1H, m, -CH- of DACH), 0.95 – 2.29 (20H, m, -CH₂- of DACH, -CH₃ of cumyl and -CH- of *i*Bu), 0.84 (6H, d, $^3J_{H-H}=6$ Hz, -CH₃ of *i*Bu), 0.75 (6H, d, $^3J_{H-H}=6$ Hz, -CH₃ of *i*Bu), 0.47 (2H, d, $^3J_{H-H}=7$ Hz, -CH₂- of *i*Bu), 0.24 (2H, d, $^3J_{H-H}=7$ Hz, -CH₂- of *i*Bu), ¹³C{¹H} NMR (101 MHz, CDCl₃) δ 171.2 (N=CH-Ar), 168.1 (Ar C), 151.8 (Ar C), 151.5 (Ar C), 143.1 (Ar C), 141.3 (Ar C), 132.0 (Ar C-H), 131.7 (Ar C-H), 127.9 (Thioph α), 127.5 (Thioph β), 125.4 (Thioph γ), 72.4 (C-H of DACH), 60.9 (C-H of DACH), 44.6 (-CH₂- of thiophenyl) 31.0 (-CH₃ of cumyl), 29.6 (-CH₃ of cumyl), 28.1 (-CH₃ of *i*Bu), 27.9 (-CH₃ of *i*Bu), 29.5 (-CH₂- of *i*Bu), 29.3 (-CH₂- of *i*Bu).

Synthesis of complex 47b. Complex **47b** was generated using a similar procedure to complex **47a** (187 mg of **L_b**, 0.350 mmol, yield=95%). Anal. Calcd. For C₄₄H₅₉InN₂O₂: C 69.27; H 7.81; N 3.67. Found: C 69.10; H 7.69; N 3.64. ¹H NMR (400 MHz, CDCl₃, 25 °C) δ 8.06 (1H, s, -N=CH-Ar), 7.02 - 7.36 (11H, m, ArH), 7.34 (1H, m, Furan α), 6.80 (1H, ArH), 6.28 (1H, m, Furan β), 6.14 (1H, m, Furan γ), 3.81 (1H, dd, $^2J_{H-H}=6$, 14 Hz, -CH₂- of furfuryl), 3.71 (1H, d, $^2J_{H-H}=6$, 14 Hz, -CH₂- of furfuryl), 2.94 (1H, m, -CH- of DACH), 2.58 (1H, m, -CH- of DACH), 0.97 – 2.31 (16H, m, -CH₂- of DACH, -CH₃ of cumyl and -CH- of *i*Bu), 0.88 (6H, m, -CH₃ of *i*Bu), 0.74 (6H, m, -CH₃ of *i*Bu), 0.50 (2H, m, -CH₂- of *i*Bu), 0.11 (2H, m, -CH₂- of *i*Bu), ¹³C{¹H} NMR (101 MHz, CDCl₃) δ 171.7 (N=CH-Ar), 168.8 (Ar C), 152.9 (Ar C), 151 (Ar C), 152.0 (Ar C), 151.8 (Ar C), 142.3 (Furan α), 141.5 (Ar C), 132.2 (Ar C-H), 131.8 (Ar C-H), 128.2 (Ar C-H), 127.8 (Ar C-H), 127.1 (Ar C-H), 127.1 (Ar C-H), 124.6 (Ar C-H), 110.8 (Furan β), 107.8 (Furan γ), 70.6 (C-H of DACH), 61.1 (C-H of DACH), 42.5(-CH₂- of furfuryl) 31.1 (-CH₃ of cumyl), 29.8

(-CH₃ of cumyl), 29.5 (-CH₃ of cumyl), 28.5 (-CH₃ of *i*Bu), 28.4(-CH₃ of *i*Bu), 28.9 (-CH₂- of *i*Bu), 29.4 (-CH₂- of *i*Bu).

Synthesis of complex 47c. Complex **47c** was generated using a similar procedure to complex **47a** (191 mg of **L_c**, 0.350 mmol, yield=95%). Anal. Calcd. For C₄₅H₆₀InN₃O: C 68.83; H 7.83; N 5.43. Found: C 69.87; H 7.61; N 5.70. ¹H NMR (400 MHz, CDCl₃, 25 °C) δ 8.52 (1H, m, Pyr γ), 8.11 (1H, s, -N=CH-Ar), 7.09 - 7.35 (11H, m, ArH), 7.61 (1H, m, Pyr α), 7.16 (1H, m, Pyr δ), 7.03 (1H, m, Pyr β), 6.79 (1H, ArH), 3.84 (2H, m, -CH₂- of pyridyl), 3.01 (1H, m, -CH- of DACH), 2.63 (1H, m, -CH- of DACH), 0.93 – 2.18 (17H, m, -CH₂- of DACH, -CH₃ of cumyl and -CH- of *i*Bu), 0.88 (6H, m, -CH₃ of *i*Bu), 0.60 (6H, m, -CH₃ of *i*Bu), 0.52 (2H, m, -CH₂- of *i*Bu), -0.07 (2H, m, -CH₂- of *i*Bu), ¹³C{¹H} NMR (101 MHz, CDCl₃) δ 171.3 (N=CH-Ar), 169.3 (Ar C), 158.4 (Ar C), 151 (Ar C), 152.0 (Ar C), 142.3 (Pyr γ), 141.3 (Ar C), 136.6 (Pyr α), 131.9 (Ar C-H), 131.4 (Ar C-H), 128.0 (Ar C-H), 127.1 (Ar C-H), 125.4 (Pyr δ), 124.4 (Pyr β), 68.4 (C-H of DACH), 61.5 (C-H of DACH), 49.5 (-CH₂- of pyridyl) 31.0 (-CH₃ of cumyl), 29.9 (-CH₃ of cumyl), 29.0 (-CH₃ of cumyl), 28.3 (-CH₃ of *i*Bu), 27.9(-CH₃ of *i*Bu), 28.2 (-CH₂- of *i*Bu), 28.1 (-CH₂- of *i*Bu).

Synthesis of complex 47d. Complex **47d** was generated using a similar procedure to complex **47a** (191 mg of **L_d**, 0.350 mmol, yield=96%). Anal. Calcd. For C₄₆H₆₁InN₂O: C 71.48; H 7.97; N 3.63. Found: C 71.74; H 7.99; N 3.57. ¹H NMR (400 MHz, CDCl₃, 25 °C) δ 7.85 (1H, s, -N=CH-Ar), 6.80 - 7.20 (11H, m, ArH), 6.61 (1H, m, ArH), 3.61 (1H, dd, ²J_{H-H}=7, 13 Hz -CH₂- of benzyl), 3.50 (1H, dd, ²J_{H-H}=7, 13 Hz -CH₂- of benzyl), 2.75 (1H, m, -CH- of DACH), 2.41 (1H, m, -CH- of DACH), 0.77 – 2.13 (17H, m, -CH₂- of DACH, -CH₃ of cumyl and -CH- of *i*Bu), 0.68 (6H, d, ³J_{H-H}=7 Hz, -CH₃ of *i*Bu), 0.53 (6H, d, ³J_{H-H}=7 Hz, -CH₃ of *i*Bu), 0.32 (2H, d, ³J_{H-H}=7 Hz, -CH₂- of *i*Bu), -0.01 (2H, d, ³J_{H-H}=7 Hz, -CH₂- of *i*Bu), ¹³C{¹H} NMR (101 MHz, CDCl₃)

δ 171.0 (N=CH-Ar), 168.2 (Ar C), 151.7 (Ar C), 151.5 (Ar C), 141.2 (Ar C), 139.8 (Ar C), 132.0 (Ar C-H), 131.5 (Ar C-H), 128.7 (Ar C-H), 127.9 (Ar C-H), 124.4 (Ar C-H), 71.7 (C-H of DACH), 61.1 (C-H of DACH), 50.1 (-CH₂- of benzyl) 30.9(-CH₃ of cumyl), 29.4 (-CH₃ of cumyl), 29.5 (-CH₃ of cumyl), 27.8 (-CH₃ of *i*Bu), 28.1 (-CH₃ of *i*Bu), 29.4 (-CH₂- of *i*Bu), 29.4 (-CH₂- of *i*Bu).

Synthesis of complex 48a. A 20 mL scintillation vial was charged with **47a** (200 mg, 0.257 mmol) in C₆H₆ (3 ml). [HNMe₂Ph][BAr^F₂₄] (253 mg, 0.266 mmol) in C₆H₆ (2 ml) was added to the stirring solution of **47a**. The reaction mixture was stirred for 4 h at r.t. The solvent was removed in vacuo to obtain a yellow residue and cold hexane (3 ml) was added to the residue. After stirring for 1 h, the supernatant was decanted off to remove the byproduct NMe₂Ph. This step was repeated at least 3 times until a pale-yellow solid precipitate formed. The product was washed with hexane (2 × 3 ml) and dried under high vacuum for a few hours. (70%). Anal. Calcd. For C₇₂H₆₂BF₂₄InN₂OS: C 54.79; H 4.10; N 1.75. Found: C 55.16; H 4.57; N 2.02. ¹H NMR (400 MHz, CDCl₃, 25 °C) δ 8.22 (1H, s, -N=CH-Ar), 7.76 (8H, br. s., *ortho* H of BAr^F₂₄), 7.62 (1H, m, ArH), 7.57 (4H, br. s., *para* H of BAr^F₂₄), 6.94 - 7.42 (14H, m, ArH), 7.36 (1H, m, Thioph α), 7.05 (1H, m, Thioph β), 6.86 (1H, m, Thioph γ), 4.38 (1H, d, ²J_{H-H}=13 Hz, -CH₂- of thiophenyl), 3.75 (1H, m, -CH₂- of thiophenyl), 3.17 (1H, m, -CH- of DACH), 2.29 (1H, m, -CH- of DACH), 0.83 – 2.04 (16H, m, -CH₂- of DACH, -CH₃ of cumyl and -CH- of *i*Bu), 0.66 (6H, m, -CH₃ of *i*Bu), 0.73 (2H, m, -CH₂- of *i*Bu), ¹³C{¹H} NMR (101 MHz, CDCl₃) δ 169.3 (N=CH-Ar), 163.9 (Ar C), 161.3-162.4 (B-C), 151.7 (Ar C), 150.0 (Ar C), 141.8 (Ar C), 140.2 (Ar C), 138.8 (Ar C), 134.9 (*ortho* C-H of BAr^F₂₄), 134.4 (ArC-H), 131.7 (ArC-H), 130.9 (ArC-H), 129.6 (Thioph γ), 128.6-129.4 (qq, ²J_{C-F} = 3, 32 Hz, *meta* C of BAr^F₂₄), 127.4, 125.6, 123.8, 121.9 (q, ¹J_{C-F} = 273 Hz, -CF₃), 128.8 Thioph β), 128.3 (Thioph α), 118.1 (Ar C), 117.6 (*para* C-H of BAr^F₂₄), 65.5 (C-H of DACH), 62.6 (C-H of DACH), 46.6 (-CH₂- of furfuryl) 32.2 (-CH₂- of *i*Bu), 30.7 (-CH₃ of cumyl),

30.8 (-CH₃ of cumyl), 28.7 (-CH₃ of cumyl), 27.6 (-CH₃ of *i*Bu), ¹⁹F{¹H} NMR (282 MHz, CDCl₃): δ -61.9.

Synthesis of complex 48b. Complex **48b** was generated using a similar procedure to complex **48a** (200 mg of **47b**, 0.262 mmol, yield=75%). Anal. Calcd. For C₇₂H₆₂BF₂₄InN₂O₂: C 55.35; H 4.15; N 1.77. Found: C 54.86; H 4.18; N 1.89. ¹H NMR (400 MHz, CDCl₃, 25 °C) δ 8.19 (1H, s, -N=CH-Ar), 7.71 (8H, br. s., *ortho* H of BAr^F₂₄), 7.62 (1H, m, ArH), 7.53 (4H, br. s., *para* H of BAr^F₂₄), 6.90 - 7.36 (12H, m, ArH), 6.21 (1H, m, Furan α), 6.14 (1H, m, Furan β), 6.13 (1H, m, Furan γ), 4.03 (1H, d, ²J_{H-H}=15 Hz, -CH₂- of furfuryl), 3.80 (1H, m, -CH₂- of furfuryl), 3.12 (1H, m, -CH- of DACH), 2.33 (1H, m, -CH- of DACH), 0.85 – 2.29 (19H, m, -CH₂- of DACH, -CH₃ of cumyl, -CH- of *i*Bu and -CH₂- of *i*Bu), 0.83 (6H, m, -CH₃ of *i*Bu), ¹³C{¹H} NMR (101 MHz, CDCl₃) δ 170.7 (N=CH-Ar), 165.7 (Ar C), 161.2-162.4 (B-C), 150.0 (Ar C), 146.1 (Furan δ), 144.2.0 (Furan γ), 141.5 (Ar C), 139.4 (Ar C), 134.9 (*ortho* C-H of BAr^F₂₄), 134.8 (ArC-H), 132.4 (ArC-H), 128.7-129.4 (qq, ²J_{C-F} = 3, 32 Hz, *meta* C of BAr^F₂₄), 127.4, 125.6, 123.8, 121.9 (q, ¹J_{C-F} = 273 Hz, -CF₃), 126.2 (Ar C-H), 125.5 (Ar C-H), 122.0 (Ar C), 117.6 (*para* C-H of BAr^F₂₄), 117.3 (Ar C), 112.3 (Furan β), 110.9 (Furan α), 64.7 (C-H of DACH), 61.6 (C-H of DACH), 42.5 (-CH₂- of furfuryl) 31.3 (-CH₃ of cumyl), 30.9 (-CH₃ of cumyl), 30.8 (-CH₂- of DACH), 30.3 (-CH₂- of *i*Bu), 28.4 (-CH₃ of cumyl), 27.9 (-CH₂- of DACH), 27.8 (-CH₃ of *i*Bu), 23.9 (-CH₂- of DACH), 23.5 (-CH- of *i*Bu), ¹⁹F{¹H} NMR (282 MHz, CDCl₃): δ -62.0.

Synthesis of complex 48c. Complex **48c** was generated using a similar procedure to complex **48a** (200 mg of **47c**, 0.259 mmol, yield=86%). Anal. Calcd. For C₇₃H₆₃BF₂₄InN₃O: C 55.72; H 4.18; N 2.64. Found: C 55.60; H 4.28; N 2.82. ¹H NMR (400 MHz, CDCl₃, 25 °C) δ 8.20 (1H, s, -N=CH-Ar), 7.76 (9H, br. s., *ortho* H of BAr^F₂₄ and Pyr γ), 7.61 (1H, m, ArH), 7.54 (4H, br. s., *para* H of BAr^F₂₄), 7.19 - 7.39 (10H, m, ArH), 7.16 (1H, m, Pyr α), 7.10 (1H, m, Pyr δ),

6.95 (2H, m, Pyr β and ArH), 4.02 (2H, m, -CH₂- of pyridyl), 3.12 (1H, m, -CH₂- of thiophenyl), 3.17 (1H, m, -CH- of DACH), 0.95 – 2.56 (20H, m, -CH₂- of DACH, -CH₃ of cumyl, -CH- of *i*Bu and -CH₂- of *i*Bu), 0.87 (6H, m, -CH₃ of *i*Bu), ¹³C{¹H} NMR (101 MHz, CDCl₃) δ 171.0 (N=CH-Ar), 167.1 (Ar C), 161.8 (B-C), 152.2 (Ar C), 152.1 (Ar C), 150.0 (Pyr β), 149.9 (Ar C), 141.9 (Pyr γ), 135.1 (*ortho* C-H of BAr^F₂₄), 134.2 (ArC-H), 132.8 (Pyr δ), 128.7-129.4 (qq, ²J_{C-F} = 3, 32 Hz, *meta* C of BAr^F₂₄), 127.4, 125.6, 123.8, 121.9 (q, ¹J_{C-F} = 273 Hz, -CF₃), 126.2 (Ar C-H), 125.5 (Ar C-H), 124.0 (Pyr α), 117.6 (*para* C-H of BAr^F₂₄), 64.2 (C-H of DACH), 60.6 (C-H of DACH), 47.3 (-CH₂- of pyridyl) 33.8 (-CH₃ of cumyl), 30.9 (-CH₃ of cumyl), 25.9 (-CH₃ of cumyl), 27.8 (-CH₃ of *i*Bu), 27.3 (-CH₂- of *i*Bu), ¹⁹F{¹H} NMR (282 MHz, CDCl₃): δ -61.8.

Synthesis of complex 48d. Complex **48d** was generated using a similar procedure to complex **48a** but was obtained in a mixture of decomposition products and could not be purified. Synthesis of **48d** in THF at -30 °C resulted in less decomposition products. However, **48d** could not be isolated. Anal. Calcd. For C₇₄H₆₄BF₂₄InN₂O: C 56.70; H 4.20; N 1.70. Found: C 55.10; H 4.50; N 1.71. ¹H NMR (400 MHz, CDCl₃, 25 °C) δ 8.36 (1H, s, -N=CH-Ar), 7.70 (8H, br. s., *ortho* H of BAr^F₂₄), 7.52 (4H, br. s., *para* H of BAr^F₂₄), 7.07 - 7.45 (14H, m, ArH), 4.17 (1H, m, -CH₂- of benzyl), 3.98 (1H, m, -CH₂- of benzyl), 3.76 (-CH₂- of THF), 3.50 (1H, m, -CH- of DACH), 3.14 (1H, m, -CH- of DACH), -0.22 – 2.31 (24H, m, -CH₂- of DACH, -CH₃ of cumyl, -CH- of *i*Bu, -CH₂- of *i*Bu and -CH₃ of *i*Bu).

Representative polymerization of epoxides using cationic complexes (48a). A 7 mL scintillation vial was charged with a solution of complex **48a** (19.0 mg, 0.012 mmol) in 0.3 mL of C₆D₆. Epichlorohydrin (0.30 mL, 3.8 mmol) was added directly to the vial by a syringe. The mixture was stirred at 25 °C for 24 h. The resulting solution was concentrated under vacuum for 3 h and then cold methanol was added to it (0 °C, 15 mL). The polymer precipitated from solution

and was isolated by decantation or centrifugation. The isolated polymer was dried under high vacuum for at least 3 h prior to analysis.

Representative polymerization of ϵ -CL using cationic complexes (48b). A 20 ml scintillation vial was charged with a solution of complex **48b** (20.0 mg, 0.013 mmol) in 0.5 ml of toluene. A solution of ϵ -CL (0.5 ml, 4.5 mmol) in 0.5 ml of toluene was added to the vial. The mixture was stirred at 100 °C for 24 h. The resulting solution was concentrated under vacuum for 3 h and then cold methanol was slowly added to the vial (0 °C, 15 mL). The polymer precipitated from the solution and was isolated by decantation of the supernatant. The isolated polymer was dried under high vacuum for at least 3 h prior to analysis.

Representative polymerization of *rac*-LA using cationic complexes (48c). A 20 ml scintillation vial was charged with a solution of complex **48c** (10.1 mg, 0.006 mmol) in 1 ml of toluene. *Rac*-LA (230 mg, 1.6 mmol) was directly added to the vial. The mixture was stirred at 100 °C for 24 h. The resulting solution was concentrated under vacuum for 3 h and then cold methanol was slowly added to the vial (0 °C, 15 mL). The polymer precipitated from the solution and was isolated by decantation of the supernatant. The isolated polymer was dried under high vacuum for at least 3 h prior to analysis.

Chapter 3: Synthesis of high molecular weight cyclic poly(lactic acid) using an air stable cationic indium catalyst

3.1 Introduction

Cyclic polymers introduce restrictions to the dynamics of polymer chains due to their lack of chain ends. This limitation in the number of conformations and movement gives cyclic polymers greater crystallinity, higher thermal stability, and lower intrinsic viscosity compared to their linear counterparts.^{106–113} While petrochemical-based cyclic polymers such as polyolefins, polystyrene and polyacrylates^{114–117} have been studied extensively, biodegradable analogues are less prevalent. For example, the physical properties of poly(lactic acid) (PLA), a biodegradable¹¹⁸ and biocompatible polymer,^{119,120} are highly dependent on the topology of the polymer chains. Unlike other topologies, such as star-shaped or cross-linked PLA, cyclic PLA (c-PLA) holds a distinct place because it differs from linear PLA only by a single bond.^{53,121,122}

Most catalysts reported for c-PLA formation produce polymers with low molecular weights or high dispersities.^{19–33} In addition, the most active catalysts are air, moisture, and functional group intolerant.¹¹³ Extant catalysts capable of forming c-PLA can be separated into three broad classes: metal catalysts, organocatalysts, and hybrid metal-organocatalyst systems (Figure 3.1).

The metal-based catalysts proceed through a coordination insertion mechanism of lactide (LA) with Lewis acidic metals (Figure 3.2a) Organotin catalysts, such as tin(II) 2-ethylhexanoate (**49**),¹³⁸ form c-PLA through conditions that increase intramolecular transesterification.^{123–127} Another report showed the formation of cyclic poly(L-lactide) (c-PLLA) with a molecular weight of 165 kg mol⁻¹ using **49** under neat conditions.¹²³ These tin systems produce 95-99% cyclic polymer, however the polymer dispersity is consistently high ($\bar{D} = 1.85 - 8.7$). High molecular

weight, broad dispersity c-PLLA can also be generated using a bis(salicylaldiminato)tin(II) catalyst (**50**).¹²⁸ A handful of other metals form c-PLA, such as a 1:1 mixture of bismuth subsalicylate and salicylic acid for the formation of c-PLLA (**51**)¹²⁹ or the *pseudo*-alumatrane complex (**52**)¹³⁰ for the formation of c-PLLA in the melt. Complex **52** was the first reported instance in which a group 13 metal complex was used to produced non-oligomeric c-PLA.

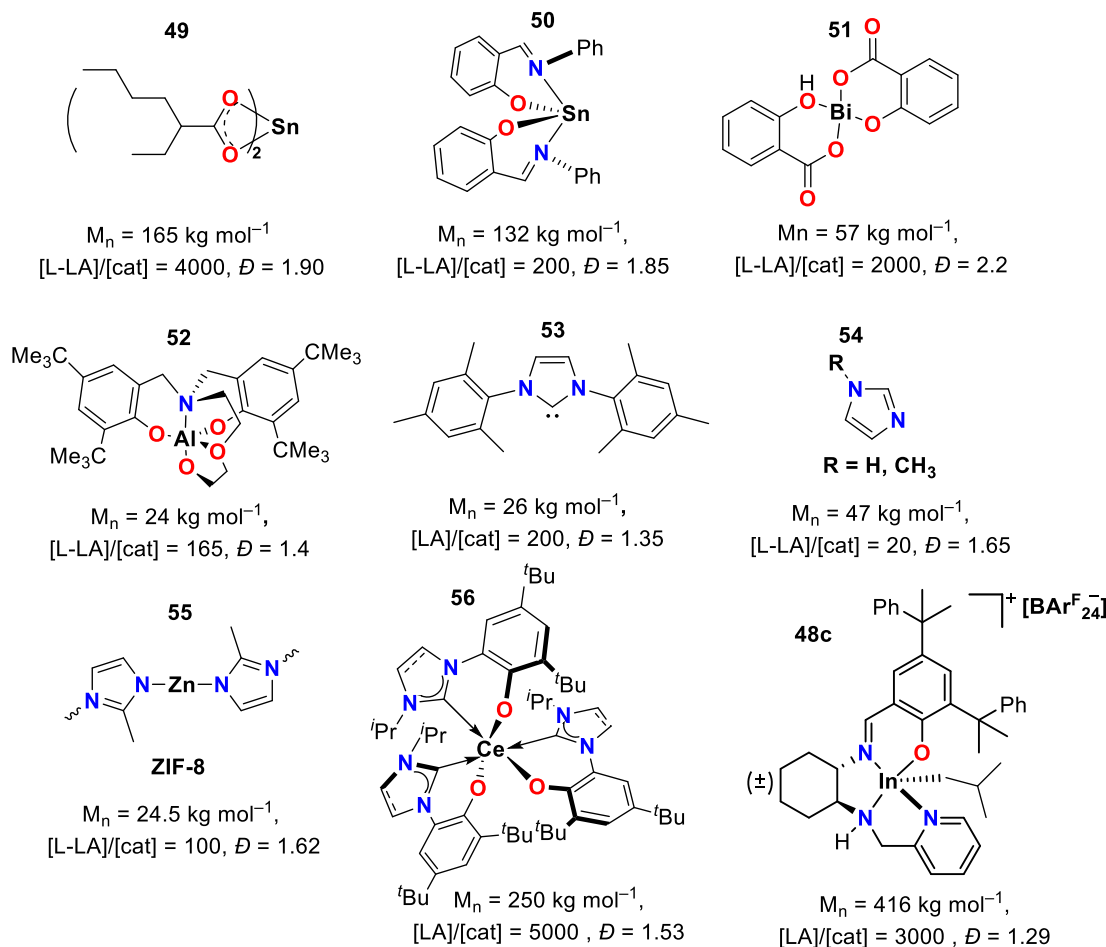


Figure 3.1. Catalysts capable of producing cyclic poly(lactide).

Organocatalysis in this reaction proceeds through a zwitterionic mechanism with a slow initiation step followed by a much faster propagation step giving rise to c-PLA, which is the kinetic product (Figure 3.2b). N-heterocyclic carbenes (NHCs) are prevalent as catalysts in the production

of c-PLA (**53**).^{131–135} Imidazole and alkylated derivatives (**54**) polymerize L-LA to give cyclic polymers; however, this system promotes extensive racemization of L-LA to form racemic c-PLA.¹³⁶

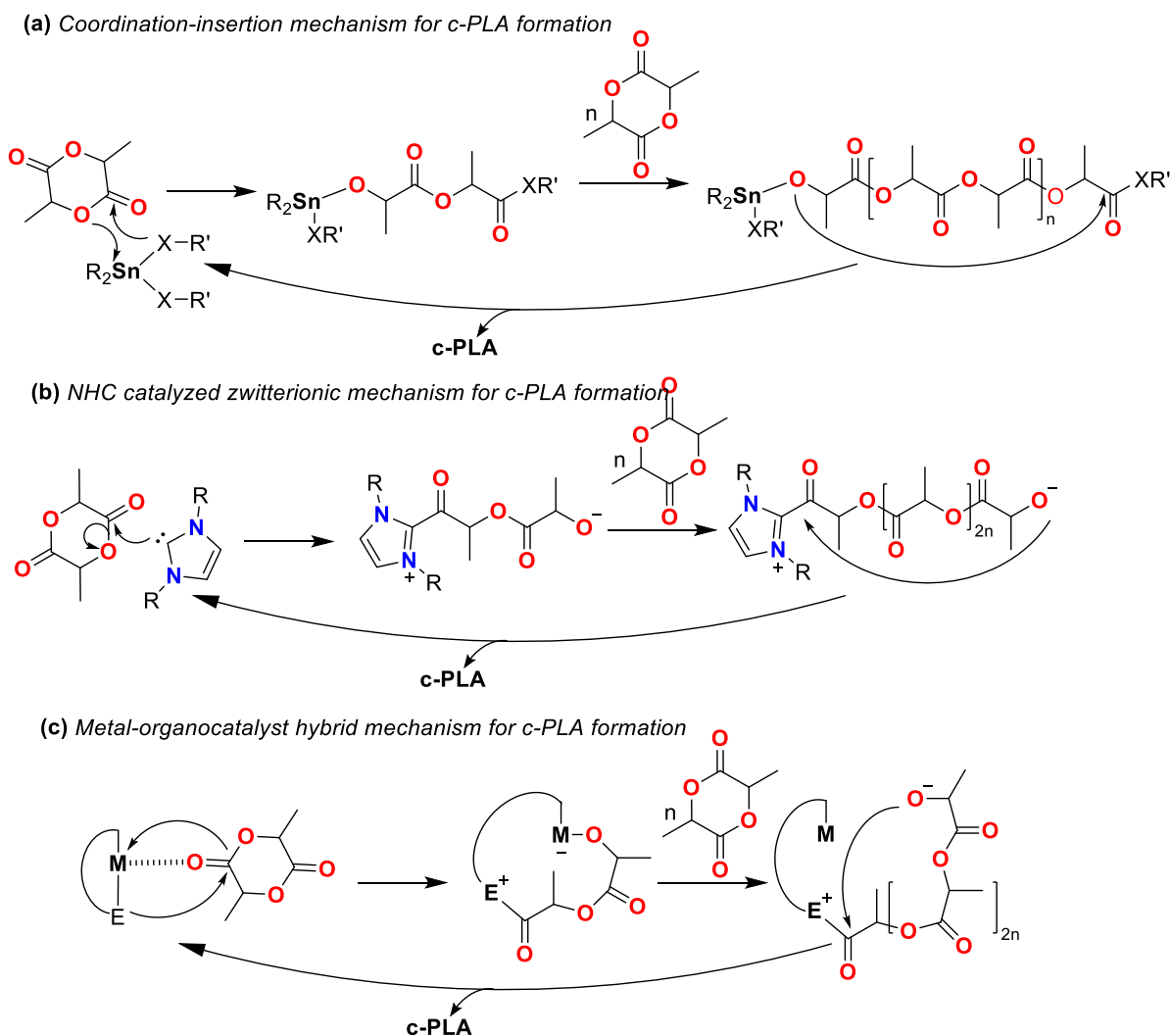


Figure 3.2. Representative mechanisms of the three major groups of catalysts.

The third class of catalysts, metal-organocatalyst systems, utilizes a Lewis acidic metal for lactide activation coupled with a hemilabile Lewis basic donor ligand capable of ring opening the monomer (Figure 3.2c). Recently, this principle was used to polymerize L-LA using the air stable,

zinc zeolitic imidazole framework, ZIF-8 (**55**); however, the resultant c-PLLA showed low molecular weights and high dispersity.¹³⁵

One of the highest molecular weights and fastest reactivities for c-PLA formation was obtained using a hybrid Ce(III)-NHC catalyst reported recently by Arnold, Williams and co-workers (**56**).¹¹³ This system was highly active and produced c-PLA with 95% cyclic fidelity, reaching higher molecular weight polymers ($\sim 400 \text{ kg mol}^{-1}$), albeit with only 60% monomer conversion. At 90% conversion, this system forms c-PLA with a maximum molecular weight of 250 kg mol^{-1} . While this benchmark system offers an efficient method for producing high molecular weight c-PLA, the lower conversions and their highly air sensitive nature can negatively impact the applicability of this system.¹³⁹ Thus, the synthesis of high molecular weight, narrow dispersity cyclic polymers remain an ongoing research challenge.

Use of a more air and functional group tolerant metal such as indium can offer a solution to this challenge.⁵³ The cationic alkylindium complexes bearing hemilabile ligands with heterocyclic side arms (**48a-c**) described in Chapter 2 are capable of ring opening polymerization of several oxygenated monomers.¹⁴⁰ One of these complexes **48c**, featuring a pyridine pendant arm, polymerized *rac*-LA to give the highest molecular weight c-PLA reported to date (Figure 3.1).

In this chapter, the polymerization of *rac*-LA with **48c** is studied showing that the resulting c-PLA has very high molecular weight and low dispersity. Additionally, the complex remains highly active even after prolonged exposure to moist air. The polymerization mechanism is explored and the thermal properties of c-PLLA, cyclic poly(D-lactide) (c-PDLA), and a stereocomplex of the two polymers are investigated. Although indium catalysts have been extensively used to polymerize LA, none of these could form cyclic PLA.^{30,40,53,102}

3.2 Results and discussion

In this section c-PLA is generated and characterized followed by an investigation into kinetics and mechanism of polymerization.

3.2.1 Generation and characterization of cyclic PLA

Table 3.1. Formation of c-PLA by ring opening polymerization of *rac*-LA using complex **48c**

Entry	[LA]/[cat]	Time (h)	Conv. ^b	M_n^c (Da)	$M_{n\text{ calc}}^d$ (Da)	\bar{D}^e	i^{*f}
1	50	24	>99	36 000	7200	1.27	0.21
2	250	24	>99	132 000	36 000	1.30	0.27
3 ^g	250	24	97	125 000	35 000	1.34	0.28
4 ^h	250	24	94	140 000	34 000	1.30	0.26
5	1000	48	90	241 000	130 000	1.42	0.54
6	2000	48	90	292 000	259 000	1.28	0.89
7	3000	48	91	416 000	393 000	1.29	0.94
8 ⁱ	250	24	>99	107 000	36 000	1.28	0.34
9 ^j	250	24	98	93 000	35 000	1.52	0.38
10 ^k	250	24	<1	-	-	-	-
11 ^l	250	24	<1	-	-	-	-
12 ^m	250	24	<1	-	-	-	-
13 ⁿ	250	24	<1	-	-	-	-

^a Reactions were performed in toluene at 100 °C, [*rac*-LA] = 0.8 M. ^b Conversion was monitored by ¹H NMR spectroscopy. ^c M_n determined through SEC in THF. ^d $M_{n\text{ Cal}}$ = calculated number averaged molecular weight = [*rac*-LA]/[cat] × conversion × molar mass of *rac*-LA. ^e Dispersity = M_w/M_n . ^f Initiation efficiency = ($M_{n\text{ Cal}}/M_n$). ^g **48c** was exposed to air for 24 h prior to use. ^h **48c** was exposed to air for 10 days prior to use. ⁱ Reaction performed with L-LA. ^j Reaction performed with D-LA. ^k Reaction performed in THF at 100 °C. ^l Reaction performed in tetrahydropyran (THP) at 100 °C. ^m Reaction performed with InBr₃ at 100 °C. ⁿ Reaction performed with 1:1 benzyl alcohol:**48c**

The goal of this project was to generate high molecular weight cyclic PLA (c-PLA) while maximizing monomer conversion. The work from the previous chapter shows that the reaction of **48c** with *rac*-LA in toluene at 100 °C forms high molecular weight c-PLA with a dispersity of 1.30.¹⁴⁰ However, the initiation efficiency, $M_{n\text{ Cal}}/M_n$, of the process was only 27% (Table 3.1,

entry 2). By lowering pre-catalyst loadings, and increasing the reaction time, the molecular weights and initiation efficiencies increase (Table 3.1, entries 5-7). With a LA:**48c** ratio of 3000, 91% of *rac*-LA is converted to obtain the highest molecular weight c-PLA reported to date (M_n 416,000 g mol⁻¹, \bar{D} = 1.29) (Table 3.1, entry 7). The dispersity of the c-PLA is consistently ~1.3, showing a high degree of reproducibility and consistency.

Currently, **48c** is the only known air stable discrete complex for c-PLA formation. To this end its reactivity after prolonged exposure to high relative humidity air (>80%) was tested. After 24 h of exposure, **48c** polymerized *rac*-LA without a significant loss of reactivity (Table 3.1, entry 3). After 10 days of exposure this complex shows similar reactivity to the complex under inert conditions, with only a 5% decrease in conversion (Table 3.1, entries 2 and 4). The resultant polymer was cyclic PLA (Figures B.5 and B.8) as confirmed by lower intrinsic viscosity.

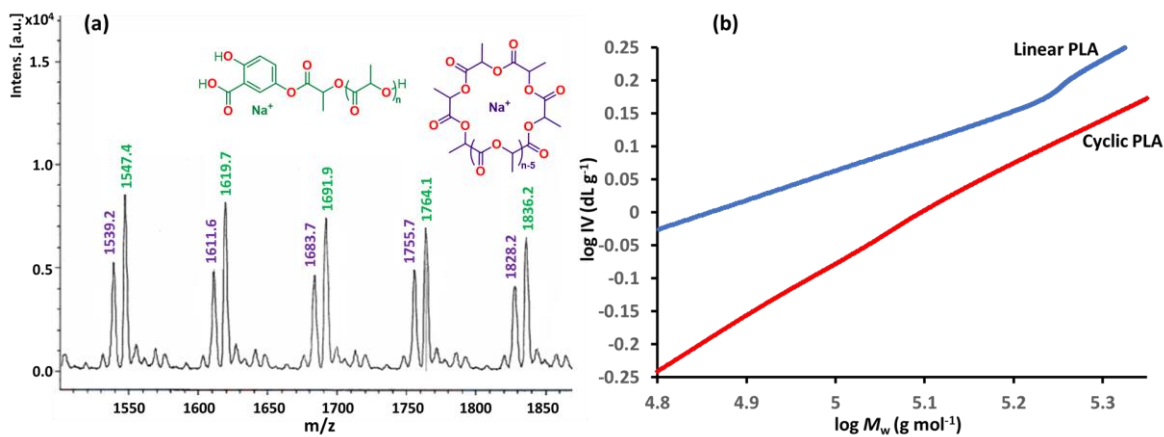


Figure 3.3. (a) Magnified MALDI-TOF spectrum of c-PLA (Table 3.1, entry 1). (b) Mark-Houwink plots for high molecular weight c-PLA (Table 3.1, entry 2) and linear PLA (Table B.2, entry 3)

Complex **48c** shows remarkable fidelity in selectively producing c-PLA in low molecular weight fractions. Matrix-assisted laser-desorption ionization time-of-flight (MALDI-TOF) mass spectrometry of a sample (Table 3.1, entry 1) shows only peaks arising from the cyclic product and the linearized polymer bearing a chain-end composed of the matrix material, 2,5-

dihydroxybenzoic acid formed during the ionization process (Figure 3.3a, Figure B.3 and B.4). To further establish its cyclic nature, a purified polymer sample was characterized using ^1H , $^{13}\text{C}\{^1\text{H}\}$, COSY, and HSQC NMR spectroscopy (Figures B.11-B.14). As a point of comparison, linear PLA was synthesized using the air and moisture stable indium catalyst **31b** previously reported by the Mehrkhodavandi group (Table B.2)⁵³ The ^1H NMR spectrum of the linear polymer shows signals from the ethoxy chain-end arising from the initiator moiety on the indium catalyst (Figure B.10). The lack of signals arising from possible chain-end groups such as methoxide or phenoxide support the formation of high purity c-PLA in the low molecular weight fractions.

In order to confirm the cyclic nature of high molecular weight fractions of c-PLA, intrinsic viscosity ($[\eta]$) measurements obtained through Size Exclusion Chromatography (SEC) were considered. Owing to their smaller hydrodynamic radius, cyclic polymers have intrinsic viscosities lowered by approximately a third in relation to their linear analogues.¹⁴¹ The Mark–Houwink plot generated for high molecular weight c-PLA (Table 3.1, entry 2) and an analogous linear PLA sample (Table B.2, entry 3) confirms that the intrinsic viscosity of the linear polymer is consistently higher than that of c-PLA (Figure 3.3b, Figures B.6, B.7 and B.9). The ratio of $[\eta]_{\text{cyclic}}/[\eta]_{\text{linear}}$ of 0.70 is in agreement with previously reported theoretical and experimental findings for c-PLA.^{137,142} The combination of MALDI-TOF spectra, NMR spectra and intrinsic viscosity data confirm the capability of **48c** to form c-PLA.

3.2.2 Catalytic behaviour of **48c**

Although the term ‘catalyst’ is used to describe most organometallic complexes used in polymerization reactions, a part of the metal complex initiates the polymerization and modifies its own structure (Figure 1.6). The complex is usually not restored to its original state, thus they are often “initiators” instead of “true catalysts”.

Complex **48c** behaves as a true catalyst rather than an initiator. To investigate, a reaction of **48c** with 250 equiv. *rac*-LA was set up and monitored at 24 h intervals. At each interval, an aliquot was removed to determine monomer conversion and molecular weight, and an additional 250 equiv. of *rac*-LA was added to the reaction mixture (Figure 3.4, Table 3.2). After each 24 h interval: (1) a small increase in polymer molecular weight, (2) a reduction in monomer conversion (99% after the first addition, while only 72% after the fifth addition), and (3) constant polymer dispersity (~1.3) were observed. While there is a minor increase in molecular weight after each addition, this is insufficient to be attributed to a ‘living’ polymerization. The increased molecular weights and lower monomer conversions are the direct result of limitations in mass transfer as the viscosity of the reaction mixture increases with each addition of monomer. The consistency of the polymer molecular weights and dispersities suggest that **48c** catalyzes the ROP LA to form c-PLA in a truly catalytic fashion.

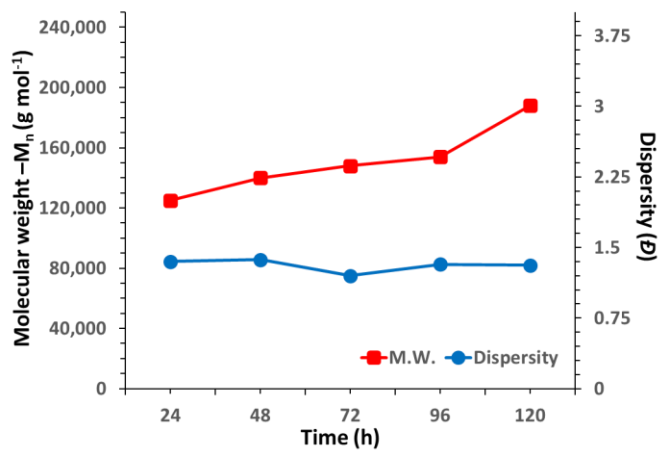


Figure 3.4. The relationship of molecular weight and dispersity at each addition of monomer at 24 h intervals

Table 3.2. Formation of c-PLA using **48c** by consecutive addition of *rac*-LA

Entry	[LA]/[cat]	Time (h)	Conv. ^b	M_n ^c (Da)	\bar{D} ^d
1	250	24	>99	125,000	1.35
2	+250	24	97	140,000	1.37
3	+250	24	86	148,000	1.20
4	+250	24	87	154,000	1.32
5	+250	24	72	188,000	1.31

^a Reactions were performed in toluene at 100 °C, [*rac*-LA] = 0.8 M.

^b Conversion was monitored by ¹H NMR spectroscopy. ^c M_n determined through SEC in THF. ^d Dispersity = M_w/M_n .

3.2.3 Mechanistic discussion

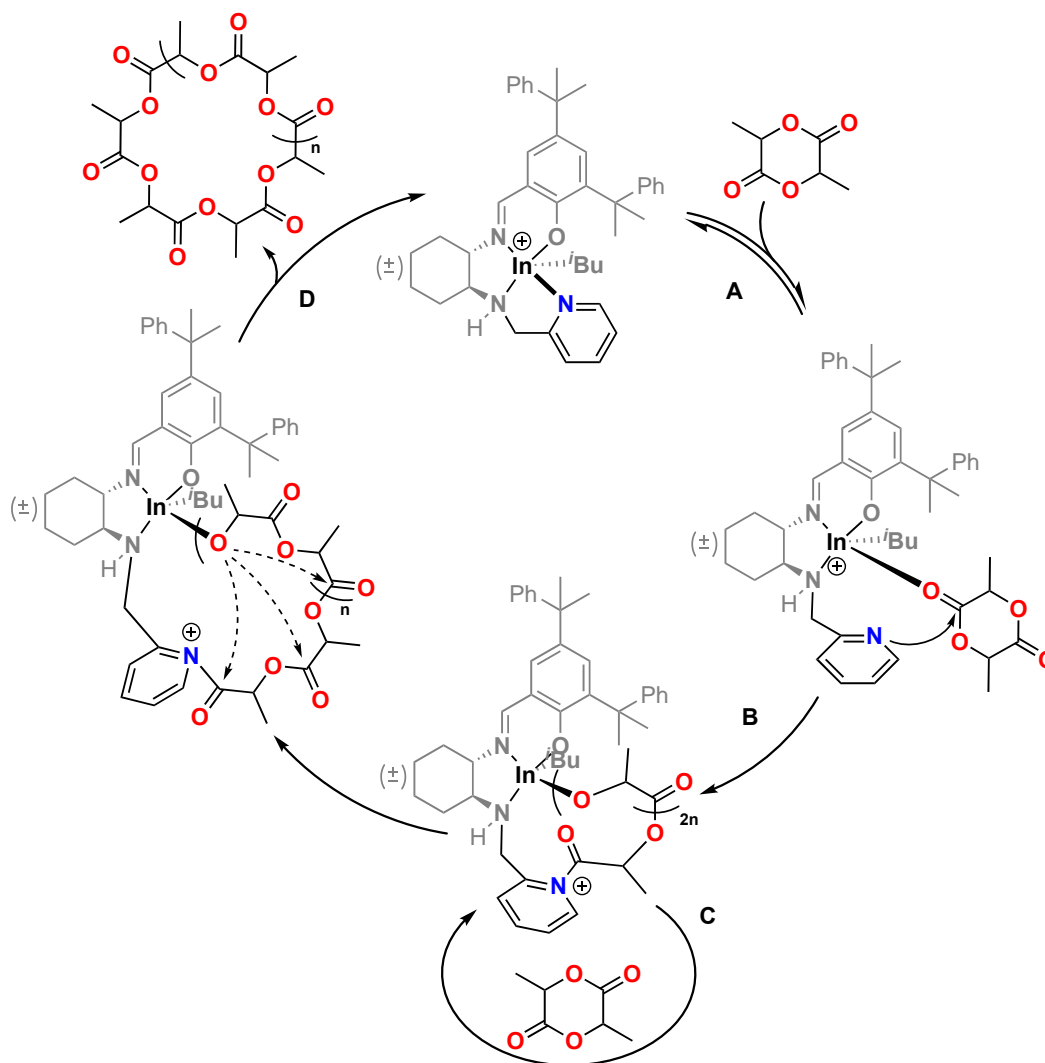


Figure 3.5. Proposed mechanism of the polymerization of LA to form c-PLA by complex **48c**.

The proposed mechanism for the polymerization of LA to form c-PLA suggests a bifunctional coordination-insertion process (Figure 3.5). The first step involves the reversible coordination of LA to the cationic indium center and the de-coordination of the pyridine donor arm (Figure 3.5A). This process depends on the Lewis acidity of the indium center as well as the dissociative potential of the pyridine pendent arm.

A modified Gutmann-Beckett experiment shows that cationic complex **48c** is significantly more Lewis acidic than its neutral dialkyl precursor complex **47c** (Figure 3.6).⁹¹ This experiment also shows that **48c** has a relative Lewis acidity comparable to InBr₃. But InBr₃ cannot polymerize LA under the experimental conditions, supporting the fact that high Lewis acidity in the absence of an initiator is insufficient for polymerization to occur (Table 3.1, entry 12).

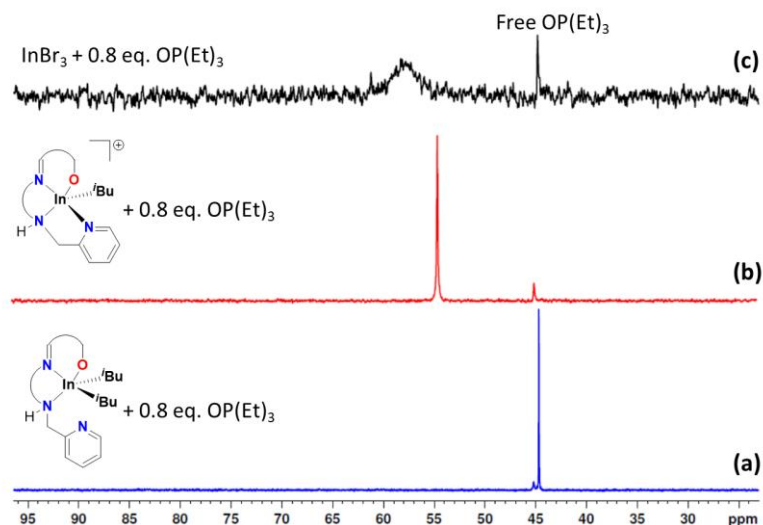


Figure 3.6. $^{31}\text{P}\{^1\text{H}\}$ NMR spectra (162 MHz, C_6D_6 , 25 °C) of a) the neutral dialkyl complex **47c** b) **48c** and c) InBr₃ after the addition of 0.8 equivalents of triethylphosphine oxide. The free OPET₃ shift is determined by the addition of a capillary inside the NMR tube containing a solution of OPET₃ in C_6D_6 .

The ability of **48c** to form c-PLA depends on the substrate-triggered hemilability of the pyridine group at high temperatures. As shown by various NMR spectroscopic techniques, the pyridine donor arm of **48c** remains coordinated to the cationic indium center in solution at room temperature (Figures A.50-A.55). This is further supported by the solid-state structure obtained using single crystal X-ray crystallography (Figure 3.7). The pyridine N-In bond length is approximately 2.25 Å. As shown in the previous chapter¹⁴⁰ detailing the hemilabile nature of this complex and related complexes, the stability and reactivity of the complexes are positively correlated to the donor ability of the pendant group. The coordinated pyridine pendant group gives

48c its stability towards high-humidity conditions. However, it was also found that the donor triggered disassociation of the pendant donor group is essential for reactivity. Additionally, high temperatures and competing donor entities can facilitate fluxional behavior in the pendant arm.¹⁴⁰

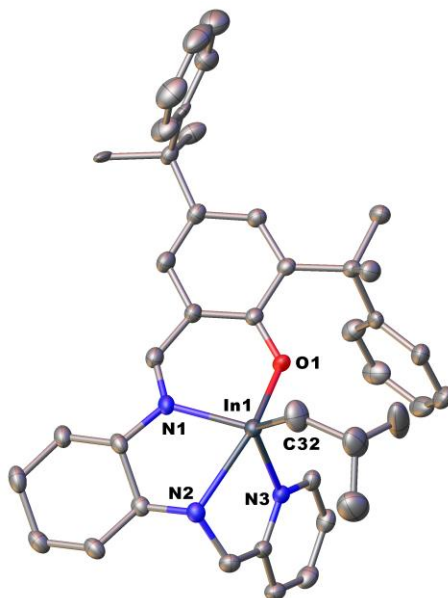


Figure 3.7. The molecular structure of the cation of **48c**. (depicted with thermal ellipsoids at 50% probability and H atoms, BarF_{24} counterion, solvent molecules as well as minor disorders omitted for clarity)

The reversible coordination of *rac*-LA to the metal center at 100 °C and its disassociation at 25 °C can be observed by ^1H NMR spectroscopy. When a 1:1 mixture of *rac*-LA and **48c** are heated in an oil bath at 100 °C for 12 h, the ^1H NMR spectrum of the mixture obtained at 25 °C immediately after the reaction shows a broad polymeric peak at $\delta = \sim 4.5\text{--}5.3$ ppm and an additional quartet at $\delta = 4.08$ ppm (Figure 3.8b). Characterization by COSY and HMBC NMR spectroscopy confirm that this peak represents a $\sim 12\%$ fraction of *rac*-LA (Figures B.24 and B.25). After 30 minutes at 25 °C, this new peak disappears (Figure 3.8c). However, upon reheating the solution to 100 °C, the reappearance of the peak indicates re-coordination of LA (Figure 3.8d).

These experiments suggest that reversible lactide coordination to complex **48c** is indeed the first step of the proposed catalytic cycle.

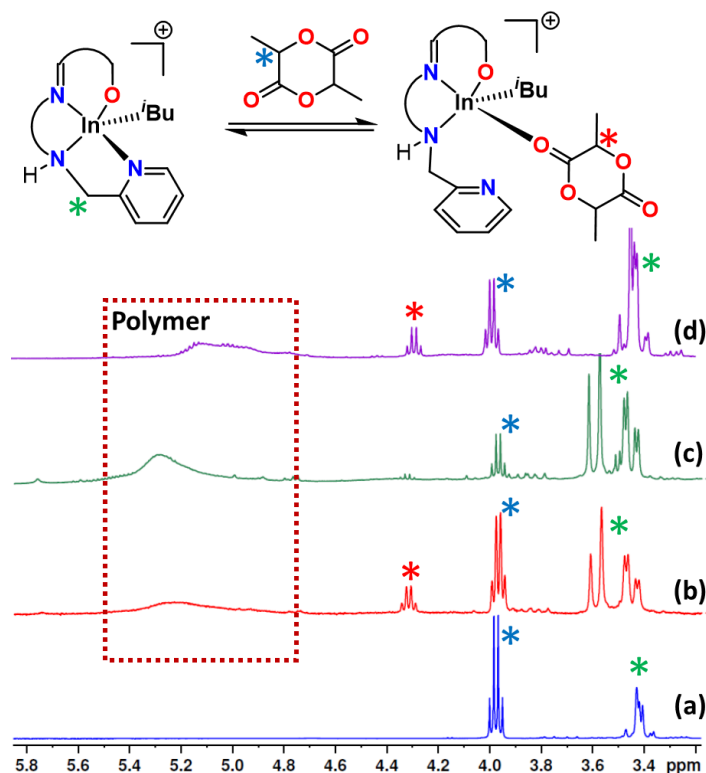


Figure 3.8. *rac*-LA methine proton region of ^1H NMR spectra (400 MHz in Tol-d_8) of a 1:1 mixture of **48c** and *rac*-LA a) at 100 °C 0 h, b) at 100 °C for 12 h, observed at 25 °C, c) after an additional 1 h at 25 °C and d) re-heated to 100 °C in the spectrometer.

Pyridine and some of its derivatives have been reported to polymerize LA.¹⁴³ Hence, at high temperatures and in the presence of donor solvents, it should be possible for the disassociated pyridine moiety to polymerize LA. However, when this reaction is conducted in donating solvents that can prevent monomer coordination, such as THF and THP at 100 °C, no reactivity was observed (Table 3.1, entries 10,11), showing that the disassociated pyridine moiety cannot polymerize LA without monomer activation by the metal center. Furthermore, no reactivity was observed at temperatures below 100 °C, *i.e.*, conditions unsuitable for the disassociation of the

pendant arm. These experiments show that for polymerization of LA to occur, the coordination of monomer to the cationic indium center and the de-coordination of the pyridine pendant group must both occur.

The second step in the mechanism entails initiation, which ensues when the lone pair on the disassociated pyridyl group attacks the activated carbonyl of the coordinated LA, ring-opening the monomer and forming an indium-centered metallocycle that incorporates a pyridinium cation (Figure 3.5B). In this process the cationic center is shifted from the metal to the pyridine-*N*. Propagation occurs through the repeated insertion of monomer molecules to the newly formed indium alkoxide bond (Figure 3.5C).

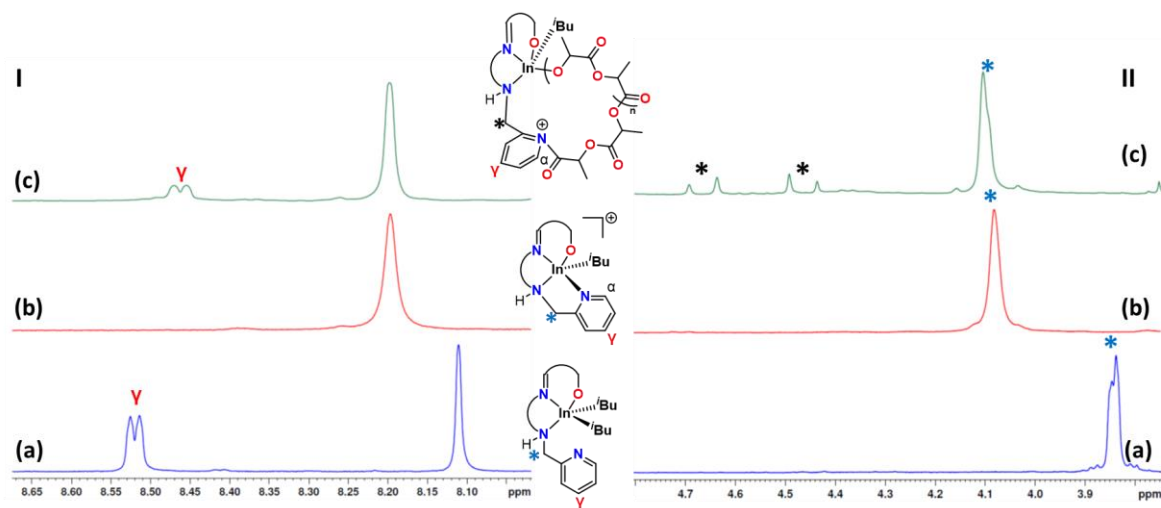


Figure 3.9. Imine (I) and methylene (II) proton regions of ^1H NMR spectra (400 MHz, 25 °C in CDCl_3) of a) **47c**, b) complex **48c** and c) 1:1 mixture *rac*-LA and **48c** heated at 100 °C for 24 h

The formation of the initial and subsequent metallacycles can be observed by NMR spectroscopy. The ^1H NMR spectrum of a 1:1 mixture of **48c** and *rac*-LA heated to 100 °C for 24 h shows the complete conversion of LA and new signals corresponding to PLA and a potential intermediate species (Figure 3.9-I). The new signals are approximately 20% of the complex as estimated by comparing the CH_2 -pyridine peaks of **48c** (overlapping at 4.10 ppm) with those of

the metallocycles ($\delta = 4.45$ and 4.65 ppm). The splitting of the methylene proton signals in Figure 3.9-IIc is due to the decreased degrees of freedom due to the metallacycle formation.¹⁴⁰ In addition, the signal for the γ -proton of the dissociated pyridine ($\delta = 8.46$ ppm) is downshifted from that of complex **48c** ($\delta = 7.76$ ppm) and resembles the same proton signal in the uncoordinated pyridyl in **47c** ($\delta = 8.52$ ppm) indicating a loss of proximity of the pyridine to indium (Figure 3.6-II).

The chain termination step happens predominantly by intramolecular chain-transfer facilitated by the spatial proximity of the two chain ends (Figure 3.5D). Additionally, the separation of peaks by 72 a.m.u on the MALDI-TOF spectrum suggests extensive transesterification in formation of c-PLA (Figures B.3-B.5). The proposed mechanism for this catalyst bears a close resemblance to the zwitterionic mechanism proposed for NHC catalysts and metal-NHC bifunctional systems (Figure 3.2c).^{137,144} Similar to the proposal by Arnold and Williams,¹¹³ to achieve high molecular weights the rate of intramolecular chain-transfer (*i.e.* macro-cyclization) has to be significantly slower than the rate of propagation.

3.2.4 Kinetics of c-PLA formation

The conversion vs. time plot obtained by measuring the conversion of monomer at several time intervals in a 24 h period using ^1H NMR spectroscopy shows a long initiation period followed by a rapid conversion of monomer to polymer (Figure 3.10a). For the first 12 h of reaction the conversion remains low ($\sim 15\%$) but stable. However, during the second 12 h period, the conversion increases rapidly to a final value of 97%. Similar to other reports of c-PLA formation,¹³³ this shows a slow initiation step (Figure 3.5A and 3.5B) and rapid propagation (Figure 3.5C) resulting in high molecular weight c-PLA.

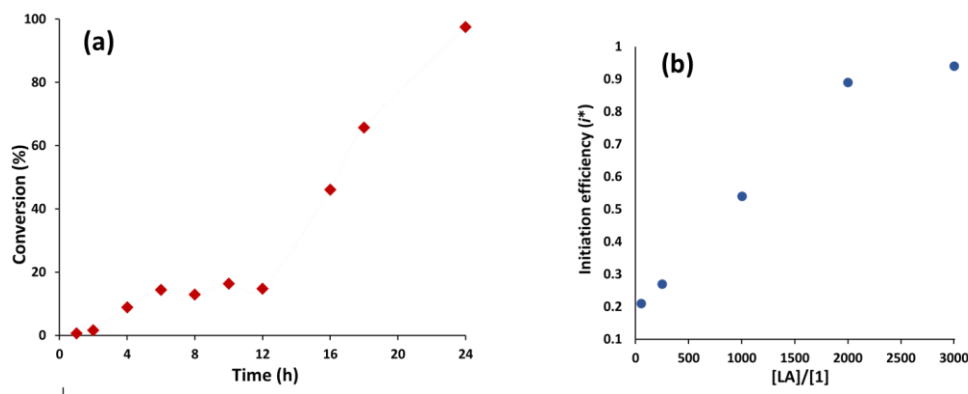


Figure 3.10. a) Conversion vs. time plot for the synthesis of c-PLA using **48c** (Reactions were performed in toluene at 100 °C, [*rac*-LA] = 0.8 M, conversion determined by ¹H NMR spectroscopy). b) Initiation efficiency vs. [LA]/[1] plot for the synthesis of c-PLA (Table 3.1)

To understand the nature of the catalyst function in more detail it is imperative to study the kinetics of the reaction and determine the reaction orders with respect to **48c** and monomer. The formation of product was observed by *in situ* ¹H NMR spectroscopy at 100 °C and the integration of the product peak with respect to the internal standard 1,3,5-trimethoxybenzene was used as an indirect measure of *rac*-LA conversion. The concentrations of [**48c**] or [LA] were varied while the other component was held constant. Concentration values were chosen to obtain reproducible measurements to avoid the deviations from linearity that arise at high conversions. The data obtained for three test concentrations were analyzed using variable time normalization analysis (VTNA), by plotting the reaction profile against the time axis multiplied by either [**48c**] (Figure 3.11a) or Σ[LA] (Figure 3.12c) raised to a numerical power where the reaction profiles overlap with each other the most when they are raised to the correct order.^{145,146} Using this methodology, this system demonstrates a first order rate dependence with respect to *rac*-LA and a zeroth order rate dependence for **48c**.

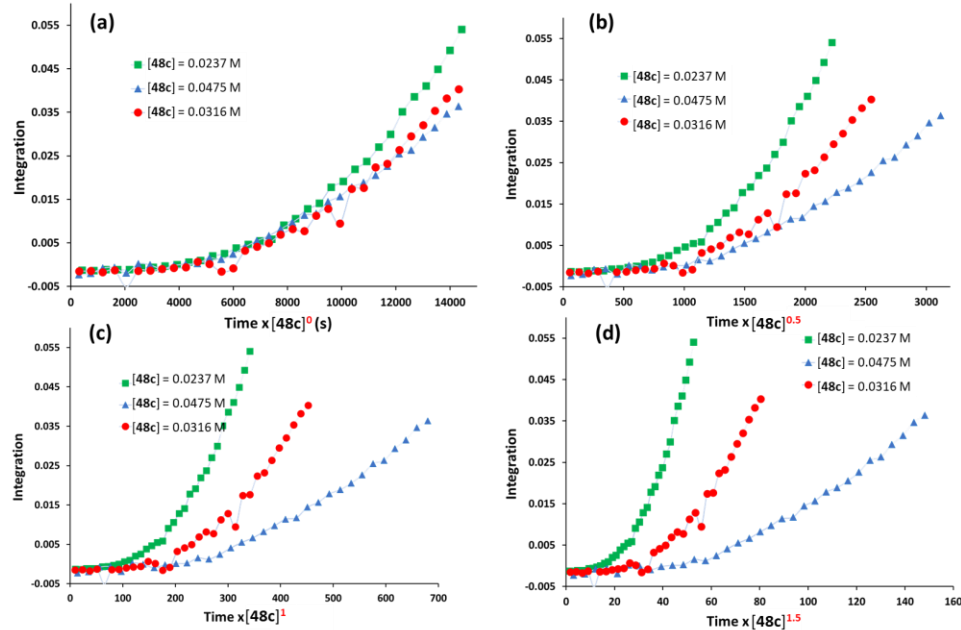


Figure 3.11. a) [48c] raised to power zero. b) [48c] raised to power 0.5. c) [48c] raised to power 1. d) [48c] raised to power 1.5. Reaction profiles overlay when [48c] is raised to the correct power. Reaction conditions: [LA] = 0.633 M; toluene d_8 ; T= 100 °C. (Integration determined with respect to 1,3,5-trimethoxybenzene).

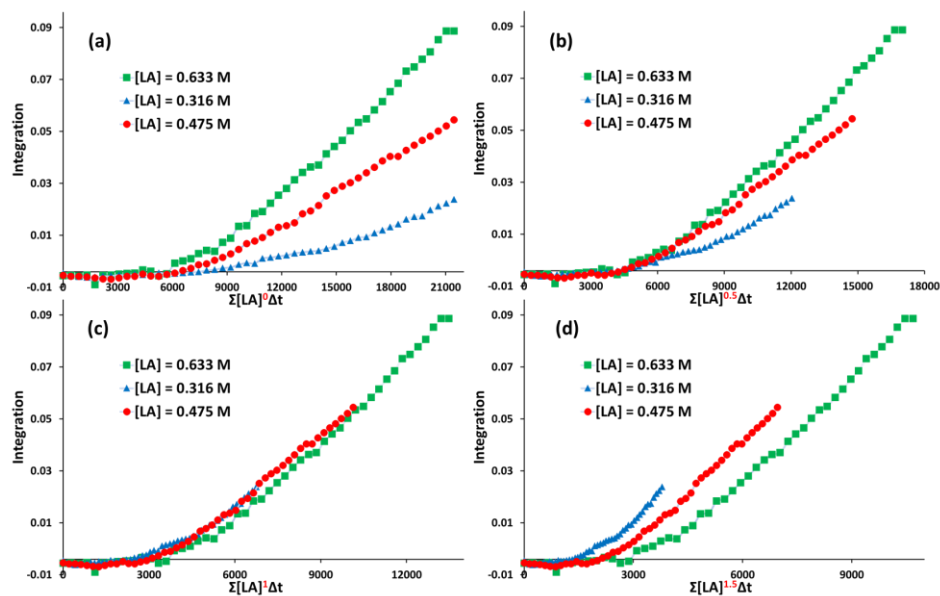


Figure 3.12. a) $\Sigma[LA]$ raised to power zero. b) $\Sigma[LA]$ raised to power 0.5. c) $\Sigma[LA]$ raised to power 1. d) $\Sigma[LA]$ raised to power 1.5. Reaction profiles overlay when $\Sigma[LA]$ is raised to the correct power. Reaction conditions: [48c] = 0.0316 M; toluene d_8 ; T= 100 °C. (Integration determined with respect to 1,3,5-trimethoxybenzene).

The apparent zeroth-order of the rate dependence with respect to **48c** may be more accurately described as a *pseudo*-zeroth order rate dependence due to low initiation efficiencies and the resulting excess of pre-catalyst present in the reaction mixture at [LA]/[**48c**] ratios <2000. This *pseudo*-zeroth order rate dependence on **48c** and the increasing initiation efficiencies with increasing monomer loadings (Figure 3.10b) show that only a small fraction of the pre-catalyst initiates the formation of c-PLA at lower [LA]/[**48c**] ratios. As the monomer loading increases, a larger fraction of the pre-catalyst is activated. Thus, the rate limiting step of the proposed catalytic cycle can be either step **A** or **B** (Figure 3.5).

While the molecular weight of c-PLA is dependent on the *rac*-LA:**48c** ratio, which gives this system characteristics of living polymerization, the stable molecular weights and dispersities of the multi-addition experiment (Table 3.2) shows that this is not the case. This apparent contradiction may be explained by the chain termination as monomer is exhausted, reforming complex **48c**, which can be reactivated upon further addition of monomer.

3.2.5 Exploration of polymer tacticity

Most studies on the formation of c-PLA have focused on the polymerization of L-LA to form c-PLLA. The reactivity of **48c** towards the polymerization of L- and D-LA to form c-PLLA and c-PDLA, respectively, was also explored. The dispersity and the initiation efficiency of the catalyst remains similar for both isomers (Table 3.1, entry 8). Owing to the difficulties in purifying the monomer, D-LA polymerizes to give a lower molecular weight and higher dispersity (Table 3.1, entry 9). The c-PLLA and c-PDLA produced using **48c** do not show racemization while c-PLA produced using *rac*-LA is atactic (Figures B.15-B.17); in comparison, bases such imidazole, and NHCs show epimerization of enantiopure monomers and form racemized c-PLA in similar reactions.^{134,136}

Table 3.3. Reported T_m values of cyclic and linear PLLA, PDLA and stereocomplexes of cyclic and linear-

PLLA/PDLA

	Polymer	M_n (g/mol) ^a	T_m (°C) ^b	T_g (°C) ^b	Catalyst	Ref
1	c-PLLA	107 000	178	59	48c	This work
2	c-PDLA	93 000	149	-	48c	This work
3 ^c	c-PLLA/c-PDLA	107 000/93 000	220	-	48c	This work
4	c-PLLA	401 000	172	62	56	¹¹³
5	c-PDLA	26 000	132	-	53	¹¹¹
6 ^c	c-PLLA/c-PDLA	30 000/26 000	179	-	53	¹¹¹
7 ^c	c-PLLA/c-PDLA	11 000/11 500	232	-	SnNaph₂	¹¹²
8	PLLA	15 000	150	-	53/BnOH	¹¹¹
9	PDLA	19 000	157	-	53/BnOH	¹¹¹
10 ^d	PLLA/PDLA	15 000/19 000	189	-	53/BnOH	¹¹¹

^a Molecular weight (M_n) determined using SEC. ^b Melting temperature and glass transition temperatures; measured using differential scanning calorimetry (DSC). ^c Stereocomplexes prepared by dissolving 1:1 mixtures of c-PLLA and c-PDLA in dichloromethane. ^d Stereocomplexes prepared by dissolving a 1:1 mixture of PLLA and PDLA in dichloromethane

The thermal properties of c-PLA produced from *rac*-LA (c-PLA) as well as c-PLLA and c-PDLA were determined using differential scanning calorimetry (DSC) (Table 3.3, Figures B.18-B.20). As expected, c-PLA is amorphous and shows a T_g of 54 °C. However, c-PLLA shows crystalline characteristics with a T_m of 178 °C similar to previously reported values (Table 3.3, entry 4).¹¹³ Interestingly, the c-PDLA synthesized using **48c** (T_m = 149 °C) has a significantly higher melting temperature than that of the polymer generated by NHC catalyst **53** (T_m = 132 °C) (Table 3.3, entry 5).¹¹¹ This difference may be attributed to the epimerization of the stereogenic centers of D-LA that occurs during polymerization by the NHC catalyst.¹¹¹ The loss of complete isotacticity leads to a lowering of the melting temperature of the prepared polymer.

Considering the lack of racemization and the high molecular weight of the cyclic polymers synthesized using **48c**, preliminary DSC analysis was conducted on a 1:1 mixture of c-PLLA and c-PDLA to determine thermal properties of a stereocomplex of the two cyclic polymers. The T_m

for the stereocomplex is approximately 220 °C, even without an annealing step (Figure B.21). While a minor endotherm is observable at 149 °C arising from residual c-PDLA, the DSC trace does not show any significant melting endotherms or a glass transition step below 195 °C, pointing to the crystalline nature of the stereocomplex. Previous studies on the T_m of c-PLLA/c-PDLA stereocomplexes suffered from significant racemization of the homopolymers during synthesis (Table 3.3, entry 6) and the need for lengthy annealing steps to achieve high melting temperatures (Table 3.3, entry 7).^{111,112}

3.3 Conclusions

The air and moisture stable complex **48c** can selectively and controllably polymerize *rac*-LA, L-LA, and D-LA to produce high molecular weight cyclic PLA in a highly reproducible fashion. Chain end group analysis by NMR spectroscopy and mass spectrometry followed by comparison of intrinsic viscosity with linear PLA conclusively support the predominant formation of cyclic polymer. The polymerization occurs through a coordination-insertion mechanism with the monomer coordinating to the cationic metal center and the subsequent ring opening being initiated by the pyridine group. The de-coordination of the hemilabile pyridine and the coordination of monomer are essential for polymerization.

Complex **48c** acts in a catalytic manner with the molecular weight of the polymer being a function of monomer: pre-catalyst ratio. Additionally, the cationic complex **48c** exhibits the remarkable ability to survive, without loss of activity, in high humidity conditions for multiple days. The air stable nature of **48c** allows it to be stored in less rigorous conditions and gives it a long and stable useful lifespan. The true catalytic behavior and stability of **48c** makes it an excellent candidate for industrial applications.

Furthermore, initial examination of polymer characteristics shows interesting thermal properties. Ultimately, the production of these high molecular weight polymers will potentially provide a route to new applications for cyclic PLA.

3.4 Experimental

General Considerations. Unless otherwise indicated, all air- and/or water-sensitive reactions were carried out under dry nitrogen using either an MBraun glove box or standard Schlenk line techniques. NMR spectra were recorded on a Bruker Avance 300 MHz, 400 MHz and 600 MHz spectrometers. ^1H NMR chemical shifts are reported in ppm versus residual protons in deuterated solvents as follows: δ 7.27 CDCl_3 , δ 7.16 C_6D_6 , $^{13}\text{C}\{^1\text{H}\}$ NMR chemical shifts are reported in ppm versus residual ^{13}C in the solvent: δ 77.2 CDCl_3 . $^{19}\text{F}\{^1\text{H}\}$ NMR chemical shifts are reported in ppm and externally referenced to neat CFCl_3 at 0 ppm. $^{31}\text{P}\{^1\text{H}\}$ NMR chemical shifts are reported in ppm and externally referenced to 85% H_3PO_4 at 0 ppm. Diffraction measurements for X-ray crystallography were made on a Bruker X8 APEX II diffraction and a Bruker APEX DUO diffraction with graphite monochromated $\text{Mo-K}\alpha$ radiation. The structures were solved by direct methods and refined by full-matrix least-squares using the SHELXTL crystallographic software of Bruker-AXS. Unless specified, all non-hydrogens were refined with anisotropic displacement parameters, and all hydrogen atoms were constrained to geometrically calculated positions but were not refined. EA CHN analysis was performed using a Carlo Erba EA1108 elemental analyzer. The elemental composition of unknown samples was determined by using a calibration factor. The calibration factor was determined by analyzing a suitable certified organic standard (OAS) of a known elemental composition. Molecular weights were determined by triple detection gel permeation chromatography (GPC-LLS) using a Waters liquid chromatograph equipped with a Water 515 HPLC pump, Waters 717 plus autosampler, Waters

Styragel columns (4.6×300 mm) HR5E, HR4 and HR2, Water 2410 differential refractometer, Wyatt tristar miniDAWN (laser light scattering detector) and a Wyatt ViscoStar viscometer. A flow rate of 0.5 mL min^{-1} was used and samples were dissolved in THF (2 mg mL^{-1}). Narrow molecular weight polystyrene standards were used for calibration purposes. Matrix-assisted laser desorption/ionization time-of-flight (MALDI-TOF) mass spectrometric analysis of isolated polymers was performed on a Bruker Autoflex MALDI-TOF equipped with a nitrogen laser (337 nm). The accelerating potential of the Bruker instrument was 19.5 kV. The polymer samples were dissolved in tetrahydrofuran (ca. 1 g/mL). The concentration of a cationization agent, sodium trifluoroacetate, in tetrahydrofuran was 1 mM. The matrix used was 2,5-dihydroxybenzoic acid (DHB) at the concentration of 20 mg/mL . A sample solution was prepared by mixing polymer, matrix, and salt in a volume ratio of 5:5:1, respectively. Differential scanning calorimetry (DSC) measurements were performed to detect the glass transition and melting temperature of the polymers using a TA instruments – Q1000. Experiments were carried out under nitrogen atmosphere with $\sim 5 \text{ mg}$ of polymer samples sealed in an aluminum pan. Starting from 0°C , samples were heated to 250°C with a 10°C/min heating rate.

Materials. Solvents (THF, pentane, toluene, hexane and diethyl ether) were collected from a Solvent Purification System from Innovative Technology, Inc. whose columns were packed with activated alumina. CDCl_3 was dried over CaH_2 , collected by vacuum distillation and degassed through a series of freeze-pump-thaw cycles. Dimethylanilinium Tetrakis(3,5-bis(trifluoromethyl)phenyl)borate ($[\text{HNMe}_2\text{Ph}][\text{BAr}^{\text{F}}_{24}]$) was generated by reacting dimethylanilinium chloride with sodium $\text{BAr}^{\text{F}}_{24}$ in diethyl ether at room temperature for 4 h. The solvent was removed under high vacuum, and addition of hexane to the residual precipitated a white solid. The white solid was isolated by vacuum filtration and dried in *vacuo* for 4 h. InCl_3

was purchased from Strem Chemicals and used without further purification. isobutylmagnesium chloride (2.0 M in Et₂O) and dimethylanilinium chloride ([HNMe₂Ph]Cl) were purchased from Aldrich and Alfa Aesar, respectively, and used as received. *rac*-lactide was recrystallized 3 times from dry toluene and dried under vacuum. In(*i*Bu)₃ was synthesized according to a previously reported procedure.¹⁰⁴

Synthesis of complex 48c. A 20 mL scintillation vial was charged with **47c** (200 mg of **47c**, 0.259 mmol, yield=86%) in C₆H₆ (3 ml). [HNMe₂Ph][BAr^F₂₄] (253 mg, 0.266 mmol) in C₆H₆ (2 ml) was added to the stirring solution of **47a**. The reaction mixture was stirred for 4 h at r.t. The solvent was removed in vacuo to obtain a yellow residue and cold hexane (3 ml) was added to the residue. After stirring for 1 h, the supernatant was decanted off to remove the byproduct NMe₂Ph. This step was repeated at least 3 times until a pale-yellow solid precipitate formed. The product was washed with hexane (2×3 ml) and dried under high vacuum for a few hours. Anal. Calcd. For C₇₃H₆₃BF₂₄InN₃O: C 55.72; H 4.18; N 2.64. Found: C 55.60; H 4.28; N 2.82. ¹H NMR (400 MHz, CDCl₃, 25 °C) δ 8.20 (1H, s, -N=CH-Ar), 7.76 (9H, br. s., *ortho* H of BAr^F₂₄ and Pyr γ), 7.61 (1H, m, ArH), 7.54 (4H, br. s., *para* H of BAr^F₂₄), 7.19 - 7.39 (10H, m, ArH), 7.16 (1H, m, Pyr α), 7.10 (1H, m, Pyr δ), 6.95 (2H, m, Pyr β and ArH), 4.02 (2H, m, -CH₂- of pyridyl), 3.12 (1H, m, -CH₂- of thiophenyl), 3.17 (1H, m, -CH- of DACH), 0.95 – 2.56 (20H, m, -CH₂- of DACH, -CH₃ of cumyl, -CH- of *i*Bu and -CH₂- of *i*Bu), 0.87 (6H, m, -CH₃ of *i*Bu), ¹³C{¹H} NMR (101 MHz, CDCl₃) δ 171.0 (N=CH-Ar), 167.1 (Ar C), 161.8 (B-C), 152.2 (Ar C), 152.1 (Ar C), 150.0 (Pyr β), 149.9 (Ar C), 141.9 (Pyr γ), 135.1 (*ortho* C-H of BAr^F₂₄), 134.2 (ArC-H), 132.8 (Pyr δ), 128.7-129.4 (qq, ²J_{C-F} = 3, 32 Hz, *meta* C of BAr^F₂₄), 127.4, 125.6, 123.8, 121.9 (q, ¹J_{C-F} = 273 Hz, -CF₃), 126.2 (Ar C-H), 125.5 (Ar C-H), 124.0 (Pyr α), 117.6 (*para* C-H of BAr^F₂₄), 64.2 (C-H of DACH), 60.6 (C-H of DACH), 47.3 (-CH₂- of pyridyl) 33.8 (-CH₃ of cumyl), 30.9 (-CH₃ of cumyl), 25.9

(-CH₃ of cumyl), 27.8 (-CH₃ of *i*Bu), 27.3 (-CH₂- of *i*Bu), ¹⁹F{¹H} NMR (282 MHz, CDCl₃): δ - 61.8.

Representative polymerization of *rac*-LA using cationic catalyst 48c. A 20 ml scintillation vial was charged with a solution of complex **48c** (10.1 mg, 0.006 mmol) in 2 ml of toluene. *rac*-LA (230 mg, 1.6 mmol) was directly added to the vial. The mixture was stirred at 100 °C for 24 h. The resulting solution was concentrated under vacuum for 3 h and then cold methanol was slowly added to the vial (0 °C, 15 mL). The polymer precipitated from the solution and was isolated by decantation of the supernatant. The isolated polymer was dried under high vacuum for at least 3 h prior to analysis.

Sample preparation for the Gutmann-Beckett method. The required complex/compound was dissolved in 0.7 mL of C₆D₆ to obtain a 20 mM concentration. This solution was mixed with 0.8 equivalents of OP(Et)₃ and transferred to an NMR tube with a J. Young valve. A sealed capillary containing a 20 mM solution of OP(Et)₃ was added to the tube and the tube was sealed. This sample was used to obtain ³¹P NMR spectra (162 MHz) at 25 °C.

Polymerization of *rac*-LA using air exposed catalyst 48c. A 10.1 mg (0.006 mmol) portion of the air exposed catalyst and *rac*-LA (230 mg, 1.6 mmol) were added to a 20 ml scintillation vial and sealed with a rubber septum. The vial was flushed in nitrogen gas and 2 ml of dry toluene was injected. The mixture was stirred at 100 °C for 24 h. The resulting solution was concentrated under vacuum for 3 h and then cold methanol was slowly added to the vial (0 °C, 15 mL). The polymer precipitated from the solution and was isolated by decantation of the supernatant. The isolated polymer was dried under high vacuum for at least 3 h prior to analysis.

Sample preparation for kinetic studies. The required amount of complex **48c** was dissolved in 0.4 mL of CD₃C₆D₅ (Tol-d₈) and transferred along with the required amount of *rac*-

LA to an NMR tube with a J. Young valve. A sealed capillary containing a known amount of 1,3,5-trimethoxybenzene in solution was added to the tube as an internal standard and the tube was sealed. This sample was used to obtain multiple ^1H NMR spectra (400 MHz) at 100 °C at regular intervals to obtain conversion data.

Chapter 4: Hemilability as a tool: exploring the mechanism of indium catalyzed coupling of epoxides and lactones

4.1 Introduction

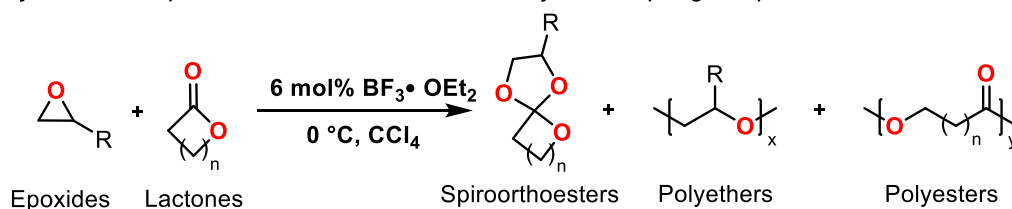
Polymers with precisely controlled alternating monomer units have properties distinct from their homo-, block- or gradient counterparts.^{147,148} Therefore, the sequence controlled synthesis of copolymers is an intriguing chemical challenge.^{149,150} This has been particularly true in the synthesis of poly(ether-*alt*-esters) from epoxides and lactones; most attempts to create structurally pure alternating copolymers form oligomers.^{151–156} One successful method for producing perfectly alternating copolymers has been the polymerization of pre-sequenced monomers.^{157–159} One such class of pre-sequenced monomers is spiro-orthoesters, molecules with three oxygen atoms bound to a common sp^3 hybridized carbon in two molecular rings, which are capable of forming poly(ether-*alt*-esters) through double ring opening polymerization reactions.^{160–162}

The synthesis of spiro-orthoesters has been dominated by the coupling of epoxides and lactones in the presence of Lewis or Brønsted acids (Figure 4.1a).^{163–167} However, this method suffers from low selectivity due to competing polymerization of the lactone and epoxide substrates. These side reactions often necessitate high temperature distillation for product isolation resulting in low yields (< 50%). While other selective synthetic procedures involving diazo precursors were reported by Coster and Lacour using rhodium and ruthenium catalysts, respectively,^{168,169} the requirement for multi-step organic syntheses to produce precursor compounds limits the scope and versatility of these methods.

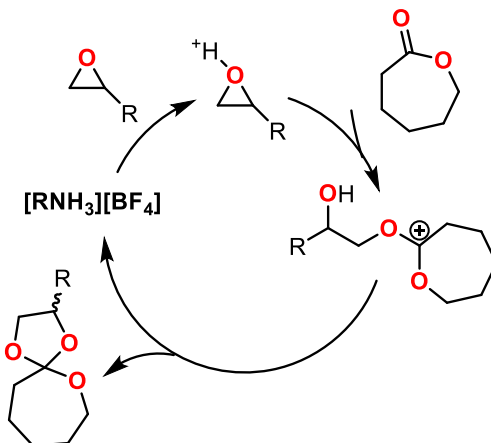
Pascault and coworkers proposed a mechanism for the formation of spiro-orthoesters from lactones and epoxides that involves activation of the epoxide *via* protonation with an acid, followed

by attack of a lactone resulting in the ring opening of the epoxide (Figure 4.1b).¹⁷⁰ The final step was ring closure and release of the spiro-orthoester product. Although this hypothesis rationalized the formation of spiro-orthoesters, the low selectivity of the reported systems has curtailed a detailed mechanistic examination of this reaction.

(a) Synthesis of spiro-orthoesters from acid-catalyzed coupling of epoxides and lactones



(b) Proposed mechanism for the formation of spiro-orthoesters by Pascault and co-workers



(c) Temperature triggered. synthesis and polymerization of spiro-orthoesters

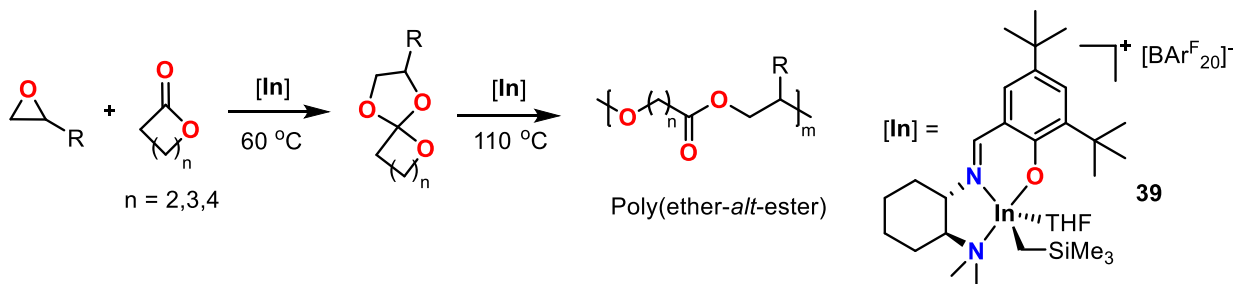


Figure 4.1. Prior studies in the coupling of epoxides and lactones.

Recently, Mehrkhodavandi and co-workers reported that a cationic alkylindium complex (**39**) catalyzed the synthesis of a range of spiro-orthoesters from various epoxides and lactones with exclusive selectivity for coupling over polymerization reactions (Figure 4.1c).⁹⁰ Subsequently, **39** was found to be capable of catalyzing the temperature-triggered double ring opening polymerization of spiro-orthoesters to yield perfectly alternating poly(ether-*alt*-ester) with the highest molecular weights reported to date ($> 40,000 \text{ g mol}^{-1}$).⁵⁹

The extended work with cationic indium catalysts in the Mehrkhodavandi group^{59,60} and the work described in Chapters 2 and 3 has shown that their stability and reactivity can be significantly influenced by the addition of a hemilabile donor arm to the ligand backbone.^{52,171} For example, adding a furfuryl pendant arm to complex **39** results in a catalyst with controlled activity and long and stable lifespan.¹⁴⁰ In this chapter, the controlled reactivity afforded by hemilability is leveraged to elucidate the mechanism of spiro-orthoester formation using cationic indium complexes with hemilabile furfuryl pendant arms. The structure-function relationship of different catalysts is explored while demonstrating that the formation of spiro-orthoesters with these compounds is governed by Michaelis-Menten-type saturation kinetics.^{172–174} Based on available information, this is the first detailed investigation of the mechanism of the metal-catalyzed formation of spiro-orthoesters from the coupling of epoxides and lactones. Elucidation of this unique mechanism will enable development of future catalysis with weak Lewis acids.

4.2 Results and discussion

This section discusses the synthesis, characterization and reactivity studies using complexes **48b** and **48e-h**. This is followed by experimental and computational studies into the cationic indium catalyzed coupling of epoxides and lactones.

4.2.1 Synthesis of compounds

The reactivity of **39** could potentially be probed by tuning the In-alkyl group and by replacing the coordinated solvent (THF) with a donor arm that can be changed both sterically and electronically. The alkane elimination reaction of trialkylindium complexes (InR_3 , $\text{R} = \text{CH}_3$, $\text{CH}_2\text{CH}(\text{CH}_3)_2$, $\text{CH}_2\text{Si}(\text{CH}_3)_3$) with proligands bearing a hemilabile furfuryl pendant group with various substituents in the α -furfuryl position ($\text{X} = \text{H}$, CH_3 , Br) forms the neutral compounds **47b** and **47e-h** (Figure 4.2). Reacting **47b** and **47e-h** with $[\text{PhNMe}_2\text{H}][\text{BAr}^{\text{F}}_{24}]$ ($\text{BAr}^{\text{F}}_{24} = \text{tetrakis}[3,5\text{-bis(trifluoromethyl)phenyl}] \text{borate}$) forms the cationic species **48b** and **48e-h**. Compounds **48b**, **48e** and **48f** will be used to probe the effect of the alkyl group while **48g** and **48h** will be used to probe the effect of the substituents on the pendant donor arms. Compound **48g** has a weakly electron donating methyl substituent at the α -position of the furan ring, while **48h** has a weakly electron withdrawing bromo group;^{175,176} both substituents have similar steric bulk.^{177,178} All new compounds were fully characterized (Figures C.1-C.48). Additionally, the solid-state molecular structures of **47e** and **48h** were determined by single-crystal X-ray crystallography. In the solid state, the hemilabile pendant arm is coordinated to the cationic indium center in the absence of external donors (Figures 4.3 and Figure C.50).¹⁴⁰

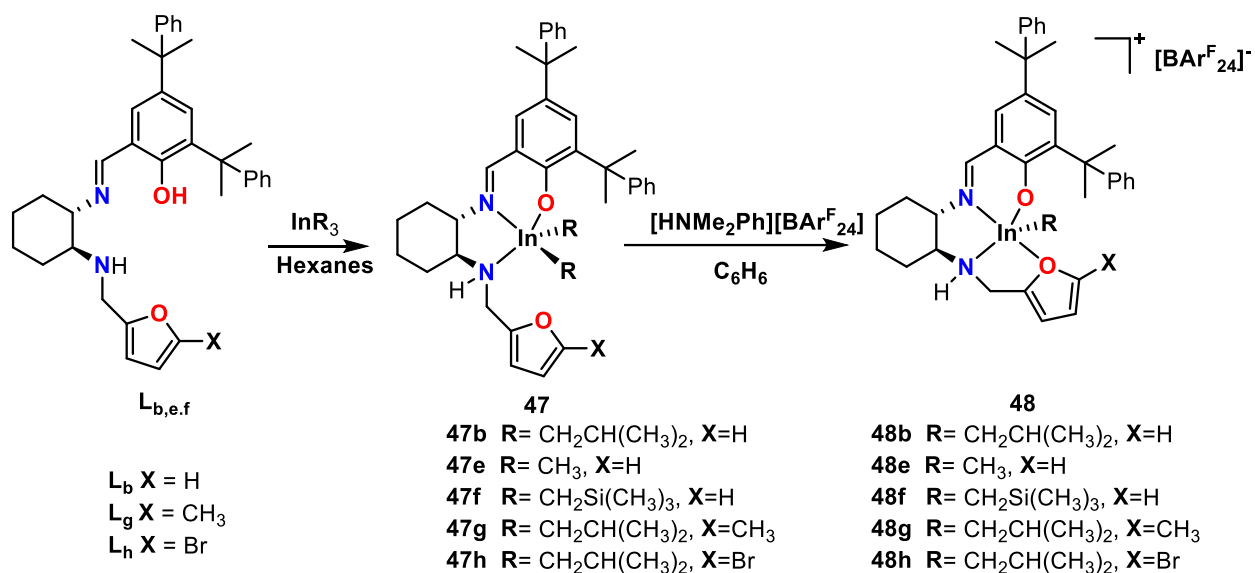


Figure 4.2. Synthesis of neutral and cationic indium complexes.

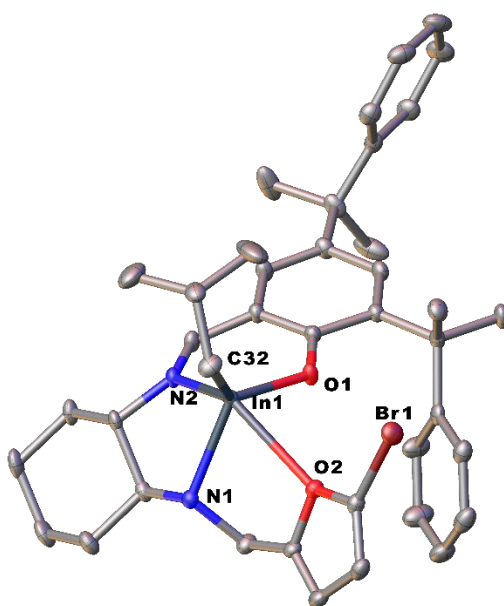


Figure 4.3. The molecular structure of **48h** depicted with thermal ellipsoids at 50% probability and H atoms, BAr^F_{24} counterion, solvent molecules, as well as minor disordered counterparts, omitted for clarity.

4.2.2 Evaluation of catalytic competency

Table 4.1 Synthesis of SOE from ϵ -caprolactone (ϵ -CL) and 1,2-epoxy-7-octene (EOE) using various cationic indium complexes.

Entry	Catalyst	In-R	Furfuryl α -X group	Conversion of EOE (%) ^b	Poly(EOE) (%) ^b	Poly(CL) (%) ^c
1	48e	CH ₃	H	48	<1	<1
2	48b	CH ₂ CH(CH ₃) ₂	H	55	<1	<1
3	48f	CH ₂ Si(CH ₃) ₃	H	78	<1	<1
4	48g	CH ₂ CH(CH ₃) ₂	CH ₃	57	<1	<1
5	48h	CH ₂ CH(CH ₃) ₂	Br	60	<1	<1
6 ^d	39	CH ₂ Si(CH ₃) ₃	-	>99	<1	<1

^a Reactions were performed in benzene for 24 h at 60 °C, [EOE] = [ϵ -CL] = 0.25 M, [catalyst] = 0.006 M. ^b Conversion was determined by ¹H NMR spectroscopy (400 MHz, C₆D₆, 25 °C) and calculated with respect to EOE. ^c Determined by ¹H NMR spectroscopy (400 MHz, C₆D₆, 25 °C). ^d Previously reported data for cationic indium complex **39**.⁹⁰

Complexes **48b** and **48e-h** were used as catalysts for the coupling of ϵ -caprolactone (ϵ -CL) and 1,2-epoxy-7-octene (EOE) to form 2-(hex-5-en-1-yl)-1,4,6-trioxaspiro[4.6]undecane (SOE) (Table 4.1). Compared to **39** (Figure 4.1c), **48b** and **48e-h** exhibit slower conversions of EOE and higher stability, making them suitable catalysts to study the specific mechanism of this reaction.

4.2.2.1 Role of the alkyl ligands in determining reactivity

The total conversion of EOE and ϵ -CL to SOE at 24-hour reaction time increases in the following order **48e** < **48b** < **48f** (Table 4.1, entries 1-3). Correspondingly, **48e** has the slowest rate of conversion of epoxide to SOE monitored over 14 hours through *in situ* ¹H NMR spectroscopy at 60 °C, followed by **48b**, with **48f** having the highest rate (Figure 4.4).

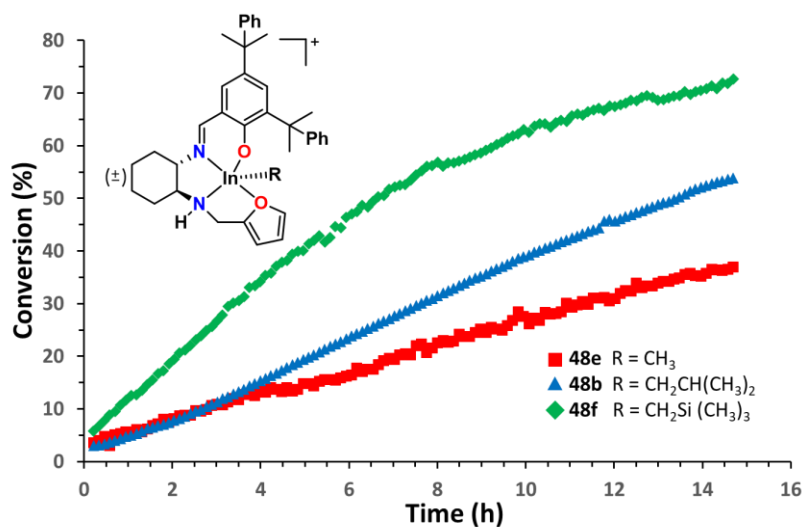


Figure 4.4. Conversion vs. time plots of **48b**, **48e**, and **48f** for the formation of SOE monitored by ¹H NMR spectroscopy (60 °C, C₆D₆, 400 MHz).

4.2.2.2 Role of the α -substituent on the hemilabile pendant arm in reactivity

Complexes **48g** and **48h** show similar conversion of EOE to SOE after 24 h (Table 4.1, entries 4,5). This is comparable to **48b**, which has an unsubstituted furfuryl pendant arm with a proton at the α -position of the furan. Furthermore, complexes **48g** and **48h** show only slightly higher conversion compared to **48b** as monitored *via in situ* ¹H NMR spectroscopy at 60 °C (Figure 4.5). It is evident from these findings that the steric bulk of the substituents on the α -position of the furfuryl pendant arm does not play a significant role in the mechanism of SOE formation. Based on these studies complex **48b** shows controlled “Goldilocks” behavior, ideal for studying the mechanism of this reaction.

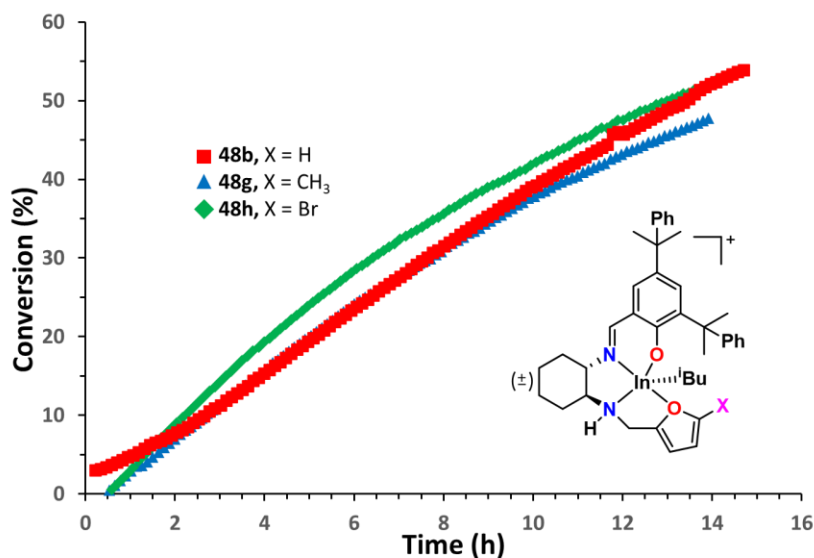


Figure 4.5. Conversion vs. time plots of **48b**, **48g**, and **48h** for the formation of SOE monitored by ^1H NMR spectroscopy (60 °C, C_6D_6 , 400 MHz) showing comparable reactivity regardless of substituents on the furan pendant arm.

4.2.3 Kinetics of spiro-orthoester formation

To identify the mechanism of SOE formation, kinetic analysis was conducted to determine the order of reaction with respect to **48b**, EOE, and $\epsilon\text{-CL}$. The SOE formation was observed by *in situ* monitoring of the SOE methyldene proton peak ($\text{R}(\text{CH}_2)_4\text{CH}=\text{CH}_2$)⁹⁰ using ^1H NMR spectroscopy at 60 °C. The concentrations of **48b**, EOE, or $\epsilon\text{-CL}$ were varied individually while the other components were kept constant. For each component, data from three different test concentrations were evaluated using Variable Time Normalization Analysis (VTNA).^{145,146} The reaction profile was plotted against the time axis multiplied by $\Sigma[\text{EOE}]$, $\Sigma[\epsilon\text{-CL}]$, or $[\textbf{48b}]$ raised to different numerical power to visually overlap the plots (Figures 4.6 and Figures C.56-C.58). Based on this analysis, the system shows first order rate dependence with respect to $[\textbf{48b}]$. However, changing either $[\text{EOE}]$ or $[\epsilon\text{-CL}]$ has no effect on the rate of reaction and shows zeroth

order rate dependence with respect to both starting substrates. This points to catalyst saturation at these reaction conditions resulting in *pseudo-zeroth* order Michaelis-Menten type kinetics.^{172–174}

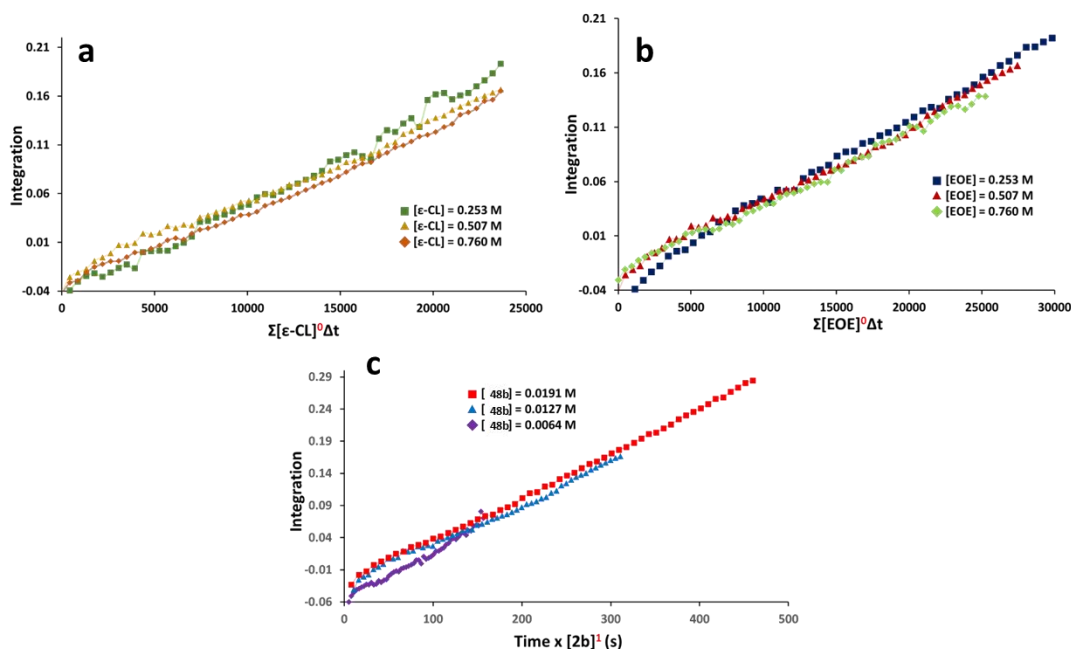


Figure 4.6. a) VTNA plots to determine the order with respect to $[\epsilon\text{-CL}]$. ($[48b] = 0.0127\text{ M}$, $[\text{EOE}] = 0.507\text{ M}$ at $60\text{ }^{\circ}\text{C}$ in benzene- d_6). b) VTNA plots to determine the order with respect to $[\text{EOE}]$ ($[48b] = 0.0127\text{ M}$, $[\epsilon\text{-CL}] = 0.507\text{ M}$ at $60\text{ }^{\circ}\text{C}$ in benzene- d_6). c) VTNA plots to determine the order with respect to $[48b]$ ($[\text{EOE}] = 0.507\text{ M}$, $[\epsilon\text{-CL}] = 0.507\text{ M}$ at $60\text{ }^{\circ}\text{C}$ in benzene- d_6).

4.2.3.1 Michaelis-Menten kinetic analysis

In systems showing Michaelis-Menten kinetics, the rate of reaction is initially linearly dependent on the concentration of starting material; however, with increasing substrate concentration the rate approaches a maximum value for a given catalyst concentration.^{140,179,180} The initial rate of SOE formation (M s^{-1}) increases when $[\text{EOE}]$ and $[\epsilon\text{-CL}]$ are increased until the rate reaches a maximum value (V_{max}) indicating that the catalyst becomes kinetically saturated (Figure 4.7a). In enzyme kinetics, the Michaelis constant (K_M) *i.e.*, the concentration of substrate at $\frac{1}{2} V_{\text{max}}$, is used as a measure of substrate affinity to catalysts. Lower K_M values correspond to

stronger affinity while higher values correspond to weaker affinity.¹⁸¹ For enzymes, K_M values range from 10^{-1} - 10^{-7} M, with the “average” enzyme possessing a K_M value of $\sim 10^{-4}$ M.¹⁸² Using the Eadie-Hofstee relationship,¹⁸³ a Michaelis constant (K_M) of 0.43 M and a V_{max} of 6.43 M s^{-1} were calculated for **48b** (Figure 4.7b).

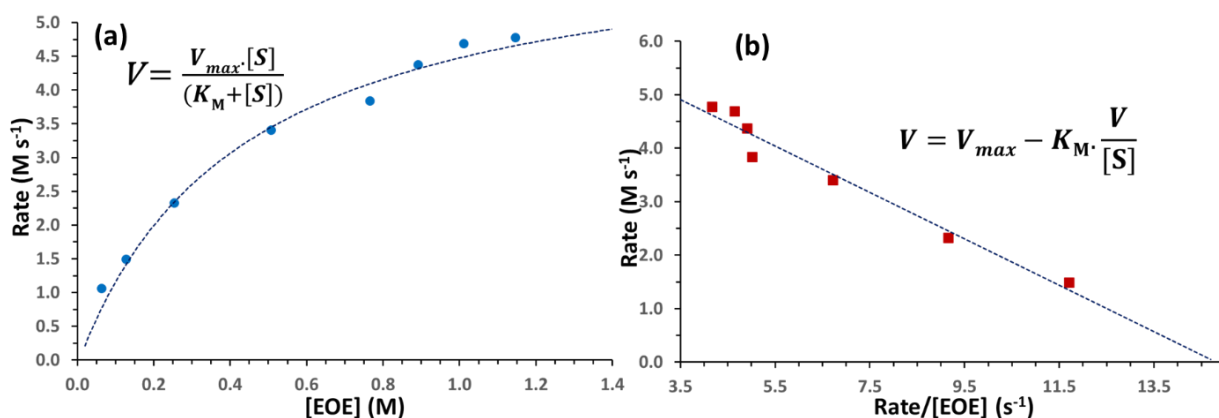


Figure 4.7. a) Saturation plot of **48b**. Line is plotted with K_M and V_{max} values extracted from the b) Eadie–Hofstee plot for **48b**.

4.2.4 Nature of the active catalyst

Understanding the nature of the active catalytic species is a fundamental step in the elucidation of the mechanism of spiro-orthoester formation.

4.2.4.1 Temperature dependent behavior of catalysts

The previous studies involving cationic alkylindium complexes bearing hemilabile ligands described in Chapter 2 have shown that the hemilability of the furfuryl pendant group has a significant effect on the reactivity of these complexes.¹⁴⁰ The change in the chemical shift of the α -proton of the furfuryl group in **48b**, **48e**, and **48f** is an excellent determinant of the fluxionality of the donor arm. Using the difference in chemical shift of this proton at 25 °C and chemical shifts at higher temperatures ($\Delta\delta$), in Variable Temperature (VT) ^1H NMR spectroscopy experiments, it is demonstrated that **48e** has the lowest fluxionality followed by higher fluxionality in **48b** (Figure

4.8 and Figures C.51-C.53). Complex **48f**, bearing the bulky $\text{CH}_2\text{Si}(\text{CH}_3)_3$ ligand, decomposes irreversibly at higher temperatures in the absence of external donor groups, showing significantly greater labile behavior than **48b** or **48e**. The more fluxional nature of the pendant arm results in higher reactivity of the cationic indium complexes in the formation of SOE with a reactivity order of **48e** < **48b** < **48f** (Table 4.1).

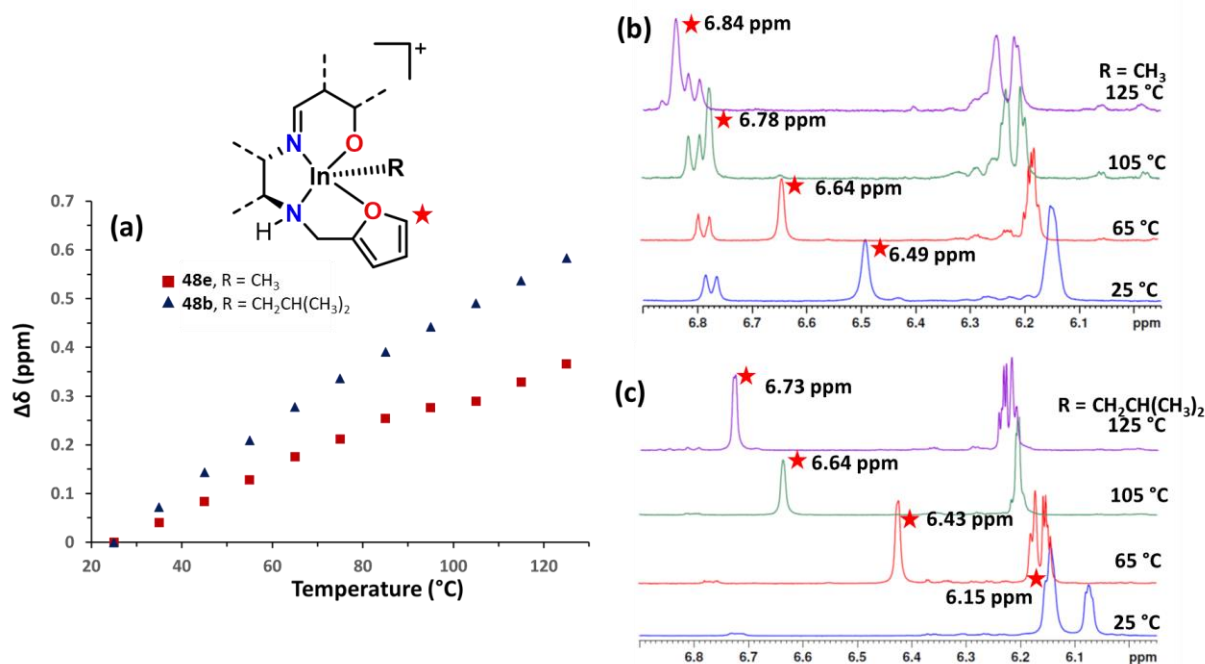


Figure 4.8. a) Downfield shift of the α proton of the furfuryl pendant arm relative to 25 °C, b) VT ^1H NMR (400 MHz, $\text{C}_6\text{D}_5\text{Br}$, 25–125 °C) spectra showing downfield migration of the α proton of the furfuryl group of **48e** and c) **48b**

To find a possible explanation for the thermal behavior of these complexes the steric bulk of the complexes were quantified using buried volume analysis (Figure 4.9).¹⁸⁴ The methyl ligand of **48e** contributes the lowest percent-buried volume to the complex, allowing for greater interaction of the furfuryl pendant group with the indium center. This renders **48e** more stable and less prone to furan dissociation. Correspondingly, the isobutyl ligand of **48b** contributes a greater

percent-buried volume. It was postulated that the increased steric crowding leads to increased fluxionality of the furfuryl pendant arm, which in turn contributes to greater catalytic activity.

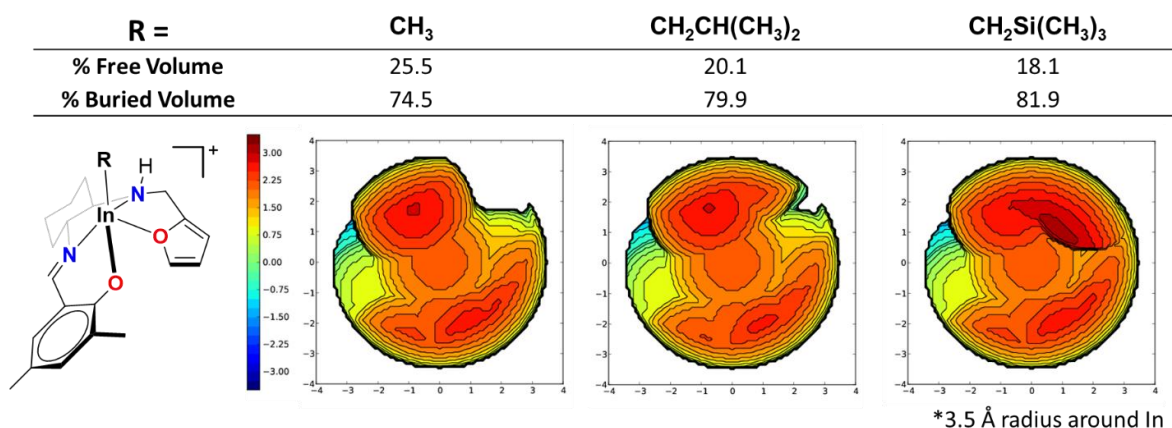


Figure 4.9. Percent buried volume (at a 3.5 Å radius around the indium center) calculation to determine steric bulk of different alkyl ligands on **48e**, **48b**, and **48f**.

While the CH₂Si(CH₃)₃ ligand of **48f** contributes a similar percent-buried volume to the isobutyl group of **48b**, it decomposes irreversibly at ~35 °C while **48b** is stable up to 125 °C in the absence of external donors *i.e.* substrate or solvent (Figure C.53). The difference in the relative stability of **48b** and **48f** is very likely electronic in nature, arising from the electron withdrawing effects of the organosilicon ligand.^{185,186} Upon disassociation of the furan moiety, the CH₂Si(CH₃)₃ ligand does not supply the indium center with enough electron density to maintain stability, leading to decomposition. However, these observations indicate that catalysis is enhanced in conditions that encourage the dissociation of the pendant arm.

4.2.4.2 Substrate coordination

Substrate coordination to the indium center and product formation can follow several possible pathways (Figure 4.10). In the first scenario, epoxide coordinates first to the catalyst and the insertion of ϵ -CL or epoxide into a coordinated epoxide results in either SOE or polyether respectively (Figure 4.10 A1, A2). Alternatively, ϵ -CL coordinates first and the insertion of

epoxide or ϵ -CL into a coordinated ϵ -CL results in a cyclic ether-ester compound or polycaprolactone (Figure 4.10 B1, B2 and Figure 4.11). However, of these pathways, only the product from path A2, SOE, is observed. While epoxides or ϵ -CL can be homopolymerized by cationic indium complexes at higher temperatures and concentrations,^{61,90,140} these polymerizations do not occur under the current reaction conditions due to the relatively low Lewis acidity of this catalyst. The relative Lewis acidity of **48b**, determined by a modified Gutmann-Becket method,^{91,92,187} is significantly lower than compounds such as BF_3 (Figure 4.1a) that can homopolymerize both ϵ -CL and epoxide under the reaction conditions used ($\delta = 78.2$ ppm for BF_3 and $\delta = 69.4$ ppm for **48b** in the $^{31}\text{P}\{^1\text{H}\}$ NMR spectrum.⁵⁹

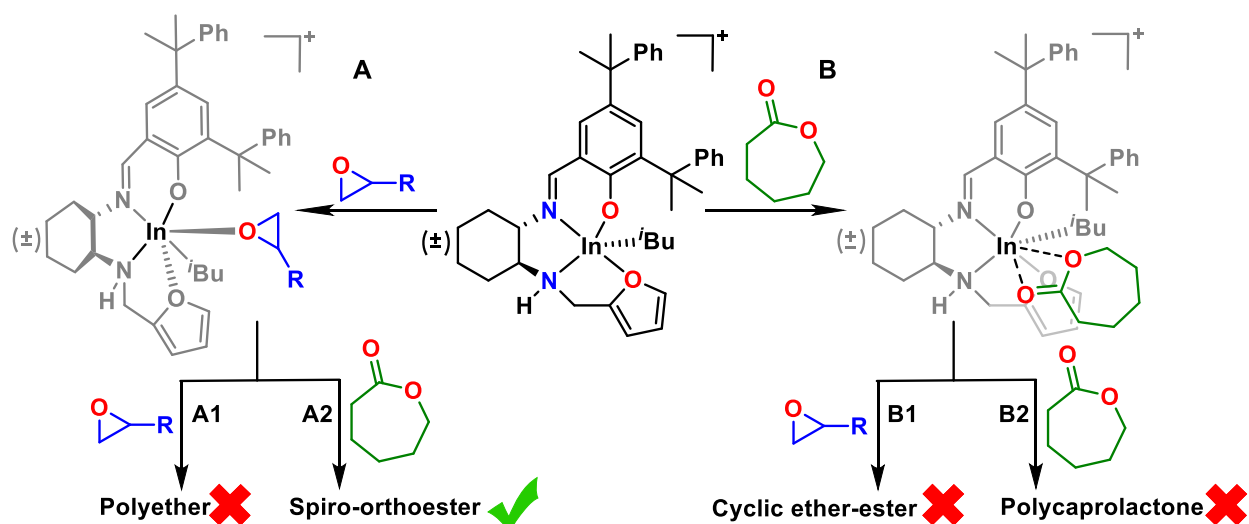


Figure 4.10. Possible pathways for substrate coordination and product formation by **48b**.

Considering neither homopolymerization products nor a cyclic ether-ester species is observed, the first step in the proposed mechanism is the activation of the catalyst by the coordination of an epoxide to the cationic center.

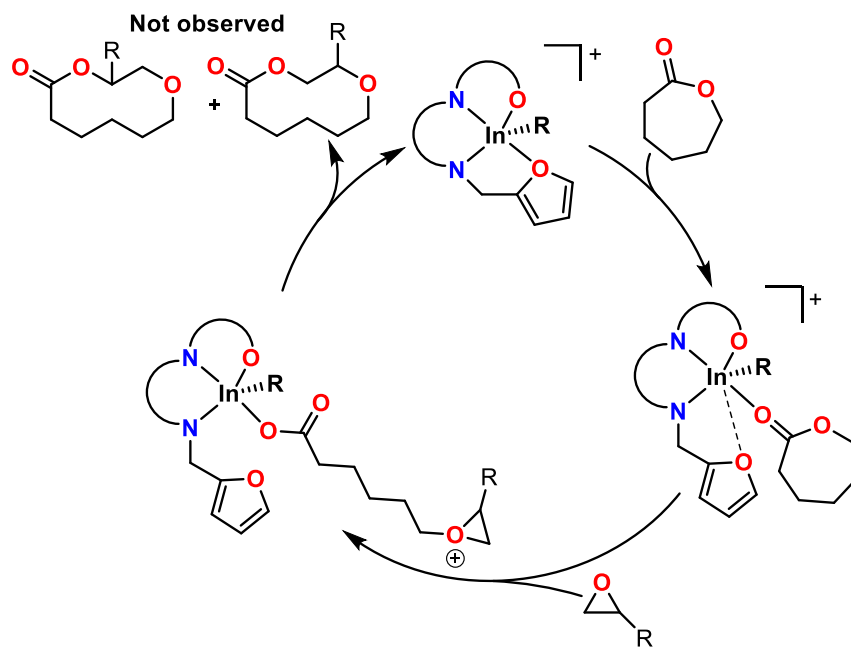


Figure 4.11. Coordination of ϵ -CL followed by attack of the epoxide is expected to result in the formation of cyclic ether-esters, which are not observed.

While the metal can accommodate either one or two epoxide molecules,¹⁴⁰ it is proposed that only one epoxide molecule is coordinated in the first step. Triethylphosphine oxide (TEPO) was used as a non-reactive model donor to approximate epoxide coordination in order to probe the impact of catalyst reactivity with either one or two epoxide molecules coordinated using a modified Gutmann-Beckett method.^{91,92,187} The $^{31}\text{P}\{^1\text{H}\}$ NMR spectrum of **48b** mixed with 1 equivalent of TEPO (**48b**•TEPO) shows a broad signal at $\delta = 69.4$ ppm. The broadness of this peak arises from the fluxional behavior of the furfuryl pendant arm at 25 °C resulting in the reversible association and dissociation of the TEPO molecule (Figures 4.12a and Figures C.54, C.55). Conversely, when 2 equivalents of TEPO are mixed with **48b** the resultant $^{31}\text{P}\{^1\text{H}\}$ NMR spectrum for **48b**•2TEPO shows a single sharp peak at $\delta = 59.6$ ppm (Figures 4.12b and Figures C.54, C.55). While both species show a downfield shift of the $^{31}\text{P}\{^1\text{H}\}$ peak of TEPO compared to free TEPO

($\delta = 45.8$ ppm), **48b**•TEPO is significantly more Lewis acidic than **48b**•2TEPO and thus expected to be the more reactive species.^{91,92}

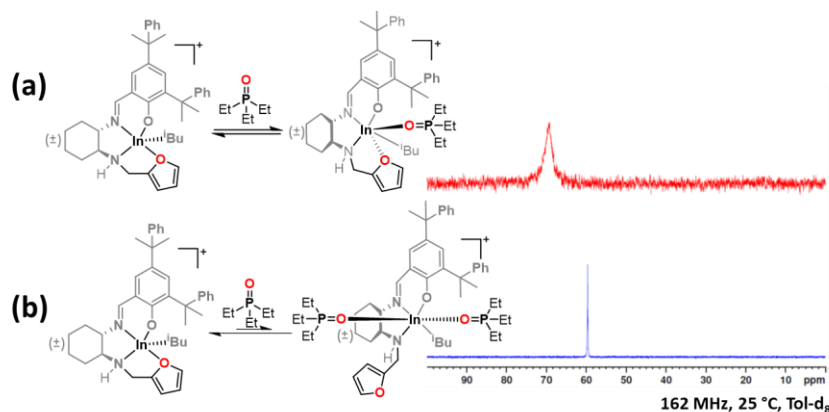


Figure 4.12. (a) Broad $^{31}\text{P}\{^1\text{H}\}$ NMR spectral peak arising from the coordination of one TEPO molecule to **48b** and (b) the sharp $^{31}\text{P}\{^1\text{H}\}$ NMR spectral peak from the coordination of two TEPO molecules to **48b**.

Additionally, computational studies show that the mono-epoxides species is more stable (~ 7 kcal mol $^{-1}$) than the bis epoxide species in benzene where the coordination of two epoxide molecules leads to the complete dissociation of the pendant furan (Figure 4.13). Thus, coordination of one epoxide molecule leads to the more stable and more active catalyst.

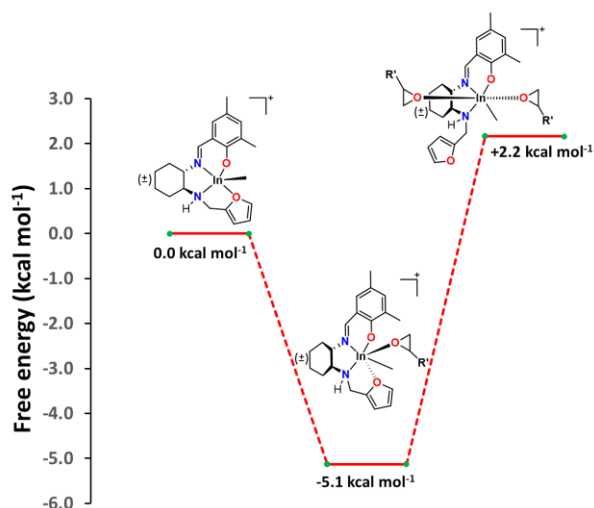


Figure 4.13. Relative stabilization energies (kcal mol $^{-1}$) of a truncated version of complex **48e** bound to one or two epoxides.

4.2.5 Proposed mechanism for spiro-orthoester formation

Based on the studies in the previous section, spiro-orthoester formation is preceded by the coordination of a single epoxide molecule resulting in the active catalytic species (Figure 4.14)

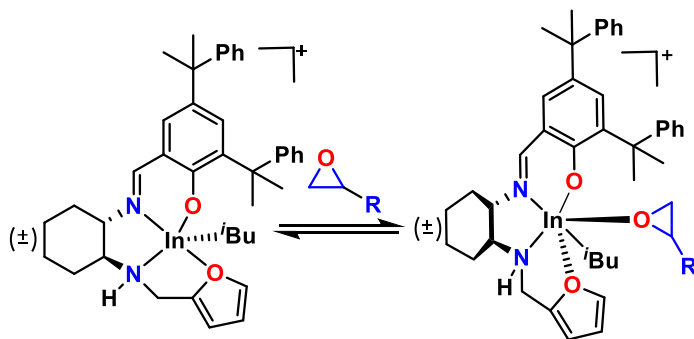


Figure 4.14. Formation of the active catalyst by coordination of epoxide to **48b**.

The first in-cycle step of the proposed mechanism involves the S_N2 attack on the epoxide by lactone and its subsequent ring opening (Figure 4.15A). This attack can occur at either carbon of the epoxide, resulting in two possible isomers. The latter steps of the cycle involve ring closing, release of the product, and re-formation of the active catalyst (Figure 4.15B).

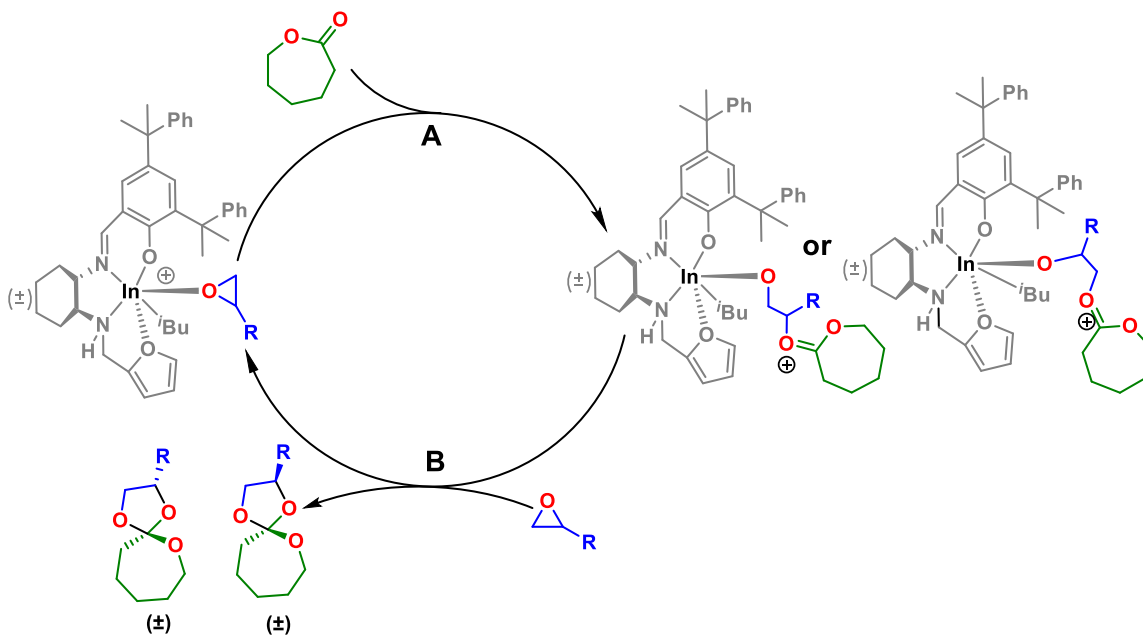


Figure 4.15. Proposed mechanism for spiro-orthoester formation by complex **48b**.

4.2.5.1 Computational studies

Computational methods were used (see Experimental and Appendix C) to gain further insights into the selective coupling of epoxide and lactone as well as the product release steps as Michaelis-Menten saturation kinetics makes it considerably more difficult to study the in-cycle steps of the proposed mechanism experimentally. These calculations were performed with a truncated **48e** as a model catalyst and 1,2-epoxybutane as a simplified model epoxide (Figure 1.16). Since all four possible stereoisomeric products are observed experimentally, only the pathway for formation of one stereoisomer was examined for brevity.

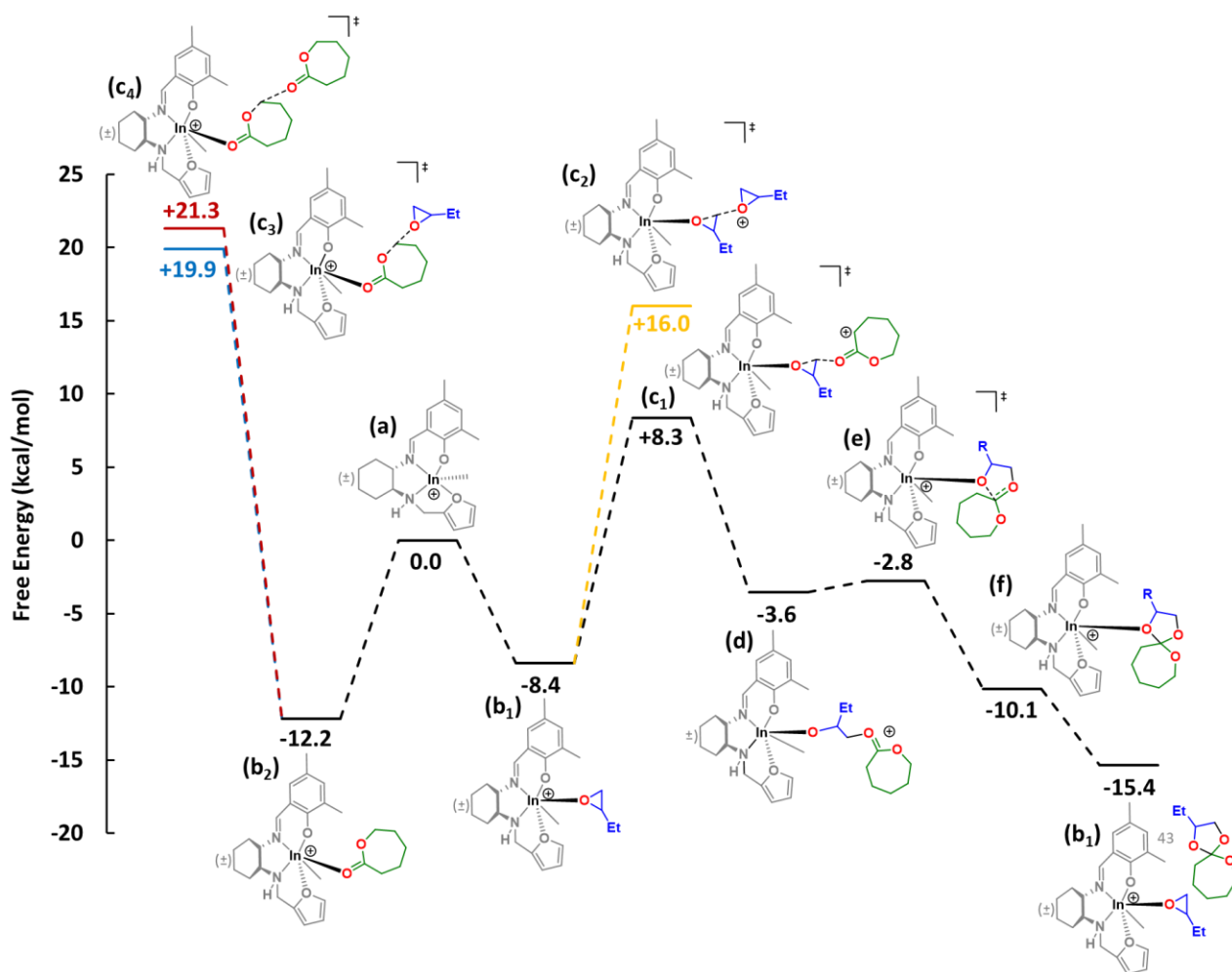


Figure 4.16. Reaction profile of the proposed mechanism of SOE formation by a truncated version of **48e**.

In the presence of ϵ -CL and epoxide, either one can coordinate to the indium center. In the case of the coordinated ϵ -CL either an epoxide or an additional ϵ -CL can ring open the coordinated lactone molecule (Figure 4.16c₃ and 4.16c₄). However, the kinetic barrier for both these scenarios is considerably larger than that of ϵ -CL inserting into a coordinated epoxide. This kinetic barrier prevents the homo-polymerization of ϵ -CL and the formation of a cyclic ether-ester species. Based on these calculations, the rate determining step (+16.7 kcal mol⁻¹) is the S_N2 attack on and the simultaneous ring opening of the coordinated epoxide by ϵ -CL, resulting in the formation of a new indium alkoxy bond (Figure 4.16d). Unlike the ring opening of the indium- ϵ -CL complexes, the ring opening of epoxides has a noticeably smaller barrier (Figure 4.16c₁ and 4.16c₂ vs. Figure 4.16c₃ and 4.16c₄). This is consistent with observed lack of homo-polymerization products or the cyclic ether-ester compound.

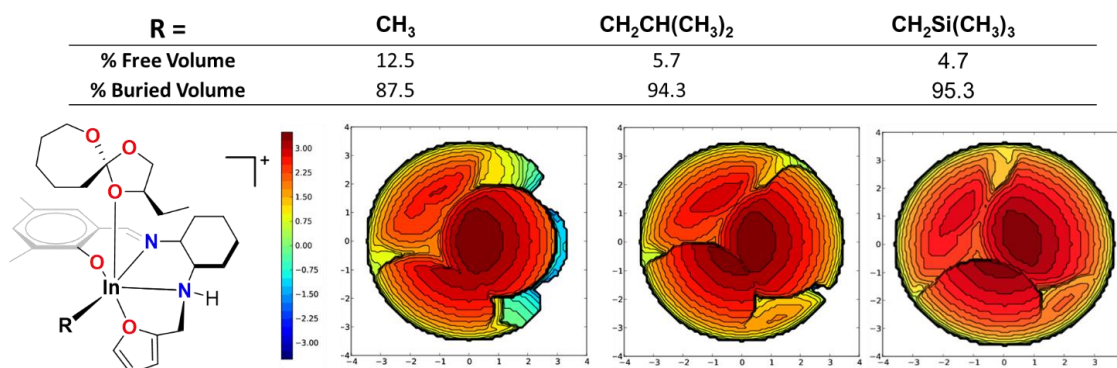


Figure 4.17. Buried volume (at a 3.5 Å radius around the indium center) calculation to determine steric bulk of different alkyl ligands on **48e-SOE**, **48b-SOE**, and **48f-SOE**.

The last step of the cycle is ring-closing by the attack on the carbonyl carbon of ϵ -CL by the indium alkoxide oxygen and the formation of spiro-orthoester. This is followed by the release of the newly formed spiro-orthoester and re-formation of the active catalyst upon the coordination of a new epoxide molecule. Apart from enhancing the fluxionality of the furan pendant arm, the steric bulk of the alkyl ligand appears to have a noteworthy effect on this last step of the catalytic

cycle. Buried volume calculations of the catalyst coordinated to the SOE show that the steric environment around **48b** and **48f** is significantly more crowded than **48e**, potentially accounting for the faster reactivity of the former two catalysts.

4.3 Conclusion

This study investigated the mechanism and catalyst design involved in the synthesis of spiro-orthoesters through the coupling of epoxides and ϵ -caprolactone experimentally and computationally. Model catalysts with different In-alkyl and substituted furfuryl pendant ligands were used to probe the structure function relationships in reactivity and mechanism. It was demonstrated that increased steric bulk, and weaker electron donation, of the alkyl ligands increases the rate of reactivity. Furthermore, weakly electron donating or withdrawing substituents on the pendant furan moiety have no significant effect on reactivity.

The main question in this study was to determine why these catalysts, in the presence of lactones and epoxides, form spiro-orthoesters exclusively in lieu of a mixture of SOE, polyether, and polyesters. The explanation lies with the kinetics of the system governed by the mild Lewis acidity of these cationic indium complexes.

These catalysts follow Michaelis-Menten type saturation kinetics, with the reaction being zeroth order with respect to both substrates and first order with respect to catalyst, with a Michaelis constant comparable to a very slow-reacting enzyme. Concurrently, the limited Lewis acidity of these systems under these reaction conditions prevents polymerization of epoxides or ϵ -caprolactone.

Finally, it is demonstrated that the reaction mechanism proceeds through the coordination of one epoxide molecule to the cationic indium center followed by the coupling to a lactone molecule resulting in the selective formation of spiro-orthoesters. These insights into the

mechanism and ligand design explain the unique selectivity for spiro-orthoesters in this system, enhance the understanding of indium in catalysis, and open doors to better and more efficient catalysis in this and related reactions.

4.4 Experimental

General Considerations. All air- and/or moisture-sensitive reactions were performed under inert and dry nitrogen atmosphere using an MBraun glove box or Schlenk line techniques unless otherwise stated. All NMR spectra were recorded on either a Bruker Avance 300 MHz or 400 MHz spectrometers. The chemical shifts on all the ^1H NMR spectra are reported in ppm and are referenced to the residual protons in deuterated solvents. ^{13}C NMR chemical shifts are reported in ppm referenced to the residual ^{13}C in the solvent.¹⁸⁸ $^{31}\text{P}\{^1\text{H}\}$ NMR chemical shifts are reported in ppm and externally referenced to 85% H_3PO_4 at 0 ppm.

X-ray diffraction measurements were carried out on a Bruker APEX DUO or Bruker X8 APEX II diffractometer equipped with graphite monochromated Mo-K_α radiation. Images were integrated using the Bruker SAINT software package, and corrected for absorption effects using SADABS. The structures were solved by direct methods and refined by full-matrix least-squares. Structure solutions were obtained using SHELXT¹⁸⁹ and refined using SHELXL¹⁹⁰ via the Olex2 interface.¹⁹¹ All non-hydrogen atoms were refined anisotropically, and all hydrogen atoms were constrained to geometrically calculated positions. A Carlo Erba EA1108 elemental analyzer was used to obtain CHN EA analysis. The elemental composition of unknown samples was determined by using calibration factor. To determine the calibration factor, a suitable certified organic standard (OAS) of known elemental composition was used.

Materials. For air- and/or moisture-sensitive reactions toluene, diethyl ether, and hexanes were collected from a Solvent Purification System from Innovative Technology, Inc. whose

columns were packed with activated alumina. CDCl_3 , C_6D_6 , and C_6H_6 were dried over CaH_2 , degassed via multiple freeze-pump-thaw cycles, and collected by vacuum distillation. Dimethylanilinium tetrakis(3,5bis(trifluoromethyl)phenyl)borate ($[\text{HNMe}_2\text{Ph}][\text{Bar}^{\text{F}}_{24}]$) was synthesized by reacting dimethylanilinium chloride with sodium $\text{Bar}^{\text{F}}_{24}$ in diethyl ether at room temperature for 4 h.⁹⁰ The solvent was removed under high vacuum, and addition of hexane to the residual precipitated a white solid. The white solid was isolated by vacuum filtration and dried in vacuo for 4 h. Isobutylmagnesium chloride (2.0 M in Et_2O), (Trimethylsilyl)methylmagnesium chloride (1.0 M in Et_2O), indium (III) chloride (InCl_3), Sodium Tetrakis(3,5bis(trifluoromethyl)phenyl)borate ($\text{Na}[\text{Bar}^{\text{F}}_{24}]$), dimethylanilinium chloride ($[\text{HNMe}_2\text{Ph}]\text{Cl}$), ϵ -caprolactone, triethoxyphosphineoxide, trimethyl indium, and 1,2-epoxy-7-octene were purchased from commercial sources. ϵ -caprolactone and 1,2-epoxy-7-octene were dried over CaH_2 , distilled and stored under molecular sieves. $\text{In}(\text{CH}_2\text{CH}(\text{CH}_3)_2)_3$ and $\text{In}(\text{CH}_2\text{Si}(\text{CH}_3)_3)_3$ were both synthesized according to a previously reported procedure.¹⁰⁴ Proligand **L_b** and complex **48b** were synthesized according to the procedure reported in Chapter 2. All other proligands were synthesized by modifying previously reported procedures.¹⁴⁰

Synthesis of Proligand L_g. To a solution of (\pm)- trans-N-((5-methylfuran-2-yl)methyl)cyclohexane-1,2-diamine (2.58 g, 12.4 mmol) in 80 mL acetonitrile (ACN) was added 3,5-dicumylsalicylaldehyde (4.3 g, 12 mmol) and heated under reflux for 16 hours equipped with a Dean-Stark apparatus. The solvent was removed in vacuo to afford the crude product in form of a solid. The crude product was purified via crystallization in pentane to afford proligand **L_g** as a yellow solid (yield~% 53) HRMS $[\text{M}+\text{H}]^+$, calculated $m/z=549.3403$. Found $m/z=549.3476$. ^1H NMR (300 MHz, CDCl_3 , 25 °C) δ 8.37 (1H, s, $-\text{N}=\text{CH}-\text{Ar}$), δ 7.40 (1H, s, ArH), δ 7.14- 7.38 (10H, m, ArH), δ 7.09 (1H, s, ArH), δ 5.90 (1H, m, furan γ), δ 5.86 (1H, m, furan β), δ 3.74 (1H, d, $^2\text{J}_{\text{H-}}$

$_{\text{H}} = 14.5 \text{ Hz}$, $-\text{CH}_2-$ of furfuryl), δ 3.63 (1H, d, $^2J_{\text{H-H}} = 14.5 \text{ Hz}$, $-\text{CH}_2-$ of furfuryl), δ 2.98 (1H, m, $-\text{CH}-$ of DACH), δ 2.61 (1H, m, $-\text{CH}-$ of DACH), δ 2.25 (3H, s, CH_3 of furan), δ 1.09-2.15 (20H, m, $-\text{CH}_2-$ of DACH and $-\text{CH}_3$ of cumyl). $^{13}\text{C}\{^1\text{H}\}$ NMR (75 MHz, CDCl_3 , 25 °C) δ 165.8 (N=CH-Ar), δ 157.9 (Ar C), δ 152.0 (Ar C), δ 151.4 (Ar C), δ 150.7 (Ar C), δ 139.7 (Ar C), δ 136.1 (Ar C), δ 129.3 (Ar C-H), δ 128.1 (Ar C-H), δ 127.0 (Ar C-H), δ 125.7 (Ar C-H), δ 125.2 (furan α), δ 118.1 (Ar C), δ 107.7 (furan γ), δ 105.9 (furan β), δ 74.4 (C-H of DACH), δ 59.4 (C-H of DACH), δ 43.4 ($-\text{CH}_2-$ of furfuryl), δ 33.8 (CH_2 of DACH), δ 31.0 (CH_2 of DACH), δ 30.3 (CH_2 of DACH), δ 29.7 ($-\text{CH}_3$ of cumyl), δ 29.4 (CH_2 of DACH), δ 24.6 ($-\text{CH}_3$ of cumyl), δ 13.7 ($-\text{CH}_3$ of furan).

Synthesis of proligand L_h . To a solution of (\pm)- trans-N-((5-bromofuran-2-yl)methyl)cyclohexane-1,2-diamine (8.22 g, 30.0 mmol) in 80 mL acetonitrile (ACN) was added 3,5-dicumylsalicylaldehyde (10.00 g, 27.9 mmol) and heated under reflux for 16 hours equipped with a Dean-Stark apparatus. The solvent was removed in vacuo to afford the crude product in form of a solid. The crude product was purified via using column chromatography using hexanes and ethyl acetate as the mobile phase to afford proligand L_h as an orange solid (yield~40%). HRMS $[\text{M}+\text{H}]^+$, calculated $m/z=613.2356$. Found $m/z=613.2429$. ^1H NMR (300 MHz, CDCl_3 , 25 °C) δ 8.34 (1H, s, $-\text{N}=\text{CH}-\text{Ar}$), δ 7.40-7.04 (12H, ArH), δ 6.14 (1H, d, furan γ), δ 5.90 (1H, d, furan β), δ 3.69 (1H, d, $^2J_{\text{H-H}} = 15 \text{ Hz}$, $-\text{CH}_2-$ of furfuryl), δ 3.61 (1H, d, $^2J_{\text{H-H}} = 15 \text{ Hz}$, $-\text{CH}_2-$ of furfuryl), δ 2.92 (1H, m, $-\text{CH}-$ of DACH), δ 2.57 (1H, m, $-\text{CH}-$ of DACH), δ 1.05-2.05 (20H, m, $-\text{CH}_2-$ of DACH and $-\text{CH}_3$ of cumyl). $^{13}\text{C}\{^1\text{H}\}$ NMR (75 MHz, CDCl_3 , 25 °C) δ 165.7 (N=CH-Ar), δ 157.9 (Ar C), δ 156.3 (Ar C), δ 150.9 (Ar C), δ 140.0 (Ar C), δ 136.3 (Ar C), δ 129.2 (Ar C-H), δ 128.2 (Ar C-H), δ 127.9 (Ar C-H), δ 126.8 (Ar C-H), δ 125.8 (Ar-H), δ 125.2 (furan α), δ 120.4 (Ar C), δ 118.2 (Ar C), δ 112.0 (furan γ), δ 109.8 (furan β), δ 74.6 (C-H of DACH), δ 59.4 (C-H of

DACH), δ 43.5 (-CH₂- of furfuryl), δ 33.8 (CH₂ of DACH) , δ 31.1-24.6 (CH₃ of cumyl and CH₂ of DACH).

Synthesis of complex 47e. To a 20 mL scintillation vial containing proligand **L_b** (167 mg, 0.313 mmol) in 4 mL hexanes was added In(CH₃)₃ and the mixture was stirred at room temperature for 16 hours. The solvent was removed under reduced pressure to afford complex **47e** in form of yellow solid (yield= 94%). Crystallization of yellow solid in hexanes at -30 °C gave yellow crystals. Anal. Calcd. For formula: C₃₈H₄₇InN₂O₂ C 67.26%; H 6.98%; N 4.13%. Found: C 66.92%; H 6.43%; N 4.16%. ¹H NMR (400 MHz, CDCl₃, 25 °C) δ 8.10 (1H, s, -N=CH-Ar), δ 7.35 (1H, m, furan α), δ 7.33-7.00 (11H, m, ArH), δ 6.79 (1H, d, Ar-H), δ 6.33 (1H, m, furan γ), δ 6.18 (1H, d, furan β), δ 3.87 (1H, m, -CH₂- of furfuryl), δ 3.55 (1H, m, -CH₂- of furfuryl), δ 2.95 (1H, m, -CH- of DACH), δ 2.57 (1H, m, -CH- of DACH), δ 2.32 (1H, m, -CH₂- of DACH), δ 2.16 (1H, m, -CH₂- of DACH), δ 1.93-0.98 (18H, m, -CH₂- of DACH and -CH₃ of cumyl), δ 1.56 (3H, s, CH₃ of furan), δ -0.42 (3H, s, In-CH₃), δ -1.14 (3H, s, In-CH₃). ¹³C{¹H} NMR (101 MHz, CDCl₃, 25 °C) δ 170.8 (N=CH-Ar), δ 168.8 (Ar C), δ 151.7 (Ar C), δ 151.4 (Ar C), δ 142.4 (furan α), δ 141.8 (Ar C), δ 133.4 (Ar C), δ 131.2 (Ar C), δ 131.0 (Ar C-H), δ 127.9 (Ar C-H), δ 127.3 (Ar C-H), δ 127 (Ar C-H), δ 126.2 (Ar C-H), δ 125.4 (Ar C-H), δ 124.3 (Ar C-H), δ 118.4 (Ar C), δ 110.7 (furan β) , δ 108.1 (furan γ) , δ 67.1 (C-H of DACH) , δ 61.3 (C-H of DACH), δ 41.4 (-CH₂- of furfuryl), δ 33.3 (CH₂ of DACH), δ 31.1 (CH₃ of cumyl), δ 29.9 (CH₂ of DACH), δ 28.2 (CH₃ of cumyl), δ 25.2 (CH₂ of DACH), δ 24.8 (CH₂ of DACH), δ -9.0 (In-CH₃).

Synthesis of complex 47f. Complex **47f** was prepared using a similar procedure as complex **47e**. To synthesize complex **47f**, proligand **L_b** (142 mg, 0.266 mmol) and In(CH₂Si(CH₃)₃)₃ (100 mg, 0.266 mmol) were used. (yield=93%). Anal. Calcd. For C₄₄H₆₃InN₂O₂Si₂: C 64.22%; H 7.72%; N 3.40%. Found: C 63.74%; H 7.50%; N 3.31. ¹H NMR

(400 MHz, CDCl₃, 25 °C) δ 8.10 (1H, s, -N=CH-Ar), δ 7.36 (1H, m, furan α), δ 7.33-7.01 (11H, m, ArH), δ 6.81 (1H, d, Ar-H), δ 6.33 (1H, m, furan β), δ 6.15 (1H, d, furan γ), δ 3.80-3.66 (2H, m, -CH₂- of furfuryl), δ 2.97 (1H, m, -CH- of DACH), δ 2.70 (1H, m, -CH- of DACH), δ 2.23 (1H, m, -CH₂- of DACH), δ 2.08 (1H, m, -CH₂- of DACH), δ 1.91-0.87 (18H, m, -CH₂- of DACH and -CH₃ of cumyl), δ -0.02 (9H, s, Si-(CH₃)₃), δ -0.22 (9H, s, Si-(CH₃)₃), δ -0.69 (2H, m, In-CH₂), δ -1.08 (2H, s, In-CH₂), ¹³C{¹H} NMR (101 MHz, CDCl₃, 25 °C) δ 171.9 (N=CH-Ar), δ 168.7 (Ar C), δ 152.6 (furan δ), δ 151.5 (Ar C), δ 142.1 (furan α), δ 141.3 (Ar C), δ 134.0 (Ar C), 132.7 (Ar C-H), 131.7 (Ar C-H), 128.0 (Ar C-H), 127.6 (Ar C-H), 127.0 (Ar C-H), 126.2 (Ar C-H), 125.5 (Ar C-H), 124.6 (Ar C-H), 118.3 (Ar C), 110.6 (furan β), 107.6 (furan γ), 70.1 (C-H of DACH), 60.7 (C-H of DACH), 42.2 (-CH₂- of furfuryl), 34.2 (CH₂ of DACH), 25.1-31.4 (CH₂ of DACH and CH₃ of cumyl), 2.8 (CH₃ of Si(CH₃)₃), 2.4 (CH₃ of Si(CH₃)₃), -0.3 (In-CH₂), -0.8 (In-CH₂).

Synthesis of complex 47g. Complex **47g** was prepared in the form of a yellow solid using a similar procedure as complex **47e**. To synthesize complex **47g**, prolignand **L_g** (186mg, 0.338 mmol) and In(CH₂CH(CH₃)₂)₃ (100mg, 0.338 mmol) were used (yield=98%). Anal. Calcd. For C₄₅H₆₁InN₂O₂ : C 69.58%; H 7.92%; N 3.61%. Found: C 69.91%; H 7.73%; N 3.59%. ¹H NMR (400 MHz, CDCl₃, 25 °C) δ 8.08 (1H, s, -N=CH-Ar), δ 7.35-7.02 (11H, m, ArH), δ 6.81 (1H, m, Ar-H), δ 6.03 (1H, m, furan γ), δ 5.90 (1H, m, furan β), δ 3.80 (1H, m, -CH₂- of furfuryl), δ 3.63 (1H, m, -CH₂- of furfuryl), δ 2.95 (1H, m, -CH- of DACH), δ 2.59 (1H, m, -CH- of DACH), δ 2.31 (1H, m, -CH- of DACH), δ 2.26 (1H, s, CH₃ of furan), δ 2.08 (1H, m, -CH₂- of DACH), δ 2.15-0.96 (20H, m, -CH₂- of DACH, CH of ⁱBu and -CH₃ of cumyl), δ 0.89 (6H, CH₃ of ⁱBu), δ 0.72 (6H, m, CH₃ of ⁱBu), δ 0.51 (2H, m, In-CH₂), δ 0.06 (2H, m, In-CH₂). ¹³C{¹H} NMR (101 MHz, CDCl₃, 25 °C) δ 171.3 (N=CH-Ar), δ 168.8 (Ar C), δ 151.8 and 150.5 (furan α and furan δ), δ 141.2 (Ar C), δ 133.2 (Ar C-H), δ 131.9 (Ar C-H), δ 131.5 (Ar C-H), δ 127.9 (Ar C-H), δ 127.5

(Ar C-H), δ 126.9 (Ar C-H), δ 125.9 (Ar C-H), δ 125.4 (Ar C-H), δ 124.4 (Ar C-H), δ 118.2 (Ar C), δ 108.5 (furan γ), δ 106.4 (furan β), δ 69.9 (C-H of DACH), δ 60.9 (C-H of DACH), δ 42.2 (-CH₂- of furfuryl), δ 34.0 (CH₂ of DACH), δ 31.1- 24.8 (CH₂ DACH, CH₃ of cumyl, In-CH₂, CH₃ of ⁱBu, CH of ⁱBu), δ 13.7 (furan CH₃).

Synthesis of complex 47h. Complex **47h** was prepared in the form of an orange solid using a similar procedure as complex **47e**. To synthesize complex **47e**, proligand **L_h** (208mg, 0.338 mmol) and In(CH₂CH(CH₃)₂)₃ (100 mg, 0.338 mmol) were used (yield=91%). Anal. Calcd. For C₄₄H₅₈BrInN₂O₂: C 62.79%; H 6.95%; N 3.33%. Found: C 64.83%; H 7.00%; N 2.97%. ¹H NMR (400 MHz, CDCl₃, 25 °C) δ 8.04 (1H, s, -N=CH-Ar), δ 7.43-6.68 (12H, ArH), δ 6.22 (1H, d, furan β), δ 6.10 (1H, d, furan γ), δ 3.80 (1H, m, -CH₂- of furfuryl), δ 3.64 (1H, m, -CH₂- of furfuryl), δ 2.93 (1H, m, -CH- of DACH), δ 2.56 (1H, m, -CH- of DACH), δ 2.23 (1H, m, -CH₂- of DACH), δ 2.04 (1H, m, -CH₂- of DACH), δ 1.87-0.92 (20H, m, -CH₂- of DACH, CH of ⁱBu and -CH₃ of cumyl), δ 0.85 (6H, CH₃ of ⁱBu), δ 0.73 (6H, m, CH₃ of ⁱBu), δ 0.46 (2H, m, In-CH₂), δ 0.10 (2H, m, In-CH₂). ¹³C{¹H} NMR (101 MHz, CDCl₃, 25 °C) δ 171.4 (N=CH-Ar), δ 168.6 (Ar C), δ 154.8 (furan delta), δ 151.8 (Ar C), δ 141.3 (Ar C), δ 133.6 (Ar C), δ 132.1 (Ar C-H), δ 131.7 (Ar C-H), δ 128.0 (Ar C-H), δ 127.6 (Ar C-H), δ 127.0 (Ar C-H), δ 125.8 (Ar C-H), δ 125.5 (Ar C-H), δ 124.5 (Ar C-H), δ 121.1 (furan α), δ 118.2 (Ar C), δ 112.2 (furan β), δ 110.5 (furan γ), δ 70.9 (C-H of DACH), δ 60.7 (C-H of DACH), δ 42.2 (-CH₂- of furfuryl), δ 33.9 (CH₂ of DACH), δ 31.2-24.8 (CH₂ DACH, CH₃ of cumyl, In-CH₂, CH₃ of ⁱBu, CH of ⁱBu), 28.9 (In-CH₂).

Synthesis of complex 48e. To a 20 mL scintillation vial containing complex **47e** (158 mg, 0.234 mmol) in 3 mL benzene (C₆H₆) was added [HNMe₂Ph][Bar^F₂₄] (243 mg, 0.234 mmol) in 2 mL benzene and the mixture was stirred for 16 hours at room temperature. The residue was washed with cold hexanes and the supernatant was discarded to remove the Nme₂Ph by-product until a

precipitate was formed. The precipitate was dried under high vacuum for a few hours (yield= 68%).

Anal. Calcd. For $C_{69}H_{56}BF_{24}InN_2O_2$: C 54.28%; H 3.7%; N 1.83%. Found: C 53.59%; H 3.58%; N 1.90%. 1H NMR (400 MHz, $CDCl_3$, 25 °C) δ 8.17 (1H, s, -N=CH-Ar), δ 7.73 (8H, br. S., ortho H of Bar^F), δ 7.64 (1H, m, ArH), δ 7.55 (4H, br. S., para H of $Bar^{F_{24}}$), 6.87- 7.42 (11H, m, ArH), 6.37 (1H, Furan α), 6.26 (1H, Furan γ), 6.21 (1H, Furan β), 4.01 (1H, m, -CH₂- of furfuryl), 3.83 (1H, m, -CH₂- of furfuryl), 2.98 (1H, m, -CH- of DACH), 0.85 – 2.38 (21H, -CH₂- of DACH, -CH₃ of cumyl, and CH of DACH), 0.13 (3H, s, In-CH₃) $^{13}C\{^1H\}$ NMR (101 MHz, $CDCl_3$) δ 170.8 (N=CH-Ar), 165.7 (Ar C), 160.7-163.1 (B-C), 151.9 (Ar C), 150.1 (Ar C), 145.9 (Ar C), 144.2 (furan α), 141.7 (Ar C), 139.6 (Ar C), 135.1 ($Bar^{F_{23}}$ ortho C), 134.4 (Ar C-H), 132.1 (Ar C-H), 130.3 (Ar C-H), 128.6-129.7 ($Bar^{F_{24}}$ meta C), 128.3- 120.7 (Ar C-H and CF₃), 117.5 ($Bar^{F_{24}}$ para C), 112.4 (furan β), 111.0 (furan γ), 64.6 (DACH CH), 61.5 (CH DACH), 42.5 (furfuryl CH₂), 30.7-23.3 (DACH CH₂ and cumyl CH₃), -7.8 (In-CH₃).

Synthesis of complex 48f. Complex **48f** was prepared using a similar procedure to complex **48e**. To synthesize complex **48f**, complex **47f** (213mg, 0.259 mmol) and [HNMe₂Ph][$Bar^{F_{24}}$] (269 mg, 0.259 mmol) were used (yield=69%). Anal. Calcd. For $C_{72}H_{64}InN_2O_2SiBF_{24}$: C 54.08%; H 4.03%; N 1.75%. Found: C 53.79%; H 4.60%; N 1.74%. 1H NMR (400 MHz, $CDCl_3$, 25 °C) δ 8.21(1H, s, -N=CH-Ar), δ 7.72 (8H, br. S., ortho H of $Bar^{F_{24}}$), δ 7.63 (1H, m, ArH), δ 7.54 (4H, br. S., para H of $Bar^{F_{24}}$), 6.98- 7.40 (11H, m, ArH), 6.23 (1H, m, Furan γ), 6.17 (1H, m, Furan β), 6.11 (1H, m, Furan α), 4.05 (1H, m, -CH₂- of furfuryl), 3.81 (1H, m, -CH₂- of furfuryl), 3.11 (1H, -CH- of DACH), 1.04 – 2.45 (21H, -CH₂- of DACH, -CH₃ of cumyl, CH of DACH), -0.11-0.07 (11H, In-CH₂ and Si(CH₃)₃), $^{13}C\{^1H\}$ NMR (100 MHz, $CDCl_3$) δ 170.9 (N=CH-Ar), 165.8 (Ar C), 161.1-162.7 (B-C), 151.8 (Ar C), 150.1 (Ar C), 145.8 (Ar C), 144.4 (furan α), 141.5 (Ar C), 139.6 (Ar C), 135.1 (C-H of ortho $Bar^{F_{24}}$), 132.5-120.7 (Ar C-H and CF₃), 117.8 ($Bar^{F_{24}}$ para C),

112.5 (furan β), 111.2 (furan γ), 64.8 (DACH CH), 61.9 (DACH CH), 42.6 (furfuryl CH₂), 31.4 (CH₃ of cumyl), 30.8 (CH₃ of cumyl and CH₂ DACH), 28.6 (CH₃ of cumyl), 28.0 (CH₂ of DACH), 23.9 (CH₂ of DACH), 23.4 (CH₂ of DACH), 2.0 (Si(CH₃)₃), 0.3 (In-CH₂).

Synthesis of complex 48g. Complex **48g** was prepared in the form of a light green solid using a similar procedure as complex **48e**. To synthesize complex **48g**, complex **47g** (271 mg, 0.349 mmol) and [HNMe₂Ph][Bar^F₂₄] (364 mg, 0.349 mmol) were used. (yield= 76%). Anal. Calcd. For C₇₃H₆₄InBF₂₄N₂O₂: C 55.39%; H 4.08%; N 1.77%. Found: C 54.98%; H 3.84%; N 1.91%. ¹H NMR (300 MHz, CDCl₃, 25 °C) δ 8.22 (1H, s, -N=CH-Ar), δ 7.73 (8H, br. S., *ortho* H of Bar^F₂₄), δ 7.60 (1H, m, ArH), δ 7.54 (4H, br. S., para H of Bar^F₂₄), 6.92- 7.44 (11H, m, ArH), 6.08 (1H, m, Furan γ), 5.98 (1H, m, Furan β), 4.09 (1H, -CH₂- of furfuryl), 3.37 (1H, -CH₂- of furfuryl), 3.21 (1H, m, -CH- of DACH), 1.15-2.40 (9H, -CH₂- of DACH, -CH- of DACH), 2.19 (3H, CH₃ of furan), 1.74 (6H, CH₃ of cumyl), 1.59-1.66 (6H, CH₃ of cumyl), 1.85 (-CH- of ⁱBu), 1.05 (2H, In-CH₂), 0.72 (6H, CH₃ of ⁱBu). ¹³C{¹H} NMR (75 MHz, CDCl₃) δ 169.1 (N=CH-Ar), δ 164.4 (Ar C), 160.9-162.8 (B-C), 154.7 (Ar C), 151.1 (Ar C), 150.0 (Ar C), 145.9 (Ar C), 141.7 (Ar C), 140.0 (Ar C), 135 (*ortho* of C-H of Bar^F), 134.7 (Ar C-H), 132.0 (Ar C-H), 130.0- 128.90 (Bar^F₂₄ *meta* C), 119.3- 128.4 (Ar C-H and CF₃), 117.7 (Bar^F₂₄ *para* C-H), 111.9 (furan γ), 108.3 (furan β), 65.5 (DACH CH), 42.8 (furfuryl CH₂), 31.4 (CH₂ DACH), 30.8, 27.8 (cumyl CH₃), 29.7 (In-CH₂), 27.7 (CH₃ of ⁱBu), 26.3 (CH of ⁱBu), 24.4 (CH₂ DACH), 23.4 (CH₂ DACH), 13.9 (furan CH₃).

Synthesis of complex 48h. Complex **48h** was prepared in the form of an orange solid using a similar procedure as complex **48e**. To synthesize complex **48h**, complex **47h** (219 mg, 0.260 mmol) and [HNMe₂Ph][Bar^F₂₄] (271 mg, 0.260 mmol) were used (yield=43%). Anal. Calcd. For C₇₂H₆₁BrInN₂O₂BF₂₄: C 52.48%; H 3.73%; N 1.7%. Found: C 51.86%; H 3.78%; N 1.66%. ¹H

NMR (400 MHz, CDCl₃, 25 °C) δ 8.20 (1H, s, -N=CH-Ar), δ 7.73 (8H, br. S., ortho H of Bar^F₂₄), δ 7.61 (1H, m, ArH), δ 7.55 (4H, br. S., para H of Bar^F₂₄), 6.79- 7.41 (11H, m, ArH), 6.36 (1H, m, Furan β), 6.14 (1H, m, Furan γ), 3.97 (1H, m, -CH₂- of furfuryl), 3.26 (1H, m, -CH- of DACH), 3.18 (1H, -CH₂- of furfuryl), 2.33 (1H, m, -CH₂- of DACH), 1.10 – 2.28 (23H, -CH₂- of DACH, CH of DACH, -CH₃ of cumyl, CH of ⁱBu, and In-CH₂), 0.78 (6H, CH₃ of ⁱBu) ¹³C{ ¹H} NMR (100 MHz, CDCl₃) δ 168.6 (N=CH-Ar), 163.9 (Ar C), 161.1-162.6 (B-C), 151.3 (Ar C), 149.9 (Ar C), 149.3 (Ar C), 142.3 (Ar C), 140.2 (Ar C), 135 (*ortho* of C-H of Bar^F₂₄), 134.5 (Ar C-H), 131.6 (Ar C-H), 129.5- 128.6 (meta C of Bar^F₂₄), 128.40-123.3 (CF₃ and Ar C-H), 120.7, 118.7, 118.2, 117.6 (*para* C-H of Bar^F₂₄), 66.3 (Furan b), 65.7 (furan a), 66.2 (CH of DACH), 65.7 (CH of DACH), 42.8 (CH₂ of furfuryl), 31.4- 23.3 (CH₂ of DACH, CH₃ of cumyl, CH of ⁱBu, In-CH₂), 27.8 (CH₃ of ⁱBu).

Representative synthesis of SOE 2-(hex-5-en-1-yl)-1,4,6-trioxaspiro[4.6]undecane using complex 48b,48e-h. A 7 mL scintillation vial was charged with ϵ -caprolactone (29 mg, 0.25 mmol) and was quantitatively added to another 7 mL scintillation vial containing the required amount of the complex **48b,48e-h** (0.006 mmol) using 0.5 mL C₆D₆. The mixture of complex and ϵ -caprolactone was quantitatively transferred to a 20 mL scintillation vial containing 1,2-epoxy-7-octene (EOE) (32 mg, 0.25 mmol) using another 0.5 mL C₆D₆ solvent. The mixture was stirred at 60 °C for 24 hours. The ¹H NMR spectrum of the reaction mixture was obtained to find the conversion and confirm the SOE product.

Sample Preparation for in situ ¹H NMR studies. A 7 mL scintillation vial was charged with ϵ -caprolactone (58 mg, 0.51 mmol) and was quantitatively added to another 7 mL scintillation vial containing the required amount of the complex **48b,48e-h** (0.013 mmol) using 0.5 mL C₆D₆. The mixture of complex and ϵ -caprolactone was quantitatively transferred to another 7 mL

scintillation vial containing 1,2-epoxy-7-octene (EOE) (64 mg, 0.51 mmol) using 0.5 mL C₆D₆. The solution was mixed thoroughly and transferred to a J. Young tube and sealed. The ¹H NMR spectrum of the reaction mixture was obtained at regular intervals at 60 °C to find the conversion and confirm the SOE product.

Sample preparation for kinetic studies. Required amounts of ε-caprolactone, 1,2-epoxy-7-octene (EOE), and complex **48b** were measured in separate 7 mL scintillation vials. Complex **48b** was quantitatively added to the vial containing ε-caprolactone using 0.5 mL C₆D₆ and the mixture was quantitatively added to the vial containing 1,2-epoxy-7-octene (EOE) using another 0.5 mL C₆D₆. The solution was mixed thoroughly and added to a J. Young tube and sealed. The sample was used for *in situ* ¹H NMR spectra for kinetic studies.

Computational studies. Density Functional Theory (DFT) calculations were performed using the Gaussian 16¹⁹² package using B3PW91 as the functional^{193,194}, LANL2DZ¹⁹⁵ basis set for indium and def2-TZVP^{196,197} for all other atoms. Accuracy of this level of theory was evaluated by comparing a truncated version of **48b.2THF**¹⁴⁰ (cumyl groups were substituted with methyl groups) with its reported crystal structure. Errors in distances and angles were below 5 and 10% respectively and were thus considered to be appropriate for further studies. Geometry optimization and frequency calculations were performed in gas phase and solvent corrections were performed using single point calculations in benzene (ε=2.2706) using the solvation model based on density.¹⁹⁸ When applicable, the most stable conformer of the molecule was studied. Frequency calculations for all optimized structures showed no imaginary frequencies except for the transition states which only had one imaginary mode. Buried volume calculations were performed using SambVca 2.1's webtool¹⁸⁴ with a 3.5 Å radius from the indium center. Hydrogen atoms were ignored for steric contributions.

Chapter 5: Conclusions and future directions

5.1 Conclusion

The aim of this thesis was to use novel ligand design to explore the behavior and reactivity of cationic indium complexes. This work was done with the following main objectives: (1) to synthesize and characterize cationic alkylindium complexes supported by hemilabile ligands, (2) to study the stability, reactivity, and reactive mechanisms of these cationic indium complexes, and (3) to use these reactivity patterns to discover new catalytic applications.

Although cationic indium complexes have potential for novel reactivity, they are difficult to study due to their propensity to decompose upon dissociation of stabilizing ligands. Chapter 2 describes the synthesis and characterization of a series of a neutral and cationic alkylindium complexes stabilized by amino-imino phenolate ligands bearing hemilabile heterocyclic donor arms. While the neutral complexes featured the non-coordinated pendant donor arm, the transformation of the neutral species into cationic species induced the coordination of the pendant donor group to form tetra-coordinate complexes. The solution and solid-state behavior of the cationic complexes were studied to determine their stability and potential for applications in catalysis. These complexes expanded the repertoire of available cationic indium catalysts.

The first examples of the catalysis of polymerization reactions by cationic indium complexes supported by hemilabile ligands were described in Chapter 2. While previous studies had reported cationic indium catalysts, their dependence on coordinated solvent molecules had made their long-term storage and large-scale synthesis difficult. The pendant donor groups with increased donicity significantly increases the stability of the new cationic indium complexes. Thus, these new hemilabile ligands offered a method to stabilize the catalysts, increasing their useful

lifespan. This has permitted larger scale synthesis of the catalysts enabling the exploration of new reactivity using new monomers.

The production of high molecular weight cyclic poly(lactic acid) (c-PLA) using the cationic alkylinidum species with a pyridyl donor arm was described in Chapter 3. This is the first study to show the use of an indium catalyst in the selective synthesis of c-PLA from *racemic*-lactide (*rac*-LA). The catalyst functions through a bifunctional Lewis acid activation, Lewis base initiation mechanism. While this system does not exhibit fast polymerization of LA, it offers a highly reproducible and controlled method to produce high molecular weight c-PLA. Future endeavors will focus on two areas, (1) large scale synthesis of high molecular weight c-PLA to explore potential real-world applications, (2) exploration of the monomer scope of this catalyst to potentially produce high molecular weight cyclic esters/thioesters. This catalytic system can potentially act as a reliable method to produce novel cyclic polymers and provide an opportunity to study their properties and possible applications.

The determination of the mechanism of spiro-orthoester synthesis from the coupling of epoxides and ϵ -CL using the controlled reactivity of cationic alkylinidum complexes stabilized by hemilabile ligands is described in Chapter 4. Alkyl ligands with weaker electron donation and larger steric bulk increases the rate of this reaction. These systems show Michaelis-Menten saturation kinetics, with a large Michaelis constant indicating low substrate affinity. Additionally, the low Lewis acidity of these cationic alkylindium catalysts do not polarize the substrate enough to form homopolymers of either of the substrates. The mechanism was determined to be initiated by epoxide coordination to the indium center followed by subsequent ring-opening by S_N2 type attack by the lactone, forming spiro-orthoesters. A closer understanding of the role of the components of these indium catalysts allows us to design ligands and catalytic systems engineered

for specific reactions or substrates. Further work in relation to this study will focus on studying the mechanism of indium catalyzed double ring opening polymerization of spiro-orthoesters to for perfectly alternating poly(ether-*alt*-esters). Additionally, the rational catalyst design to produce high molecular weight poly(ether-*alt*-esters) would allow the study of rheological properties of these polymers.

5.2 Future directions for cationic group 13 catalysts

5.2.1 Expanding the monomer scope for cationic ROP

A class of potential monomers for future polymerization studies using the cationic complexes described in Chapter 2 are the sulfur containing analogues of ϵ -caprolactone and epoxides (Figure 5.1). Sulfur-containing polymers are reported to have high refractive indices, greater degradability, and different visco-elastic properties compared to their oxygenated counterparts.^{199–201}

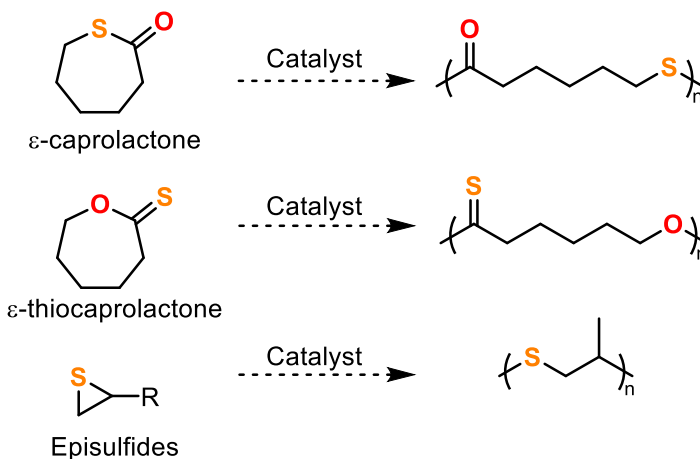


Figure 5.1. Potential sulfur containing monomers for polymerization by indium catalysts.

While there is a body of work describing the production of poly(thioesters) and poly(thionoesters) starting from ϵ -thiocaprolactone or ϵ -thionocaprolactone through bacterial synthesis,²⁰² enzymatic synthesis,²⁰³ cationic²⁰⁴ and anionic²⁰⁵ organocatalysis,^{206,207} these

systems lack the versatility and reactivity control seen with metal catalysts. Moreover, there are no reports of the use of metal catalysts in the ROP of sulfur-containing derivatives of ϵ -caprolactone.^{208,209} The cationic indium catalysts described in Chapter 2 are excellent candidates for the controlled ROP of these monomers. Further work using these indium catalysts could be done to produce block, alternating, or random copolymers of oxygen-containing and sulfur-containing monomers to produce a new class of copolymers with new optical and degradation properties.^{210–215}

5.2.2 Simplifying ligand design

The increased interest in cationic group 13 complexes has resulted in a great multitude of compounds that have multidentate ancillary ligands stabilizing them.^{83,216} Although chelating ligands can offer greater capabilities for catalyst tuning, as described in chapters 2 and 4, these ligands can require multi-step, multi-day syntheses.^{59,61,90,140} This synthetic complexity has hindered the exploration of the behavior and reactivity of these complexes as well as discouraging prospective industrial use. A potential solution to this problem is replacing intricate ligand architectures with stabilizing monodentate donor solvent ligands.²¹⁷

Considering results of the studies described in Chapters 2-4 using cationic alkylindium complexes, focus can be directed towards dialkyl group 13 cations stabilized by monodentate ligands (Figure 5.2). One of the earliest reports in this regard was by Neumüller and co-workers in the synthesis of a THF stabilized bis(isopropyl)indium species, **57**.²¹⁸ The solid-state arrangement of compound **57** consisted of $[i\text{Pr}_2\text{In}(\text{THF})_2]^+$ cations bridged by $[\text{BF}_4]^-$ ions, resulting in a continuous cation-anion chains. Subsequent work by Atwood and co-workers used bulky $t\text{Bu-NH}_2$ ligands to stabilize the dimethylgallium (**58**) and aluminum (**59**) compounds.^{219,220} The same strategy was used by Brintzinger and co-workers to produce a dimethylaluminum cation, **60**,

stabilized by two aniline molecules.²²¹ Close on their heels, Chen and Klosin synthesized a series of dialkylaluminum cations (**61**) and a cationic dimethylgallium species (**62**) stabilized by the diethyl ether solvent used as the reaction medium.²²² The methyl and octyl iterations of **61** were the first reported cationic aluminum activators in the polymerization of 1-octene. However, the reactivity of the gallium complex, **62**, was not explored.

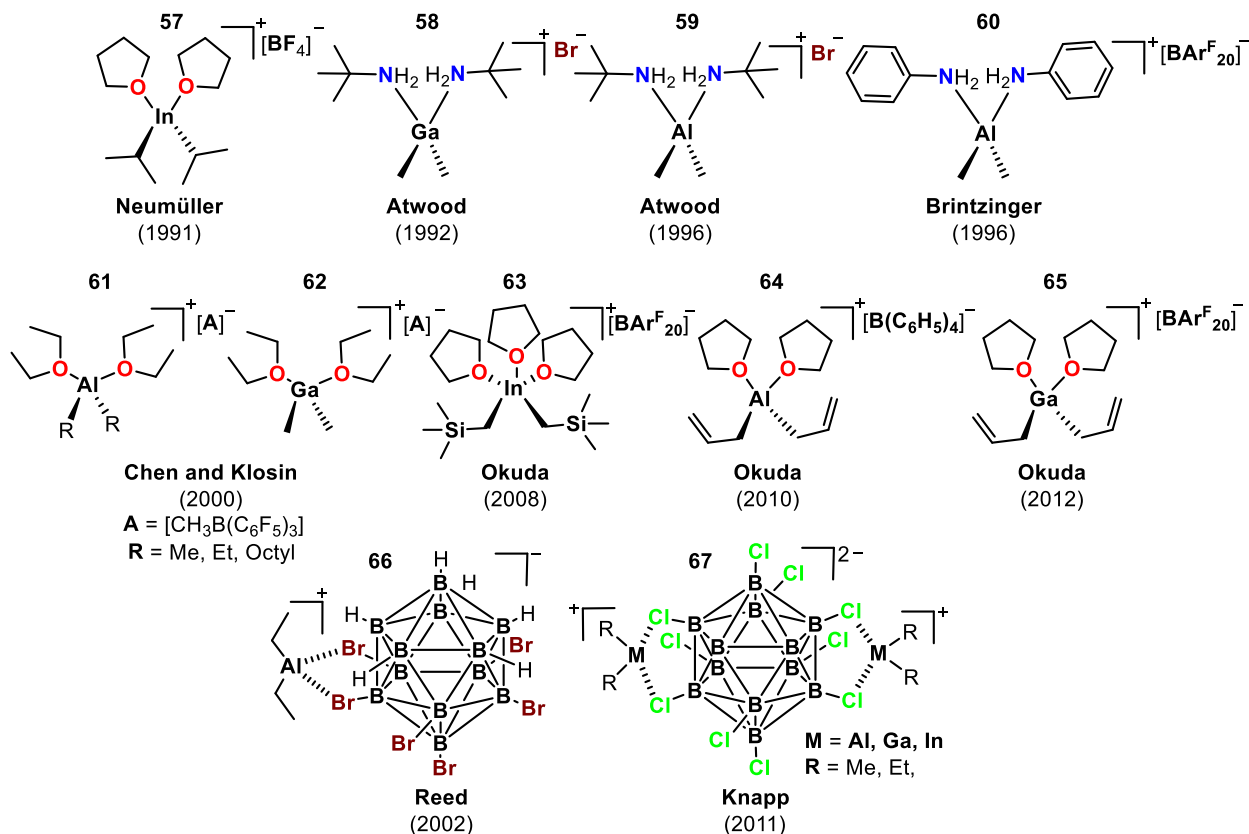


Figure 5.2. Previously reported dialkyl cations of group 13 metals stabilized by monodentate ligands.

In contrast to the tetra-coordinate indium complex **57** reported by Neumüller, Okuda and co-workers reported a penta-coordinate bis(trimethylsilylmethyl)indium complex (**63**) stabilized by three THF molecules.²²³ Complex **63** showed a square pyramidal solid-state geometry with the apical THF in closer association with the indium center compared to the basal THF molecules. Subsequently, the same group reported a bis(allyl)aluminum complex stabilized by THF (**64**).²²⁴

The solid-state structure of **64** showed two different coordination modes, a tetrahedral tetra-coordinate structure with two THF molecules and a trigonal-bipyramidal aluminum center with the allyl ligands in the equatorial plane with three THF coordinated. The two coordination modes exist in equilibrium in solution. Complex **64** could stoichiometrically react with benzophenone, allyl halides, I₂, or Br₂. The bis(allyl)gallium complex, **65**, reported by Okuda and co-workers was similar in structure and behavior to **64**.²²⁵ Complex **65** could stoichiometrically react with benzophenone and isoquinoline to produce the respective insertion complexes of gallium.

Attempts to synthesize purely ion-like group 13 dialkyl cations have turned towards using very bulky icosahedral carboranes anions as counterions. Reed and co-workers reported a diethylaluminum complex with a bromine substituted carborane counterion (**66**) capable of the catalytic ethenation of benzene, polymerization of cyclohexene oxide, and oligomerization of ethene.²²⁶ This is the only instance of catalytic activity reported for a dialkyl cation of a group 13 metal. A similar series of diethyl- and dimethyl- complexes of aluminum, gallium, indium (**67**) with a chlorinated carborane counterion were reported by Knapp and co-workers.²²⁷ While these simple cationic complexes of group 13 metals have been known for decades, their reactivity in polymerization reactions has been scarcely explored.

The recent work by Mehrkhodavandi and co-workers on cationic alkyl indium complexes and the work described in this thesis (**39** and **48a-h**) has shown the potential of these complexes as catalysts in polymerization reactions and the coupling of epoxides and lactones.^{59,90,140,171} While the work described in Chapters 1-3 demonstrate the utility of these complexes, the complexity of the ancillary ligand backbone can be a hindrance for further study of these cationic alkyl complexes and their reactivity. Therefore, dialkyl cations of group 13 metals stabilized by solvent molecules offer a simple and easily accessible platform for studying cationic complexes of group 13 metals.

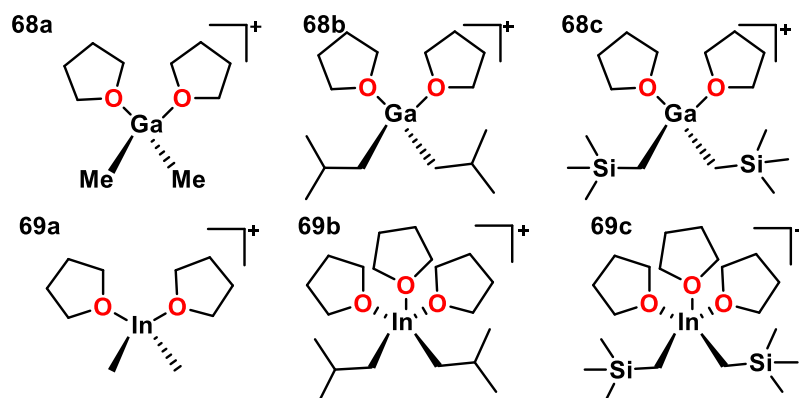


Figure 5.3. The synthesis of cationic dialkylgallium and indium complexes.

These complexes can be easily synthesized in a one-step process by the protonolysis of the neutral trialkylgallium or indium species with a Brønsted acid such as $[\text{PhNMe}_2\text{H}][\text{BAr}^{\text{F}}_{24}]$ ($\text{BAr}^{\text{F}}_{24}$ = tetrakis[3,5-bis(trifluoromethyl)phenyl]borate) in THF (Figure 5.3). Examining the reactivity of these complexes in ring opening polymerization of epoxides, ϵ -caprolactone, and spiro-orthoesters would fill a gap in the knowledge of the reactivity of dialkyl cations of group 13 metals. Additionally, the simplicity of these complexes makes them an ideal testbed to study the behavior and Lewis acidity of these complexes. While Lewis acidity can be quantified using the Gutmann-Beckett method,²²⁸ novel methods such as the fluorescent probes developed by Baumgartner and co-workers^{229,230} or computational affinity models^{231–234} may provide a better approximation of effective Lewis acidity of these in the solution phase.

Quantitatively investigating the intricate interplay between structure, Lewis acidity, and reactivity of these cationic complexes will not only address a significant knowledge gap regarding cationic group 13 complexes, but also empower future researchers to deliberately tailor catalysts for defined purposes.

Bibliography

- (1) Aldridge, S.; Downs, A. J. *The Group 13 Metals Aluminium, Gallium, Indium and Thallium: Chemical Patterns and Peculiarities*; John Wiley and Sons, 2011.
- (2) Johnson, A. L. Boron , Aluminium, Gallium , Indium and Thallium. *Annu. Rep. Prog. Chem., Sect. A: Inorg. Chem.* **2010**, *106*, 62–86.
- (3) Minami, T.; Miyata, T. Present Status and Future Prospects for Development of Non- or Reduced-Indium Transparent Conducting Oxide Thin Films. *Thin Solid Films* **2008**, *517* (4), 1474–1477.
- (4) Aguirre-Díaz, L. M.; Reinares-Fisac, D.; Iglesias, M.; Gutiérrez-Puebla, E.; Gándara, F.; Snejko, N.; Monge, M. Á. Group 13th Metal-Organic Frameworks and Their Role in Heterogeneous Catalysis. *Coord. Chem. Rev.* **2017**, *335*, 1–27.
- (5) Frost, C.; Hartley, J. New Applications of Indium Catalysts in Organic Synthesis. *Mini. Rev. Org. Chem.* **2005**, *1* (1), 1–7.
- (6) Datta, M. Recent Advances of Indium(III) Chloride Catalyzed Reactions in Organic Synthesis. *ChemistrySelect* **2021**, *6* (2), 187–216.
- (7) Aldridge, S.; Downs, A. J.; Kays, D. L. Formal Oxidation State +3: Organometallic Chemistry. In *The Group 13 Metals Aluminium, Gallium, Indium and Thallium: Chemical Patterns and Peculiarities*; John Wiley and Sons, 2011; pp 148–245.
- (8) Li, C. J.; Chan, T. H. Organic Syntheses Using Indium-Mediated and Catalyzed Reactions in Aqueous Media. *Tetrahedron* **1999**, *55* (37), 11149–11176.
- (9) Loh, T. P.; Chua, G. L. Discovery of Indium Complexes as Water-Tolerant Lewis Acids. *Chem. Commun.* **2006**, No. 26, 2739–2749.
- (10) Jung, H.-J.; Cho, Y.; Kim, D.; Mehrkhodavandi, P. Cationic Aluminum, Gallium, and

- Indium Complexes in Catalysis. *Catal. Sci. Technol.* **2021**, *11* (1), 62–91.
- (11) Carmalt, C. J.; King, S. J. Gallium(III) and Indium(III) Alkoxides and Aryloxides. *Coord. Chem. Rev.* **2006**, *250* (5–6), 682–709.
- (12) Yu, Y.; Kazemi, M. Indium Bromide (InBr₃): A Versatile and Efficient Catalyst in Organic Synthesis. *Synth. Commun.* **2021**, *51* (17), 2574–2601.
- (13) Mahato, S. K.; Acharya, C.; Wellington, K. W.; Bhattacharjee, P.; Jaisankar, P. InCl₃: A Versatile Catalyst for Synthesizing a Broad Spectrum of Heterocycles. *ACS Omega* **2020**, *5* (6), 2503–2519.
- (14) Ranu, B. C. Indium Metal and Its Halides in Organic Synthesis. *Eur. J. Org. Chem.* **2000**, *2000* (13), 2347–2356.
- (15) Singh, M. S.; Raghuvanshi, K. Recent Advances in InCl₃-Catalyzed One-Pot Organic Synthesis. *Tetrahedron* **2012**, *68* (42), 8683–8697.
- (16) Ghosh, R.; Maiti, S. Advances in Indium Triflate Catalyzed Organic Syntheses. *J. Mol. Catal. A Chem.* **2007**, *264* (1–2), 1–8.
- (17) Dagorne, S.; Normand, M.; Kirillov, E.; Carpentier, J. F. Gallium and Indium Complexes for Ring-Opening Polymerization of Cyclic Ethers, Esters and Carbonates. *Coord. Chem. Rev.* **2013**, *257* (11–12), 1869–1886.
- (18) Pérez Sestelo, J.; Sarandeses, L. A.; Martínez, M. M.; Alonso-Marañón, L. Indium(III) as π -Acid Catalyst for the Electrophilic Activation of Carbon–Carbon Unsaturated Systems. *Org. Biomol. Chem.* **2018**, *16* (32), 5733–5747.
- (19) Podlech, J.; Maier, T. C. Indium in Organic Synthesis. *Synthesis* **2003**, *2003* (05), 0633–0655.
- (20) Augé, J.; Lubin-Germain, N.; Uziel, J. Recent Advances in Indium-Promoted Organic

- Reactions. *Synthesis* **2007**, 2007 (12), 1739–1764.
- (21) Fringuelli, F.; Piermatti, O.; Pizzo, F.; Vaccaro, L. Indium Salt-Promoted Organic Reactions. *Curr. Org. Chem.* **2005**, 7 (16), 1661–1689.
- (22) Yadav, J. S.; Antony, A.; George, J.; Subba Reddy, B. V. Recent Developments in Indium Metal and Its Salts in Organic Synthesis. *Eur. J. Org. Chem.* **2010**, 2010 (4), 591–605.
- (23) Pathipati, S. R.; Van Der Werf, A.; Selander, N. Indium(III)-Catalyzed Transformations of Alkynes: Recent Advances in Carbo- and Heterocyclization Reactions. *Synthesis* **2017**, 49 (22), 4931–4941.
- (24) Pellissier, H. Enantioselective Indium-Catalyzed Transformations. *Synthesis* **2021**, 53 (08), 1379–1395.
- (25) Yadav, J.; Antony, A.; George, J.; Subba Reddy, B. Multi-Component Reactions Using Indium(III) Salts. *Curr. Org. Chem.* **2010**, 14 (4), 414–424.
- (26) Brandão, P.; Burke, A. J.; Pineiro, M. A Decade of Indium-Catalyzed Multicomponent Reactions (MCRs). *Eur. J. Org. Chem.* **2020**, 2020 (34), 5501–5513.
- (27) Fazekas, E.; Lowy, P. A.; Abdul Rahman, M.; Lykkeberg, A.; Zhou, Y.; Chambenahalli, R.; Garden, J. A. Correction: Main Group Metal Polymerisation Catalysts. *Chem. Soc. Rev.* **2023**, 52 (3), 1157–1157.
- (28) Fazekas, E.; Lowy, P. A.; Abdul Rahman, M.; Lykkeberg, A.; Zhou, Y.; Chambenahalli, R.; Garden, J. A. Main Group Metal Polymerisation Catalysts. *Chem. Soc. Rev.* **2022**, 51 (21), 8793–8814.
- (29) Hsieh, I. P.; Huang, C. H.; Lee, H. M.; Kuo, P. C.; Huang, J. H.; Lee, H. I.; Cheng, J. T.; Lee, G. H. Indium Complexes Incorporating Bidentate Substituted Pyrrole Ligand: Synthesis, Characterization, and Ring-Opening Polymerization of ϵ -Caprolactone. *Inorg.*

- Chim. Acta* **2006**, 359 (2), 497–504.
- (30) Douglas, A. F.; Patrick, B. O.; Mehrkhodavandi, P. A Highly Active Chiral Indium Catalyst for Living Lactide Polymerization. *Angew. Chem. Int. Ed.* **2008**, 47 (12), 2290–2293.
- (31) Pietrangelo, A.; Knight, S. C.; Gupta, A. K.; Yao, L. J.; Hillmyer, M. A.; Tolman, W. B. Mechanistic Study of the Stereoselective Polymerization of D, L-Lactide Using Indium(III) Halides. *J. Am. Chem. Soc.* **2010**, 132 (33), 11649–11657.
- (32) Bompart, M.; Vergnaud, J.; Strub, H.; Carpentier, J. F. Indium(Iii) Halides as Exceptionally Active, Water -Tolerant Catalysts for Cationic Polymerization of Styrenics. *Polym. Chem.* **2011**, 2 (8), 1638–1640.
- (33) Buffet, J. C.; Okuda, J.; Arnold, P. L. Chiral Indium Alkoxide Complexes as Initiators for the Stereoselective Ring-Opening Polymerization of Rac-Lactide. *Inorg. Chem.* **2010**, 49 (2), 419–426.
- (34) Horeglad, P.; Cybularczyk, M.; Litwińska, A.; Dąbrowska, A. M.; Dranka, M.; Zukowska, G. Z.; Urbańczyk, M.; Michalak, M. Controlling the Stereoselectivity of Rac-LA Polymerization by Chiral Recognition Induced the Formation of Homochiral Dimeric Metal Alkoxides. *Polym. Chem.* **2016**, 7 (11), 2022–2036.
- (35) Allan, L. E. N.; Briand, G. G.; Decken, A.; Marks, J. D.; Shaver, M. P.; Wareham, R. G. Synthesis and Structural Characterization of Cyclic Indium Thiolate Complexes and Their Utility as Initiators for the Ring-Opening Polymerization of Cyclic Esters. *J. Organomet. Chem.* **2013**, 736, 55–62.
- (36) Normand, M.; Dorcet, V.; Kirillov, E.; Carpentier, J. F. {Phenoxy-Imine}aluminum versus -Indium Complexes for the Immortal ROP of Lactide: Different Stereocontrol,

- Different Mechanisms. *Organometallics* **2013**, 32 (6), 1694–1709.
- (37) Normand, M.; Roisnel, T.; Carpentier, J. F.; Kirillov, E. Dinuclear vs. Mononuclear Complexes: Accelerated, Metal-Dependent Ring-Opening Polymerization of Lactide. *Chem. Commun.* **2013**, 49 (99), 11692–11694.
- (38) Ghosh, S.; Gowda, R. R.; Jagan, R.; Chakraborty, D. Gallium and Indium Complexes Containing the Bis(Imino)Phenoxide Ligand: Synthesis, Structural Characterization and Polymerization Studies. *Dalton Trans.* **2015**, 44 (22), 10410–10422.
- (39) Osten, K. M.; Mehrkhodavandi, P. Indium Catalysts for Ring Opening Polymerization: Exploring the Importance of Catalyst Aggregation. *Acc. Chem. Res.* **2017**, 50 (11), 2861–2869.
- (40) Yu, I.; Acosta-Ramírez, A.; Mehrkhodavandi, P. Mechanism of Living Lactide Polymerization by Dinuclear Indium Catalysts and Its Impact on Isoselectivity. *J. Am. Chem. Soc.* **2012**, 134 (30), 12758–12773.
- (41) Kremer, A. B.; Osten, K. M.; Yu, I.; Ebrahimi, T.; Aluthge, D. C.; Mehrkhodavandi, P. Dinucleating Ligand Platforms Supporting Indium and Zinc Catalysts for Cyclic Ester Polymerization. *Inorg. Chem.* **2016**, 55 (11), 5365–5374.
- (42) Diaz, C.; Fu, J.; Soobrattee, S.; Cao, L.; Nyamayaro, K.; Goonesinghe, C.; Patrick, B. O.; Mehrkhodavandi, P. Comparison of Imine- and Phosphinimine-Supported Indium Complexes: Tuning the Reactivity for the Sequential and Simultaneous Copolymerization of Lactide and ϵ -Caprolactone. *Inorg. Chem.* **2022**, 61 (8), 3763–3773.
- (43) Jung, H. J.; Nyamayaro, K.; Baalbaki, H. A.; Goonesinghe, C.; Mehrkhodavandi, P. Cooperative Initiation in a Dinuclear Indium Complex for CO₂Epoxide Copolymerization. *Inorg. Chem.* **2022**, 62 (5), 1968–1977.

- (44) Maudoux, N.; Roisnel, T.; Dorcet, V.; Carpentier, J. F.; Sarazin, Y. Chiral (1,2)-Diphenylethylene-Salen Complexes of Trier Metals: Coordination Patterns and Mechanistic Considerations in the Isoselective ROP of Lactide. *Chem. – A Eur. J.* **2014**, *20* (20), 6131–6147.
- (45) Normand, M.; Kirillov, E.; Roisnel, T.; Carpentier, J. F. Indium Complexes of Fluorinated Dialkoxy-Diimino Salen-like Ligands for Ring-Opening Polymerization of Rac -Lactide: How Does Indium Compare to Aluminum? *Organometallics* **2012**, *31* (4), 1448–1457.
- (46) Maudoux, N.; Roisnel, T.; Carpentier, J. F.; Sarazin, Y. Aluminum, Indium, and Mixed Yttrium-Lithium Complexes Supported by a Chiral Binap-Based Fluorinated Dialkoxide: Structural Features and Heteroselective ROP of Lactide. *Organometallics* **2014**, *33* (20), 5740–5748.
- (47) Quan, S. M.; Diaconescu, P. L. High Activity of an Indium Alkoxide Complex toward Ring Opening Polymerization of Cyclic Esters. *Chem. Commun.* **2015**, *51* (47), 9643–9646.
- (48) Broderick, E. M.; Guo, N.; Vogel, C. S.; Xu, C.; Sutter, J.; Miller, J. T.; Meyer, K.; Mehrkhodavandi, P.; Diaconescu, P. L. Redox Control of a Ring-Opening Polymerization Catalyst. *J. Am. Chem. Soc.* **2011**, *133* (24), 9278–9281.
- (49) Yuntawattana, N.; McGuire, T. M.; Durr, C. B.; Buchard, A.; Williams, C. K. Indium Phosphasalen Catalysts Showing High Isoselectivity and Activity in Racemic Lactide and Lactone Ring Opening Polymerizations. *Catal. Sci. Technol.* **2020**, *10* (21), 7226–7239.
- (50) Myers, D.; White, A. J. P.; Forsyth, C. M.; Bown, M.; Williams, C. K.; Myers, J. D.; Hite, A. J. P. W.; Forsyth, C. M. F.; Bown, M.; Williams, C. K. Phosphasalen Indium Complexes Showing High Rates and Isoselectivities in Rac-Lactide Polymerizations.

- Angew. Chem. Int. Ed.* **2017**, *56* (19), 5277–5282.
- (51) Thevenon, A.; Cyriac, A.; Myers, D.; White, A. J. P.; Durr, C. B.; Williams, C. K. Indium Catalysts for Low-Pressure CO₂/Epoxide Ring-Opening Copolymerization: Evidence for a Mononuclear Mechanism? *J. Am. Chem. Soc.* **2018**, *140* (22), 6893–6903.
- (52) Baalbaki, H. A.; Nyamayaro, K.; Shu, J.; Goonesinghe, C.; Jung, H. J.; Mehrkhodavandi, P. Indium-Catalyzed CO₂/Epoxide Copolymerization: Enhancing Reactivity with a Hemilabile Phosphine Donor. *Inorg. Chem.* **2021**, *60* (24), 19304–19314.
- (53) Ebrahimi, T.; Aluthge, D. C.; Patrick, B. O.; Hatzikiriakos, S. G.; Mehrkhodavandi, P. Air- and Moisture-Stable Indium Salan Catalysts for Living Multiblock PLA Formation in Air. *ACS Catal.* **2017**, *7* (10), 6413–6418.
- (54) Beament, J.; Mahon, M. F.; Buchard, A.; Jones, M. D. Salan Group 13 Complexes – Structural Study and Lactide Polymerisation. *New J. Chem.* **2017**, *41* (5), 2198–2203.
- (55) Peckermann, L.; Kapelski, A.; Spaniol, T. P.; Okuda, J. Indium Complexes Supported by 1, ω -Dithiaalkanediyl-Bridged Bis(Phenolato) Ligands: Synthesis, Structure, and Controlled Ring-Opening Polymerization of L-Lactide. *Inorg. Chem.* **2009**, *48* (12), 5526–5534.
- (56) Kapelski, A.; Okuda, J. Ring-Opening Polymerization of Rac- and Meso-Lactide Initiated by Indium Bis(Phenolate) Isopropoxy Complexes. *J. Polym. Sci. Part A: Polym. Chem.* **2013**, *51* (23), 4983–4991.
- (57) Hu, M.; Wang, M.; Zhang, P.; Wang, L.; Zhu, F.; Sun, L. Preparation and Structure of an Enantiomeric Water-Bridged Dinuclear Indium Complex Containing Two Homochiral N Atoms and Its Performance as an Initiator in Polymerization of Rac-Lactide. *Inorg. Chem. Commun.* **2010**, *13* (8), 968–971.

- (58) Blake, M. P.; Schwarz, A. D.; Mountford, P. Sulfonamide, Phenolate, and Directing Ligand-Free Indium Initiators for the Ring-Opening Polymerization of Rac-Lactide. *Organometallics* **2011**, *30* (5), 1202–1214.
- (59) Jung, H.-J. J.; Goonesinghe, C.; Mehrkhodavandi, P. Temperature Triggered Alternating Copolymerization of Epoxides and Lactones via Pre-Sequenced Spiroorthoester Intermediates. *Chem. Sci.* **2022**, *13* (13), 3713–3718.
- (60) Diaz, C.; Tomkovic, T.; Goonesinghe, C.; Hatzikiriakos, S. G.; Mehrkhodavandi, P. One-Pot Synthesis of Oxygenated Block Copolymers by Polymerization of Epoxides and Lactide Using Cationic Indium Complexes. *Macromolecules* **2020**, *53* (20), 8819–8828.
- (61) Diaz, C.; Ebrahimi, T.; Mehrkhodavandi, P. Cationic Indium Complexes for the Copolymerization of Functionalized Epoxides with Cyclic Ethers and Lactide. *Chem. Commun.* **2019**, *55* (23), 3347–3350.
- (62) Jeffrey, J. C.; Rauchfuss, T. B. Metal Complexes of Hemilabile Ligands. Reactivity and Structure of Dichlorobis(o-(Diphenylphosphino)Anisole)Ruthenium(II). *Inorg. Chem.* **1979**, *18* (10), 2658–2666.
- (63) Slone, C. S.; Weinberger, D. A.; Mirkin, C. A. The Transition Metal Coordination Chemistry of Hemilabile Ligands; John Wiley & Sons, Ltd, 2007; pp 233–350.
- (64) Braunstein, P.; Naud, F. Hemilability of Hybrid Ligands and the Coordination Chemistry of Oxazoline-Based Systems. *Angew. Chem. Int. Ed.* **2001**, *40* (4), 680–699.
- (65) Lindner, R.; van den Bosch, B.; Lutz, M.; Reek, J. N. H.; van der Vlugt, J. I. Tunable Hemilabile Ligands for Adaptive Transition Metal Complexes. *Organometallics* **2011**, *30* (3), 499–510.
- (66) Dong, K.; Sang, R.; Wei, Z.; Liu, J.; Dühren, R.; Spannenberg, A.; Jiao, H.; Neumann, H.;

- Jackstell, R.; Franke, R.; Beller, M. Cooperative Catalytic Methoxycarbonylation of Alkenes: Uncovering the Role of Palladium Complexes with Hemilabile Ligands. *Chem. Sci.* **2018**, 9 (9), 2510–2516.
- (67) Tanaka, K.; Ewing, W. R.; Yu, J.-Q. Hemilabile Benzyl Ether Enables γ -C(Sp³)-H Carbonylation and Olefination of Alcohols. *J. Am. Chem. Soc.* **2019**, 141 (39), 15494–15497.
- (68) Pérez García, P. M.; Ren, P.; Scopelliti, R.; Hu, X. Nickel-Catalyzed Direct Alkylation of Terminal Alkynes at Room Temperature: A Hemilabile Pincer Ligand Enhances Catalytic Activity. *ACS Catal.* **2015**, 5 (2), 1164–1171.
- (69) Jiménez, M. V.; Pérez-Torrente, J. J.; Bartolomé, M. I.; Lahoz, F. J.; Oro, L. A. Rational Design of Efficient Rhodium Catalysts for the Anti-Markovnikov Oxidative Amination of Styrene. *Chem. Commun.* **2010**, 46 (29), 5322–5324.
- (70) Handa, S.; Smith, J. D.; Hageman, M. S.; Gonzalez, M.; Lipshutz, B. H. Synergistic and Selective Copper/Ppm Pd-Catalyzed Suzuki–Miyaura Couplings: In Water, Mild Conditions, with Recycling. *ACS Catal.* **2016**, 6 (12), 8179–8183.
- (71) Weng, Z.; Teo, S.; Hor, T. S. A. Metal Unsaturation and Ligand Hemilability in Suzuki Coupling. *Acc. Chem. Res.* **2007**, 40 (8), 676–684.
- (72) Higman, C. S.; Nascimento, D. L.; Ireland, B. J.; Audörsch, S.; Bailey, G. A.; McDonald, R.; Fogg, D. E. Chelate-Assisted Ring-Closing Metathesis: A Strategy for Accelerating Macrocyclization at Ambient Temperatures. *J. Am. Chem. Soc.* **2018**, 140 (5), 1604–1607.
- (73) Liu, Y.; Kean, Z. S.; d’Aquino, A. I.; Manraj, Y. D.; Mendez-Arroyo, J.; Mirkin, C. A. Palladium(II) Weak-Link Approach Complexes Bearing Hemilabile N-Heterocyclic Carbene–Thioether Ligands. *Inorg. Chem.* **2017**, 56 (10), 5902–5910.

- (74) Rosen, M. S.; Stern, C. L.; Mirkin, C. A. Heteroligated PtII Weak-Link Approach Complexes Using Hemilabile N-Heterocyclic Carbene-Thioether and Phosphino-Thioether Ligands. *Chem. Sci.* **2013**, 4 (11), 4193–4198.
- (75) Hulley, E. B.; Helm, M. L.; Bullock, R. M. Heterolytic Cleavage of H₂ by Bifunctional Manganese(i) Complexes: Impact of Ligand Dynamics, Electrophilicity, and Base Positioning. *Chem. Sci.* **2014**, 5 (12), 4729–4741.
- (76) Dureen, M. A.; Stephan, D. W. Biphenylamide Ligand Complexes of Li and Al: Hemilabile Arene Donors? *J. Chem. Soc. Dalton Trans.* **2008**, No. 35, 4723–4731.
- (77) Fondong, G. L.; Njua, E. Y.; Steiner, A.; Campana, C. F.; Stahl, L. Syntheses and Structures of Zinc and Tin(II) Compounds with Hemilabile N-Silyl-Tert-Butylamido and N-Silyl-p-Tolylamido Ligands That Contain Pendent Tert-Butoxy Groups. *Polyhedron* **2011**, 30 (17), 2856–2862.
- (78) Gallegos, C.; Camacho, R.; Valiente, M.; Cuenca, T.; Cano, J. Cyclopentadienyl-Based Mg Complexes in the Intramolecular Hydroamination of Aminoalkenes: Mechanistic Evidence for Cationic: Versus Neutral Magnesium Derivatives. *Catal. Sci. Technol.* **2016**, 6 (13), 5134–5143.
- (79) Objartel, I.; Ott, H.; Stalke, D. Low-Temperature NMR and Crystal Structure Analyses of a Hemilabile Tin Complex. *Zeitschrift für Anorg. und Allg. Chemie* **2008**, 634 (12–13), 2373–2379.
- (80) Ikpo, N.; Barbon, S. M.; Drover, M. W.; Dawe, L. N.; Kerton, F. M. Aluminum Methyl and Chloro Complexes Bearing Monoanionic Aminephenolate Ligands: Synthesis, Characterization, and Use in Polymerizations. *Organometallics* **2012**, 31 (23), 8145–8158.
- (81) Plommer, H.; Reim, I.; Kerton, F. M. Ring-Opening Polymerization of Cyclohexene

- Oxide Using Aluminum Amine-Phenolate Complexes. *Dalton Trans.* **2015**, 44 (27), 12098–12102.
- (82) Dagorne, S.; Wehmschulte, R. Recent Developments on the Use of Group 13 Metal Complexes in Catalysis. *ChemCatChem* **2018**, 10 (12), 2509–2520.
- (83) Sarazin, Y.; Carpentier, J.-F. Discrete Cationic Complexes for Ring-Opening Polymerization Catalysis of Cyclic Esters and Epoxides. *Chem. Rev.* **2015**, 115 (9), 3564–3614.
- (84) Gao, J.; Zhu, D.; Zhang, W.; Solan, G. A.; Ma, Y.; Sun, W. H. Recent Progress in the Application of Group 1, 2 & 13 Metal Complexes as Catalysts for the Ring Opening Polymerization of Cyclic Esters. *Inorg. Chem. Front.* **2019**, 6 (10), 2619–2652.
- (85) Issenhuth, J.-T.; Pluvinaud, J.; Welter, R.; Bellemin-Lapponnaz, S.; Dagorne, S. Novel Neutral and Cationic Aluminium Alkyl Complexes Supported by Potentially Tridentate O,N,L-Type Aminophenolate Ligands and Their Use in Propylene Oxide Polymerization. *Eur. J. Inorg. Chem.* **2009**, 2009 (31), 4701–4709.
- (86) Plommer, H.; Murphy, J. N.; Dawe, L. N.; Kerton, F. M. Morpholine-Stabilized Cationic Aluminum Complexes and Their Reactivity in Ring-Opening Polymerization of ϵ -Caprolactone. *Inorg. Chem.* **2019**, 58 (8), 5253–5264.
- (87) Kiriratnikom, J.; Chotchatchawankul, S.; Haesuwannakij, S.; Kiatisevi, S.; Phomphrai, K. Synthesis and Characterization of Neutral and Cationic Aluminum Complexes Supported by a Furfuryl-Containing Aminophenolate Ligand for Ring-Opening Polymerization of ϵ -Caprolactone. *New J. Chem.* **2018**, 42 (11), 8374–8383.
- (88) Cross, E. D.; Tennekone, G. K.; Decken, A.; Shaver, M. P. Aluminum Amine-(*Bis*)Phenolate Complexes for Ring-Opening Polymerization of *Rac* -Lactide and ϵ -

- Caprolactone. *Green Mater.* **2013**, *1* (2), 79–86.
- (89) Robson, D. A.; Bylikin, S. Y.; Cantuel, M.; Male, N. A. H.; Rees, L. H.; Mountford, P.; Schröder, M. Neutral and Cationic Organometallic Aluminium and Indium Complexes of Mono-Pendant Arm Triazacyclononane Ligands. *J. Chem. Soc. Dalton Trans.* **2001**, No. 2, 157–169.
- (90) Jung, H.-J.; Chang, C.; Yu, I.; Aluthge, D. C.; Ebrahimi, T.; Mehrkhodavandi, P. Coupling of Epoxides and Lactones by Cationic Indium Catalysts To Form Functionalized Spiro-Orthoesters. *ChemCatChem* **2018**, *10* (15), 3219–3222.
- (91) Mayer, U.; Gutmann, V.; Gerger, W. The Acceptor Number ? A Quantitative Empirical Parameter for the Electrophilic Properties of Solvents. *Monatshefte für Chemie* **1975**, *106* (6), 1235–1257.
- (92) Welch, G. C.; Cabrera, L.; Chase, P. A.; Hollink, E.; Masuda, J. D.; Wei, P.; Stephan, D. W. Tuning Lewis Acidity Using the Reactivity of “Frustrated Lewis Pairs”: Facile Formation of Phosphine-Boranes and Cationic Phosphonium-Boranes. *Dalton Trans.* **2007**, No. 31, 3407–3414.
- (93) Kremer, A. B.; Andrews, R. J.; Milner, M. J.; Zhang, X. R.; Ebrahimi, T.; Patrick, B. O.; Diaconescu, P. L.; Mehrkhodavandi, P. A Comparison of Gallium and Indium Alkoxide Complexes as Catalysts for Ring-Opening Polymerization of Lactide. *Inorg. Chem.* **2017**, *56* (3), 1375–1385.
- (94) Sandström, M.; Persson, I.; Persson, P.; Euranto, E. K.; Brekke, T.; Aksnes, D. W.; Tokii, T. A Study of Solvent Electron-Pair Donor Ability and Lewis Basicity Scales. *Acta Chem. Scand.* **1990**, *44*, 653–675.
- (95) Cataldo, F. A Revision of the Gutmann Donor Numbers of a Series of Phosphoramides

- Including TEPA. *Eur. Chem. Bull.* **2015**, 4 (1–3), 92–97.
- (96) Horner, K. E.; Karadakov, P. B. Chemical Bonding and Aromaticity in Furan, Pyrrole, and Thiophene: A Magnetic Shielding Study. *J. Org. Chem.* **2013**, 78 (16), 8037–8043.
- (97) Katayama, M.; Shinoda, M.; Ozutsumi, K.; Funahashi, S.; Inada, Y. Reevaluation of Donor Number Using Titration Calorimetry. *Anal. Sci.* **2012**, 28 (2), 103–106.
- (98) Quattrocioni, D. G. S.; Ferreira, G. B.; da Costa, L. M.; Carneiro, J. W. de M. DFT Studies of the Interactions between the $[Ca(H_2O)_5]^{2+}$ Cation and Monofunctional Oxo, Aza, Sulfur and Phosphorous Ligands. *Comput. Theor. Chem.* **2016**, 1075, 104–110.
- (99) Li, P.; Qiu, K.-Y. Living Radical Polymerization of Methyl Methacrylate Catalyzed by CuprousN,N-Diethyldithiocarbamate. *J. Polym. Sci. Part A: Polym. Chem.* **2002**, 40 (12), 2093–2097.
- (100) Matyjaszewski, K.; Penczek, S. On-trapping in Cationic Polymerization, 2. Relative Rates of Trapping and Relative Chemical Shifts for Structurally Differing Phosphines as Trapping Agents. *Makromol. Chem.* **1981**, 182 (6), 1735–1742.
- (101) Liu, Z.; Torrent, M.; Morokuma, K. Molecular Orbital Study of Zinc(II)-Catalyzed Alternating Copolymerization of Carbon Dioxide with Epoxide. *Organometallics* **2002**, 21 (6), 1056–1071.
- (102) Aluthge, D. C.; Patrick, B. O.; Mehrkhodavandi, P. A Highly Active and Site Selective Indium Catalyst for Lactide Polymerization. *Chem. Commun.* **2013**, 49 (39), 4295–4297.
- (103) Fang, J.; Yu, I.; Mehrkhodavandi, P.; Maron, L. Theoretical Investigation of Lactide Ring-Opening Polymerization Induced by a Dinuclear Indium Catalyst. *Organometallics* **2013**, 32 (23), 6950–6956.
- (104) Beachley, O. T.; Rusinko, R. N. Preparation and Properties of

- ((Trimethylsilyl)methyl)Indium(III) Compounds. *Inorg. Chem.* **1979**, *18* (7), 1966–1968.
- (105) Murphy, A.; Pace, A.; Stack, T. D. P. Ligand and PH Influence on Manganese-Mediated Peracetic Acid Epoxidation of Terminal Olefins. *Org. Lett.* **2004**, *6* (18), 3119–3122.
- (106) Haque, F. M.; Grayson, S. M. The Synthesis, Properties and Potential Applications of Cyclic Polymers. *Nat. Chem.* **2020**, *12* (5), 433–444.
- (107) Hosoi, Y.; Takasu, A.; Matsuoka, S. I.; Hayashi, M. N-Heterocyclic Carbene Initiated Anionic Polymerization of (E,E)-Methyl Sorbate and Subsequent Ring-Closing to Cyclic Poly(Alkyl Sorbate). *J. Am. Chem. Soc.* **2017**, *139* (42), 15005–15012.
- (108) Kapnistos, M.; Lang, M.; Vlassopoulos, D.; Pyckhout-Hintzen, W.; Richter, D.; Cho, D.; Chang, T.; Rubinstein, M. Unexpected Power-Law Stress Relaxation of Entangled Ring Polymers. *Nat. Mater.* **2008**, *7* (12), 997–1002.
- (109) Ren, J. M.; Satoh, K.; Goh, T. K.; Blencowe, A.; Nagai, K.; Ishitake, K.; Christofferson, A. J.; Yiapanis, G.; Yarovsky, I.; Kamigaito, M.; Qiao, G. G. Stereospecific Cyclic Poly(Methyl Methacrylate) and Its Topology-Guided Hierarchically Controlled Supramolecular Assemblies. *Angew. Chem. Int. Ed.* **2014**, *53* (2), 459–464.
- (110) Zaldua, N.; Liénard, R.; Josse, T.; Zubitur, M.; Mugica, A.; Iturrospe, A.; Arbe, A.; De Winter, J.; Coulembier, O.; Müller, A. J. Influence of Chain Topology (Cyclic versus Linear) on the Nucleation and Isothermal Crystallization of Poly(l -Lactide) and Poly(d -Lactide). *Macromolecules* **2018**, *51* (5), 1718–1732.
- (111) Shin, E. J.; Jones, A. E.; Waymouth, R. M. Stereocomplexation in Cyclic and Linear Polylactide Blends. *Macromolecules* **2012**, *45* (1), 595–598.
- (112) Meyer, A.; Weidner, S. M.; Kricheldorf, H. R. Stereocomplexation of Cyclic Polylactides with Each Other and with Linear Poly(l-Lactide). *S. Polym. Chem.* **2019**, *10* (45), 6191–

6199.

- (113) Kerr, R. W. F.; Ewing, P. M. D. A.; Raman, S. K.; Smith, A. D.; Williams, C. K.; Arnold, P. L. Ultrarapid Cerium(III)-NHC Catalysts for High Molar Mass Cyclic Polylactide. *ACS Catal.* **2021**, 1563–1569.
- (114) Bielawski, C. W.; Benitez, D.; Grubbs, R. H. An “Endless” Route to Cyclic Polymers. *Science* (80-.). **2002**, 297 (5589), 2041–2044.
- (115) He, T.; Zheng, G. H.; Pan, C. Y. Synthesis of Cyclic Polymers and Block Copolymers by Monomer Insertion into Cyclic Initiator by a Radical Mechanism. *Macromolecules* **2003**, 36 (16), 5960–5966.
- (116) Jeong, Y.; Jin, Y.; Chang, T.; Uhlik, F.; Roovers, J. Intrinsic Viscosity of Cyclic Polystyrene. *Macromolecules* **2017**, 50 (19), 7770–7776.
- (117) Laurent, B. A.; Grayson, S. M. Synthetic Approaches for the Preparation of Cyclic Polymers. *Chem. Soc. Rev.* **2009**, 38 (8), 2202–2213.
- (118) Zhang, X.; Fevre, M.; Jones, G. O.; Waymouth, R. M. Catalysis as an Enabling Science for Sustainable Polymers. *Chem. Rev.* **2018**, 118 (2), 839–885.
- (119) Martin, O.; Avérous, L. Poly(Lactic Acid): Plasticization and Properties of Biodegradable Multiphase Systems. *Polymer (Guildf)*. **2001**, 42 (14), 6209–6219.
- (120) Ramot, Y.; Haim-Zada, M.; Domb, A. J.; Nyska, A. Biocompatibility and Safety of PLA and Its Copolymers. *Adv. Drug Deliv. Rev.* **2016**, 107, 153–162.
- (121) Shaver, M. P.; Cameron, D. J. A. Tacticity Control in the Synthesis of Poly(Lactic Acid) Polymer Stars with Dipentaerythritol Cores. *Biomacromolecules* **2010**, 11 (12), 3673–3679.
- (122) Corneillie, S.; Smet, M. PLA Architectures: The Role of Branching. *Polym. Chem.* **2015**,

6 (6), 850–867.

- (123) Kricheldorf, H. R.; Weidner, S. M. High Molar Mass Cyclic Poly(l-Lactide) Obtained by Means of Neat Tin(II) 2-Ethylhexanoate. *Polym. Chem.* **2020**, *11* (32), 5249–5260.
- (124) Kricheldorf, H. R.; Weidner, S. M.; Meyer, A. High: T_m Poly(L-Lactide)s via REP or ROPPOC of l-Lactide. *Polym. Chem.* **2020**, *11* (12), 2182–2193.
- (125) Kricheldorf, H. R.; Weidner, S. M.; Scheliga, F. Cyclic Polylactides via Simultaneous Ring-Opening Polymerization and Polycondensation Catalyzed by Dibutyltin Mercaptides. *J. Polym. Sci. Part A: Polym. Chem.* **2017**, *55* (22), 3767–3775.
- (126) Kricheldorf, H. R.; Weidner, S. M.; Scheliga, F. Cyclic Poly(Lactide)s via the ROPPOC Method Catalyzed by Alkyl- or Aryltin Chlorides. *J. Polym. Sci. Part A: Polym. Chem.* **2019**, *57* (9), 952–960.
- (127) Kricheldorf, H. R.; Weidner, S. M. High Molar Mass Cyclic Poly(L-Lactide) via Ring-Expansion Polymerization with Cyclic Dibutyltin Bisphenoxides. *Eur. Polym. J.* **2018**, *105*, 158–166.
- (128) Piromjitpong, P.; Ratanapanee, P.; Thumrongpatanaraks, W.; Kongsaree, P.; Phomphrai, K. Synthesis of Cyclic Polylactide Catalysed by Bis(Salicylaldiminato)Tin(II) Complexes. *Dalton Trans.* **2012**, *41* (41), 12704–12710.
- (129) Kricheldorf, H. R.; Weidner, S. M.; Scheliga, F. Synthesis of Cyclic Poly(L-Lactide) Catalyzed by Bismuth Salicylates—A Combination of Two Drugs. *J. Polym. Sci. Part A: Polym. Chem.* **2019**, *57* (19), 2056–2063.
- (130) Weil, J.; Mathers, R. T.; Getzler, Y. D. Y. L. Lactide Cyclopolymerization by an Alumatrane-Inspired Catalyst. *Macromolecules* **2012**, *45* (2), 1118–1121.
- (131) Brown, H. A.; Waymouth, R. M. Zwitterionic Ring-Opening Polymerization for the

- Synthesis of High Molecular Weight Cyclic Polymers. *Acc. Chem. Res.* **2013**, *46* (11), 2585–2596.
- (132) Culkin, D. A.; Jeong, W.; Csihony, S.; Gomez, E. D.; Balsara, N. P.; Hedrick, J. L.; Waymouth, R. M. Zwitterionic Polymerization of Lactide to Cyclic Poly(Lactide) by Using N-Heterocyclic Carbene Organocatalysts. *Angew. Chem.* **2007**, *119* (15), 2681–2684.
- (133) Jeong, W.; Shin, E. J.; Culkin, D. A.; Hedrick, J. L.; Waymouth, R. M. Zwitterionic Polymerization: A Kinetic Strategy for the Controlled Synthesis of Cyclic Polylactide. *J. Am. Chem. Soc.* **2009**, *131* (13), 4884–4891.
- (134) Si, G.; Zhang, S.; Pang, W.; Wang, F.; Tan, C. Stereoselective Zwitterionic Ring-Opening Polymerization of Rac-Lactide. *Polymer (Guildf)*. **2018**, *154*, 148–152.
- (135) Prasad, A. V.; Stubbs, L. P.; Ma, Z.; Yinghuai, Z. Zwitterionic Ring Opening Polymerization of Lactide by Metal Free Catalysts: Production of Cyclic Polymers. *J. Appl. Polym. Sci.* **2012**, *123* (3), 1568–1575.
- (136) Kricheldorf, H. R.; Lomadze, N.; Schwarz, G. Cyclic Polylactides by Imidazole-Catalyzed Polymerization of L-Lactide. *Macromolecules* **2008**, *41* (21), 7812–7816.
- (137) Luo, Z.; Chaemchuen, S.; Zhou, K.; Verpoort, F. Ring-Opening Polymerization of L-Lactide to Cyclic Poly(Lactide) by Zeolitic Imidazole Framework ZIF-8 Catalyst. *ChemSusChem* **2017**, *10* (21), 4135–4139.
- (138) Södergård, A.; Stolt, M. Industrial Production of High Molecular Weight Poly(Lactic Acid). In *Poly(Lactic Acid)*; John Wiley & Sons, Inc.: Hoboken, NJ, USA, 2010; pp 27–41.
- (139) Anwender, R.; Dolg, M.; Edelmann, F. T. The Difficult Search for Organocerium(IV)

- Compounds. *Chem. Soc. Rev.* **2017**, *46* (22), 6697–6709.
- (140) Goonesinghe, C.; Roshandel, H.; Diaz, C.; Jung, H.-J.; Nyamayaro, K.; Ezhova, M.; Mehrkhodavandi, P. Cationic Indium Catalysts for Ring Opening Polymerization: Tuning Reactivity with Hemilabile Ligands. *Chem. Sci.* **2020**, *11* (25), 6485–6491.
- (141) Roovers, J. Organic Cyclic Polymers. In *Cyclic Polymers*; Kluwer Academic Publishers, 2006; pp 347–384.
- (142) Zhang, X.; Waymouth, R. M. Zwitterionic Ring Opening Polymerization with Isothioureas. *ACS Macro Lett.* **2014**, *3* (10), 1024–1028.
- (143) Katiyar, V.; Nanavati, H. Ring-Opening Polymerization of L-Lactide Using N-Heterocyclic Molecules: Mechanistic, Kinetics and DFT Studies. *Polym. Chem.* **2010**, *1* (9), 1491–1500.
- (144) Patel, D.; Liddle, S. T.; Mungur, S. A.; Rodden, M.; Blake, A. J.; Arnold, P. L. Bifunctional Yttrium(III) and Titanium(IV) NHC Catalysts for Lactide Polymerisation. *Chem. Commun.* **2006**, No. 10, 1124–1126.
- (145) Burés, J. Variable Time Normalization Analysis: General Graphical Elucidation of Reaction Orders from Concentration Profiles. *Angew. Chem. Int. Ed.* **2016**, *55* (52), 16084–16087.
- (146) Burés, J. A Simple Graphical Method to Determine the Order in Catalyst. *Angew. Chem. Int. Ed.* **2016**, *55* (6), 2028–2031.
- (147) Jia, Z.; Jiang, J.; Zhang, X.; Cui, Y.; Chen, Z.; Pan, X.; Wu, J. Isotactic-Alternating, Heterotactic-Alternating, and ABAA-Type Sequence-Controlled Copolyester Syntheses via Highly Stereoselective and Regioselective Ring-Opening Polymerization of Cyclic Diesters. *J. Am. Chem. Soc.* **2021**, *143* (11), 4421–4432.

- (148) Li, J.; Stayshich, R. M.; Meyer, T. Y. Exploiting Sequence to Control the Hydrolysis Behavior of Biodegradable PLGA Copolymers. *J. Am. Chem. Soc.* **2011**, *133* (18), 6910–6913.
- (149) Mochizuki, S.; Ogiwara, N.; Takayanagi, M.; Nagaoka, M.; Kitagawa, S.; Uemura, T. Sequence-Regulated Copolymerization Based on Periodic Covalent Positioning of Monomers along One-Dimensional Nanochannels. *Nat. Commun.* **2018**, *9* (1), 1–6.
- (150) Xia, X.; Suzuki, R.; Gao, T.; Isono, T.; Satoh, T. One-Step Synthesis of Sequence-Controlled Multiblock Polymers with up to 11 Segments from Monomer Mixture. *Nat. Commun.* **2022**, *13* (1), 1–11.
- (151) Chung, K.; Endo, T.; Takata, T. Anionic Ring-Opening Copolymerization of Bicyclic Bis(γ -Lactone)s with Mono- and Bifunctional Epoxides via Double Ring-Opening Isomerization of the Bis(γ -Lactone)s and Volume Change during Copolymerization. *Macromolecules* **1995**, *28* (9), 3048–3054.
- (152) Uenishi, K.; Sudo, A.; Endo, T. Anionic Alternating Copolymerization of 3,4-Dihydrocoumarin and Glycidyl Ethers: A New Approach to Polyester Synthesis. *J. Polym. Sci. Part A: Polym. Chem.* **2008**, *46* (12), 4092–4102.
- (153) Uenishi, K.; Sudo, A.; Endo, T. Anionic Alternating Copolymerization Behavior of Bifunctional Six-Membered Lactone and Glycidyl Phenyl Ether. *J. Polym. Sci. Part A: Polym. Chem.* **2009**, *47* (14), 3662–3668.
- (154) Uenishi, K.; Sudo, A.; Endo, T. Anionic Alternating Copolymerization of a Bifunctional Six-Membered Lactone and Glycidyl Phenyl Ether: Selective Synthesis of a Linear Polyester Having Lactone Moiety. *J. Polym. Sci. Part A: Polym. Chem.* **2009**, *47* (6),

1661–1672.

- (155) Atsushi, K.; Uenishi, S.; Endo, T. Synthesis of Polyester Having Sequentially Ordered Two Orthogonal Reactive Groups by Anionic Alternating Copolymerization of Epoxide and Bislactone. *J. Polym. Sci. Part A: Polym. Chem.* **2009**, *47* (24), 6750–6757.
- (156) Van Zee, N. J.; Coates, G. W. Alternating Copolymerization of Dihydrocoumarin and Epoxides Catalyzed by Chromium Salen Complexes: A New Route to Functional Polyesters. *Chem. Commun.* **2014**, *50* (48), 6322–6325.
- (157) Nishimori, K.; Ouchi, M. AB-Alternating Copolymers via Chain-Growth Polymerization: Synthesis, Characterization, Self-Assembly, and Functions. *Chem. Commun.* **2020**, *56* (24), 3473–3483.
- (158) Qu, C.; Li, Z.; He, J. Synthesis of Copolymers with an Exact Alternating Sequence Using the Cationic Polymerization of Pre-Sequenced Monomers. *Polym. Chem.* **2018**, *9* (25), 3455–3460.
- (159) Zhao, W.; Li, F.; Li, C.; He, J.; Zhang, Y.; Chen, C. Lewis Pair Catalyzed Regioselective Polymerization of (E,E)-Alkyl Sorbates for the Synthesis of (AB)_n Sequenced Polymers. *Angew. Chem. Int. Ed.* **2021**, *60* (45), 24306–24311.
- (160) Zhou, P.; Takaishi, Y.; Duan, H.; Chen, B.; Honda, G.; Itoh, M.; Takeda, Y.; Kodzhimatov, O. K.; Lee, K. H. Coumarins and Bicoumarin from *Ferula Sumbul*: Anti-HIV Activity and Inhibition of Cytokine Release. *Phytochem.* **2000**, *53* (6), 689–697.
- (161) Ohta, T.; Maruyama, T.; Nagahashi, M.; Miyamoto, Y.; Hosoi, S.; Kiuchi, F.; Yamazoe, Y.; Tsukamoto, S. Paradisin C: A New CYP3A4 Inhibitor from Grapefruit Juice. *Tetrahedron* **2002**, *58* (33), 6631–6635.
- (162) Taniguchi, M.; Xiao, Y. Q.; Liu, X. H.; Yabu, A.; Hada, Y.; Guo, L. Q.; Yamazoe, Y.;

- Baba, K. Rivulobirin E and Rivulotririn C from *Pleurospermum Rivulorum*. *Chem. Pharm. Bull.* **1999**, 47 (5), 713–715.
- (163) Bodenbenner, K. Über Spirocyclische Orthoester. *Justus Liebigs Ann. Chem.* **1959**, 623 (1), 183–190.
- (164) Yokozawa, T.; Sato, M.; Endo, T. Preparation and Polymerization of Spiroorthoester Bearing the Perfluoroalkyl Group. *J. Polym. Sci. Part A: Polym. Chem.* **1990**, 28 (7), 1841–1846.
- (165) Nishida, H.; Sanda, F.; Endo, T.; Nakahara, T.; Ogata, T.; Kusumoto, K. Polyaddition of Bifunctional Spiro Orthoesters with Bifunctional Acid Chlorides Accompanying Double Ring-Opening Isomerization. *J. Polym. Sci. Part A: Polym. Chem.* **2000**, 38 (1), 68–73.
- (166) Chikaoka, S.; Takata, T.; Endo, T. Synthesis and Reactions of Enco-Methylene-Containing Poly(Cyclic Orthoester). *Macromolecules* **1994**, 27, 2380–2382.
- (167) Chikaoka, S.; Takata, T.; Endo, T. Cationic Ring-Opening Polymerization of Spiroorthoester: Polymer Structure, Polymerization Mechanism, and Volume Change on Polymerization. *Macromolecules* **1992**, 25 (2), 625–628.
- (168) Lombard, F. J.; Lepage, R. J.; Schwartz, B. D.; Johnston, R. C.; Healy, P. C.; Krenske, E. H.; Coster, M. J. Synthesis of Spirocyclic Orthoesters by ‘Anomalous’ Rhodium(II)-Catalysed Intramolecular C–H Insertions. *Org. Biomol. Chem.* **2018**, 16 (2), 256–261.
- (169) Tortoreto, C.; Achard, T.; Egger, L.; Guénée, L.; Lacour, J. Synthesis of Spiro Ketals, Orthoesters, and Orthocarbonates by CpRu-Catalyzed Decomposition of α -Diazo- β -Ketoesters. *Org. Lett.* **2016**, 18 (2), 240–243.
- (170) Chabanne, P.; Tighzert, L.; Pascault, J. -P. Monoepoxy Polymerization Initiated by BF₃-Amine Complexes in Bulk. III. Influence of γ -Butyrolactone on Polymer Formation. *J.*

- Appl. Polym. Sci.* **1994**, 53 (6), 787–806.
- (171) Goonesinghe, C.; Jung, H.-J.; Roshandel, H.; Diaz, C.; Baalbaki, H. A.; Nyamayaro, K.; Ezhova, M.; Hosseini, K.; Mehrkhodavandi, P. An Air Stable Cationic Indium Catalyst for Formation of High-Molecular-Weight Cyclic Poly(Lactic Acid). *ACS Catal.* **2022**, 12, 7677–7686.
- (172) García-García, A.; Serna, S.; Yang, Z.; Delso, I.; Taleb, V.; Hicks, T.; Artschwager, R.; Vakhrushev, S. Y.; Clausen, H.; Angulo, J.; Corzana, F.; Reichardt, N. C.; Hurtado-Guerrero, R. FUT8-Directed Core Fucosylation of N-Glycans Is Regulated by the Glycan Structure and Protein Environment. *ACS Catal.* **2021**, 11 (15), 9052–9065.
- (173) Calzadiaz-Ramirez, L.; Calvó-Tusell, C.; Stoffel, G. M. M.; Lindner, S. N.; Osuna, S.; Erb, T. J.; Garcia-Borràs, M.; Bar-Even, A.; Acevedo-Rocha, C. G. In Vivo Selection for Formate Dehydrogenases with High Efficiency and Specificity toward NADP⁺. *ACS Catal.* **2020**, 10 (14), 7512–7525.
- (174) Mahdavi-Shakib, A.; Sempel, J.; Babb, L.; Oza, A.; Hoffman, M.; Whittaker, T. N.; Chandler, B. D.; Austin, R. N. Combining Benzyl Alcohol Oxidation Saturation Kinetics and Hammett Studies as Mechanistic Tools for Examining Supported Metal Catalysts. *ACS Catal.* **2020**, 10 (17), 10207–10215.
- (175) Liu, S. Where Does the Electron Go? The Nature of Ortho / Para and Meta Group Directing in Electrophilic Aromatic Substitution. *J. Chem. Phys.* **2014**, 141 (19).
- (176) Liu, S. Quantifying Reactivity for Electrophilic Aromatic Substitution Reactions with Hirshfeld Charge. *J. Phys. Chem. A* **2015**, 119 (12), 3107–3111.
- (177) Chernyshov, I. Y.; Ananyev, I. V.; Pidko, E. A. Revisiting van Der Waals Radii: From Comprehensive Structural Analysis to Knowledge-Based Classification of Interatomic

- Contacts. *ChemPhysChem* **2020**, *21* (5), 370–376.
- (178) Bondi, A. Van Der Waals Volumes and Radii. *J. Phys. Chem.* **1964**, *68* (3), 441–451.
- (179) Roskoski, R. Michaelis-Menten Kinetics. In *Reference Module in Biomedical Sciences*; Elsevier, 2015.
- (180) Wijeratne, G. B.; Corzine, B.; Day, V. W.; Jackson, T. A. Saturation Kinetics in Phenolic O-H Bond Oxidation by a Mononuclear Mn(III)-OH Complex Derived from Dioxygen. *Inorg. Chem.* **2014**, *53* (14), 7622–7634.
- (181) Northrop, D. B. On the Meaning of K_m and V/K in Enzyme Kinetics. *J. Chem. Educ.* **1998**, *75* (9), 1153–1157.
- (182) Bar-Even, A.; Noor, E.; Savir, Y.; Liebermeister, W.; Davidi, D.; Tawfik, D. S.; Milo, R. The Moderately Efficient Enzyme: Evolutionary and Physicochemical Trends Shaping Enzyme Parameters. *Biochemistry* **2011**, *50* (21), 4402–4410.
- (183) Miyanaga, K.; Unno, H. Reaction Kinetics and Stoichiometry. In *Comprehensive Biotechnology, Second Edition*; Academic Press, 2011; Vol. 2, pp 33–46.
- (184) Falivene, L.; Cao, Z.; Petta, A.; Serra, L.; Poater, A.; Oliva, R.; Scarano, V.; Cavallo, L. Towards the Online Computer-Aided Design of Catalytic Pockets. *Nat. Chem.* **2019**, *11* (10), 872–879.
- (185) Thorley, K. J.; Benford, M.; Song, Y.; Parkin, S. R.; Risko, C.; Anthony, J. E. What Is Special about Silicon in Functionalised Organic Semiconductors? *Mater. Adv.* **2021**, *2* (16), 5415–5421.
- (186) Bassindale, A. R.; Glynn, S. J.; Taylor, P. G. Activating and Directive Effects of Silicon. In *Organic Silicon Compounds*; John Wiley & Sons, Ltd, 2009.
- (187) Beckett, M. A.; Strickland, G. C.; Holland, J. R.; Varma, K. S. A Convenient NMR

- Method for the Measurement of Lewis Acidity at Boron Centres: Correlation of Reaction Rates of Lewis Acid Initiated Epoxide Polymerizations with Lewis Acidity. *Polymer (Guildf)*. **1996**, 37 (20), 4629–4631.
- (188) Fulmer, G. R.; Miller, A. J. M.; Sherden, N. H.; Gottlieb, H. E.; Nudelman, A.; Stoltz, B. M.; Bercaw, J. E.; Goldberg, K. I. NMR Chemical Shifts of Trace Impurities: Common Laboratory Solvents, Organics, and Gases in Deuterated Solvents Relevant to the Organometallic Chemist. *Organometallics* **2010**, 29 (9), 2176–2179.
- (189) Sheldrick, G. M.; IUCr. SHELXT – Integrated Space-Group and Crystal-Structure Determination. *Acta Cryst.* **2015**, 71 (1), 3–8.
- (190) Sheldrick, G. M. Crystal Structure Refinement with SHELXL. *Acta Cryst.* **2015**, 71 (1), 3–8.
- (191) Dolomanov, O. V.; Bourhis, L. J.; Gildea, R. J.; Howard, J. A. K.; Puschmann, H. OLEX2: A Complete Structure Solution, Refinement and Analysis Program. *J. Appl. Cryst.* **2009**, 42 (2), 339–341.
- (192) Frisch, M. J.; Trucks, G. W.; Schlegel, H. B.; Scuseria, G. E.; Robb, M. A.; Cheeseman, J. R.; Scalmani, G.; Barone, V.; Petersson, G. A.; Nakatsuji, H.; Li, X.; Caricato, M.; Marenich, A. V.; Bloino, J.; Janesko, B. G.; Gomperts, R.; Mennucci, B.; Hratch, D. J. Gaussian 16, Revision A.03. *Gaussian, Inc., Wallingford CT, 2016*.
- (193) Becke, A. D. Density-functional Thermochemistry. III. The Role of Exact Exchange. *J. Chem. Phys.* **1993**, 98 (7), 5648–5652.
- (194) Perdew, J. P. Density-Functional Approximation for the Correlation Energy of the Inhomogeneous Electron Gas. *Phys. Rev. B* **1986**, 33 (12), 8822.
- (195) Wadt, W. R.; Hay, P. J. Ab Initio Effective Core Potentials for Molecular Calculations.

- Potentials for Main Group Elements Na to Bi. *J. Chem. Phys.* **1985**, 82 (1), 284–298.
- (196) Weigend, F.; Ahlrichs, R. Balanced Basis Sets of Split Valence, Triple Zeta Valence and Quadruple Zeta Valence Quality for H to Rn: Design and Assessment of Accuracy. *Phys. Chem. Chem. Phys.* **2005**, 7 (18), 3297–3305.
- (197) Schäfer, A.; Horn, H.; Ahlrichs, R. Fully Optimized Contracted Gaussian Basis Sets for Atoms Li to Kr. *J. Chem. Phys.* **1992**, 97 (4), 2571–2577.
- (198) Marenich, A. V.; Cramer, C. J.; Truhlar, D. G. Universal Solvation Model Based on Solute Electron Density and on a Continuum Model of the Solvent Defined by the Bulk Dielectric Constant and Atomic Surface Tensions. *J. Phys. Chem. B* **2009**, 113 (18), 6378–6396.
- (199) Illy, N.; Mongkhoun, E. Thiolactone Chemistry, a Versatile Platform for Macromolecular Engineering. *Polym. Chem.* **2022**, 13 (32), 4592–4614.
- (200) Kricheldorf, H. R.; Schwarz, G. Poly(Thioester)S. *J. Macromol. Sci. A* **2007**, 44 (6), 625–649.
- (201) Seefried, C. G.; Koleske, J. V. Lactone Polymers.V. Viscoelastic Properties of Polycaprolactone and Polyethiocaprolactone. *J. Macromol. Sci. B* **1974**, 10 (4), 579–589.
- (202) Wübbeler, J. H.; Steinbüchel, A. New Pathways for Bacterial Polythioesters. *Curr. Opin. Biotechnol.* **2014**, 29 (1), 85–92.
- (203) Shimokawa, K.; Kato, M.; Matsumura, S. Enzymatic Synthesis and Chemical Recycling of Polythiocaprolactone. *Macromol. Chem. Phys.* **2011**, 212 (2), 150–158.
- (204) Sanda, F.; Jirakanjana, D.; Hitomi, M.; Endo, T. Cationic Ring-Opening Polymerization of ϵ -Thionocaprolactone: Selective Formation of Polythioester. *J. Polym. Sci. Part A: Polym. Chem.* **2000**, 38 (22), 4057–4061.

- (205) Sanda, F.; Jirakanjana, D.; Hitomi, M.; Endo, T. Anionic Ring-Opening Polymerization of ϵ -Thionocaprolactone. *Macromolecules* **1999**, *32* (24), 8010–8014.
- (206) Bannin, T. J.; Kieseewetter, M. K. Poly(Thioester) by Organocatalytic Ring-Opening Polymerization. *Macromolecules* **2015**, *48* (16), 5481–5486.
- (207) Datta, P. P.; Kieseewetter, M. K. Controlled Organocatalytic Ring-Opening Polymerization of ϵ -Thionocaprolactone. *Macromolecules* **2016**, *49* (3), 774–780.
- (208) Purohit, V. B.; Pięta, M.; Pietrasik, J.; Plummer, C. M. Recent Advances in the Ring-Opening Polymerization of Sulfur-Containing Monomers. *Polym. Chem.* **2022**, *13* (34), 4858–4878.
- (209) Wang, L.; Ren, W. Synthesis of Polythioesters. In *Sulfur-Containing Polymers: From Synthesis to Functional Materials*; John Wiley & Sons, 2021.
- (210) Ivanchenko, O.; Authesserre, U.; Coste, G.; Mazières, S.; Destarac, M.; Harrisson, S. ϵ -Thionocaprolactone: An Accessible Monomer for Preparation of Degradable Poly(Vinyl Esters) by Radical Ring-Opening Polymerization. *Polym. Chem.* **2021**, *12* (13), 1931–1938.
- (211) Zhang, C. J.; Hu, L. F.; Yang, J. L.; Cao, X. H.; Zhang, X. H. Alternating Copolymerization of γ -Selenobutyrolactone with Episulfides for High Refractive Index Selenium-Containing Polythioesters. *Eur. Polym. J.* **2020**, *133*.
- (212) Duchiron, S. W.; Pollet, E.; Givry, S.; Avérous, L. Enzymatic Synthesis of Poly(ϵ -Caprolactone-Co- ϵ -Thiocaprolactone). *Eur. Polym. J.* **2017**, *87*, 147–158.
- (213) Le Luyer, S.; Quienne, B.; Bouzaid, M.; Guégan, P.; Caillol, S.; Illy, N. Bio-Based Poly(Ester-Alt-Thioether)s Synthesized by Organo-Catalyzed Ring-Opening Copolymerizations of Eugenol-Based Epoxides and N -Acetyl Homocysteine Thiolactone.

- Green Chem.* **2021**, *23* (19), 7743–7750.
- (214) Yue, T. J.; Wang, L. Y.; Ren, W. M. The Synthesis of Degradable Sulfur-Containing Polymers: Precise Control of Structure and Stereochemistry. *Polym. Chem.* **2021**, *12* (46), 6650–6666.
- (215) Puchelle, V.; Latreyte, Y.; Girardot, M.; Garnotel, L.; Levesque, L.; Coutelier, O.; Destarac, M.; Guégan, P.; Illy, N. Functional Poly(Ester-Alt-Sulfide)s Synthesized by Organo-Catalyzed Anionic Ring-Opening Alternating Copolymerization of Oxiranes and γ -Thiobutyrolactones. *Macromolecules* **2020**, *53* (13), 5188–5198.
- (216) Dagonne, S.; Atwood, D. A. Synthesis, Characterization, and Applications of Group 13 Cationic Compounds. *Chem. Rev.* **2008**, *108* (10), 4037–4071.
- (217) Kühn, F. E.; Ismeier, J. R.; Schön, D.; Xue, W.-M.; Zhang, G.; Nuyken, O. Solvent Stabilized Transition Metal Cations as Initiators for Cyclopentadiene Polymerization. *Macromol. Rapid Commun.* **1999**, *20*, 555–559.
- (218) Neumüller, B.; Gahlmann, F. Diorganoindiumfluoride. Die Kristallstrukturen von [IPr₂In(THF)₂][BF₄] Und (MesBO)₃. *J. Organomet. Chem.* **1991**, *414* (3), 271–283.
- (219) Atwood, D. A.; Jones, R. A.; Cowley, A. H.; Bott, S. G.; Atwood, J. L. Structural Characterization of a Dialkylgallium Cation: X-Ray Crystal Structure of [Me₂Ga(TBuNH₂)₂][Br]. *J. Organomet. Chem.* **1992**, *425* (1–2), C1–C3.
- (220) Atwood, D.; Jegier, J. Halide Effects in the Formation of Four-Coordinate, Cationic Aluminum. *Inorg. Chem.* **1996**, *35* (15), 4277–4282.
- (221) Wrobel, O.; Schaper, F.; Brintzinger, H. H. Bulky Siloxyaluminum Alkyls as Models for Al₂Me₆-Treated Silica Gel Surfaces. Characterization of a Dimethylaniline-Stabilized Dimethylaluminum Cation. *Organometallics* **2004**, *23* (4), 900–905.

- (222) Klosin, J.; Roof, G. R.; Chen, E. Y. X.; Abboud, K. A. Ligand Exchange and Alkyl Abstraction Involving (Perfluoroaryl)Boranes and -Alanes with Aluminum and Gallium Alkyls. *Organometallics* **2000**, *19* (23), 4684–4686.
- (223) Peckermann, I.; Robert, D.; Englert, U.; Spaniol, T. P.; Okuda, J. Neutral and Cationic Trimethylsilylmethyl Complexes of Indium. *Organometallics* **2008**, *27* (18), 4817–4820.
- (224) Lichtenberg, C.; Robert, D.; Spaniol, T. P.; Okuda, J. Bis(Allyl)Aluminum Cation, Tris(Allyl)Aluminum, and Tetrakis(Allyl) Aluminate: Synthesis, Characterization, and Reactivity. *Organometallics* **2010**, *29* (21), 5714–5721.
- (225) Lichtenberg, C.; Spaniol, T. P.; Okuda, J. Bis(Allyl)Gallium Cation, Tris(Allyl)Gallium, and Tetrakis(Allyl)Gallate: Synthesis, Characterization, and Reactivity. *Inorg. Chem.* **2012**, *51* (4), 2254–2262.
- (226) Kim, K. C.; Reed, C. A.; Long, G. S.; Sen, A. Et₂Al⁺ Alumenium Ion-like Chemistry. Synthesis and Reactivity toward Alkenes and Alkene Oxides. *J. Am. Chem. Soc.* **2002**, *124* (26), 7662–7663.
- (227) Kessler, M.; Knapp, C.; Zogaj, A. Cationic Dialkyl Metal Compounds of Group 13 Elements (E = Al, Ga, In) Stabilized by the Weakly Coordinating Dianion [B₁₂Cl₁₂]²⁻. *Organometallics* **2011**, *30* (14), 3786–3792.
- (228) Erdmann, P.; Greb, L. What Distinguishes the Strength and the Effect of a Lewis Acid: Analysis of the Gutmann–Beckett Method. *Angew. Chem. Int. Ed.* **2022**, *61* (4).
- (229) Bentley, J. N.; Elgadi, S. A.; Gaffen, J. R.; Demay-Drouhard, P.; Baumgartner, T.; Caputo, C. B. Fluorescent Lewis Adducts: A Practical Guide to Relative Lewis Acidity. *Organometallics* **2020**, *39* (20), 3645–3655.
- (230) Gaffen, J. R.; Bentley, J. N.; Torres, L. C.; Chu, C.; Baumgartner, T.; Caputo, C. B. A

- Simple and Effective Method of Determining Lewis Acidity by Using Fluorescence. *Chem* **2019**, 5 (6), 1567–1583.
- (231) Jupp, A. R.; Johnstone, T. C.; Stephan, D. W. The Global Electrophilicity Index as a Metric for Lewis Acidity. *Dalton Trans.* **2018**, 47 (20), 7029–7035.
- (232) Böhrer, H.; Trapp, N.; Himmel, D.; Schleep, M.; Krossing, I. From Unsuccessful H₂-Activation with FLPs Containing B(OHfip)₃ to a Systematic Evaluation of the Lewis Acidity of 33 Lewis Acids Based on Fluoride, Chloride, Hydride and Methyl Ion Affinities. *Dalton Trans.* **2015**, 44 (16), 7489–7499.
- (233) Christe, K. O.; Dixon, D. A.; McLemore, D.; Wilson, W. W.; Sheehy, J. A.; Boatz, J. A. On a Quantitative Scale for Lewis Acidity and Recent Progress in Polynitrogen Chemistry. *J. Fluor. Chem.* **2000**, 101 (2), 151–153.
- (234) Greb, L. Lewis Superacids: Classifications, Candidates, and Applications. *Chem. Eur. J.* **2018**, 24 (68), 17881–17896.

Appendices

Appendix A - Data associated with Chapter 2.

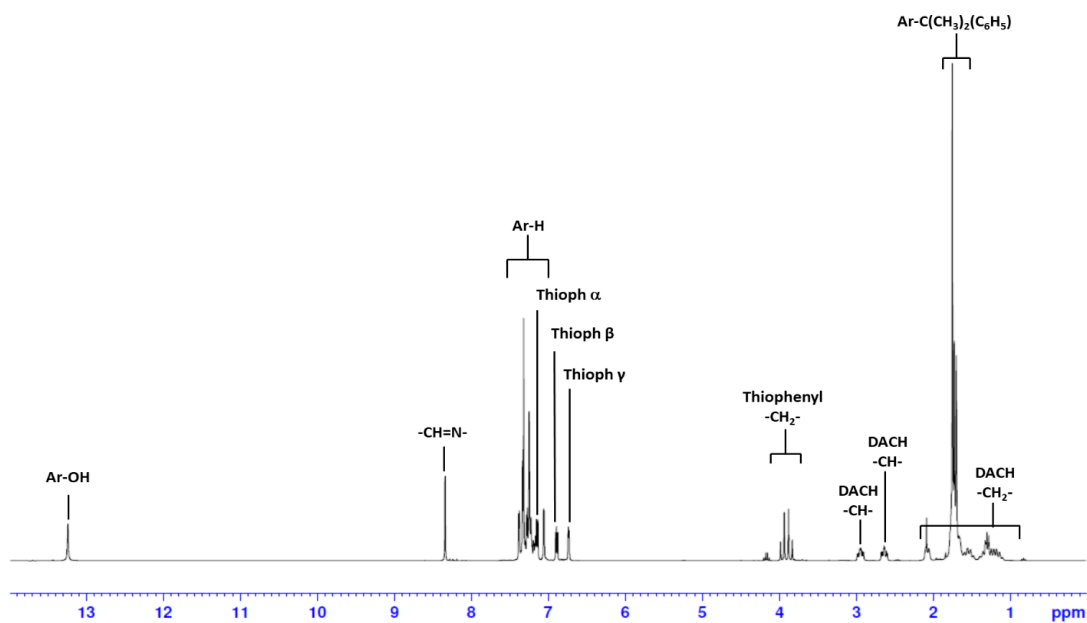


Figure A.1. ^1H NMR spectrum (400 MHz, CDCl_3 , 25 °C) of **L_a**

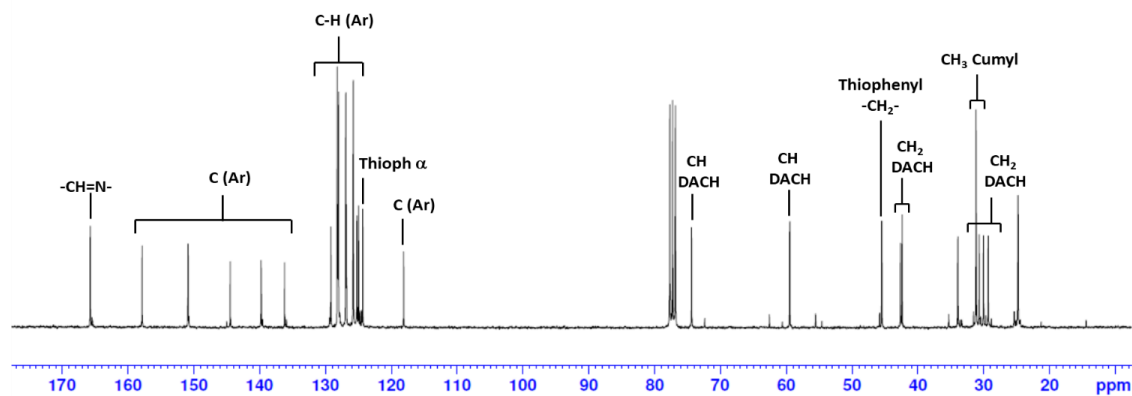


Figure A.2. $^{13}\text{C}\{^1\text{H}\}$ NMR spectrum (101 MHz, CDCl_3 , 25 °C) of **L_a**

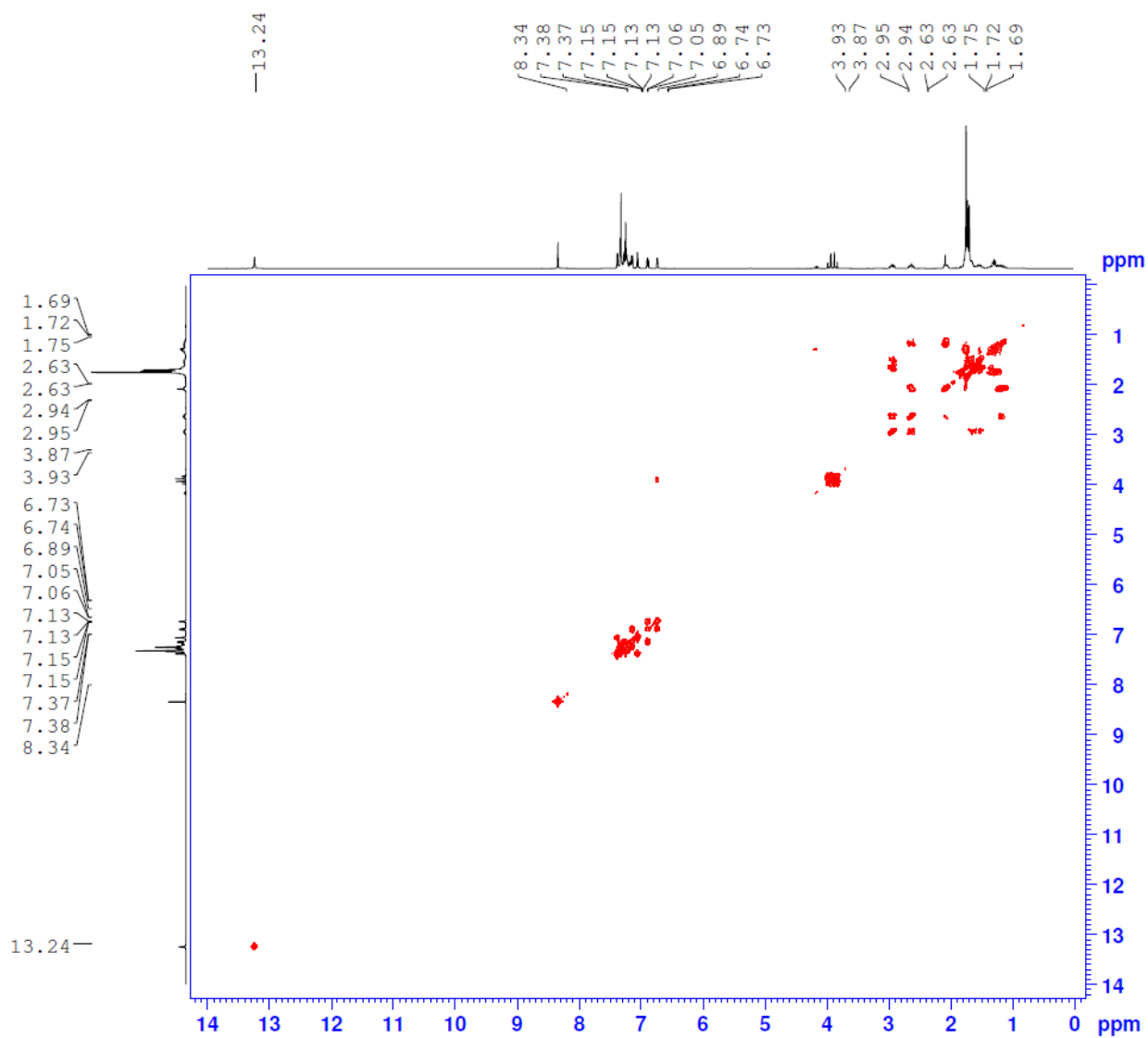


Figure A.3. 2D ^1H - ^1H COSY NMR spectrum (400 MHz, CDCl_3 , 25 $^\circ\text{C}$) of **L_a**

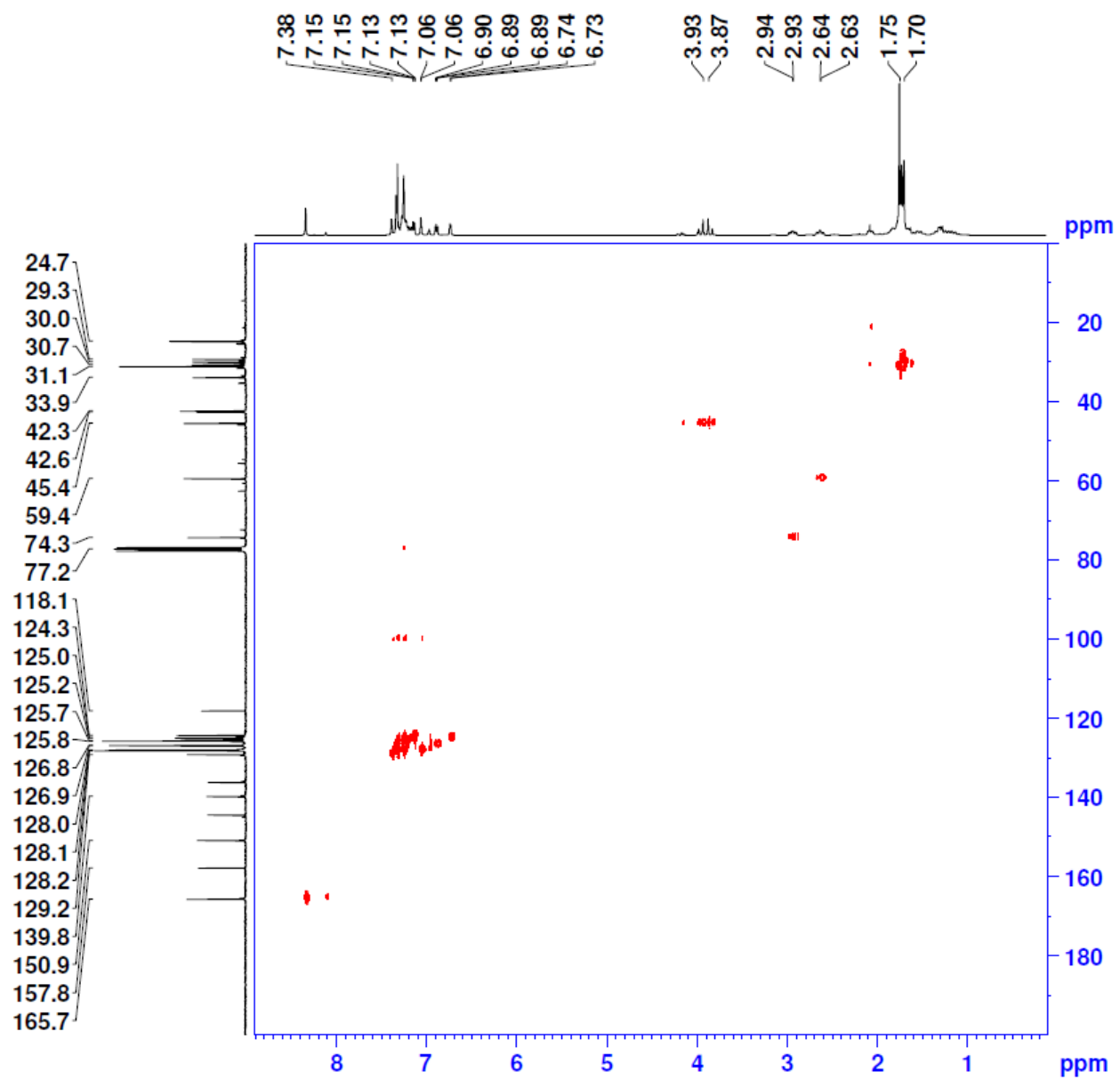


Figure A.4. ^1H - ^{13}C Heteronuclear Single Quantum Coherence (HSQC) NMR spectrum (CDCl_3 , 25 $^\circ\text{C}$) of **L_a**

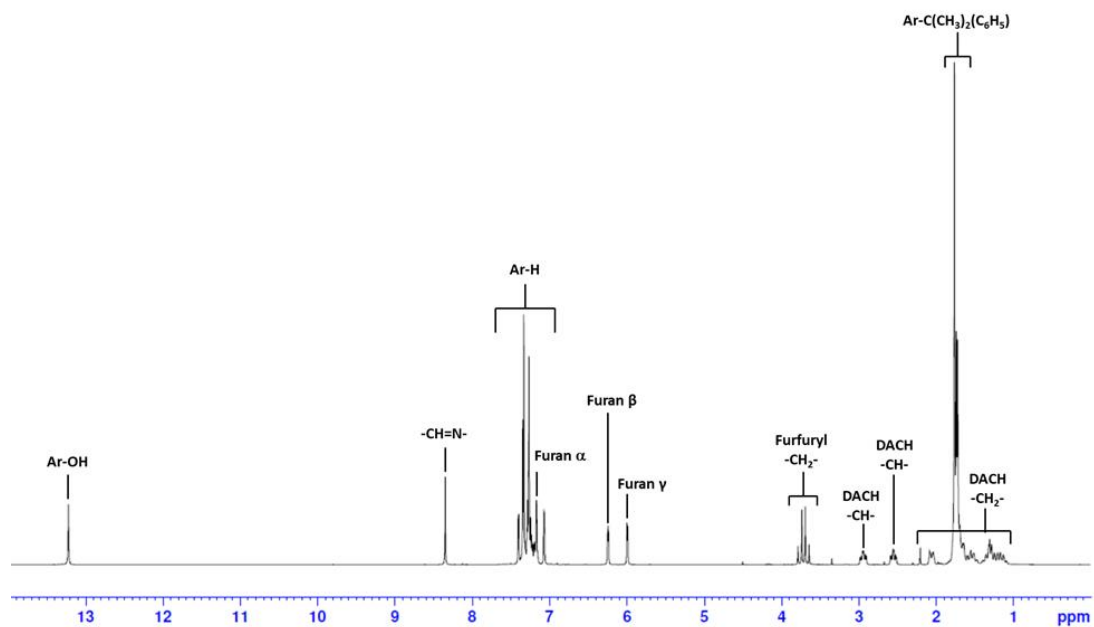


Figure A.5. ^1H NMR spectrum (400 MHz, CDCl_3 , 25 $^\circ\text{C}$) of L_b

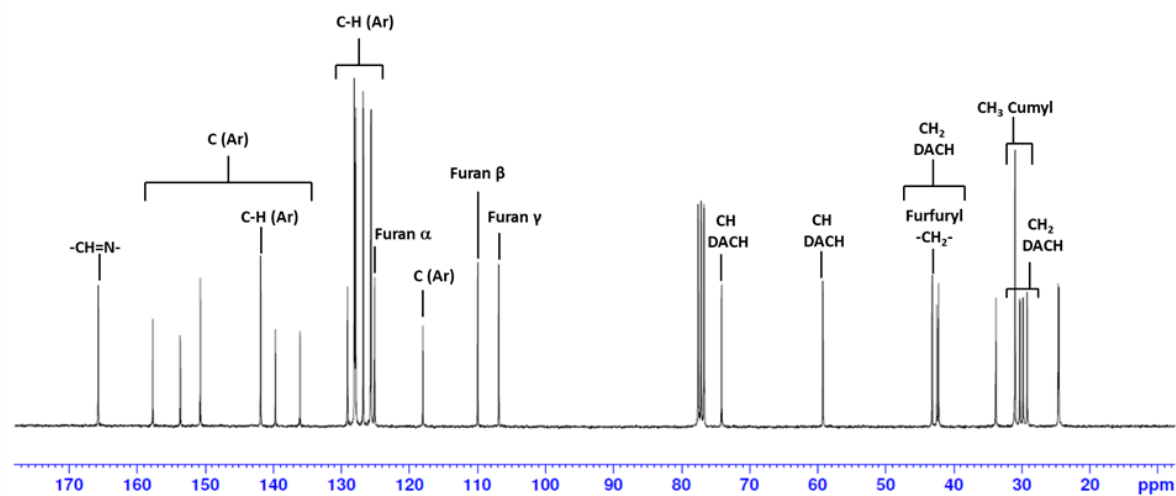


Figure A.6. $^{13}\text{C}\{^1\text{H}\}$ NMR spectrum (101 MHz, CDCl_3 , 25 $^\circ\text{C}$) of L_b

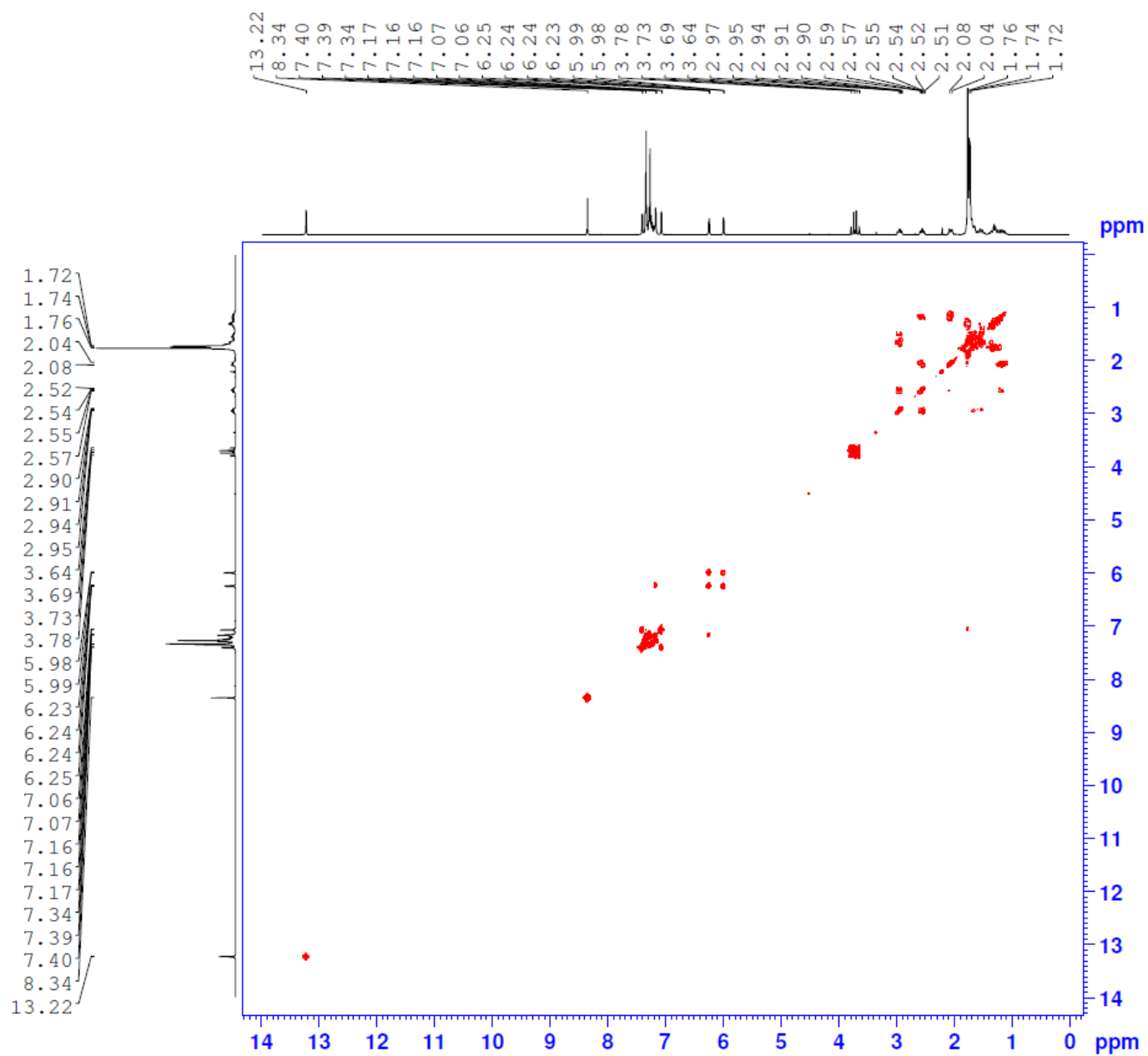


Figure A.7. ^1H - ^1H COSY NMR spectrum (400 MHz, CDCl_3 , 25 $^\circ\text{C}$) of **L_b**

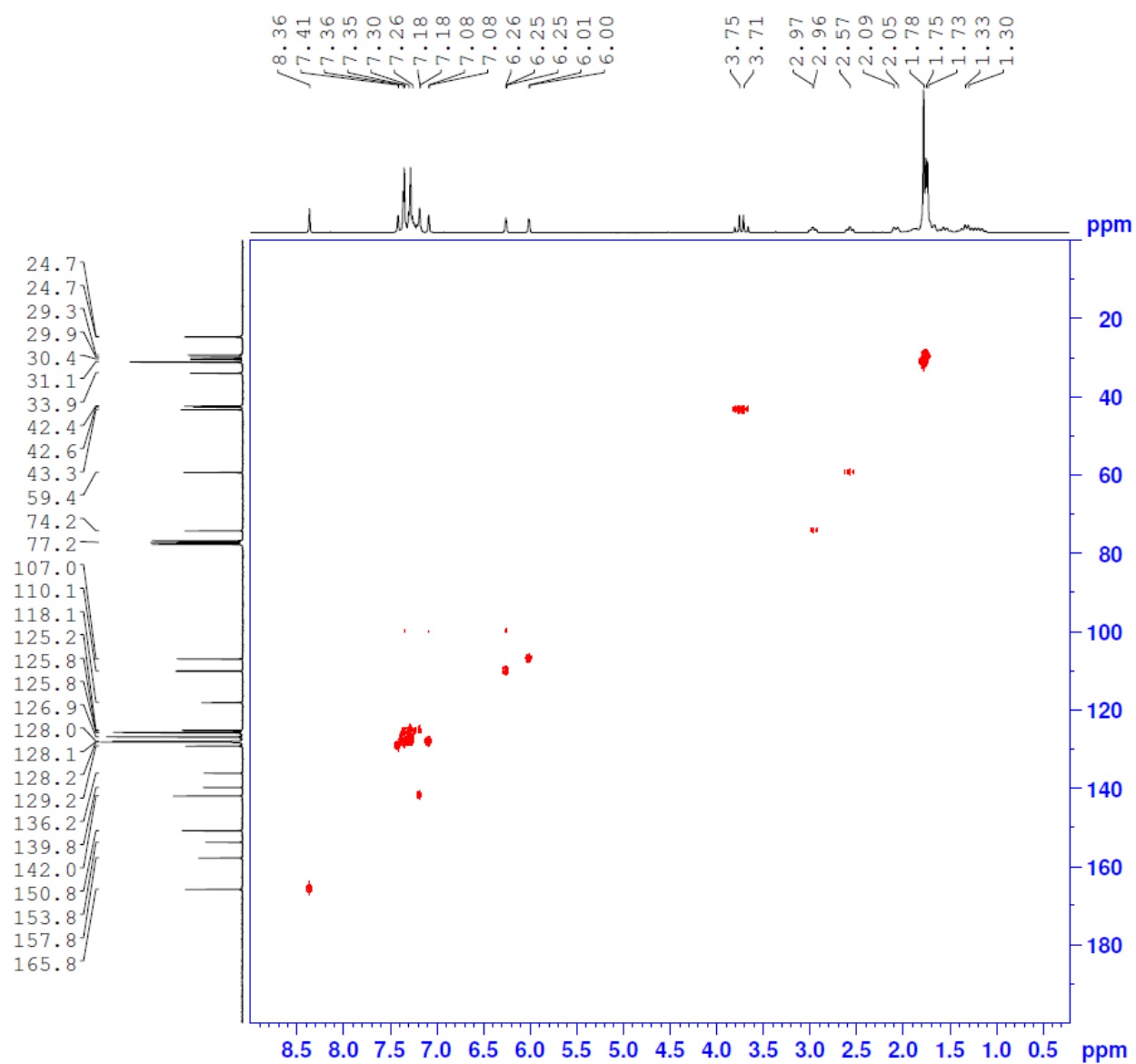


Figure A.8. ^1H - ^{13}C Heteronuclear Single Quantum Coherence (HSQC) NMR spectrum (CDCl_3 , 25 $^\circ\text{C}$) of **L_b**

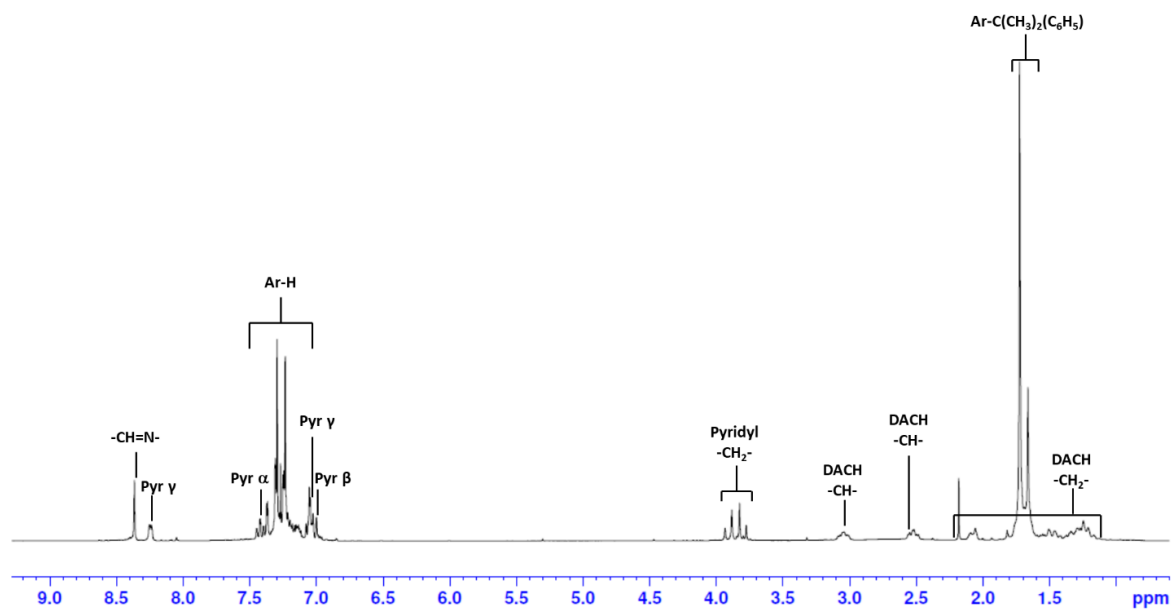


Figure A.9. ¹H NMR spectrum (400 MHz, CDCl₃, 25 °C) of **L_c**

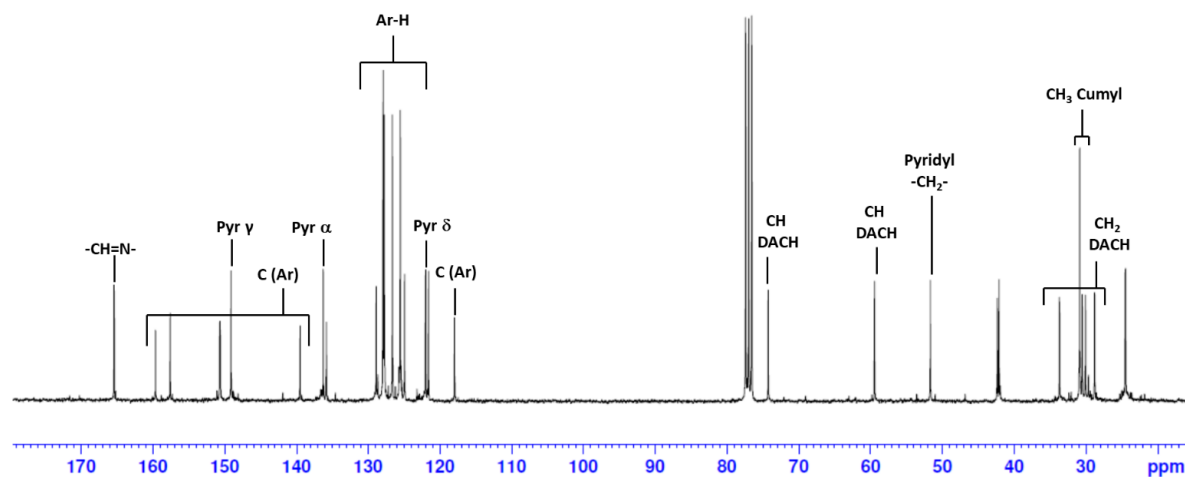


Figure A.10. ¹³C{¹H} NMR spectrum (101 MHz, CDCl₃, 25 °C) of **L_c**

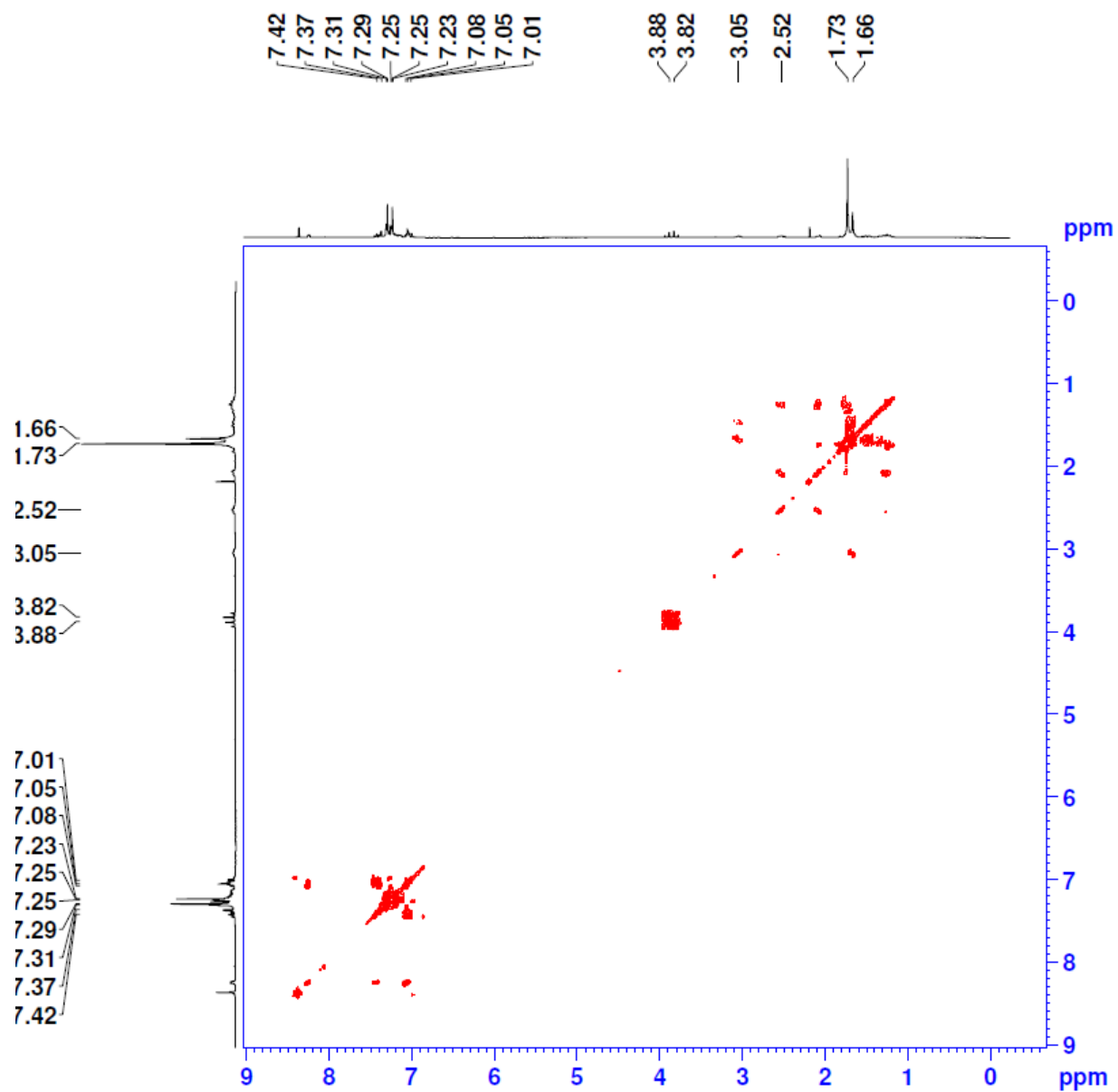


Figure A.11. ^1H - ^1H COSY NMR spectrum (400 MHz, CDCl_3 , 25 $^\circ\text{C}$) of L_c

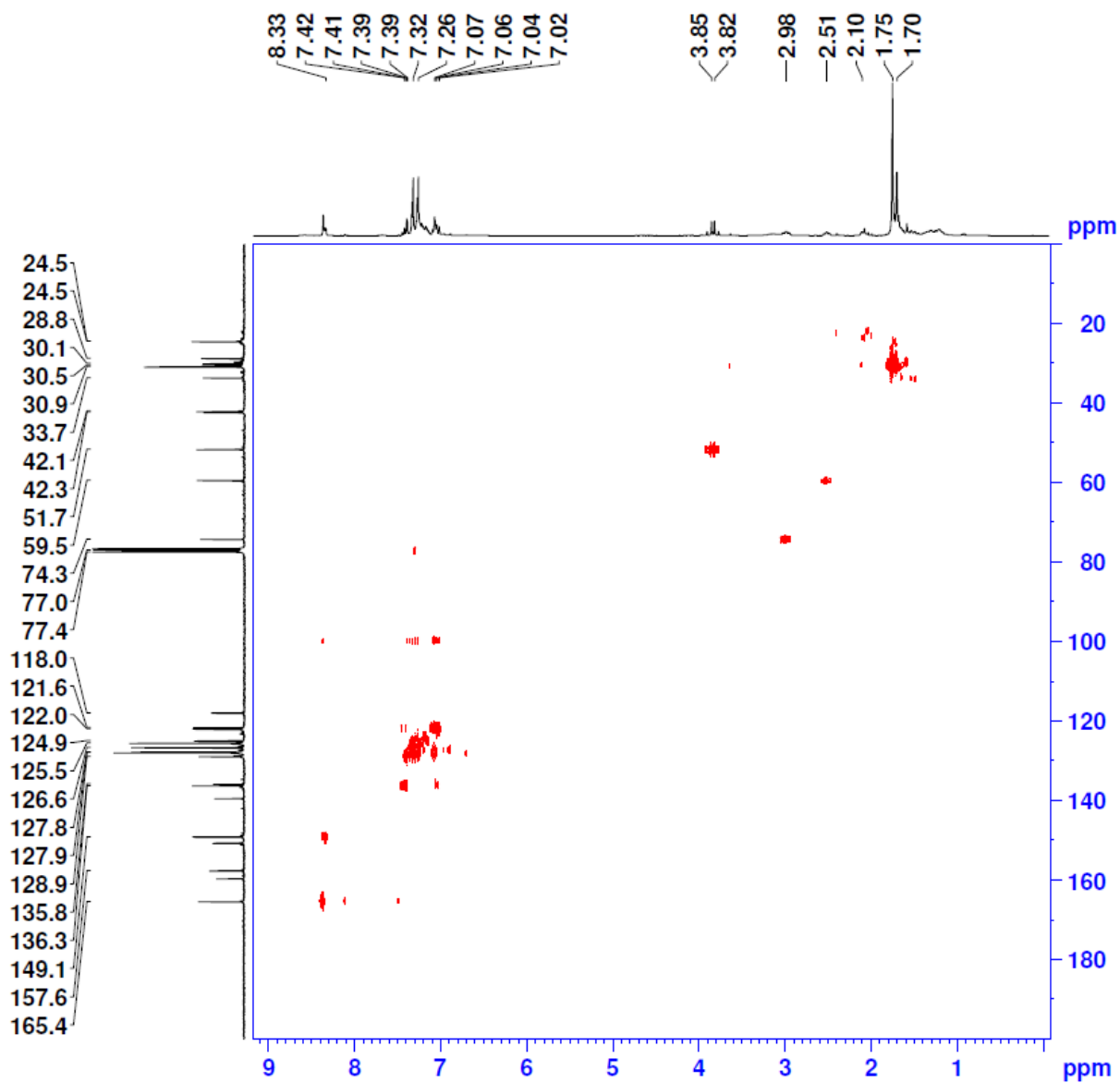


Figure A.12. ^1H - ^{13}C Heteronuclear Single Quantum Coherence (HSQC) NMR spectrum (CDCl_3 , 25°C) of **Lc**

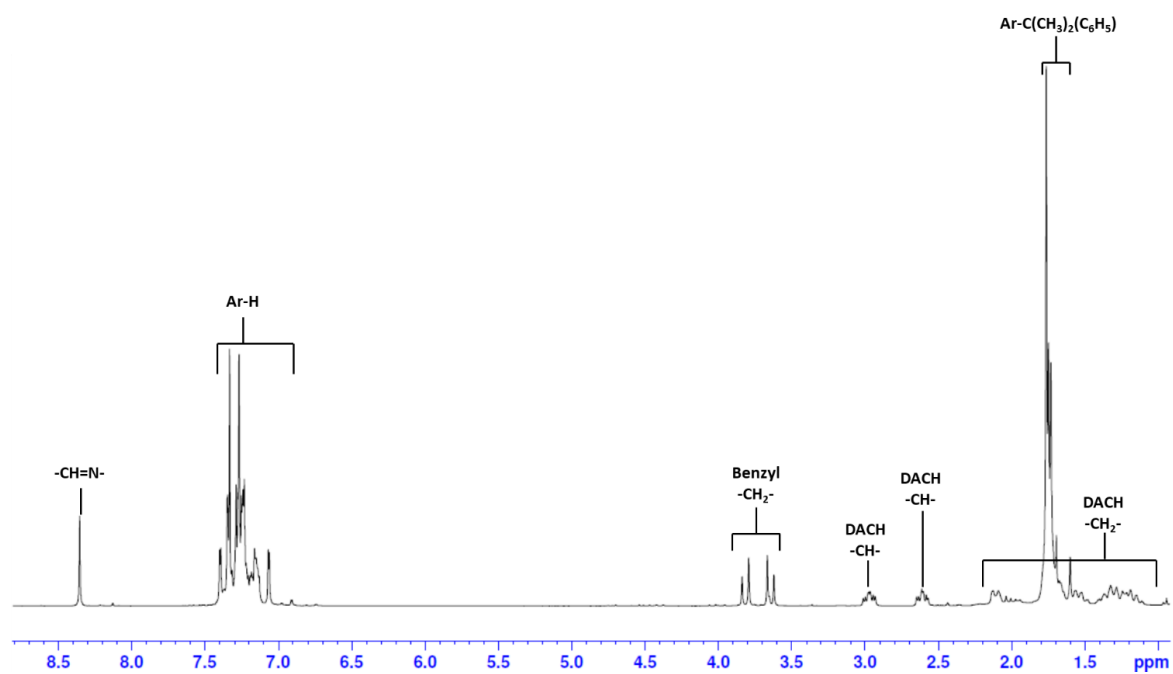


Figure A.13. ¹H NMR spectrum (400 MHz, CDCl₃, 25 °C) of **L_d**

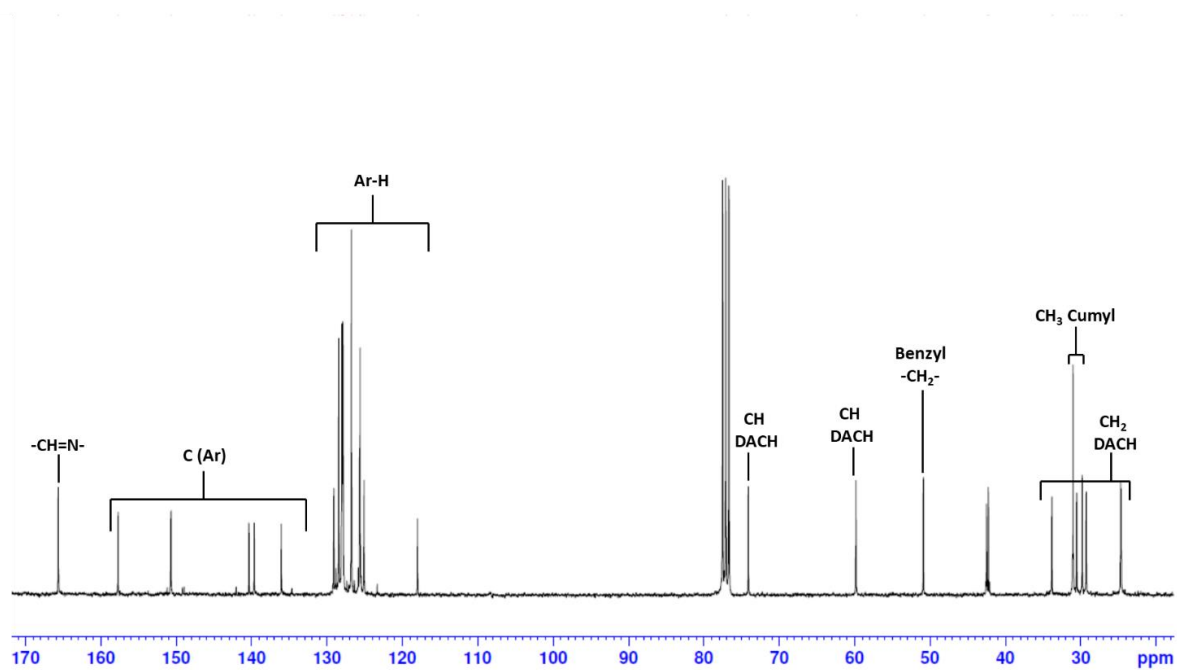


Figure A.14. ¹³C{¹H} NMR spectrum (101 MHz, CDCl₃, 25 °C) of **L_d**

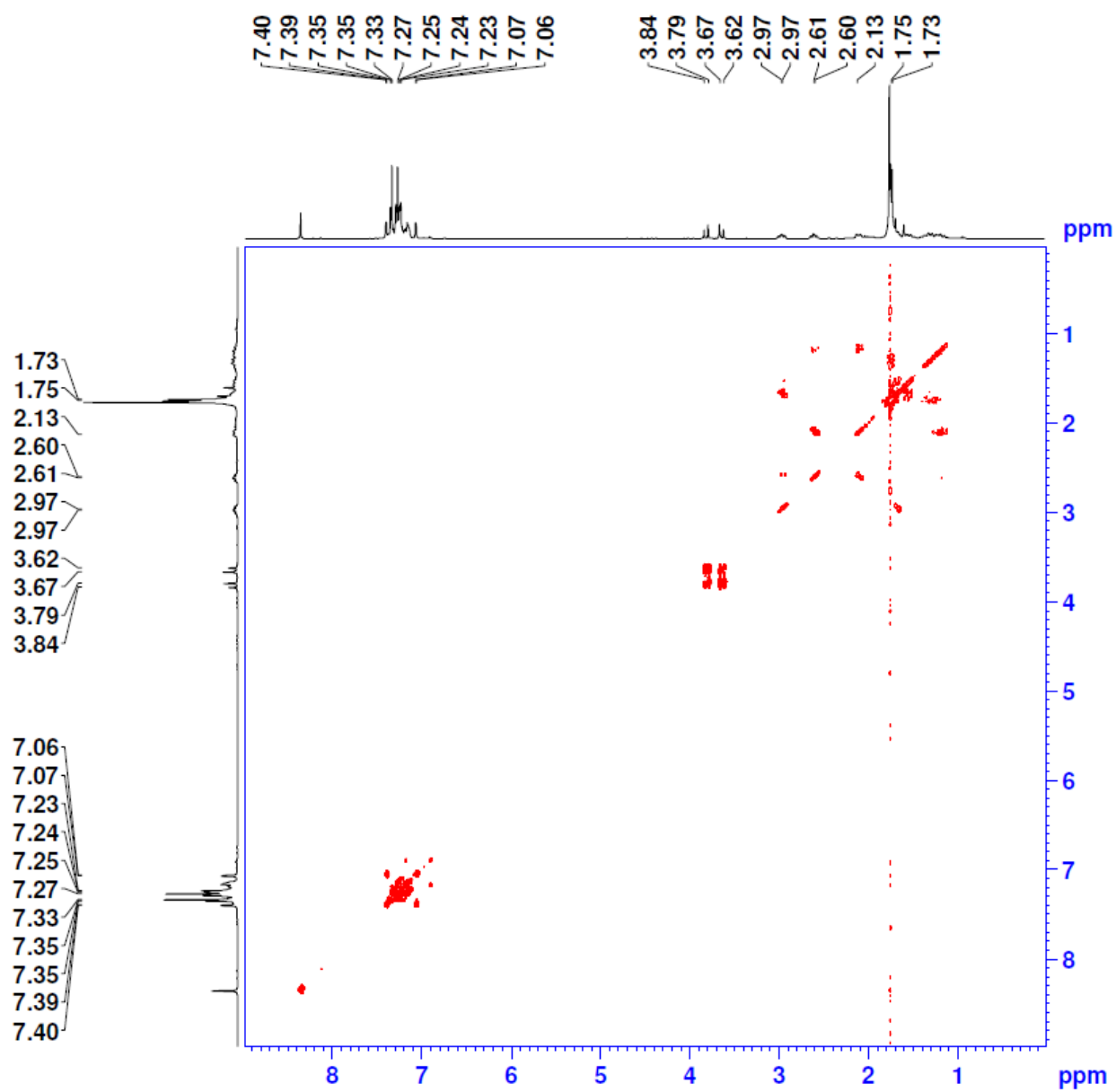


Figure A.15. 2D ^1H - ^1H COSY NMR spectrum (400 MHz, CDCl_3 , 25 $^\circ\text{C}$) of **La**

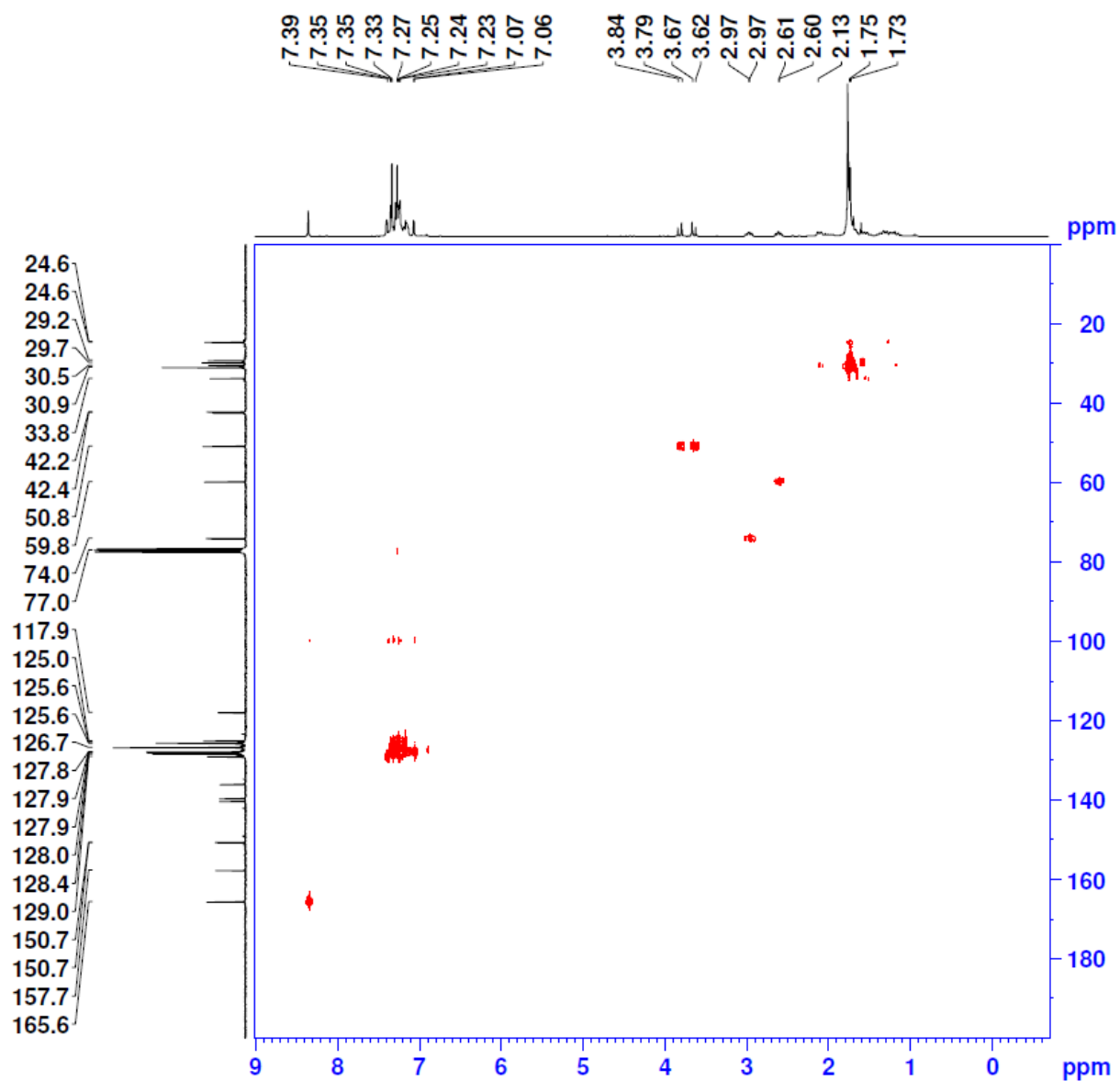


Figure A.16. ^1H - ^{13}C Heteronuclear Single Quantum Coherence (HSQC) NMR spectrum (CDCl_3 , 25 $^\circ\text{C}$) of **Ld**

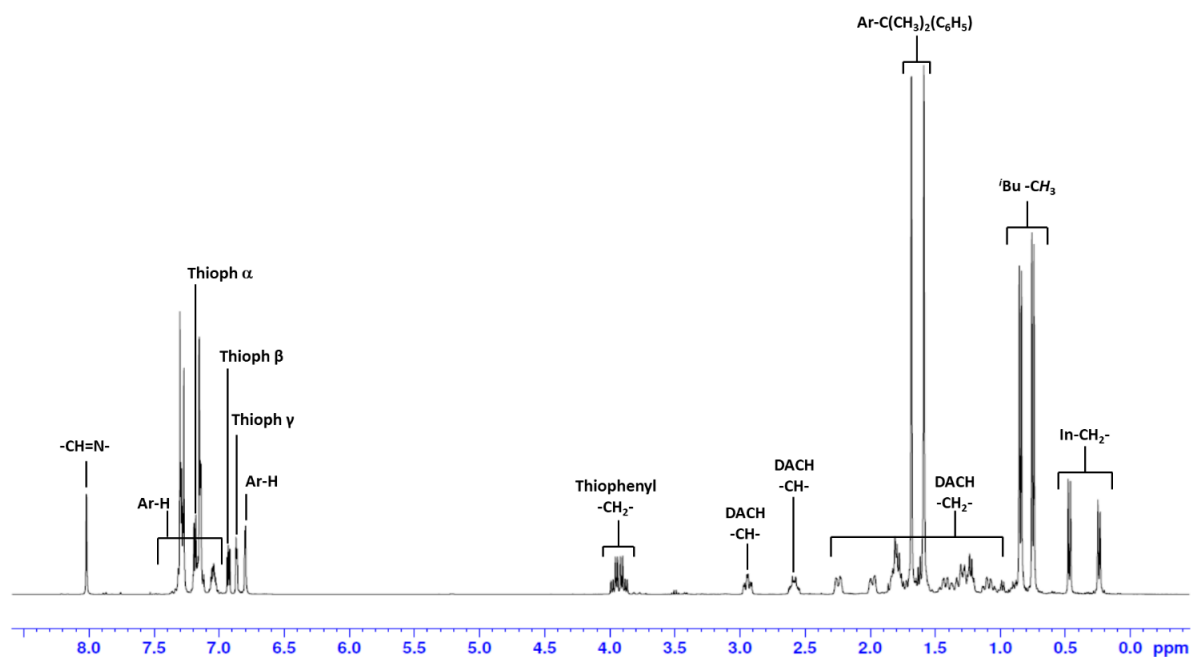


Figure A.17. ^1H NMR spectrum (400 MHz, CDCl_3 , 25 °C) of **47a**

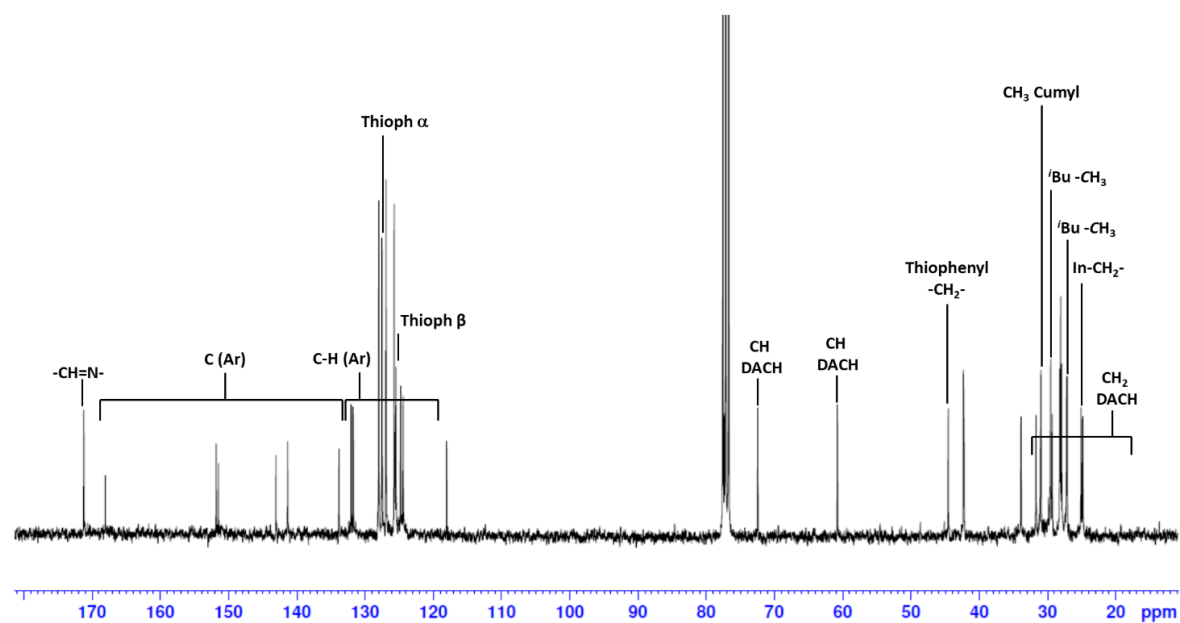


Figure A.18. $^{13}\text{C}\{^1\text{H}\}$ NMR spectrum (101 MHz, CDCl_3 , 25 °C) of **47a**

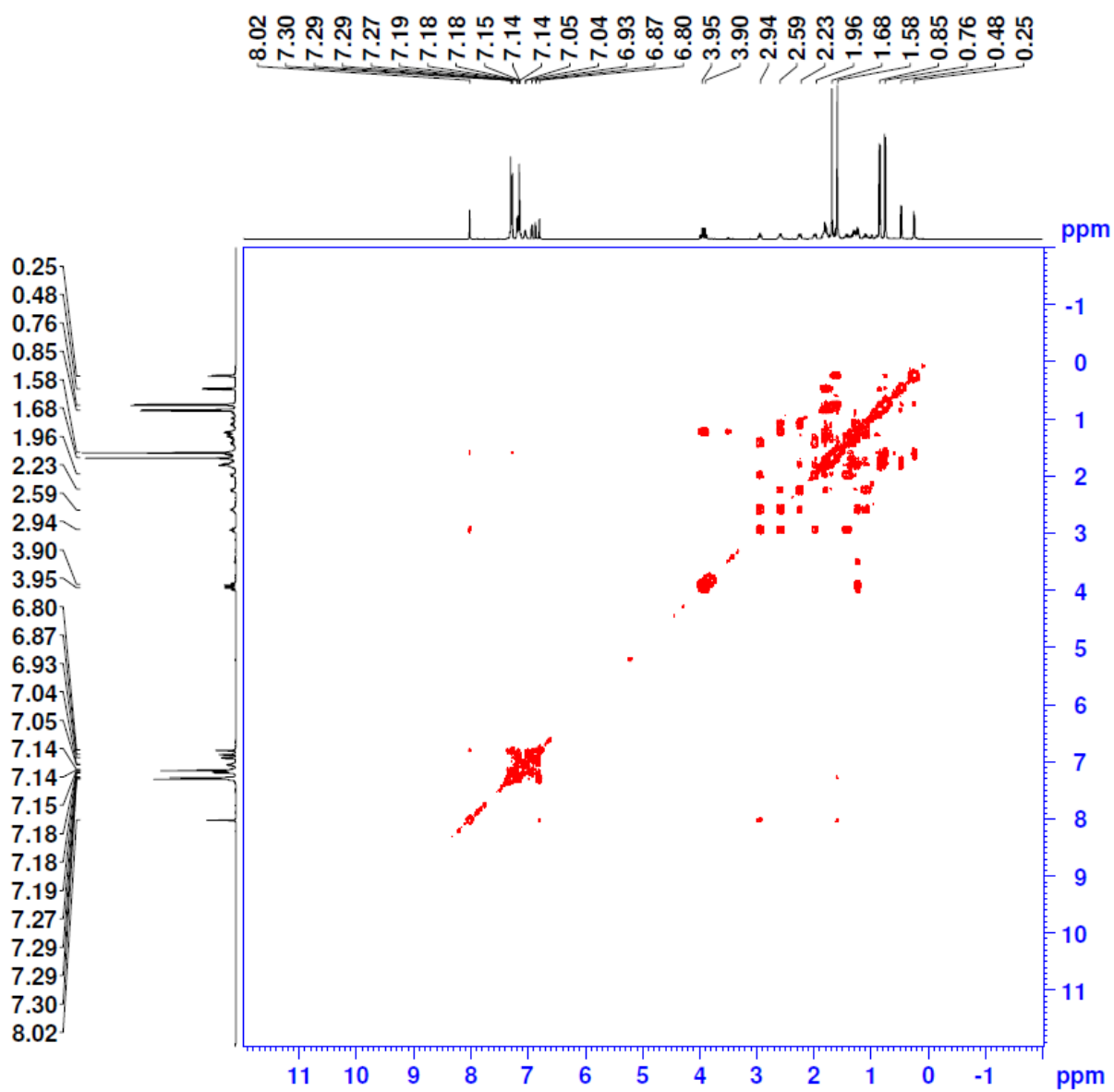


Figure A.19. ^1H - ^1H COSY NMR spectrum (400 MHz, CDCl_3 , 25 °C) of **47a**

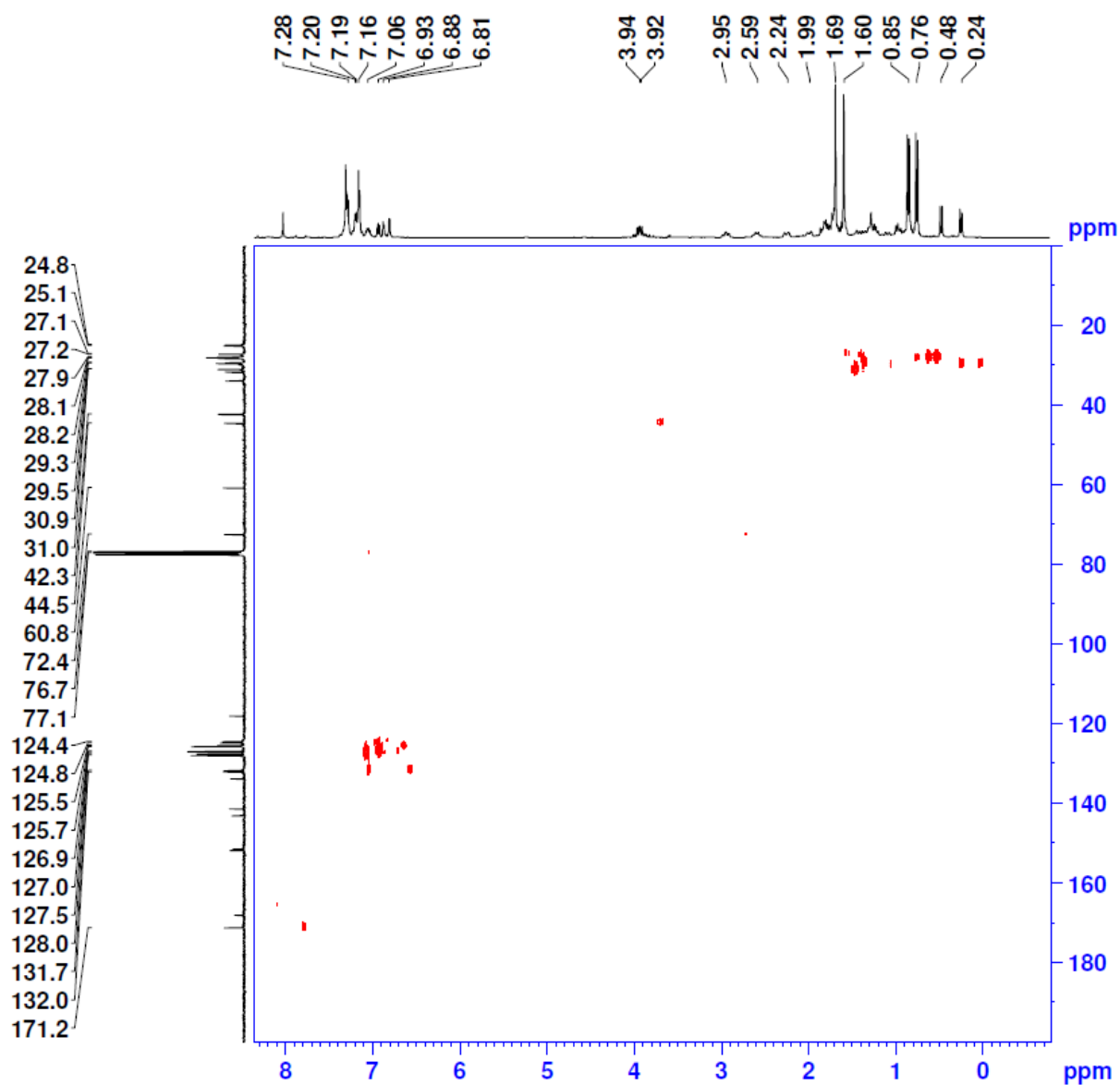


Figure A.20. ^1H - ^{13}C Heteronuclear Single Quantum Coherence (HSQC) NMR spectrum (CDCl_3 , 25 $^\circ\text{C}$) of **47a**

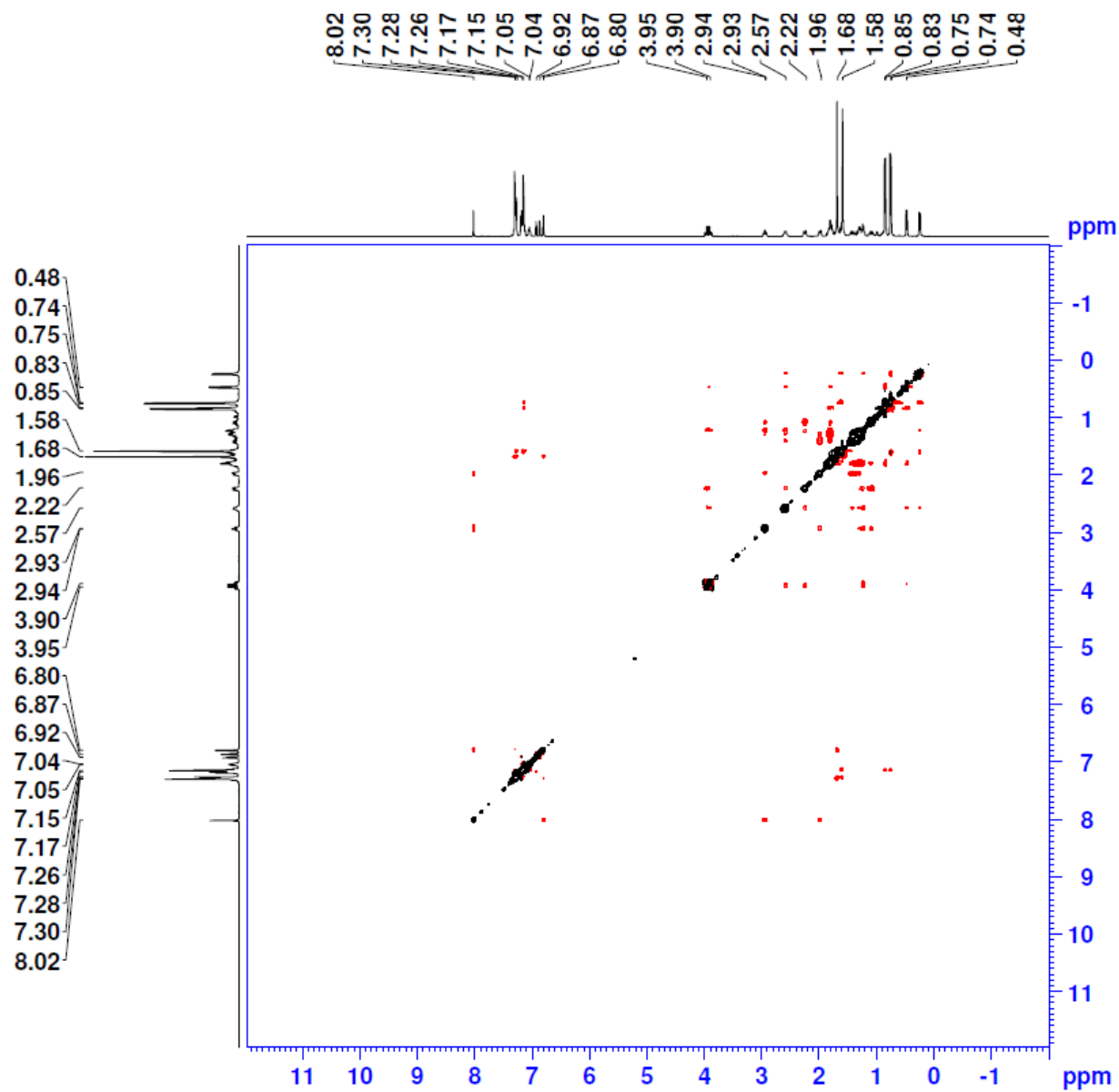


Figure A.21. Nuclear Overhauser Effect spectroscopy (NOESY) NMR spectrum (400 MHz, CDCl₃, 25 °C) of **47a**

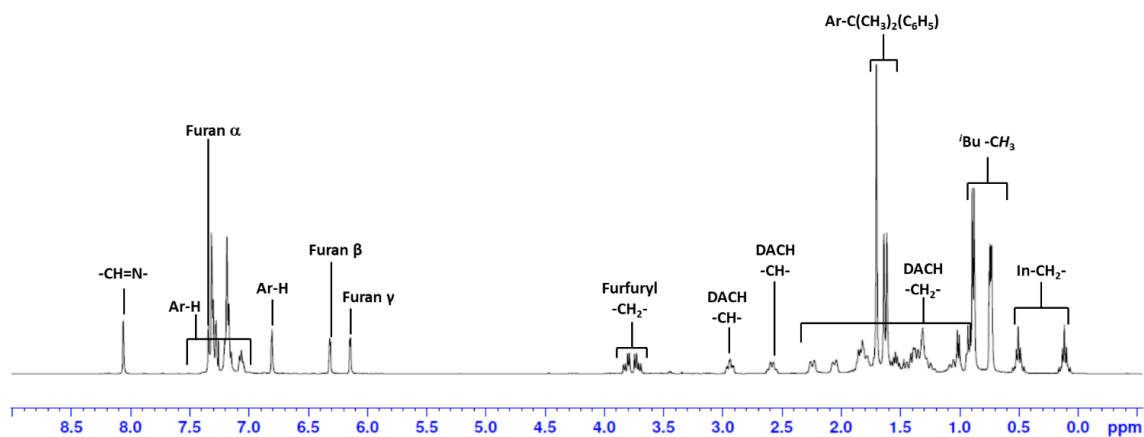


Figure A.22. ^1H NMR spectrum (400 MHz, CDCl_3 , 25 $^\circ\text{C}$) of **47b**

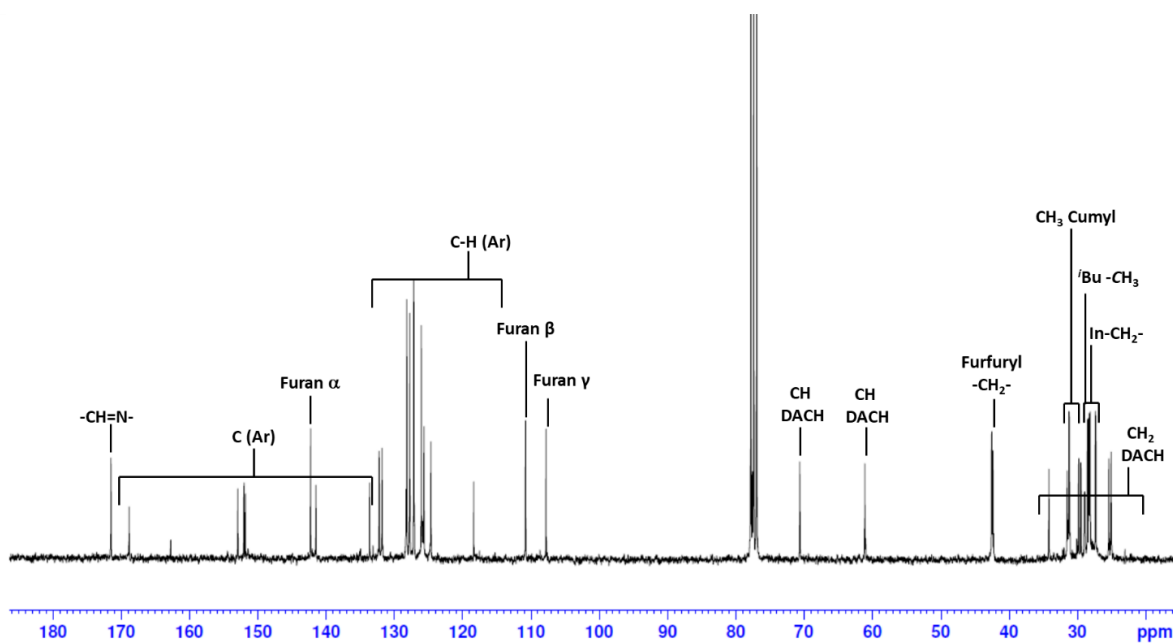


Figure A.23. $^{13}\text{C}\{^1\text{H}\}$ NMR spectrum (101 MHz, CDCl_3 , 25 $^\circ\text{C}$) of **47b**

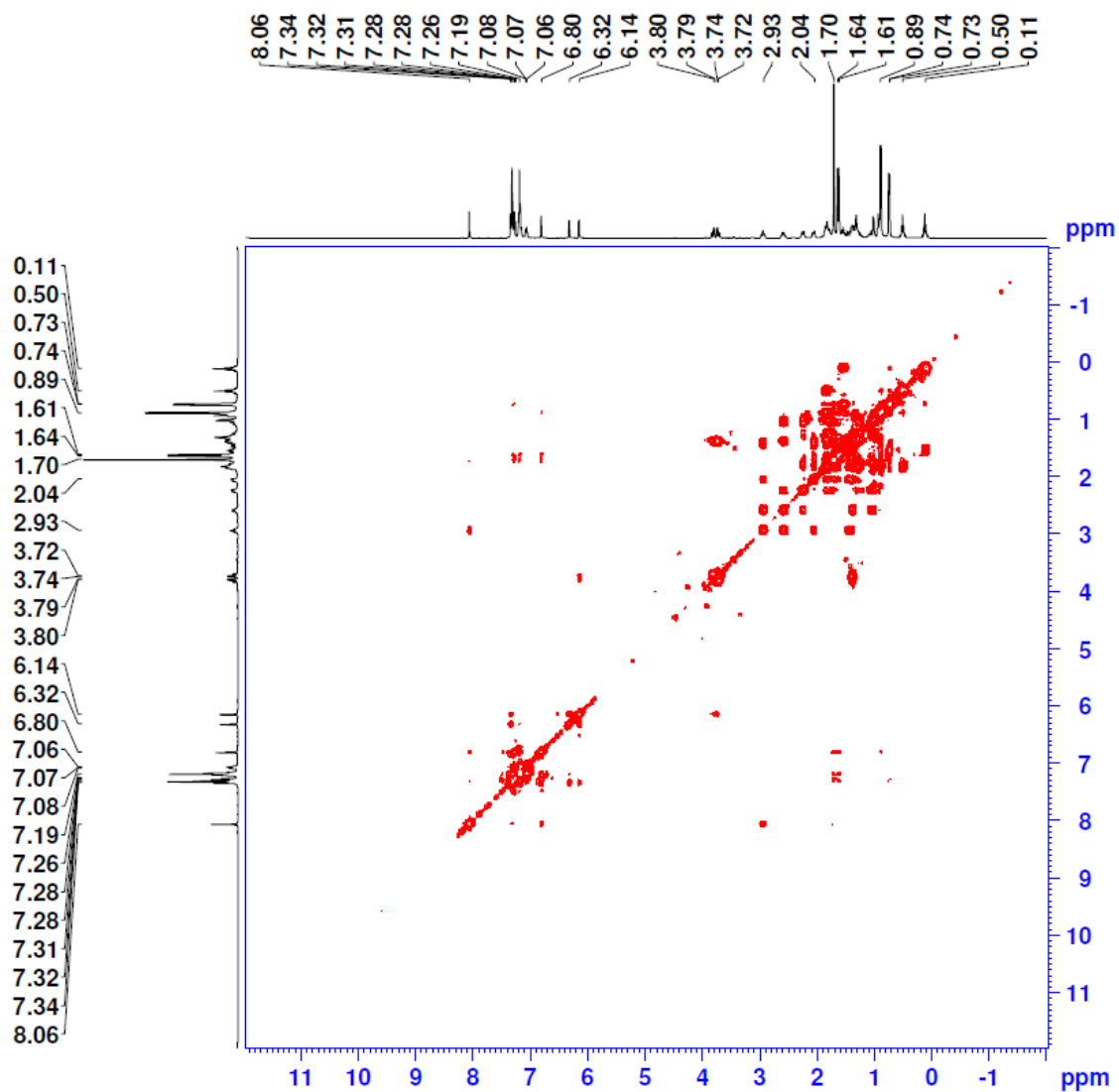


Figure A.24. ^1H - ^1H COSY NMR spectrum (400 MHz, CDCl_3 , 25 °C) of **47b**

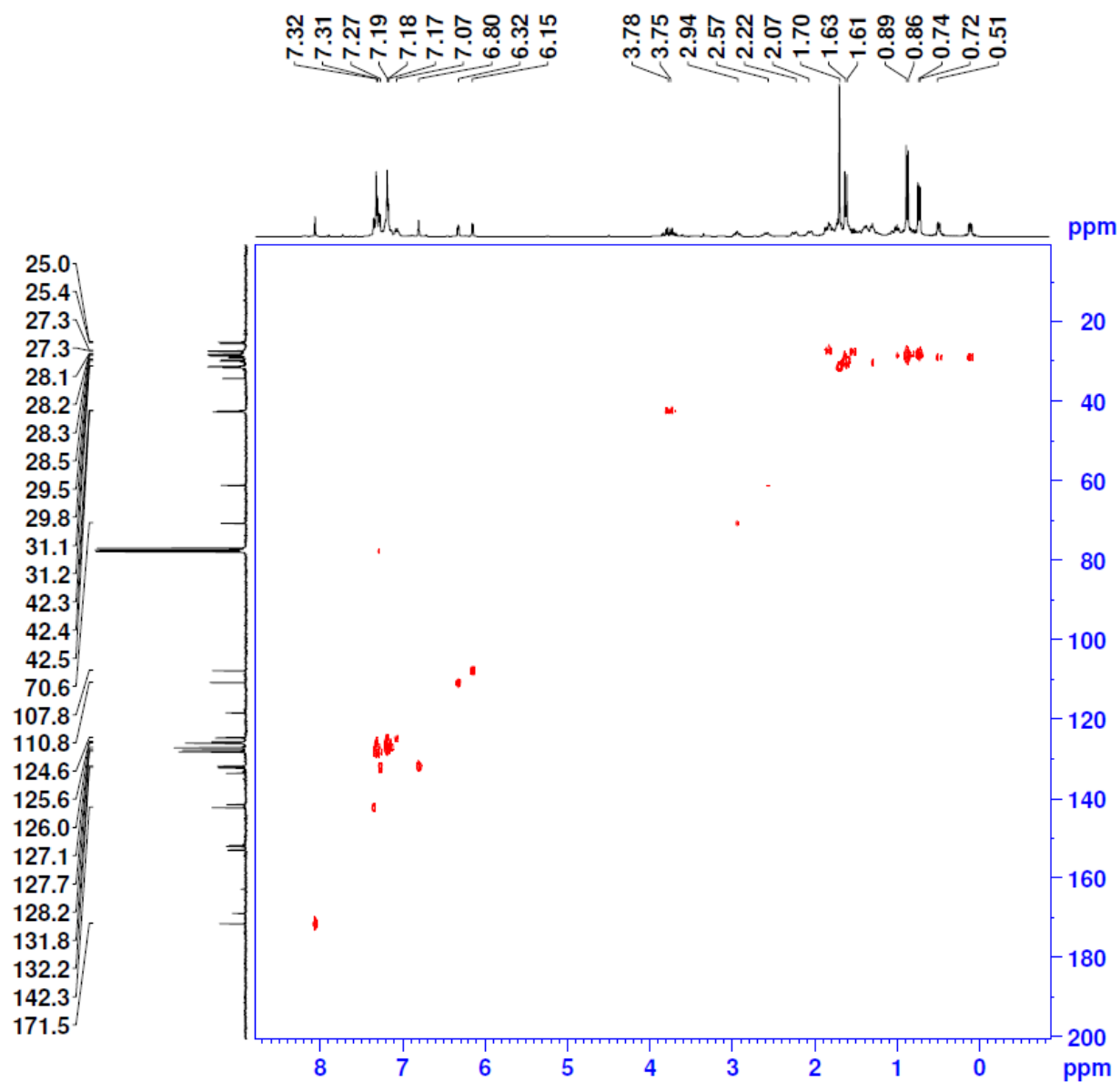


Figure A.25. ^1H - ^{13}C Heteronuclear Single Quantum Coherence (HSQC) NMR spectrum (CDCl_3 , 25 $^\circ\text{C}$) of **47b**

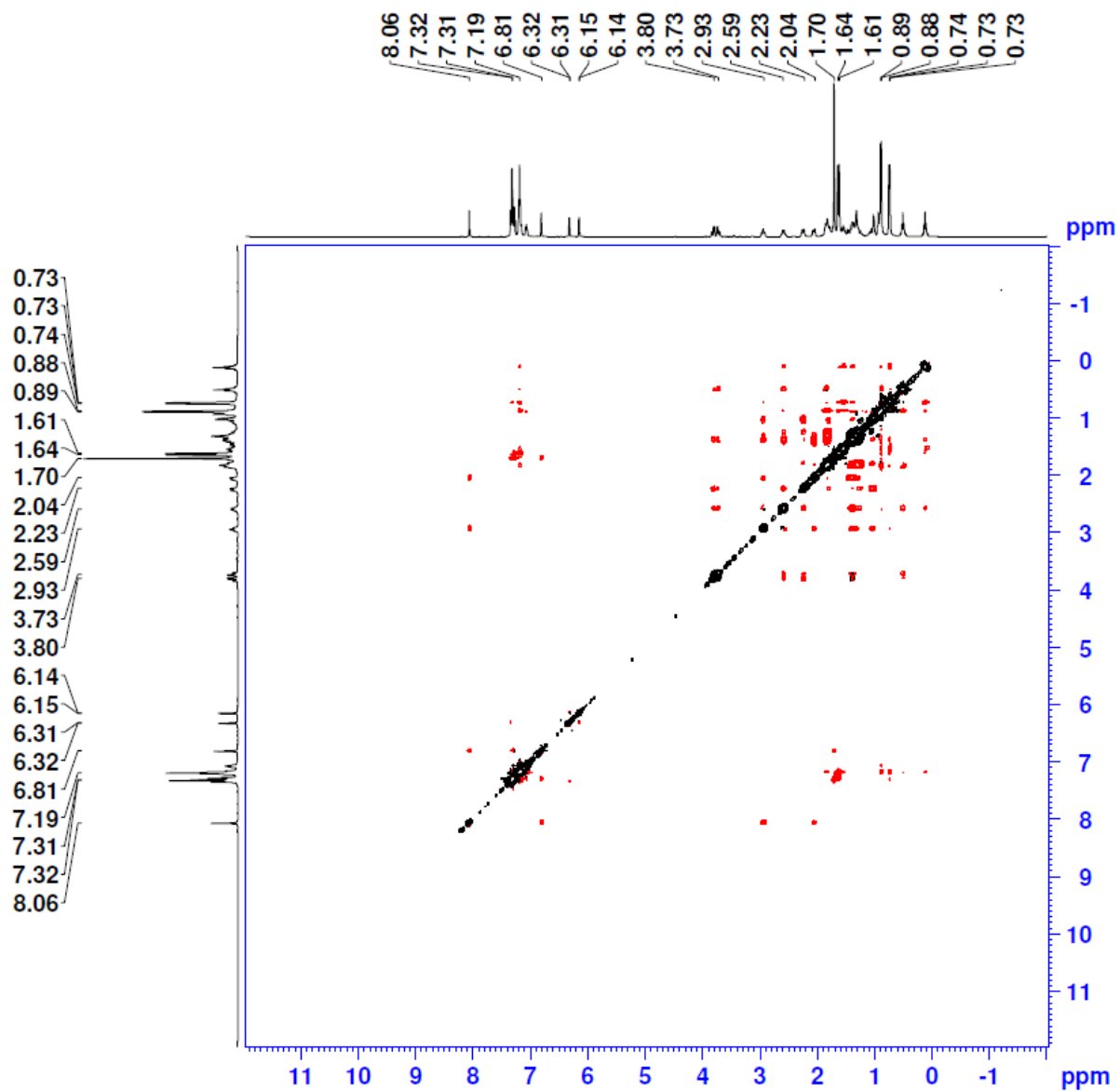


Figure A.26. Nuclear Overhauser Effect spectroscopy (NOESY) NMR spectrum (400 MHz, CDCl₃, 25 °C) of **47b**

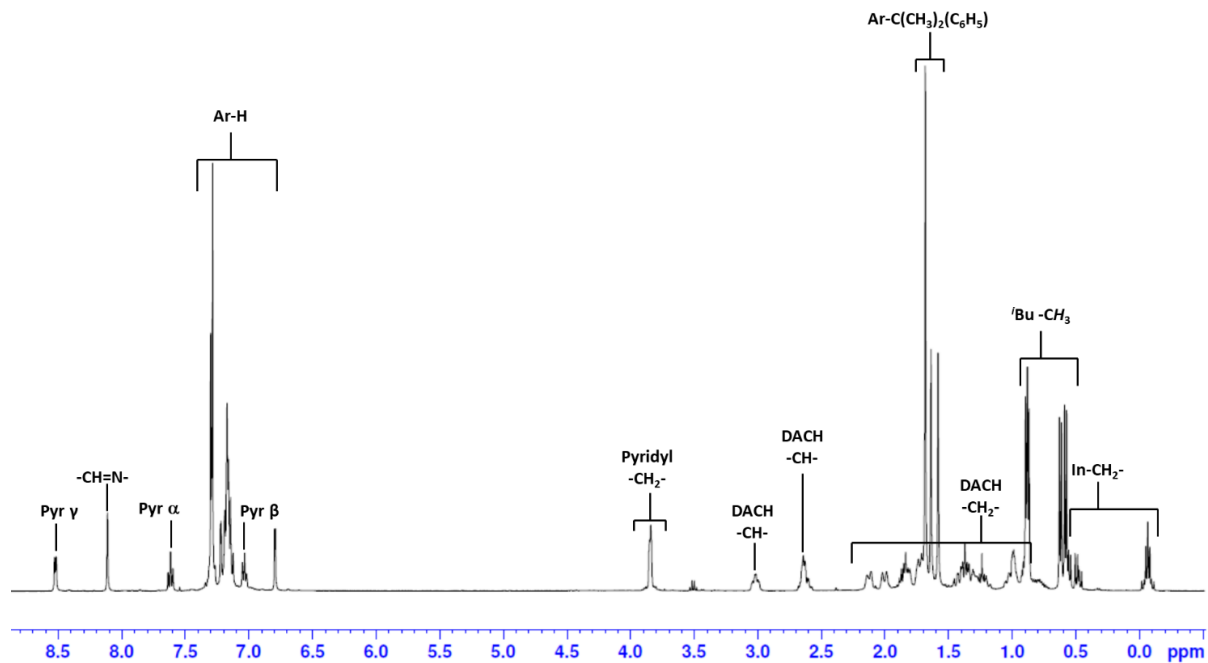


Figure A.27. ^1H NMR spectrum (400 MHz, CDCl_3 , 25 $^\circ\text{C}$) of **47c**

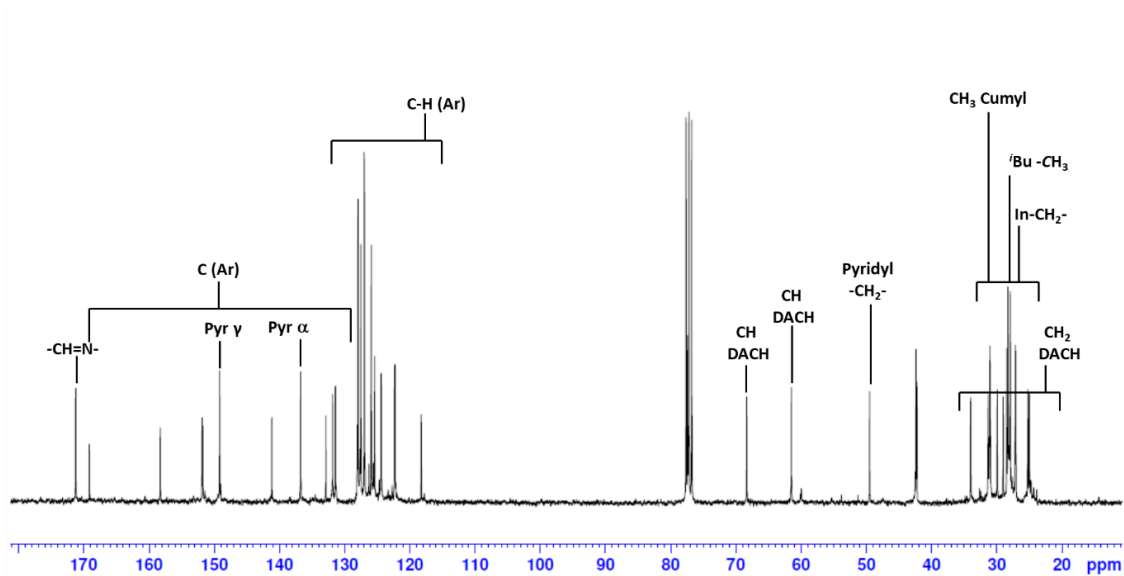


Figure A.28. $^{13}\text{C}\{^1\text{H}\}$ NMR spectrum (101 MHz, CDCl_3 , 25 $^\circ\text{C}$) of **47c**

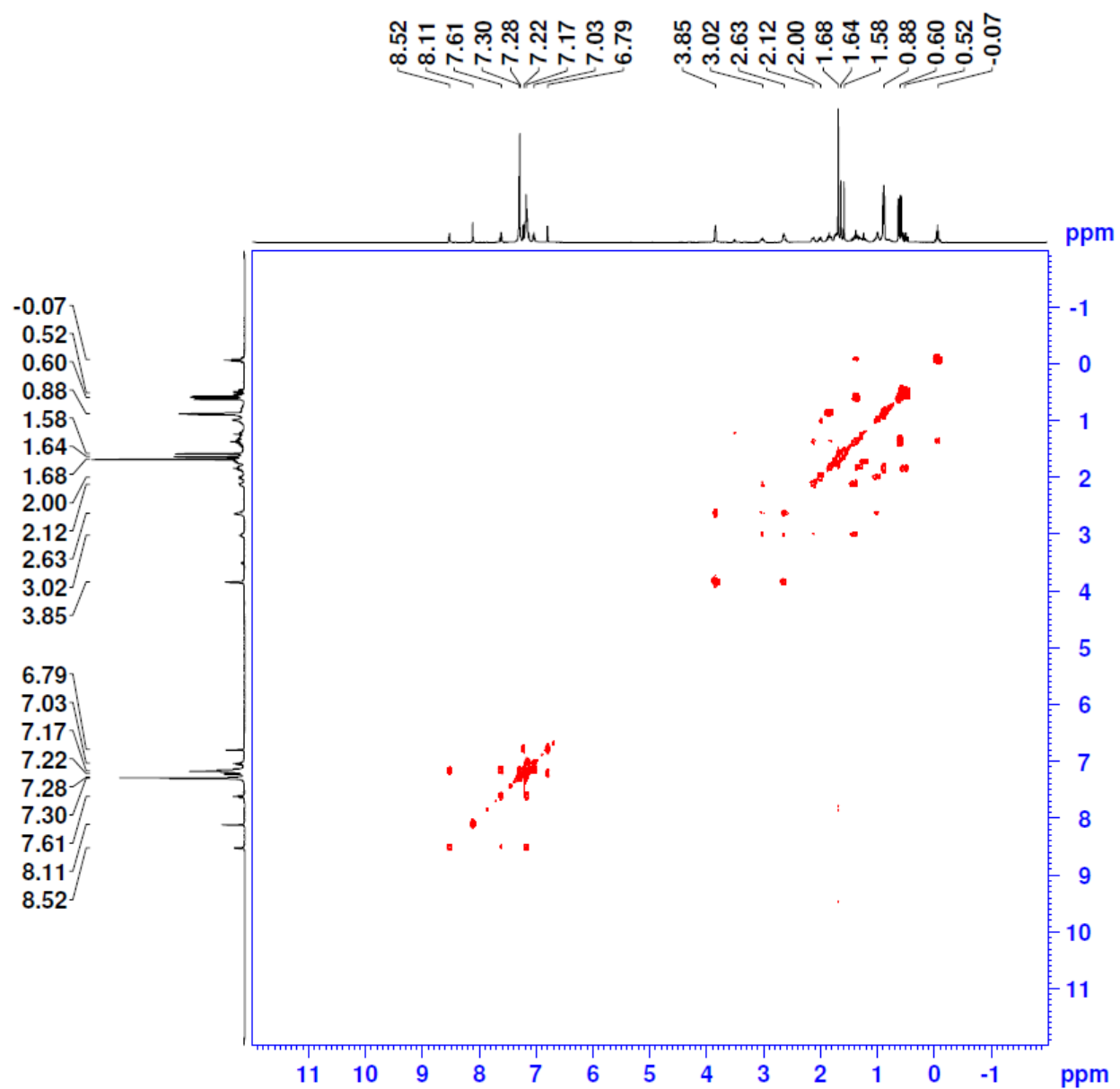


Figure A.29. ^1H - ^1H COSY NMR spectrum (400 MHz, CDCl_3 , 25 $^\circ\text{C}$) of **47c**

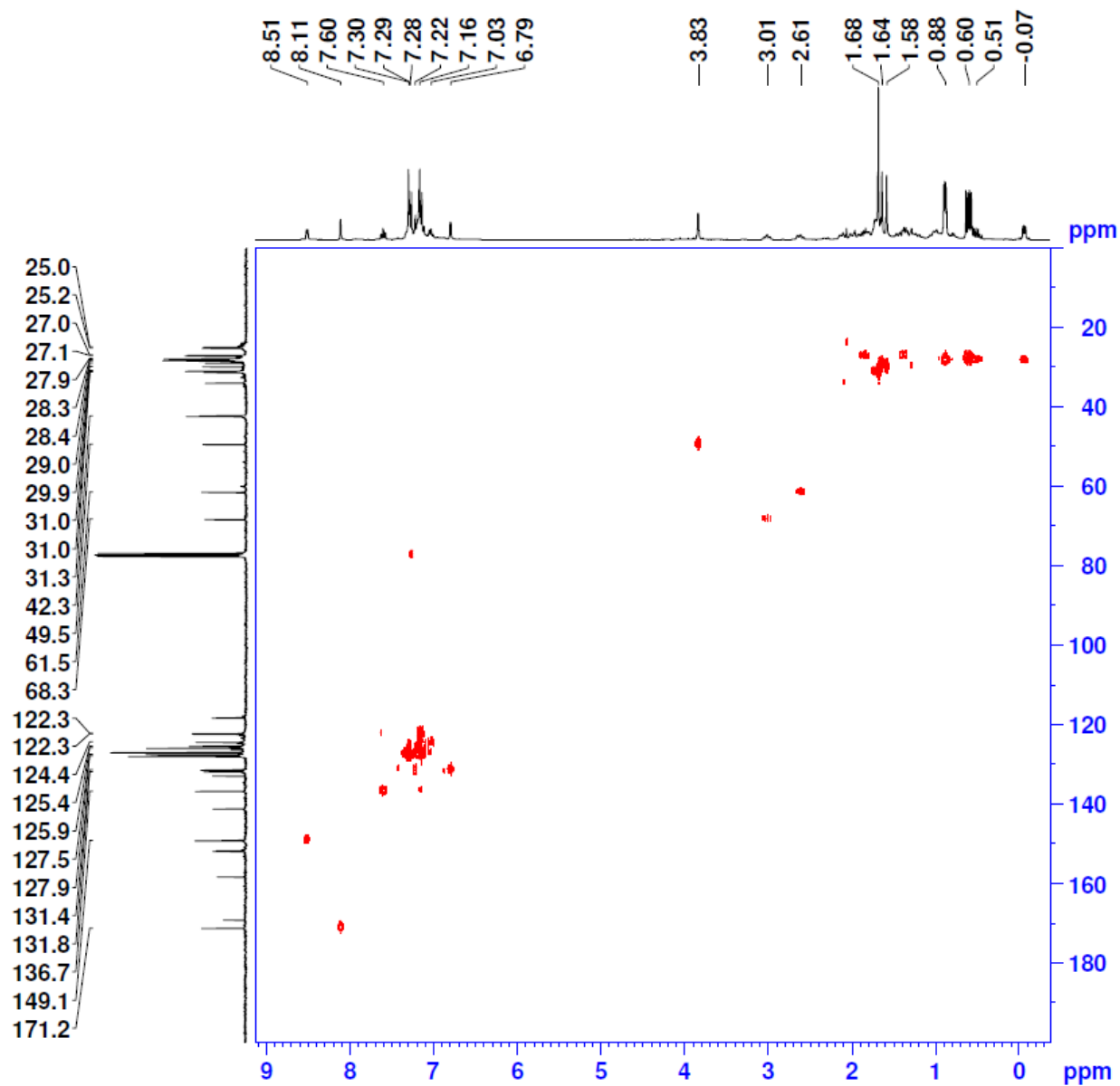


Figure A.30. ^1H - ^{13}C Heteronuclear Single Quantum Coherence (HSQC) NMR spectrum (CDCl_3 , 25 $^\circ\text{C}$) of **47c**

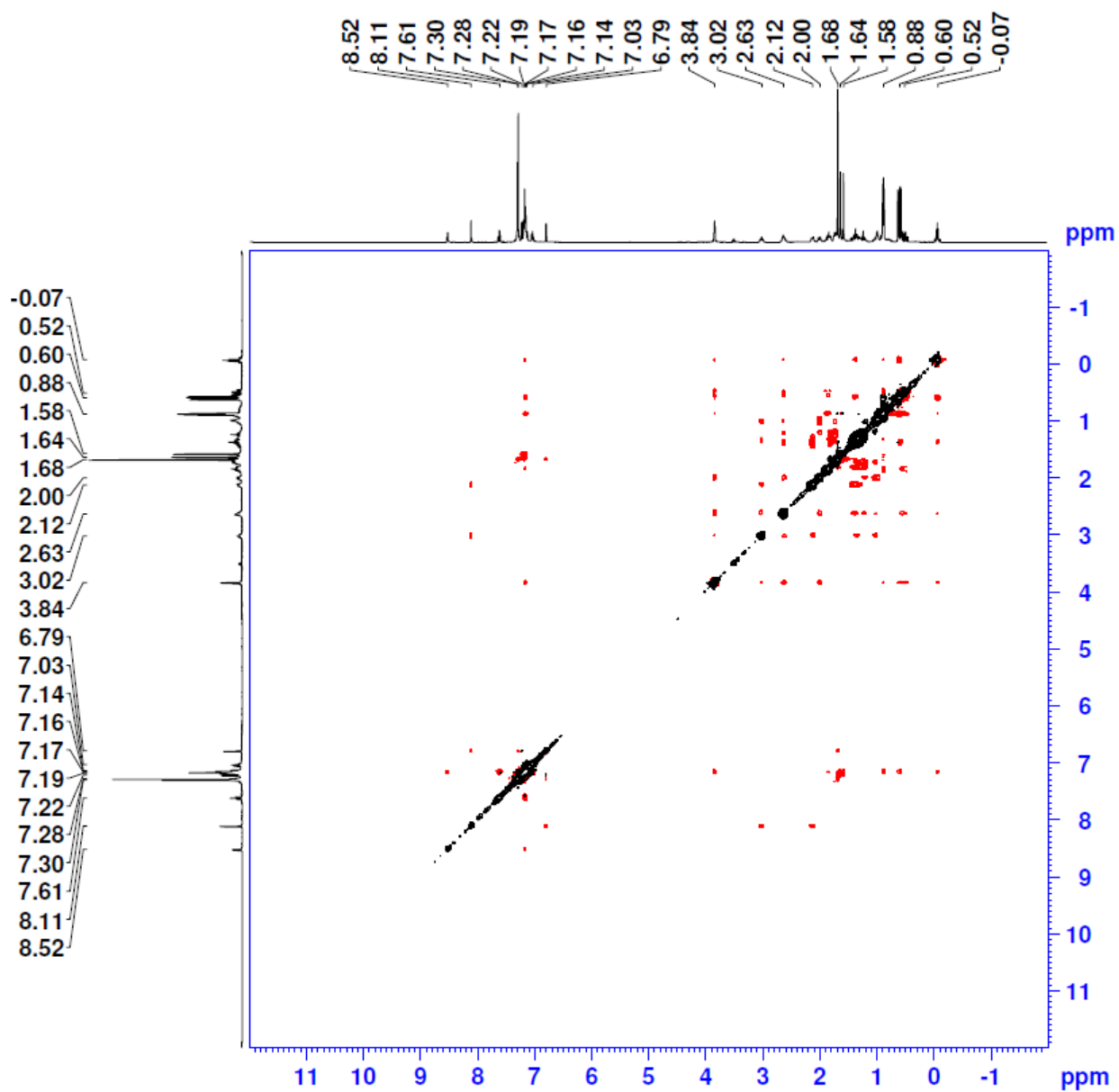


Figure A.31. Nuclear Overhauser Effect spectroscopy (NOESY) NMR spectrum (400 MHz, CDCl₃, 25 °C) of **47c**

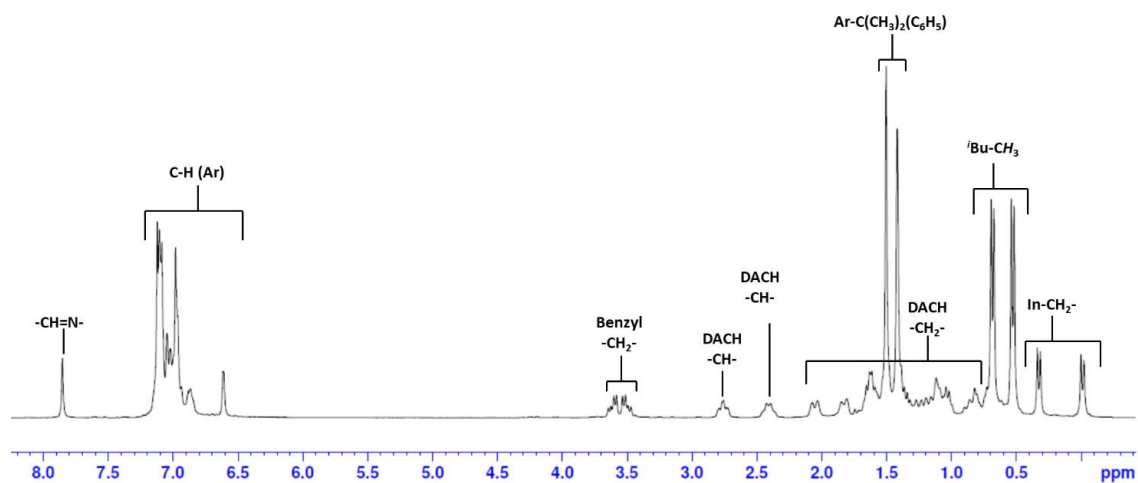


Figure A.32. ^1H NMR spectrum (400 MHz, CDCl_3 , 25 $^\circ\text{C}$) of **47d**

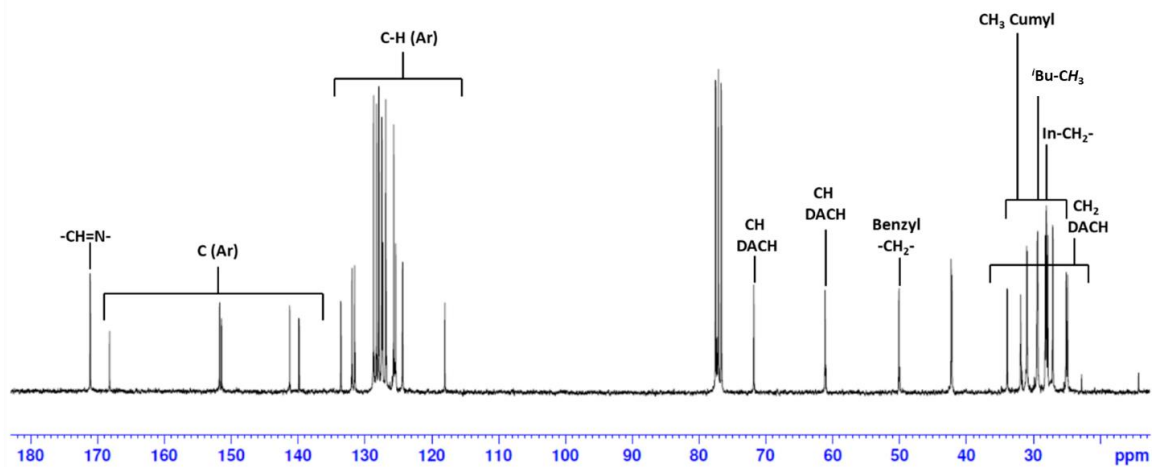


Figure A.33. $^{13}\text{C}\{^1\text{H}\}$ NMR spectrum (101 MHz, CDCl_3 , 25 $^\circ\text{C}$) of **47d**

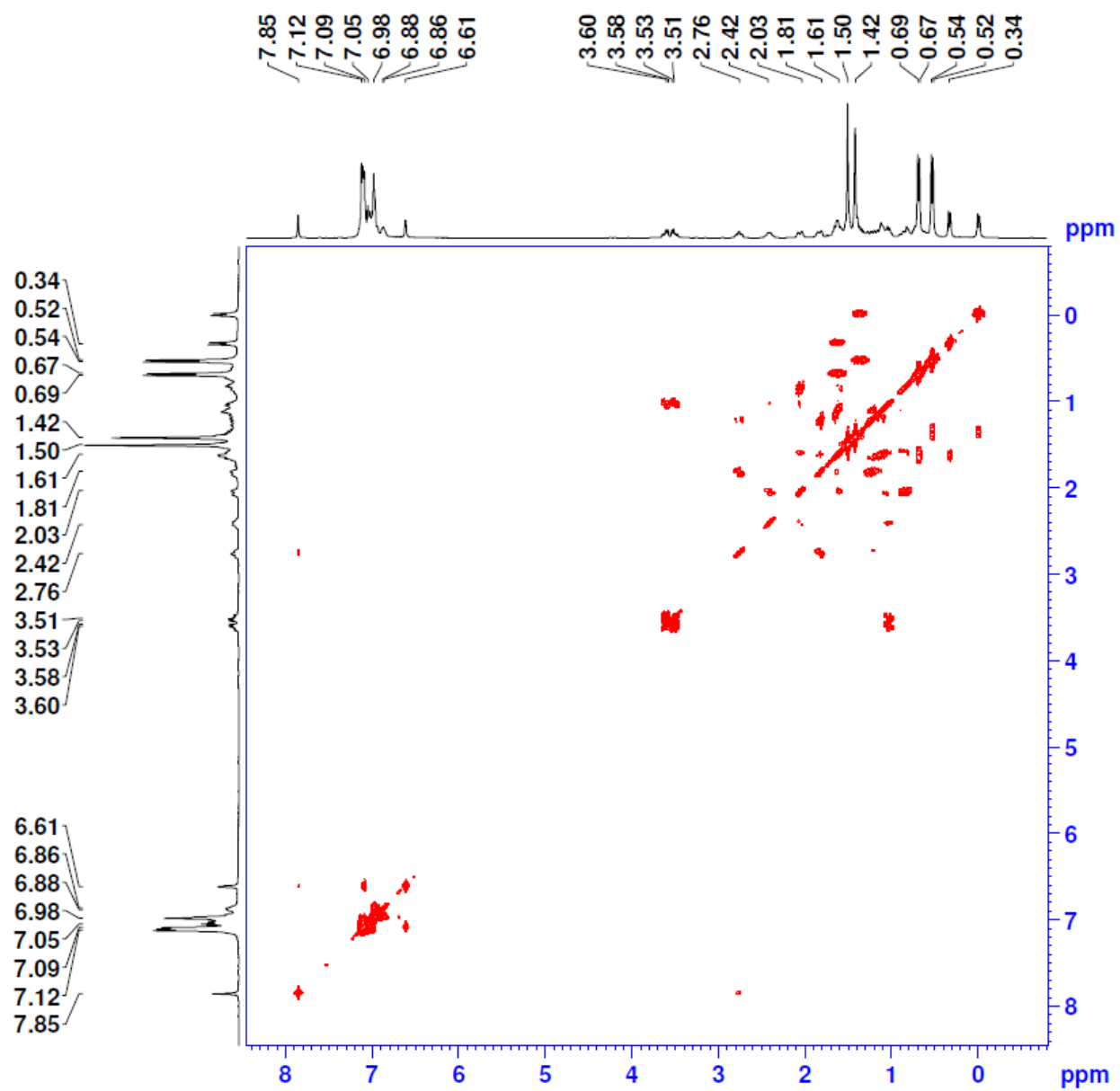


Figure A.34. ^1H - ^1H COSY NMR spectrum (400 MHz, CDCl_3 , 25 °C) of **47d**

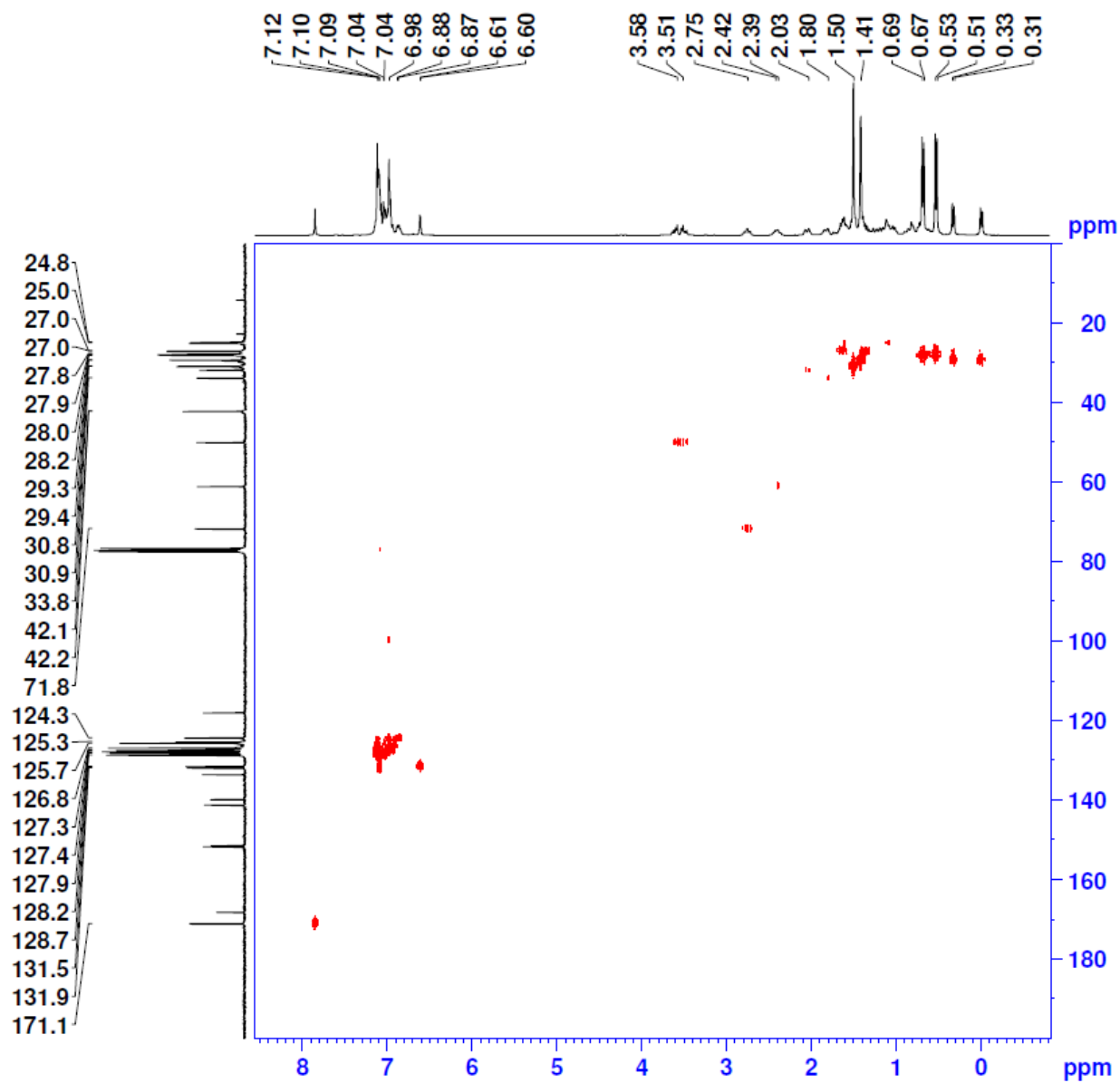


Figure A.35. ^1H - ^{13}C Heteronuclear Single Quantum Coherence (HSQC) NMR spectrum (CDCl_3 , 25 $^\circ\text{C}$) of **47d**

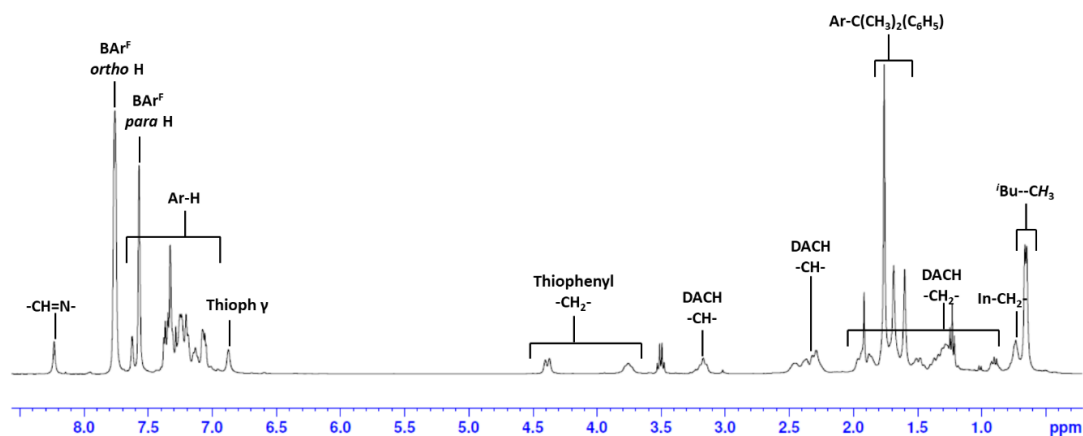


Figure A.36. ^1H NMR spectrum (300 MHz, CDCl_3 , 25 $^\circ\text{C}$) of **48a**. (Residual diethyl ether q, 3.48 and t, 1.22 ppm)

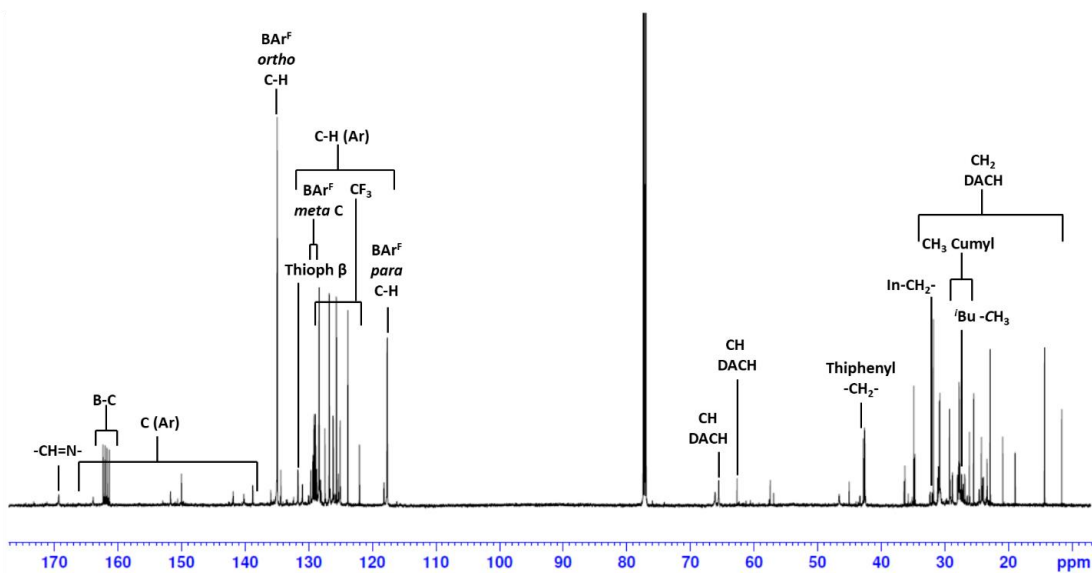


Figure A.37. $^{13}\text{C}\{^1\text{H}\}$ NMR spectrum (151 MHz, CDCl_3 , 25 $^\circ\text{C}$) of **48a**

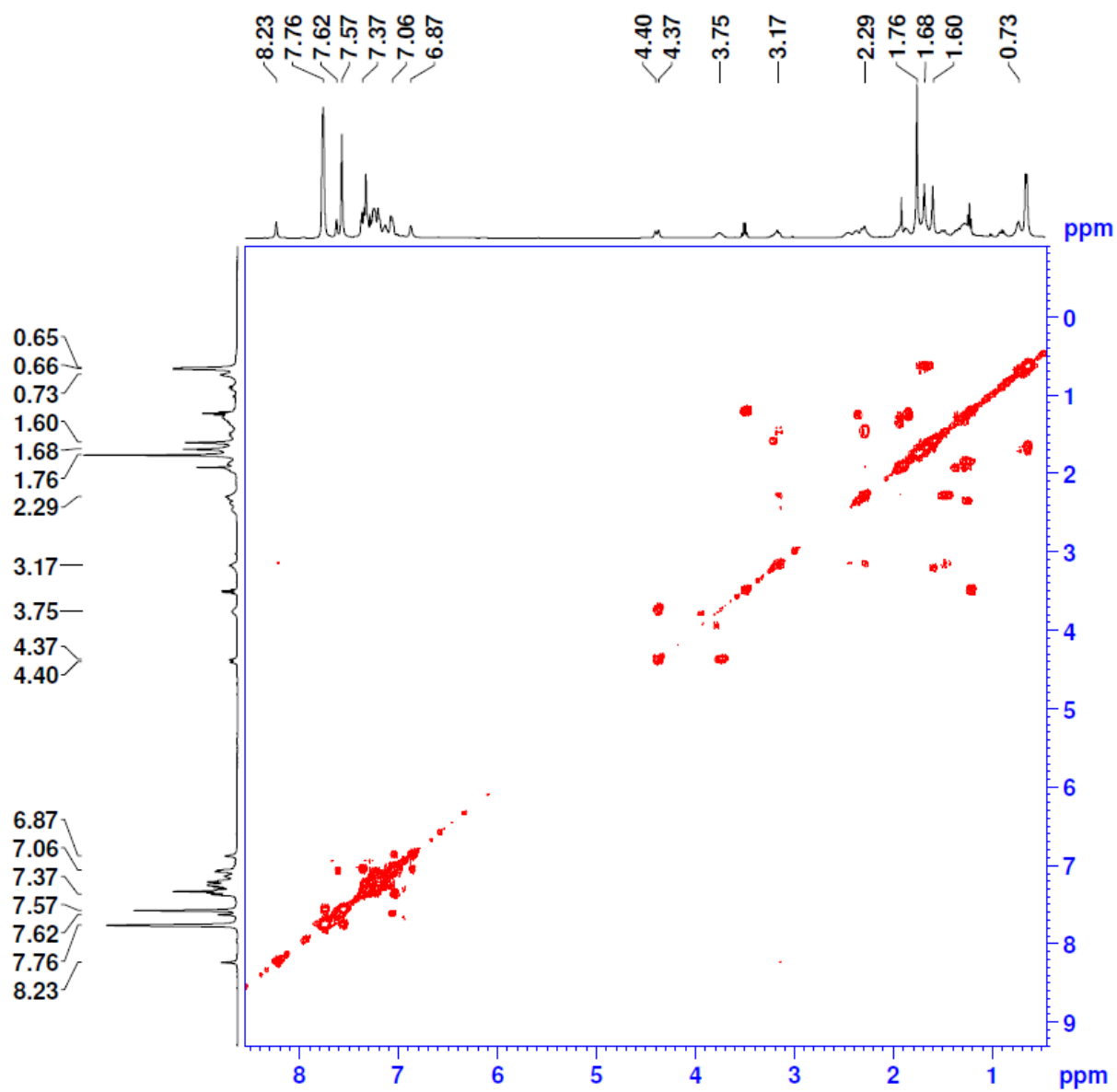


Figure A.38. ^1H - ^1H COSY NMR spectrum (400 MHz, CDCl_3 , 25 $^\circ\text{C}$) of **48a**

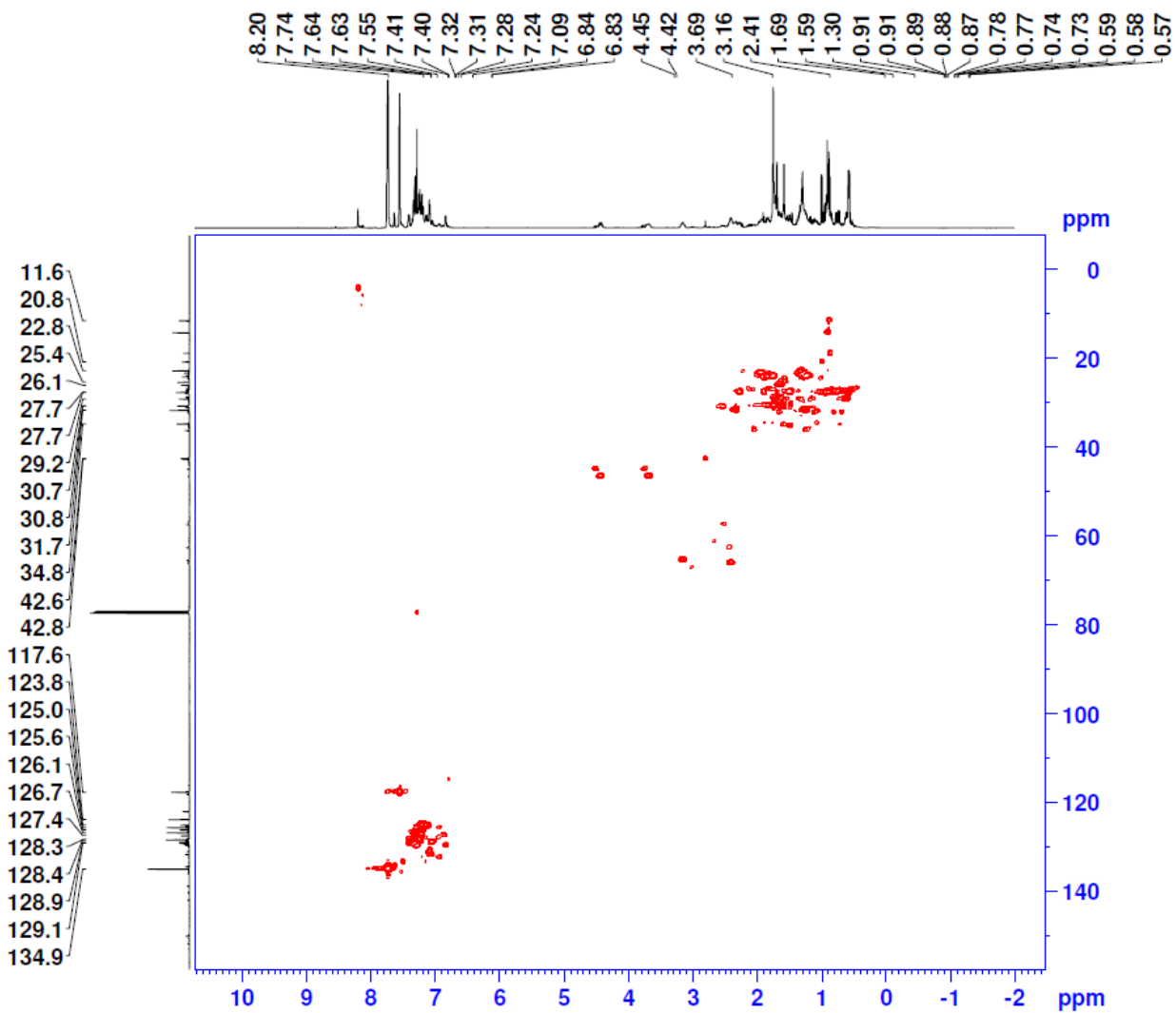


Figure A.39. ^1H - ^{13}C Heteronuclear Single Quantum Coherence (HSQC) NMR spectrum (CDCl_3 , 25 $^\circ\text{C}$) of **48a**

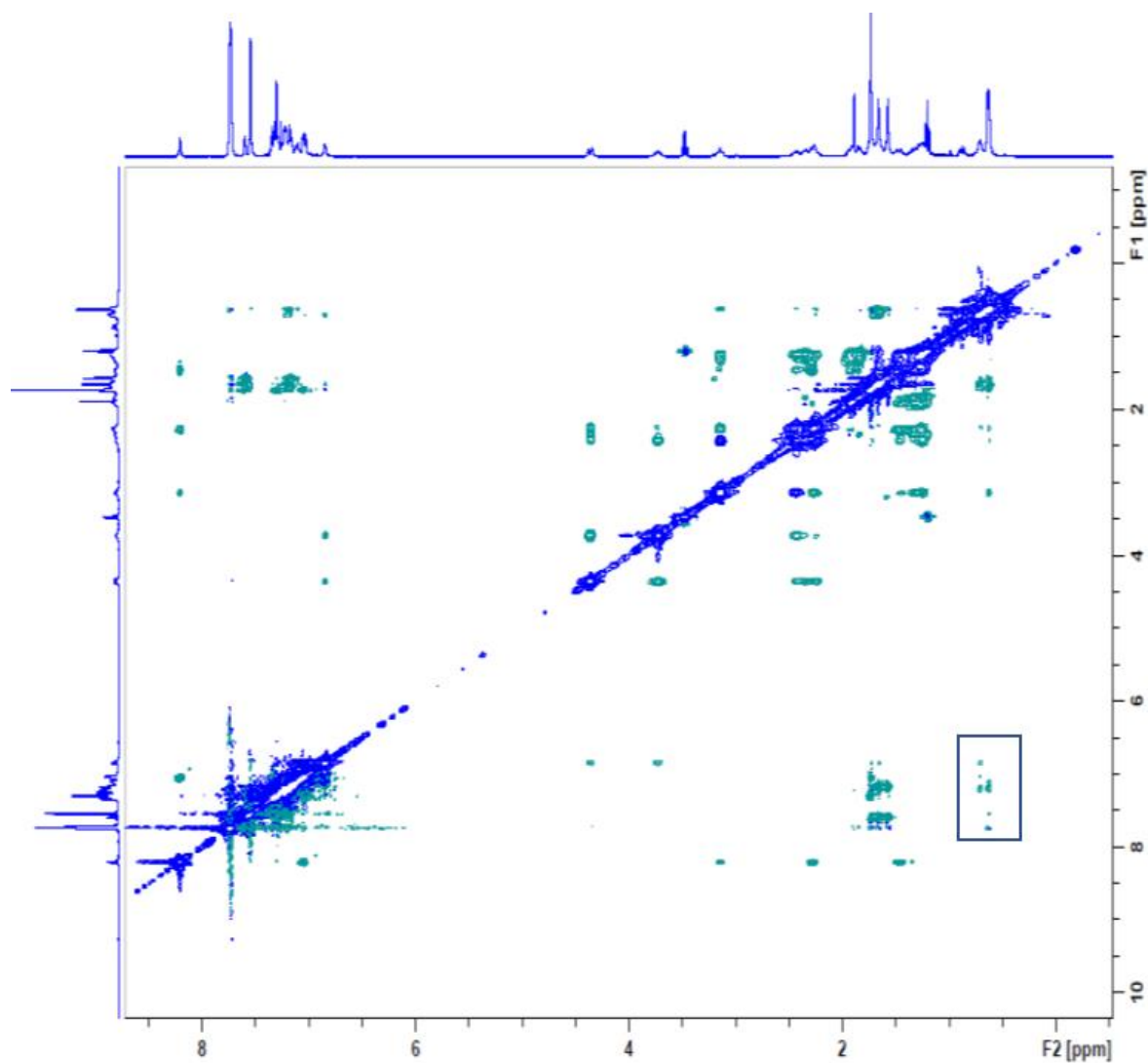


Figure A.40. Nuclear Overhauser Effect spectroscopy (NOESY) NMR spectrum (400 MHz, CDCl₃, 25 °C) of **48a**

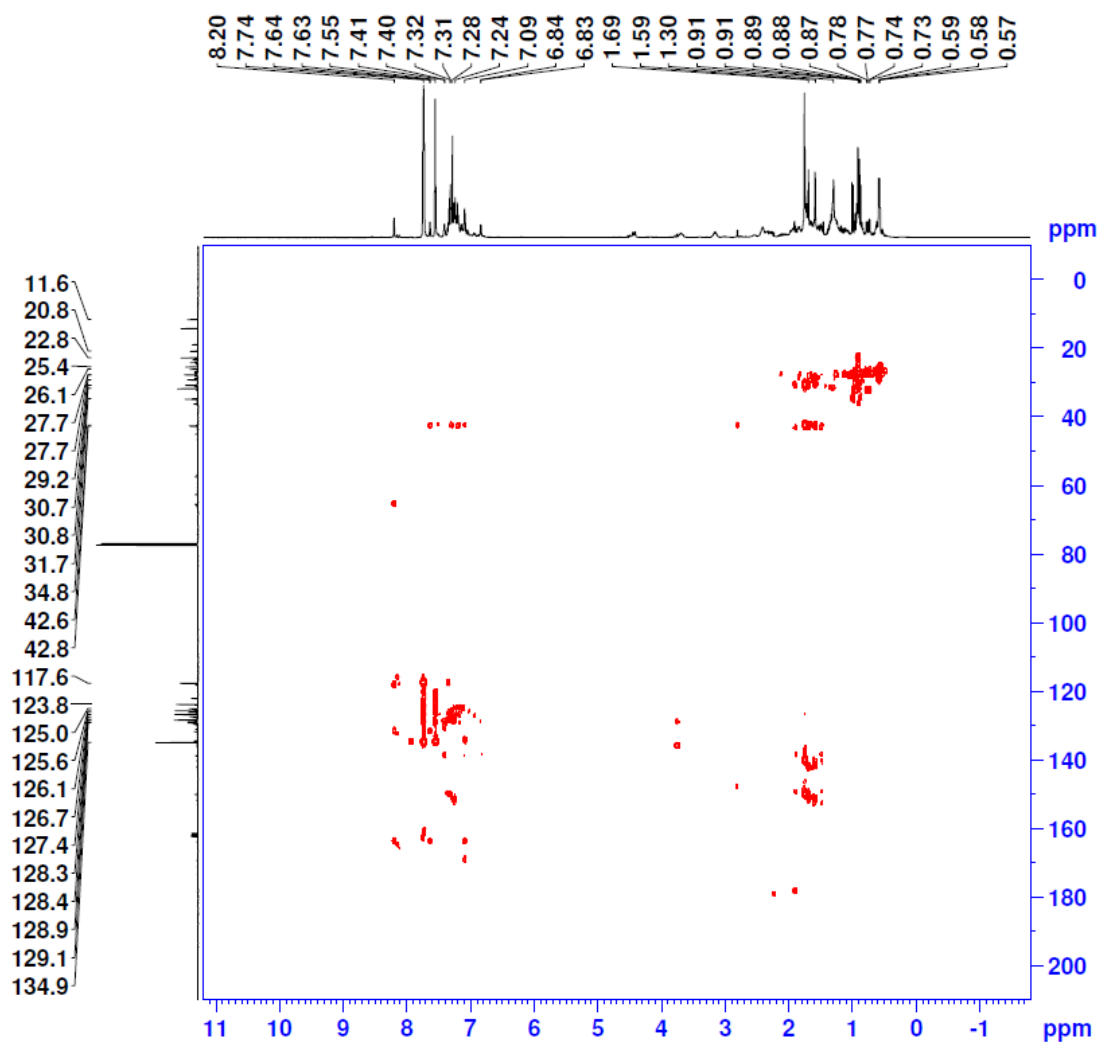


Figure A.41. ^1H - ^{13}C Heteronuclear Multiple Bond Correlation (HMBC) NMR spectrum (CDCl_3 , 25 $^\circ\text{C}$) of **48a**

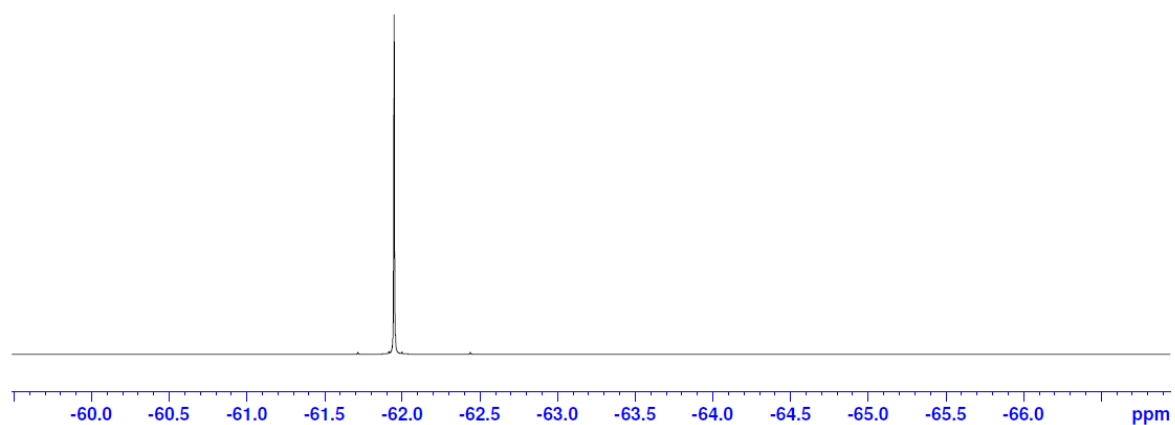


Figure A.42. $^{19}\text{F}\{^1\text{H}\}$ NMR spectrum (282 MHz, CDCl_3 , 25 °C) of **48a**

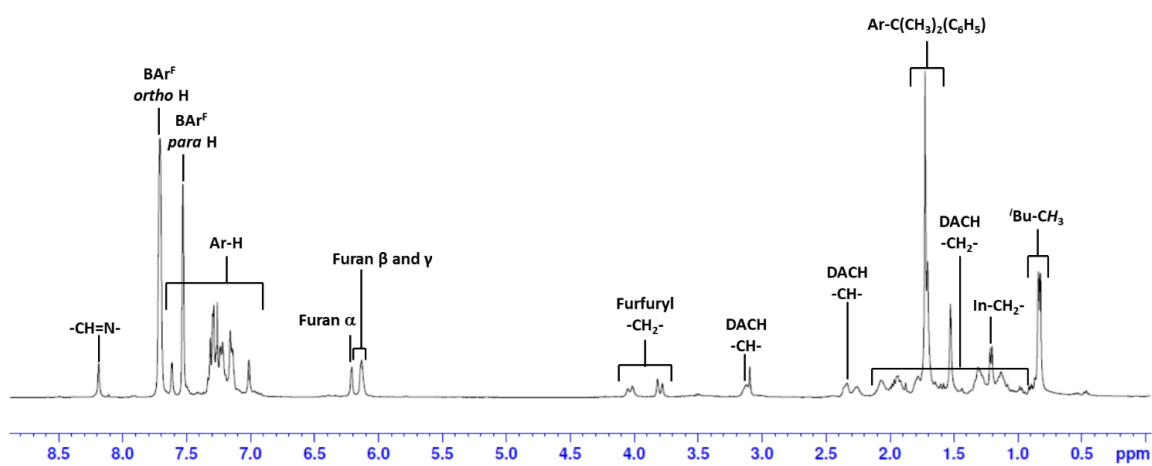


Figure A.43. ^1H NMR spectrum (300 MHz, CDCl_3 , 25 °C) of **48b**

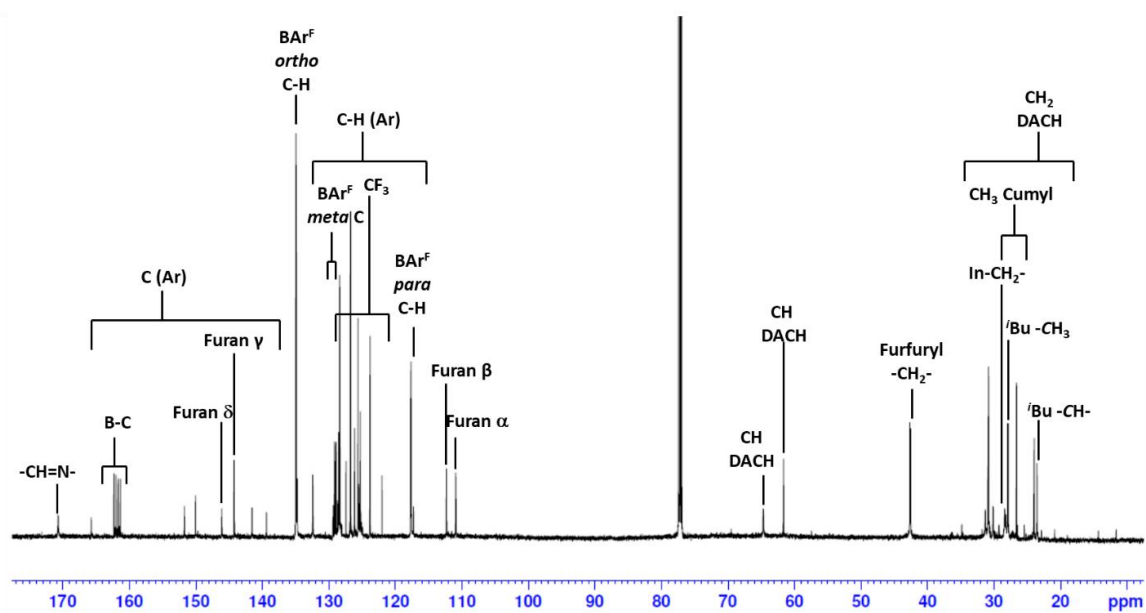


Figure A.44. $^{13}\text{C}\{^1\text{H}\}$ NMR spectrum (151 MHz, CDCl_3 , 25 °C) of **48b**

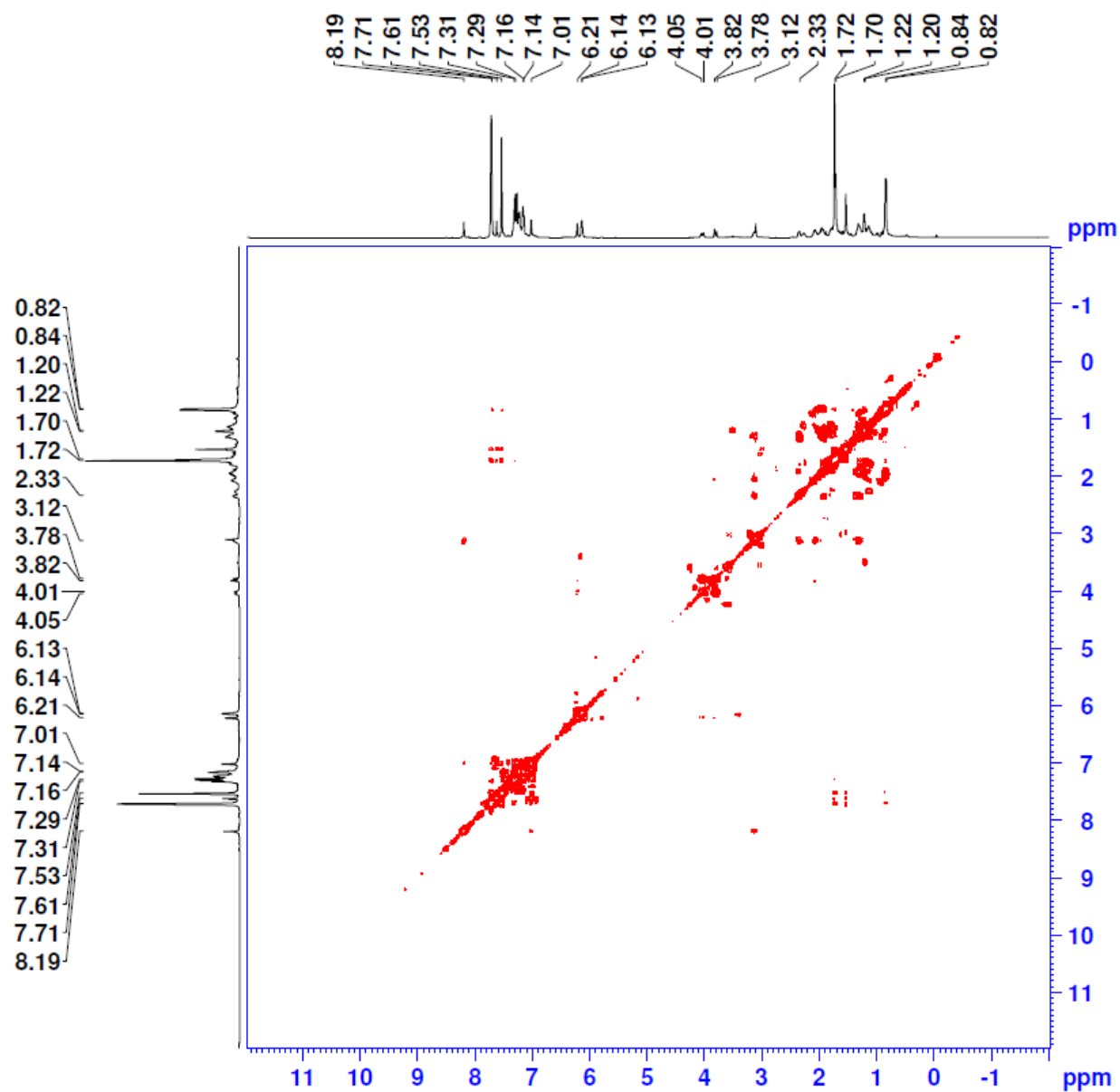


Figure A.45. ^1H - ^1H COSY NMR spectrum (400 MHz, CDCl_3 , 25 °C) of **48b**

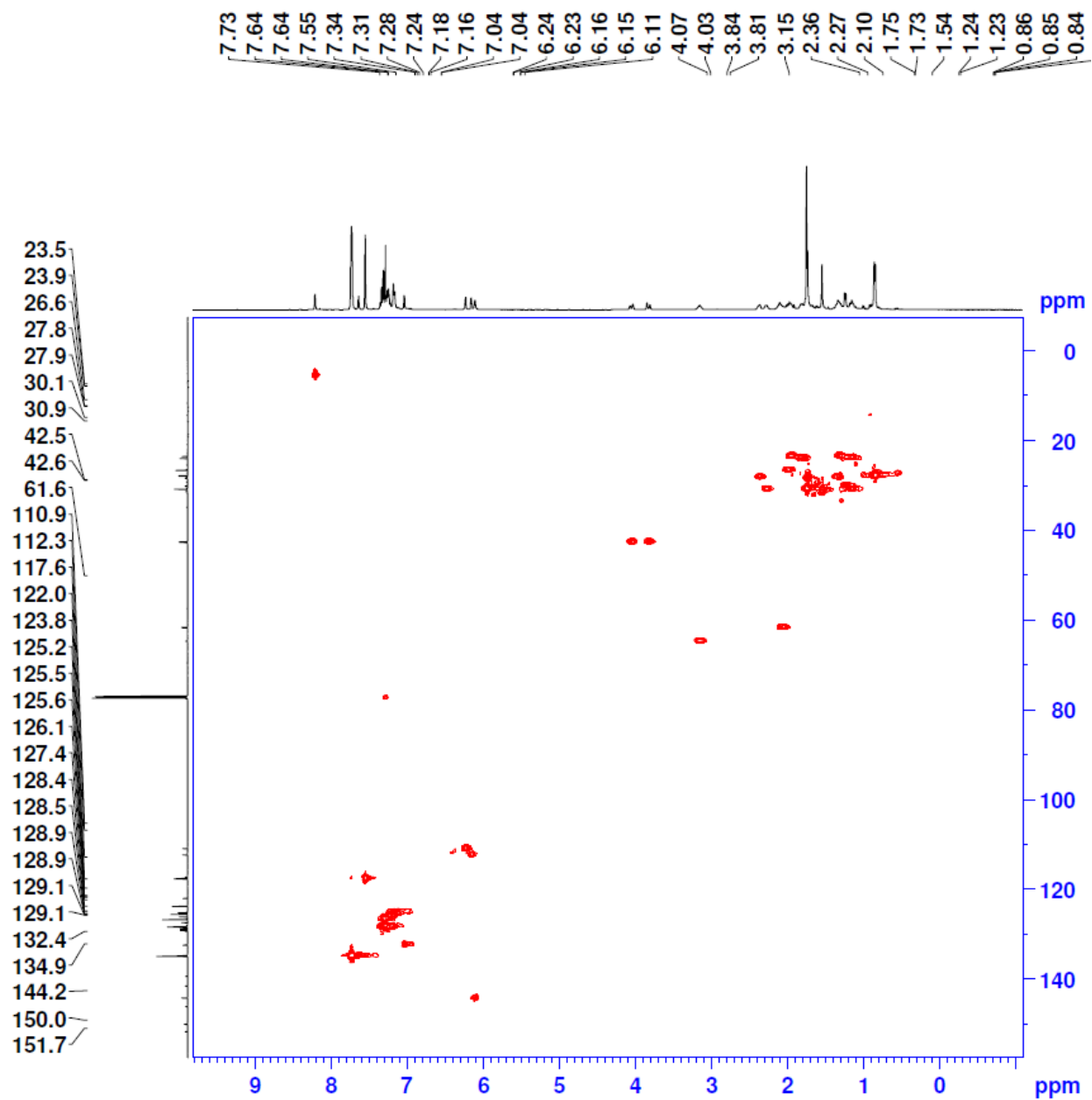


Figure A.46. ^1H - ^{13}C Heteronuclear Single Quantum Coherence (HSQC) NMR spectrum (CDCl_3 , 25 °C) of **48b**

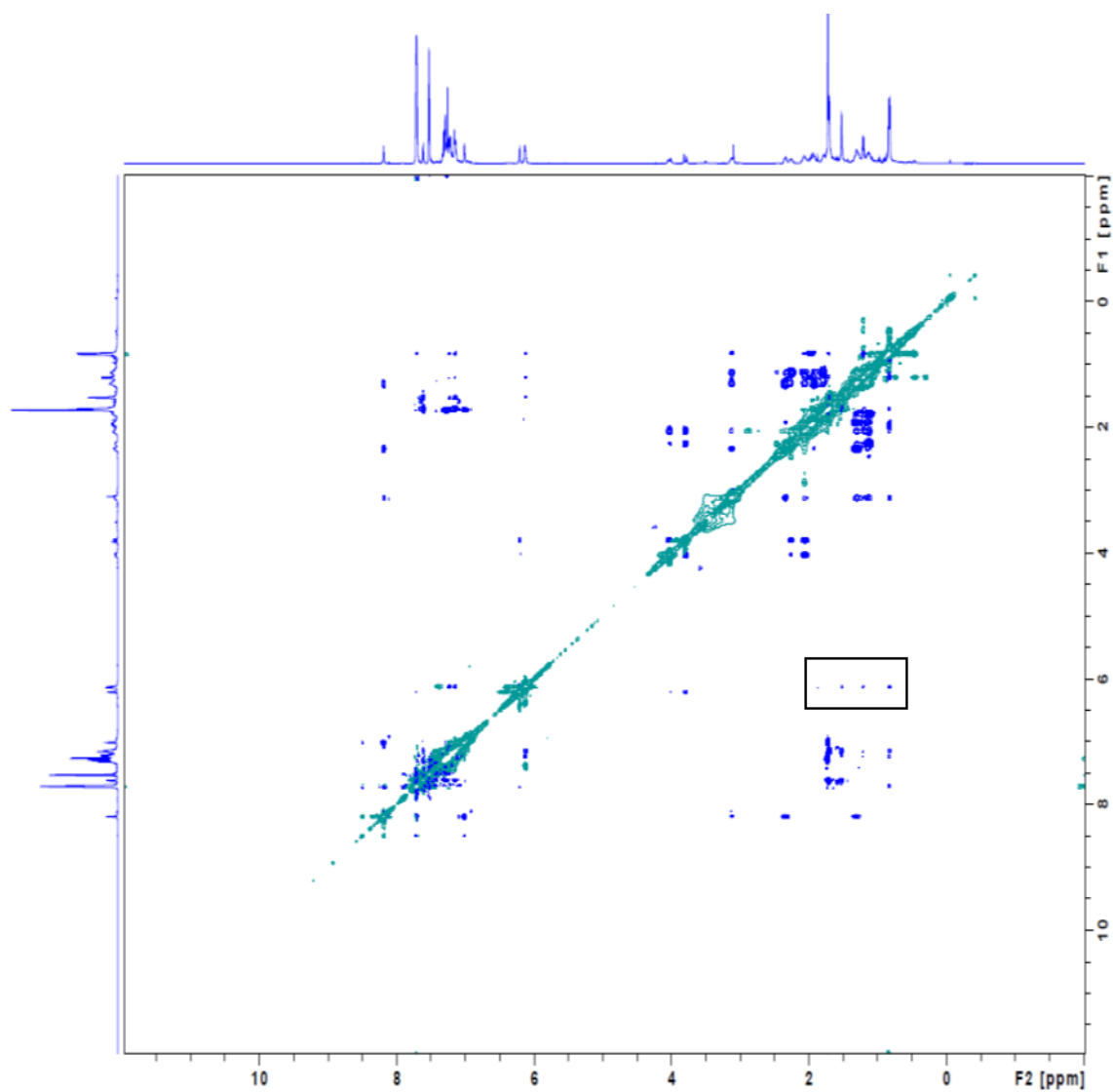


Figure A.47. Nuclear Overhauser Effect spectroscopy (NOESY) NMR spectrum (400 MHz, CDCl₃, 25 °C) of **48b**

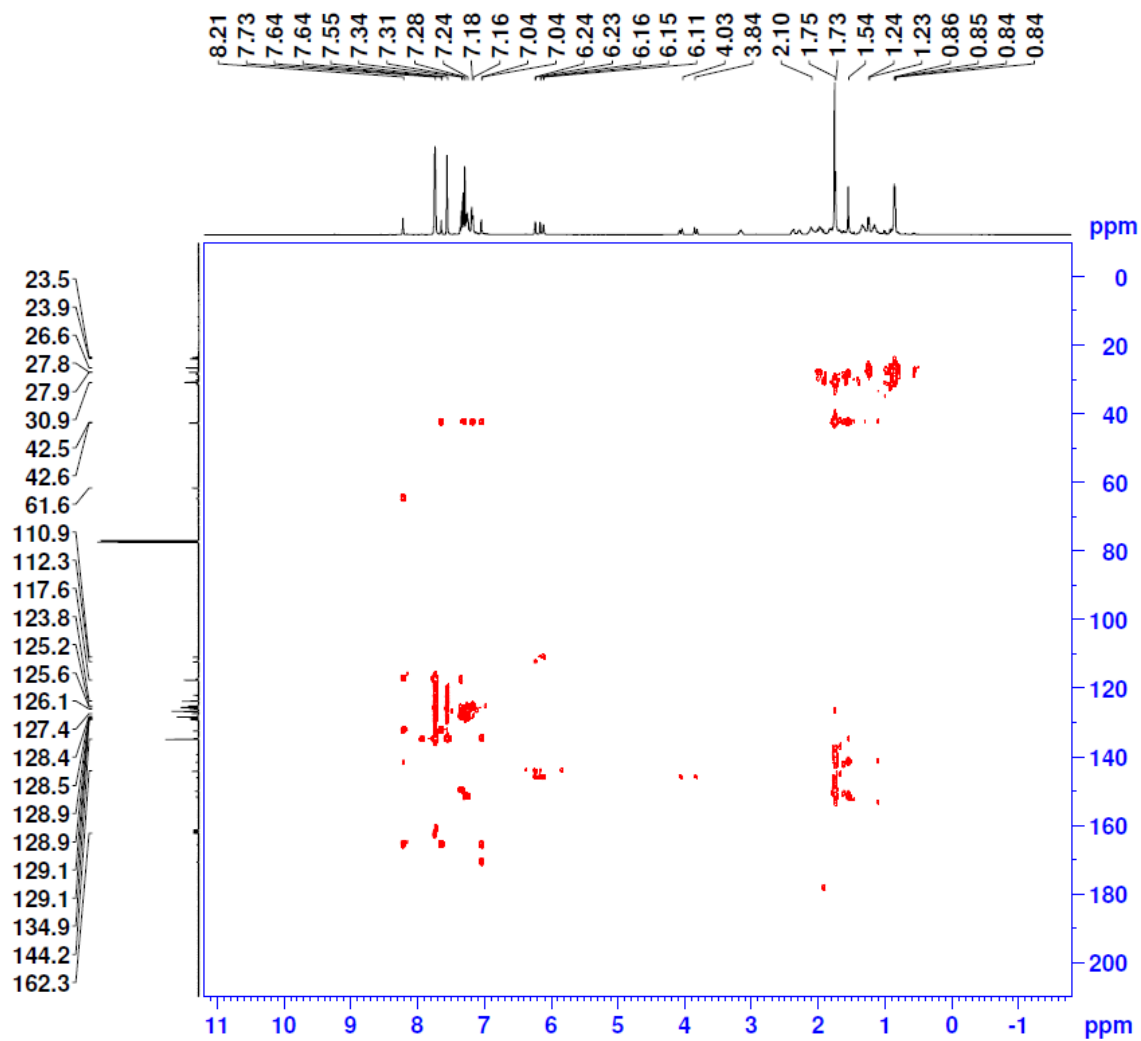


Figure A.48. ¹H-¹³C Heteronuclear Multiple Bond Correlation (HMBC) NMR spectrum (CDCl₃, 25 °C) of **48b**

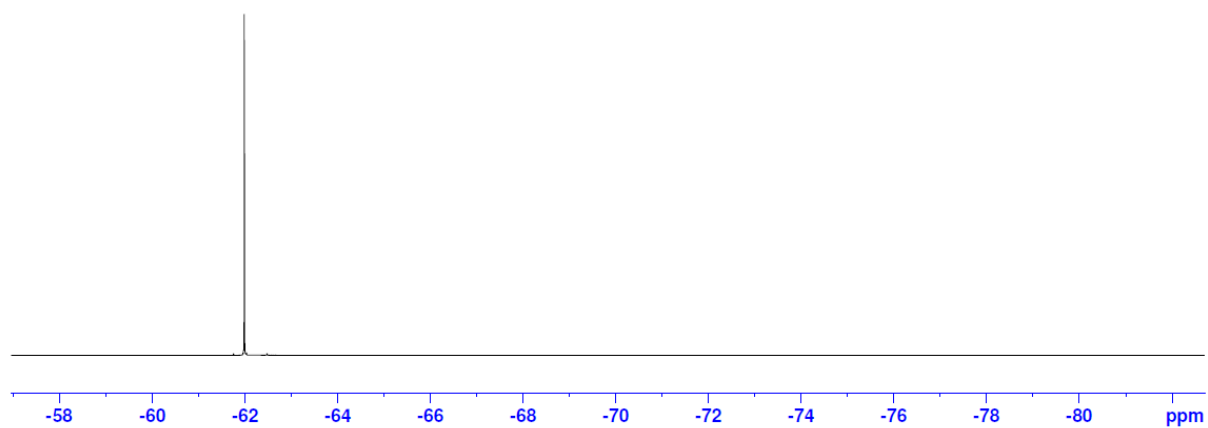


Figure A.49. $^{19}\text{F}\{^1\text{H}\}$ NMR spectrum (282 MHz, CDCl_3 , 25 °C) of **48b**

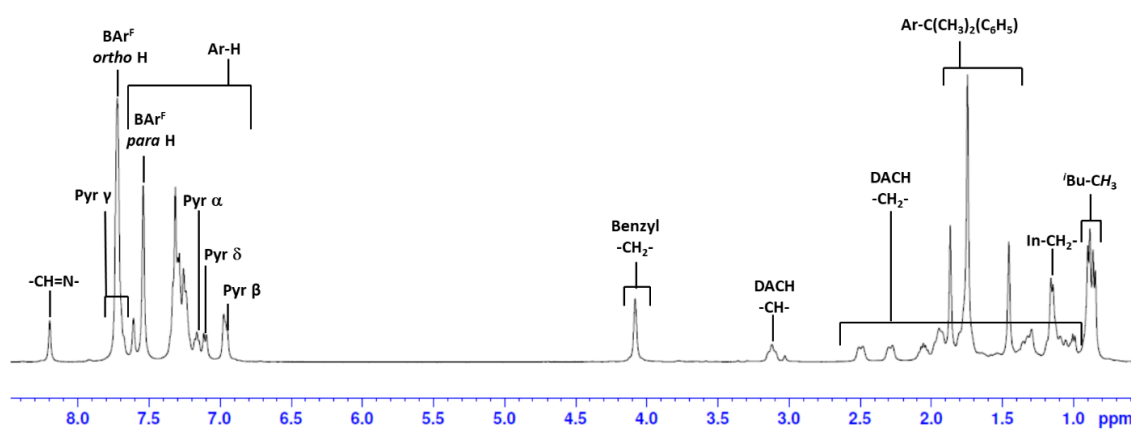


Figure A.50. ^1H NMR spectrum (300 MHz, CDCl_3 , 25 °C) of **48c**

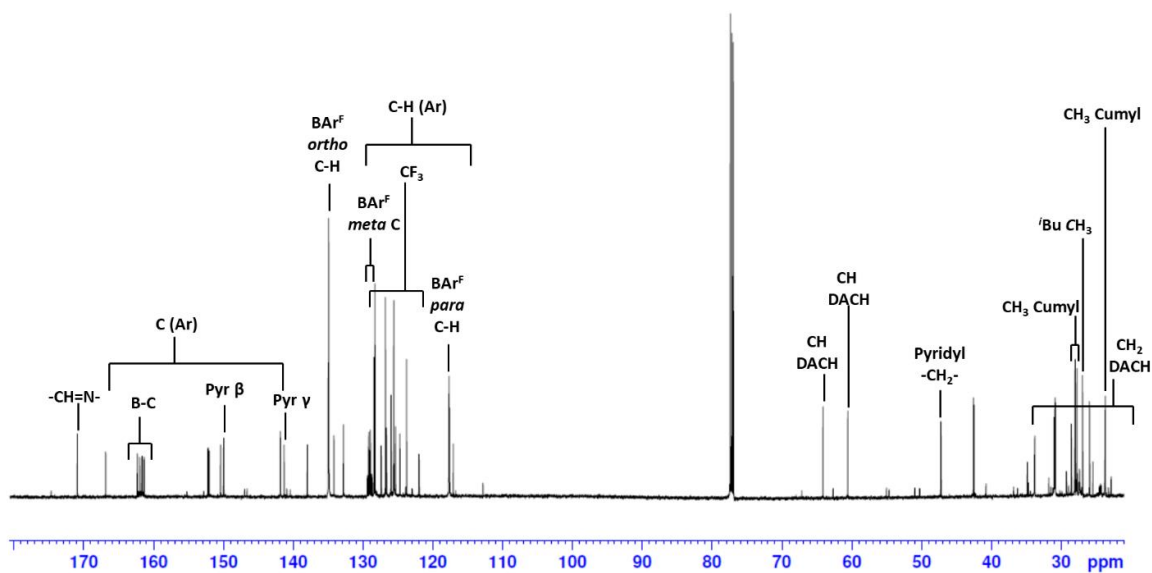


Figure A.51. $^{13}\text{C}\{^1\text{H}\}$ NMR spectrum (151 MHz, CDCl_3 , 25 °C) of **48c**

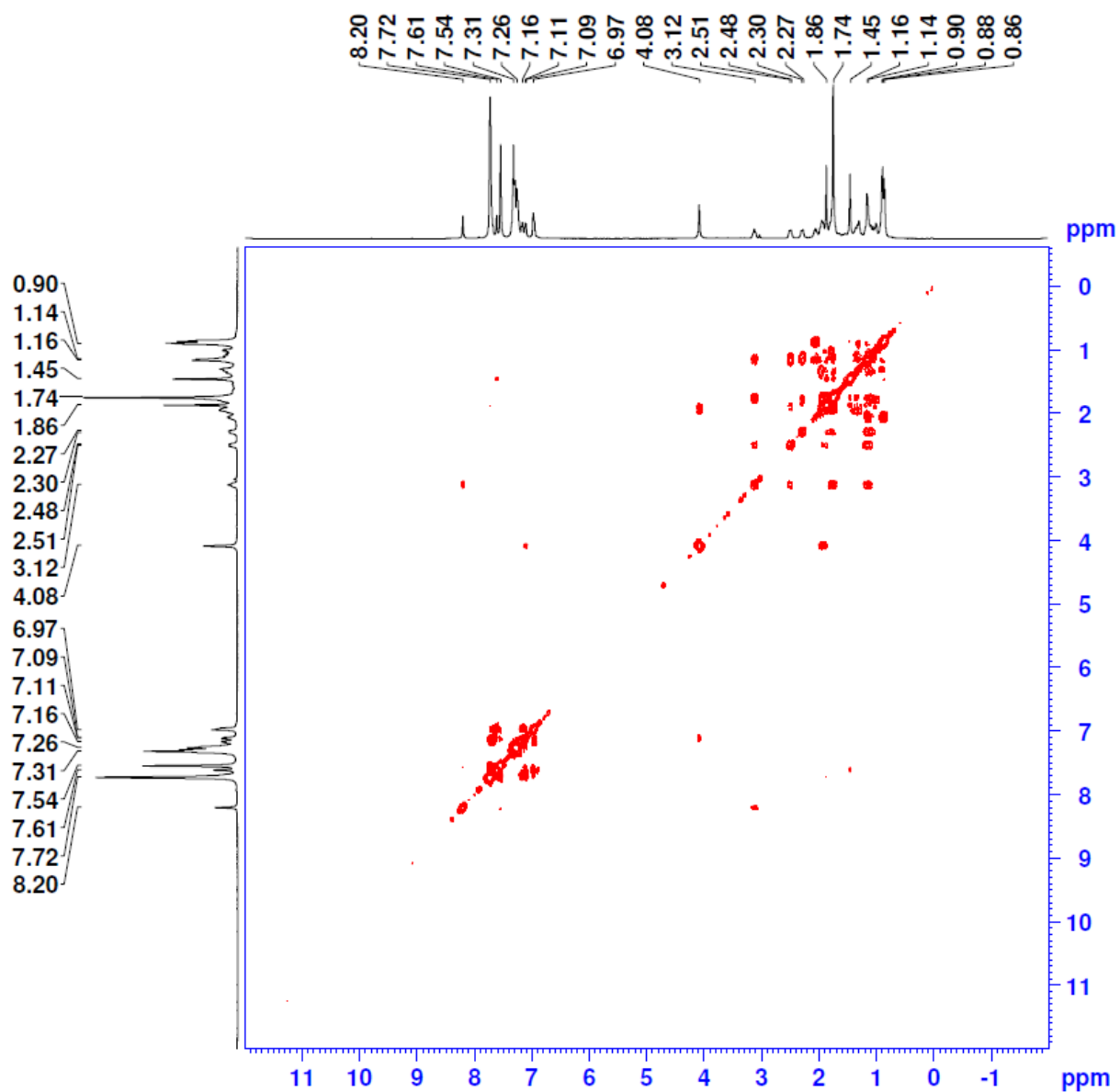


Figure A.52. ^1H - ^1H COSY NMR spectrum (400 MHz, CDCl_3 , 25 $^\circ\text{C}$) of **48c**

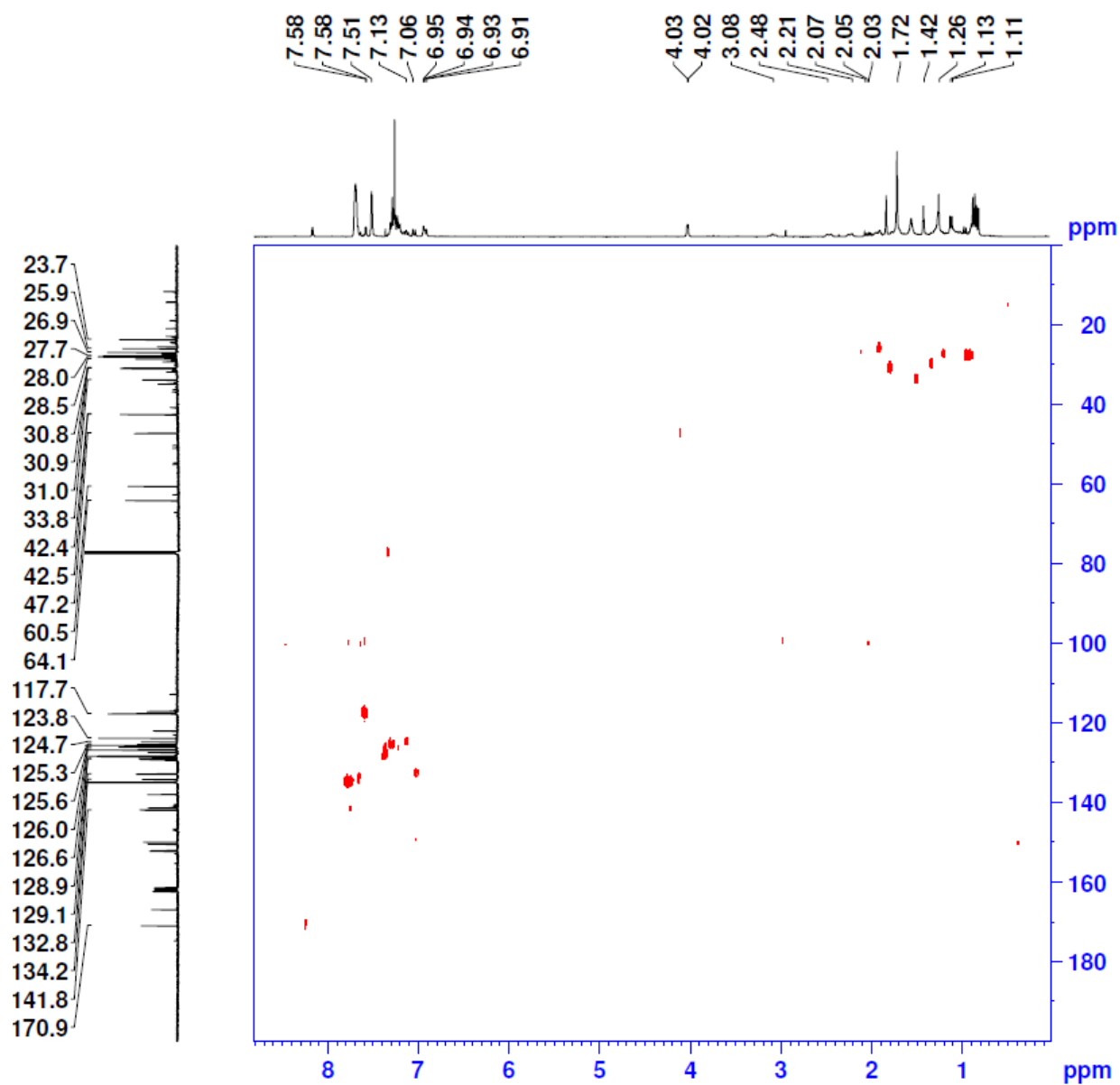


Figure A.53. ^1H - ^{13}C Heteronuclear Single Quantum Coherence (HSQC) NMR spectrum (CDCl_3 , 25 $^\circ\text{C}$) of **48c**

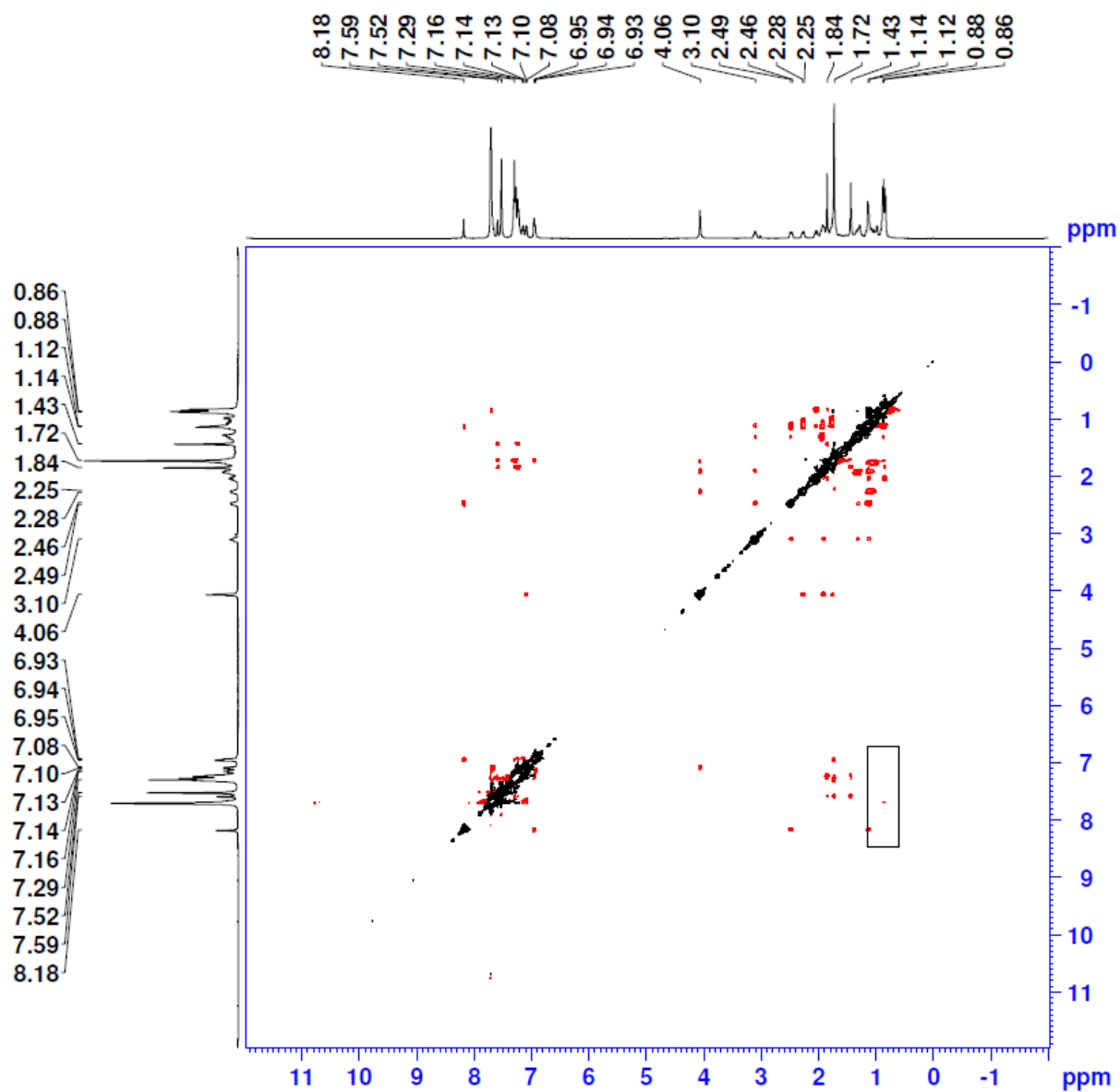


Figure A.54. Nuclear Overhauser Effect spectroscopy (NOESY) NMR spectrum (400 MHz, CDCl_3 , 25 °C) of **48c**

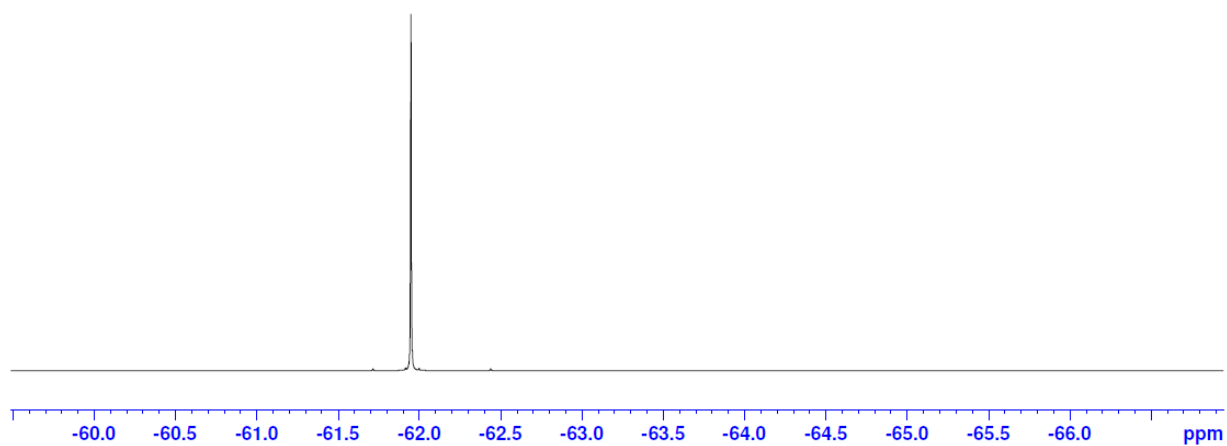


Figure A.55. $^{19}\text{F}\{^1\text{H}\}$ NMR spectrum (282 MHz, CDCl_3 , 25 °C) of **48c**

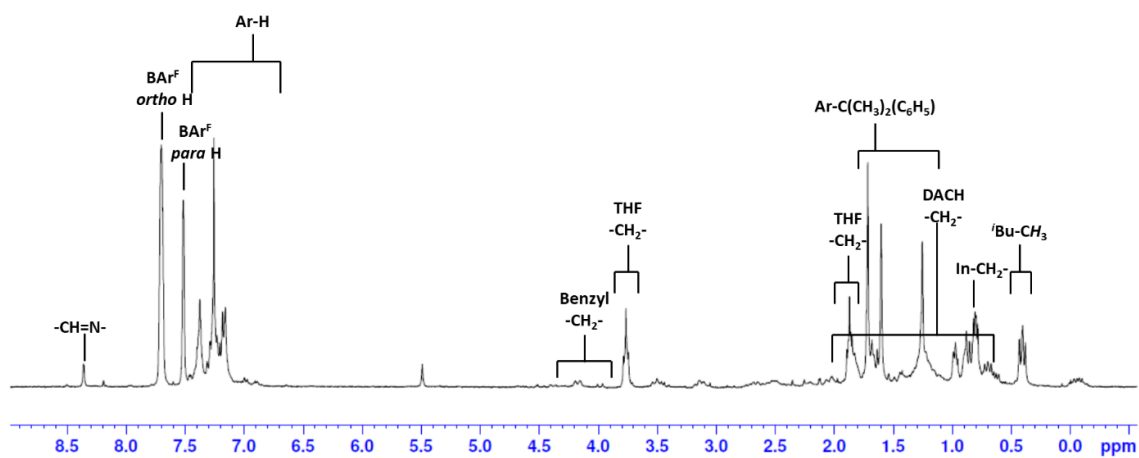
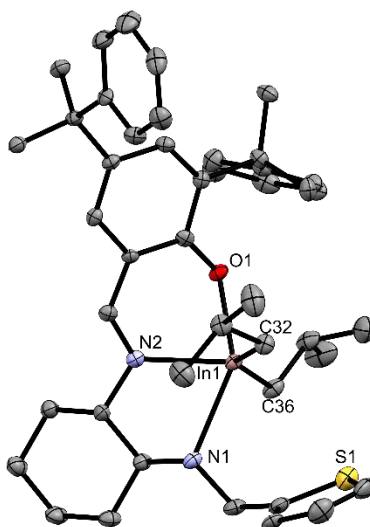
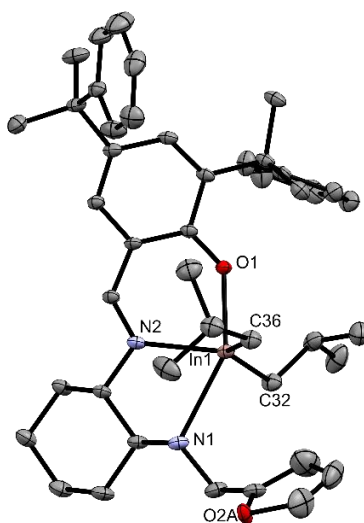


Figure A.56. ^1H NMR spectrum (300 MHz, CDCl_3 , 25 °C) of **48d**



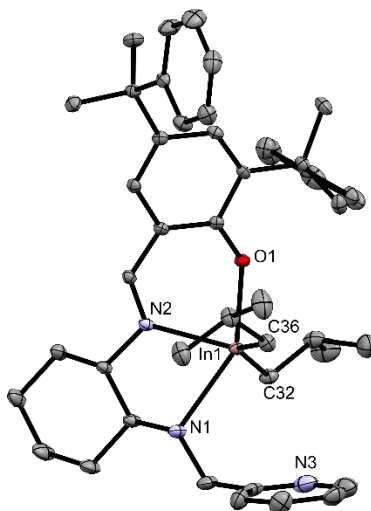
Selected bond distance (Å) and angles (°) for complex 47a				
Bond distances	In1-N1	2.510(3)	In1-C32	2.165(4)
	In1-N2	2.293(3)	In1-C36	2.169(4)
	In1-O1	2.205(3)		
Bond Angles	O1-In1-C32A	98.0(1)	O1-In1-N1	147.4(1)
	O1-In-C36	95.0(1)	N1-In1-C32	99.4(1)
	C32-In1-C36	135.0(2)	N1-In1-C36	91.9(1)
	N1-In1-N2	69.6(1)		

Figure A.57. The molecular structure of complex **47a**. (depicted with thermal ellipsoids at 50% probability and H atoms, as well as solvent molecules omitted for clarity).



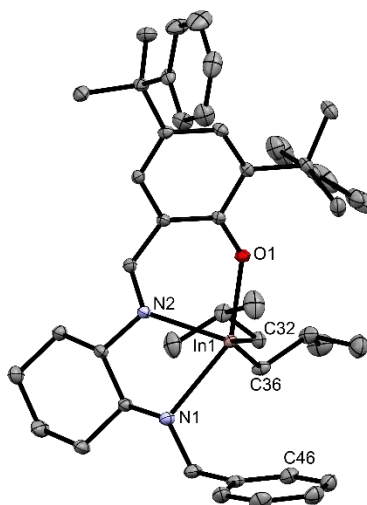
Selected bond distance (Å) and angles (°) for complex 47b				
Bond distances	In1-N1	2.548(1)	In1-C32	2.178(2)
	In1-N2	2.269(2)	In1-C36	2.187(3)
	In1-O1	2.203(1)		
Bond Angles	O1-In1-C32A	94.00(7)	O1-In1-N1	148.60(6)
	O1-In-C36	101.95(8)	N1-In1-C32	90.98(8)
	C32-In1-C36	129.61(9)	N1-In1-C36	98.52(8)
	N1-In1-N2	70.31(6)		

Figure A.58. The molecular structure of complex **47b**. (depicted with thermal ellipsoids at 50% probability and H atoms, minor disorders as well as solvent molecules omitted for clarity).



Selected bond distance (Å) and angles (°) for complex 47c .				
Bond distances	In1-N1	2.510(2)	In1-C32	2.174(2)
	In1-N2	2.286(1)	In1-C36	2.170(2)
	In1-O1	2.209(2)		
Bond Angles	O1-In1-C32A	94.72(7)	O1-In1-N1	148.01(6)
	O1-In-C36	97.68(7)	N1-In1-C32	92.82(7)
	C32-In1-C36	135.39(8)	N1-In1-C36	98.55(7)
	N1-In1-N2	69.95(6)		

Figure A.59. The molecular structure of complex **47c**. (depicted with thermal ellipsoids at 50% probability and H atoms, as well as solvent molecules omitted for clarity).



Selected bond distance (Å) and angles (°) for complex 47d .				
Bond distances	In1-N1	2.516(2)	In1-C32	2.170(1)
	In1-N2	2.286(1)	In1-C36	2.176(1)
	In1-O1	2.206(1)		
Bond Angles	O1-In1-C32A	97.49(5)	O1-In1-N1	148.14(4)
	O1-In-C36	94.38(5)	N1-In1-C32	98.34(5)
	C32-In1-C36	136.55(6)	N1-In1-C36	92.87(5)
	N1-In1-N2	69.81(4)		

Figure A.60. The molecular structure of complex **47d**. (depicted with thermal ellipsoids at 50% probability and H atoms, as well as solvent molecules omitted for clarity).

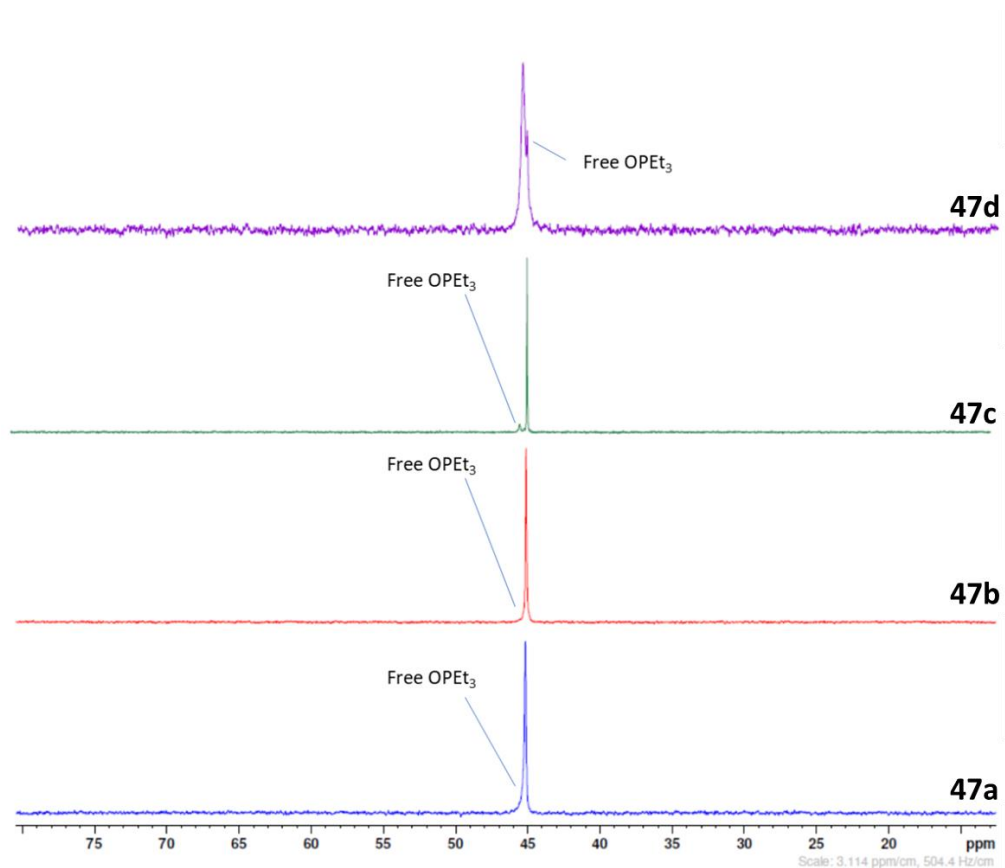


Figure A.61. $^{31}\text{P}\{^1\text{H}\}$ NMR spectra (162 MHz, C_6D_6 , 25 °C) of **47a**, **47b**, **47c**, and **47d** after the addition of 0.8 equivalents of OPEt_3 . The free triethylphosphine oxide shift is determined by the addition of a capillary inside the NMR tube containing a solution of triethylphosphine oxide in C_6D_6 .

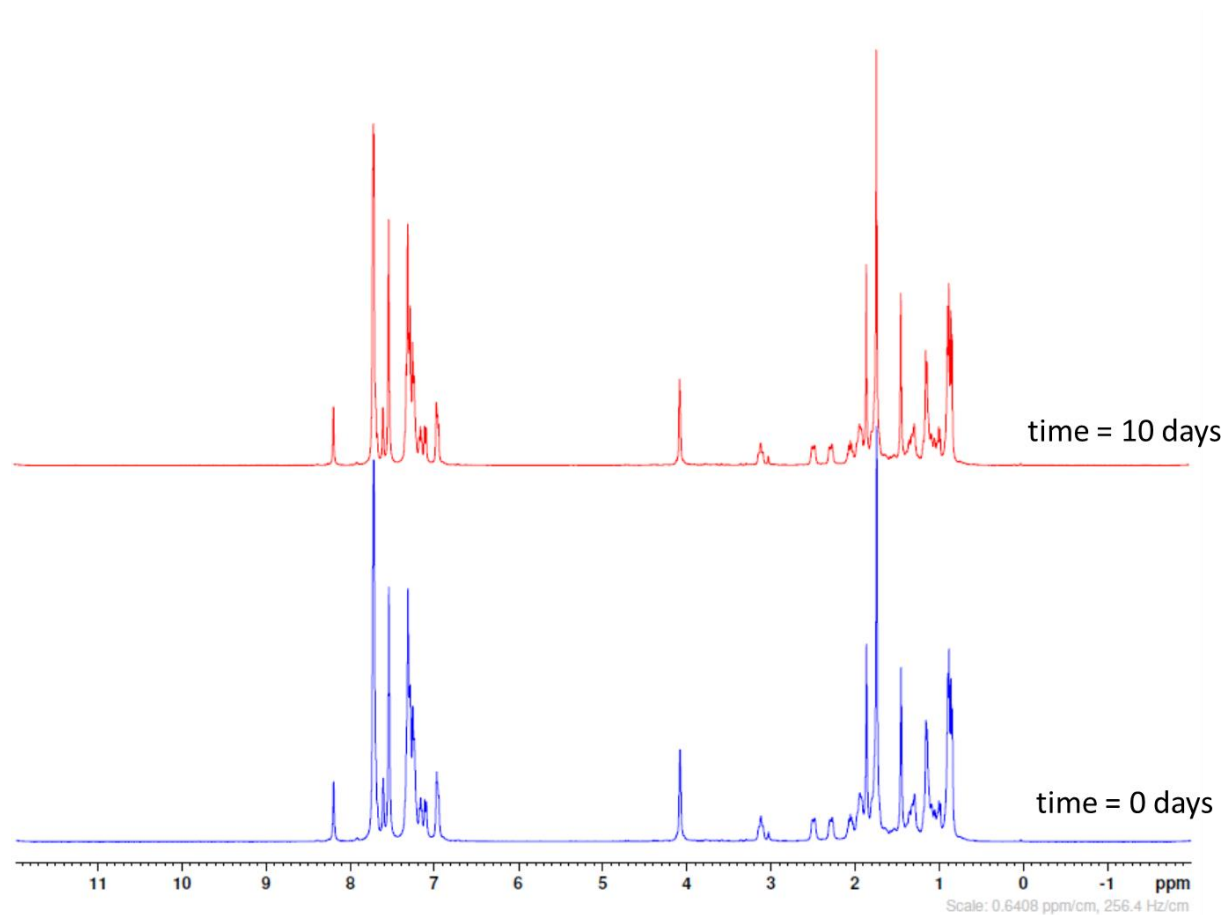


Figure A.62. ^1H NMR spectra of **48c** before (time = 0 days) and after (time = 10 days) exposure to air for 10 days continuously. No significant changes were observed.

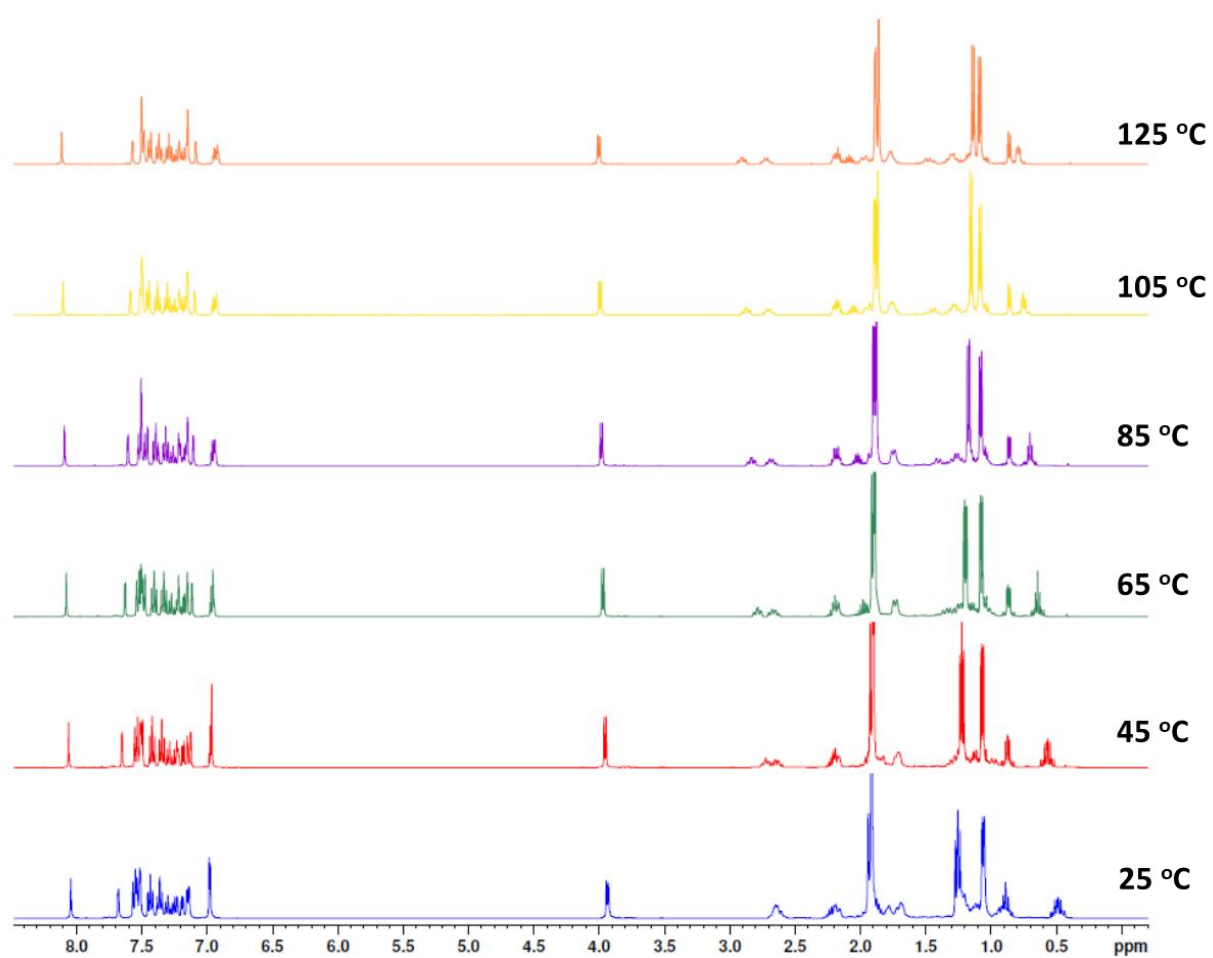


Figure A.63. Variable temperature (VT) ¹H NMR spectra (400 MHz, C₆D₅Br, 25 to 125 °C) of **47a**. Shifts observed were reversible. C₆D₅Br is taken as a reference.

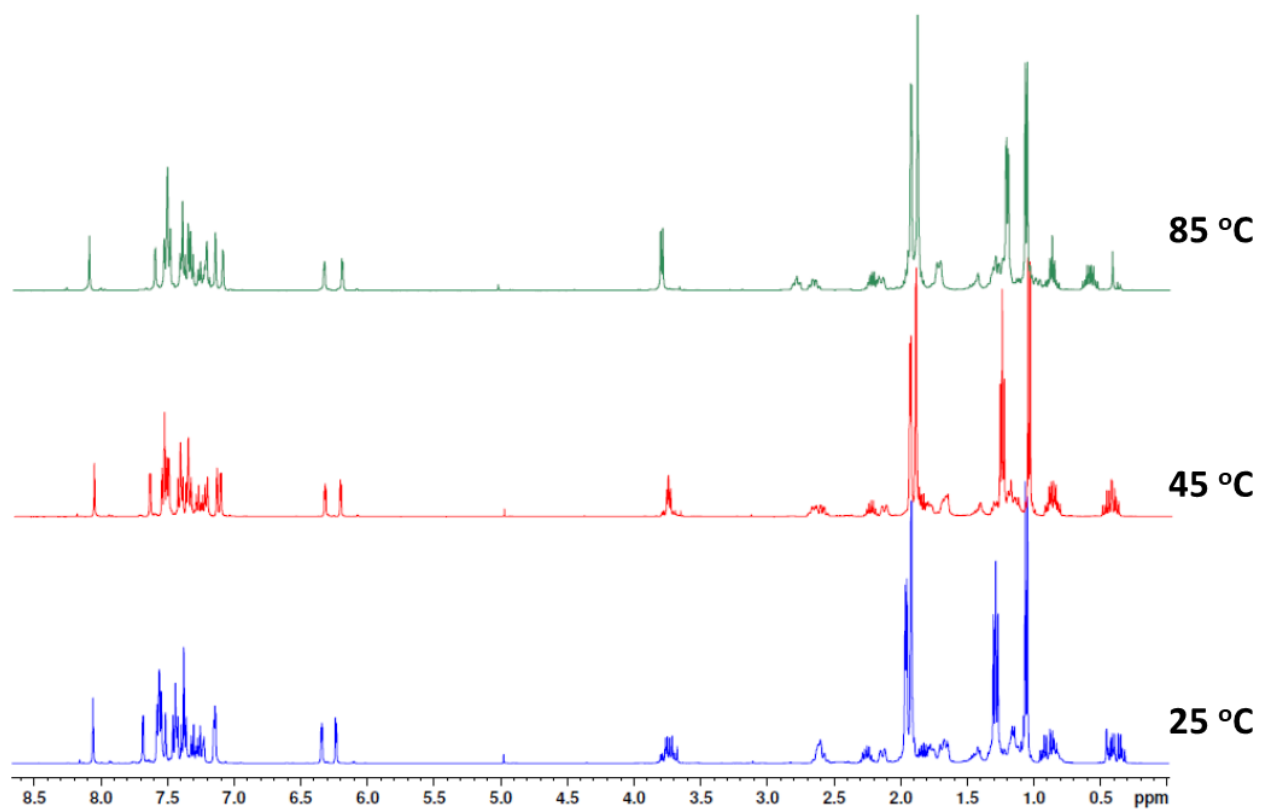


Figure A.64. Variable temperature (VT) ¹H NMR spectra (400 MHz, C₆D₅Br, 25 to 85 °C) of **47b**. Shifts observed were reversible. C₆D₅Br is taken as a reference.

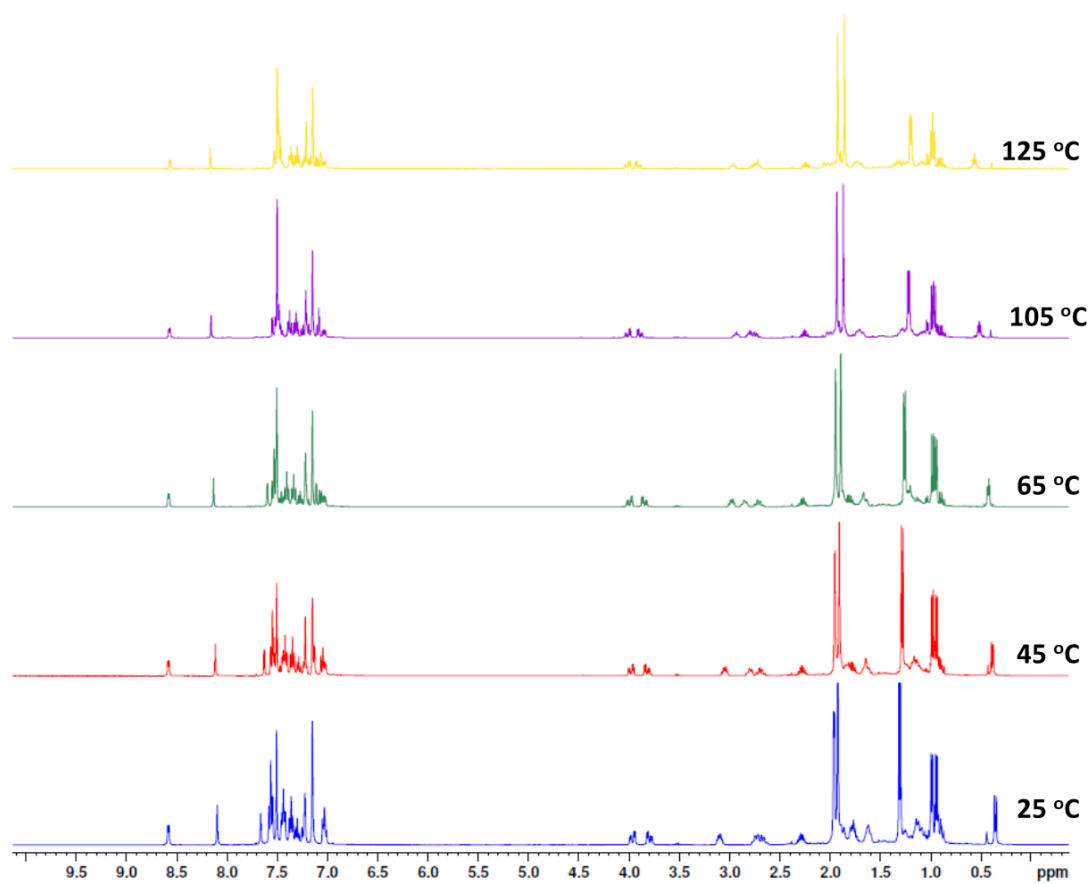


Figure A.65. Variable temperature (VT) ¹H NMR spectra (400 MHz, C₆D₅Br, 25 to 85 °C) of **47c**. Shifts observed were reversible. C₆D₅Br is taken as a reference.

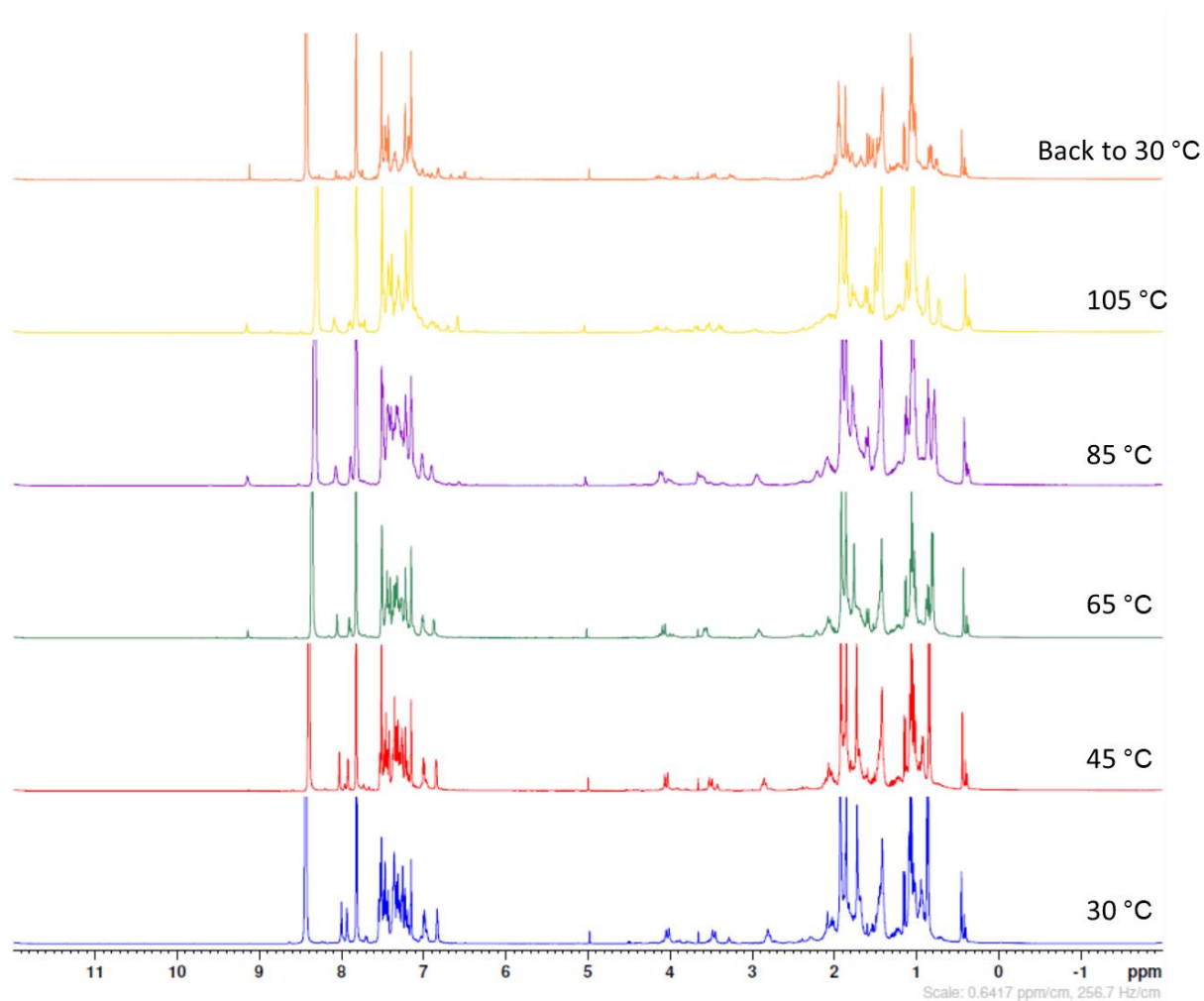


Figure A.66. Variable temperature (VT) ¹H NMR spectra (400 MHz, C₆D₅Br, 30 to 105 °C) of **48a**. Shifts observed were irreversible. C₆D₅Br is taken as a reference.

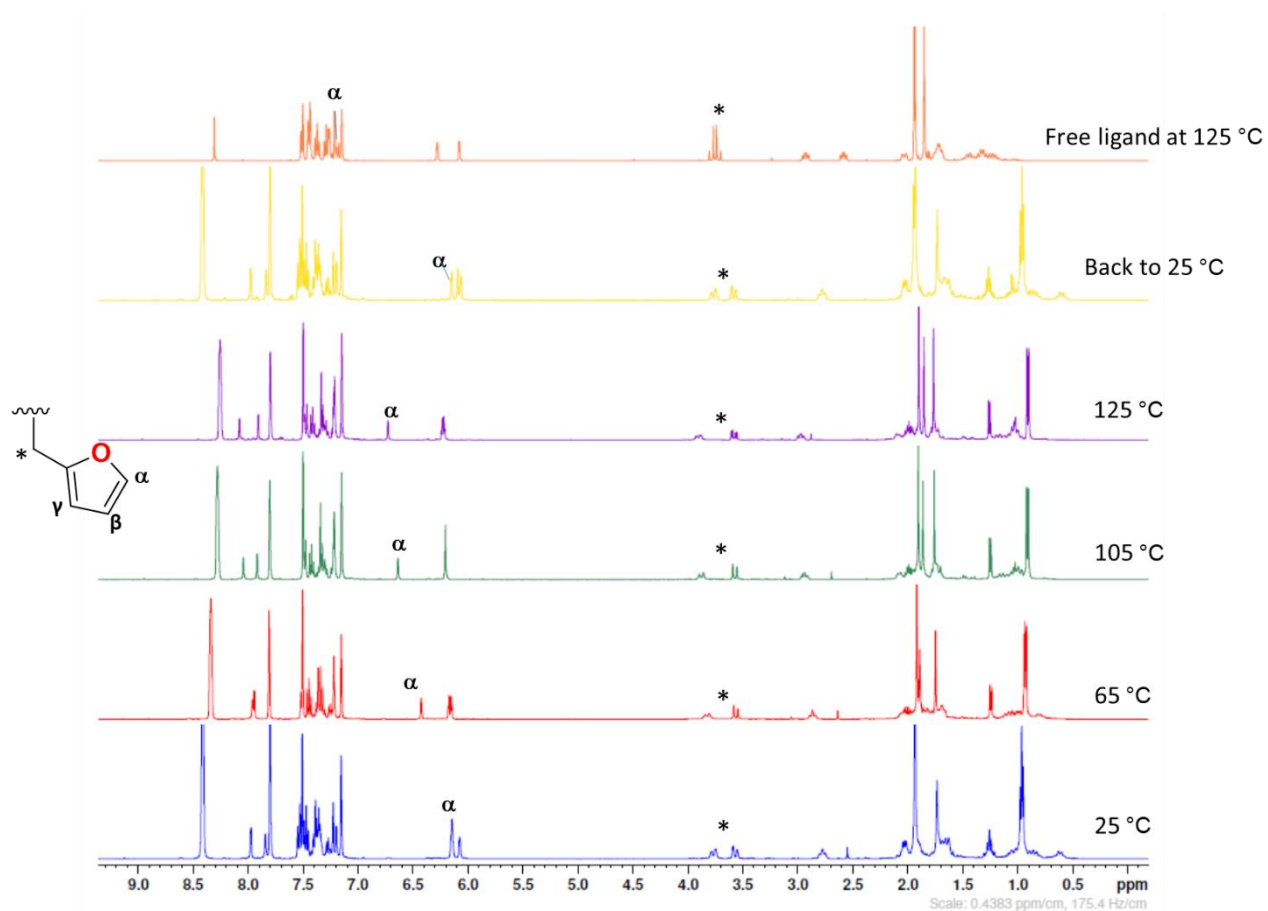


Figure A.67. Variable temperature (VT) ^1H NMR spectra (400 MHz, $\text{C}_6\text{D}_5\text{Br}$, 25 to 125 °C) of **48b** free ligand **L_b**.

Shifts observed were reversible. $\text{C}_6\text{D}_5\text{Br}$ is taken as a reference.

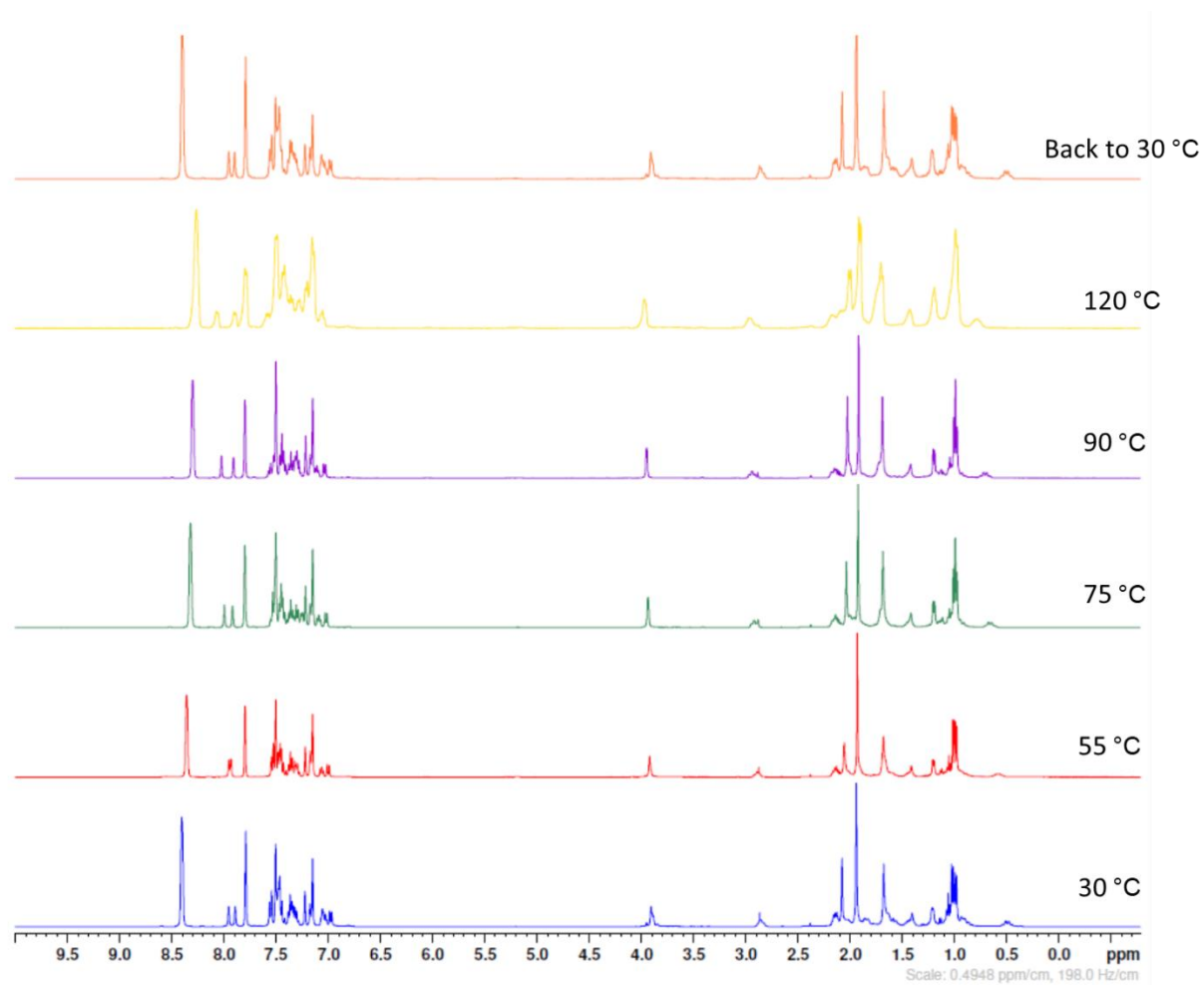
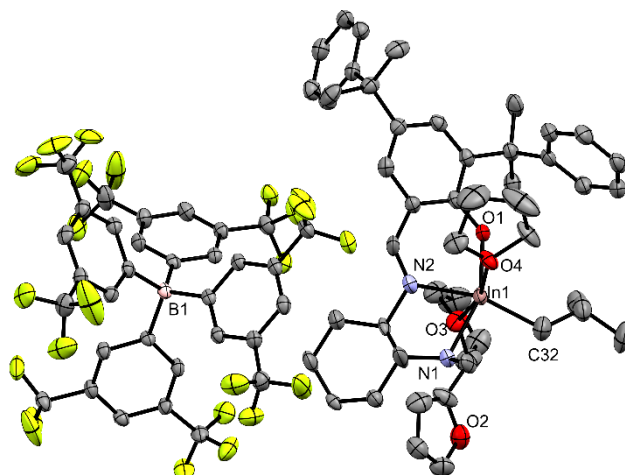


Figure A.68. Variable temperature (VT) ^1H NMR spectra (400 MHz, $\text{C}_6\text{D}_5\text{Br}$, 30 to 120 °C) of **48c**. Shifts observed were reversible. $\text{C}_6\text{D}_5\text{Br}$ is taken as a reference.



Selected bond distance (Å) and angles (°) for complex 48b.2THF				
Bond distances	In1-N1	2.468(5)	In1-O3	2.392(4)
	In1-N2	2.179(5)	In1-O4	2.354(4)
	In1-O1	2.127(3)	In1-C32	2.128(7)
Bond Angles	O1-In1-C32	112.9(2)	O1-In1-N1	156.3(1)
	O3-In1-O4	166.3(1)	N1-In1-C32	90.4(2)
	N1-In1-N2	72.9(2)		

Figure A.69. Molecular structures of complex **48b.2THF** (depicted with thermal ellipsoids at 50% probability and H atoms, minor disorders as well as solvent molecules omitted for clarity)

Table A.1. Selective crystal data for **47b**, **47d**, **47a**, **47c** and **48b.2THF**

	1b	1d	1a	1c	2b.2THF
empirical formula	C ₄₄ H ₅₉ In N ₂ O ₂	C ₄₆ H ₆₁ In N ₂ O	C ₄₄ H ₅₉ In N ₂ O S	C ₄₅ H ₆₀ In N ₃ O	C ₈₈ H ₉₂ B F ₂₄ In N ₂ O ₆
Fw	762.75	772.78	778.81	773.78	1855.26
<i>T</i> (K)	296.15	273(2)	100	296.15	100
<i>a</i> (Å)	17.5732(15)	18.4020(6)	18.3672(15)	18.3804(16)	12.616(3)
<i>b</i> (Å)	13.8493(11)	13.9008(5)	14.0583(12)	13.9887(12)	13.343(3)
<i>c</i> (Å)	18.4226(15)	18.4542(7)	17.9736(14)	18.328(2)	26.255(5)
α (deg)	90	90	90	90	80.163(3)
β (deg)	117.891(2)	119.051(2)	118.8140(10)	119.839(2)	76.369(3)
γ (deg)	90	90	90	90	85.869(3)
volume (Å ³)	3962.81	4126.72	4066.39	4087.71	4229.90
<i>Z</i>	4	4	4	4	2
cryst syst	monoclinic	monoclinic	monoclinic	monoclinic	triclinic
space group	<i>P</i> 2 ₁ / <i>c</i>	<i>P</i> 2 ₁ / <i>n</i>	<i>P</i> 2 ₁ / <i>c</i>	<i>P</i> 2 ₁ / <i>c</i>	<i>P</i> -1
<i>d</i> _{calc} (g/cm ³)	1.278	1.244	1.272	1.257	1.457
μ (Mo K α) (cm ⁻¹)	6.34	6.08	6.67	6.14	3.87
2 θ _{max} (deg)	61.3	61.2	55.8	61.0	54.6
absor corr (<i>T</i> _{min} , <i>T</i> _{max})	0.7005, 0.7461	0.909, 0.986	0.982, 0.997	0.6730, 0.7461	0.9887, 0.9977
total no. of reflns	63957	65464	9204	56696	18759
no. of indep reflns (<i>R</i> _{int})	12154 (0.0394)	12665 (0.0445)	9204 (0.0890)	12417 (0.0461)	18759(0.1605)
residuals (refined on <i>F</i> ²): <i>R</i> ₁ ^a ; <i>wR</i> ₂	0.0523, 0.0887	0.0354, 0.0634	0.0773, 0.1436	0.0465, 0.0808	0.0983, 0.2141
GOF	1.023	1.032	1.067	1.094	1.036
no. obsrvns [<i>I</i> > 2 σ (<i>I</i>)]	9858	9908	9510	9643	9841
residuals (refined on <i>F</i> ² : <i>R</i> ₁ ^a ; <i>wR</i> ₂ ^b)	0.0524, 0.0802	0.0273, 0.0600	0.0550, 0.1339	0.0373, 0.0772	0.0794, 0.2047

$$^a R_1 = \Sigma ||F_o| - |F_c|| / \Sigma |F_o|, ^b wR_2 = [\Sigma (w (F_o^2 - F_c^2)^2) / \Sigma w(F_o^2)_2]^{1/2}$$

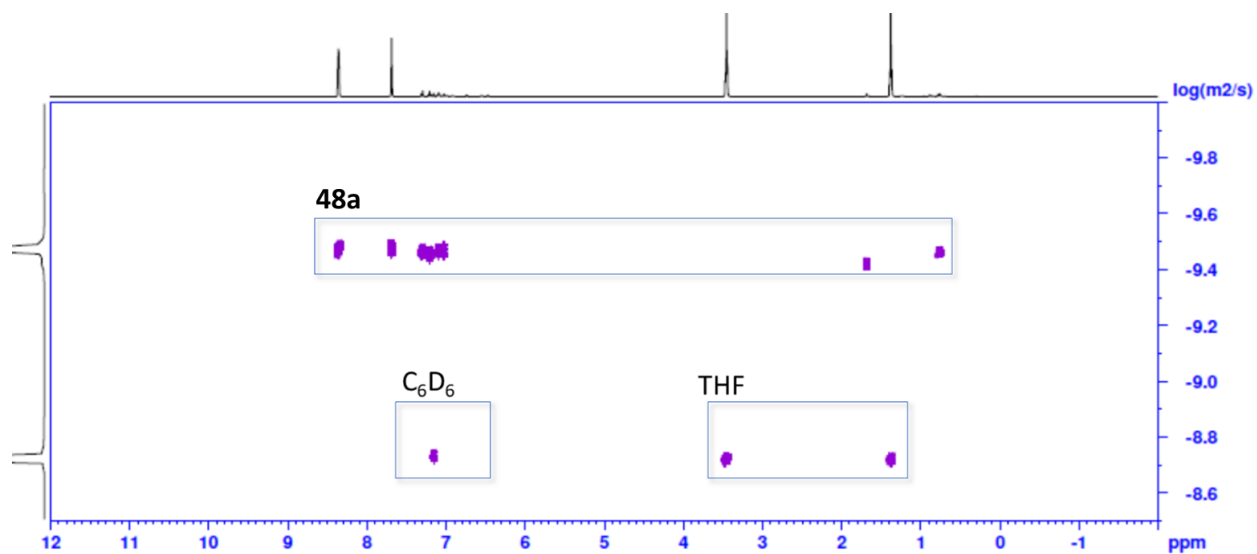


Figure A.70. DOSY-NMR of the mixture of THF and **48a** (400MHz, $\Delta = 1.2$ s, $\delta = 400$ μ s, C_6D_6 , 25 $^{\circ}C$).

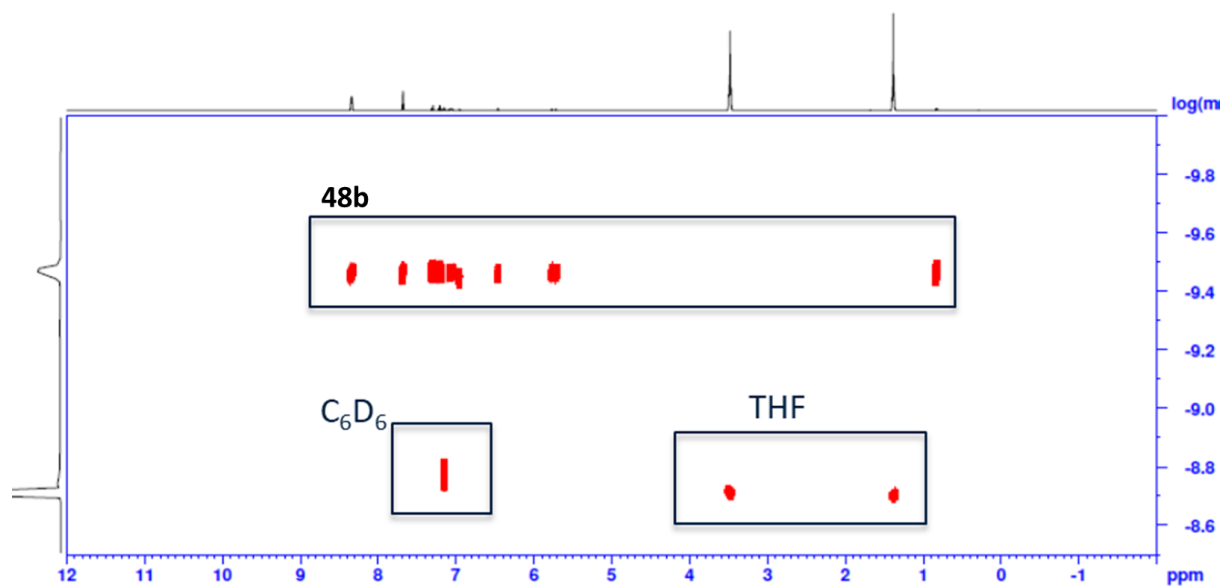


Figure A.71. DOSY-NMR of the mixture of THF and **48b** (400MHz, $\Delta = 1.2$ s, $\delta = 400$ μ s, C_6D_6 , 25 $^{\circ}C$).

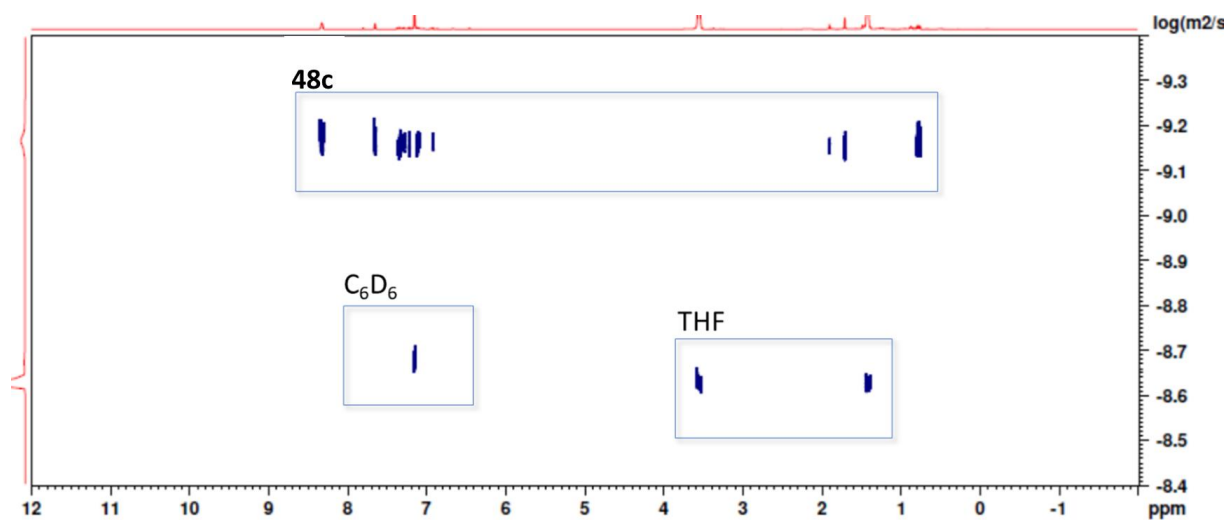


Figure A.72. DOSY-NMR of the mixture of THF and **48c** (400MHz, $\Delta = 0.55$ s, $\delta = 400$ μ s, C₆D₆, 25 °C).

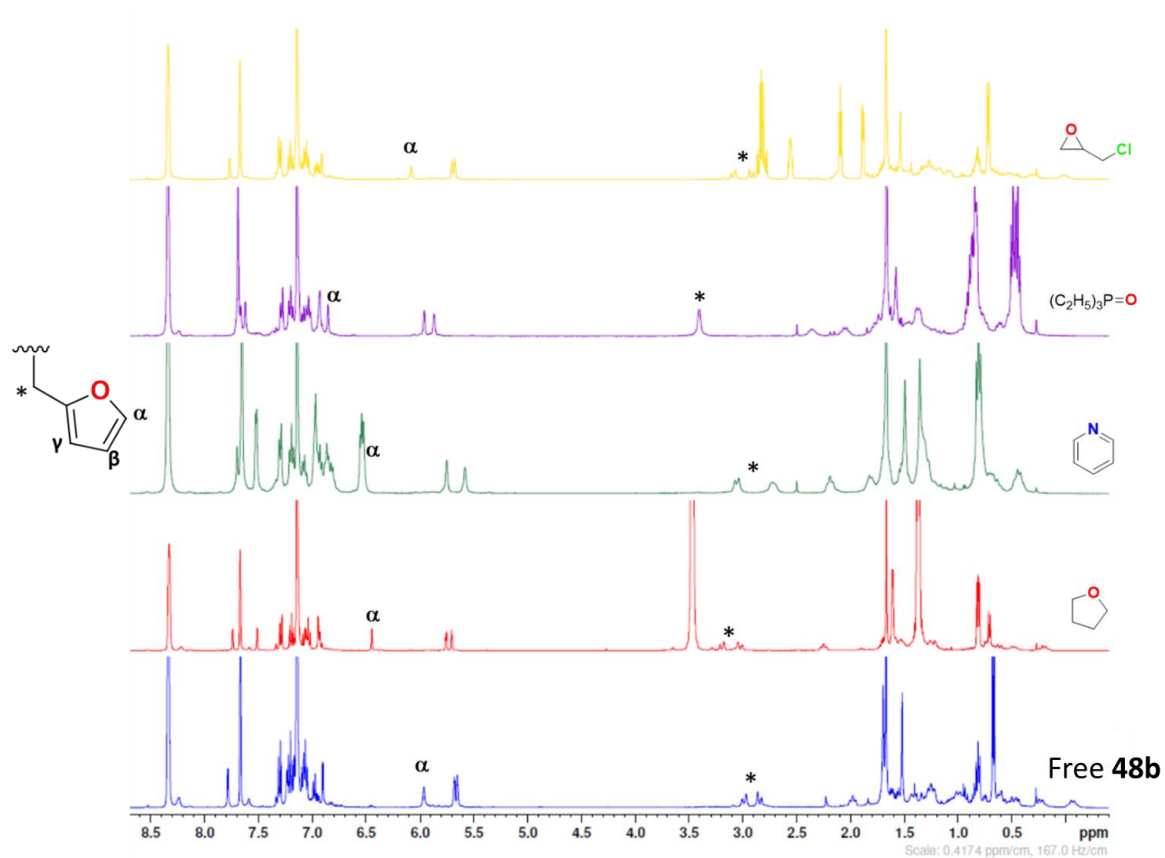


Figure A.73. ^1H NMR of spectra of **48b** in the presence of THF, pyridine, triethylphosphine oxide and epichlorohydrin (400 MHz in C_6D_6 at 25 $^\circ\text{C}$).

Appendix B - Data associated with Chapter 3.

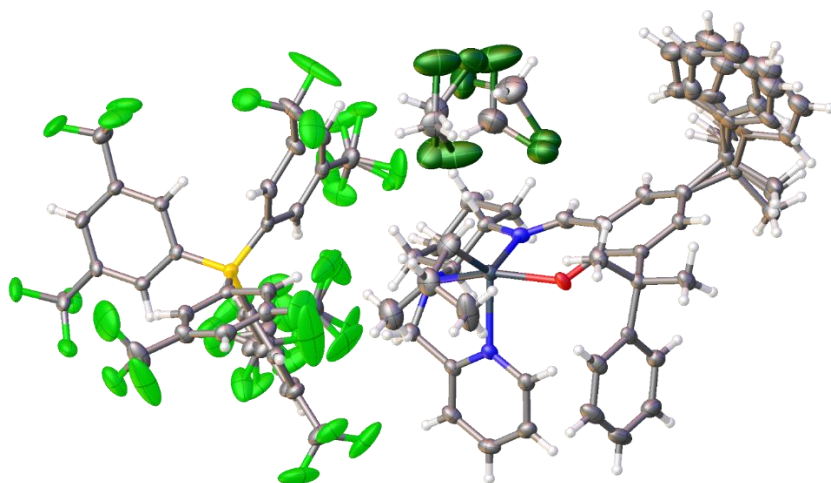
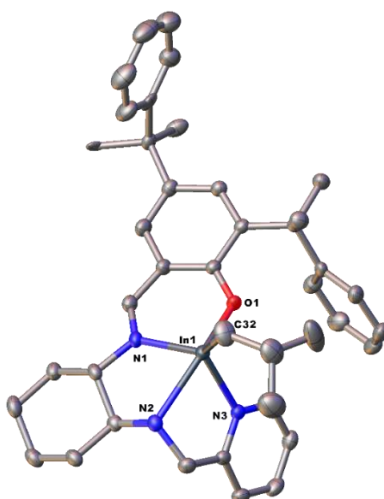


Figure B.1. Asymmetric unit of complex **48c**. Material crystallizes in P-1 and is disordered



Bond Distances	In1-N1	2.193(2)	In1-N3	2.252(2)
	In1-N2	2.390(2)	In1-C32	2.154(3)
	In1-O1	2.1093(18)		
Bond Angles	O1-In1-C32	107.92(12)	O1-In1-N3	88.64(8)
	O1-In1-N1	85.44(8)	N2-In1-C32	103.81(12)
	N1-In1-N2	74.60(8)	N3-In1-C32	122.74(12)
	N2-In1-N3	72.65(8)	O1-In1-N2	148.22(8)
			N1-In1-N3	103.23(8)

Figure B.2. Molecular structure of the cation of complex **48c** (depicted with thermal ellipsoids at 50% probability and H atoms, BARF_{24} counterion, solvent molecules, as well as minor disorders omitted for clarity)

Table B.1. Crystal data for complex **48c**

	48c
empirical formula	C _{74.58} H _{66.22} BCl _{3.25} F _{24.09} InN ₃ O
Fw	1718.96
<i>T</i> (K)	273.15
<i>a</i> (Å)	12.7732(14)
<i>b</i> (Å)	13.1111(14)
<i>c</i> (Å)	22.821(2)
α (deg)	90.294(2)
β (deg)	92.587(2)
γ (deg)	93.439(2)
volume (Å ³)	3810.9(7)
<i>Z</i>	2
cryst syst	triclinic
space group	P-1
<i>d</i> _{calc} (g/cm ³)	1.498
μ (Mo K α) (cm ⁻¹)	0.528
2 θ _{max} (deg)	58.34
absor corr (<i>T</i> _{min} , <i>T</i> _{max})	0.7005, 0.7461
total no. of reflns	20636
no. of indep reflns (<i>R</i> _{int})	20636 (0.0394)
Data/restraints/parameters	20636/1785/1262
residuals (refined on <i>F</i> ²): <i>R</i> ₁ ; <i>wR</i> ₂	0.0842, 0.1424
GOF	1.125
no. obsrvns [<i>I</i> > 2 σ (<i>I</i>)]	9858
residuals (refined on <i>F</i> ² : <i>R</i> ₁ ^{<i>a</i>} ; <i>wR</i> ₂ ^{<i>b</i>})	0.0560, 0.1424
^{<i>a</i>} <i>R</i> ₁ = $\Sigma F_o - F_c / \Sigma F_o $, ^{<i>b</i>} <i>wR</i> ₂ = $[\Sigma (w(F_o^2 - F_c^2))^2 / \Sigma w(F_o^2)_2]^{1/2}$	

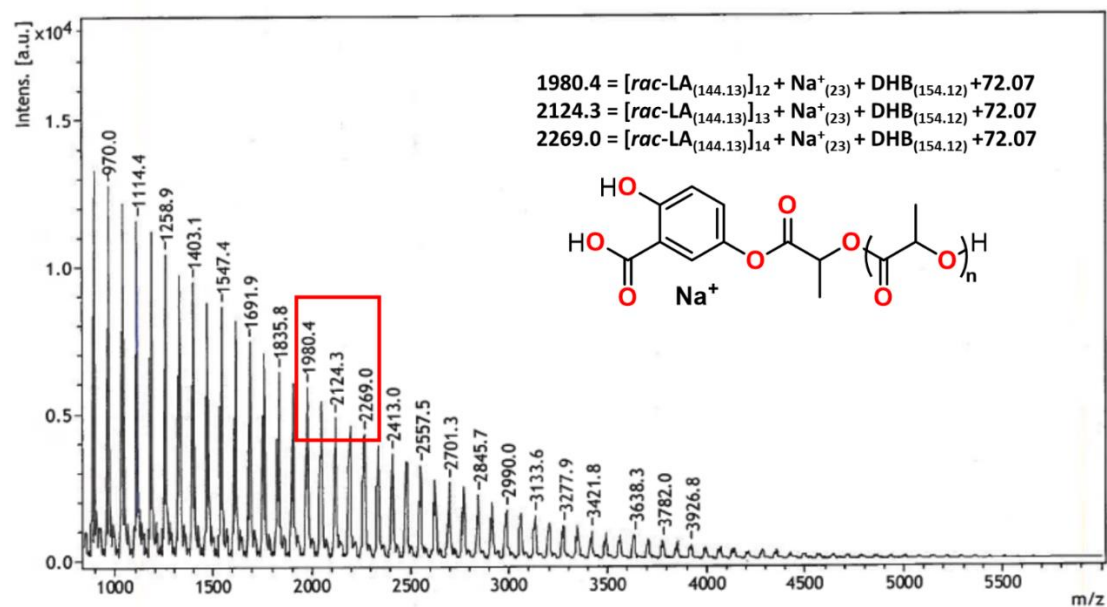


Figure B.3. MALDI-TOF spectrum of c-PLA isolated from polymerization of 50 equivalents of *rac*-LA with **48c** in toluene at 100 °C for 24 hours (Table 3.1, entry 1)

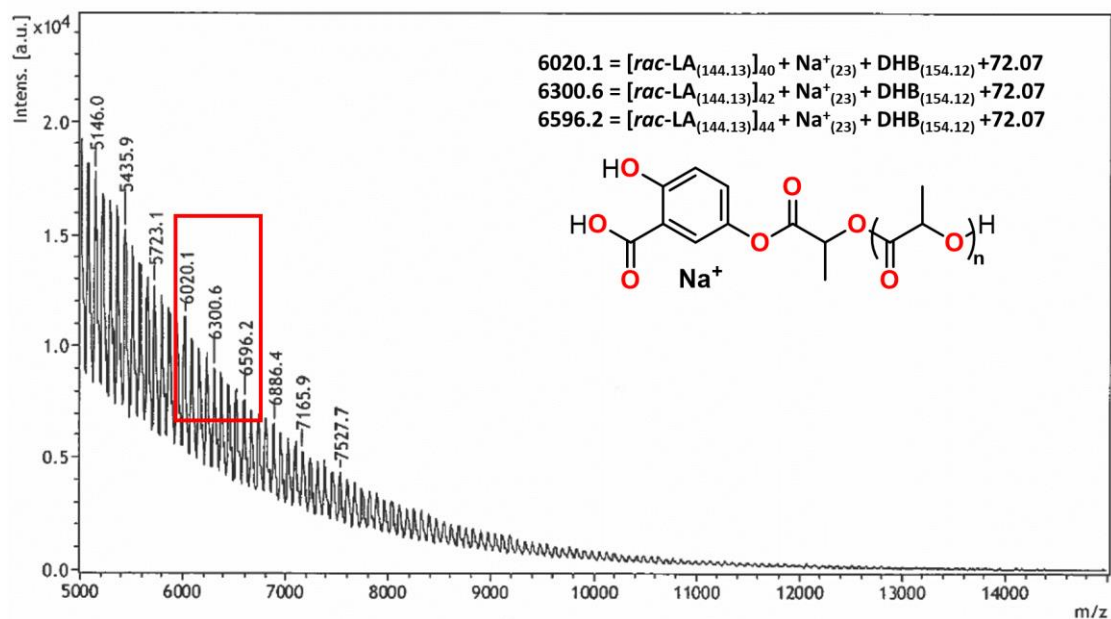


Figure B.4. High molecular weight fraction MALDI-TOF spectrum of c-PLA isolated from polymerization of 50 equivalents of *rac*-LA with **1** in toluene at 100 °C for 24 hours (Table 3.1, entry 1)

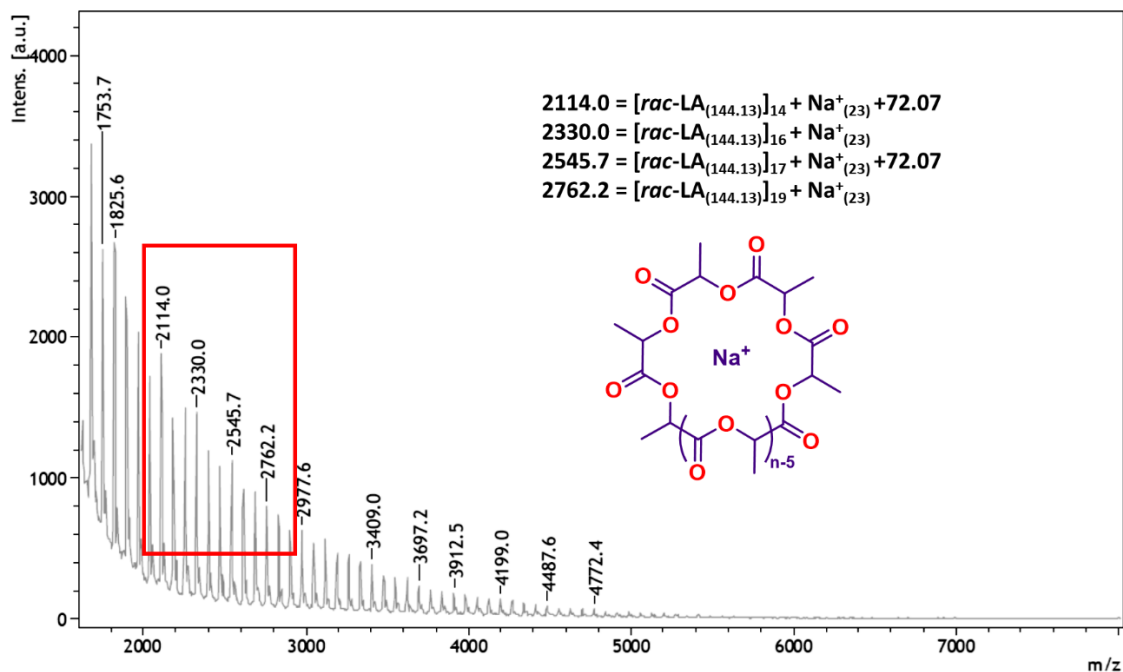


Figure B.5. MALDI-TOF spectrum of c-PLA (Table 3.1, entry 4)

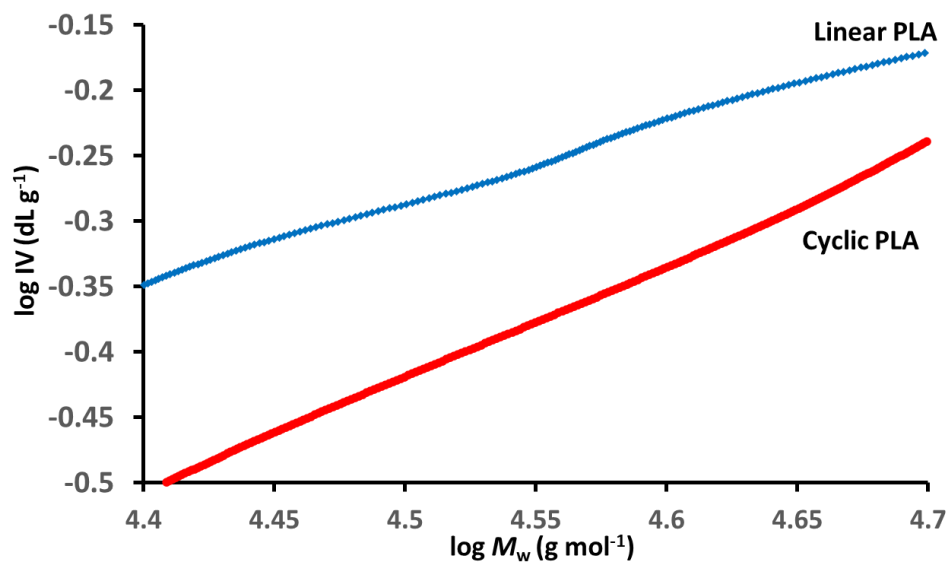


Figure B.6. Mark-Houwink plots for c-PLA (Table 3.1, entry 1) and linear PLA (Table B.2, entry 1)

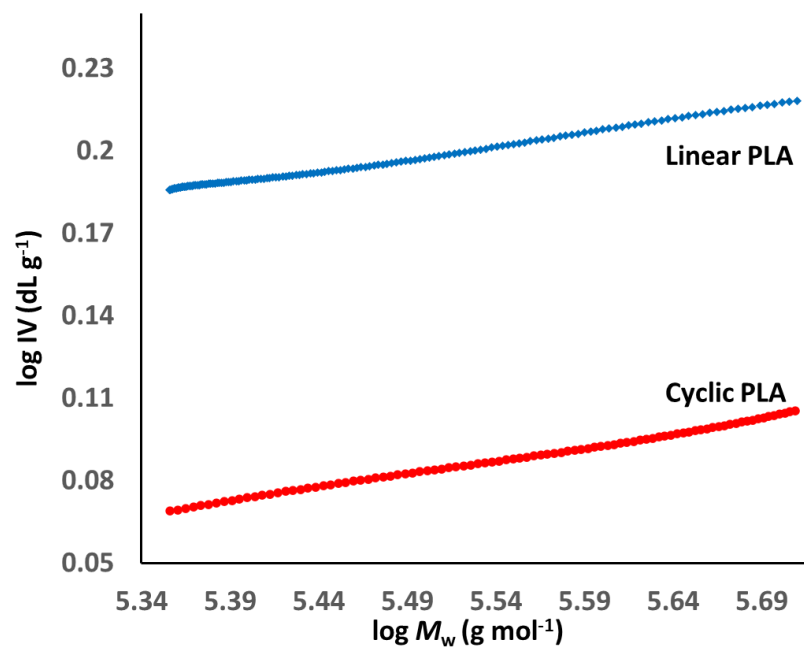


Figure B.7. Mark-Houwink plots for high molecular weight c-PLA (Table 3.1, entry 2) and linear PLA (Table B.2, entry 3)

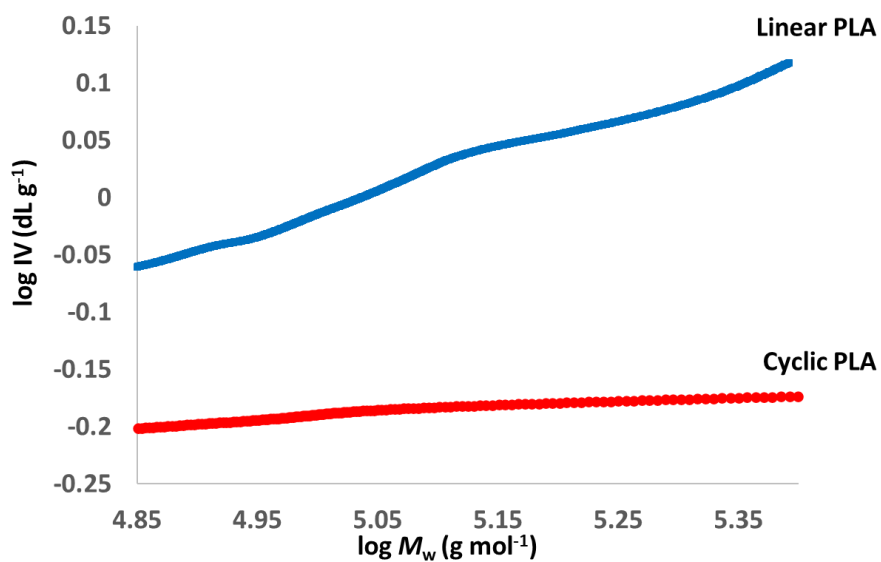


Figure B.8. Mark-Houwink plots for high molecular weight c-PLA (Table 3.1, entry 4) and linear PLA (Table B.2, entry 3)

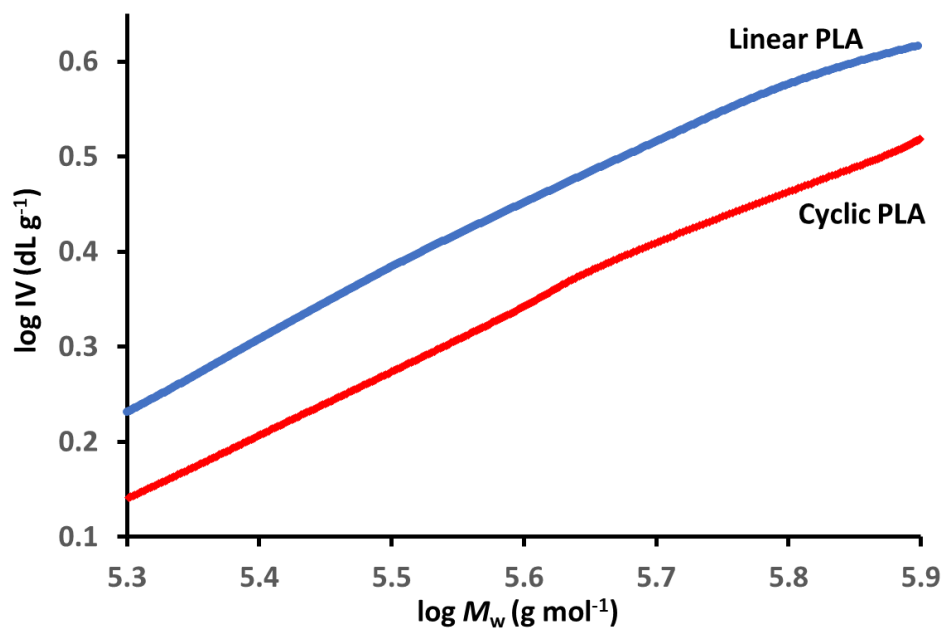


Figure B.9. Mark-Houwink plots for high molecular weight c-PLA (Table 3.1, entry 7) and linear PLA (Table B.2, entry 4)

Table B.2. Synthesis of linear PLA using **31b**⁵³

Entry	[LA]/[cat]	Time (h)	Conv. ^b	M_n^c	\bar{D}^d
1	250	24	>99	42 000	1.31
2	690	24	>99	104 000	1.07
3	870	24	>99	127 000	1.06
4	1250	24	>99	180 000	1.08

^a Reactions were performed in toluene at 100 °C, [*rac*-LA] = 0.8 M. ^b Conversion was monitored by ¹H NMR spectroscopy. ^c M_n determined through SEC in THF. ^d Dispersity = M_w/M_n .

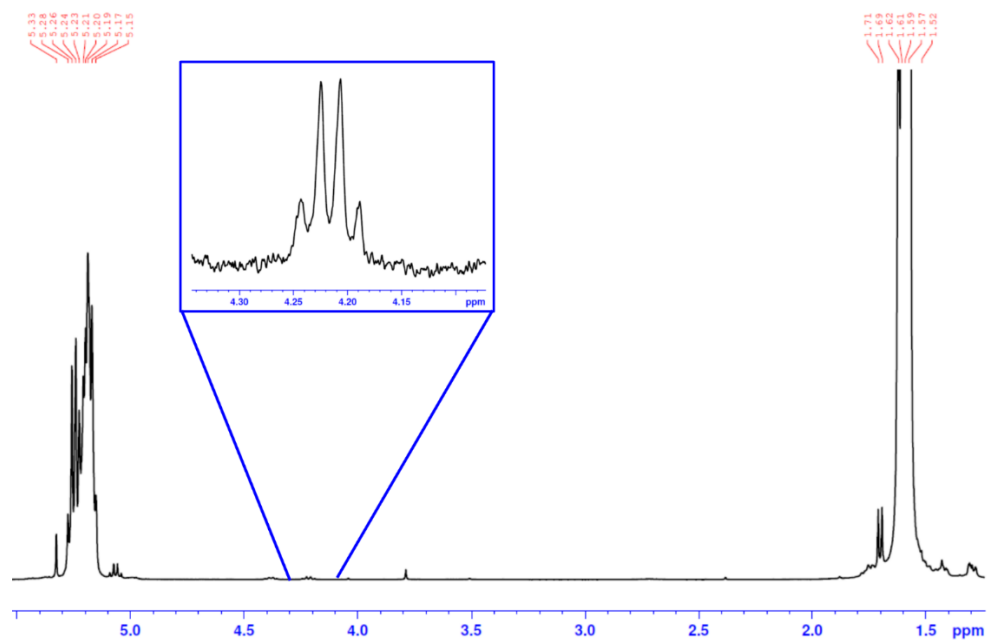


Figure B.10. ^1H NMR spectrum (400 MHz, CDCl_3 , 25 $^\circ\text{C}$) of linear PLA (Table B.2, entry 1). Inset- methylene protons of ethoxy chain end group.

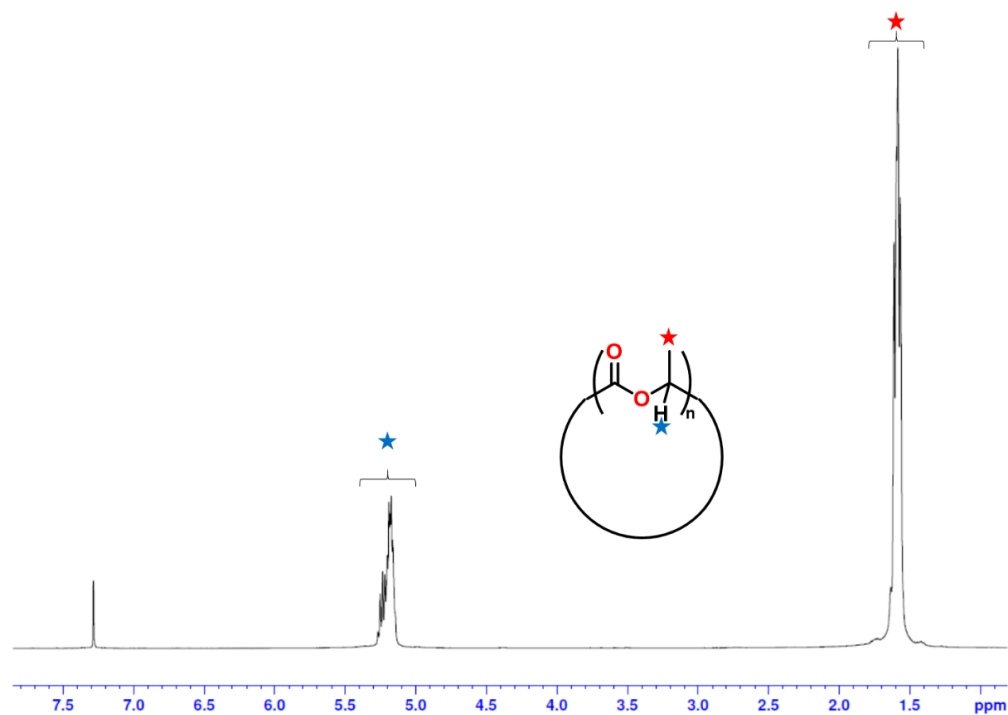


Figure B.11. ^1H NMR spectrum (300 MHz, CDCl_3 , 25 $^\circ\text{C}$) of c-PLA (Table 3.1, entry 1)

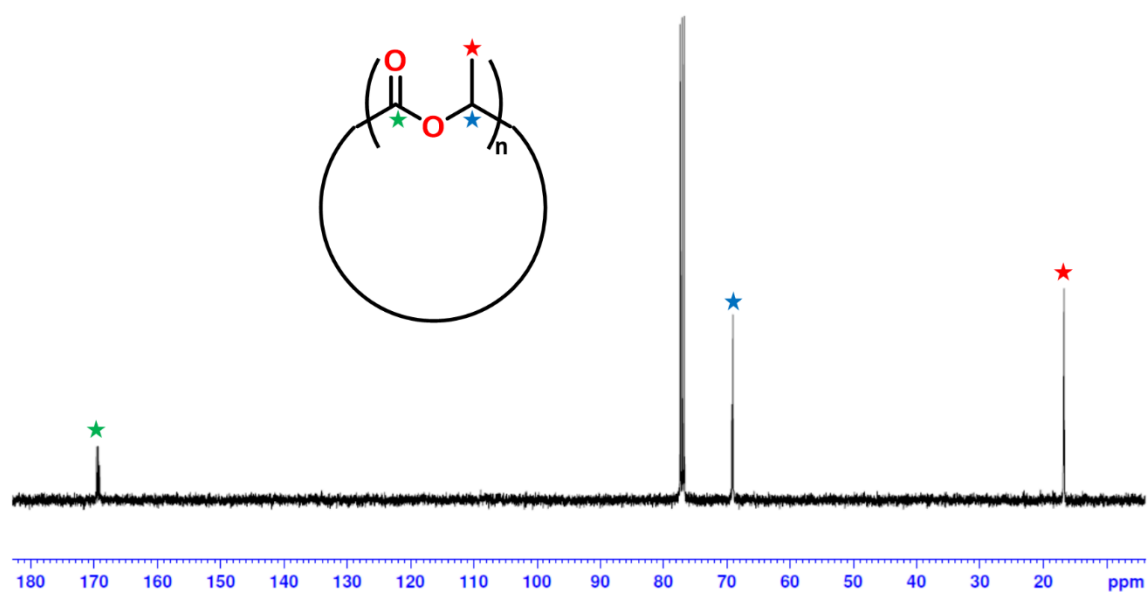


Figure B.12. $^{13}\text{C}\{^1\text{H}\}$ NMR spectrum (151 MHz, CDCl_3 , 25 °C) c-PLA (Table 3.1, entry 1)

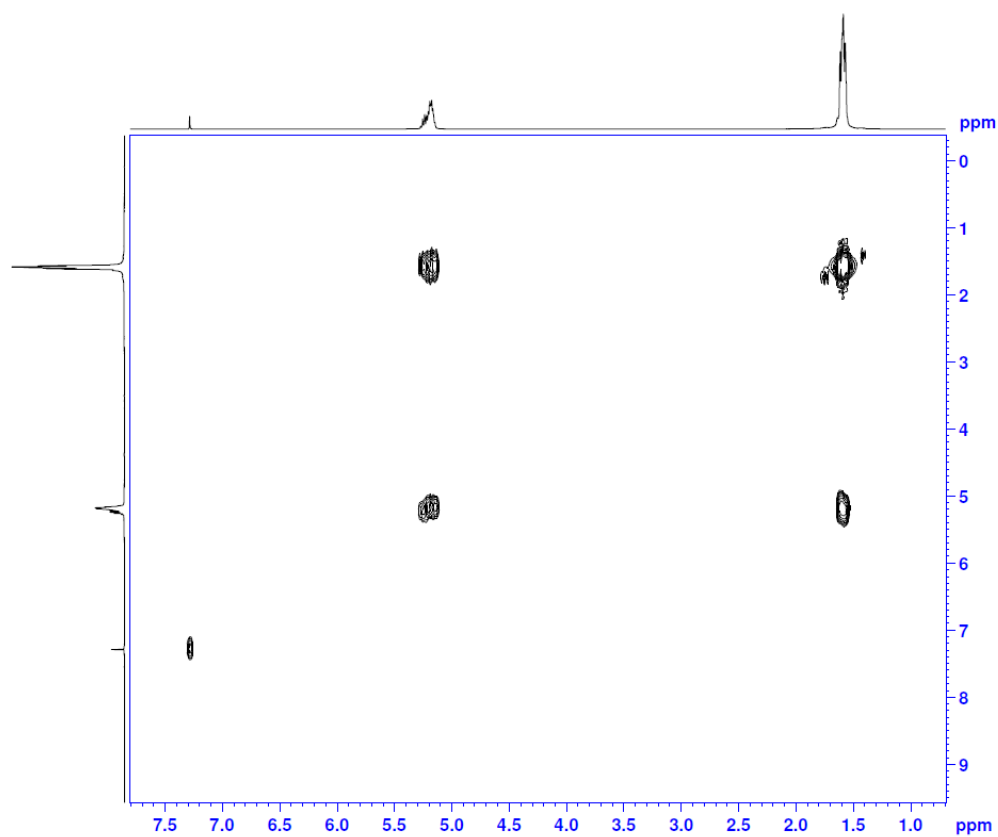


Figure B.13. $^1\text{H}-^1\text{H}$ COSY NMR spectrum (400 MHz, CDCl_3 , 25 °C) of c-PLA (Table 3.1, entry 1)

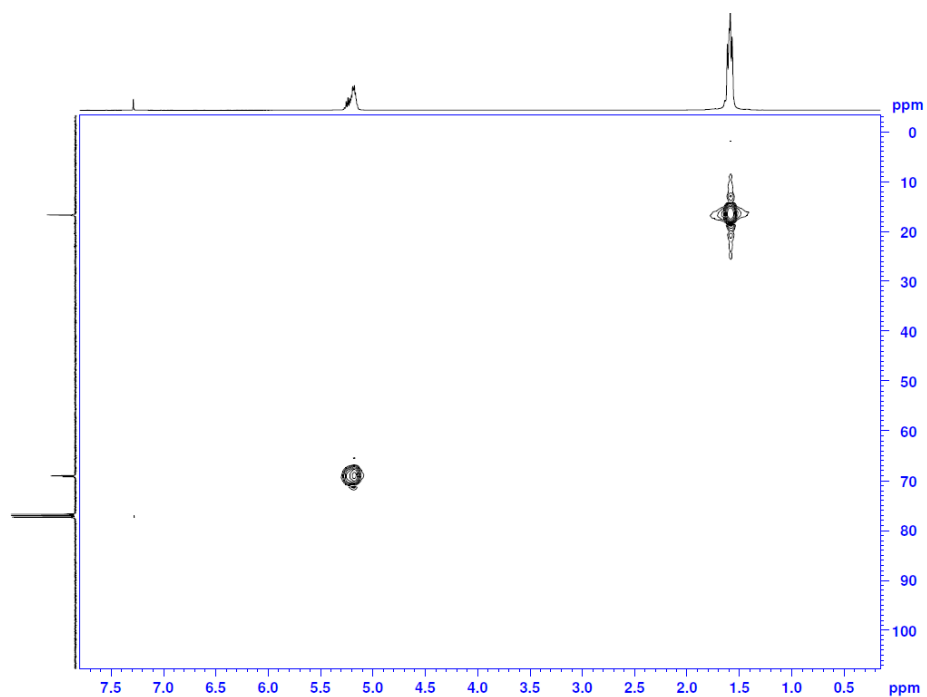


Figure B.14. ^1H - ^{13}C Heteronuclear Single Quantum Coherence (HSQC) NMR spectrum (CDCl_3 , 25 °C) of c-PLA
(Table 3.1, entry 1)

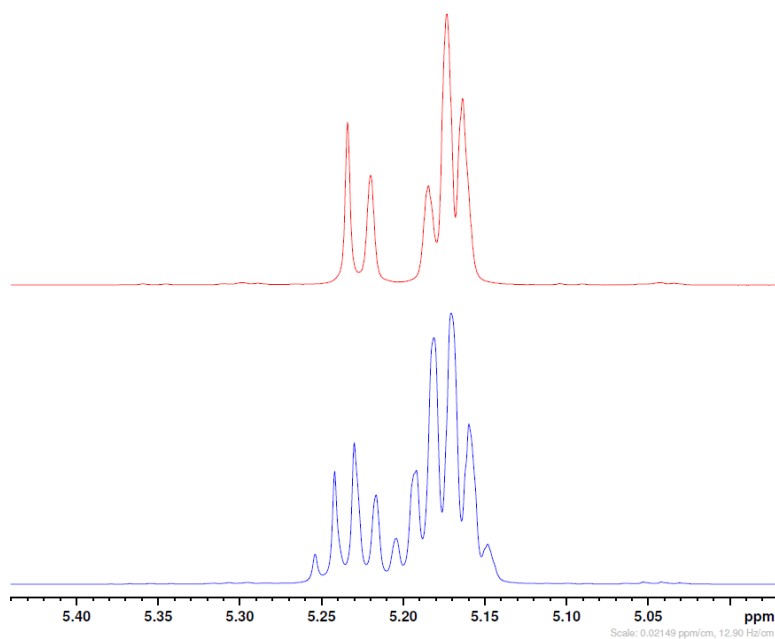


Figure B.15. Methine region of c-PLA polymer ^1H NMR spectrum (600 MHz, CDCl_3 , 25 $^\circ\text{C}$) (Bottom). $^1\text{H}\{^1\text{H}\}$ NMR spectrum (600 MHz, CDCl_3 , 25 $^\circ\text{C}$) of c-PLA (Top). The methine protons of the polymer are decoupled. ($P_m = 0.46$)

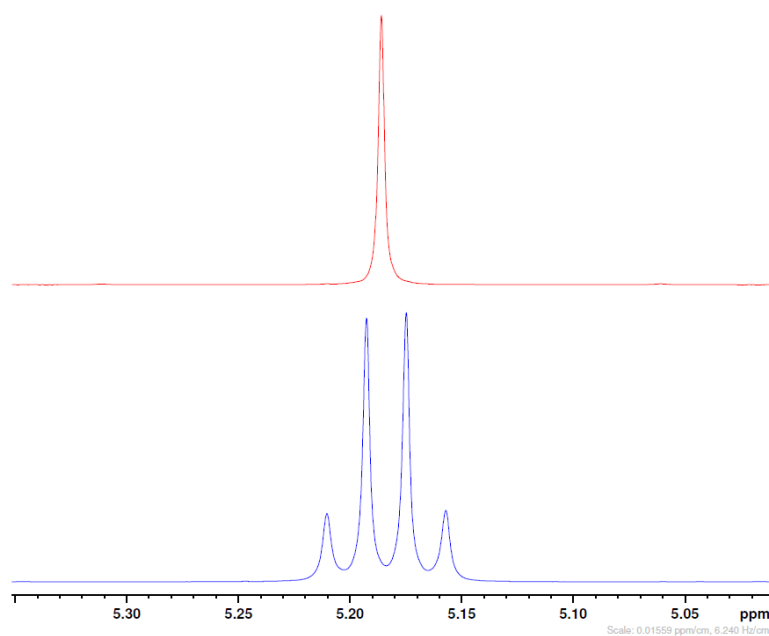


Figure B.16. Methine region of c-PLLA polymer ^1H NMR spectrum (600 MHz, CDCl_3 , 25 $^\circ\text{C}$) (Bottom). $^1\text{H}\{^1\text{H}\}$ NMR spectrum (600 MHz, CDCl_3 , 25 $^\circ\text{C}$) of c-PLLA (Top). The methine protons of the polymer are decoupled.

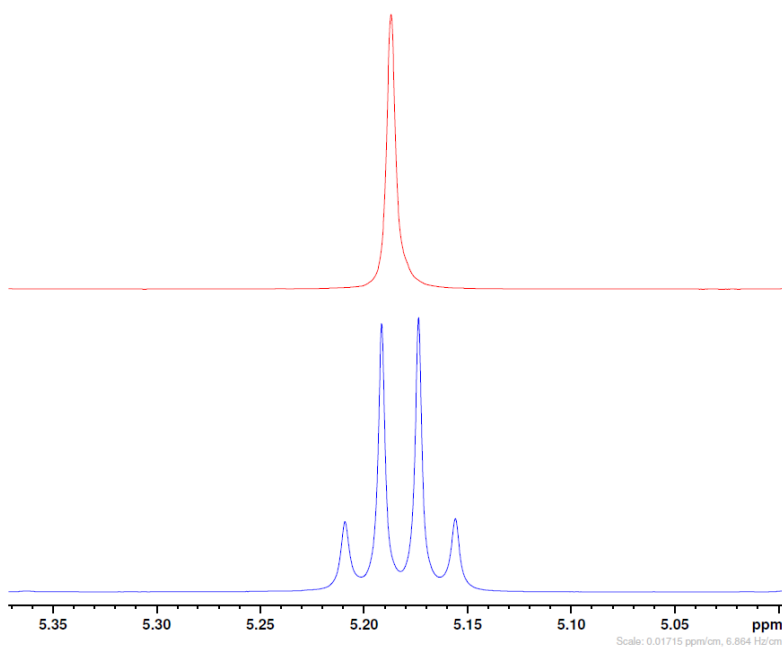


Figure B.17. Methine region of c-PDLA polymer ^1H NMR spectrum (600 MHz, CDCl_3 , 25 $^\circ\text{C}$) (Bottom). $^1\text{H}\{^1\text{H}\}$ NMR spectrum (600 MHz, CDCl_3 , 25 $^\circ\text{C}$) of c-PDLA (Top). The methine protons of the polymer are decoupled.

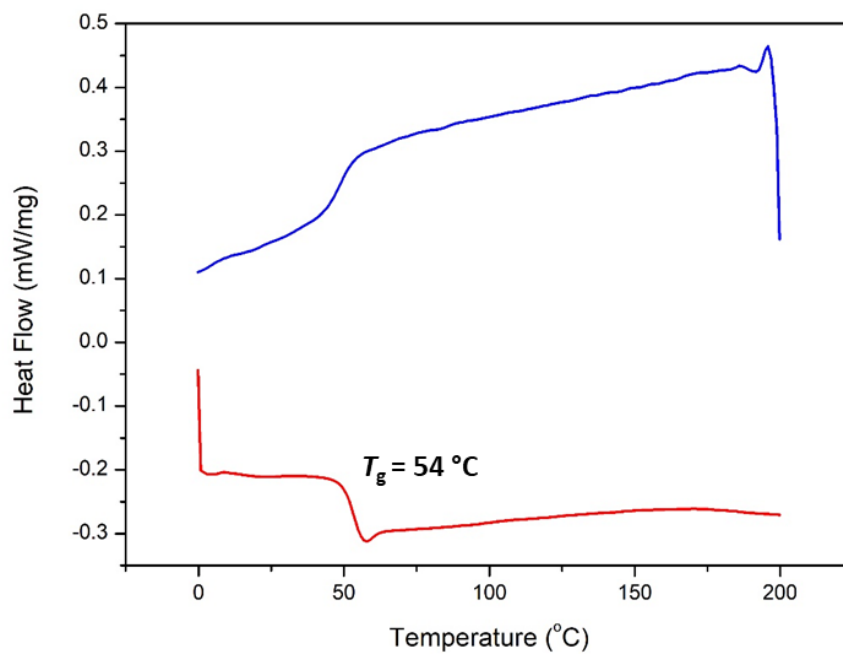


Figure B.18. DSC thermogram of c-PLA produced with **48c** (Table 3.1, entry 7)

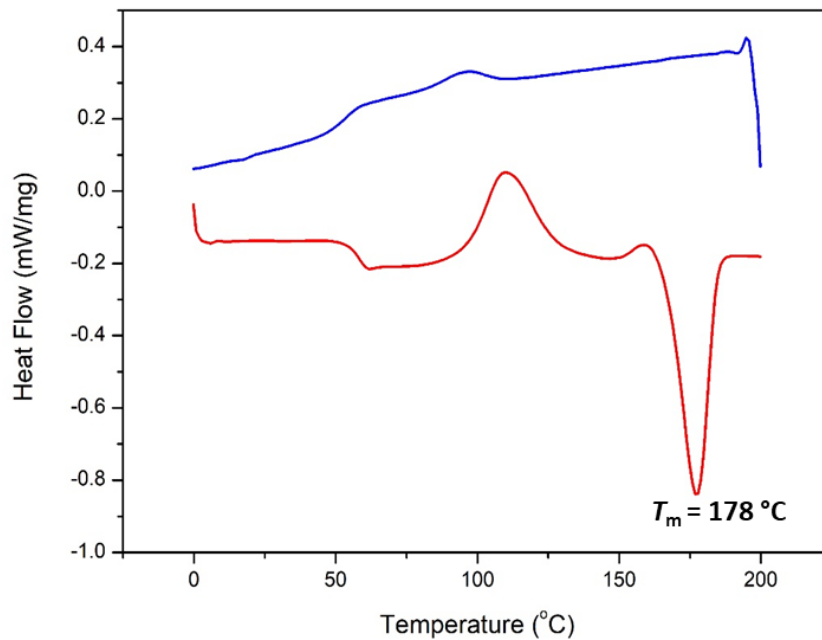


Figure B.19. DSC thermogram of c-PLLA produced with **48c** (Table 3.1, entry 8)

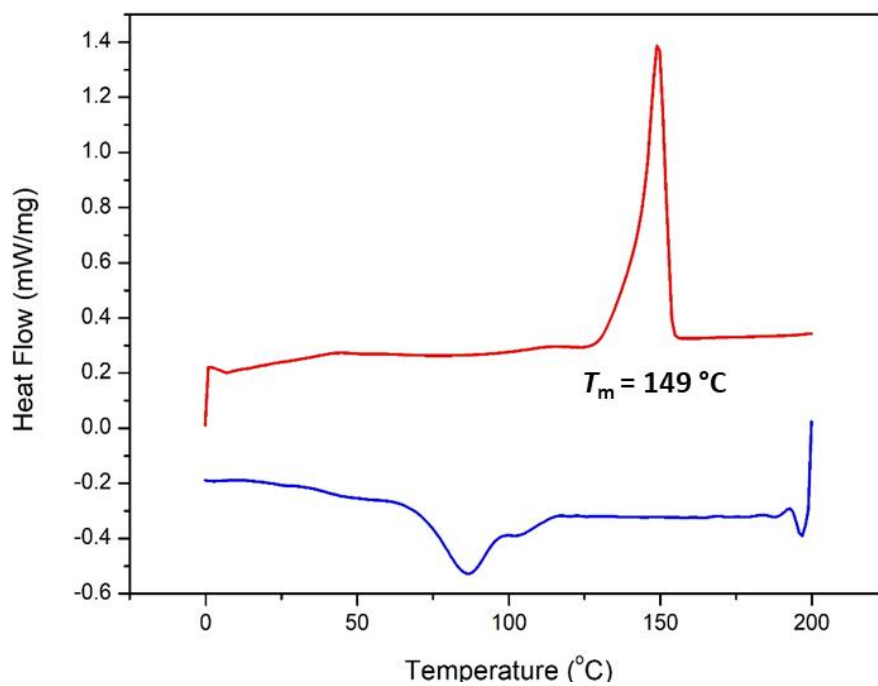


Figure B.20. DSC thermogram of c-PDLA produced with **48c** (Table 3.1, entry 9)

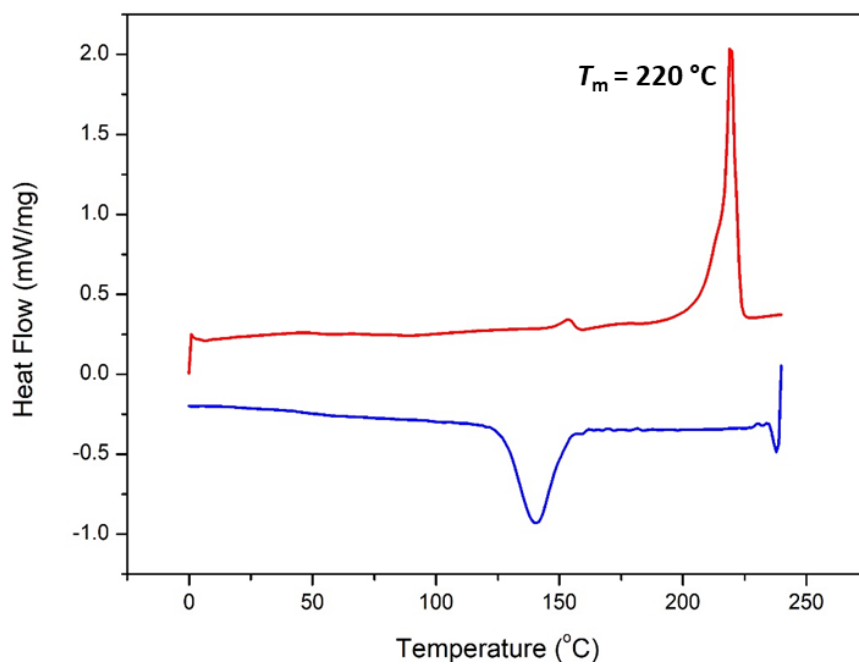


Figure B.21. DSC thermogram of the c-PLLA/c-PDLA stereocomplex

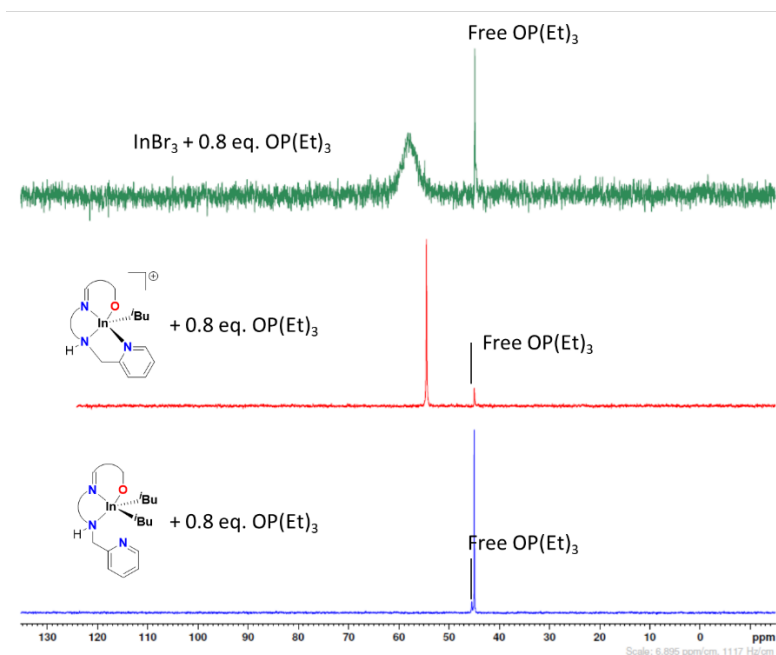


Figure B.22. $^{31}\text{P}\{^1\text{H}\}$ NMR spectra (162 MHz, C_6D_6 , 25 °C) of **48c**, neutral dialkyl indium precursor and InBr_3 after the addition of 0.8 equivalents of OP(Et)_3 . The free triethylphosphine oxide shift is determined by the addition of a capillary inside the NMR tube containing a solution of triethylphosphine oxide in C_6D_6 .

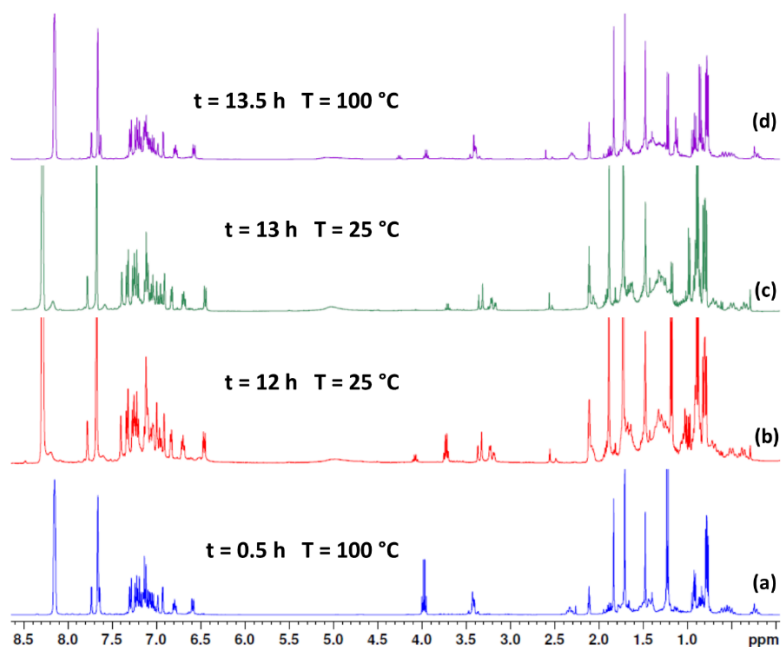


Figure B.23. *rac*-LA methine proton region of ^1H NMR spectra (400 MHz in Tol-d_8) of a 1:1 mixture of **48c** and *rac*-LA a) at 100 °C, b) after being heated at 100 °C for 12 h and observed at 25 °C, c) after an additional 1 h h at 25 °C and d) re-heated to 100 °C in the spectrometer.

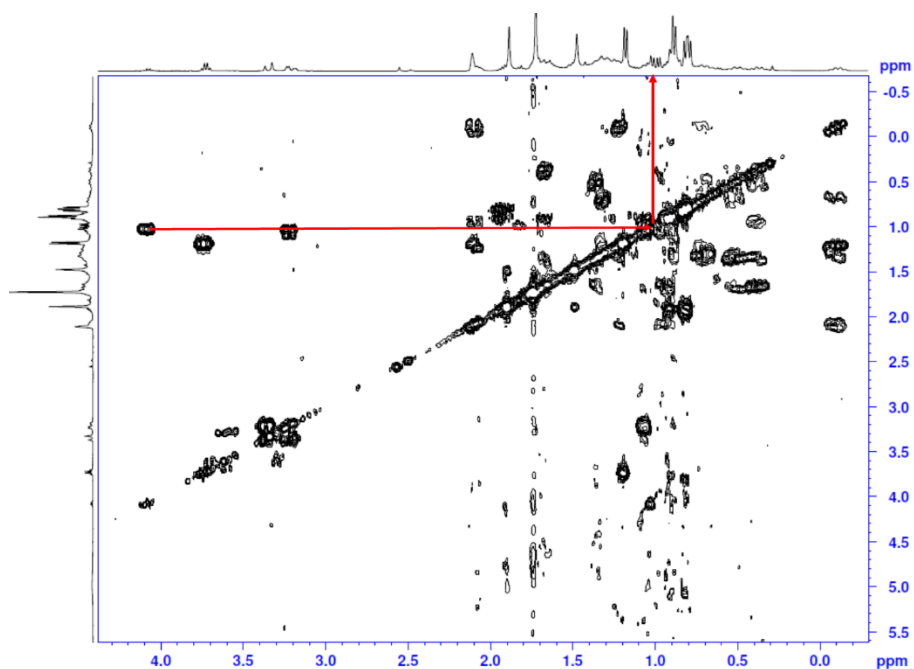


Figure B.24. ^1H - ^1H COSY NMR spectrum (400 MHz, Tol-d_8 25 °C) of Figure B.23b

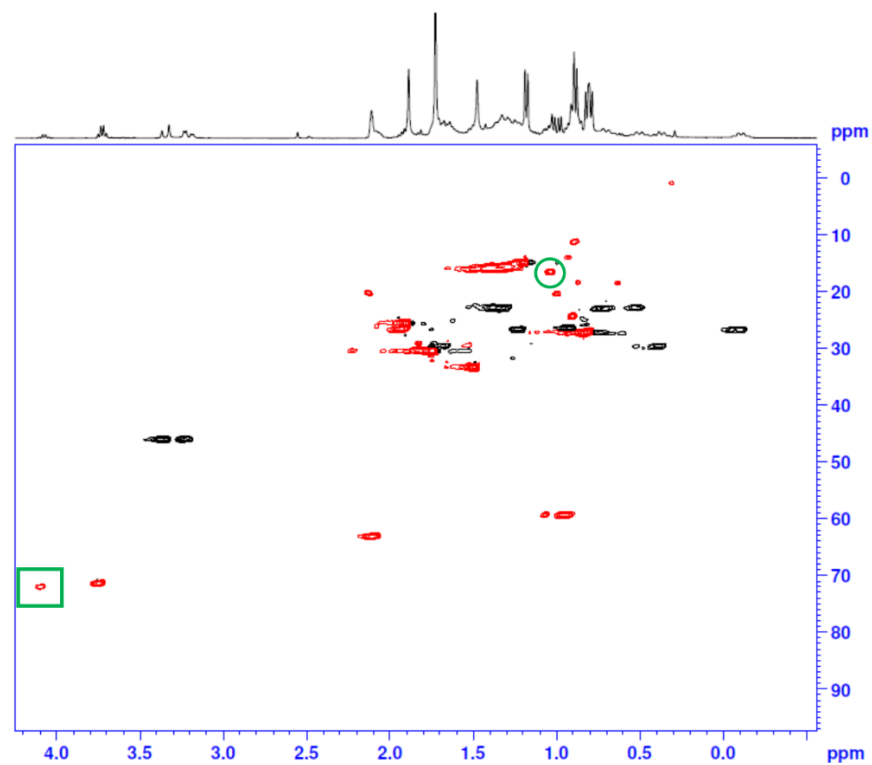


Figure B.25. Heteronuclear Multiple Bond Correlation (HMBC) NMR spectrum (400 MHz, Tol- d_8 25 °C) of Figure B.23b (Red – methine/methyl peaks, black – methylene peaks). Methine and methyl peaks of the coordinated *rac*-LA are in the green box and circle respectively).

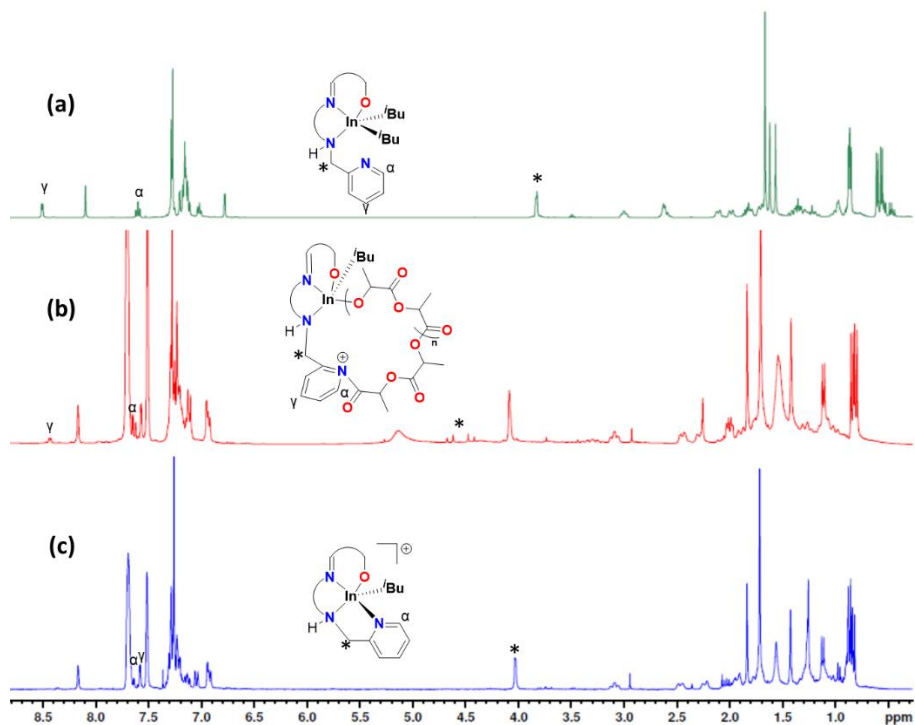


Figure B.26. ^1H NMR spectra (400 MHz, CDCl_3 , 25 $^\circ\text{C}$) of (a) **47c**, (b) **48c** + 1 eq. of *rac*-LA heated to 100 $^\circ\text{C}$ for 24 h, and (c) **48c**

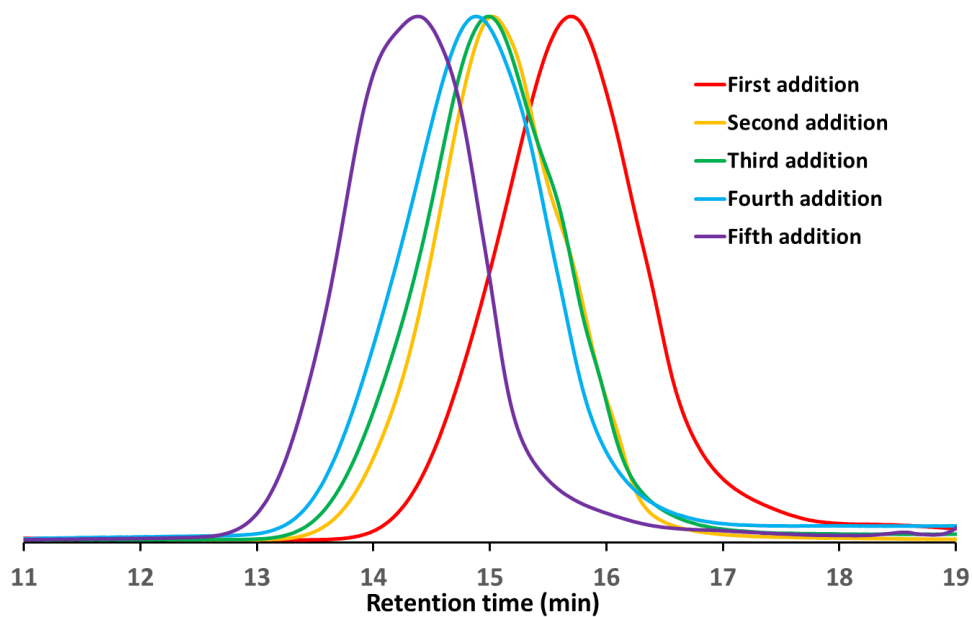


Figure B.27. SEC traces of c-PLA produced with **48c** (Table 3.2, entries 1-5)

Table B.3. Cyclic PLA produced by literature reported methods

Entry	[LA]/[cat]	M_n (Da)	Conversion %	\bar{D} (M_w/M_n)	Reference
1	5000	401 000	60	1.17	113
2	4000	165 000	100	1.90	123
3	1500	83 000	-	2.79	124
4	200	19 000	Incomplete	2.10	125
5	1000	54 000	97	2.40	126
6	1000	41 000	97	3.00	127
7	200	132 200	89	1.85	128
8	2000	57 000	97	2.20	129
9	407	32 350	39	1.20	130
10	200	26 000	92	1.35	132
11	200	31 400	91	1.16	133
12	100	7 500	55	1.09	134
13	200	39 363	90	1.42	135
14	20	47 000	91	1.65	136
15	100	24 500	96	1.62	137
16	3000	416 000	91	1.29	<i>This work</i>

Appendix C - Data associated with Chapter 4.

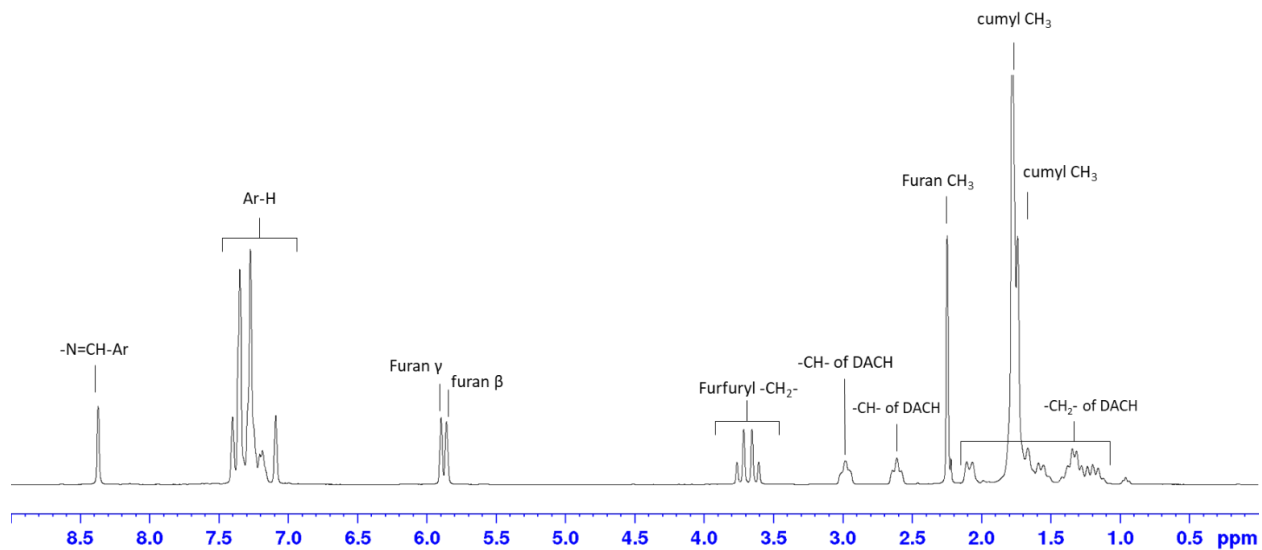


Figure C.1. ^1H NMR spectrum (300MHz, CDCl_3 , 25 °C) of proligand **L_g**. DACH= diaminocyclohexane

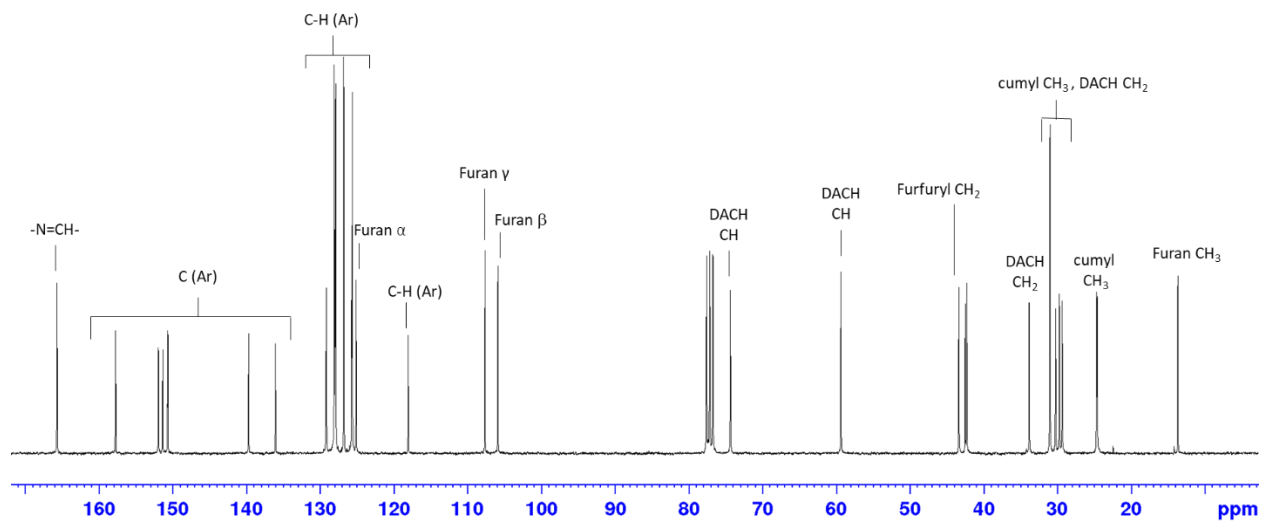


Figure C.2. $^{13}\text{C}\{^1\text{H}\}$ NMR spectrum (75MHz, CDCl_3 , 25 °C) of proligand **L_g**

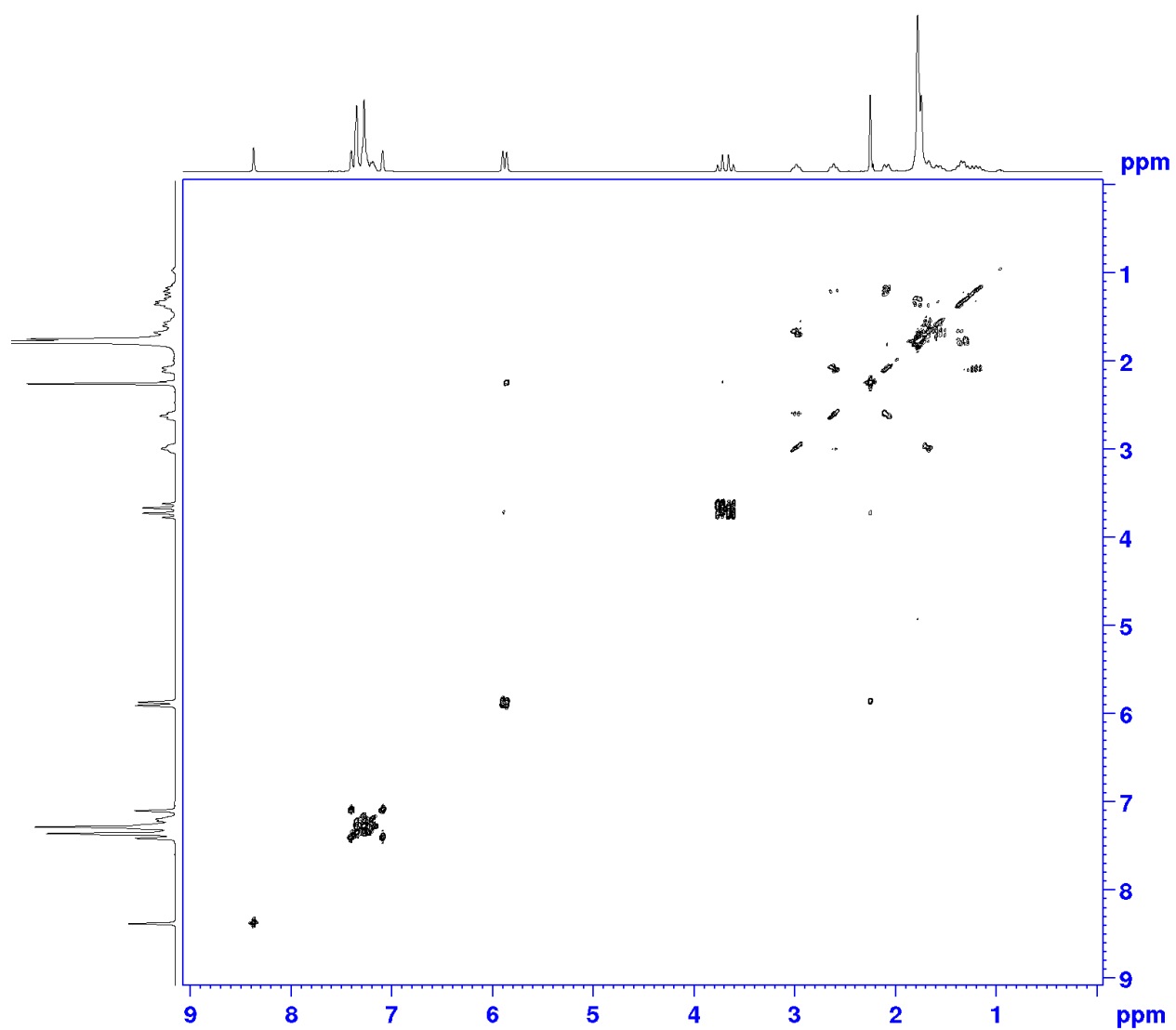


Figure C.3. 2D ^1H - ^1H COSY NMR spectrum (300 MHz, CDCl_3 , 25 °C) of **L_g**

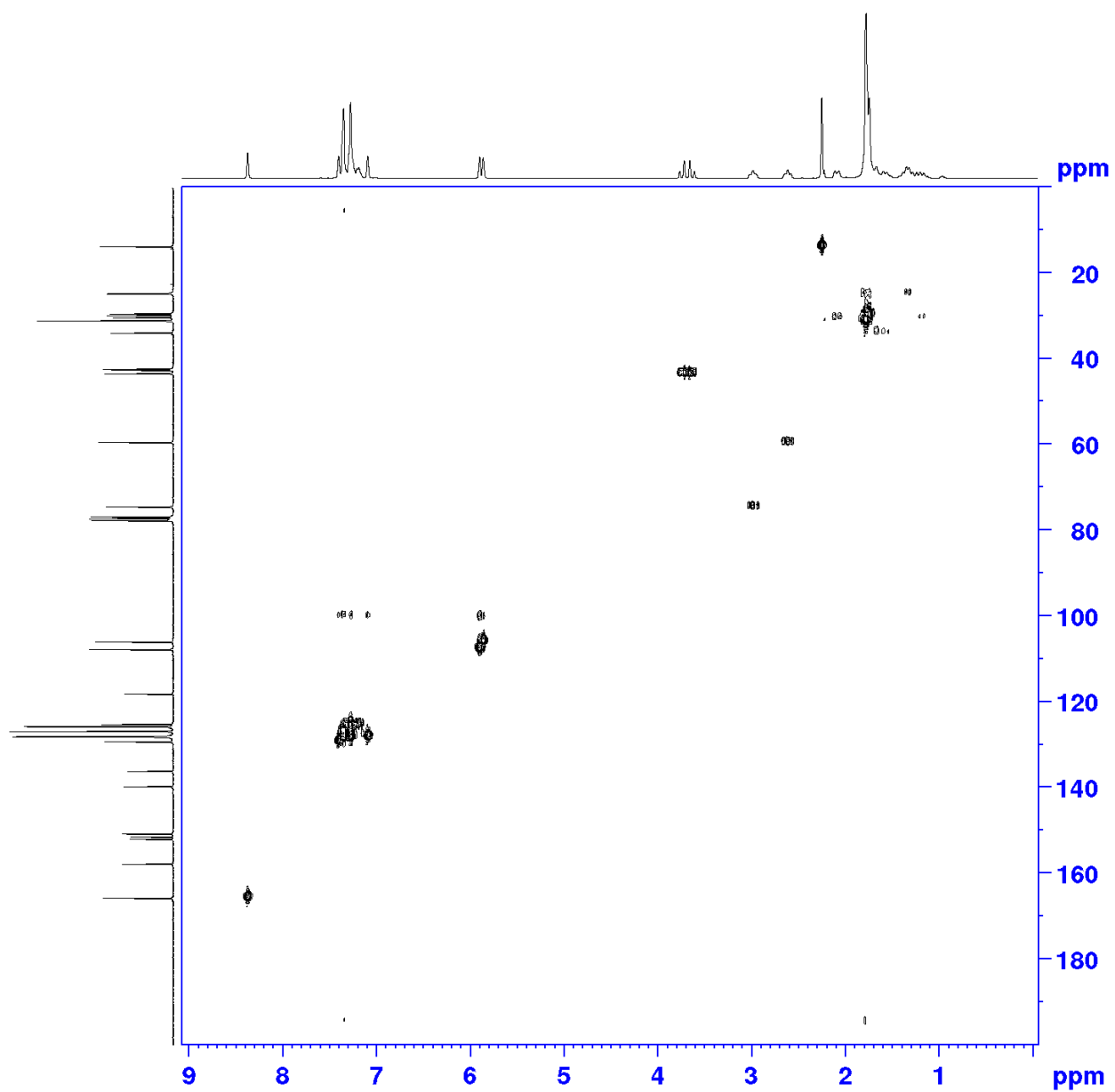


Figure C.4. 2D ^1H - ^{13}C Heteronuclear Single Quantum Coherence (HSQC) NMR spectrum (CDCl₃, 25 °C) of **L_g**

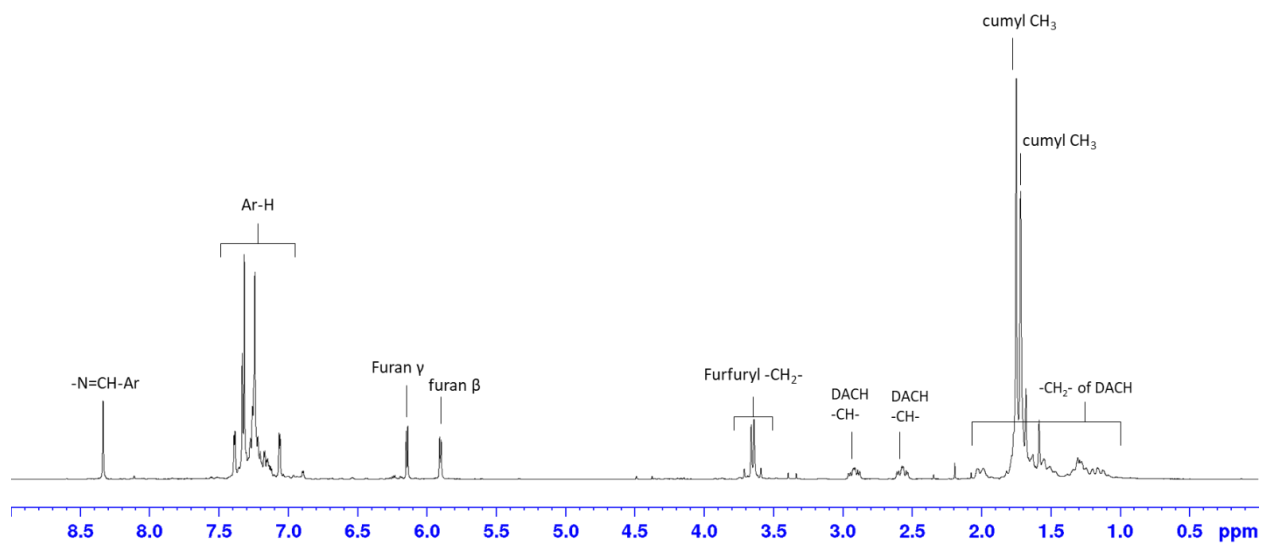


Figure C.5. ^1H NMR spectrum (300MHz, CDCl_3 , 25 °C) of proligand L_h

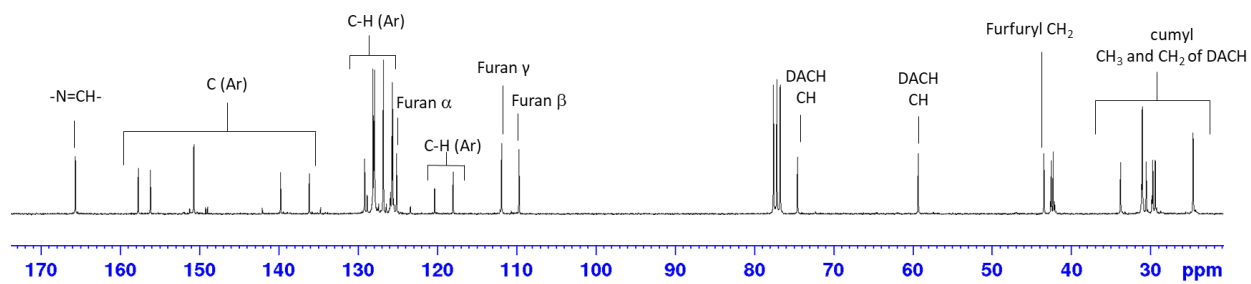


Figure C.6. $^{13}\text{C}\{^1\text{H}\}$ NMR spectrum (75MHz, CDCl_3 , 25 °C) of proligand L_h

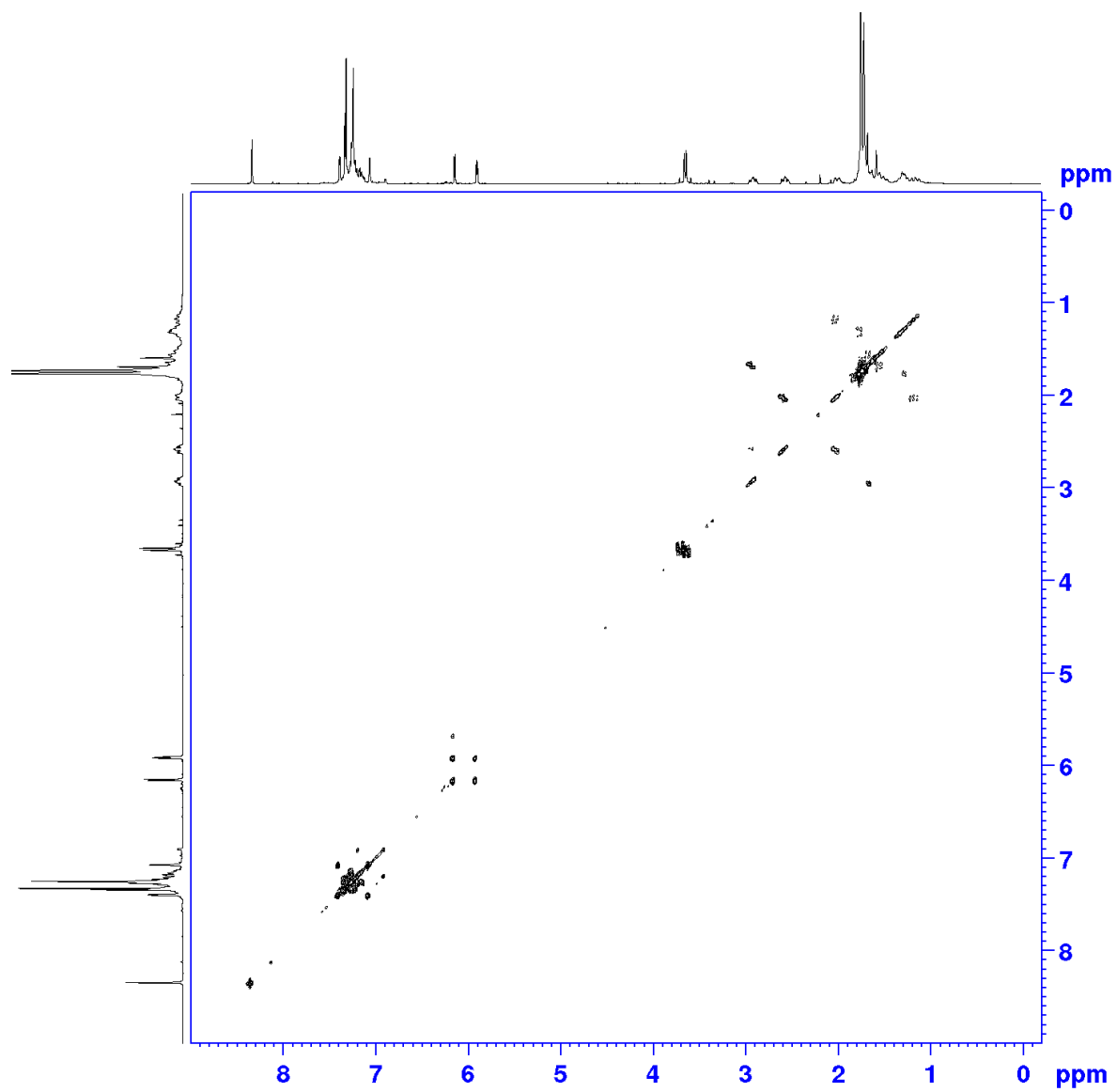


Figure C.7. 2D ^1H - ^1H COSY NMR spectrum (300 MHz, CDCl_3 , 25 °C) of **Lh**

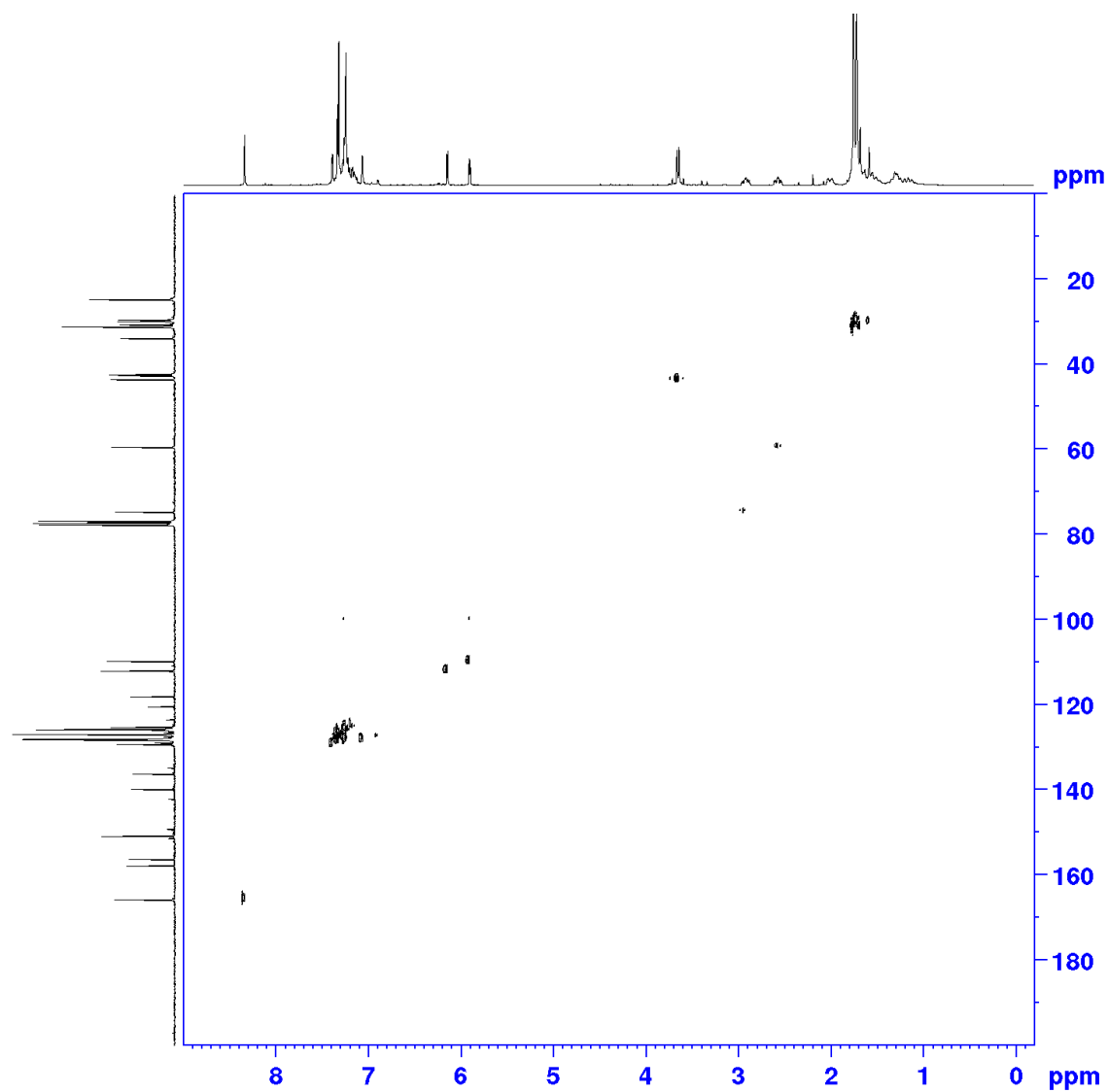


Figure C.8. 2D ^1H - ^{13}C Heteronuclear Single Quantum Coherence (HSQC) NMR spectrum (CDCl_3 , 25 $^\circ\text{C}$) of **L_h**

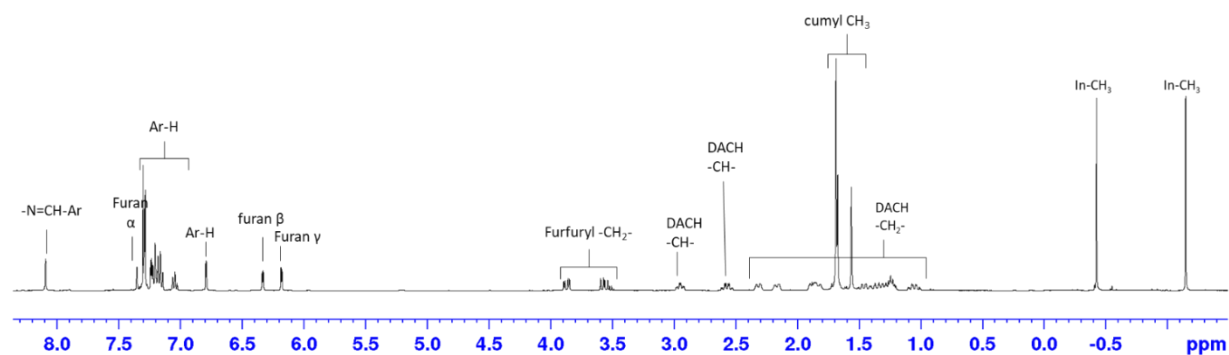


Figure C.9. ^1H NMR spectrum (400 MHz, CDCl_3 , 25 $^\circ\text{C}$) of complex **47e**

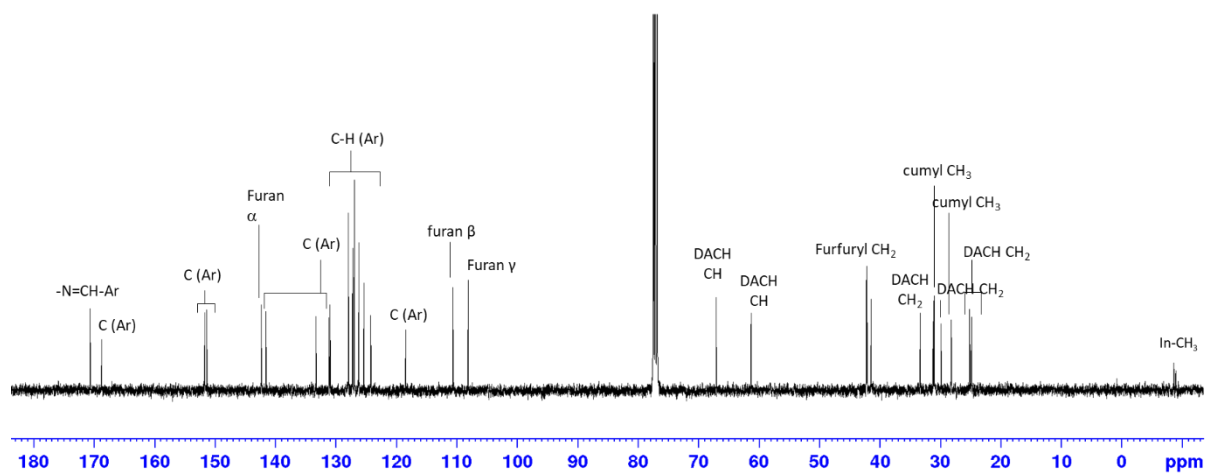


Figure C.10. $^{13}\text{C}\{^1\text{H}\}$ NMR spectrum (100 MHz, CDCl_3 , 25 $^\circ\text{C}$) of complex **47e**

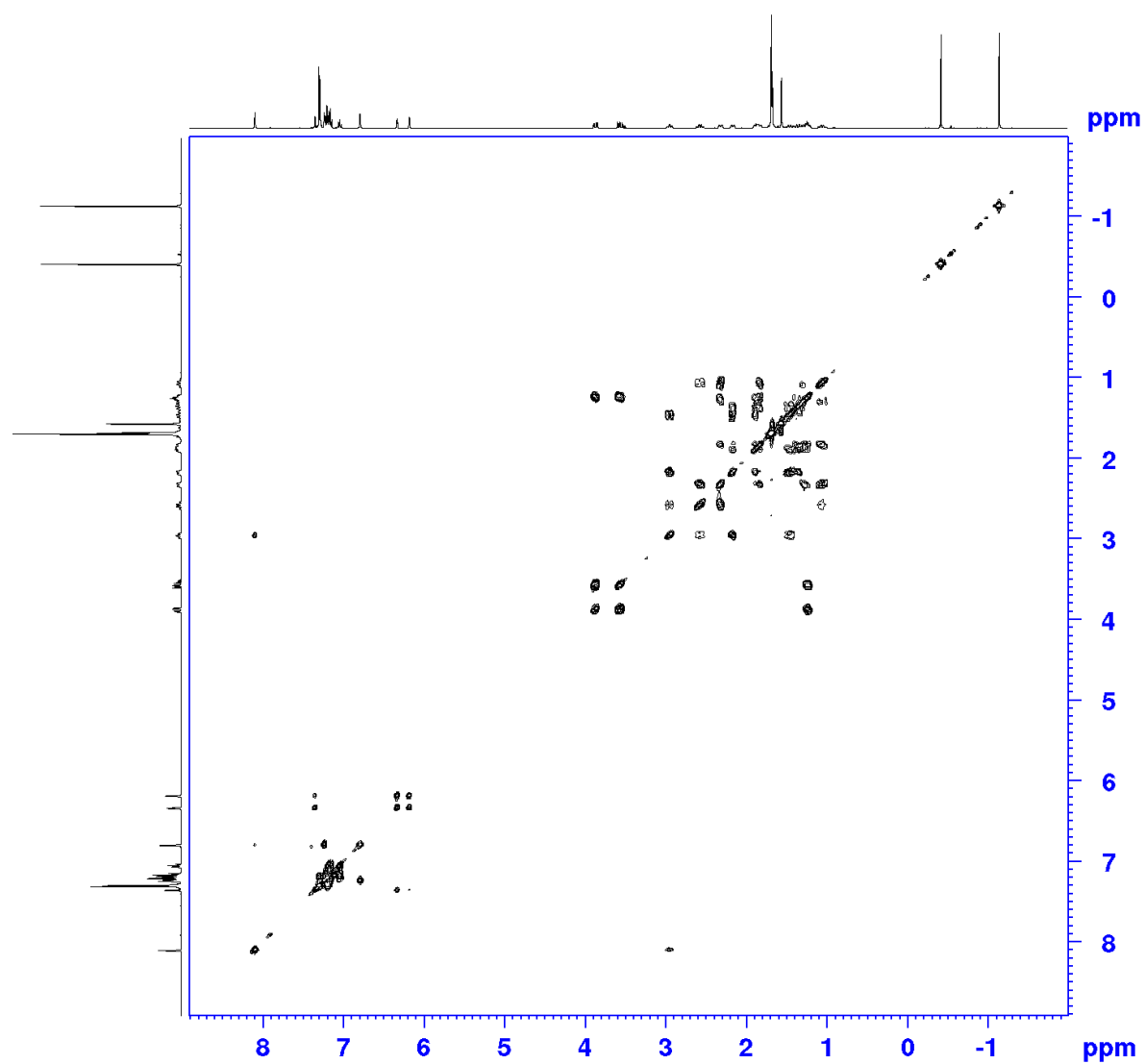


Figure C.11. ^1H - ^1H COSY NMR spectrum (400 MHz, CDCl_3 , 25 °C) of complex **47e**

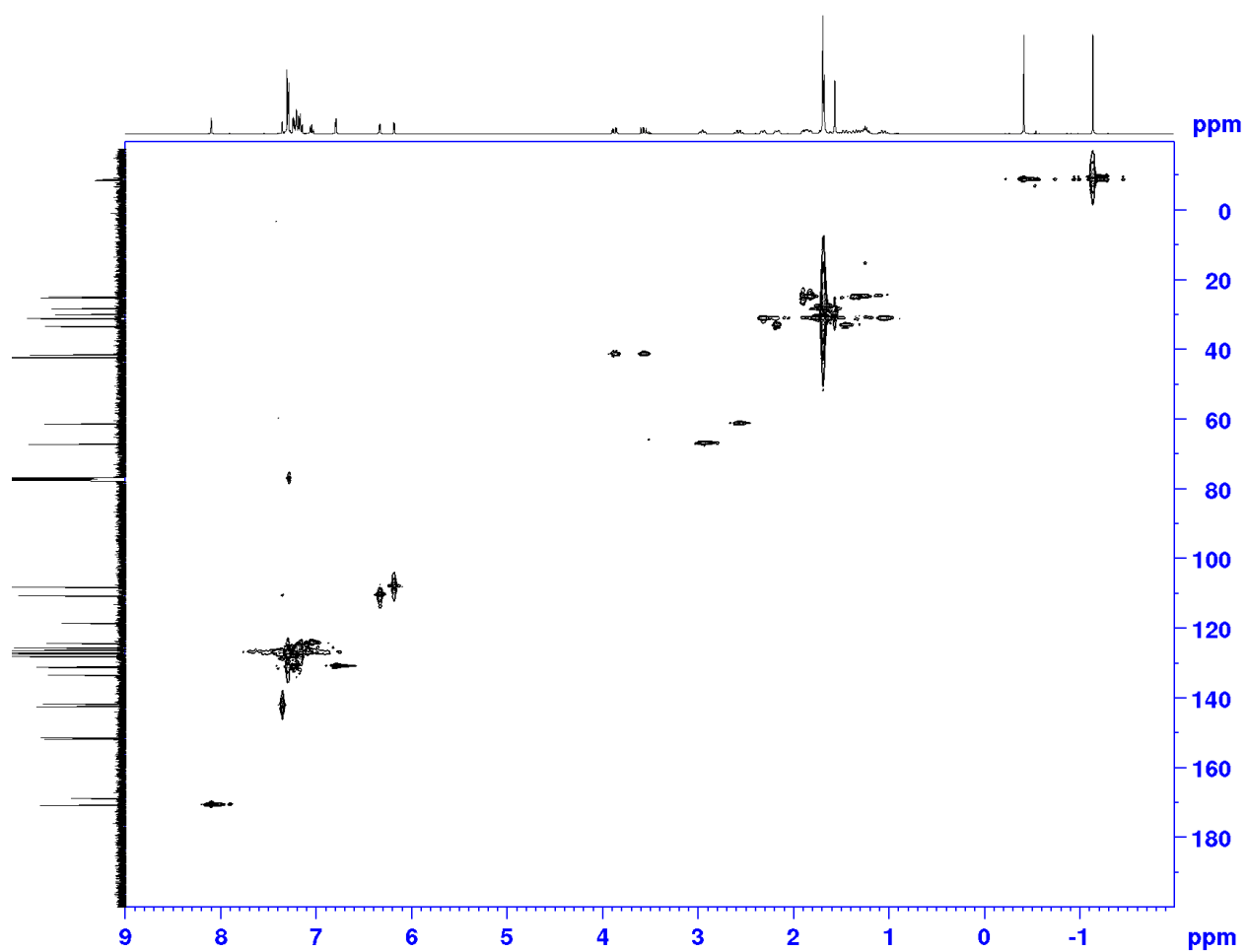


Figure C.12. 2D ^1H - ^{13}C Heteronuclear Single Quantum Coherence (HSQC) NMR spectrum (CDCl_3 , 25 $^\circ\text{C}$) of complex **47e**

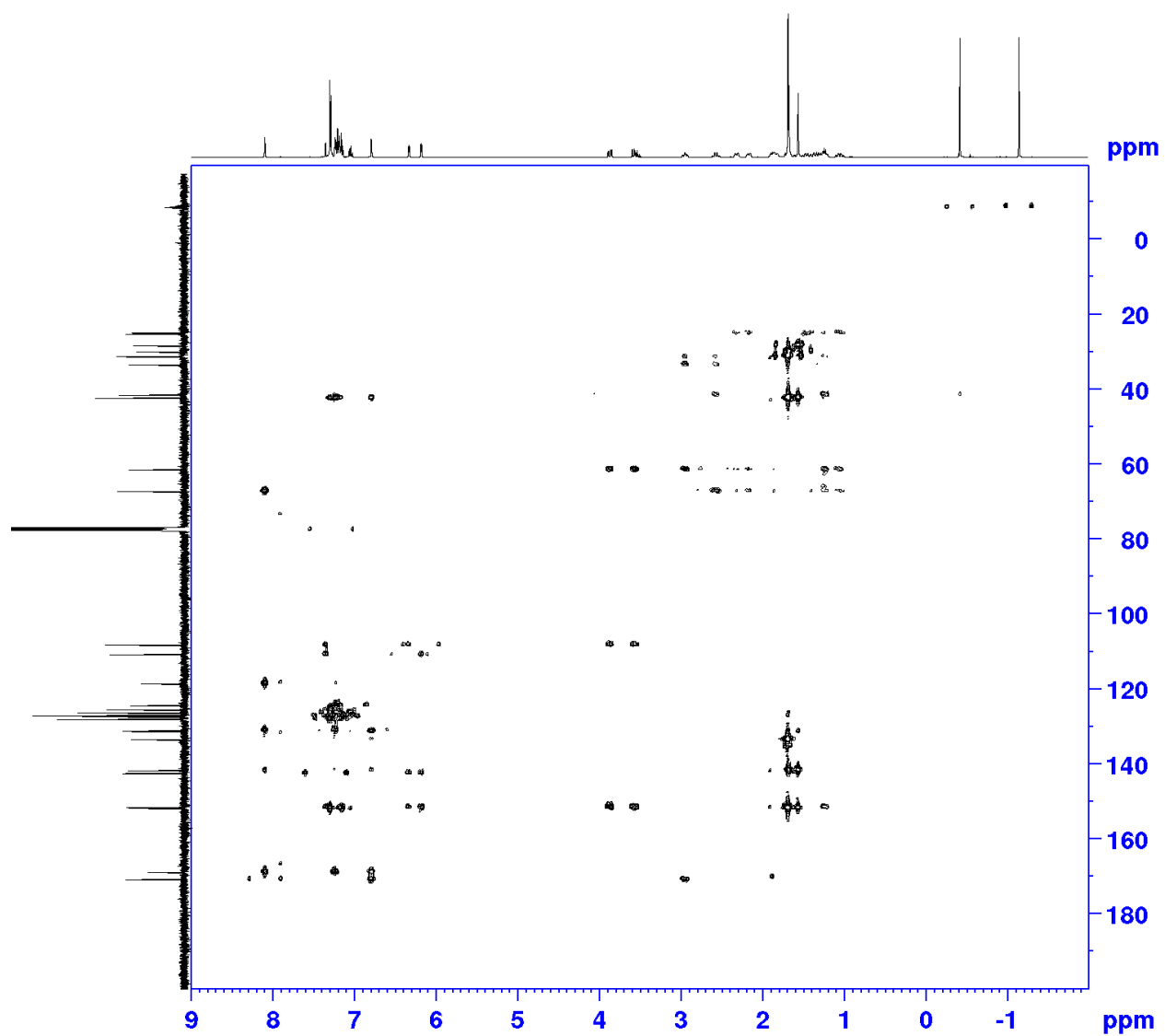


Figure C.13. ^1H - ^{13}C Heteronuclear Multiple Bond Correlation (HMBC) NMR spectrum (CDCl_3 , 25 $^\circ\text{C}$) of complex

47e

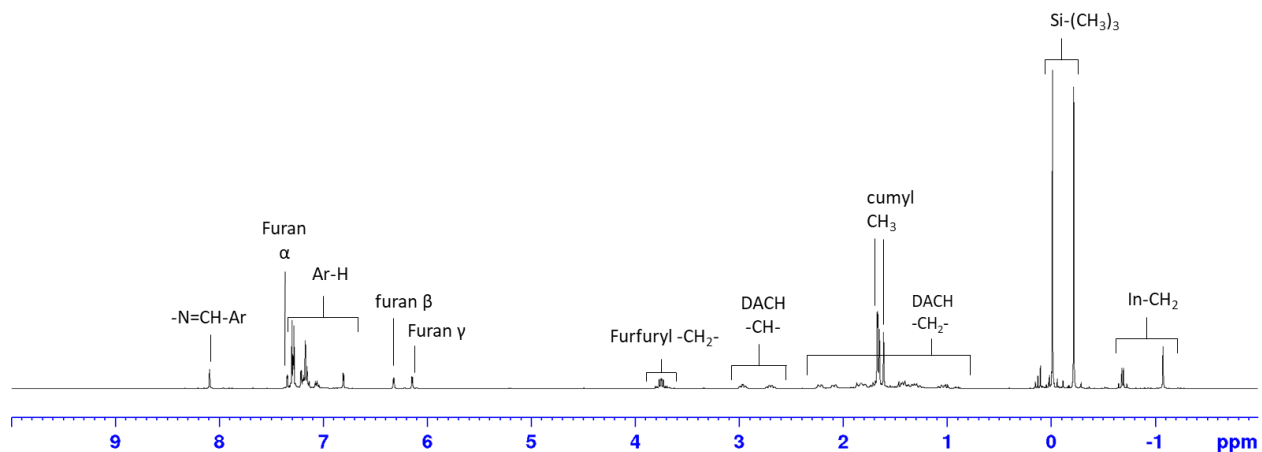


Figure C.14. ^1H NMR spectrum (400 MHz, CDCl_3 , 25 $^\circ\text{C}$) of complex **47f**

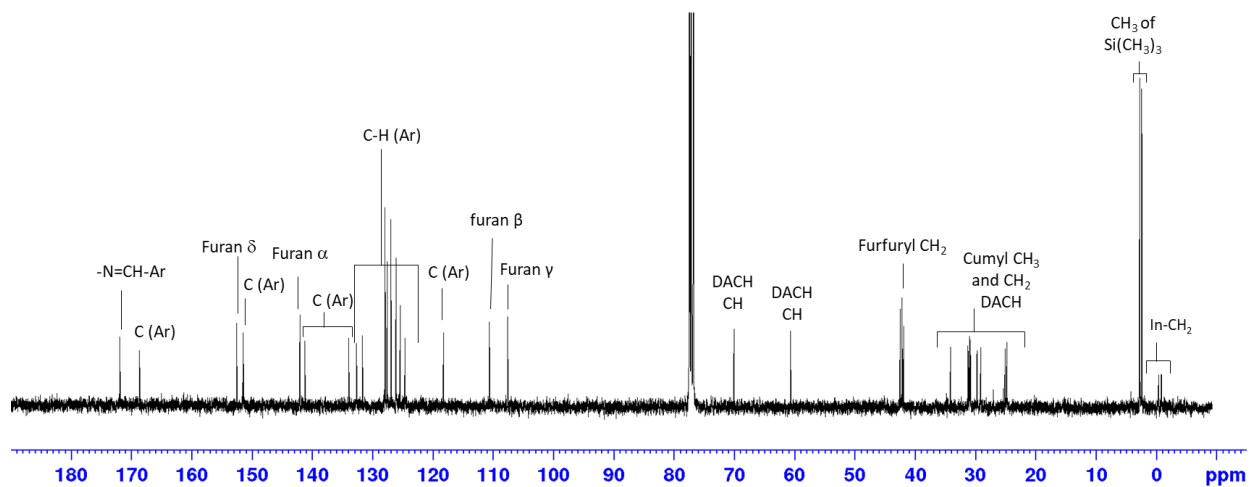


Figure C.15. $^{13}\text{C}\{^1\text{H}\}$ NMR spectrum (100 MHz, CDCl_3 , 25 $^\circ\text{C}$) of complex **47f**

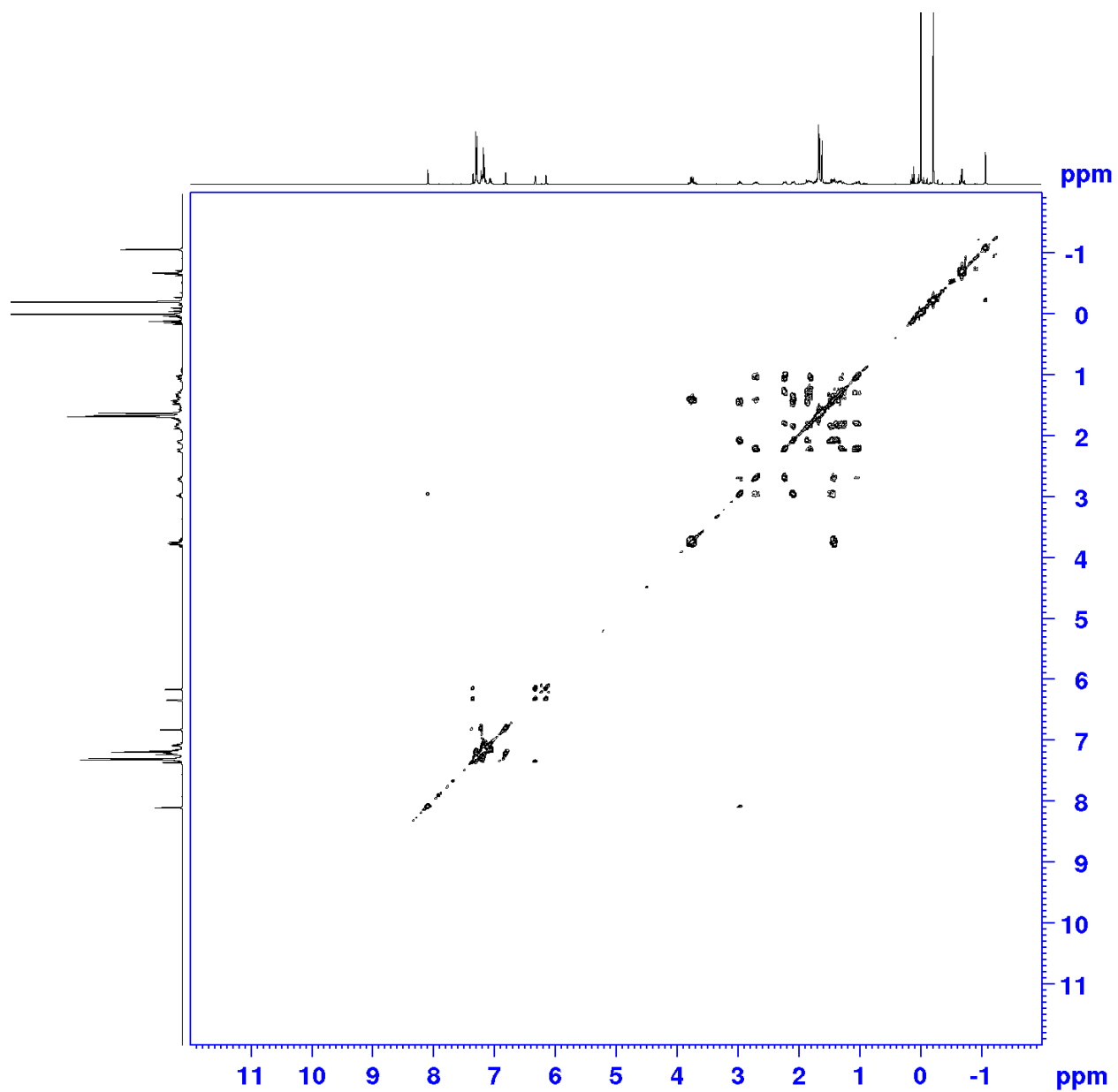


Figure C.16. ^1H - ^1H COSY NMR spectrum (400 MHz, CDCl_3 , 25 °C) of complex **47f**

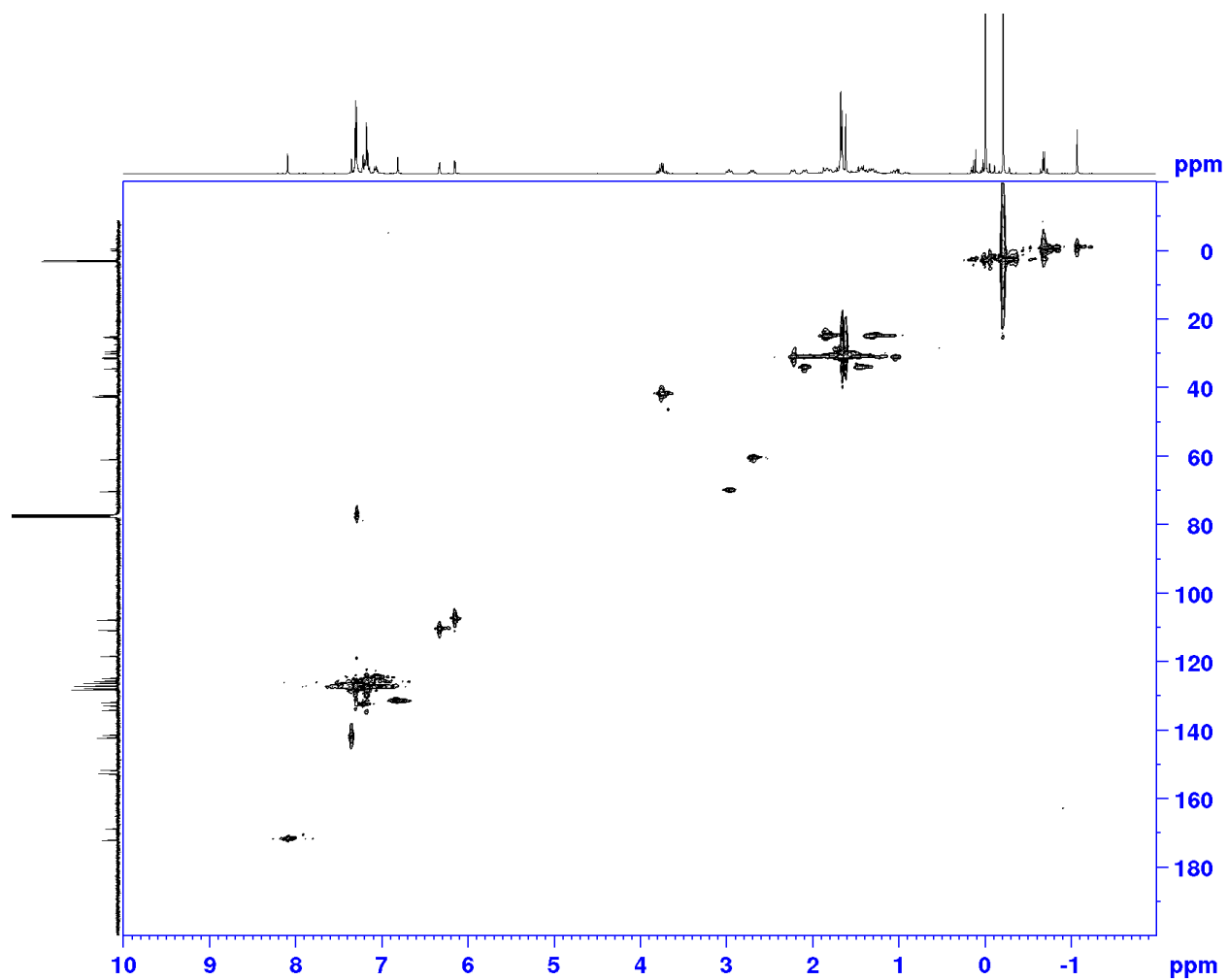


Figure C.17. 2D ^1H - ^{13}C Heteronuclear Single Quantum Coherence (HSQC) NMR spectrum (CDCl_3 , 25 $^\circ\text{C}$) of complex **47f**

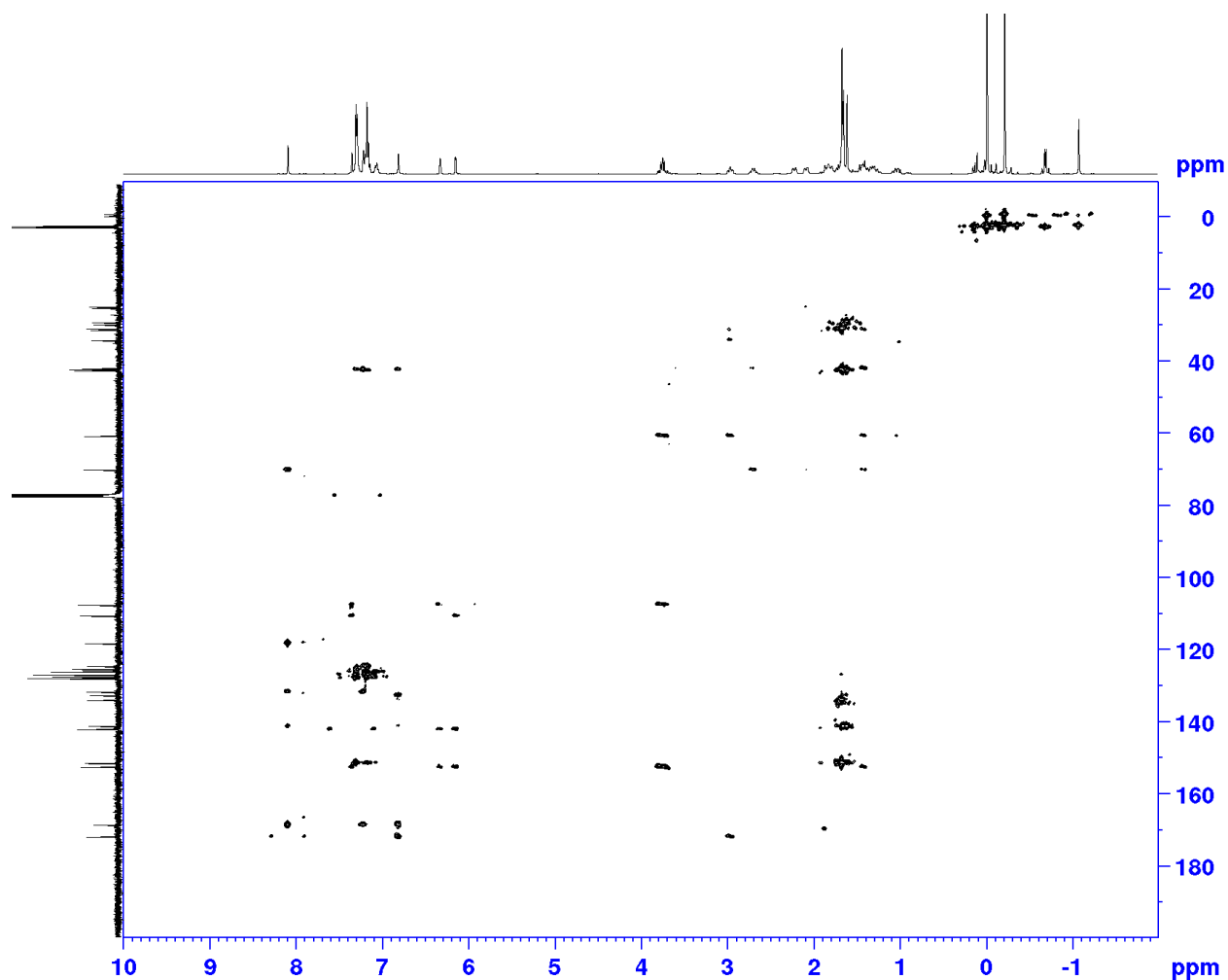


Figure C.18. 2D ^1H - ^{13}C Heteronuclear Multiple Bond Correlation (HMBC) NMR spectrum (CDCl_3 , 25 $^\circ\text{C}$) of complex **47f**

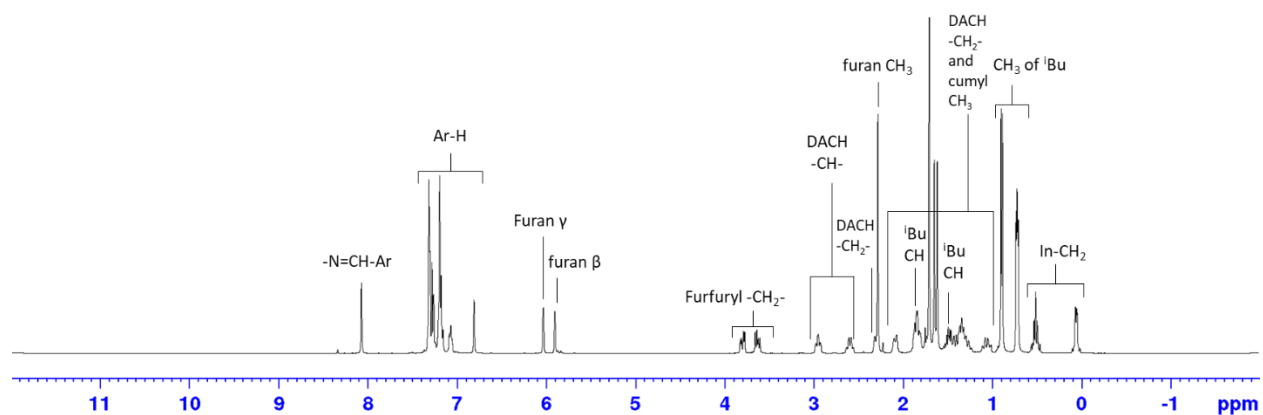


Figure C.19. ^1H NMR spectrum (400 MHz, CDCl_3 , 25 $^\circ\text{C}$) of complex **47g**

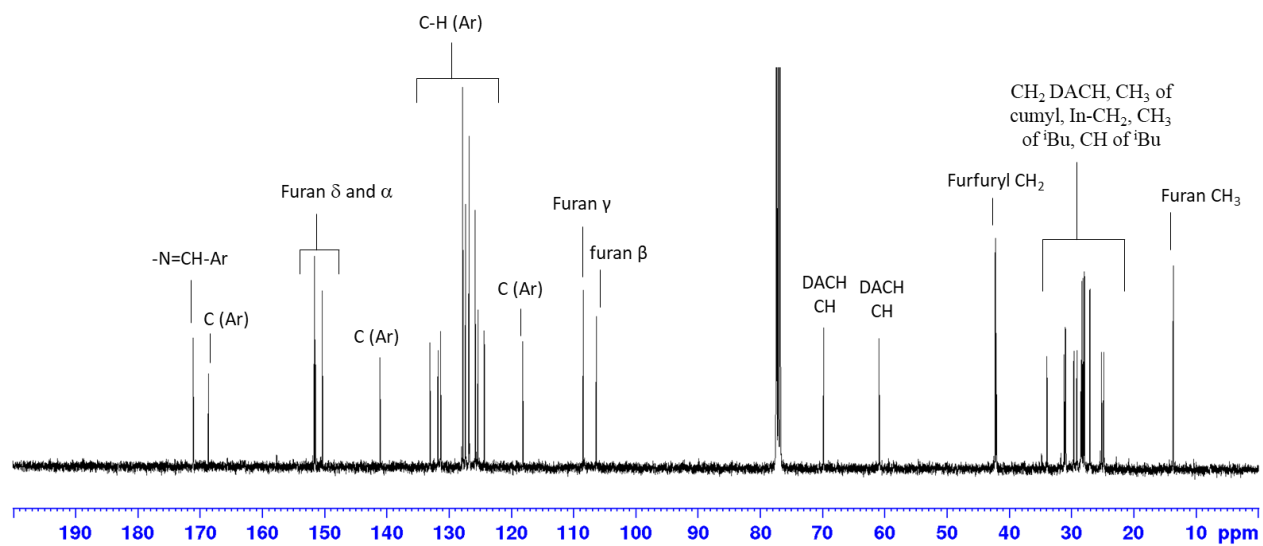


Figure C.20. $^{13}\text{C}\{^1\text{H}\}$ NMR spectrum (100 MHz, CDCl_3 , 25 °C) of complex **47g**

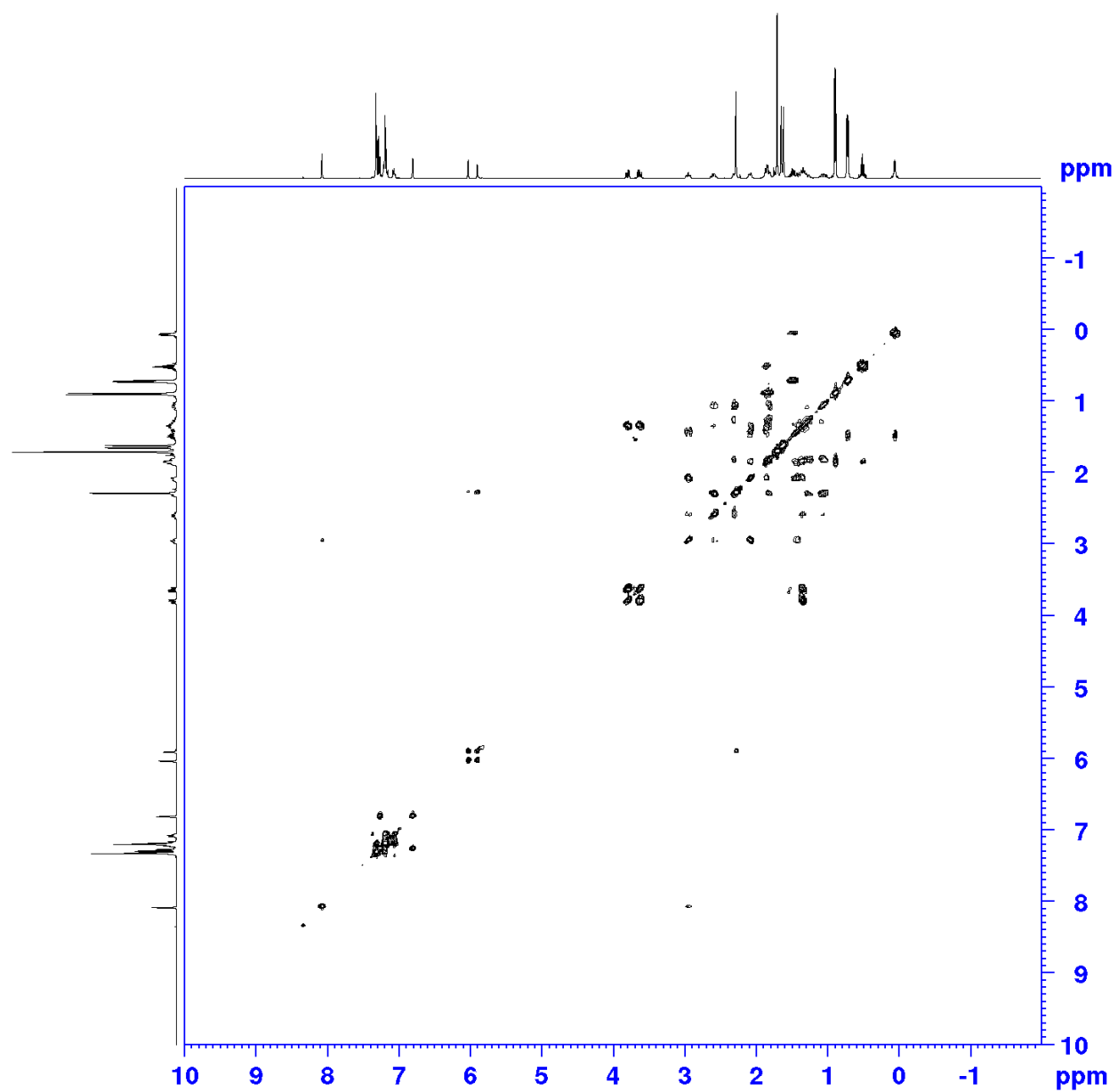


Figure C.21. ^1H - ^1H COSY NMR spectrum (400 MHz, CDCl_3 , 25 °C) of complex **47g**

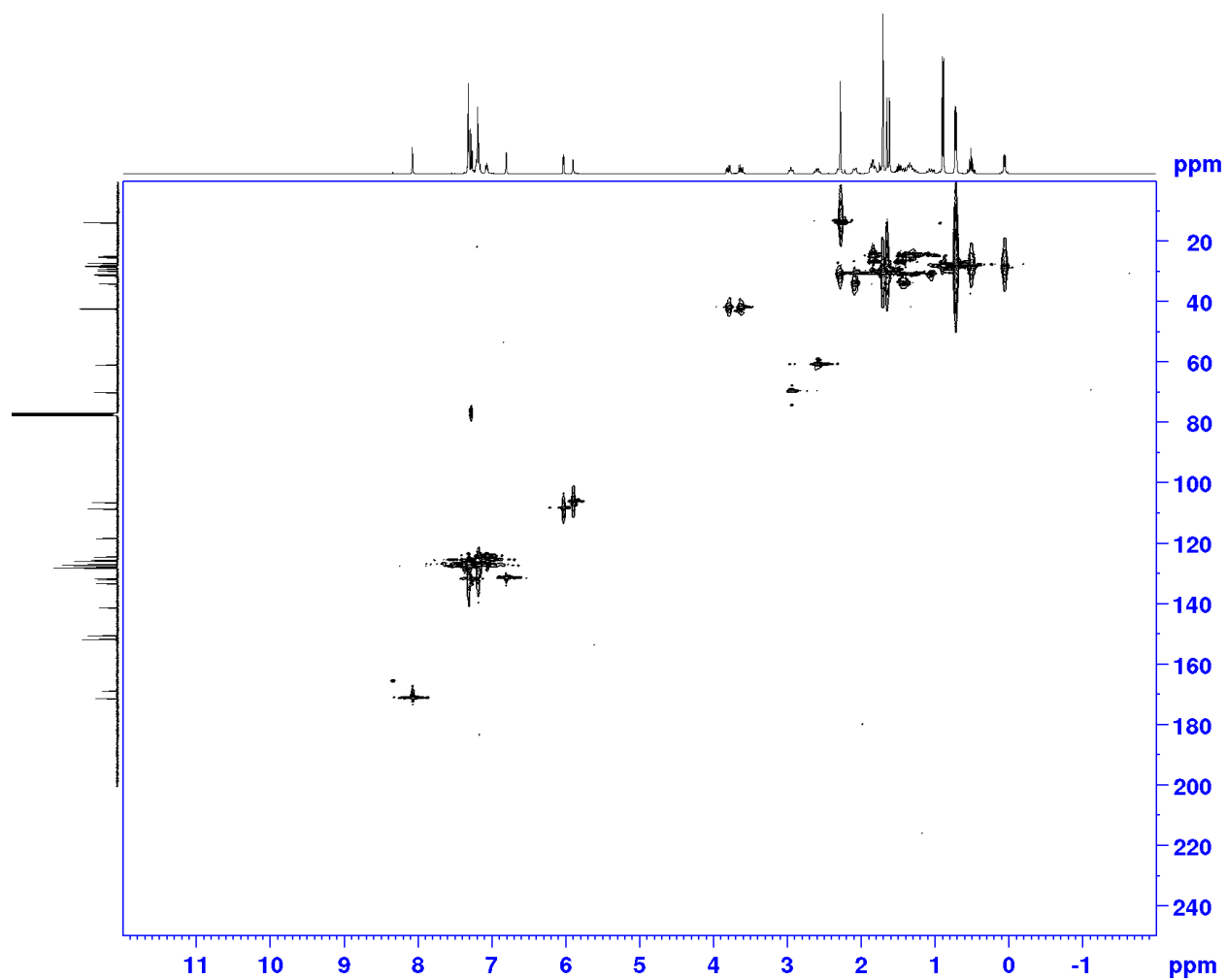


Figure C.22. 2D ^1H - ^{13}C Heteronuclear Single Quantum Coherence (HSQC) NMR spectrum (CDCl_3 , 25 $^\circ\text{C}$) of complex **47g**

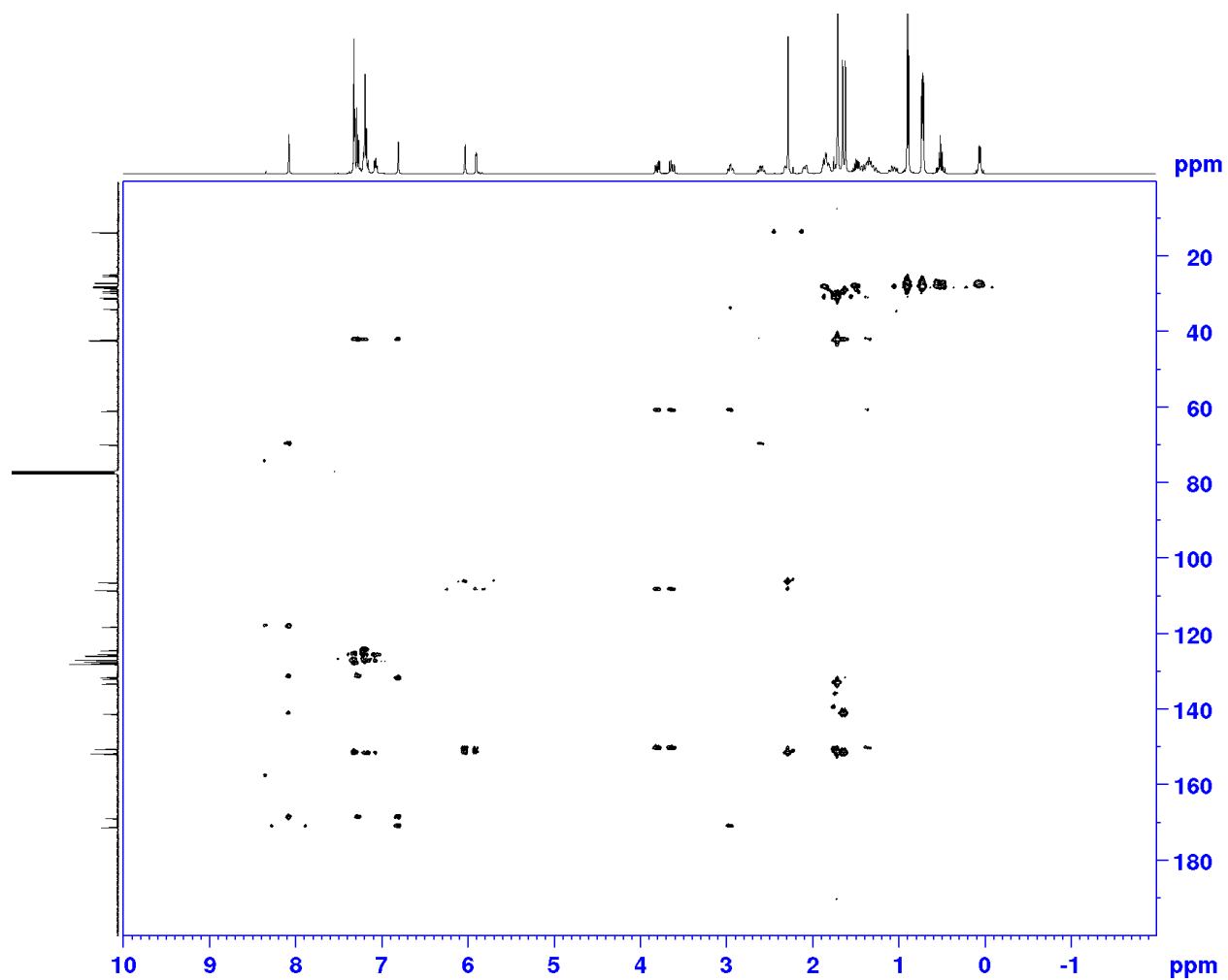


Figure C.23. ^1H - ^{13}C Heteronuclear Multiple Bond Correlation (HMBC) NMR spectrum (CDCl_3 , 25 $^\circ\text{C}$) of complex

47g

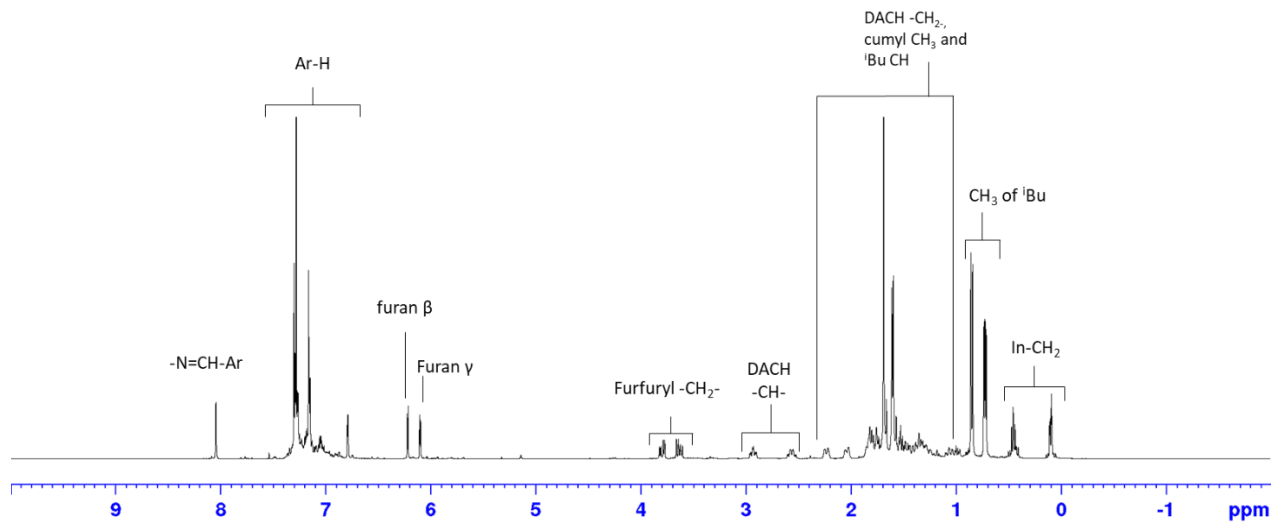


Figure C.24. ^1H NMR spectrum (400 MHz, CDCl_3 , 25 °C) of complex **47h**

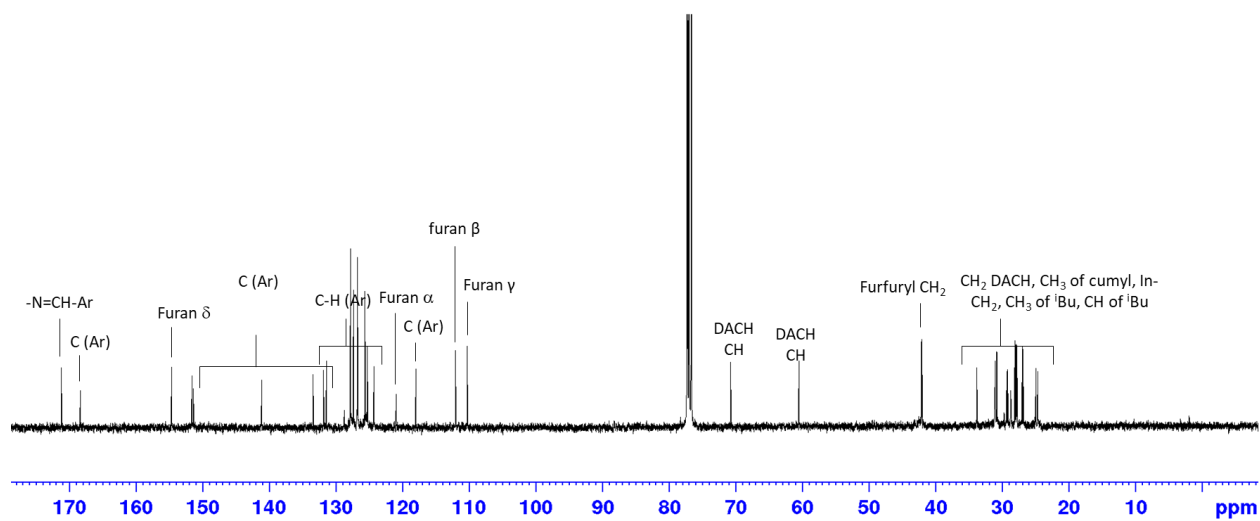


Figure C.25. $^{13}\text{C}\{^1\text{H}\}$ NMR spectrum (100 MHz, CDCl_3 , 25 °C) of complex **47h**

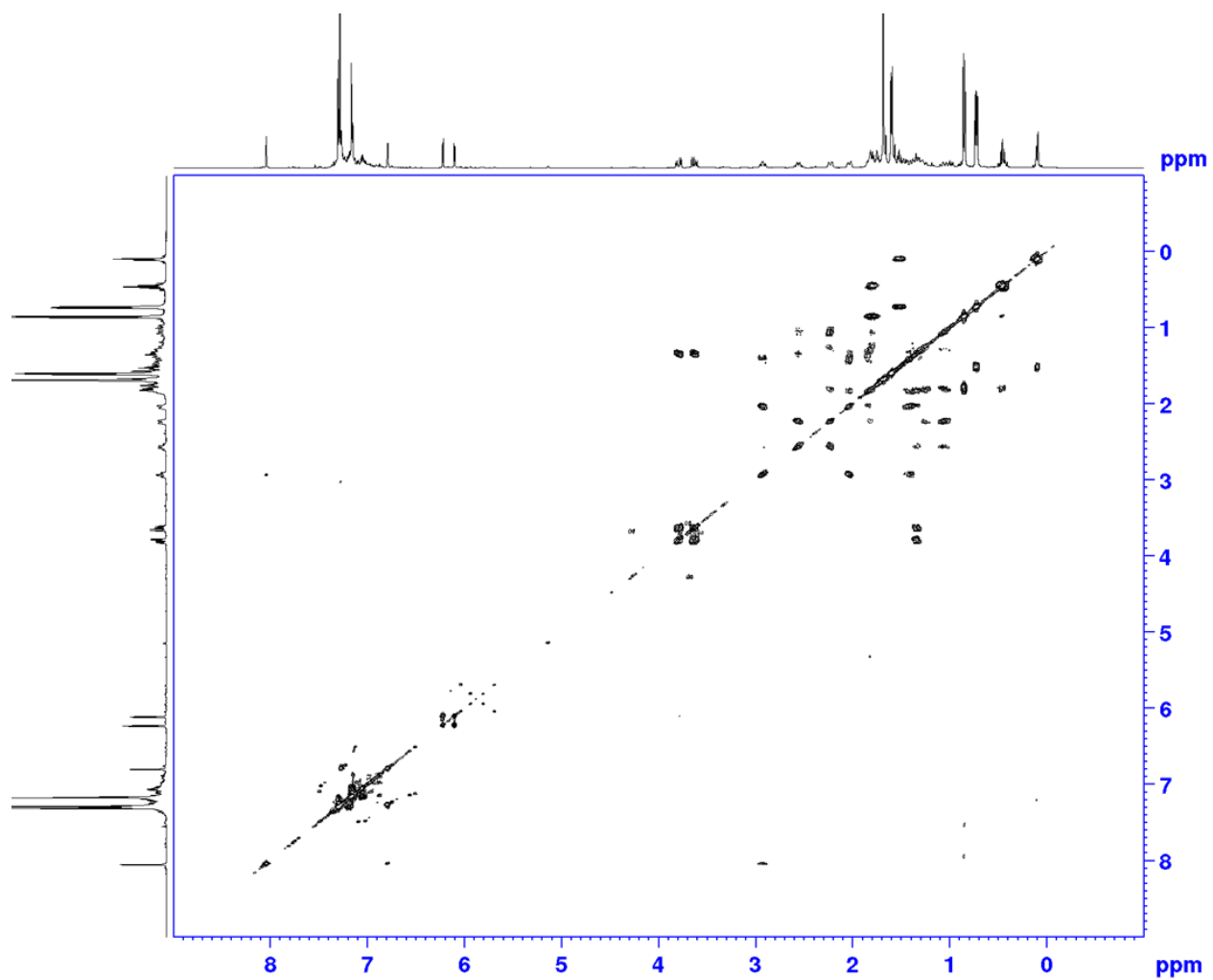


Figure C.26. ^1H - ^1H COSY NMR spectrum (400 MHz, CDCl_3 , 25 °C) of complex **47h**

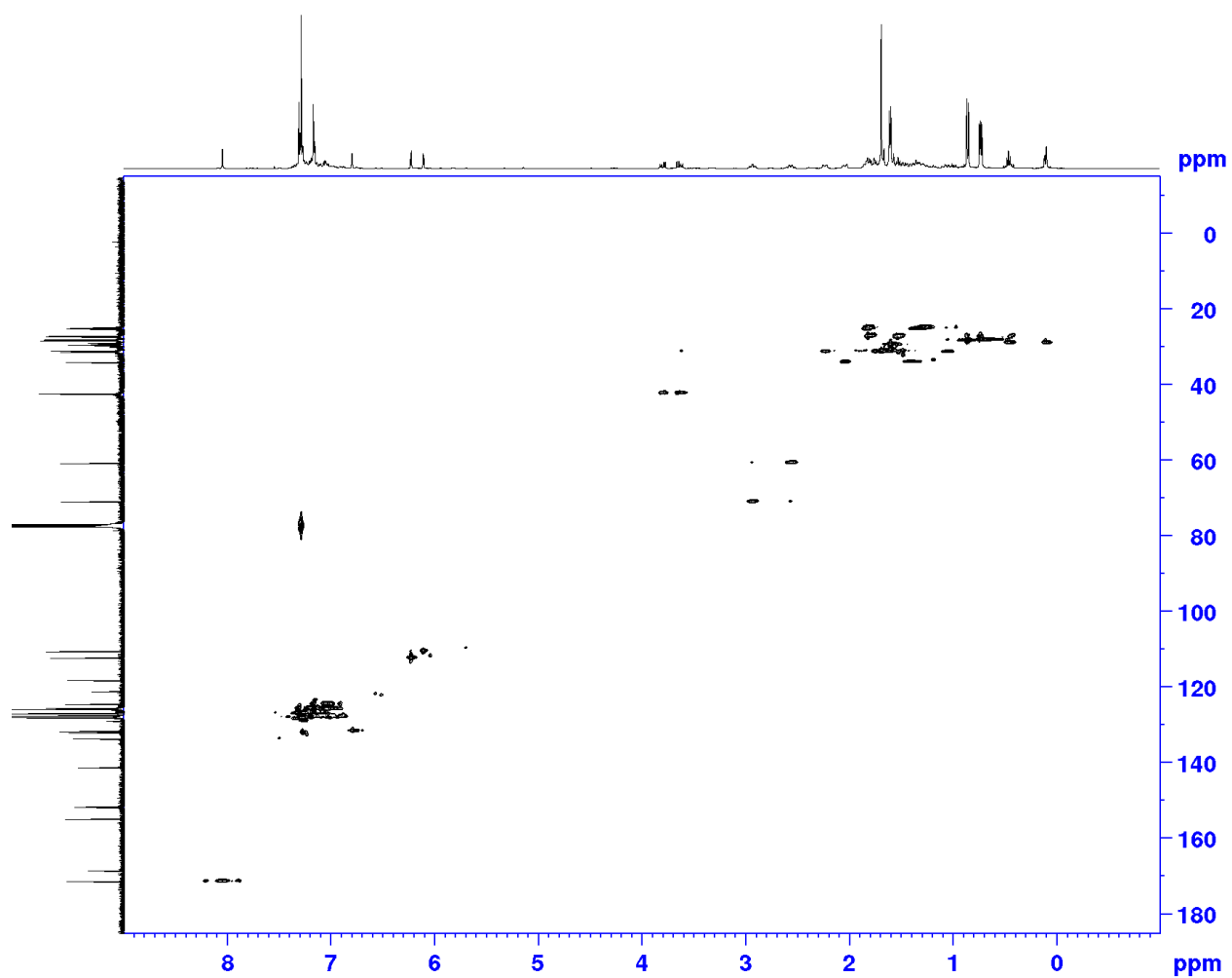


Figure C.27. 2D ^1H - ^{13}C Heteronuclear Single Quantum Coherence (HSQC) NMR spectrum (CDCl_3 , 25 $^\circ\text{C}$) of complex **47h**

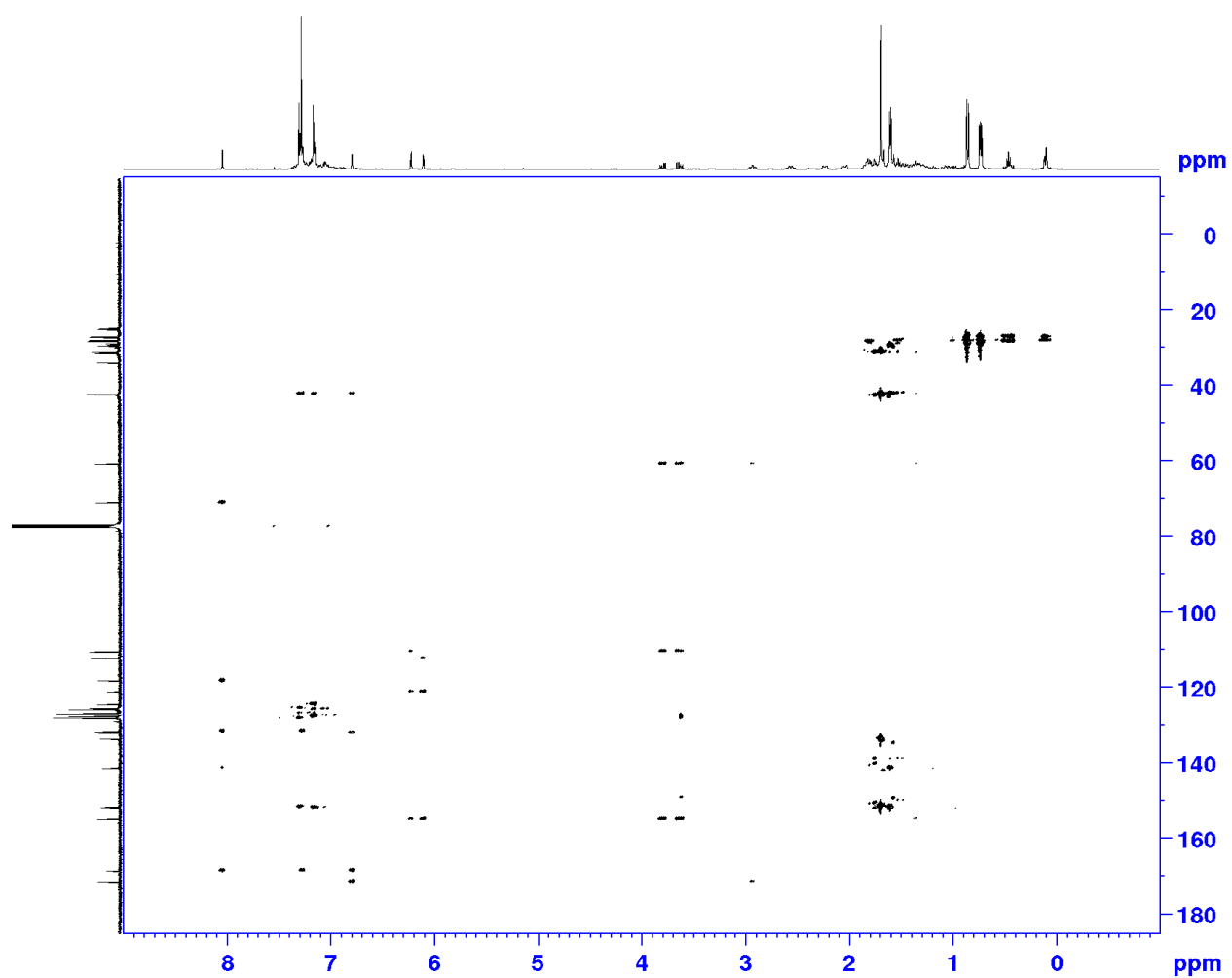


Figure C.28. ^1H - ^{13}C Heteronuclear Multiple Bond Correlation (HMBC) NMR spectrum (CDCl_3 , 25 $^\circ\text{C}$) of complex **47h**

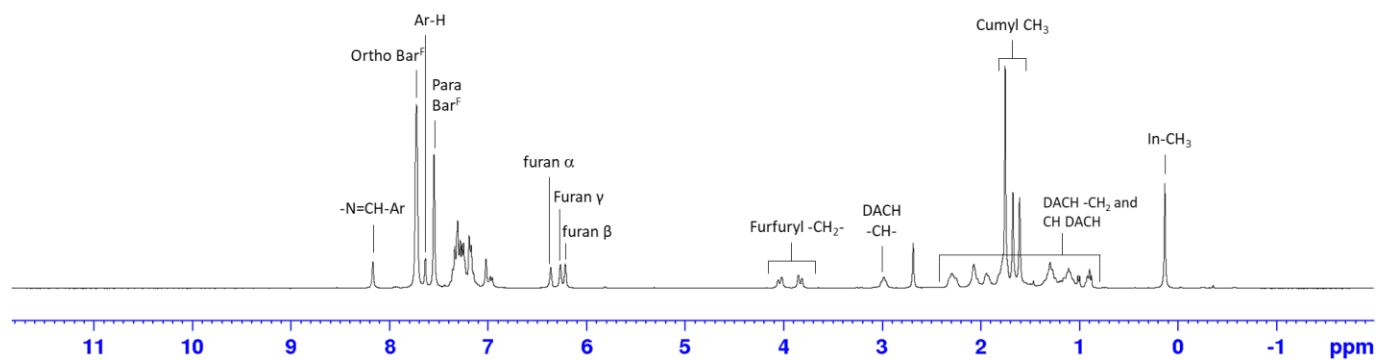


Figure C.29. ^1H NMR spectrum (CDCl_3 , 400 MHz, 25 °C) of complex **48e**

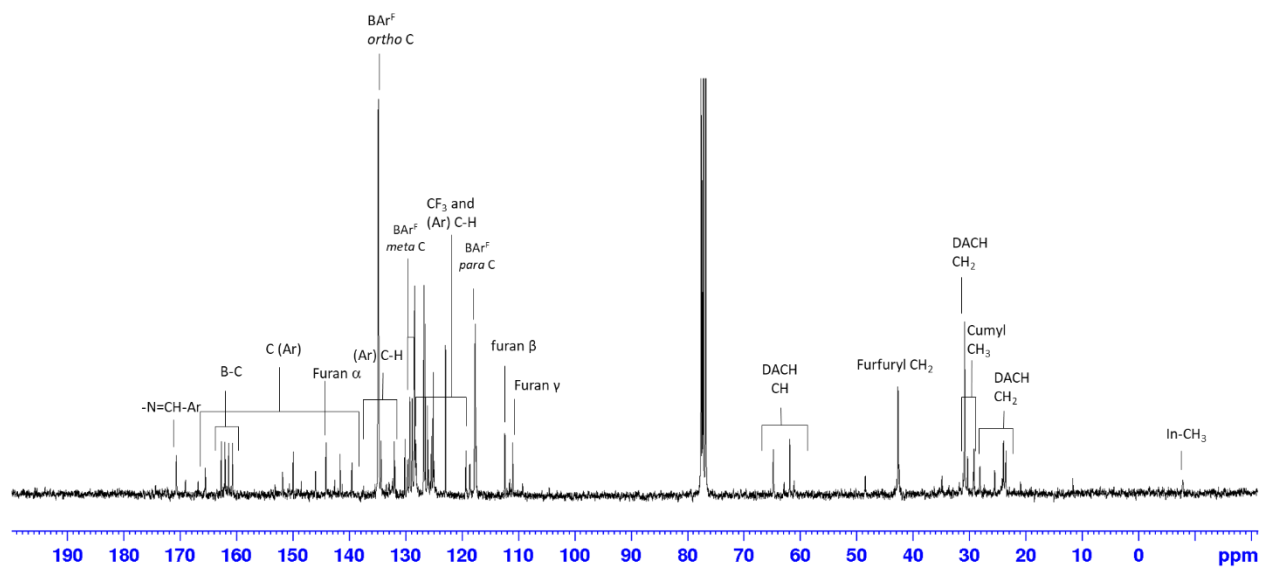


Figure C.30. $^{13}\text{C}\{^1\text{H}\}$ NMR spectrum (75MHz, CDCl_3 , 25 °C) of complex **48e**

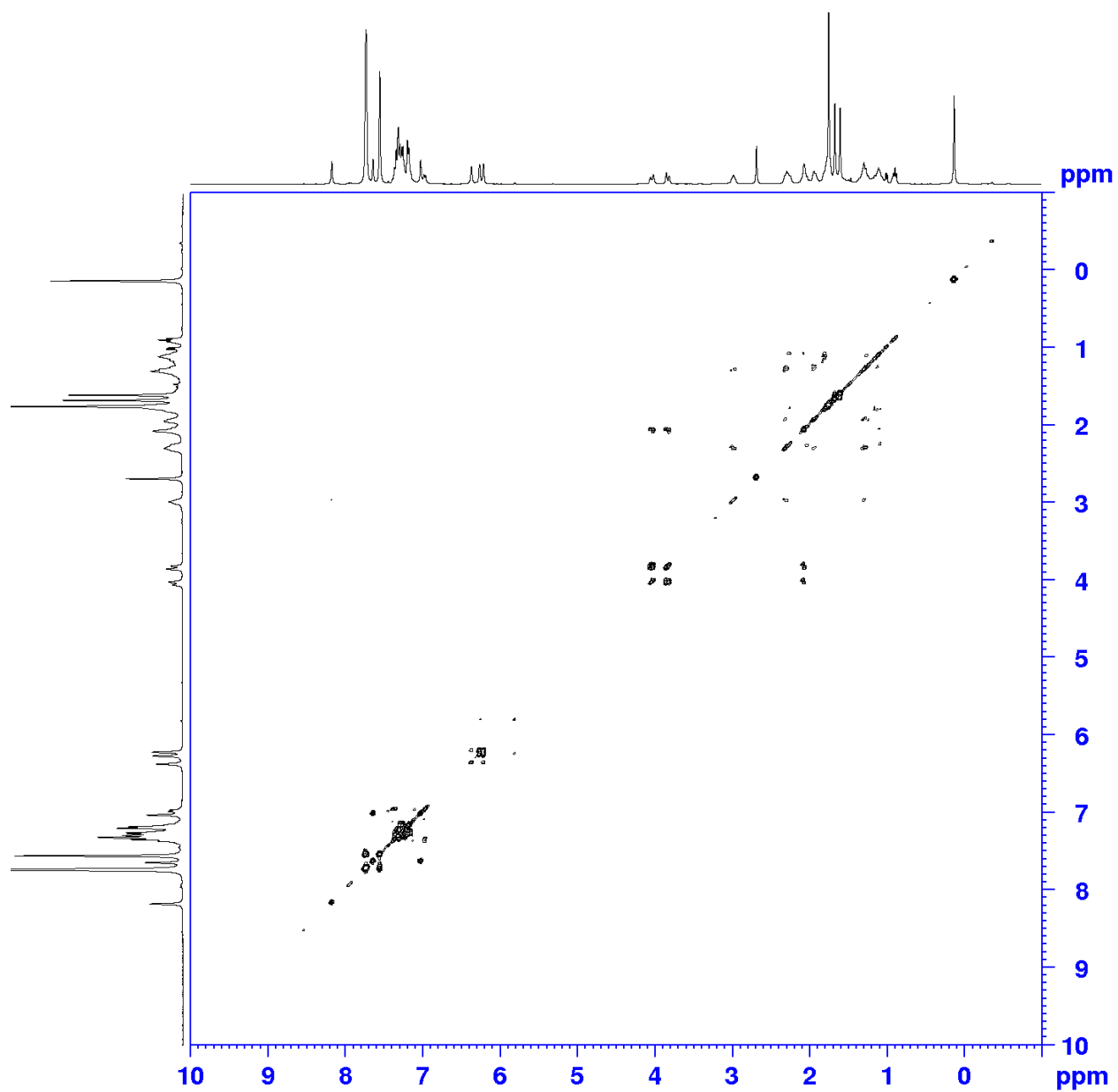


Figure C.31. ^1H - ^1H COSY NMR spectrum (400 MHz, CDCl_3 , 25 °C) of complex **48e**

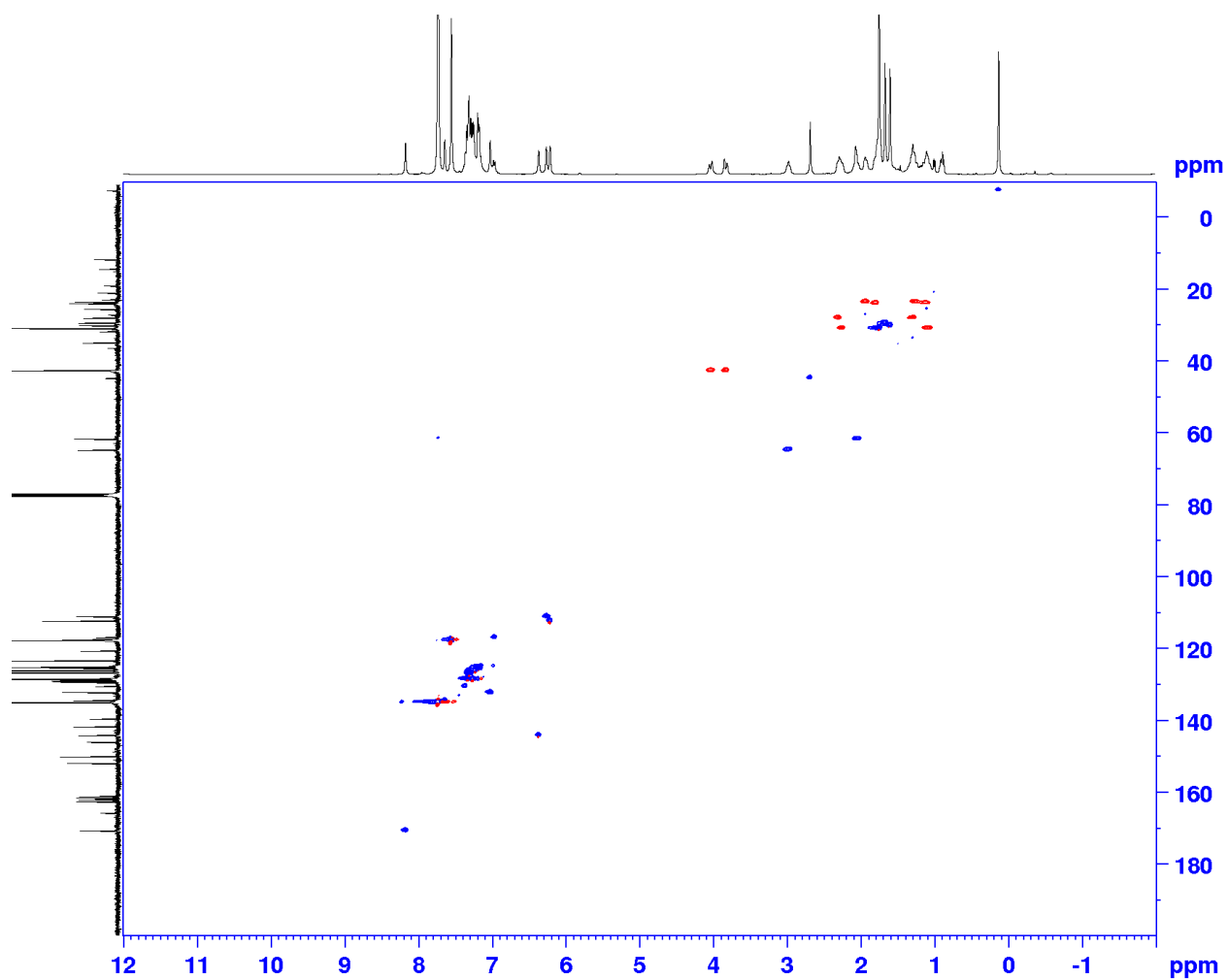


Figure C.32. 2D ^1H - ^{13}C Heteronuclear Single Quantum Coherence (HSQC) NMR spectrum (CDCl_3 , 25 $^\circ\text{C}$) of complex **48e**

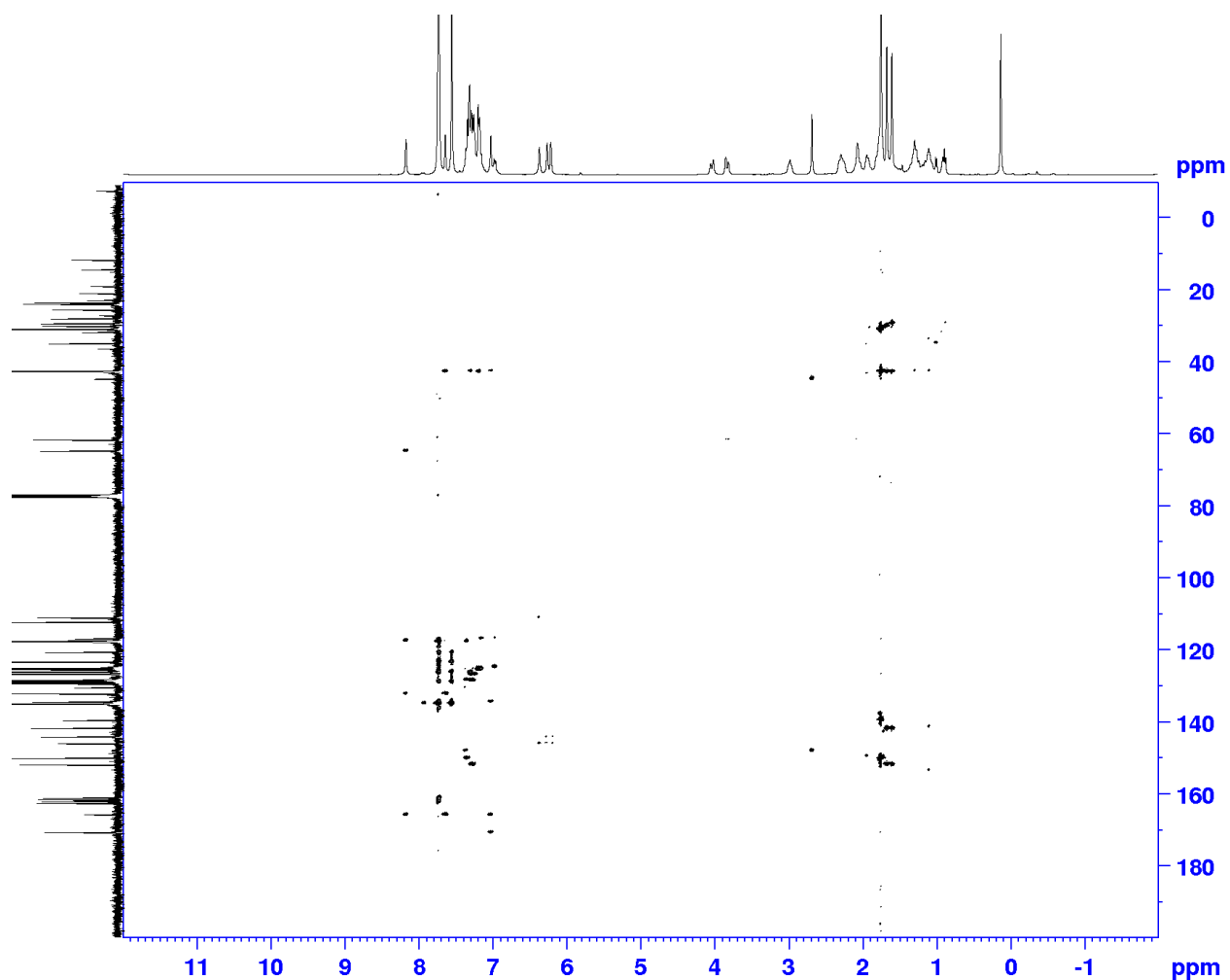


Figure C.33. ^1H - ^{13}C Heteronuclear Multiple Bond Correlation (HMBC) NMR spectrum (CDCl_3 , 25 $^\circ\text{C}$) of complex **48e**

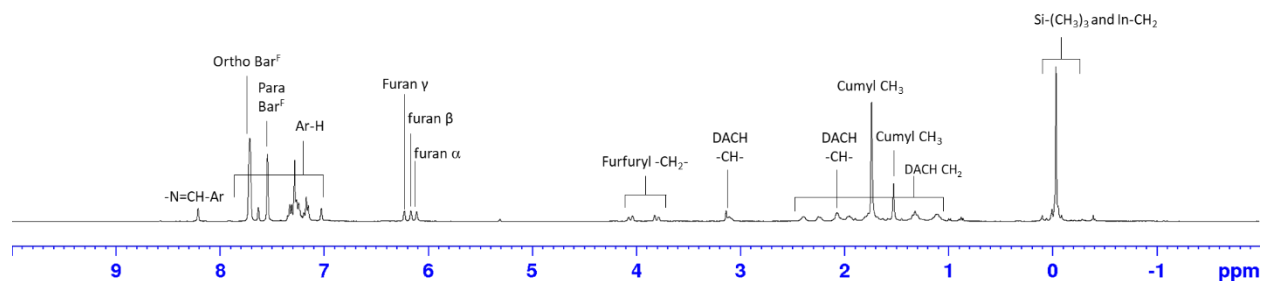


Figure C.34. ^1H NMR spectrum (CDCl_3 , 400 MHz, 25 $^\circ\text{C}$) of complex **48f**

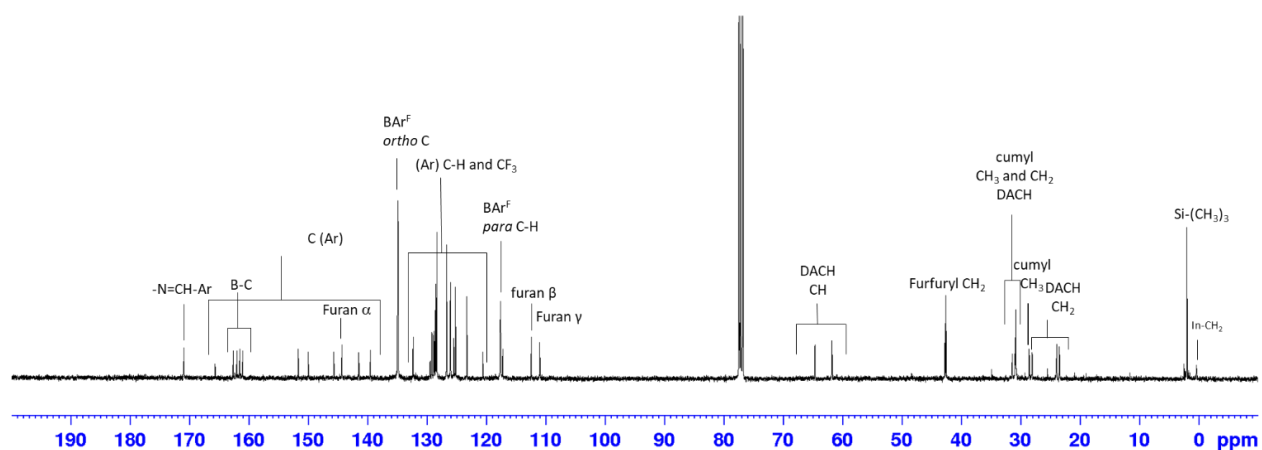


Figure C.35. $^{13}\text{C}\{^1\text{H}\}$ NMR spectrum (100 MHz, CDCl_3 , 25 °C) of complex **48f**

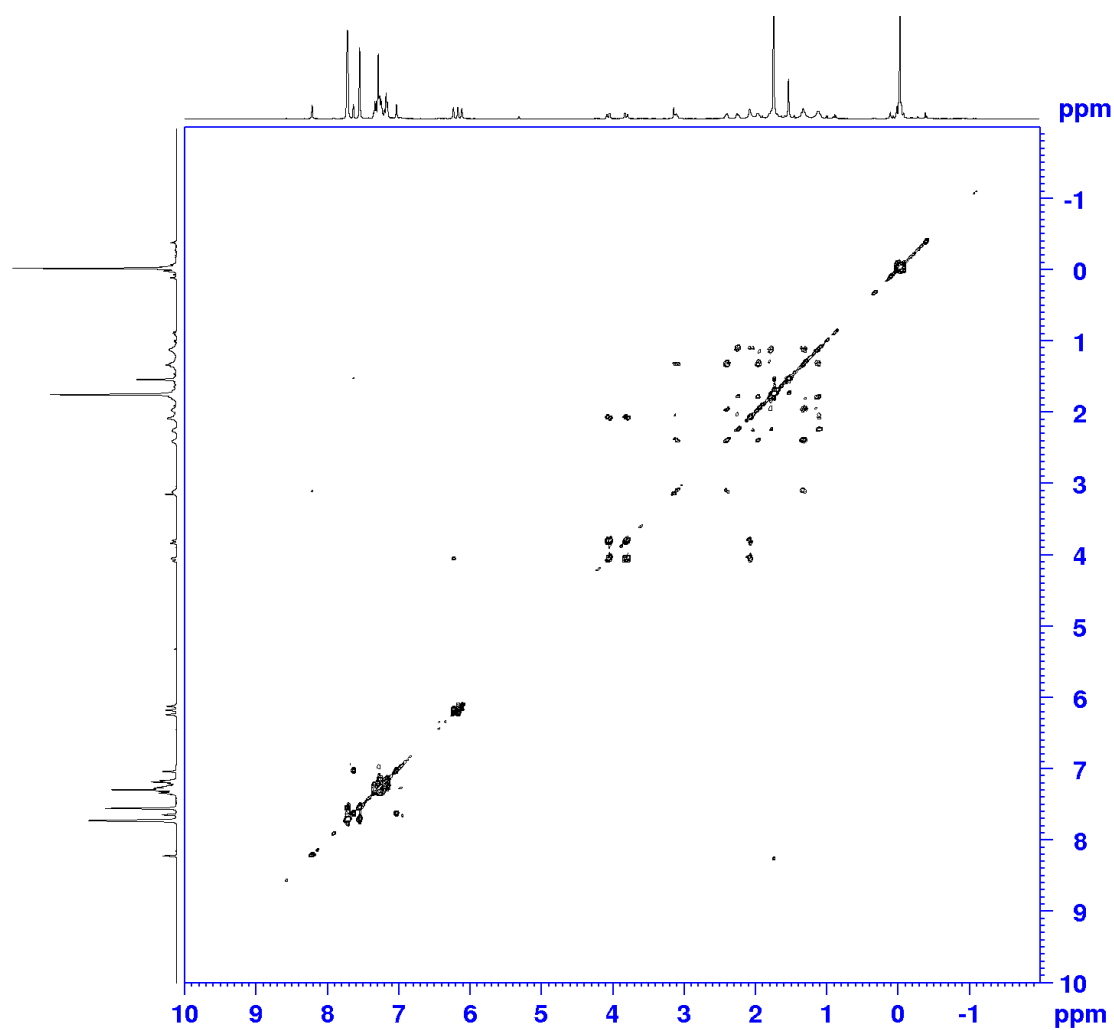


Figure C.36. ^1H - ^1H COSY NMR spectrum (400 MHz, CDCl_3 , 25 °C) of complex **48f**

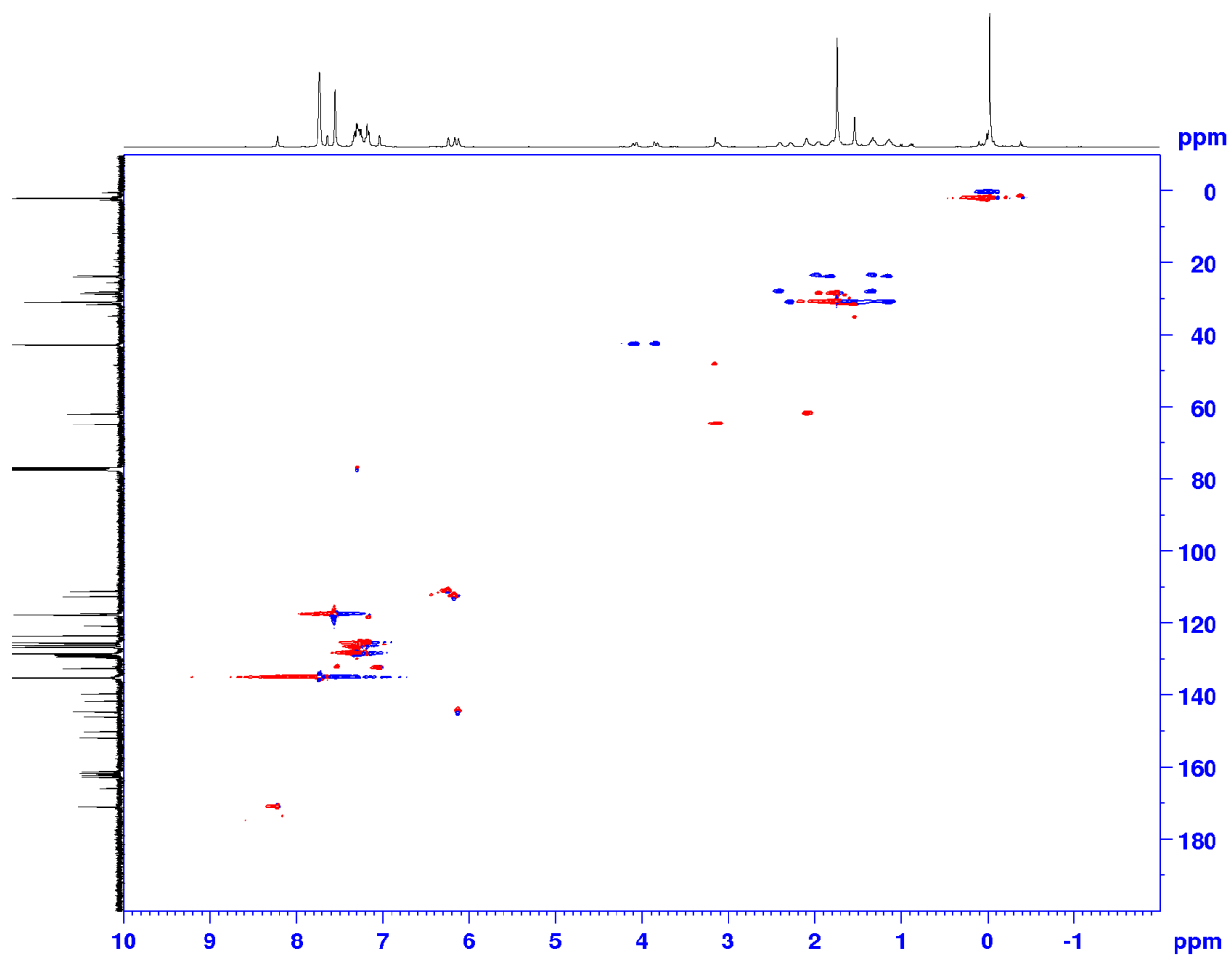


Figure C.37. 2D ^1H - ^{13}C Heteronuclear Single Quantum Coherence (HSQC) NMR spectrum (CDCl_3 , 25 $^\circ\text{C}$) of complex **48f**

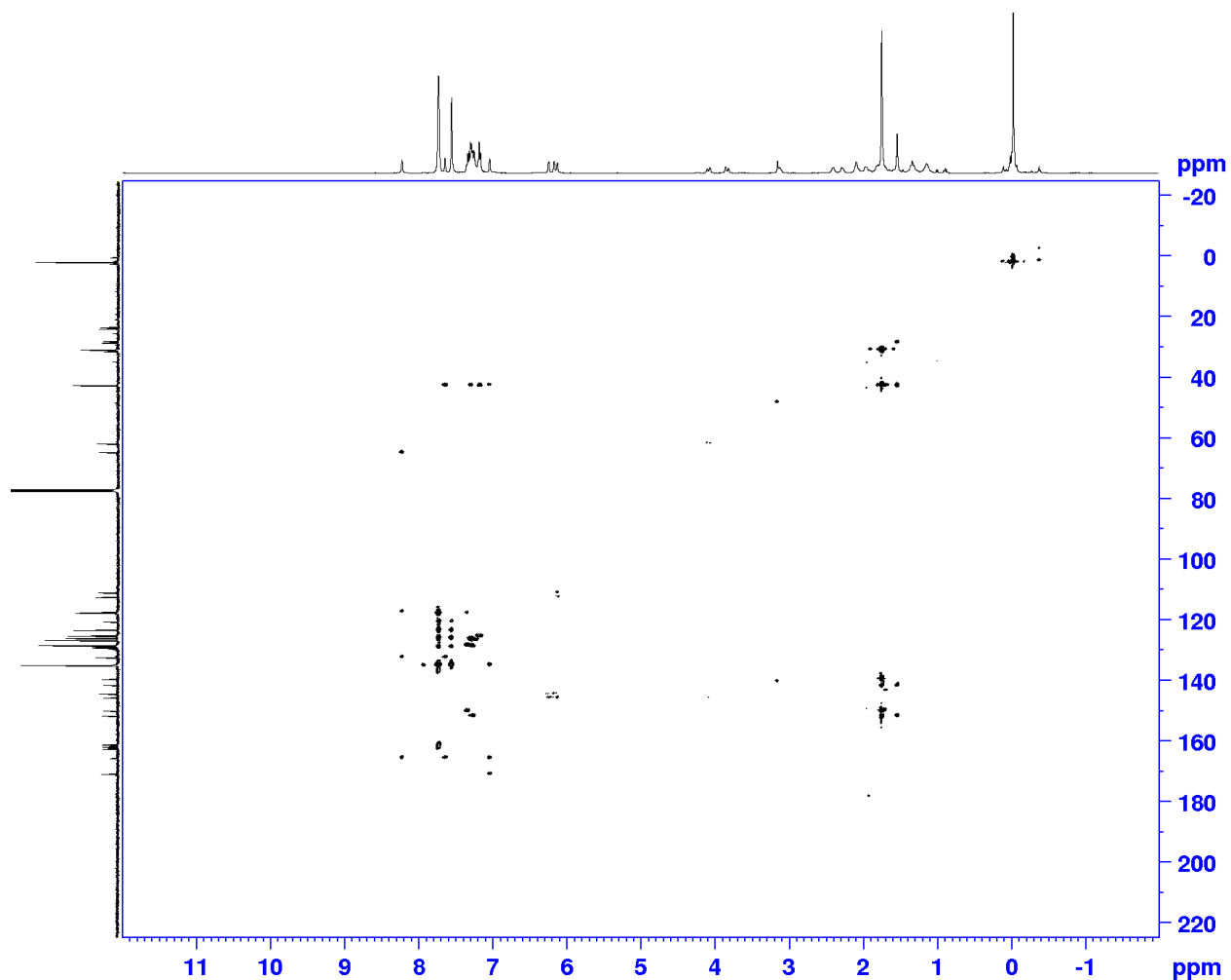


Figure C.38. ^1H - ^{13}C Heteronuclear Multiple Bond Correlation (HMBC) NMR spectrum (CDCl_3 , 25 $^\circ\text{C}$) of complex **48f**

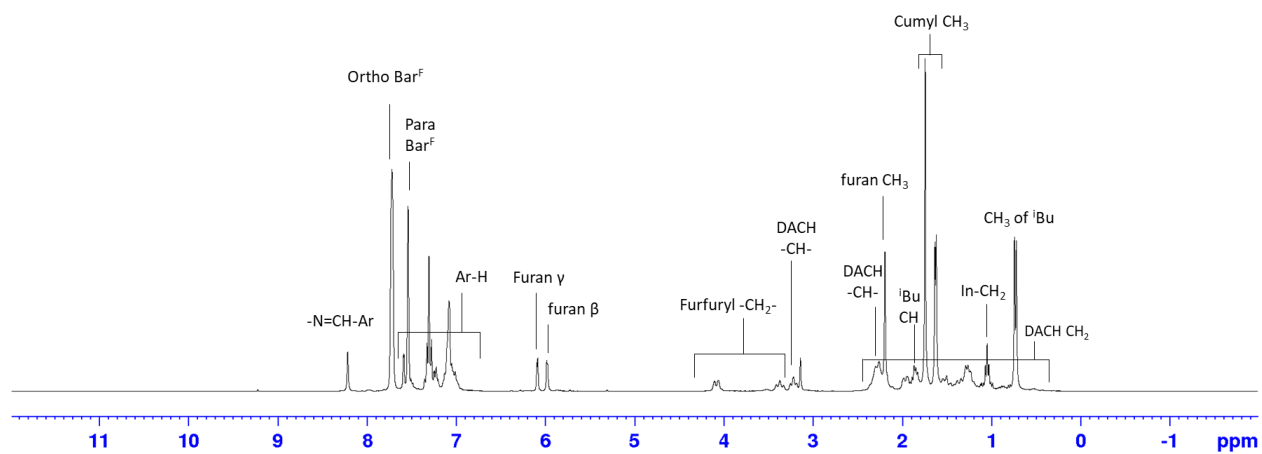


Figure C.39. ^1H NMR spectrum (CDCl_3 , 300 MHz, 25 $^\circ\text{C}$) of complex **48g**

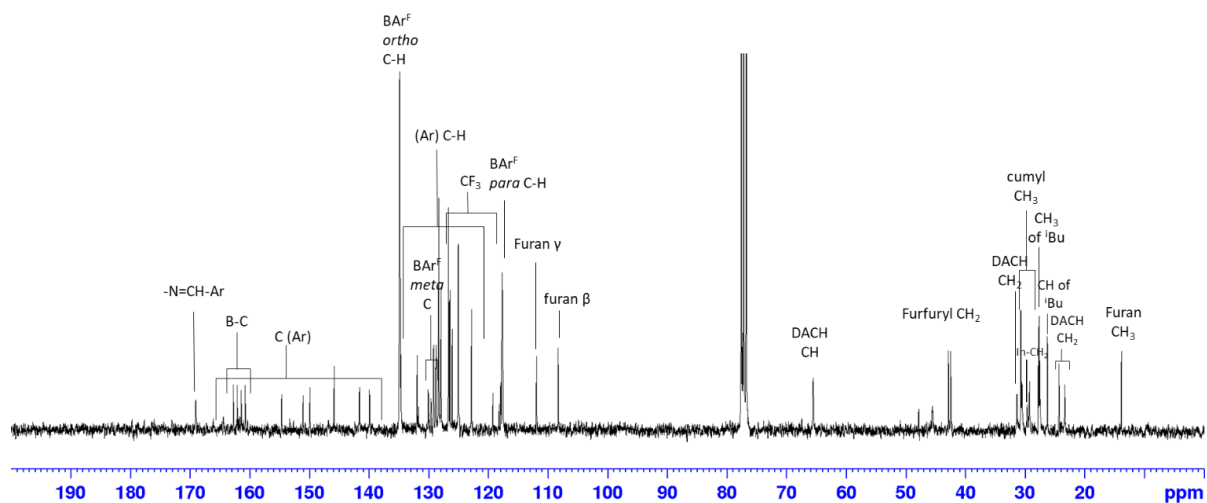


Figure C.40. $^{13}\text{C}\{^1\text{H}\}$ NMR spectrum (75 MHz, CDCl_3 , 25 °C) of complex **48g**

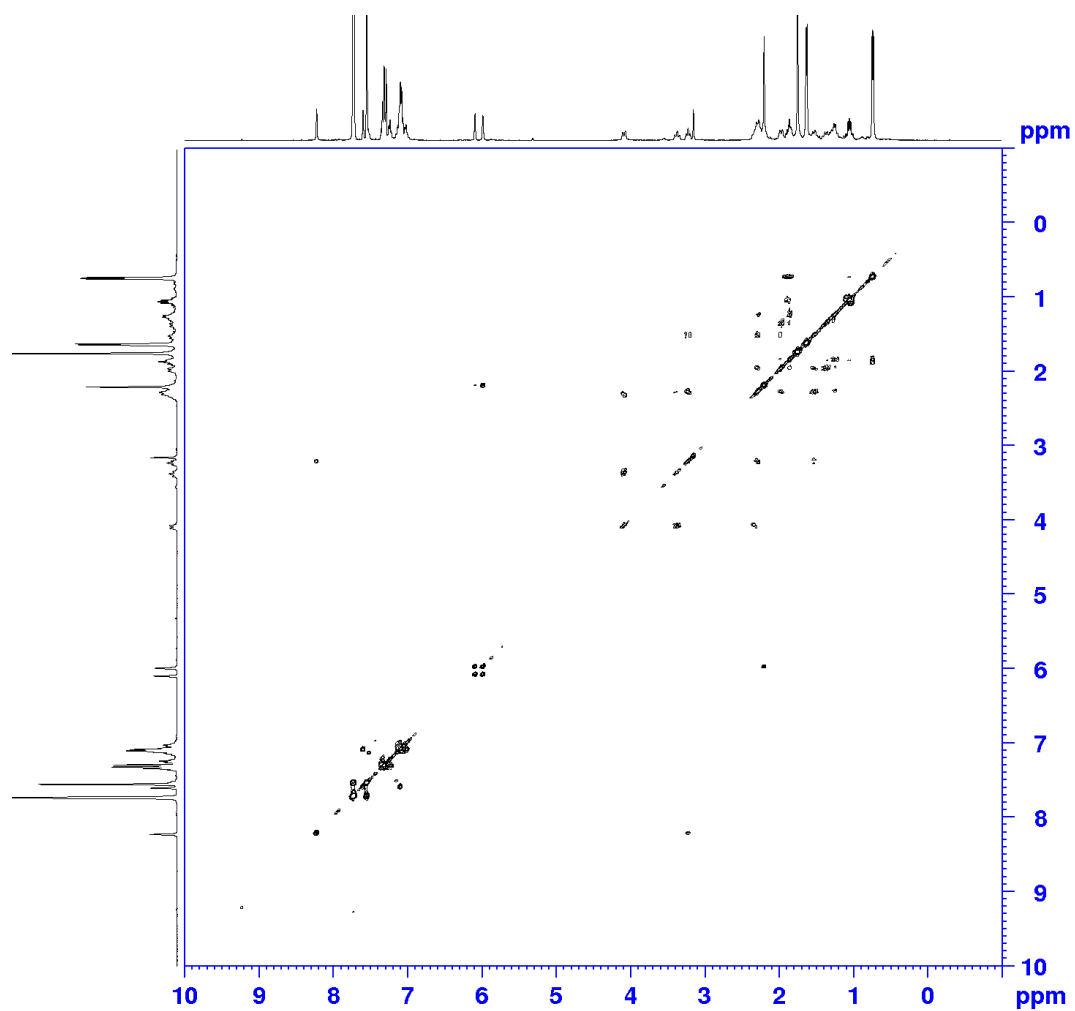


Figure C.41. ^1H - ^1H COSY NMR spectrum (400 MHz, CDCl_3 , 25 °C) of complex **48g**

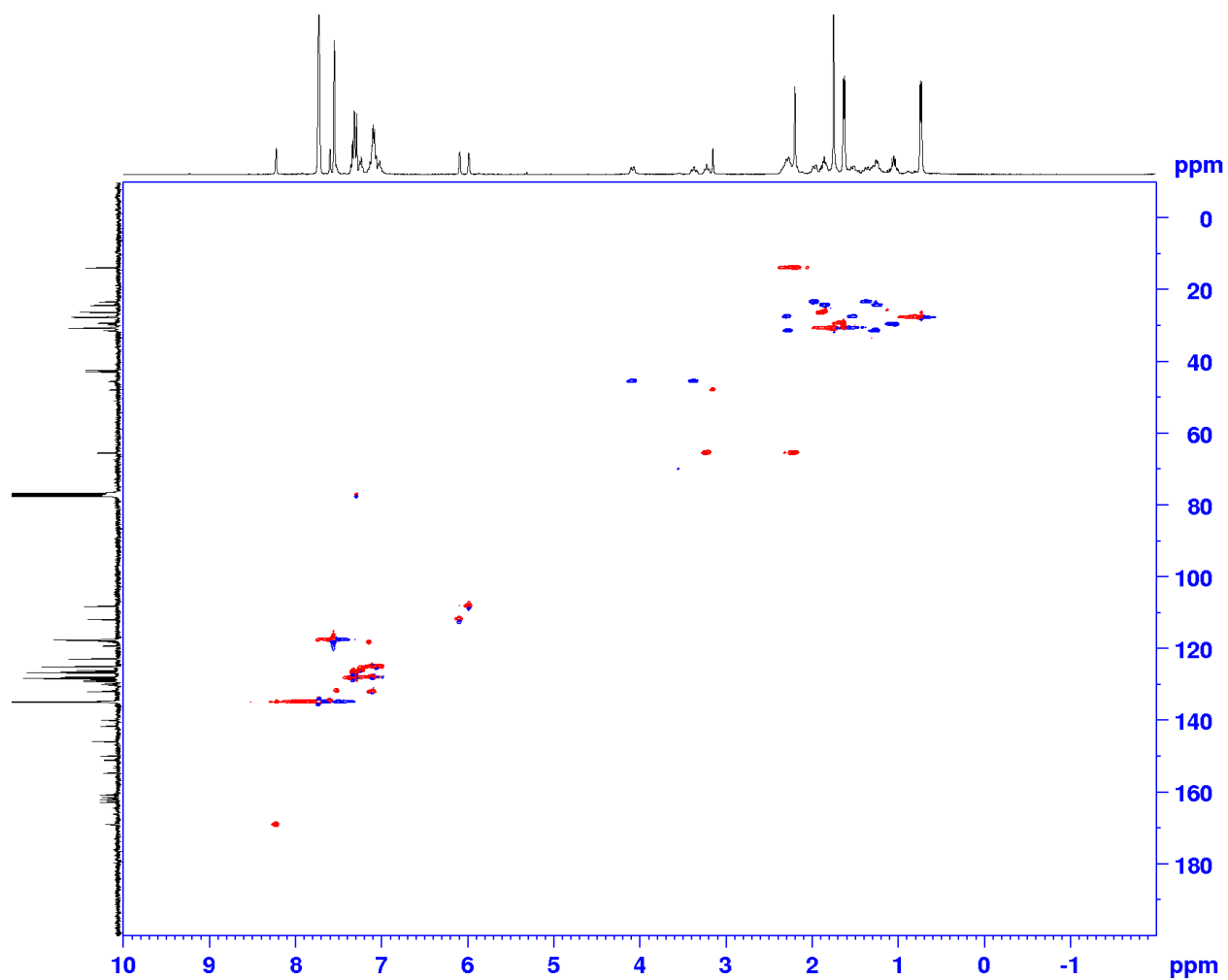


Figure C.42. 2D ^1H - ^{13}C Heteronuclear Single Quantum Coherence (HSQC) NMR spectrum (CDCl_3 , 25 $^\circ\text{C}$) of complex **48g**

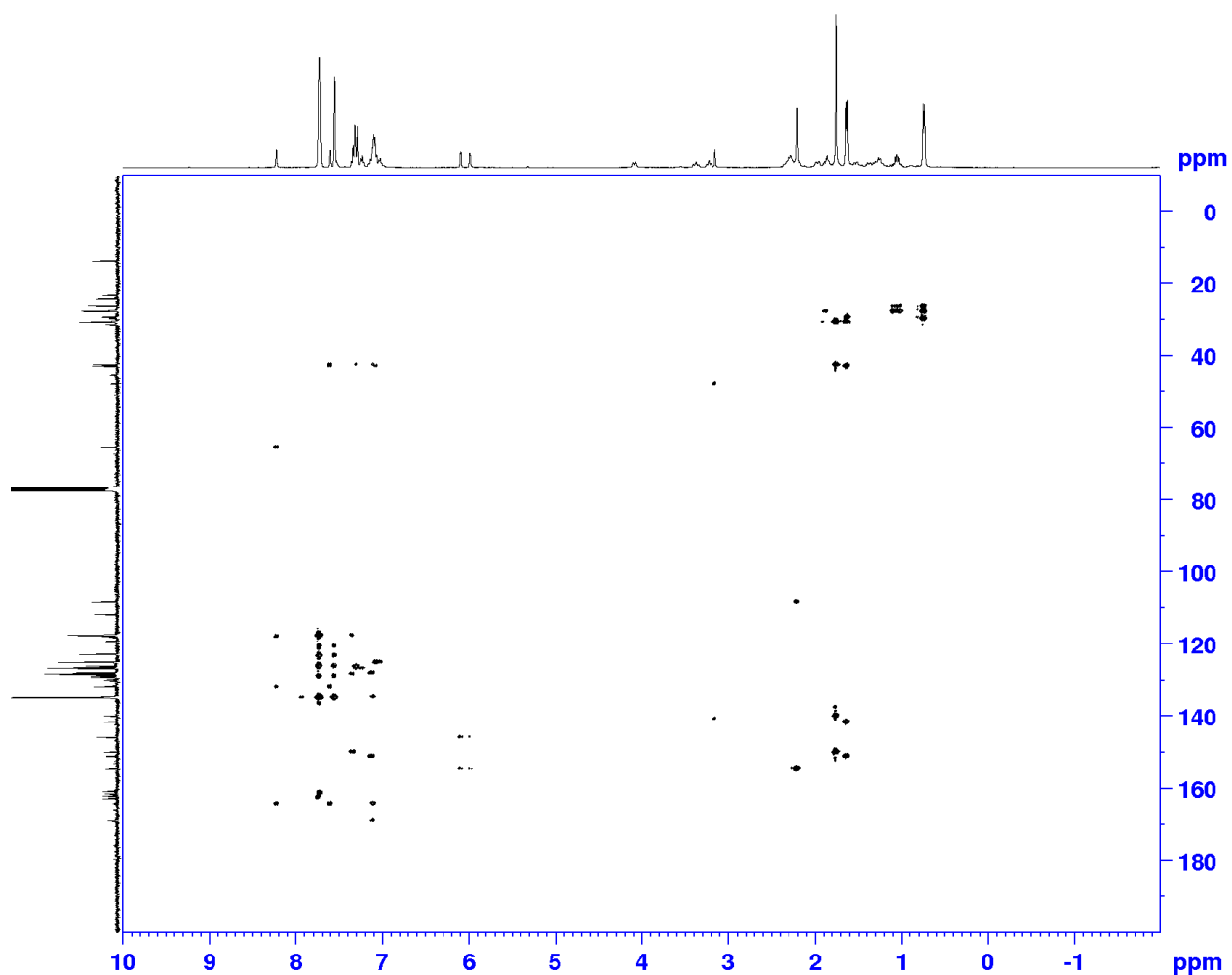


Figure C.43. ^1H - ^{13}C Heteronuclear Multiple Bond Correlation (HMBC) NMR spectrum (CDCl_3 , 25 $^\circ\text{C}$) of complex **48g**

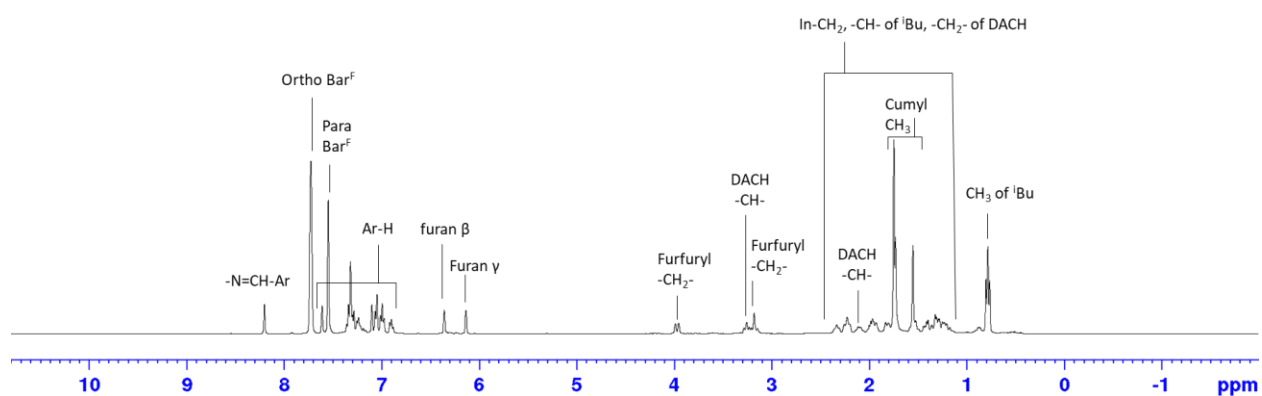


Figure C.44. ^1H NMR spectrum (CDCl_3 , 400 MHz, 25 $^\circ\text{C}$) of complex **48h**

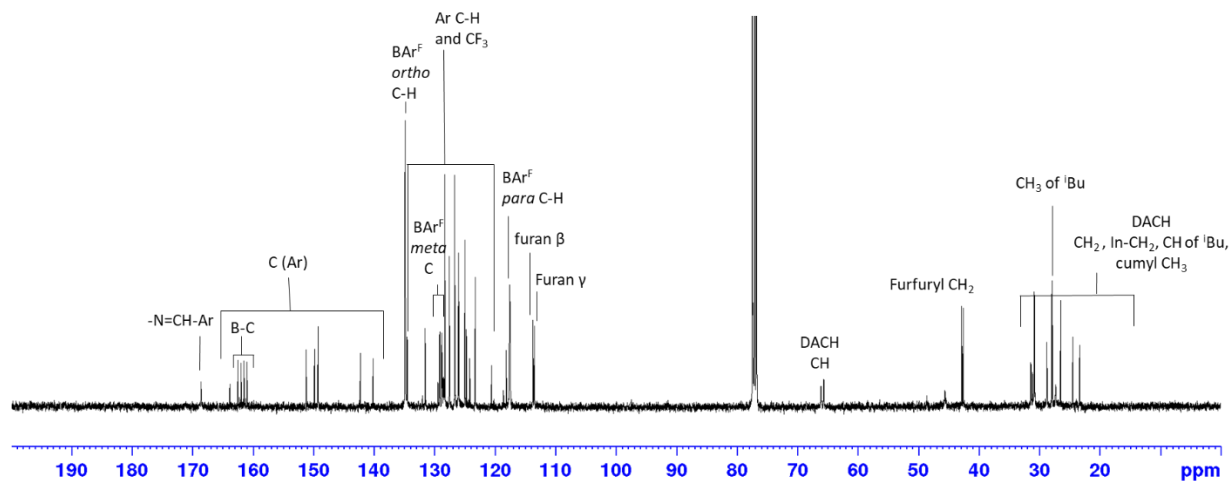


Figure C.45. $^{13}\text{C}\{^1\text{H}\}$ NMR spectrum (100 MHz, CDCl_3 , 25 °C) of complex **48h**

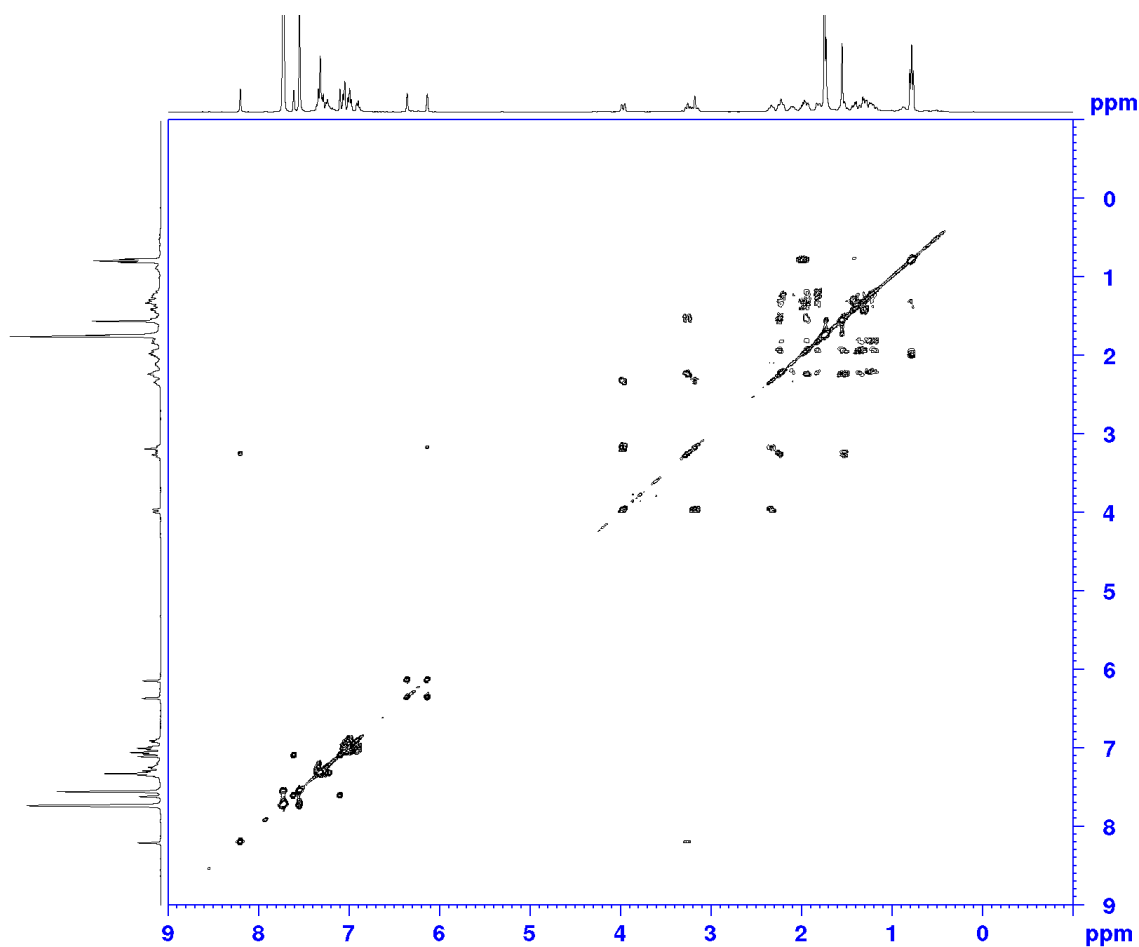


Figure C.46. ^1H - ^1H COSY NMR spectrum (400 MHz, CDCl_3 , 25 °C) of complex **48h**

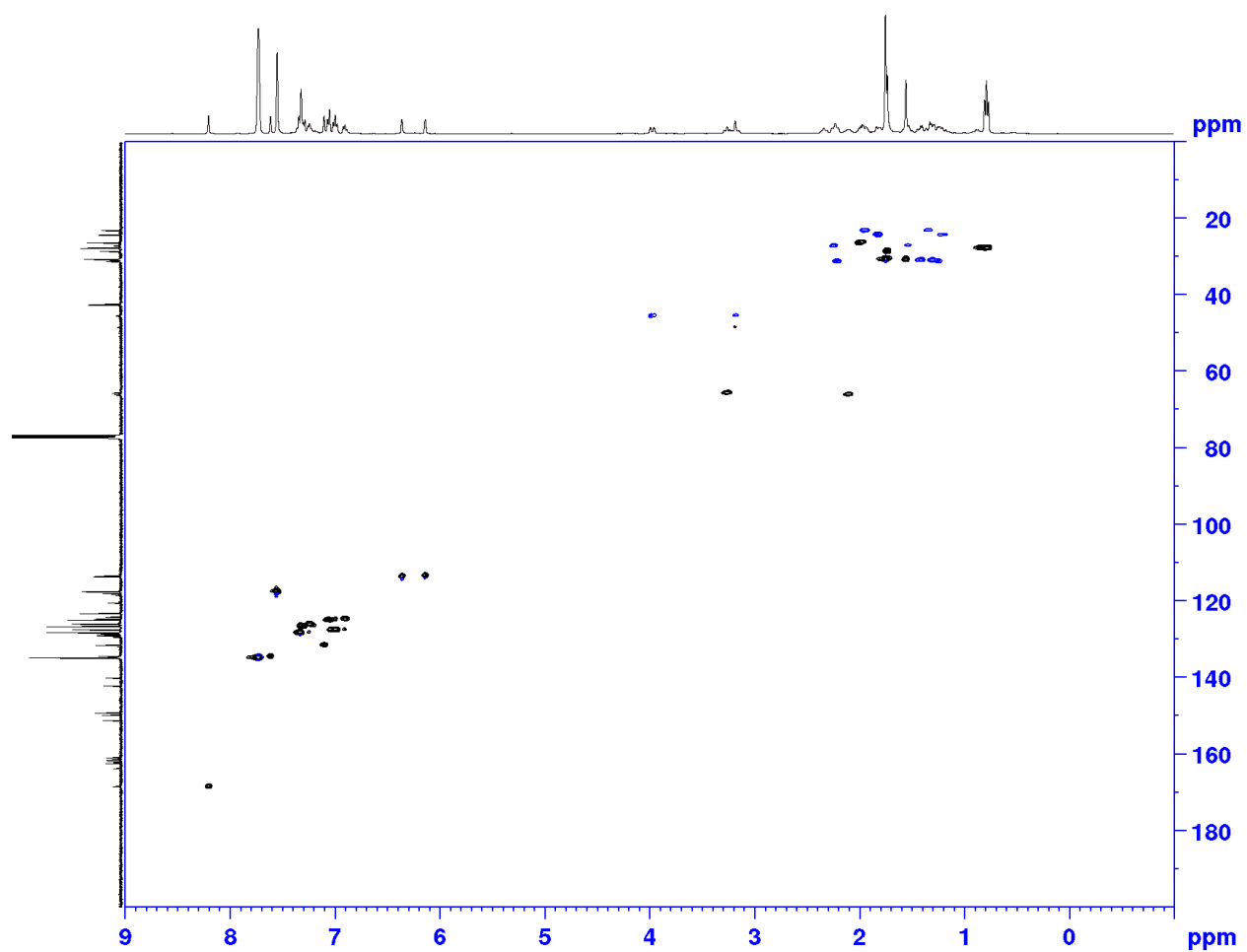


Figure C.47. 2D ^1H - ^{13}C Heteronuclear Single Quantum Coherence (HSQC) NMR spectrum (CDCl_3 , 25 $^\circ\text{C}$) of complex **48h**

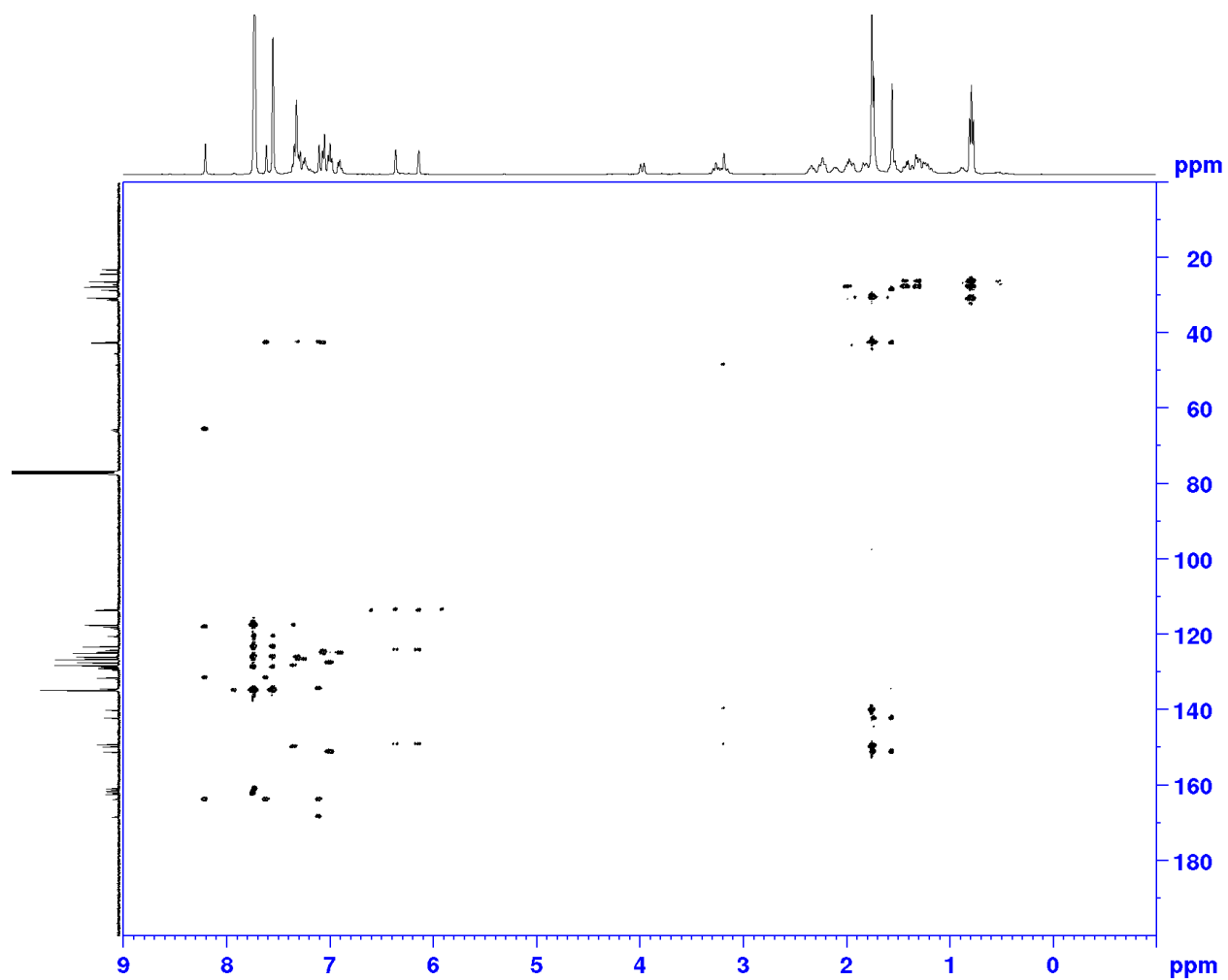
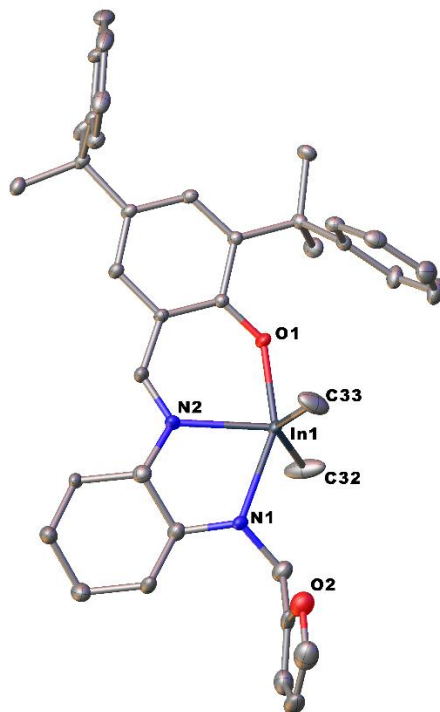


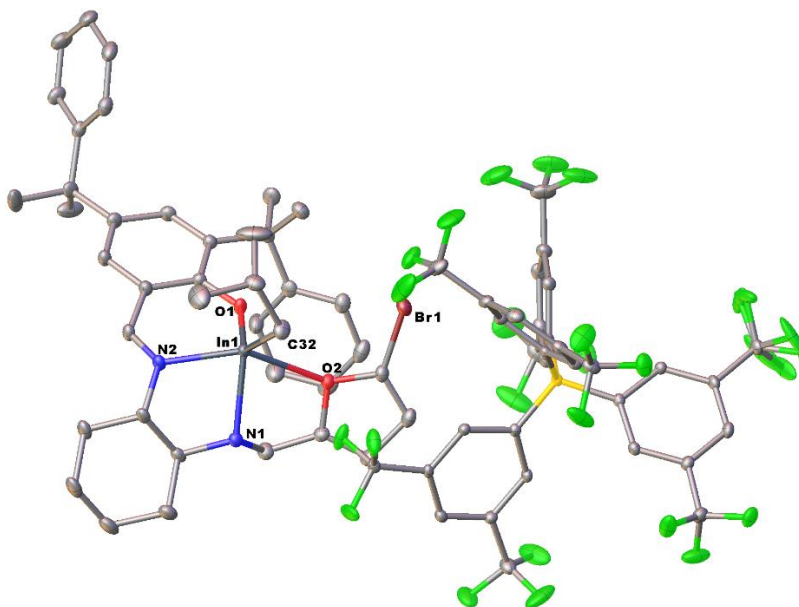
Figure C.48. ^1H - ^{13}C Heteronuclear Multiple Bond Correlation (HMBC) NMR spectrum (CDCl_3 , 25 $^\circ\text{C}$) of complex

48h



Selected bond length (Å) and angles (°) for complex 47e .				
Bond Distances	In1-N1	2.4593(17)	In1-C32	2.150(3)
	In1-N2	2.2921(18)	In1-C33	2.164(3)
	In1-O1	2.1623(15)		
Bond Angles	O1-In1-C32	93.62(9)	O1-In1-N1	154.54(6)
	O1-In1-C33	101.64(9)	N1-In1-C32	92.69(9)
	C32-In1-C33	137.37(17)	N1-In1-C33	90.14(9)
	N1-In1-N2	72.05(6)		

Figure C.49. The molecular structure of complex **47e**. (Depicted with thermal ellipsoids at 50% probability and H atoms and minor disorders omitted for clarity).



Selected bond length (Å) and angles (°) for complex 48h .				
Bond Distances	In1-N1	2.3118(17)	In1-O2	2.5845(14)
	In1-N2	2.1795(16)	In1-C32	2.140(2)
	In1-O1	2.0570(13)		
Bond Angles	O1-In1-C32	127.77(7)	O1-In1-N1	109.13(6)
	O1-In1-O2	77.83(5)	N1-In1-C32	118.28(7)
	N1-In1-N2	75.18(6)		

Figure C.50. The molecular structure of complex **48h**. (Depicted with thermal ellipsoids at 50% probability and H atoms and minor disorders omitted for clarity).

Table C.1. Selected crystal data

	Complex 47e	Complex 48h
Identification code	mo_pm280_0m	mo_pm282_0m
Empirical formula	C ₃₈ H ₄₇ InN ₂ O ₂	C ₇₂ H ₆₁ BBrF ₂₄ InN ₂ O ₂
Formula weight	678.59	1647.76
Temperature/K	296.15	90
Crystal system	monoclinic	monoclinic
Space group	P2 ₁ /c	P2 ₁ /c
a/Å	12.3599(5)	13.3231(11)
b/Å	19.2656(8)	39.918(3)
c/Å	14.2292(6)	13.5270(11)
$\alpha/^\circ$	90	90
$\beta/^\circ$	98.8620(10)	100.9150(10)
$\gamma/^\circ$	90	90
Volume/Å ³	3347.8(2)	7063.9(10)
Z	4	4
$\rho_{\text{calc}}/\text{g}/\text{cm}^3$	1.346	1.549
μ/mm^{-1}	0.741	1.010
F(000)	1416.0	3312.0
Crystal size/mm ³	0.043 × 0.02 × 0.02	0.025 × 0.025 × 0.011
Radiation	MoK α (λ = 0.71073)	MoK α (λ = 0.71073)
2 θ range for data collection/ $^\circ$	3.334 to 65.224	3.114 to 61.086
Index ranges	-15 ≤ h ≤ 18, -28 ≤ k ≤ 28, -21 ≤ l ≤ 21	-19 ≤ h ≤ 19, -57 ≤ k ≤ 57, -19 ≤ l ≤ 19
Reflections collected	60479	179985
Independent reflections	12198 [R _{int} = 0.0168, R _{sigma} = 0.0122]	21581 [R _{int} = 0.0564, R _{sigma} = 0.0337]
Data/restraints/parameters	12198/0/394	21581/0/962
Goodness-of-fit on F ²	1.037	1.061
Final R indexes [I >= 2 σ (I)]	R ₁ = 0.0426, wR ₂ = 0.1082	R ₁ = 0.0385, wR ₂ = 0.0806
Final R indexes [all data]	R ₁ = 0.0460, wR ₂ = 0.1111	R ₁ = 0.0547, wR ₂ = 0.0862
Largest diff. peak/hole / e Å ⁻³	3.30/-0.91	0.61/-0.84
Flack parameter		

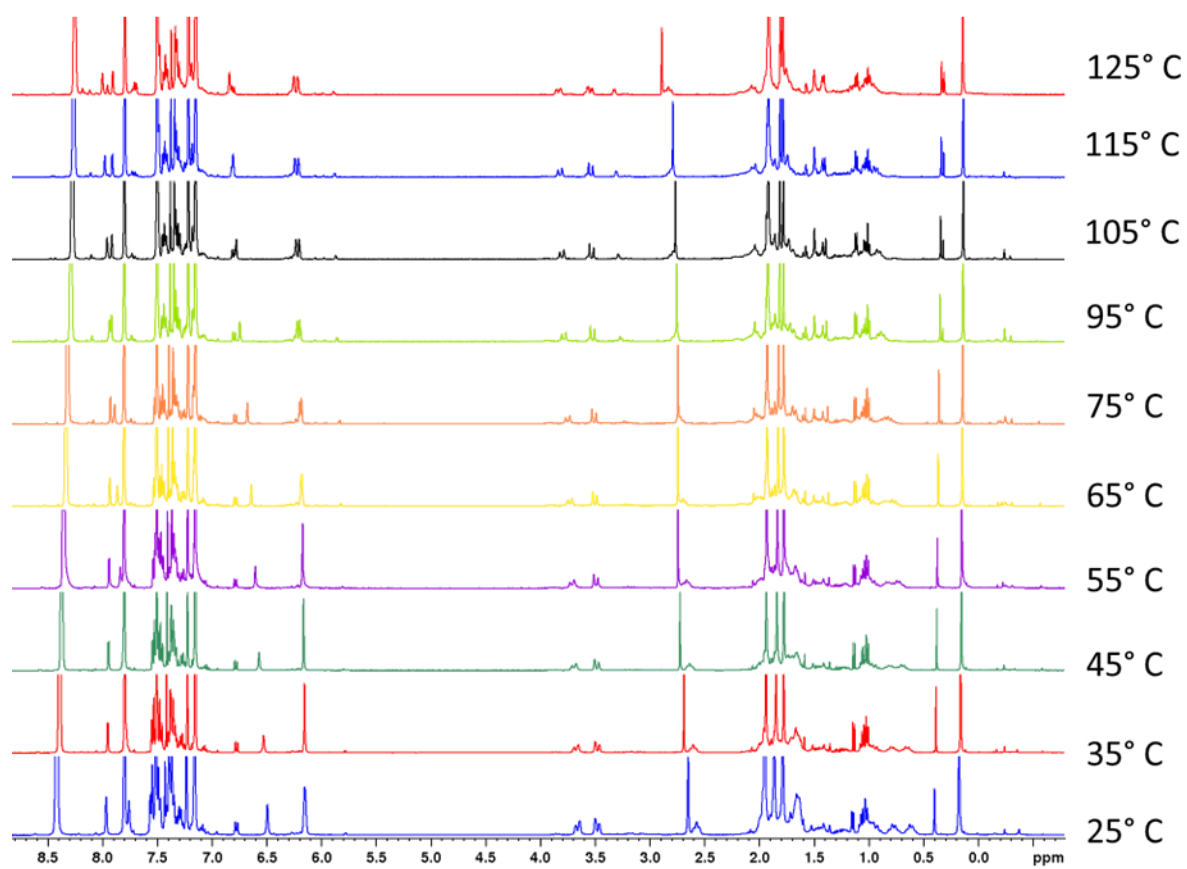


Figure C.51. Reversible Variable Temperature ^1H NMR spectrum of complex **48e** from 25° C to 125° ($\text{C}_6\text{D}_5\text{Br}$, 400 MHz)

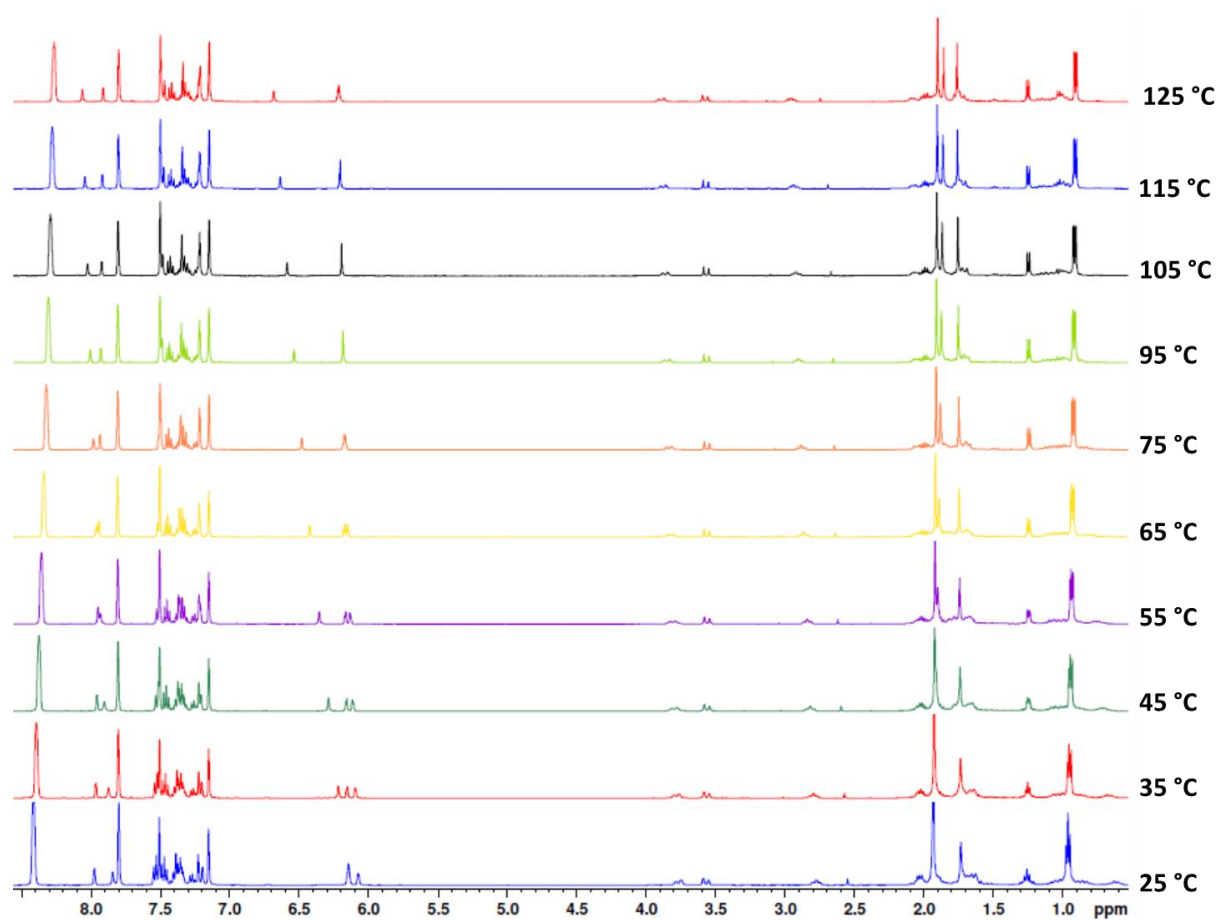


Figure C.52. Reversible variable temperature ^1H NMR spectrum of complex **48b** from 25 °C to 125 °C

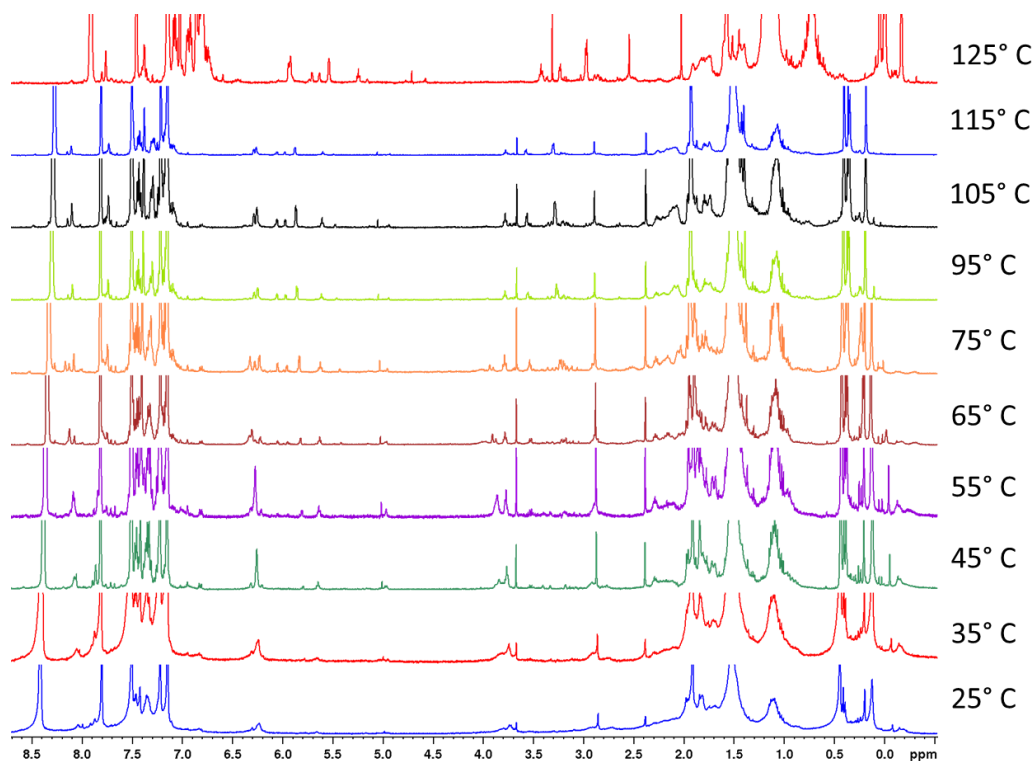


Figure C.53. Variable Temperature ^1H NMR spectrum of complex **48f** from 25 °C to 125 °C. Irreversible decomposition happens above 35 °C ($\text{C}_6\text{D}_5\text{Br}$, 400 MHz)

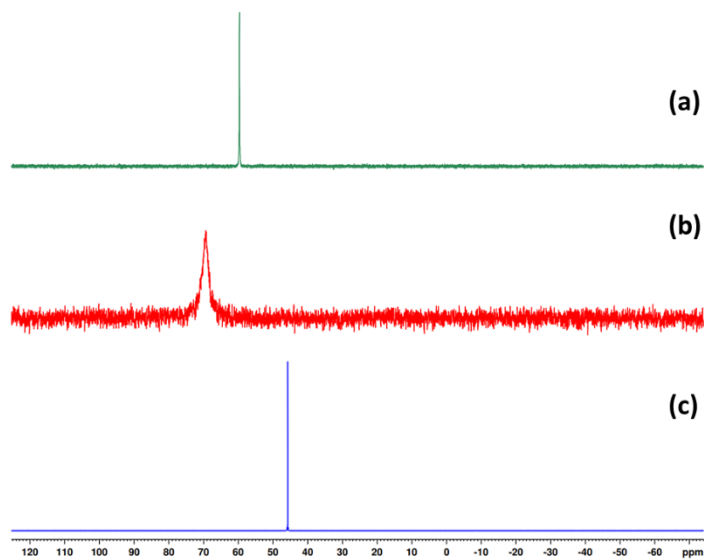


Figure C.54. a) $^{31}\text{P}\{^1\text{H}\}$ NMR spectrum of complex **48b** and 2 equivalents of TEPO, b) $^{31}\text{P}\{^1\text{H}\}$ NMR spectrum of complex **48b** and 1 equivalent of TEPO, c) $^{31}\text{P}\{^1\text{H}\}$ NMR spectrum of free TEPO. (162 MHz, toluene- d_8 , 25 °C).

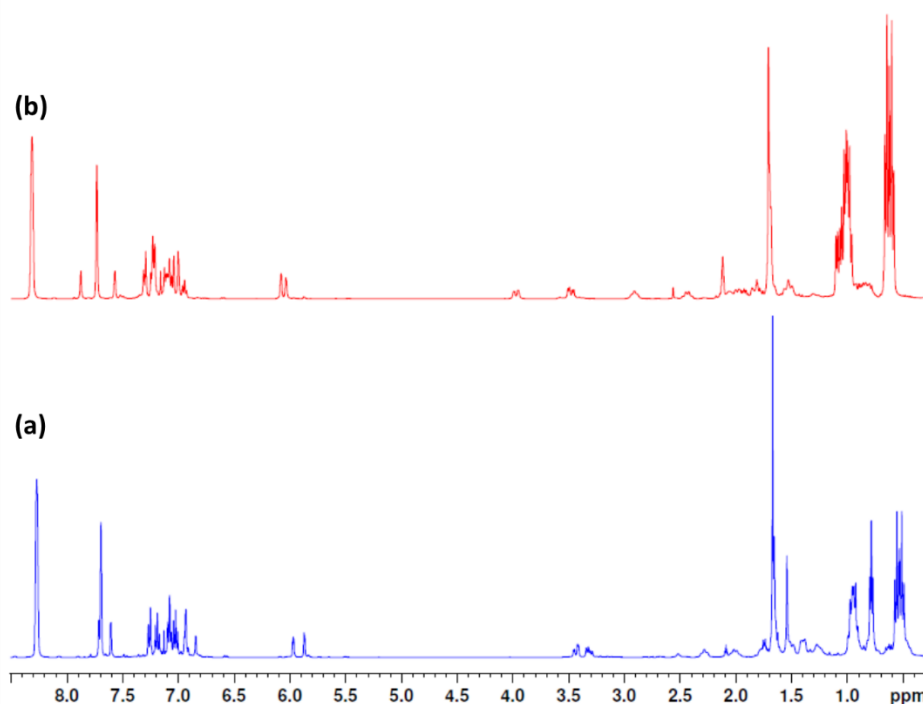


Figure C.55. a) ^1H NMR spectrum of complex **48b** and 1 equivalent of TEPO, b) ^1H NMR spectrum of complex **48b** and 1 equivalent of TEPO. (400 MHz, toluene- d_8 , 25° C)

Reaction order with respect to [48b]

In order to determine the order of reaction with respect to [**48b**], Variable Time Normalization analysis (VTNA) was used.^{145,146} Three reaction profiles were obtained using three different concentrations of **48b** (0.0064, 0.0127, and 0.0191 M) while keeping the concentration of EOE (0.507 M) and ϵ -CL (0.507 M) constant. Integration of the SOE product was determined from the ^1H NMR. By normalizing the time axis by multiplying the time with [**48b**] raised to the correct reaction order, the reaction profiles converge. Four different orders have been plotted (Figure B.56). With 1 as the reaction order with respect to **48b**, the reaction profiles overlap with each other the most.

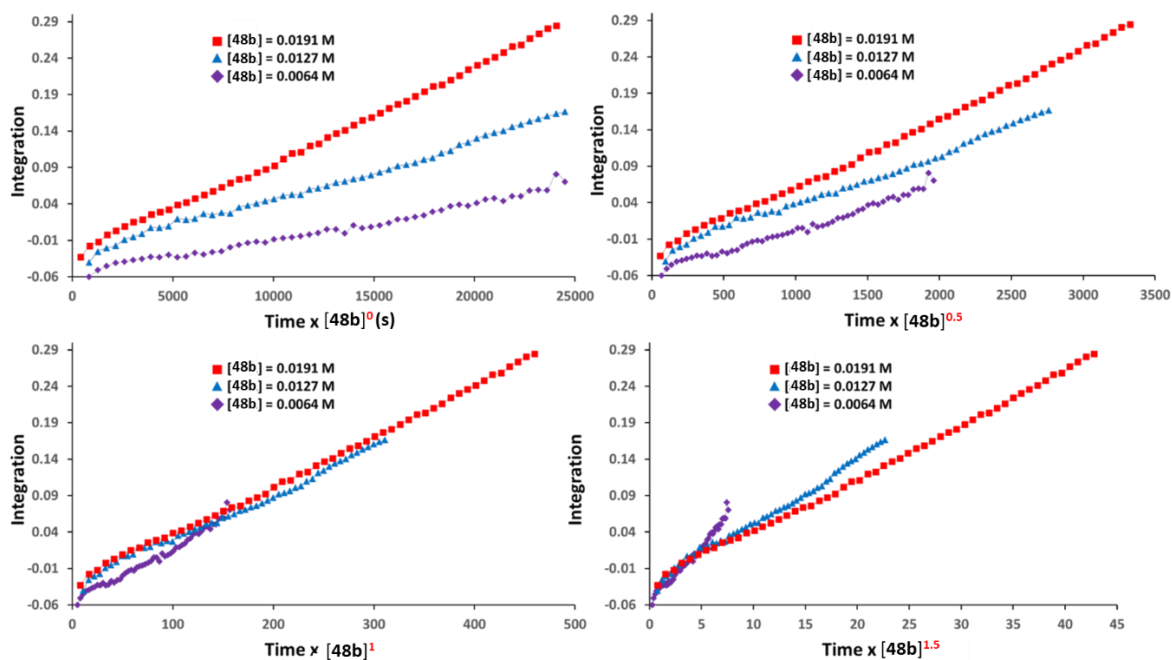


Figure C.56. a) Reaction profile when raised to power zero. b) Reaction profile when raised to power 0.5. c)

Reaction profile when raised to power 1. d) Reaction profile when raised to power 1.5. Reaction conditions:

$$[\text{EOE}] = [\epsilon\text{-CL}] = 0.507 \text{ M}; \text{C}_6\text{D}_6; 60^\circ \text{C}$$

Reaction order with respect to $[\epsilon\text{-CL}]$

In order to determine the order of reaction with respect to $[\epsilon\text{-CL}]$, Variable Time Normalization analysis (VTNA) was used.^{145,146} Three reaction profiles were obtained using three different concentrations of $\epsilon\text{-CL}$ (0.253, 0.507, and 0.760 M) while keeping the concentration of EOE (0.507 M) and **48b** (0.0127 M) constant. Integration of the SOE product was determined from the ^1H NMR. By normalizing the time axis by multiplying the time with $[\epsilon\text{-CL}]$ raised to the correct reaction order, the reaction profiles converge. Four different orders have been plotted (Figure C.57). With zero as the reaction order with respect to $\epsilon\text{-CL}$, the reaction profiles overlap with each other the most.

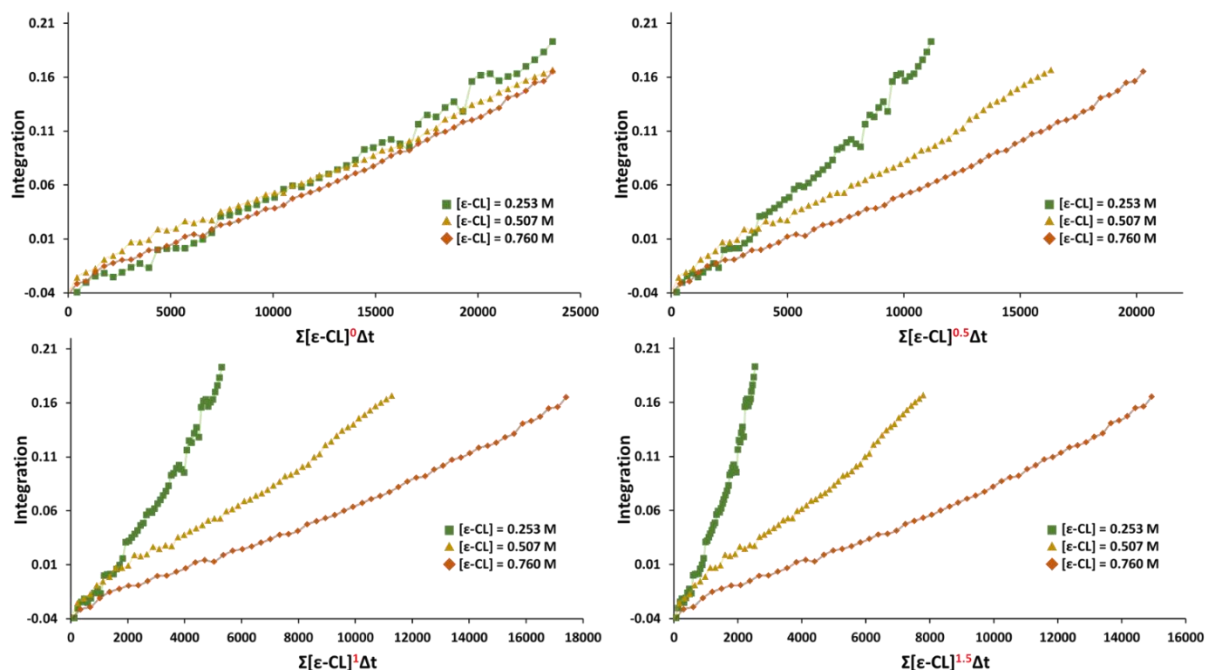


Figure C.57. a) Reaction profile when raised to power zero. b) Reaction profile when raised to power 0.5. c)

Reaction profile when raised to power 1. d) Reaction profile when raised to power 1.5. Reaction conditions:

$$[\text{EOE}]=0.507 \text{ M}, [\mathbf{48b}] = 0.0127 \text{ M}; \text{C}_6\text{D}_6; 60^\circ \text{C}$$

Reaction order with respect to [EOE]

In order to determine the order of reaction with respect to [EOE], Variable Time Normalization analysis (VTNA) was used.^{145,146} Three reaction profiles were obtained using three different concentrations of EOE (0.253, 0.507, 0.760 M) while keeping the concentration of ϵ -CL (0.507 M) and **48b** (0.0127 M) constant. Integration of the SOE product was determined from the ^1H NMR. By normalizing the time axis by multiplying the time with [EOE] raised to the correct reaction order, the reaction profiles converge. Four different orders have been plotted (Figure C.58). With zero as the reaction order with respect to EOE, the reaction profiles overlap with each other the most.

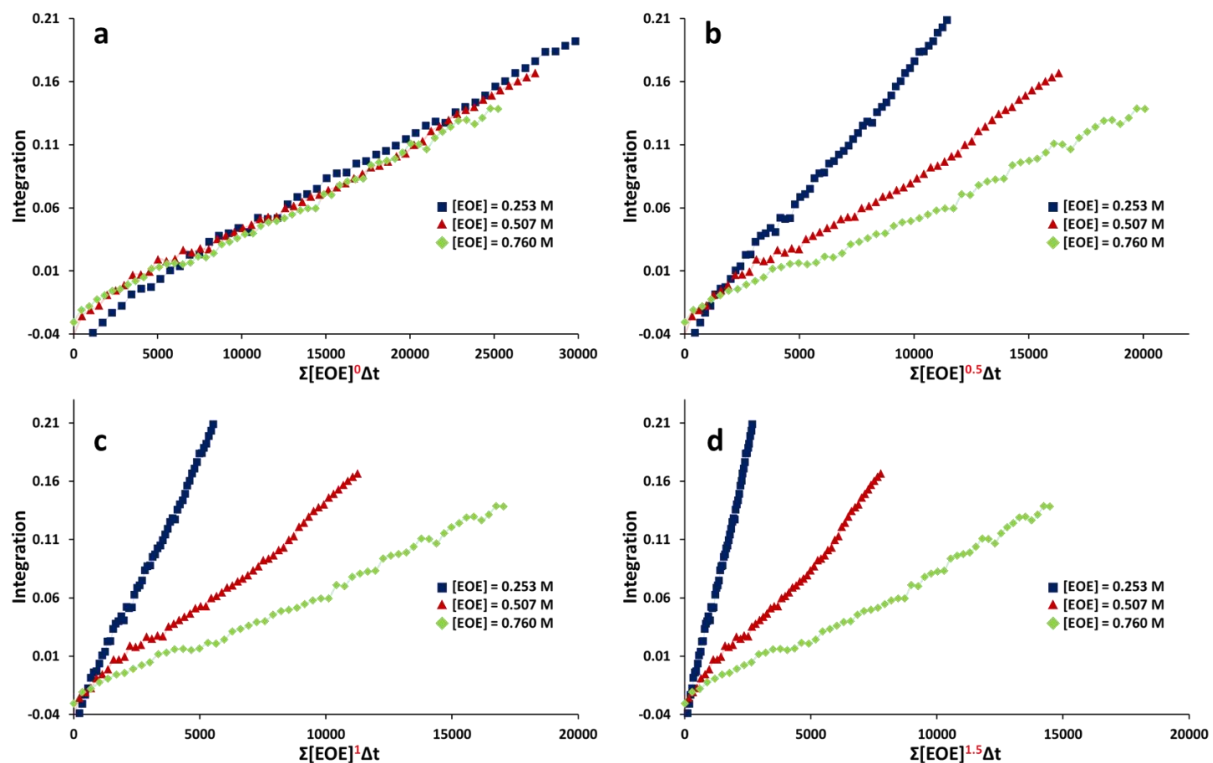


Figure C.58. a) Reaction profile when raised to power zero. b) Reaction profile when raised to power 0.5. c) Reaction profile when raised to power 1. d) Reaction profile when raised to power 1.5. Reaction conditions: $[\epsilon\text{-CL}] = 0.507\text{ M}$, $[\mathbf{48b}] = 0.0127\text{ M}$; C_6D_6 ; 60°C

R =	CH_3	$\text{CH}_2\text{CH}(\text{CH}_3)_2$	$\text{CH}_2\text{Si}(\text{CH}_3)_3$
% Free Volume	15.8	11.3	9.2
% Buried Volume	84.2	88.7	90.8

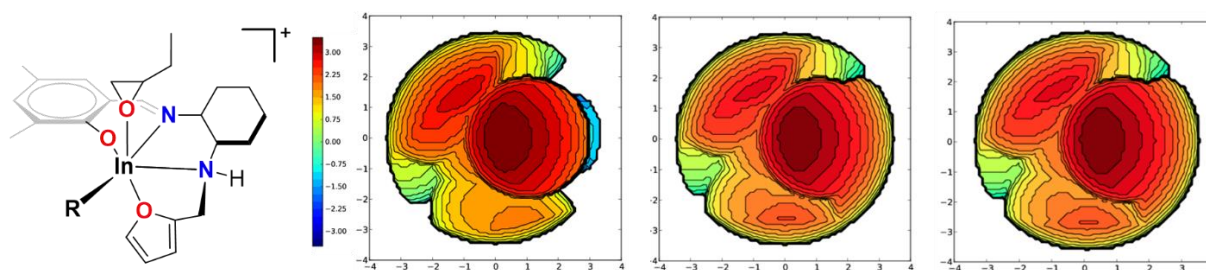


Figure C.59. Buried volume (at a 3.5 \AA radius around the indium center) calculation to determine steric bulk of different alkyl ligands on $\mathbf{48e}$ -epoxide, $\mathbf{48b}$ -epoxide, and $\mathbf{48f}$ -epoxide.

Table C.2. Crystallographic and computational comparison of bond distances and angles of **48b.2THF**

Distances (Å)			
Bond	X-ray Crystallography	DFT	% error*
In-O _(THF1)	2.39229	2.38305	0.386
In-O _(THF2)	2.35365	2.40974	2.38
In-O _(phenoxy)	2.12711	2.04549	3.84
In-N _(amine)	2.46772	2.45516	0.509
In-N _(imine)	2.17899	2.2153	1.66
In-C	2.12847	2.16668	1.80
Angles (°)			
Angle	X-ray Crystallography	DFT	% error*
O _(phenoxy) -In-N _(imine)	84.216	85.275	1.26
N _(imine) -In-N _(amine)	72.866	73.434	0.780
N _(amine) -In-C	90.444	95.458	5.54
C-In-O _(phenoxy)	112.920	106.023	6.11
N _(imine) -In-C	162.362	168.564	3.82
O _(phenoxy) -In-N _(amine)	156.282	158.077	1.149
O _(phenoxy) -In-O _(THF1)	86.067	93.845	9.03
O _(phenoxy) -In-O _(THF2)	85.794	87.046	1.46
N _(imine) -In-O _(THF1)	79.288	80.964	2.11
N _(imine) -In-O _(THF2)	88.949	88.820	0.145
N _(amine) -In-O _(THF1)	95.385	88.025	7.72
N _(amine) -In-O _(THF2)	87.721	87.345	0.429
C-In-O _(THF1)	97.101	96.222	0.905
C-In-O _(THF2)	96.204	93.454	2.86
O _(THF1) -In-O _(THF2)	166.308	169.628	2.00
*(DFT - Crystal /Crystal) x 100			